# Passive Acoustic Monitoring on the Eastern Nova Scotian Shelf Slope and in the Gully Marine Protected Area

N.A. Cochrane and H.B. Moors-Murphy

Department of Fisheries & Oceans
Maritimes Region
Ocean and Ecosystem Sciences Division
Bedford Institute of Oceanography
PO Box 1006
Dartmouth, NS
B2Y 4A2

2017

**Canadian Technical Report of Fisheries and Aquatic Sciences 3236**

Fisheries and Oceans Canada | Pêches et Océans Canada

Canada

**Canadian Technical Report of Fisheries and Aquatic Sciences**

Technical reports contain scientific and technical information that contributes to existing knowledge but which is not normally appropriate for primary literature. Technical reports are directed primarily toward a worldwide audience and have an international distribution. No restriction is placed on subject matter and the series reflects the broad interests and policies of Fisheries and Oceans Canada, namely, fisheries and aquatic sciences.

Technical reports may be cited as full publications. The correct citation appears above the abstract of each report. Each report is abstracted in the data base *Aquatic Sciences and Fisheries Abstracts*.

Technical reports are produced regionally but are numbered nationally. Requests for individual reports will be filled by the issuing establishment listed on the front cover and title page.

Numbers 1-456 in this series were issued as Technical Reports of the Fisheries Research Board of Canada. Numbers 457-714 were issued as Department of the Environment, Fisheries and Marine Service, Research and Development Directorate Technical Reports. Numbers 715-924 were issued as Department of Fisheries and Environment, Fisheries and Marine Service Technical Reports. The current series name was changed with report number 925.

**Rapport technique canadien des sciences halieutiques et aquatiques**

Les rapports techniques contiennent des renseignements scientifiques et techniques qui constituent une contribution aux connaissances actuelles, mais qui ne sont pas normalement appropriés pour la publication dans un journal scientifique. Les rapports techniques sont destinés essentiellement à un public international et ils sont distribués à cet échelon. II n'y a aucune restriction quant au sujet; de fait, la série reflète la vaste gamme des intérêts et des politiques de Pêches et Océans Canada, c'est-à-dire les sciences halieutiques et aquatiques.

Les rapports techniques peuvent être cités comme des publications à part entière. Le titre exact figure au-dessus du résumé de chaque rapport. Les rapports techniques sont résumés dans la base de données *Résumés des sciences aquatiques et halieutiques*.

Les rapports techniques sont produits à l'échelon régional, mais numérotés à l'échelon national. Les demandes de rapports seront satisfaites par l'établissement auteur dont le nom figure sur la couverture et la page du titre.

Les numéros 1 à 456 de cette série ont été publiés à titre de Rapports techniques de l'Office des recherches sur les pêcheries du Canada. Les numéros 457 à 714 sont parus à titre de Rapports techniques de la Direction générale de la recherche et du développement, Service des pêches et de la mer, ministère de l'Environnement. Les numéros 715 à 924 ont été publiés à titre de Rapports techniques du Service des pêches et de la mer, ministère des Pêches et de l'Environnement. Le nom actuel de la série a été établi lors de la parution du numéro 925.

Canadian Technical Report of
Fisheries and Aquatic Sciences 3236

2017

# PASSIVE ACOUSTIC MONITORING ON THE EASTERN NOVA SCOTIAN SHELF SLOPE AND IN THE GULLY MARINE PROTECTED AREA

by

N.A. Cochrane and H.B. Moors-Murphy

Department of Fisheries & Oceans
Maritimes Region
Ocean and Ecosystem Sciences Division
Bedford Institute of Oceanography
PO Box 1006
Dartmouth, NS
B2Y 4A2

Cat. No. Fs97-6/3236E-PDF ISBN 978-0-660-23609-4 ISSN 1488-5379

Correct citation for this publication:

Cochrane, N.A. and Moors-Murphy, H.B. 2017. Passive acoustic monitoring on the eastern Nova Scotian Shelf Slope and in the Gully Marine Protected Area. Can. Tech Rep. Fish. Aquat. Sci. 3236: xii + 306 p.

## TABLE OF CONTENTS

## LIST OF FIGURES

## ABSTRACT

Cochrane, N.A. and Moors-Murphy, H.B. 2016. Passive acoustic monitoring on the eastern Nova Scotian Shelf Slope and in the Gully Marine Protected Area. Can. Tech Rep. Fish. Aquat. Sci. 3236: xii + 306 p.

Time and spectral domain characteristics of ocean acoustic noise ≤ 8 kHz monitored at three eastern Scotian Shelf /Slope deep water sites are examined. Important spectral features included winter ~20 Hz fin whale vocalizations and 30 to 200 Hz enhancements from vessel-radiated noise (companion report). Early Gully MPA canyon recordings were strongly contaminated by pseudo-noise from strong near-bottom $O_1$ and $K_1$ period tidal currents, the problem effectively mitigated in later deployments. Longer deployments appeared affected by instrumental sensitivity drifts, probably from water ingress into over-pressured hydrophone electronics. Noise spectral amplitudes above several hundred hertz were dominantly wind-related, confirmed by detailed regressions between ~ 5 kHz noise levels and Sable Island winds. Select long duration spectral levels are compared to published measures off Cape Hatteras and off California. Recommendations regarding future noise monitoring programs are made.

## RÉSUMÉ

Cochrane, N.A. and Moors-Murphy, H.B. 2016. La surveillance acoustique passive de la partie est du plateau/talus néo-écossais et dans la zone de protection marine du Gully. Rapp. tech. can. sci. halieut. aquat. 3236: xii + 306 p.

Les caractéristiques temporelles et du domaine spectral des bruits sous-marins d'une fréquence inférieure ou égale à 8 kHz observés à trois sites en eaux profondes de la partie est du plateau/talus néo-écossais sont examinées. D'importantes caractéristiques spectrales comprennent des vocalisations de rorqual commun se situant à environ 20 Hz en hiver et des exaltations de 30 à 200 Hz du bruit rayonné des navires (rapport complémentaire). Les premiers enregistrements du canyon de la ZPM du Gully sont fortement contaminés par le pseudo-bruit des forts courants de marée des périodes $K_1$ et $O_1$, près du fond, et le problème a été efficacement atténué au cours des déploiements ultérieurs. Les déploiements plus longs semblent avoir été touchés par une dérive en sensibilité des instruments, probablement à cause d'infiltration d'eau dans les composants électroniques de l'hydrophone soumis à un surcroît de pression. Des amplitudes spectrales au-delà de plusieurs centaines de hertz étaient principalement reliées au vent, ce qui est confirmé par des régressions détaillées entre des niveaux de bruit d'environ 5 kHz et les vents de l'île de Sable. Des niveaux spectraux de longue durée déterminés sont comparés aux mesures prises au large du cap Hatteras et au large de la Californie (mesures publiées). Des recommandations sont à l'heure actuelle formulées en ce qui concerne les futurs programmes de surveillance du bruit.

# 1. INTRODUCTION

This report examines the properties of passive acoustic data collected using JASCO Applied Sciences **A**utonomous **M**ultichannel **A**coustic **R**ecorders (AMARs) at three deep water sites on the slope of the Nova Scotian Shelf extending, with short breaks, over a two-year period from mid October 2012 to late September 2014. One site was located in the large, ecologically and biologically diverse submarine canyon known as "The Gully", itself situated within the wider Gully Marine Protected Area (MPA). The two remaining sites were located to the east of the MPA, between the Gully and Shortland Canyon and between Shortland and Haldimand Canyons respectively. We examine both the time and the spectral domain properties of the resultant datasets.

First presented are methods, then an overview of the main characteristics of the AMAR datasets, followed by more detailed analysis of important features. The analysis includes a comparison of several more reliable spectral noise averages with analogous measures elsewhere. Since continuous learning is vital to refining technique, limitations of these datasets such as mooring generated pseudo-noise, possible non-stationary instrumental noise, and apparent instrumental sensitivity drifts during extended deployments are examined. Finally, recommendations are made in regard to future extensions of the Scotian Shelf/Slope acoustic monitoring efforts.

In regard to organization, this report contains several appendices that treat specialized topics and systematically present the computed spectral data. Appendix 1 describes detailed AMAR instrumental frequency response characteristics, Appendix 2 examines the evidence for systematic system sensitivity drifts, Appendix 3 examines the influence of local winds in determining high frequency spectral levels, while Appendix 4 contains the extensive collection of spectral plots in multiple formats.

One analytical effort addressed local vessel noise. This topic was considered too extensive and specialized for inclusion here and has been prepared as a parallel companion report (Cochrane and Moors-Murphy 2017).

All dates and times are reported in UTC.

# 2. METHODS

## 2.1. ACOUSTIC RECORDINGS

### *2.1.1. Recording Sites*

The passive acoustic data analysed in this report were recorded at three geographically well-separated mooring sites or stations on the eastern Scotian Slope, all in water depths of the order of 1500 m. The three mooring stations (Fig. 1) were designated "MidGul"

(site in the Gully), "GulSho", (site halfway between the Gully and Shortland canyon), and "ShoHald" (site halfway between the Shortland and Haldimand canyons). The three sites were occupied repetitively over four successive deployments spanning mid October 2012 to late September 2014 with modest (27 - 52 day) inter-deployment time gaps. The four successive deployment periods were designated "Winter 2012-13", "Summer 2013", "Winter 2013-14", and "Summer 2014" (deployments capitalized in text). Station and deployment particulars appear in Table 1.

### *2.1.2. Instrumentation*

At each station, acoustic data were internally recorded by a single AMAR suspended about 60 m above the ocean floor on a submerged mooring (Figs. 2 and 3). Each AMAR was equipped with a single omnidirectional, wide-band hydrophone mounted above and proximate to (within ~1 m) the instrument pressure case. Geospectrum M8E-51 hydrophones were used for the first year of data collection (Winter 2012-13 and Summer 2013 deployments), while Geospectrum M8Q-51 hydrophones were used for the second year (Winter 2013-14 and Summer 2014 deployments). The complete AMAR mooring assemblies including railroad wheel anchors were free-dropped from the surface. At the end of the recording period, moorings were recovered, minus the anchors, by use of a Benthos acoustic release. The mooring sites were characterized by substantial short range bathymetric variation resulting in deployment depth uncertainties of about ± 100 m based on vessel echosoundings at drop time. For the Winter 2012-13 and Summer 2014 deployments (only), the near-bottom Benthos releases were acoustically ranged providing, presumably, more accurate depths and positions (Table 1). The Summer 2014 moorings were also equipped with MicroCAT temperature/pressure recorders mounted just below the AMARs, again, to furnish more refined depths.

### *2.1.3. Recorded Data Sequencing and Format*

The AMARs recorded acoustic data on a duty cycle that alternated between low and high frequency sampling reflected in the respective digitization rates. For the low frequency (LF) data collection, during Winter 2012-13 and Summer 2013 one individual data series was extracted every 900 s (15 min). This series consisting of 780 s (13 min) of data sampled continuously at a 16 kHz rate. During Winter 2013-14 and Summer 2014 one series was extracted every 1200 s (20 min) consisting of 1070 s (~18 min) of continuous 16 kHz sampling. Within the remaining 120 or 130 s inter-series sampling gaps, the data collection switched to high frequency (HF) sampling either at a 125 kHz (Winter 2012-13 and Summer 2013) or 375 kHz (Winter 2013-14 and Summer 2014) rate. The high frequency (HF) data collection facilitated parallel marine mammal vocalization studies not presented in the current report. This initial report mainly considers physical acoustic data characteristics and limits itself to the LF AMAR data digitized at 16 kHz to 24-bit resolution.

Data files, one new low frequency and one high frequency file initiating every 15 or 20 min depending on the deployment, were off-loaded from the AMAR by JASCO Applied Sciences and delivered to DFO in standard single channel (monaural) WAVE (.wav) file

format, with separate file collections for the low and high frequency sampling. File start times, in UTC, to one second precision were encoded into the data file names. Start time accuracies were limited by the drifts of the AMAR internal clocks, which may accumulate systematic offsets up to several minutes from true time over a 5 – 6 month deployment. Clock drift is important if AMAR times must be related to an external time base, such as when correlating recorded acoustic levels with AIS determined vessel positions (e.g. Cochrane and Moors-Murphy 2017). Clock drift also presents a challenge if multiple AMAR time bases must be related to determine the direction of sound arrival from marine mammal vocalizations, explosions, earthquakes, etc.

### *2.1.4. AMAR Frequency Response Characteristics*

Ocean sounds of interest encompass a wide range of acoustic frequencies. Each AMAR instrument with hydrophone is characterized by an amplitude frequency response measured and supplied by the manufacturer (JASCO Applied Sciences) in tabular form (see Appendix 1). In addition, the absolute acoustic calibration of each AMAR system with hydrophone was measured at a reference frequency of 250 Hz, a frequency at which the instruments are entering the level portion of their mid-band responses.

Power spectral amplitudes presented in this report were quantitatively corrected for recording system calibrations and frequency responses, the latter using empirical mathematical approximations to the tabulated responses. Corrections were also applied for the recording system DC offset. While offsets drift slightly over a deployment, use of a mean offset is sufficient for practical purposes.

Strong evidence will be presented that at least some AMARs displayed slow downward drifts in instrumental sensitivity over the course of extended deployments (see Appendices 2 and 3), an effect acknowledged by the manufacturer. The origin of these apparent sensitivity drifts remains speculative but was most likely related to slow water ingress into the hydrophones or the hydrophone electronics due to deployment hydrostatic pressures exceeding the tested limits of the hydrophone assemblies. AMAR system noise levels also increased during the later stages of some long deployments. The noise character was again suggestive of water infiltration into the hydrophones or electronics, although it is not known with certainty if the sensitivity drifts and the changing instrumental noise levels shared a common cause. Because confident quantification of the sensitivity drifts was not possible, and because of the increased noise characterizing the later stages of some deployments, data for the most critical analyses were chosen from earlier portions of specific deployments.

## 2.2. DATA PROCESSING

### *2.2.1. Time Domain Characterization*

The total time series obtained from each individual AMAR for each deployment were extracted and carefully inspected as the initial analytical step. The methodology followed that employed by Cochrane (2007) for the inspection of passive acoustic data collected

during the 2003 Marathon Canada Ltd. 3-D Scotian Slope seismic survey (Lee and Hurley 2005). Time series were first corrected for their long-term arithmetic means (means subtracted) then converted to a calibrated floating point internal format in units of μPa by multiplication by the AMAR-specific **mid-band** calibration factor (μPa/digitizing interval). Time domain data were then plotted in the form of successive 300 s interval estimates of: 1) the maximum instantaneous 0 – peak acoustic amplitude; 2) the root mean square (RMS) acoustic amplitude averaged over the entire interval; 3) the maximum RMS amplitude computed over consecutive 1 s sub-intervals within the interval; and, 4) the minimum RMS amplitude computed over similar 1 s sub-intervals. Amplitudes were plotted in units of dB re 1 μPa (i.e. 20 log amplitude in μPa), vs. decimal day of year (DOY). DOY 0.0 marks the start of Jan. 1$^{st}$ of the relevant year while DOY 1.0 is the end of Jan. 1$^{st}$ etc., continuing to the end of the deployment and resetting to 0.0 if a new calendar year begins during the deployment.

Additional information is furnished by the Probability Density Functions (PDFs) of the simple time domain signal descriptors above for all three stations (Figs. 13 – 18). Plot-specific analysed time periods were adjusted to be identical for each station. Corrupted data encountered at any station resulted in removal of the corresponding time period at the two remaining stations (a minor consideration). Plot Y-axes indicate the probability of specific acoustic quantities lying within a 1 dB bin centered on corresponding X-axes acoustic levels. Probabilities were normalized such that the area under each plotted curve is unity.

### *2.2.2. Spectral Domain Characterization*

Power spectral analysis with its many derivative applications usually constitutes the most fundamental and meaningful form of time series analyses. The spectral analysis technique employed for the AMAR datasets was an adaptation of the averaged periodogram method of Welch (1967). It consisted of sub-sampling the original recorded, discontinuous (arising from alternation between LF and HF sampling) digital time series in **locally** consecutive, non-overlapping time sub-series of $2^n$ points duration. Our sampling of the original time series in analyses was normally quite sparse; a trade-off between analysis time and estimate stability. Typically only 10 or 20 consecutive and contiguous (i.e. non-overlapping) subseries of 8192 to 32768 pts length were analysed from the start of each individual data file. For each spectral estimate time domain sub-series, properly scaled to μPa, the linear trend was first removed followed by the resultant sub-series mean. A time domain Hanning window function was then applied. The sub-series complex Fourier transform was computed, squared, and summed over corresponding positive (+ve) and negative (–ve) frequencies (or doubled for +ve frequencies only), followed by corrections to remove the average effect of the Hanning window application. This resulted in the production of a raw sub-series spectral estimate or sub-estimate (sometimes denoted a "periodogram" in reference to a single sub-series). Individual sub-series spectral estimates distributed systematically over the total length of the specified spectral analysis time period were arithmetically averaged to produce the final power spectral estimate. No spectral prewhitening was applied to the original time series even though ocean acoustic power spectra tend to be quite red.

For consistency with Parseval's theorem, power spectral amplitudes extracted using this methodology were scaled to be variance conserving, that is, the frequency integral of the power spectral density expressed in **linear** units of $\mu Pa^2/Hz$ over the entire +ve range of frequencies should equal the variance of the analysed time series. This was numerically verified, agreement to within several percent normally being obtained. The limiting factors were probably the interaction of the spectral pre-conditioning (Hanning window and linear trend removal) with various non-random characteristics of the underlying time series.

All quantitative spectral responses reproduced in this report were additionally corrected for the known amplitude-frequency responses of the AMAR recording systems. In instances where the statistical properties of the spectral sub-estimates were themselves examined (as below), the frequency response corrections were applied to the spectral sub-estimates prior to arithmetic averaging. It should be noted that after instrumental frequency response corrections, the resultant spectra are variance conserving in regard to a hypothetical acoustic time series measured without alteration by the (measurement) instrument response. This underlying time series is usually unknown for geophysical field data but constitutes the entity whose properties we wish to examine. For our analyses the AMAR system phase responses were immaterial since cross-spectral estimation was not employed.

The statistical properties of the spectral sub-estimates, themselves arithmetically averaged to derive total time series power spectral amplitudes, were examined following the general methods of Merchant et al. (2013). Spectral sub-estimate properties were computed and graphically displayed in the frequency domain. These included the sub-estimate arithmetic mean (i.e. standard power spectral amplitude) and a measure of its variance, as well as the sub- estimate PDF mode, median, and cumulative amplitude distribution function. Subtle changes in sub-estimate PDF character over frequency or time can often reveal distinct, contrasting physical processes or provide information about instrumental limitations or malfunctions not evident from inspection of the power spectrum in isolation.

Three basic forms of spectral analysis and display were performed on our entire acoustic database:

1) High resolution spectrograms:

- Sub-series length – 32768 pts at 16 kHz sampling rate (2.048 s duration), for a basic spectral resolution of 0.4882 Hz not including spectral window effects.
- Total time series length – one calendar month, start and finish coinciding with actual calendar month. Equipment deployment or recovery within a specific month or equipment malfunctions occasionally forced total analysis durations of less than a month.
- Sparse sampling – 20 x 32768 pt. consecutive, non-overlapping sub-series selected from each successive data file. Considering acquisition data file sequencing, 40.96 s of time-continuous data were analysed every 15 min for the Winter 2012-13 and

Summer 2013 deployments and every 20 min for the Winter 2013-14 and Summer 2014 deployments. Spectral sub-estimates generated from each 32768 pt sub-series were averaged without hierarchy over the entire one month calendar period when possible.

- Plotted were sound pressure spectral amplitudes (decibel form) vs. frequency (log scale) extending from about 2 Hz to the 8 kHz Nyquist (blue curves). Also plotted were indicators of the spectral sub-estimate variance (about their arithmetic means) in the form of a 2nd set of curves (black) drawn 1 S.D. (i.e. $\sqrt{Sub-estimate\ \ Variance}$ ) above the power spectral amplitude curves.

2) Medium resolution spectrograms with statistics:

- Sub-series length – 8192 pts @ 16 kHz sampling rate (0.512 s duration), for a basic spectral resolution of 1.953 Hz not including spectral window effects.
- Total time series length – one calendar month, start and finish coinciding with actual calendar month. Deployment and recoveries, or malfunctions sometimes forced total analysis durations of less than a month.
- Sparse sampling – 20 x 8192 pt. consecutive, non-overlapping sub-series selected from each successive data file. Considering acquisition data file sequencing, 10.24 s of time-continuous data were analysed every 15 min for the Winter 2012-13 and Summer 2013 deployments while 10.24 s of data were analysed every 20 min for the Winter 2013-14 and Summer 2014 deployments. Spectral estimates generated from each 8192 pt sub-series were averaged without hierarchy over the entire one month period when possible.
- More information was plotted than with the high resolution spectral estimates. Plotted, were overall power spectral densities (i.e. arithmetic average of sub-series estimates) from 10 Hz to the 8 kHz Nyquist as white curves on coloured backgrounds. The solid colour backgrounds constitute a colour encoded representation of the frequency specific PDF amplitude of all spectral sub-estimates over the entire analysed recoding period. Normalized PDFs were computed for incremental 0.1 dB width bins in the spectral amplitude domain.[1] The trend of the PDF mode (i.e. the PDF peak amplitude or most probable sub-estimate amplitude) can be traced in the amplitude vs. frequency domain by discerning the right-most spectral key colour appearing at any given acoustic frequency. Also, five (5) black overlay curves trace the PDF cumulative percentile distributions. Individual curves from bottom to top represent sub-estimate 1, 5, 50, 95, and 99 percentile lines respectively. The central curve is the PDF median, i.e. the 50% curve; half of the spectral sub-estimate amplitudes falling on either side of this line.

[1] The normalization employed for the colour-encoded data ensured that the probabilities of given frequency spectral estimates falling within specific contiguous 0.1 dB incremental spectral amplitude bins when summed over all possible amplitude bins yields unity. Consequently, if one uses these probabilities to define a PDF function continuous in the spectral amplitude domain, the integral of the same PDF over the total amplitude domain will be 0.1. The reader may find it more natural to multiply the charted PDF's by factor of 10 to define a more conventional probability per 1 dB amplitude increment thereby yielding a probability integral of unity.

3) One-third (1/3) octave averaged spectral sections, the objective being the production of long duration frequency vs. time graphical sections with colour encoded spectral amplitudes:
   - Sub-series length for underlying spectral estimates prior to 1/3 octave frequency averaging - 32768 pts @ 16 kHz sampling rate (2.048 s duration), for a basic spectral resolution of 0.4882 Hz not including spectral window effects.
   - Total time series length – 10 consecutive sub-series drawn from the beginning of each recorded file and further averaged over the required number of successive data files to produce either hourly or daily power spectral estimates. Since the Winter 2012-13 and Summer 2013 deployments generated data files at 15 min intervals while the Winter 2013-14 and Summer 2014 deployments generated files at 20 min intervals, hourly 1/3 octave power spectral estimates produced from the first two deployments averaged over a total of 2.048 s x 10 x 4 = 81.92 s of data while hourly spectral estimates from the latter two deployments averaged over 2.048 s x 10 x 3 = 61.44 s of data.
   - Plotted as spectral amplitude colour sections were the high resolution spectral estimates (above bullet) averaged in 1/3 octave width bins. The first frequency bin was arbitrarily centered on 5 Hz and each successively higher bin centered at the central frequency of the preceding bin x $2^{1/3}$. Each bin encompassed high resolution spectral estimates lying within a multiplicative factor of $2^{-1/6}$ below to $2^{1/6}$ above the respective bin central frequency. The methodology ensured that bin centers and boundaries were equally spaced in the logarithmic frequency domain. It should be emphasized that high resolution spectral estimates falling within any one bin were **arithmetically averaged, not summed,** so that the resultant bin spectral levels continued to be referenced to a 1 Hz bandwidth. It should also be noted that under this methodology there exists a slight ~0.7% mismatch between the arithmetic and geometric bin central frequencies which can be ignored for all practical purposes.

# 3. RESULTS AND DISCUSSION

## 3.1. INTRODUCTION

### *3.1.1. Time Domain Plots*

When the four time domain descriptors (maximum instantaneous 0 – peak acoustic amplitude, average RMS acoustic amplitude, maximum RMS amplitude and minimum RMS amplitude) were overlaid and viewed at relatively high time resolution, instrument malfunctions such as increases in instrumental noise levels were readily spotted, as well as specific physical acoustic events and phenomena such tidal periodicities in acoustic levels and proximate ship passages. When viewed in suitably time compressed formats so as to encompass entire deployments, these plots also provided valuable hints of long-term drifts in instrument sensitivities or systematically changing instrumental or ambient noise levels, effects which can be later explored and quantified using specialized analyses.

As an example, Figs. 4 - 6 display sample 10-day (start of 26 Nov to end of 5 Dec 2012) time domain amplitude statistics for each of the three stations extracted from the Winter 2012-13 deployment. Figure 4 is for the MidGul station where tidal flow induced acoustic noise was exceptionally high, while Figs. 5 and 6 show GulSho and ShoHald stations, respectively, where analogous tidal flow induced noise levels appeared much lower or absent. Similar plots time-compressed to include the entire Winter 2012-13 deployment period are shown for the same three stations in Figs. 7 - 12. Time domain stats for the remaining three post-Winter 2012-13 deployments were of superficially similar appearance and are not reproduced in this report. Recourse was made to analogous time domain statistical descriptors in the preliminary stages of the analysis of individual ship passages (Cochrane and Moors-Murphy 2017).

Figs. 13 - 18 show multiple station PDF plots for the same statistical descriptors over successive deployment periods. For display, the two long winter deployments are divided into separate pre- and post- Jan 1$^{st}$ time intervals. It is observed that most PDF plots, as plotted linear in decibels, display a slightly asymmetric Gaussian type appearance often with low amplitude tails extending toward higher acoustic levels. These plots differ in only minor ways between stations. The notable exception is MidGul station for both the Winter 2012-13 and Summer 2013 deployments (only) where the PDF tails are much more pronounced and in some cases display a 2$^{nd}$ peak i.e. resulting in a bimodal PDF distribution. The exceptions often give the appearance of, or are at least compatible with, a multi-state system; a certain range of times are characterized by a more ordinary distribution of acoustic levels while other times are characterized by much higher observed levels.

Note that the time domain signal descriptors and their PDFs pertain not to the ambient acoustic environments sampled by the AMAR systems but rather to the acoustic signals **actually recorded** by these systems. The two entities differ because of the characteristic LF and HF response roll-offs of the measurement systems, namely, 20 dB/decade (6 dB/octave) LF roll-offs with low end -3 dB points at ~20 Hz and modest HF roll-offs above ~5 kHz (Appendix 1). In other words, the time domain acoustic measures, as presented, convey information about the temporal-statistical character of the ambient acoustic environments, but only within the band-limited context imposed by the AMAR instrumental frequency responses. In contrast, the power spectral plots to follow are corrected for the instrumental frequency response making them more directly representative of ambient conditions.

### *3.1.2. Spectral Domain Plots*

The high resolution spectra are presented in Appendix 4 figure series A4-1. The medium resolution spectra with indicators of the principal statistical properties of spectral sub-estimates are reproduced in Appendix 4 figure series A4-2. Within each of these figure series, plots for the three stations are ordered geographic west to east (MidGul, GulSho, then ShoHald), and the sequence repeated for successive deployments. For each of the high and medium resolution spectrograms produced, figure designations start with the

basic figure sequence number (e.g. A4-1), followed by a dash, station, dash, year, dash, and finally the three-letter month abbreviation (with months presented in chronological order from deployment). The 1/3 octave averaged spectral sections appear in Appendix 4 figure series A4-3. Figure numbering is conventional for station, followed by a dash and the deployment designation, namely: "W2012", "S2013", "W2013", and "S2014" for the four AMAR deployments in chronological sequence. For winter deployments the spectral section was divided into pre- ("-1") and post-Jan 1$^{st}$ ("-2") segments. Summer deployment spectral sections appear as single continuous plots without suffix designations.

## 3.2. PRINCIPAL DATA CHARACTERISTICS

### *3.2.1. General*

The principal qualitative characteristics of the underlying acoustic time series are well illustrated in the 1/3 octave averaged spectral sections (Fig. series A4-3). Consider the typical section of Fig. A4-3-GulSho-W2013-1 initiating on 16 Nov. 2013 inclusive and extending to the end of calendar year 2013. Immediately evident is the markedly red nature of the power spectra, i.e. spectral power as scaled in fixed bandwidth units (1 Hz) *generally* falls off rapidly on proceeding from low to high acoustic frequencies. However, such spectral fall-offs constitute a far from a regular fixed process as is detailed in the immediately following sub-sections and also in section 3.3.7.

### *3.2.2. Fin Whale Line*

Prominent is a strong line at about 20 Hz that extends across the entire displayed temporal section with only modest short-term variation but fading slightly in amplitude near the end of the calendar year (Fig. A4-3-GulSho-W2013-1). This well-known spectral feature characterizing virtually all fall and winter acoustic recordings from the Northwest Atlantic region arises from fin whale vocalizations (Watkins et al. 1987, Delarue 2008). Fin whale vocalizations are examined more closely in section 3.3.2 below, not from a biological perspective but because their vocalization signatures play such a dominant seasonal role in shaping the overall low frequency ocean noise spectrum.

### *3.2.3. Long Period Fluctuations in Spectral Levels*

Continuing our examination of Fig. A4-3-GulSho-W2013-1, in the frequency range >200 Hz one observes a series of irregular, long period (2–4 day) temporal fluctuations in spectral level. With the employed frequency domain smoothing, little detailed structure is apparent between 200 Hz to the 8 kHz Nyquist apart from a general fall-off of levels with increasing frequency. Short duration spectral sections at much higher frequency and time resolutions often reveal a variety of transitory marine mammal calls within this frequency range. Standard ocean acoustics texts (e.g. Clay and Medwin 1977) indicate that most ocean noise in this frequency range originates from near-surface bubbles produced by wind driven ocean–atmosphere interaction processes. Cursory examination of simultaneous spectral sections from MidGul and ShoHald (Figs. A4-3-MidGul-

W2013-1 and A4-3-ShoHald-W2013-1) reveals similar long period spectral fluctuations that appear highly correlated in both time and level with those observed at GulSho. Therefore, it seems reasonable to ascribe the slowly varying high frequency acoustic levels mainly to systematic fluctuations in regional wind fields. Below 200 Hz apparent wind correlated spectral features, while still discernable, become increasing mixed with noise from alternative sources having differing temporal dependencies. Some apparent wind correlated signals persisting below 200 Hz may arise more from storm-related interacting wave fields, and even storm induced ocean turbulence (wind correlated but mediated through less direct mechanisms). The higher frequency wind origin acoustic noise is examined in detail in Appendix 3.

### *3.2.4. Shipping Noise Band*

From about 30 Hz to at least 100 Hz, another broad band of enhanced spectral levels is observed. While these enhancements are fairly continuous over the entire displayed time interval, they do display temporal fluctuations not obviously correlated with the wind driven noise at higher frequencies. In contrast to the fin whale narrow vocalization band occurring not far below the lower boundary, this broad noise band displays much less seasonal variability. Standard texts ascribe this band to ship-radiated noise. On detailed examination of the relevant ship noise or "shipping" band in Fig. A4-3-GulSho-W2013-1, a time domain granularity is observed consisting of discrete narrow vertical line-like features signifying enhanced spectral levels persisting for intervals up to several hours. The less intense of these features tend to broaden or become less-peaked in time and display relatively less high frequency content. With ever decreasing amplitude, these features also tend to become less distinct individually until merging into a diffuse, virtually continuous background. We interpret the horizontal (i.e. temporal) granularity as arising from individual ship passages. The comparatively few ships passing quite close to the mooring are readily discerned as individual acoustic events, these peaking sharply in time, often with simultaneous brief bursts of spectral content above 100 Hz. Contributions from increasingly distant ship passages tend to merge progressively into a virtually continuous, fairly constant amplitude ambient background. The cases for which passage of individual ships can be readily discerned and identified are analysed in detail by Cochrane and Moors-Murphy (2017).

### *3.2.5. Pseudo-Noise*

In Fig. A4-3-GulSho-W2013-1, some events dominantly of very low acoustic frequency are discerned in the frequency range from 5 Hz to as high as 40 Hz. For instance, between decimal days 357.2 and 359.9 a series of six successive, equally spaced acoustic enhancement events are observed in the 5 – 10 Hz range. Graphical scaling from the plot reveals an inter-maximum event spacing lying within estimation error of the 12.42 hour $M_2$ tidal period. The question arises: if tidally related, do these acoustic features result from freely propagating sound fields generated by tidal turbulence remote from the mooring hardware, or alternatively; are these features pseudo-noise, i.e. hydrophone signals caused locally from current vortex shedding from the hydrophone or from the mooring hardware possibly enhanced by the excitation of pre-existing resonant

vibrational modes of the mooring cabling or other mooring components? Perhaps during the examined three day interval tidal currents peaked or otherwise fortuitously combined with non-tidal origin current fields in the manner necessary to push instantaneous current vectors beyond a threshold required to excite strong mooring vibrations (the latter also explaining why the observed repetition period might be $M_2$ rather than ½ $M_2$).

Proceeding forward in time to the post-Jan 1st portion of the Winter 2013-14 GulSho deployment (Fig. A4-3-GulSho-W2013-2) one observes the gradual emergence of a low frequency, generally ≤ 10 - 12 Hz, rumble. The rumble intensity increases from about Jan. 1st (New Year) to the end of deployment. Hints of tidal periodicities within the rumble are evident, especially prior to day 50, and even pre-Jan. 1st, but these become less clear as rumble amplitudes subsequently build. Again this could be pseudo-noise; vibrations generated by the interaction of the aging mooring hardware with the ambient current fields comprised of both tidal and non-tidal components. Other explanations considered include:

- A slow AMAR hardware failure such as water infiltration into the hydrophones or hydrophone electronics. This seems unlikely if tidal periodicities are indeed present but such periodicities are not obvious after the phenomena is well established and has grown in amplitude. This explanation does demand serious consideration.
- Seasonal increases in ultra-low frequency marine mammal vocalizations. A separate analysis of cetacean calls indicate that fin, humpback and blue whale calls peak in Dec - Jan (Martin et al. 2014; Kowarski et al. 2015; Moors-Murphy et al. In prep.[2]), with the proportion of files with these calls present decreasing substantially in the February - April period (though a secondary smaller peak in humpback whale calls occurs at the end of March and beginning of May; Kowarski et al. 2015). Sei whale calls (another low frequency vocalizer) peak in June-Aug (Krieg 2016). The rumble disappears completely after the one month time gap between cessation of the Winter 2013-14 deployment recording on April 5th and on the beginning of the Summer 2014 deployment on May 5th (Fig. A4-3-GulSho-S2014). Since observed whale temporal vocalization patterns are distinctly different from that of the low frequency rumble, this indicates that low frequency baleen whale calls are not the originating source. The low frequency noise is also broader in frequency range than most baleen whale calls. Somewhat similar rumble effects are observed within the same time period at MidGul (Fig. A4-3-MidGul-W2013-2) and ShoHald (Fig. A4-3-ShoHald-W2013-2), but the detailed time-amplitude patterns differ significantly. At MidGul the effect begins only after day 45 and is less extreme. At ShoHald, while a suggestion of a similar effect exists, it is much lower than at either GulSho or MidGul – this latter observation also modestly argues against a biological explanation.

[2] Moors-Murphy, H.B., J.W. Lawson, B. Rubin, E. Marotte, G. Renaud, A. Buren, and C. Fuentes-Yaco. Occurrence of blue whales (*Balaenoptera musculus*) off Nova Scotia, Newfoundland, and Labrador. DFO Can. Sci. Advis. Sec. Res. Doc. 2017 (in preparation).

- Distant exploration seismic surveys. On the Scotian Slope seismic surveys are frequently detected, at very low acoustic levels, originating from distant areas around the periphery of the Atlantic Basin where the direct propagation paths are not blocked by intervening land masses. For GulSho where levels < 10 Hz were most pronounced, high time resolution sonograms showed **no** evidence of periodic seismic pulses. For MidGul and ShoHald where < 10 Hz noise levels were lower, seismic pulses could sometimes be detected but it did not appear that the majority of the noise rising in amplitude with time was characterized by a pulsed mechanism.

In conclusion, the very low frequency noise appears most compatible with origins linked either to deterioration of the AMAR hydrophone/hydrophone electronics or to physical deterioration of the mooring. Whether electronic or mechanical in origin, this noise is unlikely to represent a remotely generated, freely propagating acoustic sound field, i.e. a field which would be present in the absence of the mooring. It therefore constitutes one form of pseudo-noise not representative of the true ambient noise background. The special case of extremely high pseudo-noise levels observed during early MidGul deployments will be deferred to section 3.3.4.

## 3.3. DETAILED DATA CHARACTERISTICS

### *3.3.1. General*

We now consider the quantitatively more informative power spectral plots and the broader acoustic dataset in general. First examined is a typical amplitude vs. frequency power spectrum believed little contaminated by instrumental or pseudo-noise. The data was selected from the relatively quiet pre-Jan 1$^{st}$ portion of the GulSho Winter 2013-14 deployment, specifically for the month of December. Figure A4-2-GulSho-2013-Dec shows the conventional power spectral density (white line) with sub-estimates and stats. Figure A4-1-GulSho-2013-Dec shows the conventional power spectrum (blue line) for the same month at four times the spectral resolution with estimates extending further into the low frequency regime. Note that spectral levels in both figures are in good amplitude agreement though differing in frequency resolution.

### *3.3.2. Fin Whale Spectral Lines*

Again prominent is the narrow 20 Hz fin whale feature, rising 12–13 dB above the surrounding spectral background levels, and of about 10 Hz total width on the higher spectral resolution plot. On examining the corresponding 1/3 octave spectral sections from MidGul and ShoHald (Figs. A4-3-MidGul-W2013-1 and A4-3-ShoHald-W2013-1 respectively) the same feature is detected at roughly the same amplitude thus indicating the phenomenon is geographically widespread. On extending our examination of the 20 Hz line over all catalogued 1/3 octave spectral sections (i.e. all stations and all deployments) several recurrent characteristics are observed:

- A total absence in mid-summer
- Start-up in late summer – about the beginning of September

- A gradual spectral amplitude rise to relatively steady peak levels maintained through the months of November and December
- A drop in amplitude starting around the Jan 1st and continuing to about the end of March when vocalizations tend to disappear into ambient background, although a low level residual can at times be detected to the end of May which marks the beginning of the summer quiet period.

These observations are consistent with analyses of fin whale calls in other studies (Martin et al. 2014).

### *3.3.3. Shipping Related Spectral Noise*

Returning to Fig. A4-2-GulSho-2013-Dec, the spectral enhancement extending from at least 30 Hz to about 200 Hz corresponds to that traditionally ascribed to ship noise. Its broad nature and temporal persistence makes accurate discernment of its amplitude above the otherwise baseline ambient background virtually impossible. Over the wider frequency range. ignoring bumps, overall spectral trends are red. The spectral amplitude fall-off with frequency is estimated as roughly 9 dB/octave between 2 and 15 Hz (start of fin whale peak), consistent with the textbook 8 – 10 dB/octave "deep-sea" rate suggested by Urick (1975). The fall-off reduces to about 3.9 dB/ octave from 500 Hz to the 8 kHz Nyquist, the within-range slope actually increasing with frequency, as compared to a 5 or 6 dB/octave rate suggested by Urick for an inclusive but broader frequency range.

Further examining the spectral plot with statistics (Fig. A4-2-GulSho-2013-Dec), it is observed that the conventional power spectral amplitude, the spectral sub-estimate median, and the sub-estimate mode generally parallel each other but do not coincide. While the power spectral amplitude is relatively insensitive to the length of the spectral sub-series used in its estimation (8192 samples or 0.512 s in time) - except for the resultant degree of spectral smoothing - this is less true in regard to the forms of the sub-estimate distribution functions. With the chosen analytical parameters the spectral mode tends to lie very slightly above the spectral median while the power spectral amplitudes lay just over 4 dB above the median, the separation between the power spectral amplitude and the sub-estimate median increasing slightly toward the low frequency end. On examining the wider family of similar plots (other months, stations and deployments) one notes a tendency for the sub-estimate distribution functions to display slightly narrower central peaks below about 200 Hz. Narrower peaks would appear characteristic of the dominantly ship-generated noise that also appears to fluctuate less, or at least in a slightly different statistical manner than the dominantly wind-correlated noise above 200 Hz.

The separation between the power spectral amplitude and the sub-estimate amplitude median increases markedly when a significant fraction of the total spectral noise power arises from infrequent or intermittent loud events i.e. isolated events with separations in time large compared to the individual spectral sub-sample duration and with an accumulated duration constituting but a small fraction of the total analysis interval. Such events might arise from sporadic loud marine mammal calls, very close ship passages, seismic airgun or echosounder pulses, or intermittent mooring strumming, among other possibilities. With reference to Fig. A4-2-GulSho-2012-Dec, the corresponding GulSho

station spectral plot for the year previous, notice the pronounced sharp spectral amplitude spike at about 1100 Hz (of uncertain origin) with only a slight analogous effect observed in the corresponding spectral sub-estimate median.[3] Narrow bandwidth anomalies in spectral amplitude vs. median separations occur more frequently in the 40 – 100 Hz range, as might be expected from close ship passages or extended duration fishing activities in the vicinity of the mooring. Less frequently, as with the 1100 Hz line above, narrow lines are visible in the monthly high resolution spectra well above 100 Hz. Again, these lines at exceptionally high frequencies appear to originate from shipboard machinery, the lines acquiring an enhanced visibility by lying within the steeply falling portion of the relevant oceanic noise power spectra in the transition region between shipping and wind-dominated spectral power. One case investigated in detail is the occurrence of strong but narrow ~420 Hz lines in the Summer 2013, June spectra for MidGul and ShoHald (best observed in Figs. A4-1-MidGul-2013-Jun and A4-1-ShoHald-2013-Jun), but barely noticeable at GulSho (Fig. A4-1-GulSho-2013-Jun). AIS analysis combined with higher **time** resolution spectral estimates (Fig. 19) allowed confident identification of the source, namely a 53,800 GT container vessel which passed MidGul and ShoHald moorings on June 12th at lateral ranges of only 2.4 and 4.4 km respectively while travelling just over 17 kts. The total time duration of high level 420 Hz signals at MidGul and ShoHald was only 20–30 min. Therefore, reliable amplitude quantifications of the passages in the original Figure series A4-1 plots were on the edge of being problematic considering the sparse ~41s of continuous acoustic sampling every 15 min employed. The same vessel also passed GulSho at about 9 km range resulting in comparative spectral levels 5 – 10 dB lower, very close to ambient background.

### *3.3.4. Pseudo-Noise Spectral Signatures*

An extreme separation between conventional spectral vs. sub-estimate median power occurs at MidGul during the initial Winter 2012-13 deployment. Consider the month of December (Fig. A4-2-MidGul-2012-Dec). Variable but generally large separations, as much as 13 dB, between spectral levels and median powers are observed between 10 Hz and several hundred Hz. In addition, a sequence of decreasing amplitude harmonically related spectral peaks at approximately 40 Hz frequency intervals are clearly observed starting around 120 Hz, while the 40 Hz fundamental and the 80 Hz first harmonic are only just discernable above broader band noise. Again these peaks are strongly evident in the power spectral amplitudes but are comparatively weak in the corresponding sub-estimate medians. With high certainty these anomalously large separations characterize pseudo-noise arising from cable strumming and/or other current-induced mechanical vibrations of the mooring equipment. Reference to the corresponding 1/3 octave spectral section (Fig. A4-3-MidGul-W2012-1) on which individual periods of pseudo-noise are readily discerned reveals that the time durations characterizing the highest levels of noise

[3] The immediately following spectral dip has a different probably instrumentation-related origin with the mean, mode, and all percentile lines about equally affected.

excitations are relatively brief i.e. the pseudo-noise possesses a low duty-cycle.[4] The principle is that sporadic high level noise bursts, whether of a true or pseudo nature, can markedly increase average spectral levels with comparatively minor effects on the spectral median and mode **if their overall duty-cycle is relatively low**.

Returning to Fig. A4-2-MidGul-2012-Dec, it is intriguing that the 20 Hz fin whale peak is clearly delineated by both the spectral sub-estimate median and mode while the anticipated corresponding peak in the power spectral amplitude is totally obscured by pseudo-noise (compare to simultaneous plots from the less pseudo-noise contaminated GulSho and ShoHald in Figs. A4-2-GulSho-2012-Dec and A4-2-ShoHald-2012-Dec respectively). This raises the interesting possibility that in similar cases of severe high amplitude, low duty cycle noise contamination, provided one is pre-informed as to the normal relationship between standard power spectral levels and the spectral sub-estimate medians and modes, it may be possible to reconstruct reasonably accurate estimates of the underlying uncontaminated power spectra by working backwards from less affected sub-estimate median or mode measures. This would constitute a potential processing approach for, in essence, suppressing unwanted noise components of a certain statistical character in acoustic power spectral estimation.

### *3.3.5. Pseudo-Noise Patterns within MidGul Dataset*

3.3.5.1. General Observations

On examining 1/3 octave spectral sections over all deployments and all stations (Figure series A4-3), the sections for MidGul during the Winter 2012-13 deployment (Figs. A4-3-MidGul-W2012-1 and A4-3-MidGul_W2012-2) stand out as exceptional in regard to their high amplitude, repetitive spectral response patterns at 300 Hz and below.[5] The low frequency spectral response patterns are observed to recur at about roughly 25.4 hour intervals with a longer period superimposed spectral amplitude modulation of about 321 hours duration. The periodically recurrent noise patterns are broadband from 5 Hz to about 300 Hz with brief higher frequency bursts occasionally approaching 2 kHz. The spectral noise power scaled /Hz is biased toward the lowest frequencies with broad enhancements in the 10 – 13 and 40 – 70 Hz ranges as well as around 120 Hz, the frequency region where the high resolution monthly spectral plots displayed a sequence of strong lines. Noise in the very low frequency 5 – 7 Hz range remains intense with amplitudes usually, but not invariably, correlating strongly with times of marked enhancement at the higher frequencies (i.e. alternative processes may be contributing to the observed very low frequency regime. The high resolution MidGul monthly spectral plots reveal a persistent peak in the 4 – 7 Hz range as well as high continuum levels at MidGul in this same very low frequency range (for example, Figs. A4-1-MidGul2012-Oct to A4-1-MidGul-2013-Apr incl.). As noted above, the Winter 2012-13 December

[4] The term "duty-cycle" is used loosely. While pseudo-noise is often observed to be highly periodic over periods of 5 – 10 days substantial irregularities and longer term variability are also observed, nevertheless a quasi-periodic pattern persists.

[5] Similar repetitive patterns are also observed in the Winter 2012-13 MidGul time domain data statistical descriptors – compare Fig. 2 for MidGul with Figs. 3 and 4 for GulSho and ShoHald stations respectively.

MidGul standard power spectral plot (Fig. A4-2-MidGul-2012-Dec) is characterized by marked low frequency amplitude enhancements and multiple discrete frequency harmonic peaks strongly indicative of ocean current excitation.

3.3.5.2. Noise Envelope Characteristics

The low frequency repetitive patterns on the 1/3 octave spectral sections convey the impression of an amplitude envelope of two superimposed, nearly equal amplitude sinusoidal time series both of near-diurnal (i.e. 24 hour) periodicity but with sufficiently frequency separation to generate a 321 hour repetitive beat pattern. Detailed physical oceanographic characterizations of the Gully area including the general area of MidGul have been published by Greenan et al. (2013, 2014). Their results revealed markedly enhanced tidal $O_1$ (25.81934 hr) and $K_1$ (23.93447 hr) period near bottom currents at two moored multiple current meter stations along the Gully central canyon axis. The ocean current ellipses at these stations were tightly aligned along the Gully axis with current amplitudes increasing rapidly within 100 m of the bottom. Their nearest current meter mooring to MidGul (# 1589 or "SG11") was located on the Gully axis about 8.6 km NW of our station. Their maximum $K_1$ current was 0.19 m/s and the maximum $O_1$ current was 0.16 m/s; both measured at 1542 m depth, 98 m above bottom. In contrast, the near semi-diurnal $M_2$ (12.42060 hr) maximum tidal current was 0.093 m/s, considerably lower. Apart from the Gully, deep Scotian Slope tidal currents are dominantly of $M_2$ periodicity with typical near-bottom maximum speeds of several cm/s. The order of magnitude higher and dominantly diurnal deep current velocities along the Gully axis stand out in stark contrast. We believe that these strong, near-diurnal Gully deep axial current fields are likely responsible for the excitation of near-diurnal repetitive patterns in the Winter 2012-13 MidGul spectral sections.

Additional confirmation comes from quantitative study of observed MidGul noise level periodicities. A periodogram (i.e. complex Fourier transform amplitudes squared vs. frequency) with a box car time weighted window for maximum frequency discrimination was computed for a 16384 pt time series of successive acoustic **envelope** amplitudes sampled at 15 min intervals. The 15 min envelope amplitude was defined as the RMS amplitude of the first 300 s of each AMAR data file, with successive data files following at 15 min intervals. The envelope amplitude time series commenced at day 286.0 (00:00 12 Oct. 2012) and extended over a continuous time span of 170.67 days. The resulting periodogram is presented in Fig. 20. The logarithmic horizontal axis has been plotted in period rather than frequency.

Amplitude spikes are observed at the discrete computed periods closest to the theoretical $O_1$, $K_1$, and $M_2$ tidal periodicities, the resolution in periodicity near the diurnal (24 hr) period being about 0.14 hours. Detailed inspection of the spike denoted "$K_1$" (Fig. 20) reveals it to be indeed of slightly less than pure diurnal periodicity strongly indicating that the $O_1$ and $K_1$ marked spikes are actually excited by these tidal components. This is further supported by the observation that the $O_1$ and $K_1$ amplitudes are comparable (even considering the spill-over between spectral bins) as was the case for the deep tidal current amplitudes reported by Greenan et al. (2014). A clear $M_2$ period tidal component is also distinctly observed but at a considerably lower amplitude. The $K_1$ vs. $O_1$ additive beat

period, in theory: 1 /((1/23.93447 hr) – (1/25.81934 hr)) = 327.86 hr; is also consistent with the location of a long period spike in the periodogram (although resolution at this much longer periodicity is low, ~26 hr). It is interesting that the acoustic envelope excitations occur at the same periodicities as the tidal currents - not at ½ of the same periodicities - implying that only one extreme of the combined tidal ellipses was successful in generating high levels of pseudo-noise. On examination of monthly tidal current rose plots for the 1542 m RCM at station mooring 1589 (Greenan et al. 2013) a definite asymmetry is noted with currents stronger in the NW directed direction than in the SE. This would suggest that during maximum amplitude tidal flows when the $K_1$ and $O_1$ components are nearly in phase, considerable asymmetry in the combined component tidal ellipses is present from non-linearities in tidal component superposition (or some other effect). When combined with possible flow thresholding effects and further non-linearities for existing sustained acoustic mooring vibrations, this could well account for the largely diurnal character of the corresponding mooring noise envelope.

Figure 21 is a 10 day time domain expanded portion of the spectral section of Fig. A4-3-MidGul-W2012-1, showing the complexity of the acoustic pseudo-noise phenomena. Separate noise excitations can frequently be observed for each direction of the dominantly diurnal flow pattern but the contributions from one direction of flow appear highly dominant, hence the near-diurnal character of the envelope when the $O_1$ and $K_1$ components are nearly in phase. One general consequence of the highly non-linear generation process is the production of sum and difference frequencies. The $O_1$, $K_1$ period difference frequency is the same as the (linear process) beat frequency while the $O_1$, $K_1$ component sum frequency corresponds exactly to the $M_2$ tidal period, giving an alternative and possibly more plausible general mechanism as to why both sum and difference tidal components might be present in the envelope of the AMAR noise signal. The precise physical generation mechanisms aside, the clear detection of known dominant tidal current periodicities in the signal envelope agues strongly for a tidal excitation origin.

Knowing that $O_1$, $K_1$ tidal nulls recur at a periodicity of 13.66 days (327.86 hr) suggests that tidal pseudo-noise might be suppressed by simply restricting analysis to time series sub-sets proximate to predicated nulls. This was explored for the MidGul, Nov. 2012 data. Lacking knowledge of tidal current phases at depth, we chose the deep and well defined tidal pseudo-noise null visually observed at decimal DOY 287.9 (14 Oct. 2012 21:36) and forward extrapolated to predict successive nulls over the next 1½ months. Resultant spectra with stats for data acceptance windows of 1.00 and 0.50 days centered on the predicted tidal beat nulls for the month of Nov. 2012 are shown in Figs. 22 and 23 respectively. Corresponding computed spectra for GulSho and ShoHald for the same data decimation (0.50 day windows centered on MidGul nulls)[6] are shown for comparison in Figs. 24 and 25. Note the recovery of the 20 Hz fin whale power spectral line and the good general agreement of MidGul spectral levels with those from GulSho and ShoHald. While pseudo-noise is greatly attenuated for MidGul using this selection

[6] Resultant spectra from GulSho and ShoHald are shown to illustrate the effects of similar data decimation on stations believed little affected by pseudo-noise.

procedure, the extreme decimation (only two sampling periods per month) precludes any notion of a representative monthly spectral average.

3.3.5.3. High Time Resolution Spectral Properties

It is instructive to examine the high resolution spectral properties of Winter 2012-13 MidGul pseudo-noise within sufficiently short time windows that any causal driving current flows might be assumed to remain relatively constant. This has accomplished in the neighbourhood of a representative but otherwise arbitrarily chosen time domain pseudo-noise peak occurring at 14:24 03 Dec. 2012 (2012 DOY 337.6; see Fig. A4-3-MidGul-W2012-1). Detailed spectra within three brief time windows were examined: high flow conditions at DOY 337.6, medium flow conditions at 337.8, and low flow conditions at DOY 338.0 based upon the observed local character of the section.[7] The standard recorded signal time domain statistics are shown in Fig. 26. From the nearest AMAR-recorded acoustic files to each of the chosen time windows, pressure signal power spectral densities were computed using 38 consecutive non-overlapping time series each of 131,072 pts (8.192 s) duration.

Resulting spectra appear in Figs. 27 and 28, the former plotted on a conventional logarithmic frequency axis and the latter on a linear frequency axis covering 0 - 100 Hz. Examining the linear axis plot, for the "strong" tidal flow a series of strong regular harmonic lines are observed between about 13 and 83 Hz at about 14 Hz spacings. For "medium" flows similar but lower amplitude lines, with a suggestion of a dual-peaked structure, are observed between about 7 and 50 Hz at 8 – 9 Hz spacings. For the lowest flow there is a suggestion of a few very low amplitude peaks at 5 – 6 Hz spacings above 30 Hz, but the winter fin whale vocalization peak at 20 Hz obscures the observations. At still lower frequencies the fundamental and lower harmonics are not obviously present.

As to excitation, vortex shedding from the 0.25" outside diameter coated steel cable would be expected to induce traverse cable oscillations. The characteristic vortex shedding frequency is given by:

$$f_s = S\ v/\mathrm{d}$$

where $v$ the current speed, d the cable diameter in units compatible with $v$, and $S$ is the dimensionless Strouhal number, usually characterised by a value of about 0.18 (Urick 1975).

We have no exact in-situ measure of $v$ or its variation long the length of the mooring. The above cited measurements of Greenan et al. for $O_1$ and $K_1$ tidal currents in-phase at depth suggest a value of the order of 0.35 m/s may be appropriate. Taking $d$ = 0.00635 m, $f_s$ computes to 9.9 Hz. Orthogonal traverse oscillations of the mooring cable perpendicular to the current flow are excited at $f_s$ while in-line oscillations would be

[7] The terminology "high excitation" rather than "high flow" etc. might be more appropriate since the strong asymmetry in excitation by the tidal ellipse is not well understood. Nevertheless, we will assume in this discussion that excitation is primarily related to the magnitude of the flow.

excited at 2 $f_s$ (Ketchman 1981). While the exact conversion mechanism of cable motion to hydrophone electrical impulse is obscure, it seems reasonable that considering non-linearities in the excitation process that one should observe a series of pseudo-noise spectral lines at $f_s$ and its lower harmonics. For our "high" flow case the primary frequency was observed to be about 14 Hz. This frequency seems reasonably compatible with the estimated $f_s$ of 9.9 Hz, considering that $v$ on which $f_s$ is linearly dependent was little more than conjectural. Consistent with this approach for the case of "medium" flows, at least, harmonic amplitudes are lower and shifted to a lower primary frequency. Further support is lent to a vortex shedding excitation by examination of the earlier high time resolution spectral section of Fig. 21 covering somewhat analogous periods of high pseudo-noise excitation at MidGul during Winter 2012-13. It can be observed that during the most intense pseudo-noise events, low frequency smoothed spectral amplitudes peak around 14 Hz simultaneous with maximum tidal currents (presumed indicated by maximum pseudo-noise intensities), the spectral peaks falling to lower frequencies systematically and roughly symmetrically on either side of inferred peak flows.

The computed excitation frequencies appear to be considerably higher than the primary transverse resonant frequencies of the tensioned long mooring cables which are anticipated to lie, very roughly, in the 1 Hz range. Therefore, vortex shedding would not be expected to efficiently excite lower order resonant modes of the cables themselves at least during higher current flows. However, higher order cable modes and independent higher frequency mechanical resonances may exist in isolated portions of the mooring hardware and if sufficiently undamped, either or both might well be strongly excited at specific tidal flows (vortex shedding frequency and its harmonics). Such resonances, if present, might account for the higher frequency harmonic peaks appearing in the one month high resolution spectral plots for MidGul for Winter 2012-13 and Summer 2013, each monthly plot encompassing a wide range of tidal current flows.

### *3.3.6. Mitigation of Gully Canyon Pseudo-Noise*

The existence of pseudo-noise in the Winter 2012-13 MidGul recordings was recognized during the subsequent analysis but, unfortunately, not within the time frame necessary to take mitigative actions for the Summer 2013 deployment. In consequence, the Summer MidGul deployment was also affected by pseudo-noise (Fig. A4-3-MidGul-S2013) - but to a less extreme degree, possibly a fortuitous consequence of a slightly altered station location characterized by a bottom depth of only 1580 m vs. 1780 m (at minimum) for the initial Winter 2012-13 deployment (Table 1). The following Winter 2013-14 and final Summer 2014 MidGul (only) deployments replaced the standard 3/16" steel mooring cables, plastic jacketed to a 0.25" outside diameter, by similar outside diameter fuzz faired rope (Yale Cordage "Aracom Miniline") and also used more streamlined SUB floats for both the top end and near bottom buoyancy (Fig. 3, compare to standard configuration Fig. 2) in an effort to damp out current-induced cable strumming or other oscillatory hardware behaviour. In addition, the target location was altered slightly to ensure a shallower bottom depth more consistent with that achieved in Summer 2013. Consulted BIO physical oceanographic personnel believed that the modestly shallower MidGul station water depths would likely result in a less extreme deep tidal current

regime than encountered on the initial Winter 2012-13 deployment, a fact consistent with the Summer 2013 observations. Examination of MidGul spectral sections from the Winter 2013-14 and Summer 2014 MidGul deployments (Figs. A4-3-MidGul-W2013-1 and 2, and A4-3-MidGul-S2014 respectively) demonstrate that these efforts were successful in suppressing, at minimum, the more obvious high-level pseudo-noise components.

### *3.3.7. Multi-Month and Multi-Station Spectral Summaries*

How do computed spectral levels vary month-to-month and from station-to-station? Superimposed monthly high resolution power spectral density plots for each AMAR for each deployment are presented in Figs. 29 - 40. In these plots the spectral curves for successive months are colour-coded. Further, choosing the months of June and December, located sufficiently early in the respective deployments to be little influenced by possible calibration drift or spurious instrumentation noise (further discussed below) we have plotted 3-station spectral overlay summaries for either June or December for each of the deployments in Figs. 41 to 44 respectively. Several inferences can be drawn from these figures:

1) In nearly all instances on proceeding from lower to higher frequencies a marked change in noise spectral character is observed at around 150 Hz. Above 150 Hz, monthly spectra tend to be comparatively smooth and monotonically decreasing with frequency. Any deviations from this pattern tend to be localized in frequency (i.e. discrete lines). In addition, above 150 Hz, decibel shifts between month-to-month spectral levels tend to be systematic with only minor frequency dependence, the shifts showing a slight tendency to decrease with increasing frequency. Below 150 Hz, systematic shifts are also observed, these often of higher magnitude – but less consistent over time than at higher frequencies. The above observations are illuminated by an investigation of meteorological influences on ambient noise in Appendix 3 where it was demonstrated that above approximately 150 Hz ambient noise was correlated to the inferred local wind field in a highly systematic manner. Both the spectral frequency response and its functional dependence on wind speed largely conformed to that anticipated from an extensive accumulated literature, the extraordinarily deep depths of our deployments and our use of a geographically remote wind reference being limiting factors in comparing our spectral wind responses to those observed elsewhere. Excepting the Winter 2012-13 deployment, month-by-month shifts in acoustic levels in the wind dominated regime tended to show similar patterns at all stations with a total seasonal range of 6 – 7 dB with highest levels in mid-winter and lowest levels in mid-summer.

2) For the longer Winter 2012-13 and the Winter 2013-14 deployments at frequencies above 150 Hz, downward trends in spectral levels with increasing time are observed for post-deployment elapsed times exceeding about three months. This phenomenon, examined in detail in Appendix 2 may arise largely from systematic reductions in AMAR instrumental acoustic sensitivities with time, perhaps related to the extended and unusually deep nature of these deployments. Instrumental sensitivity drifts are

difficult to examine in isolation since above 150 Hz acoustic noise spectra become strongly wind dependent and wind fields vary seasonally as well as on shorter time scales. Appendix 3 quantifies the effects of wind on high frequency noise levels and, in the process, produces strong evidence that inferred instrumental sensitivity drifts are indeed real **for the initial Winter 2012-13 datasets** and are not mere artefacts of seasonally changing wind fields, the sensitivity drifts apparently varying with instrument. Sensitivity drifts are suspected for other data sets, especially Winter 2013-14, but the evidence is less conclusive. The summer sets were definitely too short to be definitive (the Summer 2013 datasets used the same model hydrophone as in the clearly anomalous Winter 2012-13 datasets). No local Scotian Shelf exploration seismic surveys were in progress during the two winter deployments which might produce an enhanced and varying noise background.

3) For the initial Winter 2012-13 deployment for frequencies below about 150 Hz and extending down to the 2 Hz plot cut off, systematic downward shifts in spectral levels similar to those seen above 150 Hz are observed at all three stations. However, below 30 Hz, month-to-month decibel shifts were markedly larger than above 150 Hz. The several month hiatus in drift initiation seemingly evident at higher frequencies is also less clear. In the Winter 2013-14 deployments below about 12 Hz, MidGul and GulSho show systematic upward drifts in spectral levels over time totalling at least 15 dB. The drifts start early in the deployment and continue to the end of the recording period. In contrast, ShoHald displays a much lower amplitude drift during the same time period, spectral levels rising only modestly from November to February and then falling slightly in March and April. The contrasting multi-low frequency range behaviours would suggest that the causative mechanisms are largely local since true seasonal ambient noise level shifts would be expected to be geographically widespread affecting all three stations similarly. The fact that low frequency spectral levels at MidGul and GulSho evolve upwards over time rather than downwards, as observed above 150 Hz at all frequencies and stations in Winter 2012-13, suggests an **additive** noise mechanism that counteracts any opposing effect from possibly declining instrumental sensitivities. The gradual evolution of very low frequency rumbles at MidGul and, especially, at GulSho, with hints of a similar but much less pronounced effect at ShoHald are described above (section 3.2.5). This rumble is most likely indicative of a slowly evolving electronic or perhaps even mechanical malfunction which injects increasing levels spectral noise of a highly red character, most evident at < 12 Hz, over the course of deployments. Any instrumental sensitivity drift hypothesis **by itself** reasonably accounting for the time variation of the Winter 2012-13 data over the **entire** observed frequency range would require a drift component which is frequency dependent. Systematic decibel shifts in sensitivity below 30 Hz appear to be clearly higher than those above 150 Hz, assuming that both true ambient noise and locally generated pseudo-noise are subject to the same system response characteristics. Conversations with JASCO (Bruce Martin, personal communication Jan. 2016) indicated a suspicion of water infiltration into AMAR hydrophone coupling capacitors. Might such a process induce a frequency-dependent response characteristic? Might the very low frequency rumble evident in the later Winter 2013-14 deployment possible also arise from water infiltration?

In terms of the quantitative performance of the AMARs one observes from the instrumental frequency response characteristics displayed in Appendix 1 that the electronic response roll-off below 10 Hz is quite extreme. Any errors present in estimating this response for individual instruments, anomalous drifts over time in this response characteristic, or the presence of a real post-filtering electronic noise floor associated with the data would be magnified by the often quite extreme spectral response corrections applied following spectral estimation to compensate for the projected low-frequency roll-off. In consequence, the quantitative reliability of AMAR data might be expected to decline as one dips into the highly corrected frequency regime below roughly 10 Hz.

4) A strong spectral peak in the 4 – 6 Hz region is observed in the initial Winter 2012-13 deployments at all three stations. On careful examination a similar peak is detectable through all deployments and at all stations (though this may be obscured by the low frequency rumble when the same is present at high level) with the notable exceptions of MidGul on the Winter 2013-14 and Summer 2014 deployments. These two exceptions were the only instances in which haired fairing was utilized on the mooring cable with the intent of damping mooring line vibrations or oscillations. Therefore, the 4 – 6 Hz peak is likely a product of pseudo-noise[8] and, consequently, unrepresentative of true ambient background. These peaks may possibly represent excitation of preferred overtones of the fundamental natural vibration periods of the longer mooring cables by mild low current, low frequency vortex shedding. Because of the evidence for mooring oscillations and the additional existence of a rumble signal of possible electronic origin, it is seems prudent that the very low frequency spectral regimes observed at all of our stations should be regarded as upper bounds to the true ambient noise background.

5) Ship noise usually appears as a modest spectral bump most pronounced between 30 and 100 Hz. For the two extended winter deployments, it is unclear whether the temporal drifts in shipping band acoustic levels more closely resemble the drifts observed above 150 Hz or those below 30 Hz. For ship noise, the low frequency spectral tail is obscured by the spectral extension of the low frequency rumble especially at Winter 2013-14 MidGul and GulSho.

6) Spectral responses at all Winter 2012-13 and Summer 2013 stations are characterized by a series of sharply defined minor dips starting just above 1 kHz, the patterns being nearly identical at all stations. Corresponding dips are absent for the Winter 2013-14 and Summer 2014 deployments. This might be due to the use of Geospectrum M8Q

[8] "Pseudo-sound" (we use analogous "pseudo-noise") usually refers to pressure fluctuations at a hydrophone or other sound measuring device originating from local sources as opposed to pressure fluctuations originating remotely and conveyed by acoustic waves freely propagating in the water medium. In our specific case we could broaden the definition to also include non-stationary acoustic noise originating from anomalous operation of the measurement device itself as distinguished from the normal stationary instrumentation noise floor.

hydrophones for the latter two deployments in contrast to the Geospectrum M8E hydrophones employed for the two earlier deployments. However, hydrophones on the latter two deployments were intentionally mounted less proximate to the of the AMAR pressure case end-caps, a possible alternative explanation.

7) Firm conclusions regarding comparative true ambient noise levels at the various recording sites, including systematic seasonal variabilities, are difficult to formulate because of the existence of non-ambient noise contributions in the lower frequency ranges and suspected - but poorly characterized - instrument sensitivity drifts quite possibly affecting the total frequency range. In the instances where residual mooring generated pseudo-noise, possible sensitivity drifts, and anomalous instrumental noise were all anticipated to be low, such as within the wind-dominated frequency range from several hundred Hz to the 8 kHz Nyquist cut-off during the **early months** of all deployments, the noise levels for the same monthly average at all three sites were close to identical (Figs. 41 – 44). For the December 2013 (Fig. 43) and, especially, the June 2014 (Fig. 44) data, less exact, but still reasonably good, agreements extend downward to about10 Hz at all sites.

### 3.4. COMPARISONS WITH "CLASSIC" DEEP WATER NOISE SPECTRA

How do the AMAR spectral levels, especially those believed to be little compromised by pseudo-noise and other anomalous effects, compare with similar long-term, deep-water noise measurements collected elsewhere? The recognition of slowly rising (decadal time scale) low frequency noise levels in virtually all ocean basins due to progressively increasing shipping densities and the transition to ever larger vessels makes this issue of some environmental importance. Classic ocean noise level measurements, some interpreted as demonstrating upward movements over time, are summarized by Dahl et al. (2007). Apart from shipping, other systematic long-term ocean processes also potentially influence ocean noise levels. These include shifts in average wind speed due to climate change (mainly affecting frequencies above a few hundred hertz) and slow changes in ocean sound absorption arising from systematic changes in ocean temperature structure and/or pH, the absorption effects probably minor compared to the shipping related changes (Hester et al 2008; Joseph and Chiu 2010; Reeder and Chiu 2010; Udovydchenkov et al. 2010). Spectral curves collected in the 1963 - 1965 and 1994 – 2001 periods from the U.S. Navy SOSUS array west of Pt. Sur, California (Andrew et al. 2002; Wenz 1969) are plotted in Fig. 45. These were collected at a depth of 1359 m, a depth range roughly comparable to our AMARs. Also plotted are the measurements of McDonald et al. (2006) at another offshore California site, "San Nicolas South", SW of San Nicolas Island from Nov. 2003 to March 2004. Observations were at 1090 m depth, 10 m off bottom. Also shown are earlier SOSUS measurements by Wenz (1968a, b) rescaled into conventional acoustic units by McDonald et al. (2006) and spanning Nov. 2003 to March 2004 at essentially the same San Nicolas South location.

Comparable baseline data from deeper water sites in the western Atlantic basin are scarce. Most published acoustic spectral levels from the Scotian Shelf region (e.g. Zakarauskas et al. 1990; Desharnais and Collison 2001) are confined to shallow waters

and/or are of brief temporal duration, therefore, not well suited for comparison with our AMAR averages. Possibly more suitable are selected deeper water noise recordings off the south-central U.S. east coast from a collection recently reported by Wiggins (2015). These were obtained using HARP bottom mount packages (Wiggins and Hildebrand 2007) with hydrophones mounted about 10 m above bottom – much closer to bottom than our AMARs but comparable to the Californian data. Plotted in Fig. 45 are scaled spectra from Wiggins' "Hatteras (Site 1)" station directly east of Cape Hatteras in about 960 m of water. Spectra were derived from about 1.4 years of gapped data collected between March 2012 and March 2014. Also plotted is a spectral curve from a 2nd Wiggins "Cherry Point Deep (Site 3)" station SE of Cape Hatteras in about 900 m of water. This spectral curve was derived from about 1.2 years of gapped data collected between August 2011 and June 2013. Included in Fig. 45 are standard text book deep ocean sound level bounding curves for "heavy shipping" for sea state 6 and "light shipping" for sea state 1 (Urick 1975). Since Urick's shipping levels date from about five decades prior to contemporary times their current relevance might be questioned.

For comparison with the above reference measurements, ShoHald acoustic spectral levels from December 2013 and June 2014 were selected as best representative of the true ambient Scotian Slope background at 10 Hz and above. Spectral averages for both months are plotted in Fig. 45. During both June and December, noise levels at ShoHald were the lowest of the three AMAR stations, with little obvious evidence of pseudo-noise contamination at ≥10 Hz. In addition, a fairly close correspondence between the PDFs for time domain average, minimum, and maximum RMS levels for 300 s sub-intervals for both months is observed (Figs. 16 and 17), which argues for little sporadic high level noise contamination. While the BP Canada "Tangier" exploration seismic survey was in progress during the June 2014 period and seismic pulses could be discerned on some acoustic records, the averaged spectral levels appeared little affected. Spectral levels down to 10 Hz were nearly identical to those observed at the same station in June 2013. Significantly, the selected spectra for both December 2013 and June 2014 were computed from data recorded sufficiently close to the instrument deployment times that any drifts in instrumental calibration should be essentially negligible. Both spectra were also collected using the same model hydrophone. The power spectral levels for ShoHald plotted in Fig. 45 were scaled from higher resolution spectral curves as point readings at 1/3 octave frequency intervals, as opposed to 1/3 octave binned spectral averages. Since the underlying spectral curves were quite featureless, excepting the 20 Hz fin whale vocalization line, little information was believed lost by the sparse frequency domain sampling. Close ship passages were not eliminated from the defining spectral computations. Indirect indications in the form of fairly constant or, at least only slightly changing, decibel spacings between the regular power spectral level, the spectral sub-estimate median, and the sub-estimate mode through the entire plotted frequency ranges (Figs. A4-2-ShoHald-2013-Dec and A4-2-ShoHald-2014-Jun) argue against brief high level transient events such as close ship passages contributing unduly to the overall spectral levels for the two examples chosen.

Above 300 Hz, the ShoHald spectral levels for December are observed to be about 6 dB higher than those for June, an effect almost certainly attributable to comparatively higher

December wind fields and seas states. Below 300 Hz the otherwise contrasting seasonal ShoHald levels shift rapidly to more comparable values within the shipping-dominated noise band, ignoring the narrow 20 Hz peak in December from fin whale vocalizations. Nevertheless, some seasonal variation appears to persist down to frequencies as low as 70 Hz. Our June ShoHald levels agree reasonably well with levels at the two Wiggins deep-water stations but our December ShoHald levels are markedly higher than those reported by Wiggins above about 70 – 100 Hz, perhaps reflecting stronger winter winds at our higher latitude station. Wiggins (2015) believed fin whale vocalizations were responsible for the enhancements near 20 Hz at his deep water stations while some mooring strumming was believed responsible for the anomalously high spectral readings below 20 Hz at his Site 3 "Cherry Pt. Deep" station. Examining the off-California data, within the shipping-dominated spectral range and up to 400 Hz, the highest available frequency for comparison, our ShoHald June data, falls very close to the 2003 - 2004 San Nicolas Island data. However, it is likely that the San Nicolas shipping noise levels, especially those below 50 Hz, have continued to increase during the one decade observation time gap preceding our AMAR observations. Our ShoHald levels also fall somewhere between the mid-1960's and late 1990's spectral levels reported off Pt. Sur, California.

## 4. RECOMMENDATIONS FOR FUTURE MONITORING

Informed by both the present study results and the results from analogous passive acoustic studies elsewhere, several recommendations regarding future long term acoustic monitoring studies in the Scotian Shelf/Slope area are provided below.

Observing the historical Californian noise data, it is of interest that the rates of increase in 40 Hz shipping noise over time at both Pt. Sur and San Nicholas South are comparable (~0.3 dB/yr) while average absolute levels at the two stations for reasonably comparable time periods appear to systematically differ by about 6 – 7 dB (higher at Pt. Sur; also see McDonald et al. 2006). This demonstrates that deep water shipping noise levels can vary significantly even within the same general geographic region due to varying distances to heavily travelled shipping lanes and likely, to a lesser degree, acoustic propagation effects. Therefore, if future passive acoustic monitoring is attempted within our region to elucidate long term anthropogenic influences, attention should be given to:

- Closely duplicating mooring locations and hydrophone depths;
- Avoiding localized commercial fishing hot spots;
- Using sufficiently long averaging times to produce representative ambient noise samples cognizant of the high variability in wind speeds and sea states during especially the winter months; and,
- Reducing mooring strumming effects and hydrophone flow noise as much as practical. Avoiding areas of known enhanced bottom currents, for instance those known to be present along the Gully central axis, is strongly recommended unless the effectiveness of pseudo-noise suppression techniques can be conclusively demonstrated.

The latter challenge could well necessitate mounting measurement packages with hydrophones near or on-bottom similar to the HARP packages of Wiggins and

Hildebrand (2007) or our earlier Scotian Shelf OBS hydrophone-equipped units (Cochrane 2007). However, near-bottom mounting would be disadvantageous in areas of high bottom topography as well as forcing acoustic measurement very close to a major physical boundary. At present, excepting the physical AMAR unit itself, most of the mooring hardware is the in-house responsibility of DFO. The construction of low noise acoustic moorings is a specialized skill where even minor mechanical details can be important, and where much can be learned from experienced technical personnel elsewhere, including the accumulated literature. Care should be taken to systematically document the pseudo-noise characteristics of various mooring hardware configurations as part of a long term iterative learning and refinement process. This necessitates systematic feedback from acoustic data analysts to mooring design and assembly personnel.

With regards to the AMAR instruments themselves, the acoustic calibration drifts encountered during at least the Winter 2012-13 deployments are clearly unacceptable for definitive long term quantitative monitoring. At the present time, the phenomenon remains poorly understood in terms of its origin, its magnitude, its detailed character, reproducibility, and the range of operational conditions likely to trigger its occurrence (or to guarantee its non-occurrence). A means of periodically checking the total measurement system acoustic calibration or the calibration stability in-situ may be required. This might be achieved by programmed periodic transmission of pulses from a proximate calibrated acoustic source. Further, lower drift AMAR internal clocks in conjunction with an acceptable geographic distribution of recorders would enable long baseline triangulation of discrete acoustic events. While triangulation would not be especially advantageous for the range of investigations pursued in this document, new analytical possibilities would be opened for the same datasets. Better timekeeping is currently technically possible but the necessary trade-offs against enhanced power consumption and costs are judged disadvantageous. Better solutions are welcome and should also include protocols for electronically measuring precise residual clock offsets both immediately before and after deployments. Another possibility would be the use of short baseline hydrophone pairs or arrays to explore the time-spatial correlation properties of recorded noise thereby enabling more reliable separation of free propagating vs. mooring generated noise, enabling discernment of arrival directions (requires geometric controls), and providing a way of detecting sensitivity drift or other anomalous behaviour of individual acoustic channels. In terms of field operational protocols, the collection of CTD or sound speed profiles at both instrument deployment and recovery should be routine as well as the employment of a proven methodology for determining precise post-deployment hydrophone depths and locations.

## 5. ACKNOWLEDGEMENTS

The authors graciously acknowledge that this work was not accomplished in isolation. We especially thank Jay Barthelotte and Adam Hartling of the Technical Operations Group, Ocean Physics Section, BIO, for their capable design and fabrication of the AMAR moorings. Bruce Martin, Applied Science Manager, JASCO Applied Sciences, provided vital support in understanding the response characteristics of the AMAR

instruments and served as a knowledgeable and efficient liaison for instrumental data transfers from JASCO to BIO. Pierre Clement, Coastal Ecosystem Science Division, furnished satellite-relayed AIS data received from exactEarth and greatly assisted in understanding its principal characteristics (most AIS-based analysis appears in the companion report addressing vessel noise). Blair Greenan of BIO's Ocean Sciences Division provided expert knowledge regarding the deep ocean current regime in the central Gully. The officers and crew of CCGS *HUDSON* performed proficiently deploying and retrieving our AMAR moorings. Thanks are also extended to the Senior Scientists of several *HUDSON* cruises who went out of their way to accommodate our special mooring deployment/retrieval requirements.

Sincerely appreciated and of great value were the critiques of advanced drafts of this manuscript by David Barclay, Department of Oceanography, Dalhousie University and Pamela Emery, Ocean and Ecosystem Sciences Division, BIO. However, the authors should make clear that the reviewers served in an advisory capacity only and that the report's contents should neither be considered as necessarily reflecting their views nor as necessarily carrying their full endorsement.

Principal computations were performed using Lahey-Fujitsu Fortran 95 v 5.6 with integrated Winteracter v 8.0. Graphics were provided by Matlab v 5.1.0.421.

This work was supported by DFO SPERA (**S**trategic **P**rogram for **E**cosystem-Based **R**esearch and **A**dvice) funding.

## 6. REFERENCES


Andrew, R.K., Howe, B.M., Mercer, J.A., and Dzieciuch, M.A. 2002. Ocean ambient sound: Comparing the 1960s with the 1990s for a receiver off the California coast. Acoust. Res. Lett. Online 3(2): 65–70. http://scitation.aip.org/content/asa/journal/arlo/browse [follow links] (accessed 11 February, 2016).

Clay, C.S., and Medwin, H. 1977. Acoustical oceanography: Principles and applications. John Wiley & Sons, New York. 544 p.

Cochrane, N.A. 2007. Ocean bottom acoustic observations in the Scotian Shelf Gully during an exploration seismic survey – A detailed study. Can. Tech. Rep. Fish. Aquat. Sci. 2747: viii + 73 p.

Cochrane, N.A. and Moors-Murphy, H. 2017. Extraction of vessel acoustic source levels and total sound exposure levels from passive acoustic recordings on the eastern Nova Scotian Shelf Slope and in the Gully Marine Protected Area. Can. Tech. Rep. Fish. Aquat. Sci. 3237. In press.

Dahl, P.H., Miller, J.H., Cato, D.H., and Andrew, R.K. 2007. Underwater ambient noise. Acoustics Today Jan. 2007: 23–33.

Delarue, J. 2008. Northwest Atlantic fin whale vocalizations: Geographic variations and implications for stock assessments. Thesis (M. Phil. in Human Ecology) College of the Atlantic, Bar Harbour, Maine. xi + 99 p.

Desharnais, F., and Collison, N.E.B. 2001. Background noise levels in the area of the Gully, Laurentian Channel and Sable Bank. Proceedings of Oceans 2001, Hawaii, HI, Nov. 2001: 1348–1355.

Greenan, B.J.W., Petrie, B.D., and Cardoso, D.A. 2014. Mean circulation and high-frequency flow amplification in the Sable Gully. Deep-Sea Res. II 104: 20–34.

Greenan, B.J.W., Petrie, B.D., Cardoso, D., Harrison, W.G., Head, E.J.H., and Li, W.K.W. 2013. Physical, chemical and biological variability of the Sable Gully 2006-07. Can. Tech. Rep. Hydrogr. Ocean. Sci. 293: ix + 261 p.

Hester, K.C., Peltzer, E.T., Kirkwood, W.J., and Brewer, P.G. 2008. Unanticipated consequences of ocean acidification: A noisier ocean at lower pH. Geophys. Res. Lett. 35. L19601, doi:10.1029/2008GL034913: 5 p.

Joseph, J.E., and Chiu, Ching-Sang. 2010. A computational assessment of the sensitivity of ambient noise to ocean acidification. J. Acoust. Soc. Am. 128(3): EL144–EL149.

Ketchman, J. 1981. Vibration induced in towed linear underwater array cables. IEEE J. Ocean. Eng. OE-6(3): 77-87.

Kowarski, K., Evers, C., Moors-Murphy, H.B., and Martin, B. 2015. Year-round monitoring of humpback whale (*Megaptera novaeangliae*) calls in the Gully MPA and adjacent areas. Proc. Acoustics Week in Canada 2015. Oct. 6 – 9, Halifax, NS: 2 p.

Krieg, P. 2016. Evidence of song vocalization by Sei whales (*Balaenoptera Borealis*) in The Gully submarine canyon off Nova Scotia, Canada. Honors Thesis (B.Sc.) Dalhousie University, Halifax, NS: 51 p.

Lee K., Bain, H., and Hurley, G.V. (eds.) 2005. Acoustic monitoring and marine mammal surveys in the Gully and outer Scotian Shelf before and during active seismic programs. Environmental Studies Research Funds (ESRF) Report 151: xx + 154 p.

Martin, B., Korarski, K., Mouy, X., and Moors-Murphy, H. 2014. Recording and identification of marine mammal vocalizations on the Scotia slope and shelf. Proc. IEEE-MTS Oceans 2014, 14 – 19 Sept., St. John's, NL: 6 p.

McDonald, M.A., Hildebrand, J.A., and Wiggins, S.M. 2006. Increases in deep ocean ambient noise in the Northeast Pacific west of San Nicolas Island, California. J. Acoust. Soc. Am. 120(2): 711–718.

Merchant, N.D., Barton, T.R., Thompson, P.M., Pirotta, E., Dakin, D.T., and Dorociez, J. 2013. Spectral probability density as a tool for ambient noise analysis. J. Acoust. Soc. Am. 133(4): EL262–EL267.

Reeder, D.B., and Chiu, Ching-Sang. 2010. Ocean acidification and its impact on ocean noise: Phenomenology and analysis. J. Acoust. Soc. Am. 128(3): EL137–EL143.

Udovydchenkov, I.A., Duda, T.F., Doney, S.C., and Lima, I.D. 2010. Modeling deep ocean shipping noise in varying acidity conditions. J. Acoust. Soc. Am. 128(3): EL130–EL136.

Urick, R.J. 1975. Principles of underwater sound. McGraw-Hill, New York. xiii + 384 p.

Watkins, W.A., Tyack, P., Moore, K.E., and Bird, J.E. 1987. The 20-Hz signals of finback whales (*Balaenoptera physalus*). J. Acoust. Soc. Am. 82(6): 1901–1912.

Welch, P.D. 1967. The use of fast Fourier transform for the estimation of power spectra: A method based on time averaging over short, modified periodograms. IEEE Trans. Audio and Electroacoust. AU-15: 70–73.

Wenz, G.M. 1968a. Properties of low-frequency, deep water ambient noise west of San Diego, California. Navy Undersea Warfare Center Technical Publication TP-39. p. 48. [Quoted by McDonald et al. (2006), original document not procured].

Wenz, G.M. 1968b. Properties of low-frequency, deep water ambient noise southwest of Pacific Beach, Washington. Navy Undersea Warfare Center Technical Publication TP-90, p. 38. [Quoted by McDonald et al. (2006), original document not procured].

Wenz, G.M. 1969. Low-frequency deep-water ambient noise along the Pacific Coast of the United States. U.S. Navy J. Underwater Acoust. 19: 423–444. [Quoted by McDonald et al. (2006), original document not procured].

Wiggins, S.M. 2015. Low – frequency ambient noise offshore of North Carolina and Florida 2007-2014 Final Report. Marine Physical Laboratory, Scripps Institution of Oceanography. Report No. MPL TM-556 (April 2015). 16 p. http://cetus.ucsd.edu/Publications/Reports/WigginsTM556-2015.pdf (accessed 11 January, 2016).

Wiggins, S.M., and Hildebrand, J.A. 2007. High-frequency acoustic recoding package (HARP) for broad-band, long-term marine mammal monitoring. Proceedings: International Symposium on Underwater Technology 2007 and International Workshop on Scientific Use of Submarine Cables & Related Technologies 2007, IEEE Tokyo, Japan: 551 – 557. http://escholarship.org/uc/item/0p6832s1 (accessed 11 January, 2016).

Zakarauskas, P., Chapman, D.M.F., and Staal, P.R. 1990. Underwater acoustic ambient noise levels on the eastern Canadian continental shelf. J. Acoust. Soc. Am. 87(5): 2064–2071.

**Table 1.** AMAR station deployment periods, locations, and water depths.

| Deployment | | Deployed | Recovered | Lat. | Long. | Drop Depth | Benthos Release Depth | MicroCAT Depth |
|---|---|---|---|---|---|---|---|---|
| unit/station no. | | dd-mmm-yy | dd-mmm-yy | dec.deg. | dec.deg. | m | m | m |
| **Winter 2012-13** | | | | | | | | |
| ***MidGul*** | 127/1833 | 12-Oct-12 | 10-Apr-13 | 43.85088 | -58.91864 | 1780 | 1914 | ----- |
| ***GulSho*** | 145/1832 | 12-Oct-12 | 10-Apr-13 | 43.86833 | -58.59861 | 1516 | 1435 | ----- |
| ***ShoHald*** | 144/1831 | 12-Oct-12 | 10-Apr-13 | 44.08836 | -58.06505 | 1700 | 1789 | ----- |
| **Summer 2013** | | | | | | | | |
| ***MidGul*** | 127/1849 | 07-May-13 | 26-Sep-13 | 43.86225 | -58.90997 | 1580 | ----- | ----- |
| ***GulSho*** | 145/1850 | 08-May-13 | 26-Sep-13 | 43.86376 | -58.58818 | 1583 | ----- | ----- |
| ***ShoHald*** | 144/1851 | 08-May-13 | 26-Sep-13 | 44.09772 | -58.05636 | 1545 | ----- | ----- |
| **Winter 2013-14** | | | | | | | | |
| ***MidGul*** | 143/1859 | 15-Nov-13 | 06-Apr-14 | 43.86225 | -58.90997 | 1525 | ----- | ----- |
| ***GulSho*** | 194/1860 | 15-Nov-13 | 06-Apr-14 | 43.86163 | -58.58790 | 1530 | ----- | ----- |
| ***ShoHald*** | 197/1861 | 15-Nov-13 | 07-Apr-14 | 44.09742 | -58.05631 | 1550 | ----- | ----- |
| **Summer 2014** | | | | | | | | |
| ***MidGul*** | 143/1868 | 03-May-14 | 26-Sep-14 | 43.86408 | -58.90825 | 1614 | 1536 | 1487 |
| ***GulSho*** | 194/1869 | 03-May-14 | 26-Sep-14 | 43.86367 | -58.35481 | 1573 | 1618 | 1539 |
| ***ShoHald*** | 197/1870 | 03-May-14 | 26-Sep-14 | 44.16318 | -58.10422 | 1559 | 1560 | 1625 |

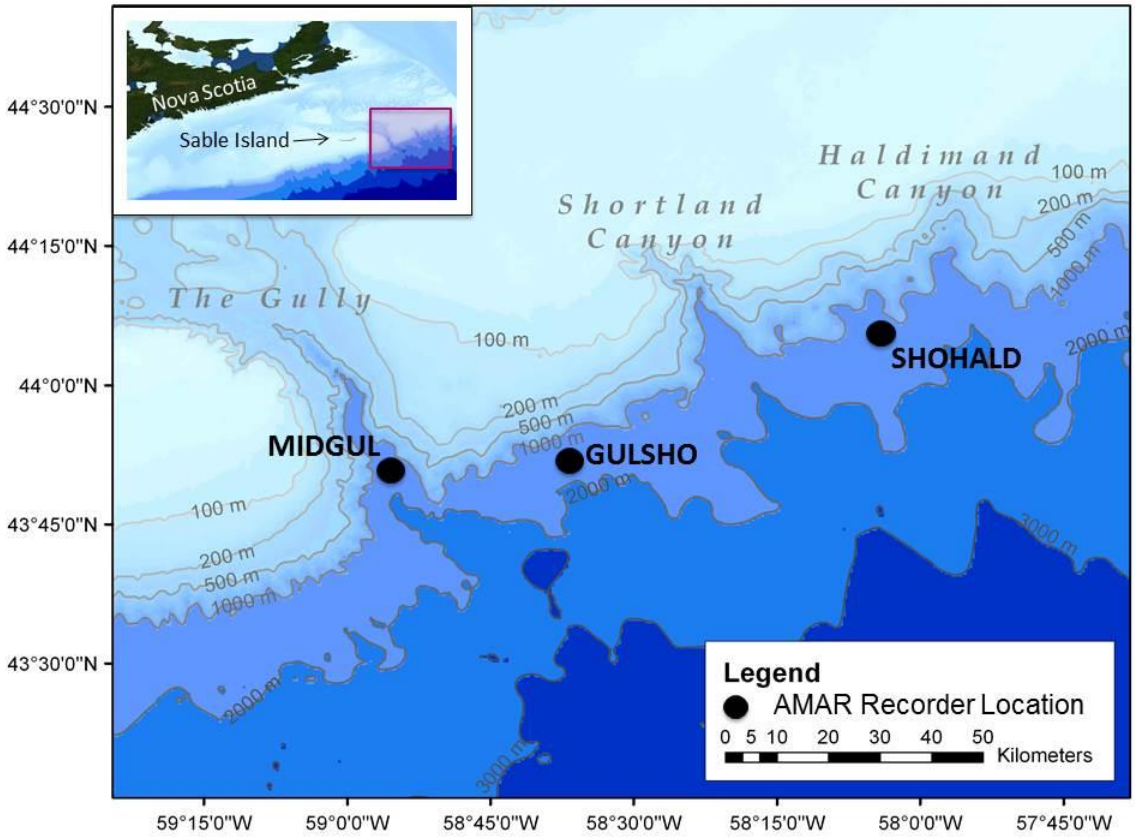


**Figure 1.** AMAR recording sites. Consult Table 1 for locations and depths.

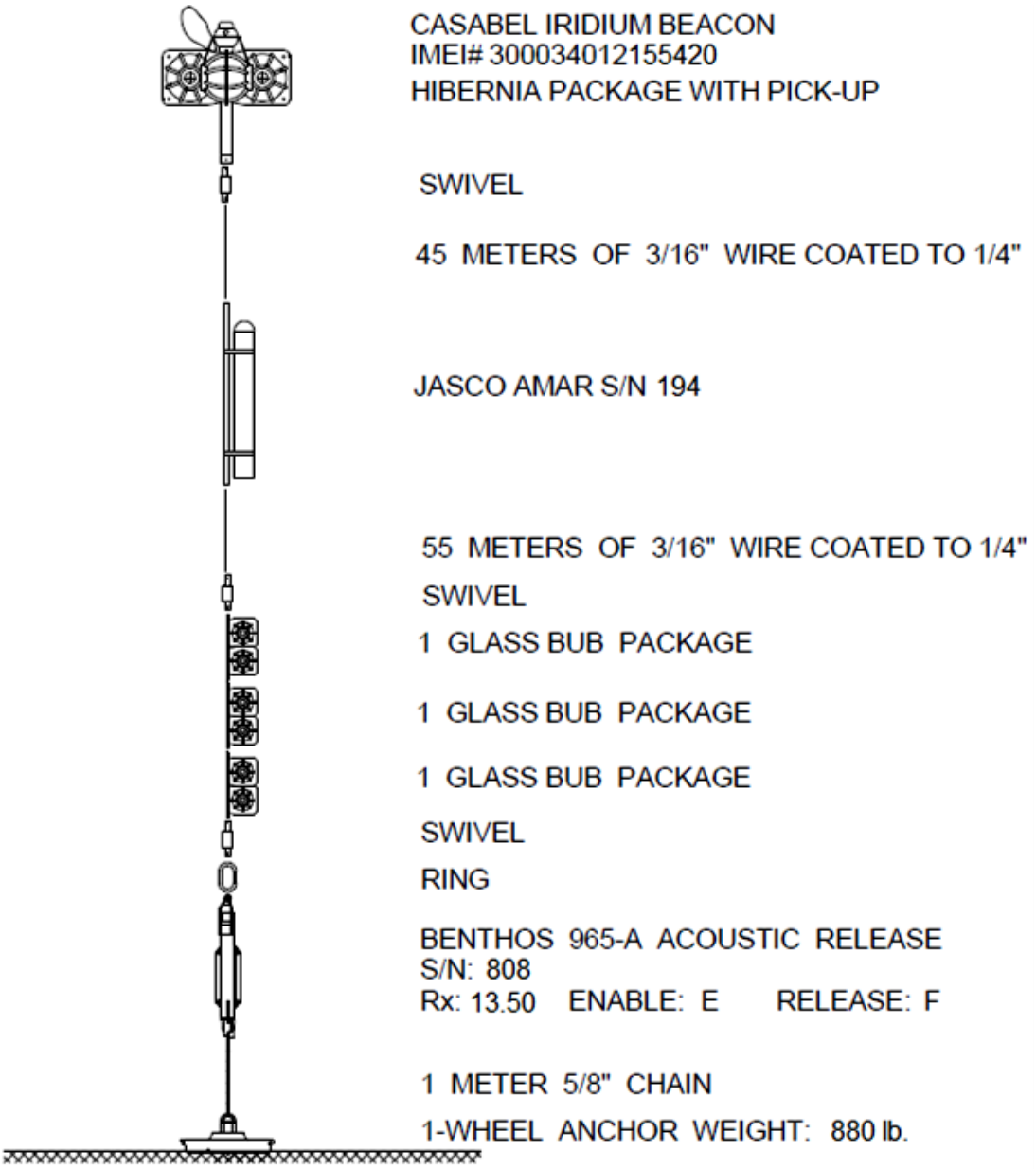


**Figure 2.** Sample mooring configuration similar to those employed at all stations for all deployments excepting the MidGul Winter 2013-14 and Summer 2014 deployments. Summer 2014 deployments also included a MicroCAT recorder mounted just below the AMAR recorder. Figure provided by J. Barthelotte with revisions by N. Cochrane.

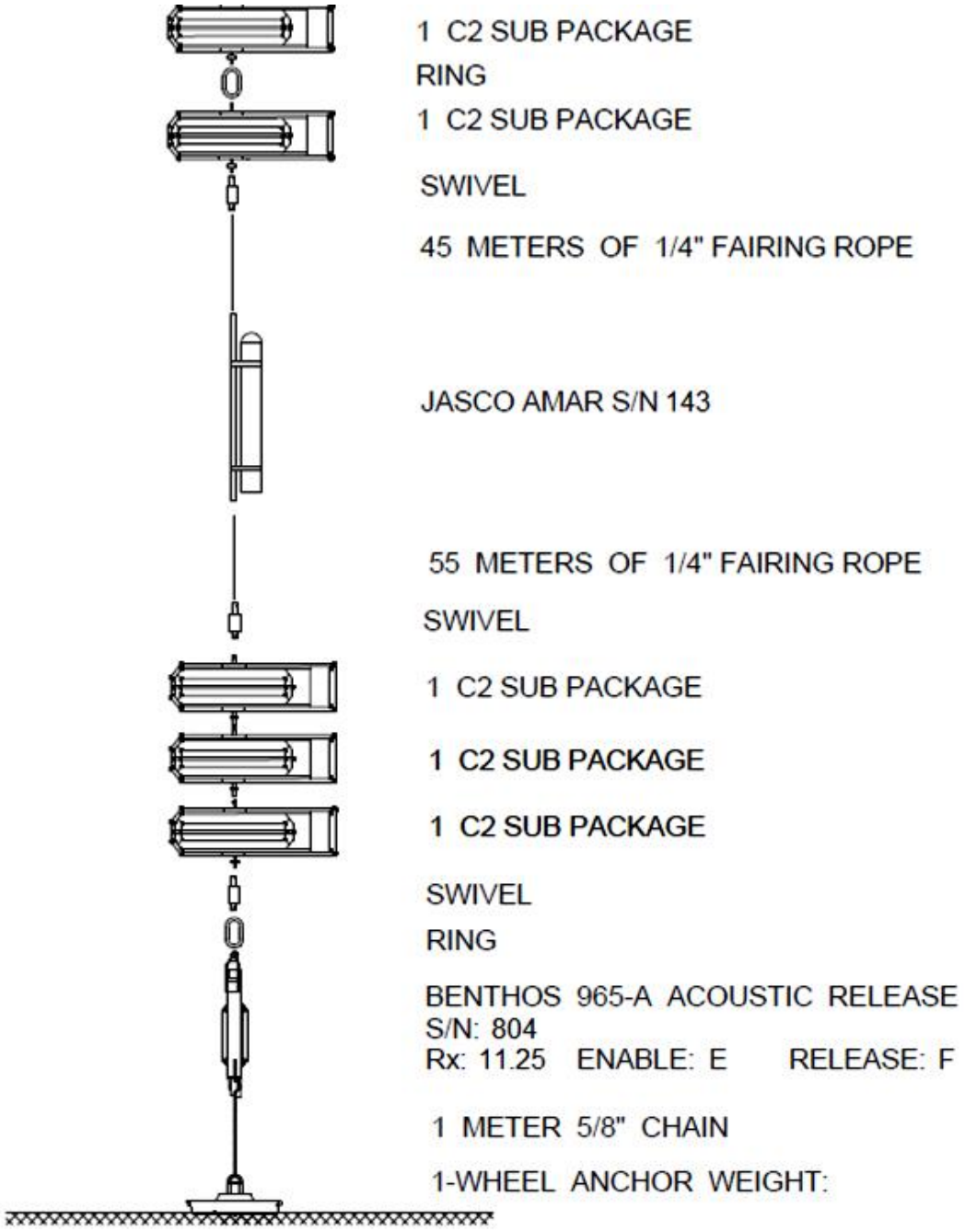


**Figure 3.** Sample mooring configuration similar to those employed at MidGul for the Winter 2013-14 and Summer 2014 deployments. Summer 2014 deployment also included a MicroCAT recorder mounted just below AMAR recorder. Figure provided by J. Barthelotte with revisions by N. Cochrane.

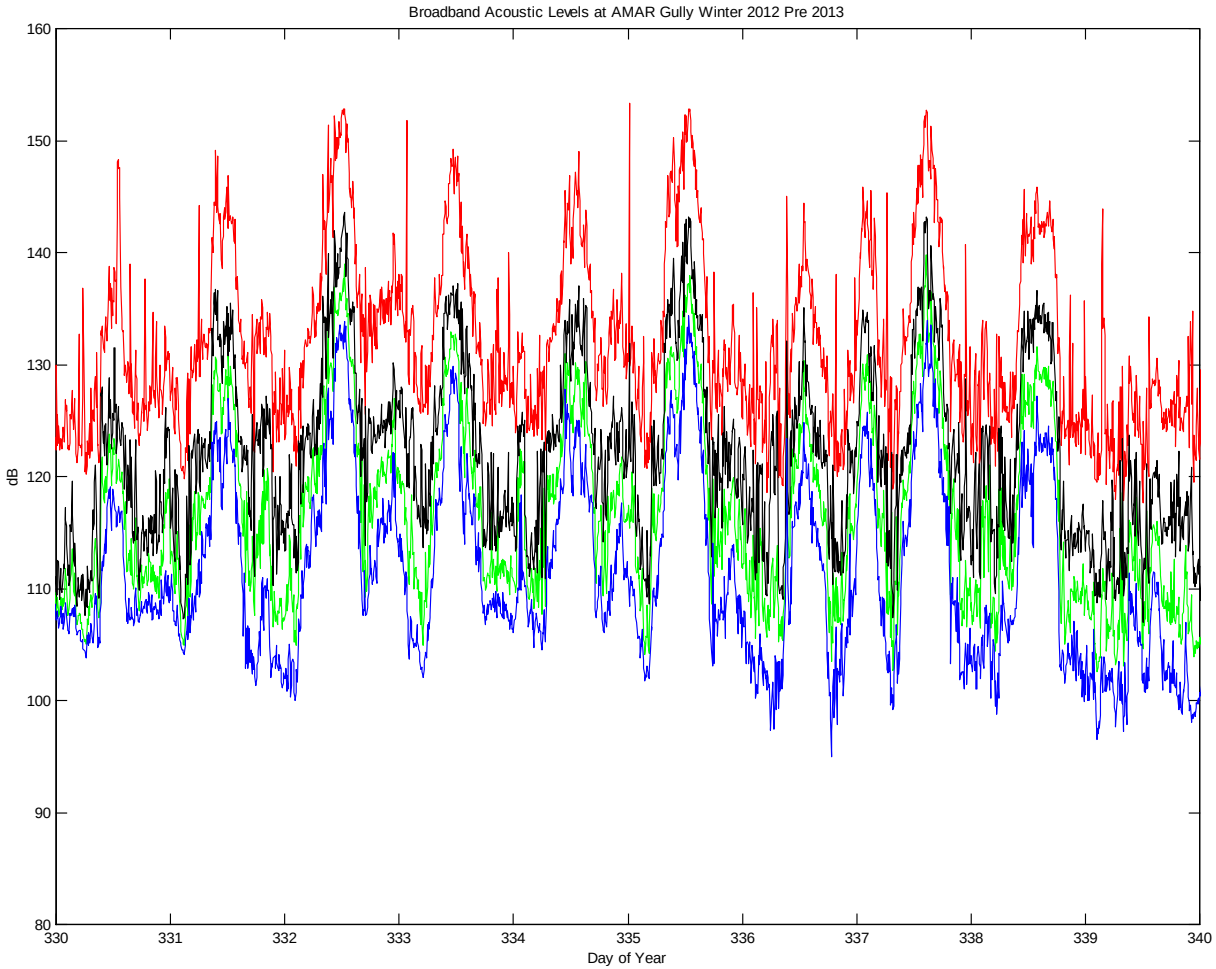


**Figure 4.** Sample broadband acoustic levels at MidGul for a 10 day period during Winter 2012–13 deployment. Red – Maximum instantaneous 0–peak acoustic amplitude over consecutive 300 s recording intervals. Green - RMS amplitude averaged over same 300 s interval. Black - Maximum RMS amplitude averaged over any consecutive 1 s interval within 300 s interval. Blue - Minimum RMS level averaged over any consecutive 1 s interval within 300 s interval.

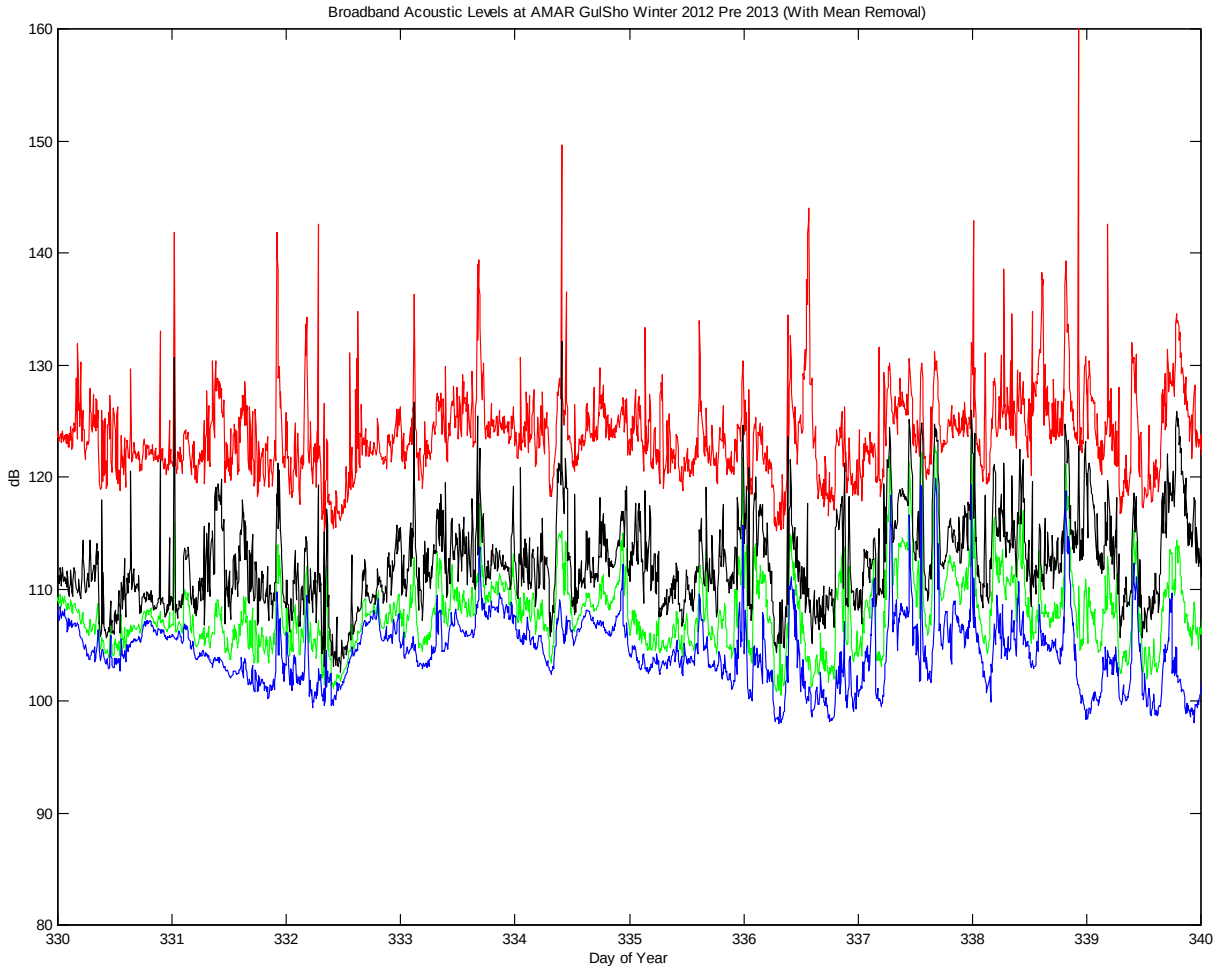


**Figure 5.** Sample broadband acoustic levels at GulSho for a 10 day period during Winter 2012–13 deployment. Red – Maximum instantaneous 0 – peak acoustic amplitude over consecutive 300 s recording intervals. Green – RMS amplitude averaged over same 300 s interval. Black – Maximum RMS amplitude averaged over any consecutive 1 s interval within 300 s interval. Blue – Minimum RMS level averaged over any consecutive 1 s interval within 300 s interval.

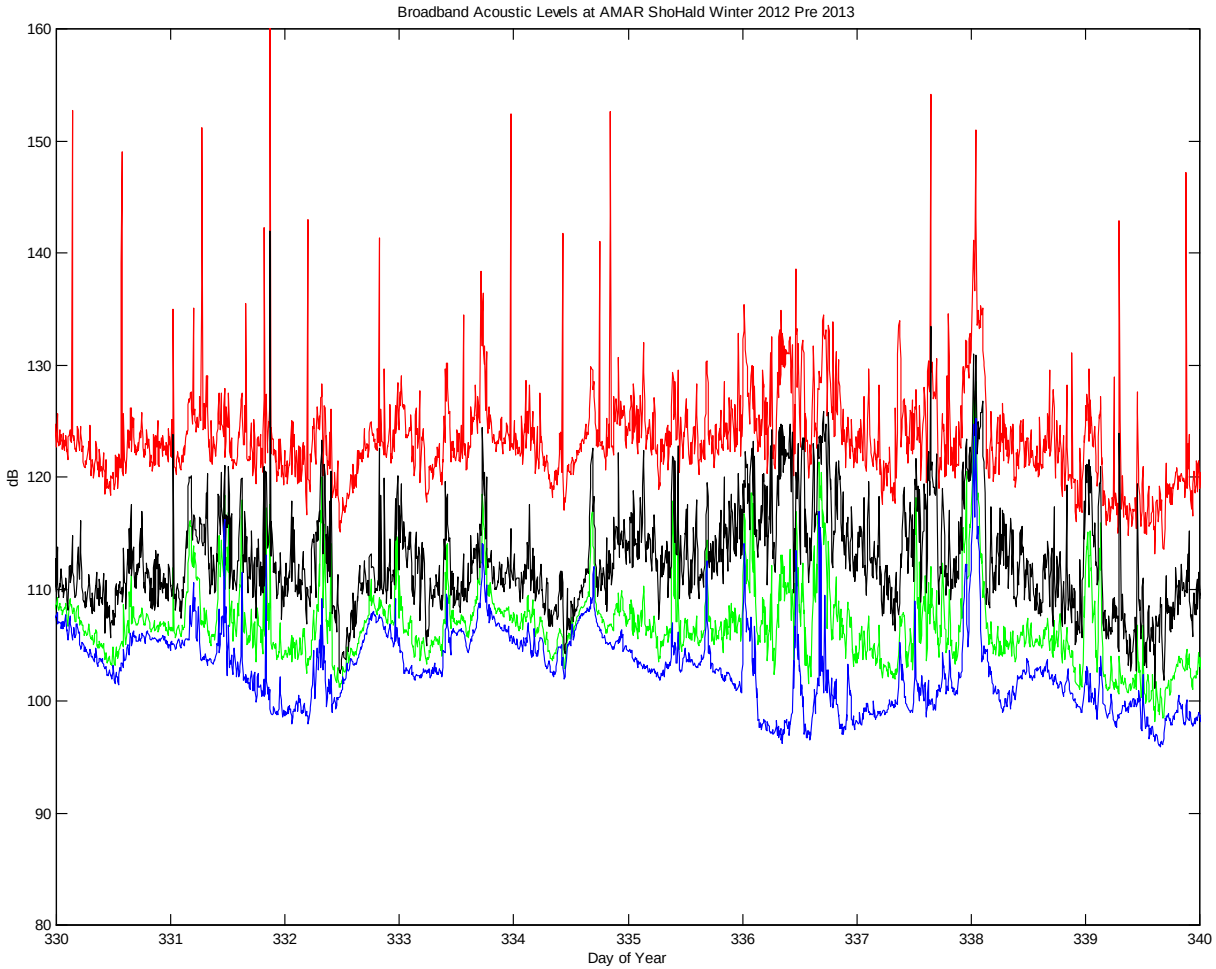


**Figure 6.** Sample broadband acoustic levels at ShoHald for a 10 day period during Winter 2012–13 deployment. Red – Maximum instantaneous 0 – peak acoustic amplitude over consecutive 300 s recording intervals. Green – RMS amplitude averaged over same 300 s interval. Black – Maximum RMS amplitude averaged over any consecutive 1 s interval within 300 s interval. Blue – Minimum RMS level averaged over any consecutive 1 s interval within 300 s interval.

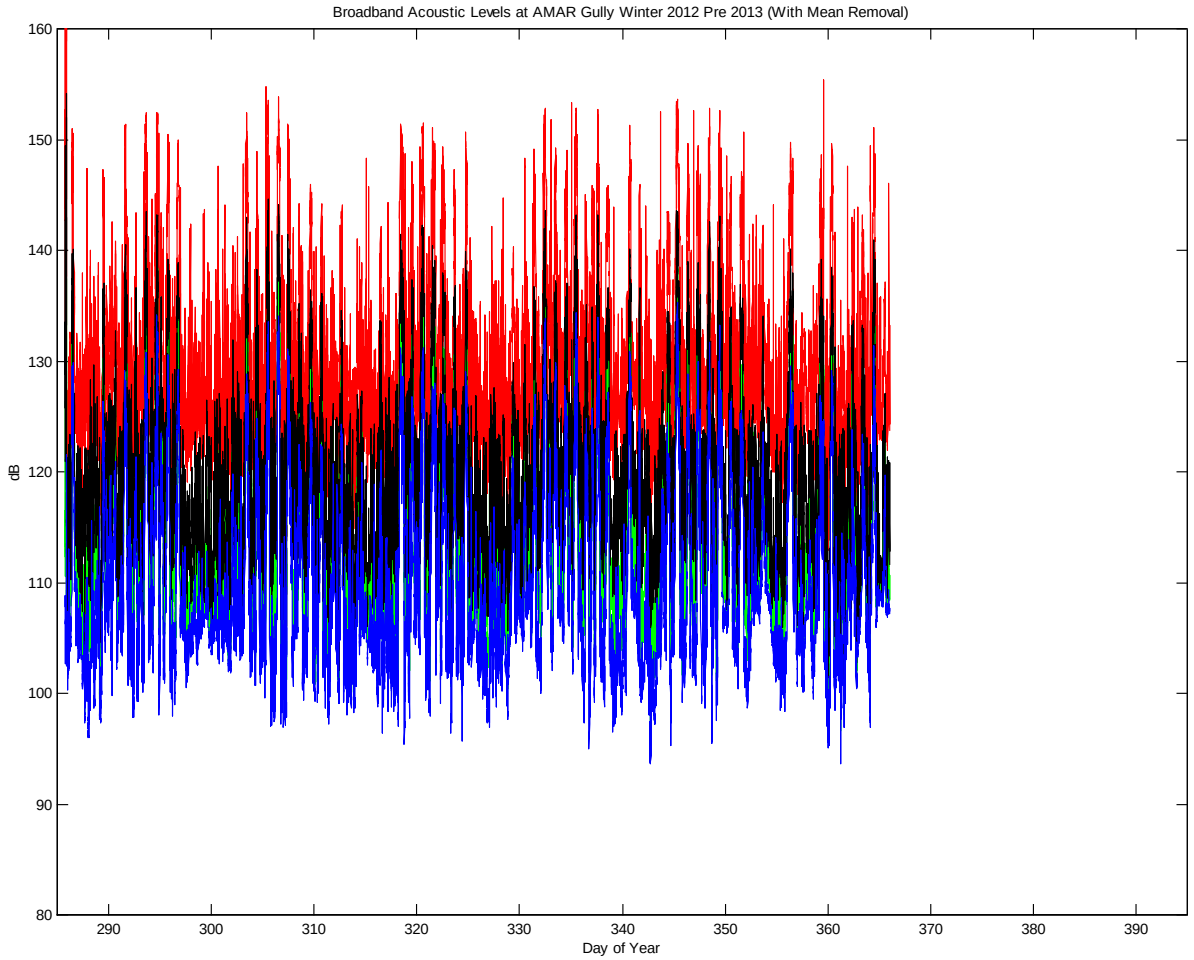


**Figure 7.** Sample broadband acoustic levels at MidGul for Year 2012 portion of Winter 2012–13 deployment. Red – Maximum instantaneous 0 – peak acoustic amplitude over consecutive 300 s recording intervals. Green – RMS amplitude averaged over same 300 s interval. Black – Maximum RMS amplitude averaged over any consecutive 1 s interval within 300 s interval. Blue – Minimum RMS level averaged over any consecutive 1 s interval within 300 s interval.

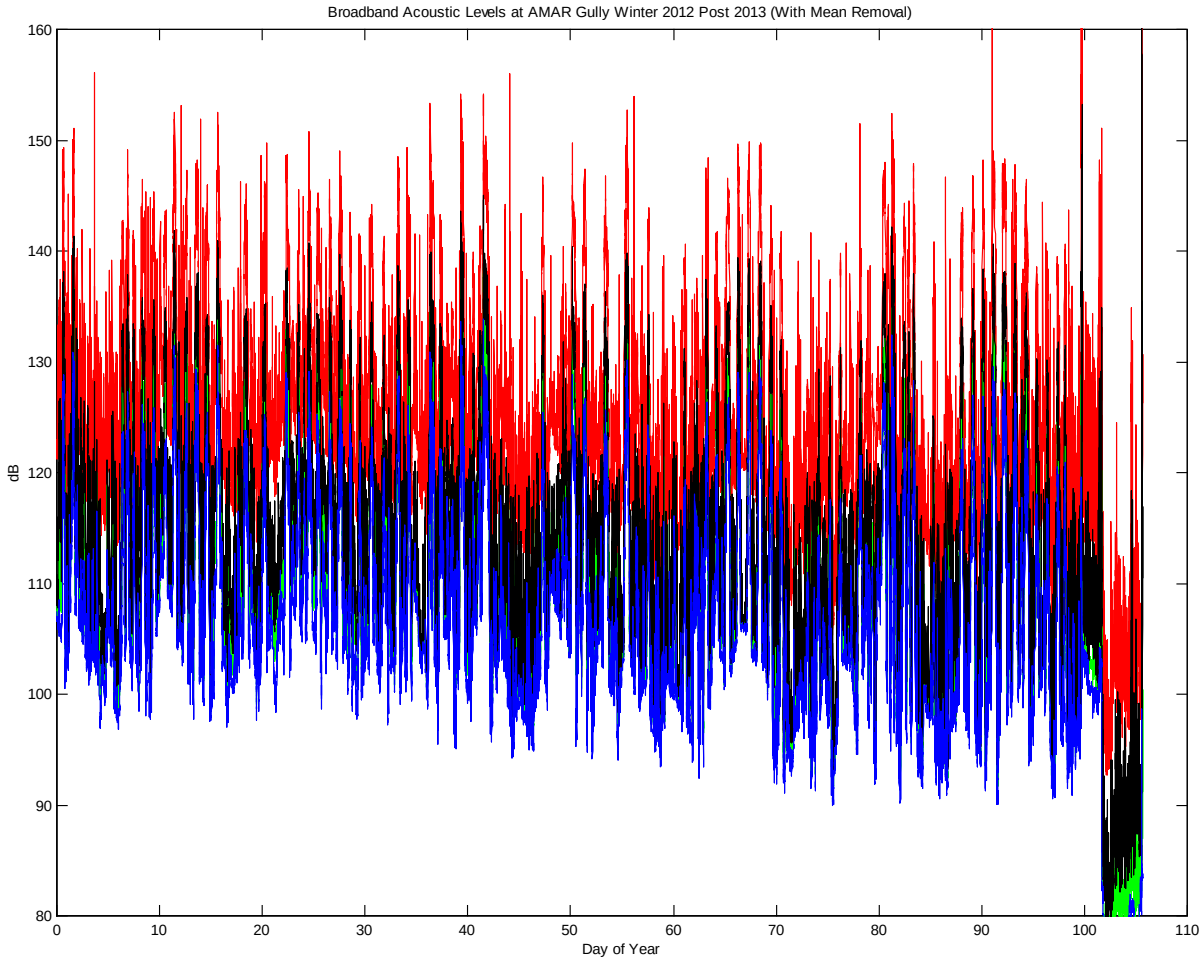


**Figure 8.** Sample broadband acoustic levels at MidGul for Year 2013 portion of Winter 2012–13 deployment. Red – Maximum instantaneous 0 – peak acoustic amplitude over consecutive 300 s recording intervals. Green – RMS amplitude averaged over same 300 s interval. Black – Maximum RMS amplitude averaged over any consecutive 1 s interval within 300 s interval. Blue – Minimum RMS level averaged over any consecutive 1 s interval within 300 s interval.

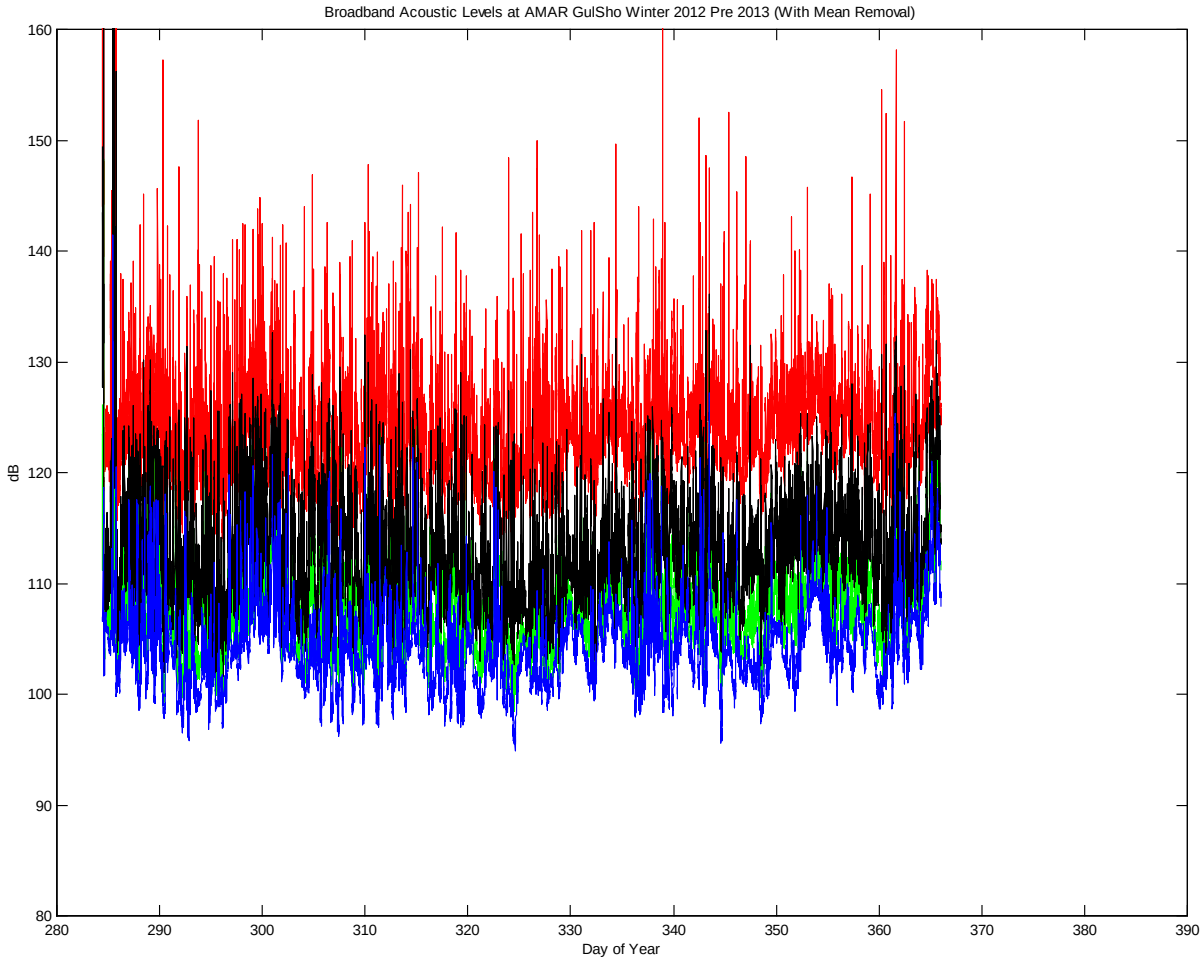


**Figure 9.** Sample broadband acoustic levels at GulSho for Year 2012 portion of Winter 2012–13 deployment. Red – Maximum instantaneous 0 – peak acoustic amplitude over consecutive 300 s recording intervals. Green – RMS amplitude averaged over same 300 s interval. Black – Maximum RMS amplitude averaged over any consecutive 1 s interval within 300 s interval. Blue – Minimum RMS level averaged over any consecutive 1 s interval within 300 s interval.

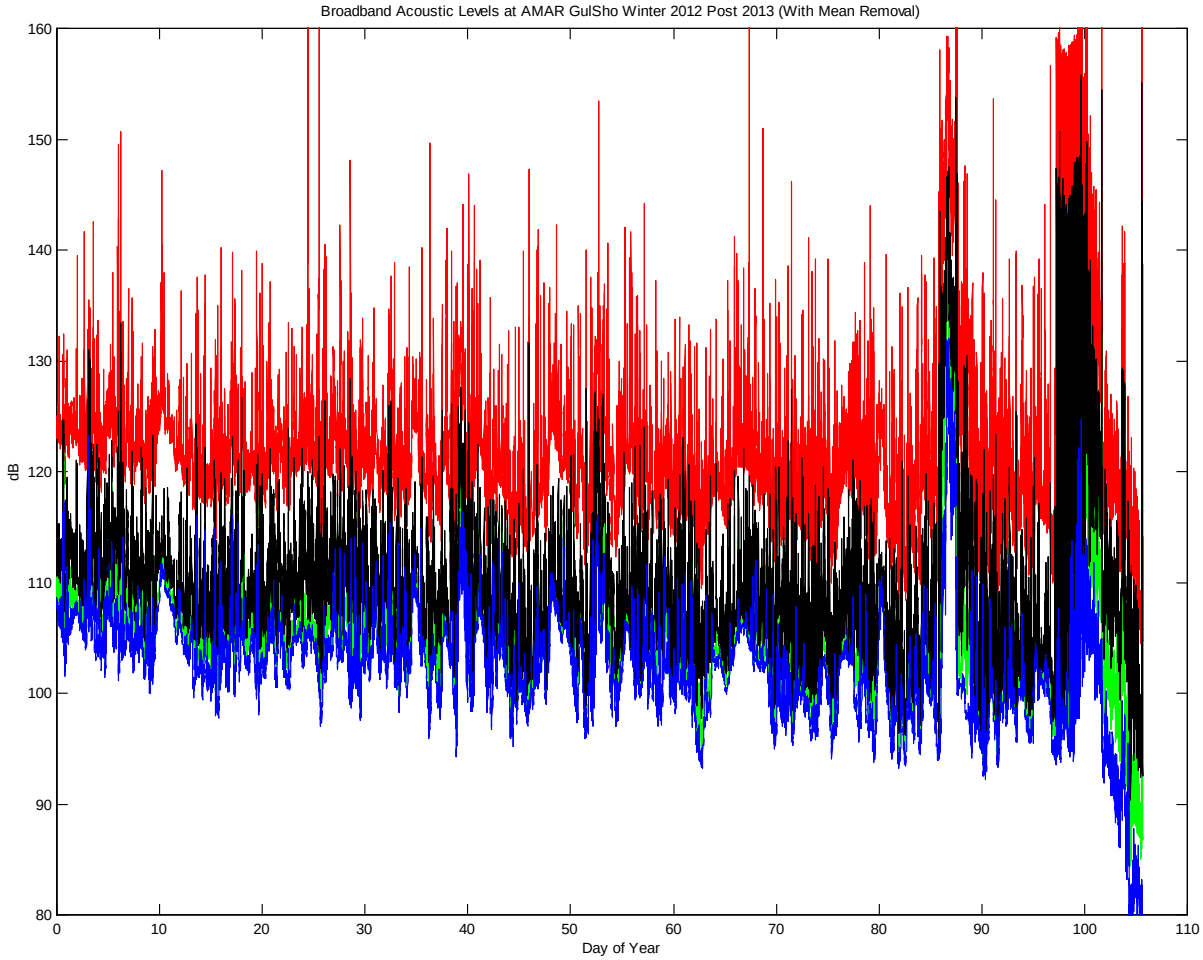


**Figure 10.** Sample broadband acoustic levels at GulSho for Year 2013 portion of Winter 2012–13 deployment. Red – Maximum instantaneous 0 – peak acoustic amplitude over consecutive 300 s recording intervals. Green – RMS amplitude averaged over same 300 s interval. Black – Maximum RMS amplitude averaged over any consecutive 1 s interval within 300 s interval. Blue – Minimum RMS level averaged over any consecutive 1 s interval within 300 s interval.

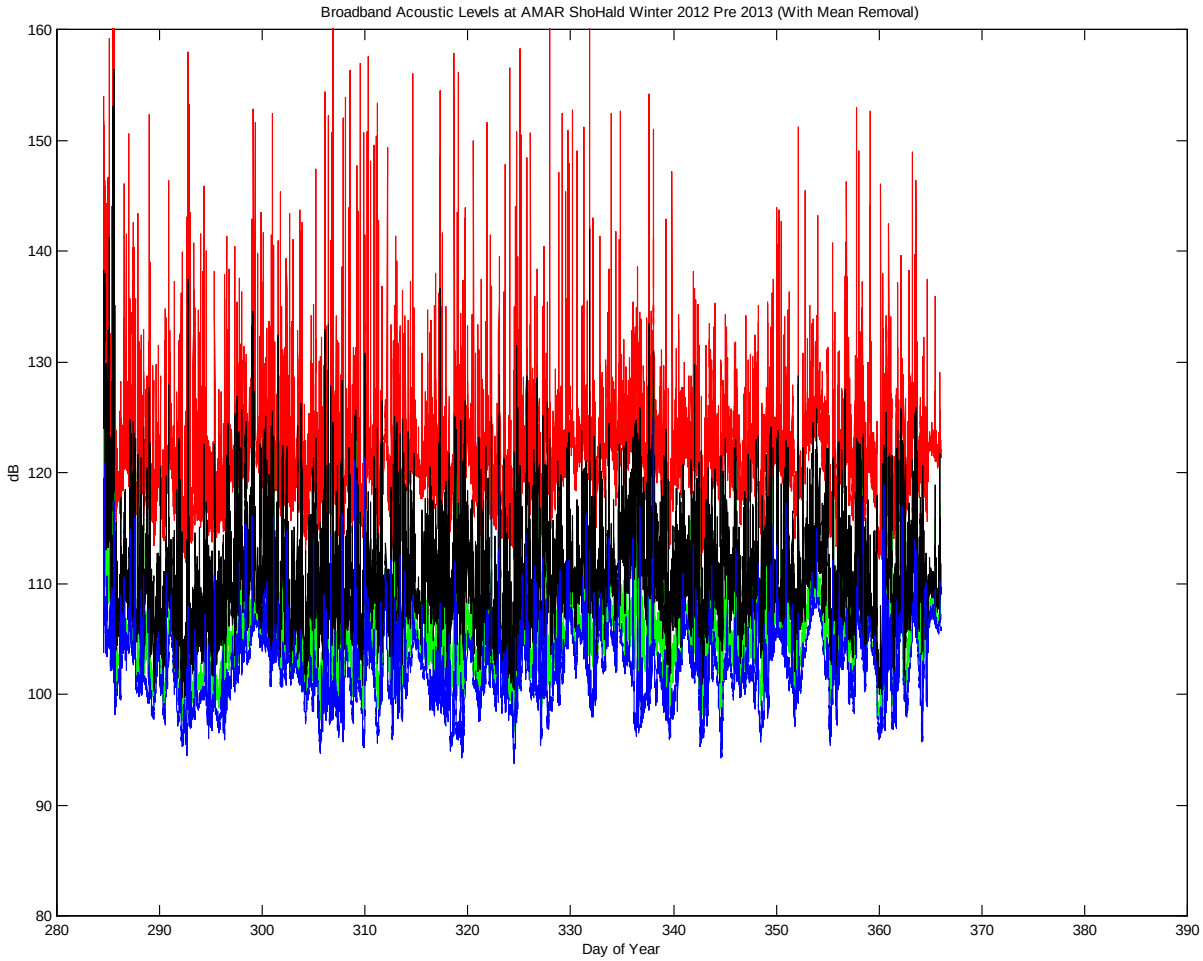


**Figure 11.** Sample broadband acoustic levels at ShoHald for Year 2012 portion of Winter 2012–13 deployment. Red – Maximum instantaneous 0 – peak acoustic amplitude over consecutive 300 s recording intervals. Green – RMS amplitude averaged over same 300 s interval. Black – Maximum RMS amplitude averaged over any consecutive 1 s interval within 300 s interval. Blue – Minimum RMS level averaged over any consecutive 1 s interval within 300 s interval.

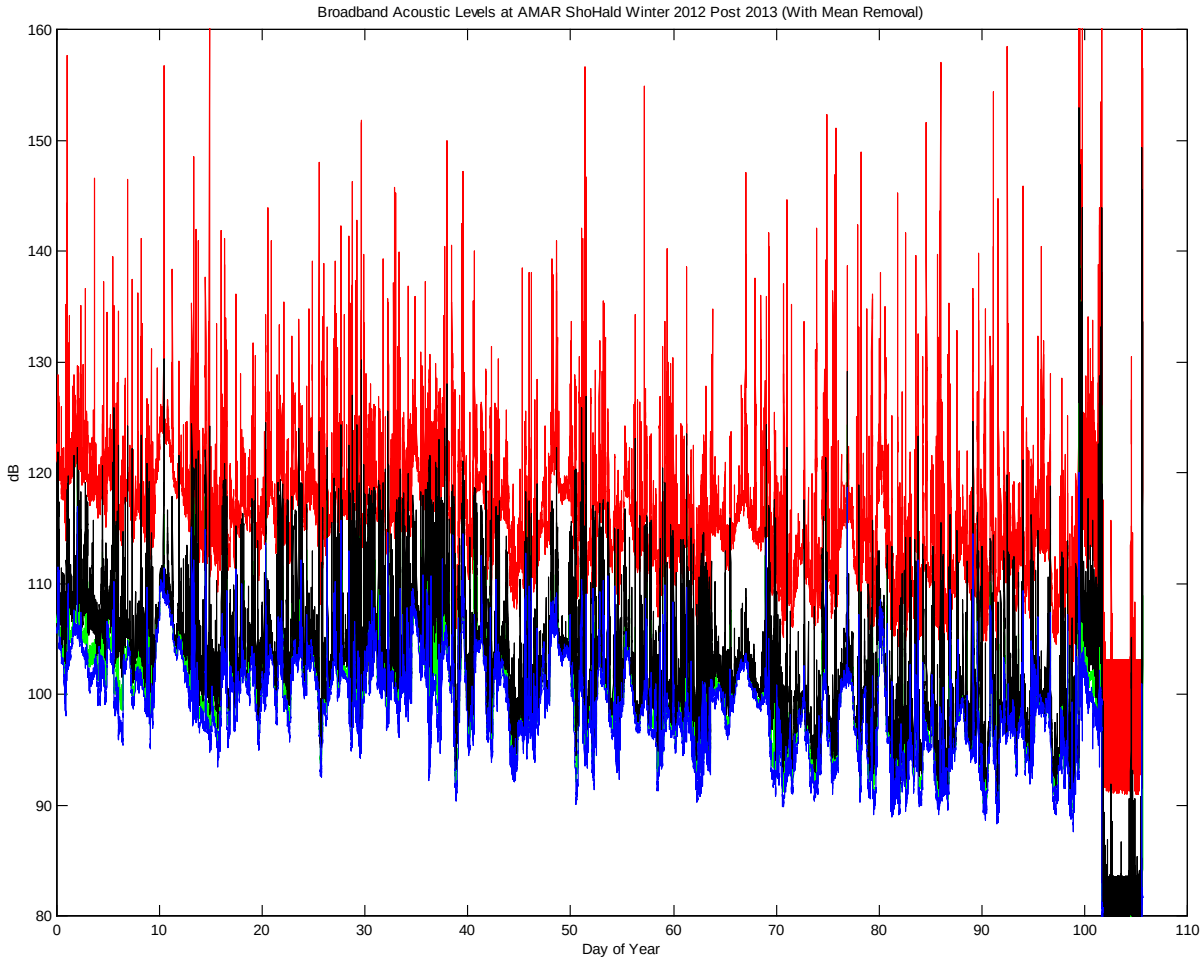


**Figure 12.** Sample broadband acoustic levels at ShoHald for Year 2013 portion of Winter 2012–13 deployment. Red – Maximum instantaneous 0 – peak acoustic amplitude over consecutive 300 s recording intervals. Green – RMS amplitude averaged over same 300 s interval. Black – Maximum RMS amplitude averaged over any consecutive 1 s interval within 300 s interval. Blue – Minimum RMS level averaged over any consecutive 1 s interval within 300 s interval.

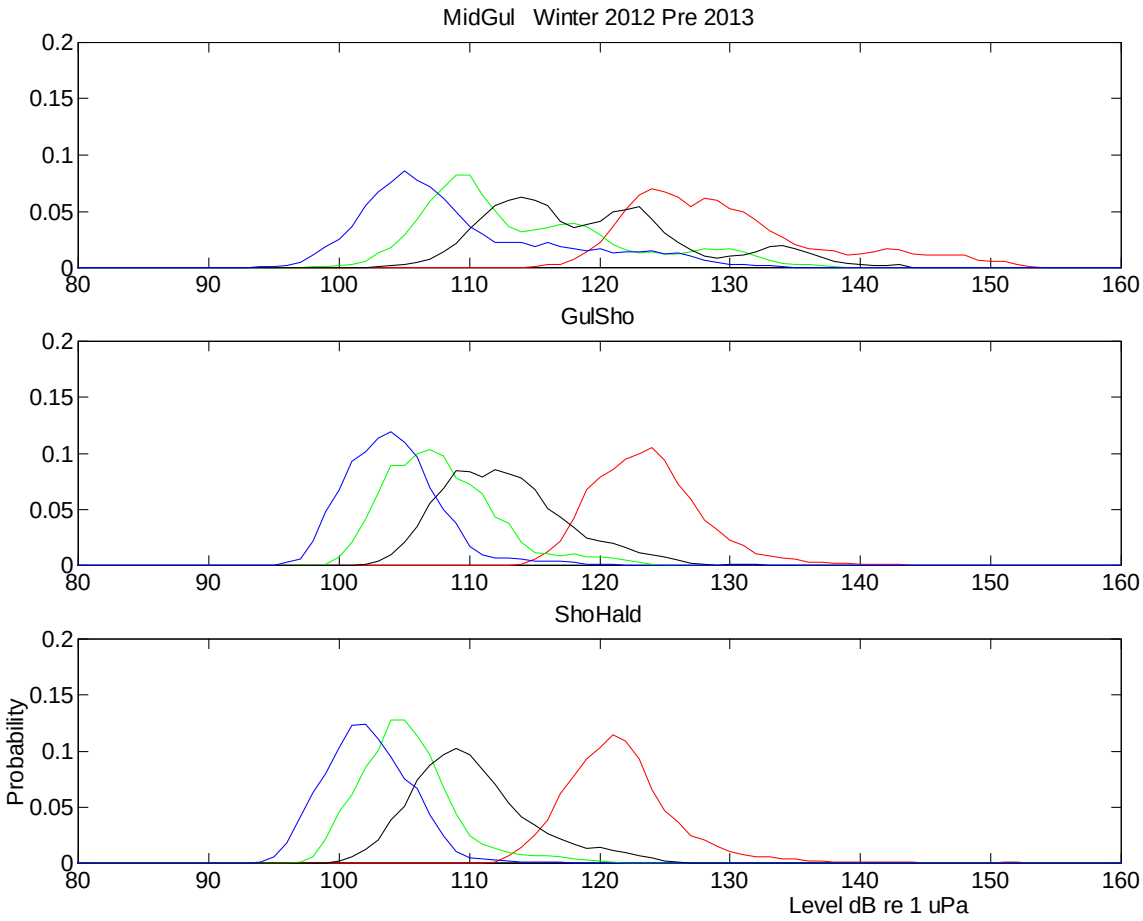


**Figure 13.** Instrumental signal level probability density functions for pre New Year, Winter 2012-13 deployment period (DOY 286.0 to 366.0) at MidGul, GulSho, and ShoHald. Red - Maximum 0-peak acoustic amplitudes over consecutive 300 s sampling intervals. Green - RMS amplitudes averaged over consecutive 300 s intervals. Black - Maximum RMS amplitudes as averaged over any consecutive 1 s interval within 300 s interval. Blue - Minimum RMS amplitudes as averaged over any consecutive 1 s interval within 300 s intervals.

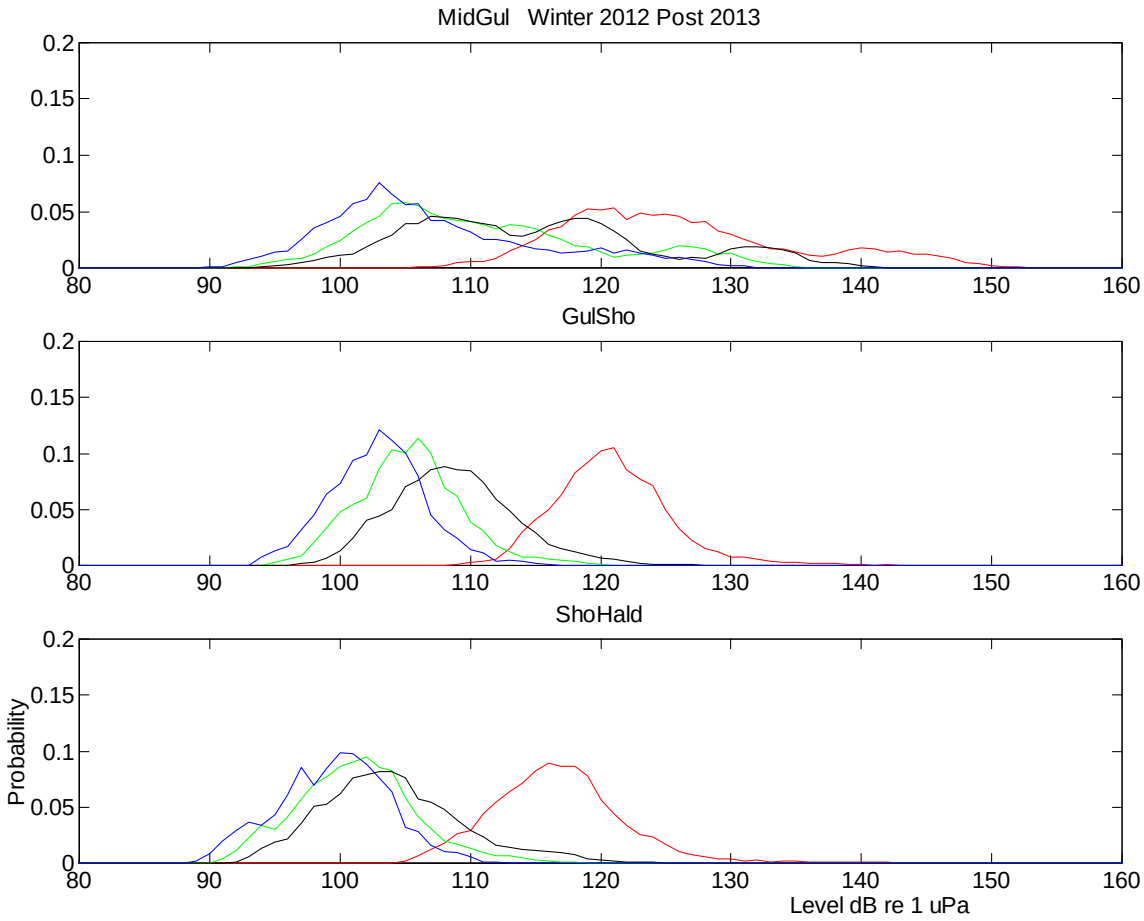


**Figure 14.** Instrumental signal level probability density functions for post New Year, Winter 2012-13 deployment period (DOY 0.0 to 85.0) at MidGul, GulSho, and ShoHald. Red - Maximum 0-peak acoustic amplitudes over consecutive 300 s sampling intervals. Green - RMS amplitudes averaged over consecutive 300 s intervals. Black - Maximum RMS amplitudes as averaged over any consecutive 1 s interval within 300 s interval. Blue - Minimum RMS amplitudes as averaged over any consecutive 1 s interval within 300 s intervals.

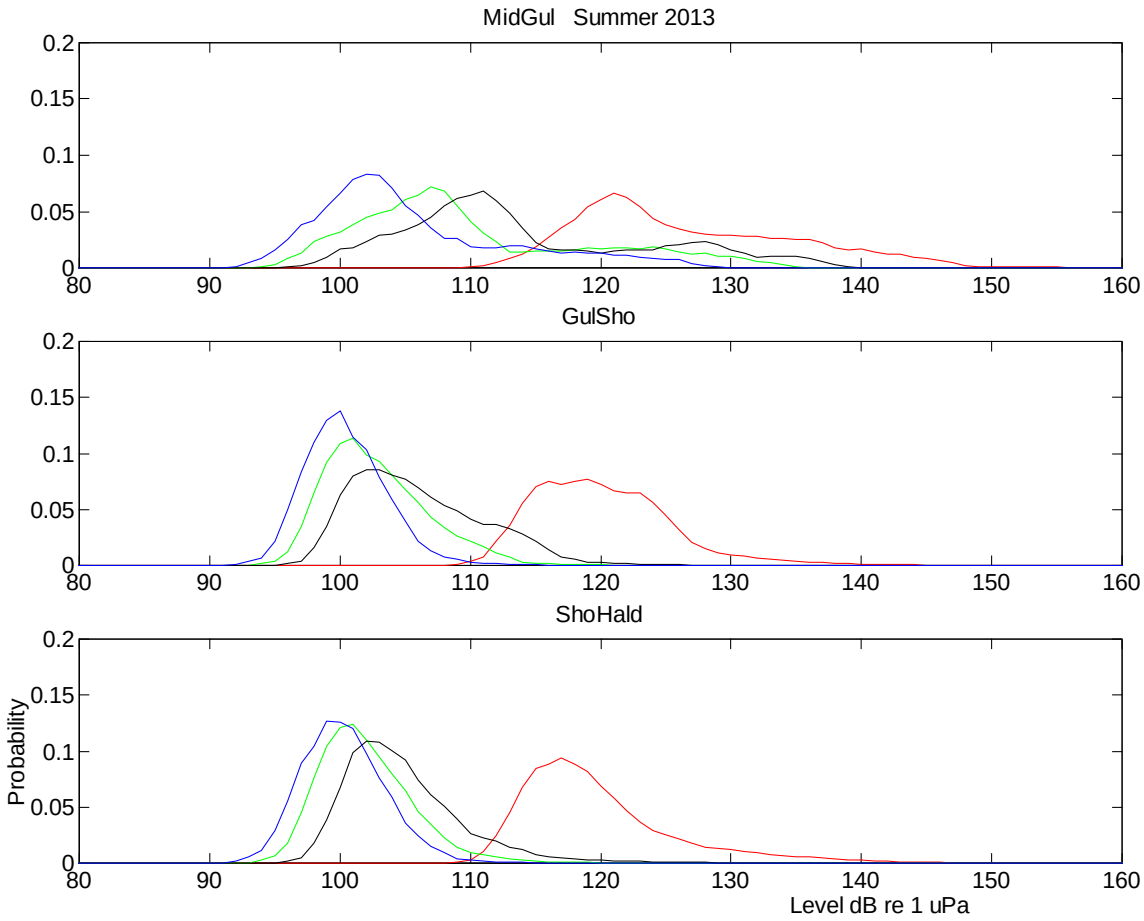


**Figure 15.** Instrumental signal level probability density functions for Summer 2013 deployment period (DOY 128.0 to 266.0) at MidGul, GulSho, and ShoHald. Red - Maximum 0-peak acoustic amplitudes over consecutive 300 s sampling intervals. Green - RMS amplitudes averaged over consecutive 300 s intervals. Black - Maximum RMS amplitudes as averaged over any consecutive 1 s interval within 300 s interval. Blue - Minimum RMS amplitudes as averaged over any consecutive 1 s interval within 300 s intervals.

.

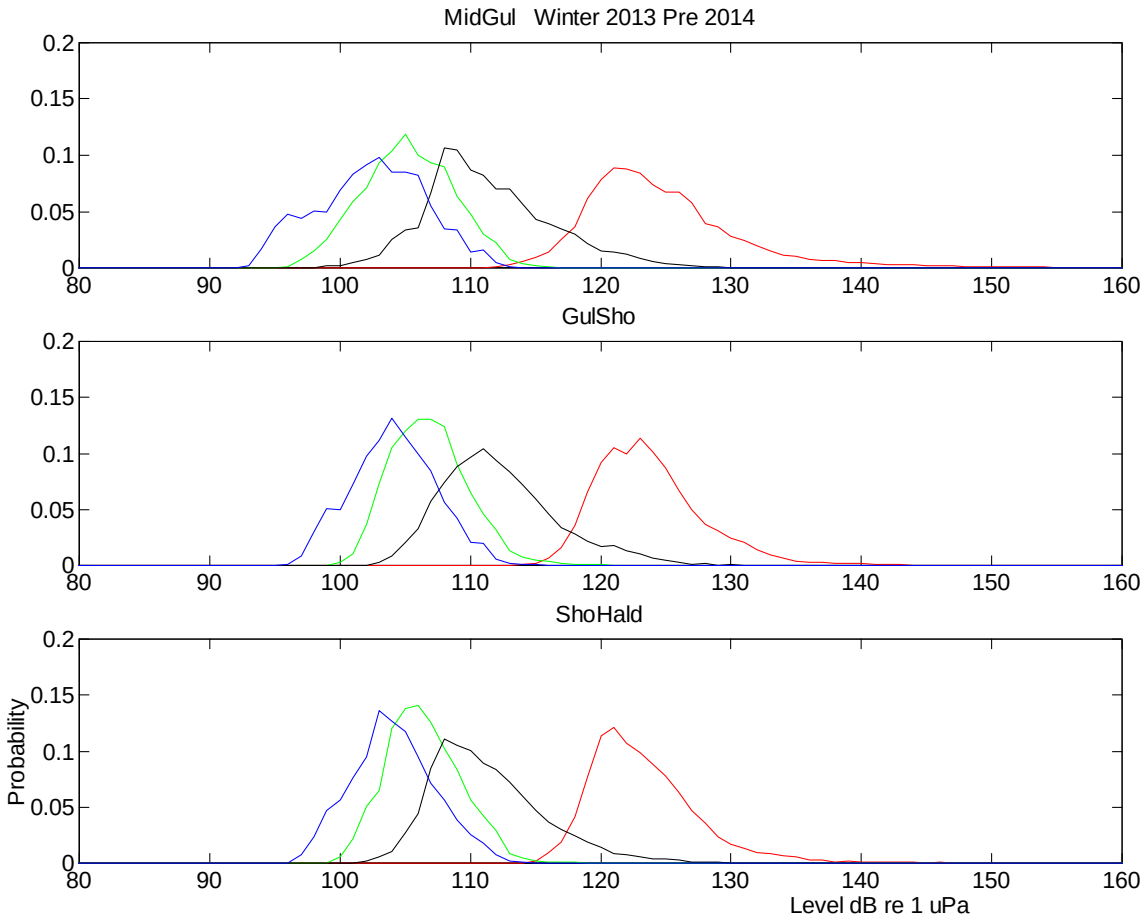


**Figure 16.** Instrumental signal level probability density functions for pre New Year, Winter 2013-14 deployment period (DOY 319.0 to 365.0) at MidGul, GulSho, and ShoHald. Red - Maximum 0-peak acoustic amplitudes over consecutive 300 s sampling intervals. Green - RMS amplitudes averaged over consecutive 300 s intervals. Black - Maximum RMS amplitudes as averaged over any consecutive 1 s interval within 300 s interval. Blue - Minimum RMS amplitudes as averaged over any consecutive 1 s interval within 300 s intervals.

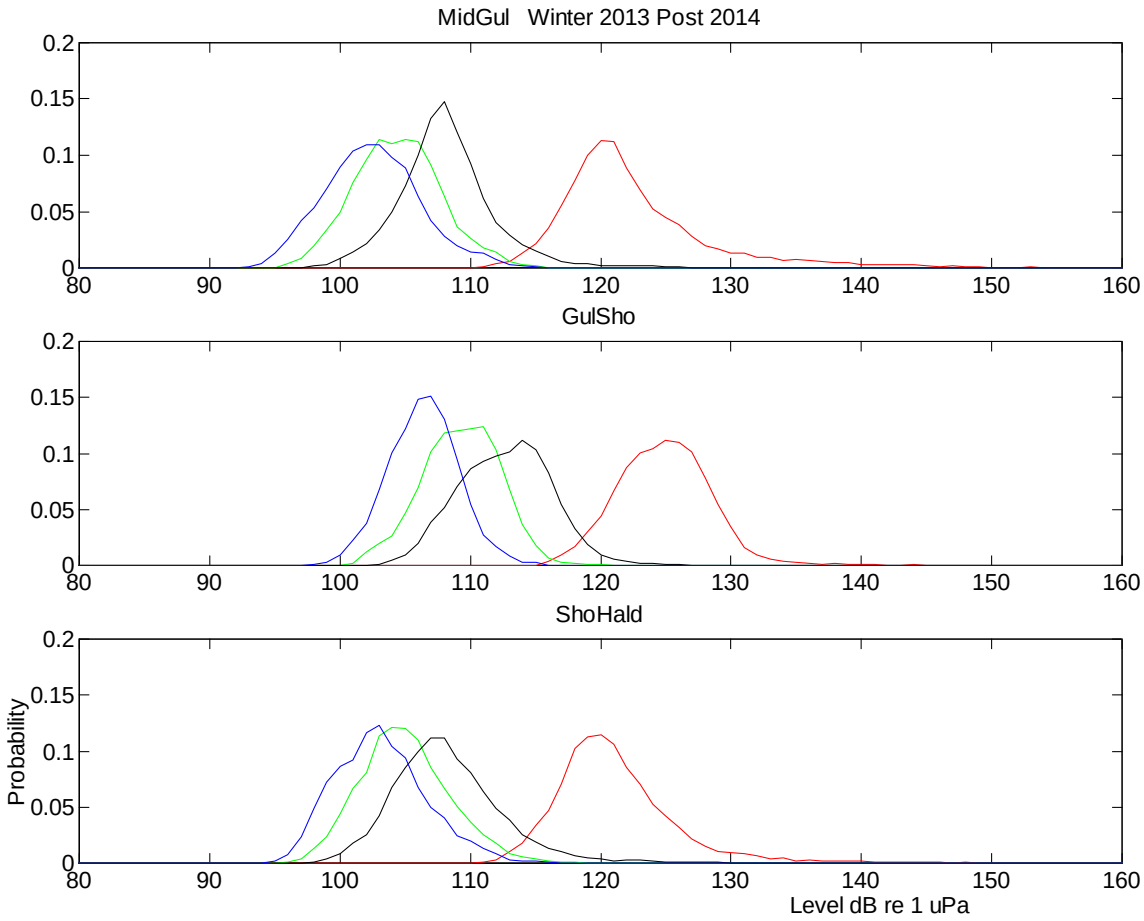


**Figure 17.** Instrumental signal level probability density functions for post New Year, Winter 2013-14 deployment period (DOY 0.0 to 95.0) at MidGul, GulSho, and ShoHald. Red - Maximum 0-peak acoustic amplitudes over consecutive 300 s sampling intervals. Green - RMS amplitudes averaged over consecutive 300 s intervals. Black - Maximum RMS amplitudes as averaged over any consecutive 1 s interval within 300 s interval. Blue - Minimum RMS amplitudes as averaged over any consecutive 1 s interval within 300 s intervals.

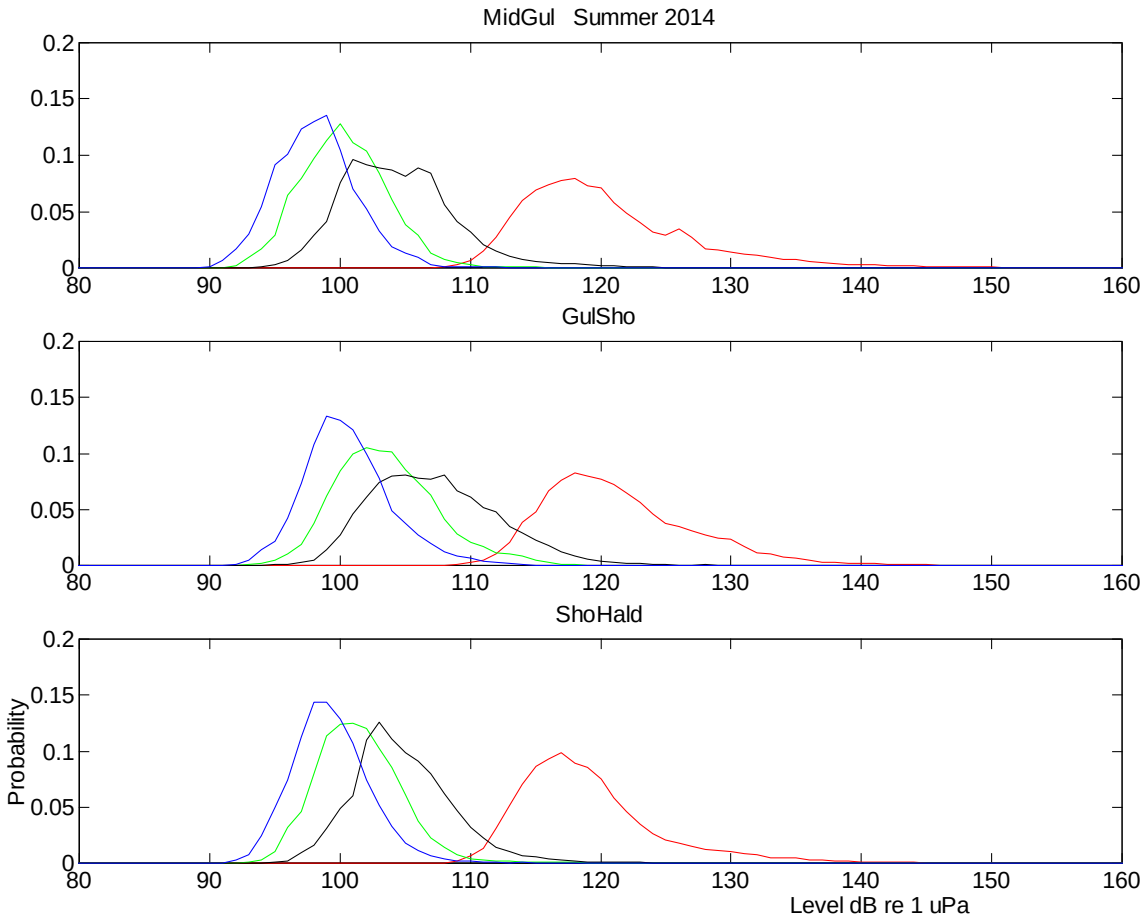


**Figure 18.** Instrumental signal level probability density functions for Summer 2014 deployment period (DOY 124.0 to 261.0) at MidGul, GulSho, and ShoHald. Red - Maximum 0-peak acoustic amplitudes over consecutive 300 s sampling intervals. Green - RMS amplitudes averaged over consecutive 300 s intervals. Black - Maximum RMS amplitudes as averaged over any consecutive 1 s interval within 300 s interval. Blue - Minimum RMS amplitudes as averaged over any consecutive 1 s interval within 300 s intervals.

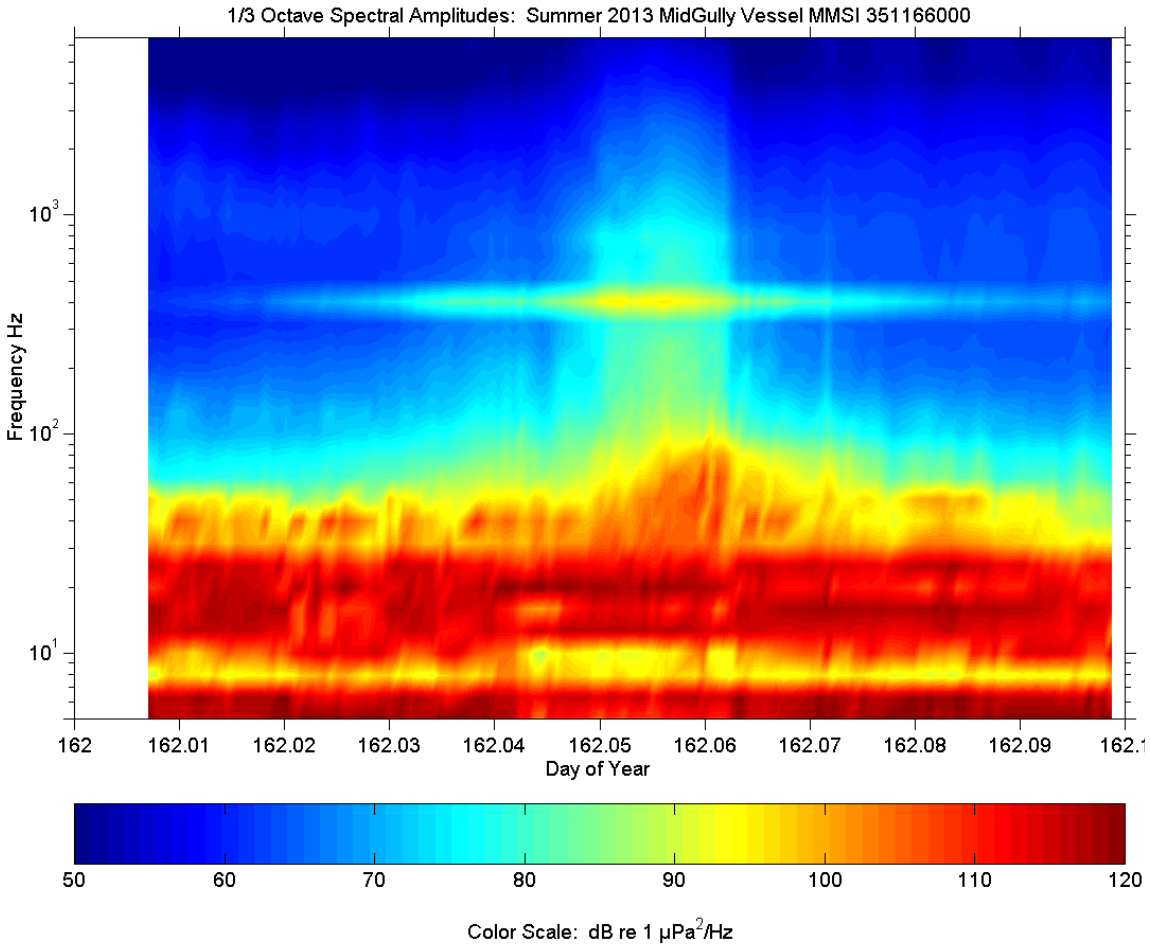


**Figure 19.** High time resolution 1/3 octave spectral section of the passage of a container vessel past MidGul at a minimum lateral range of about 2.4 km on 12 June 2013. Spectral estimates generated at 60 s time intervals except as limited by inter-record time gaps. Note the isolated prominent spectral line at about 420 Hz.

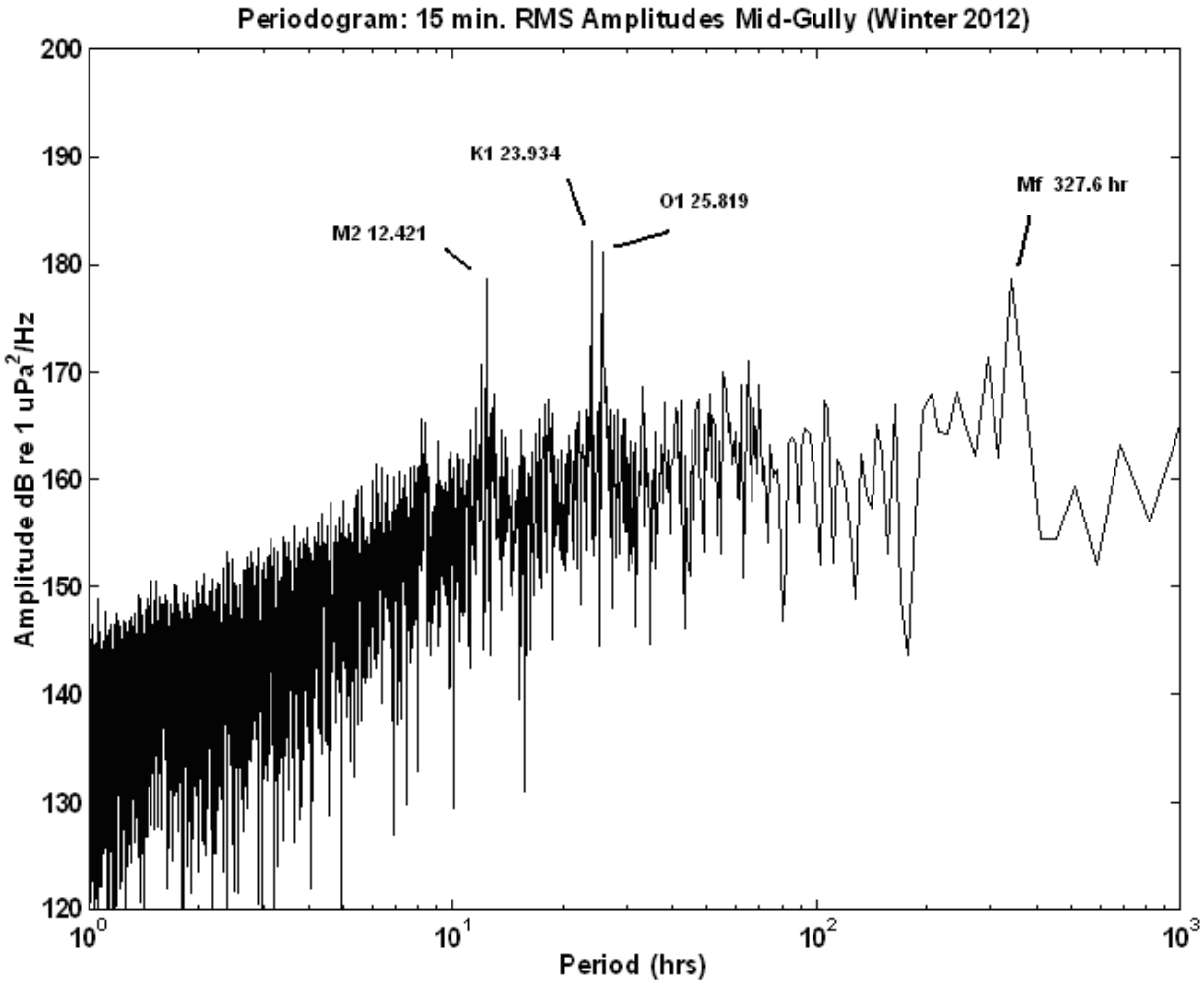


**Figure 20.** Periodogram computed from 170.67 day time series of RMS signal amplitudes sampled at 15 min intervals at MidGul during the Winter 2012-13 deployment.

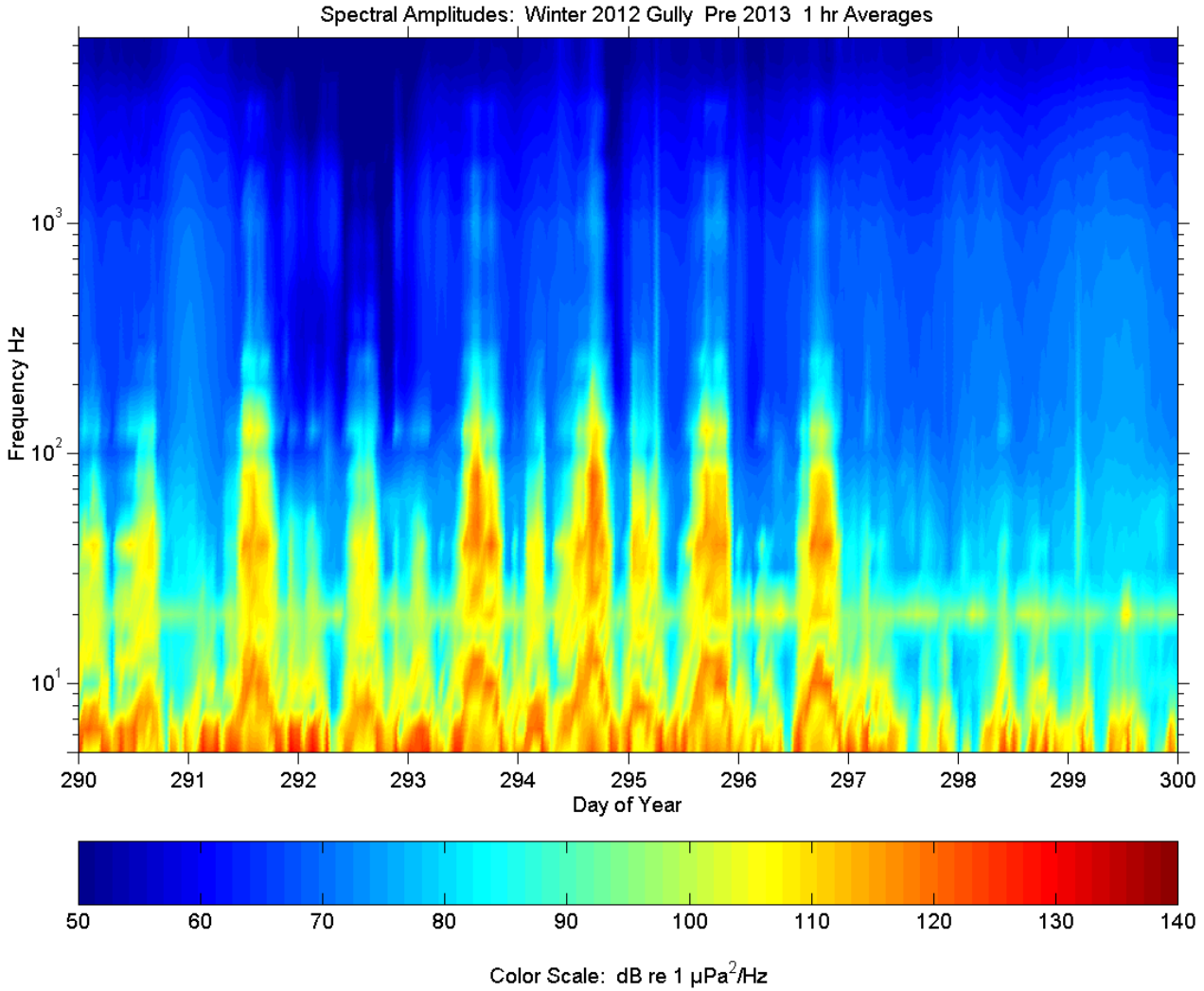


**Figure 21.** Power spectral density (1/3 octave) time x frequency section for 10 day duration sub-period expanded from Fig. A4-3-MidGul-W2012-1 to better illustrate time dependence of recorded pseudo-noise.

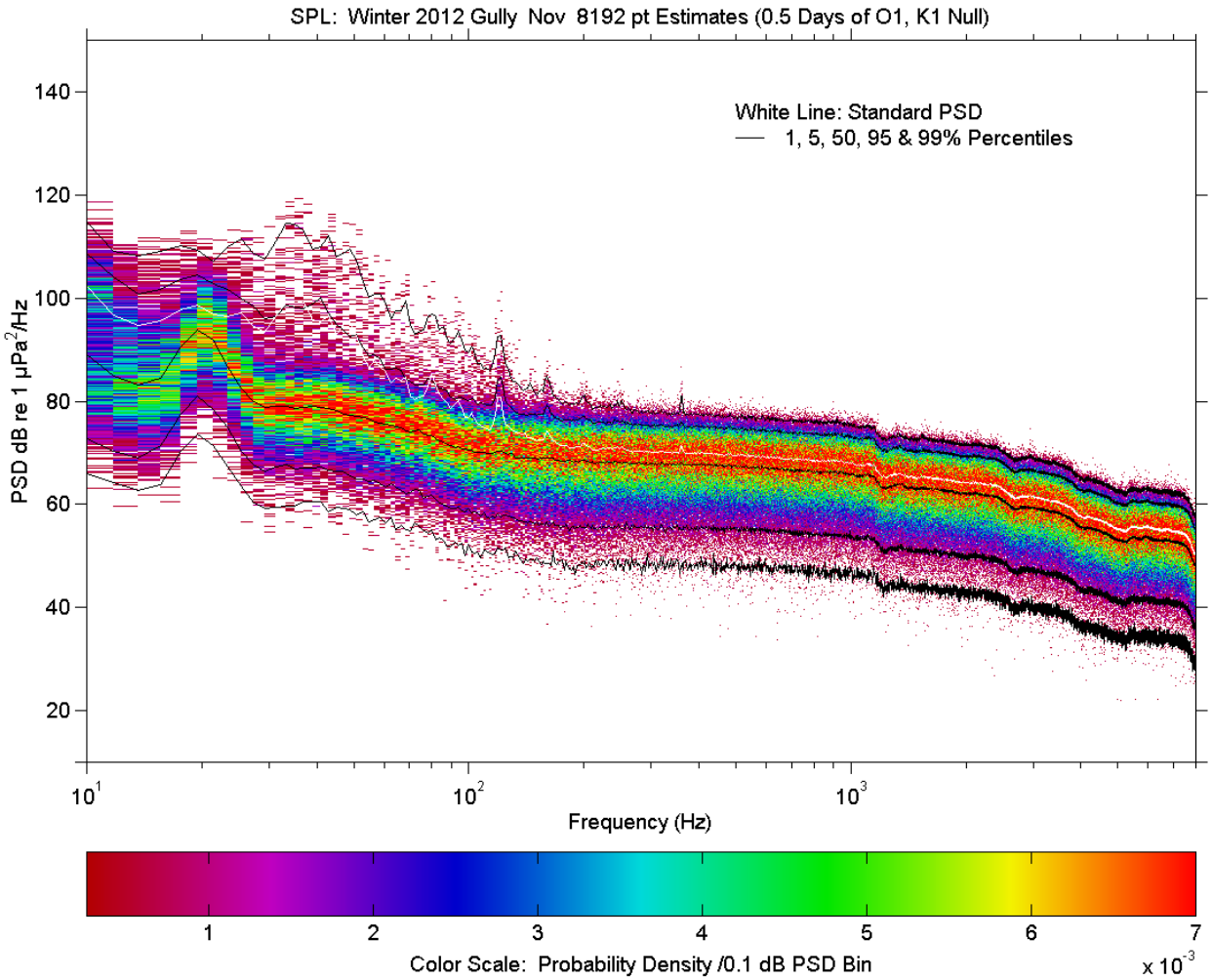


**Figure 22.** Medium resolution power spectral density with stats as in Fig. A4-2-MidGul-2012-Nov but restricting analysed data to within 1 day windows centered on predicted $O_1$, $K_1$ tidal current noise nulls.

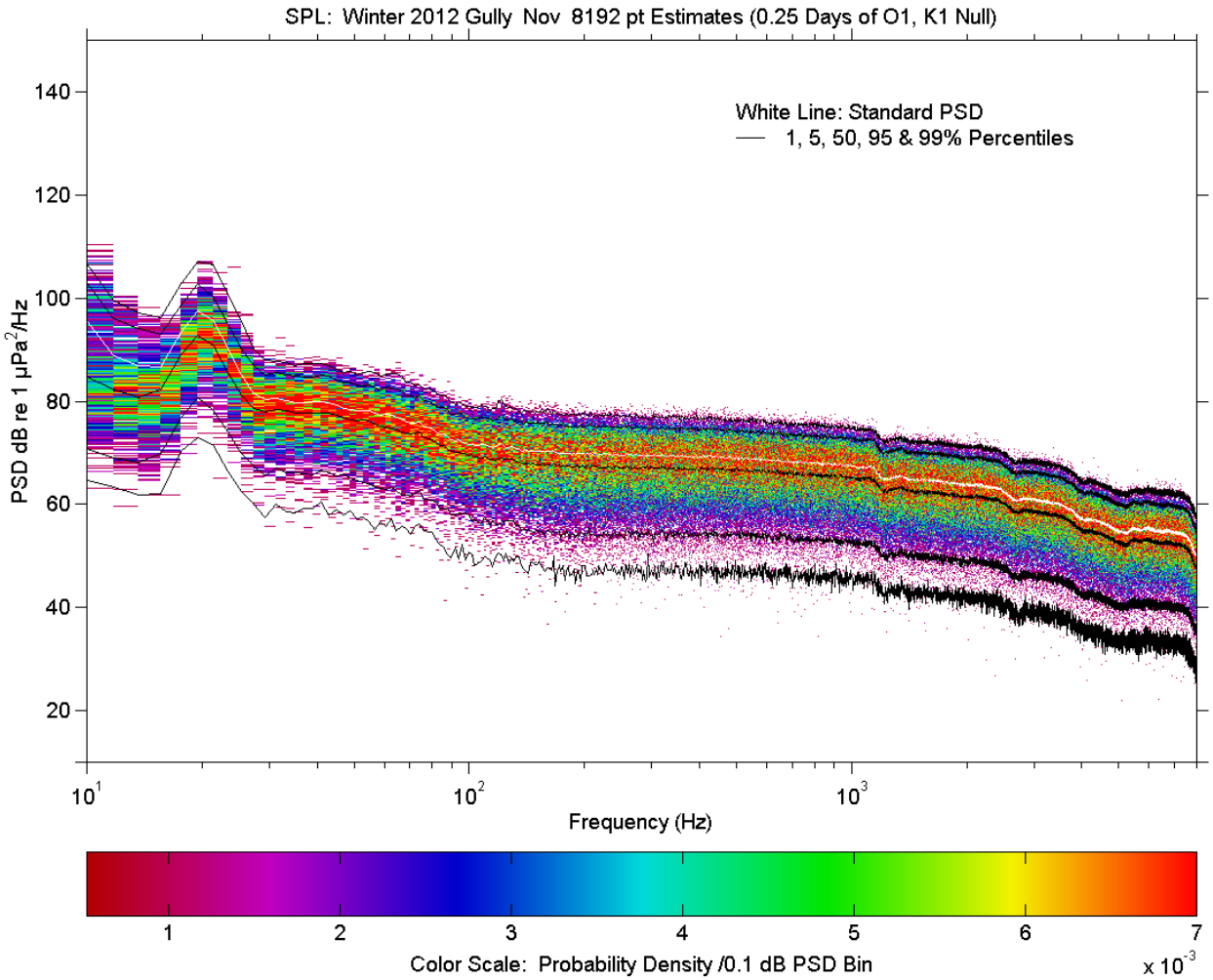


**Figure 23**. Medium resolution power spectral density with stats as in Fig. A4-2-MidGul-2012-Nov but restricting analysed data to within 0.5 day windows centered on predicted $O_1$, $K_1$ tidal current noise nulls.

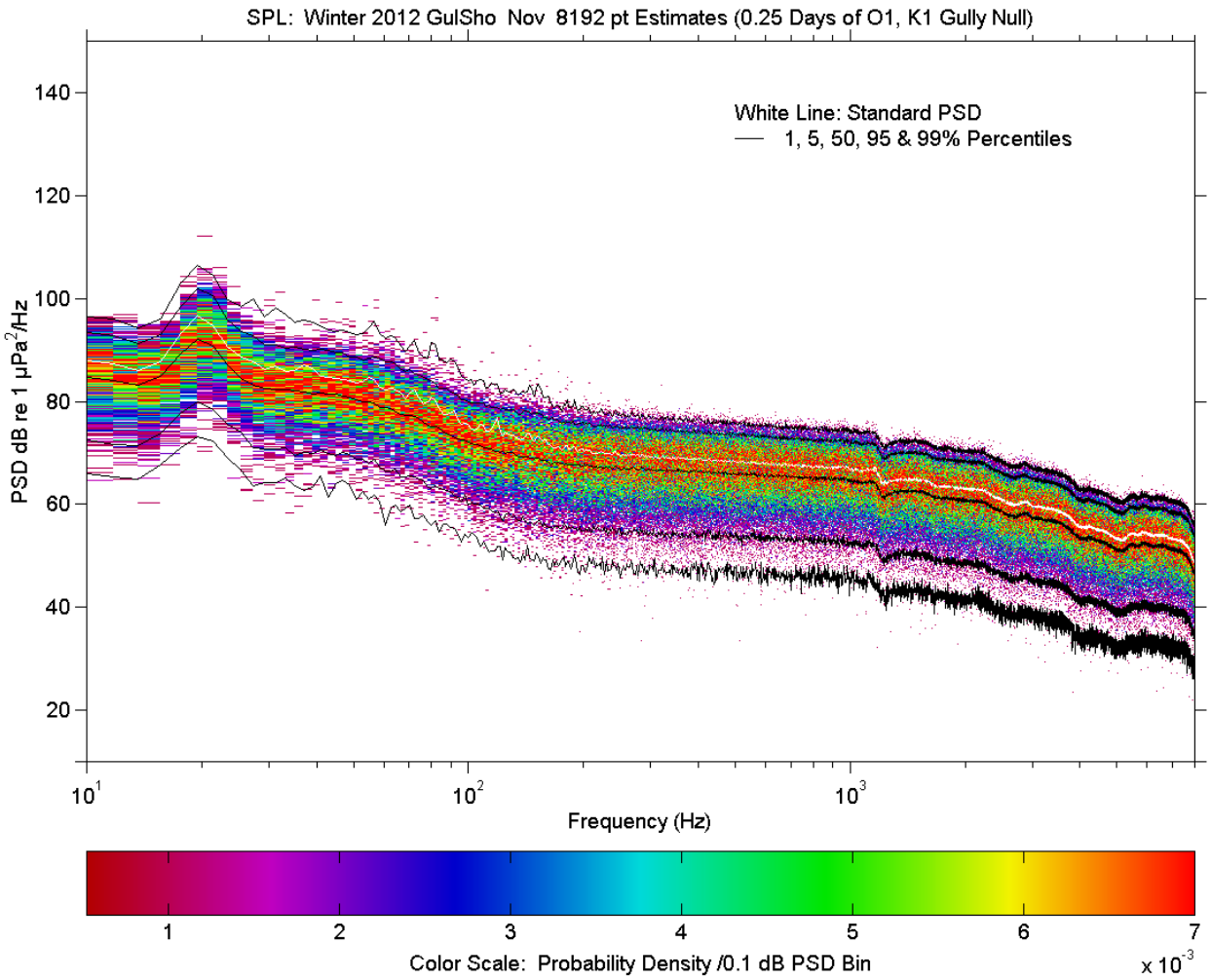


**Figure 24.** Medium resolution power spectral density with stats as in Fig. A4-2-GulSho-2012-Nov but restricting analysed data to within 0.5 day windows centered on predicted $O_1$, $K_1$ tidal current noise nulls.

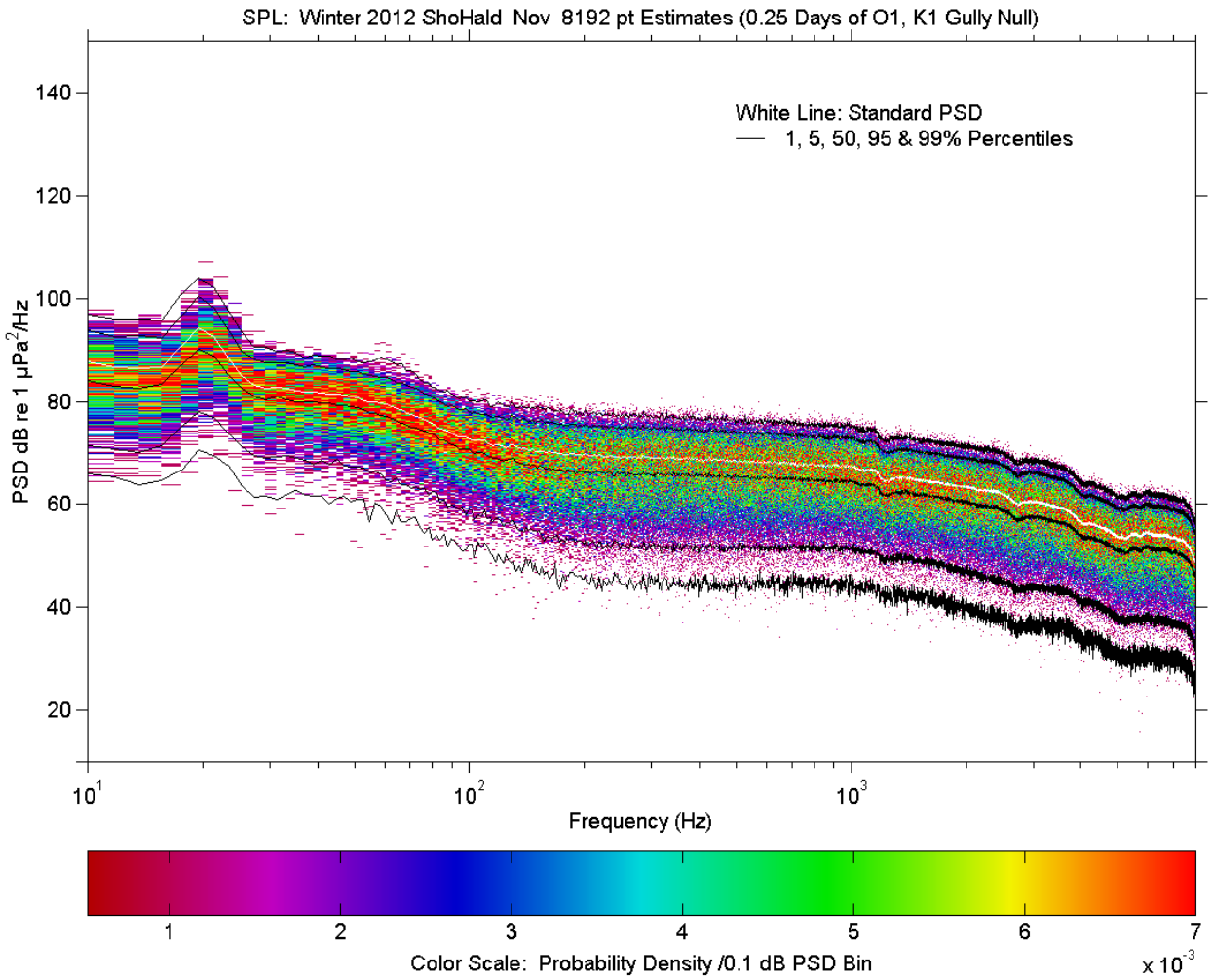


**Figure 25.** Medium resolution power spectral density with stats as in Fig. A4-2-ShoHald-2012-Nov but restricting analysed data to within 0.5 day windows centered on predicted $O_1$, $K_1$ tidal current noise nulls.

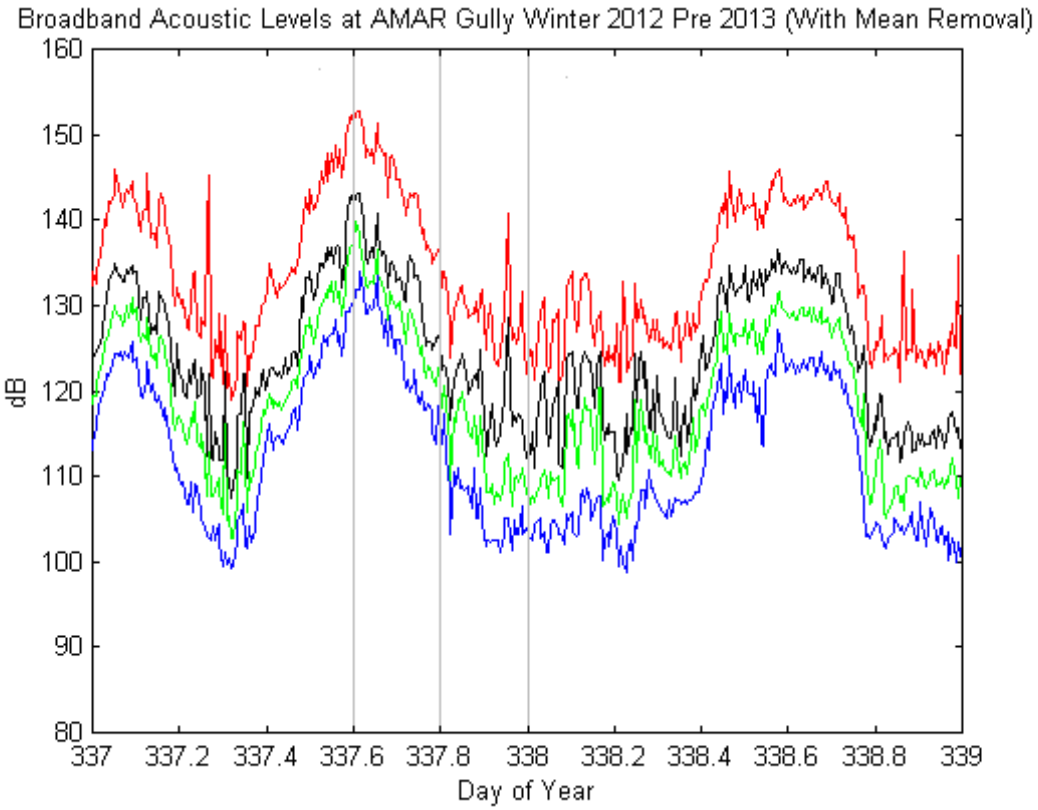


**Figure 26.** Broadband acoustic levels at MidGul for a 2 day period during the Winter 2012–13 deployment with marked analysis times for spectral study of mooring pseudo-noise. Red - Maximum 0-peak acoustic amplitudes over consecutive 300 s sampling intervals. Green - RMS amplitudes averaged over consecutive 300 s intervals. Black - Maximum RMS amplitudes as averaged over any consecutive 1 s interval within 300 s interval. Blue - Minimum RMS amplitudes as averaged over any consecutive 1 s interval within 300 s intervals. Grey vertical lines indicate, left to right, chosen spectral analysis times corresponding to high, medium, and low mooring current excitations respectively.

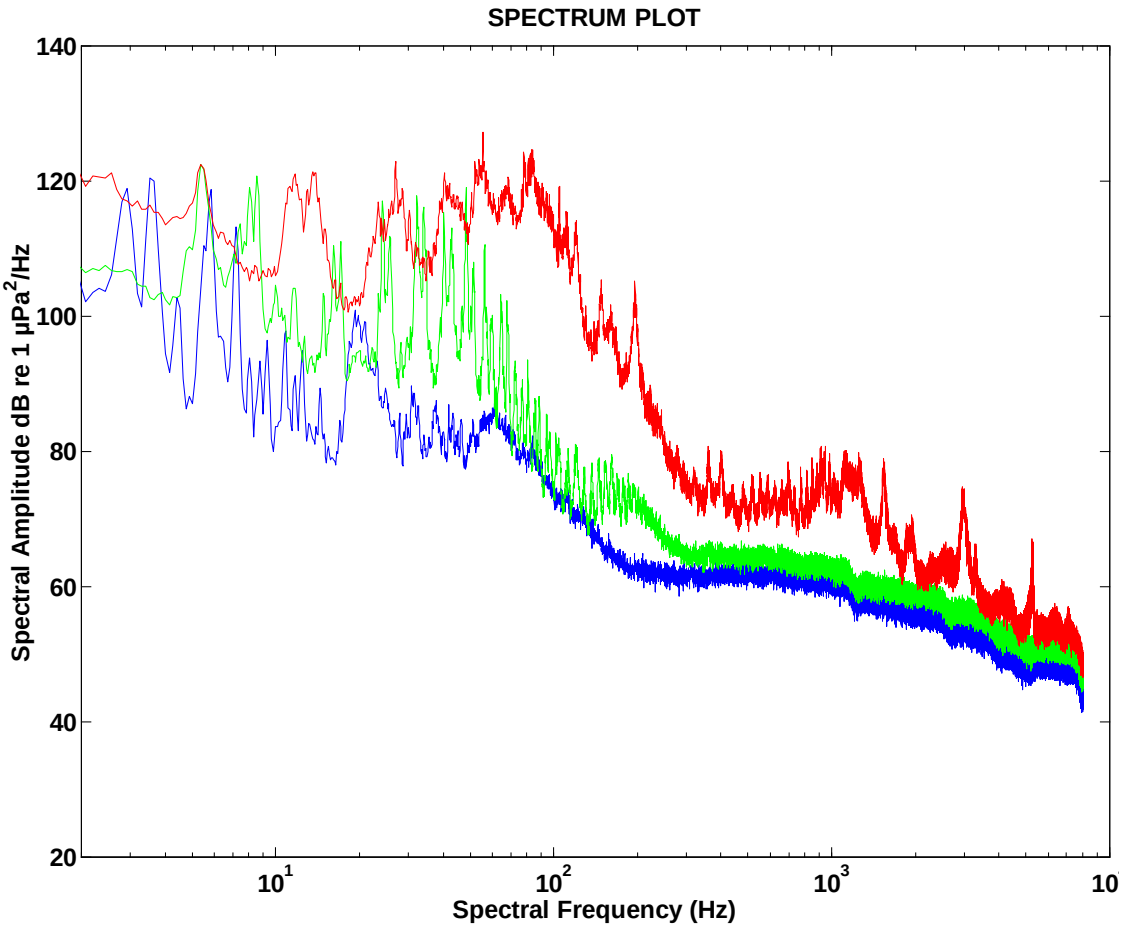


**Figure 27.** Acoustic sound pressure level power spectral density vs. frequency (log scale) for MidGul on Winter 2012-13 deployment for instances of high (red), medium (green), and low (blue) mooring ocean excitation currents using brief observation windows near DOYs 337.6, 337.8, and 338.0 respectively of year 2012.

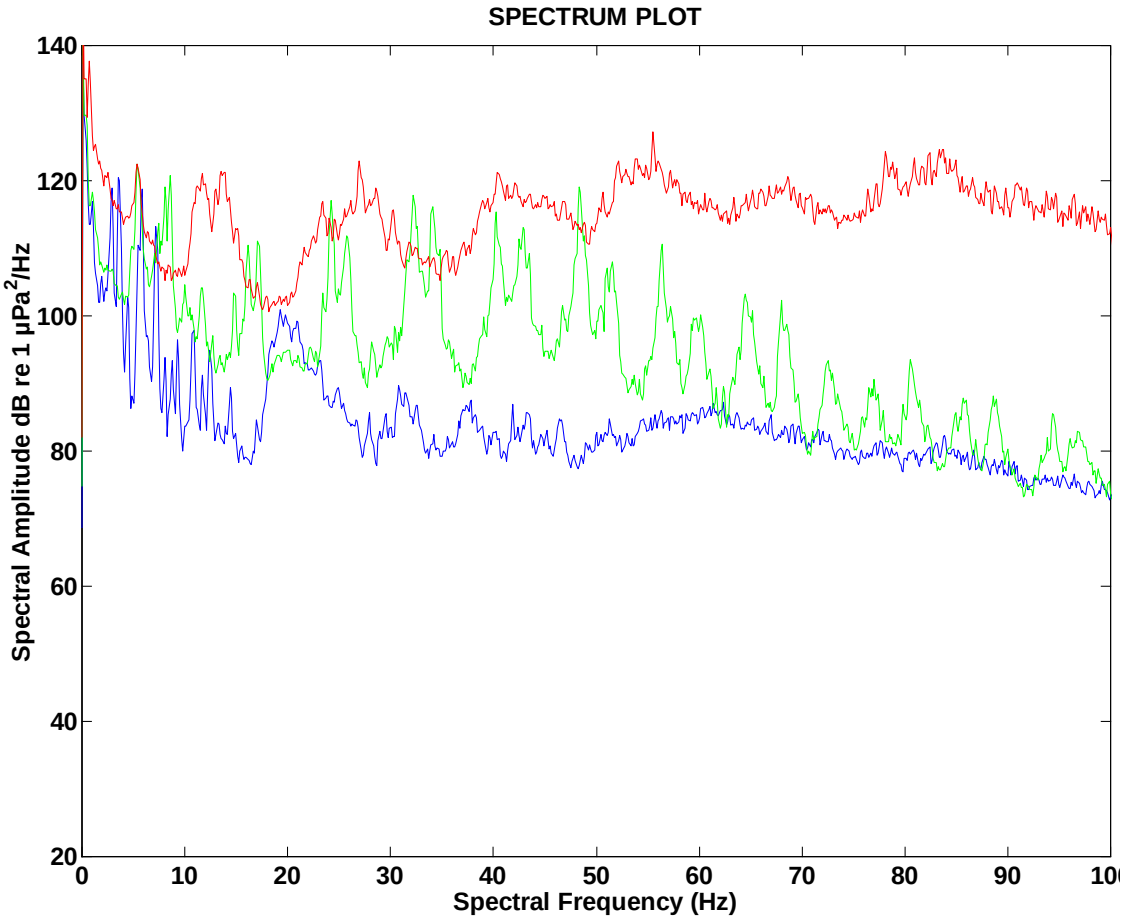


**Figure 28.** Acoustic sound pressure level power spectral density vs. frequency (linear scale) for MidGul on Winter 2012-13 deployment for instances of high (red), medium (green), and low (blue) mooring ocean excitation currents using brief observation windows near DOYs 337.6, 337.8, and 338.0 respectively of year 2012 (compare Fig. 27).

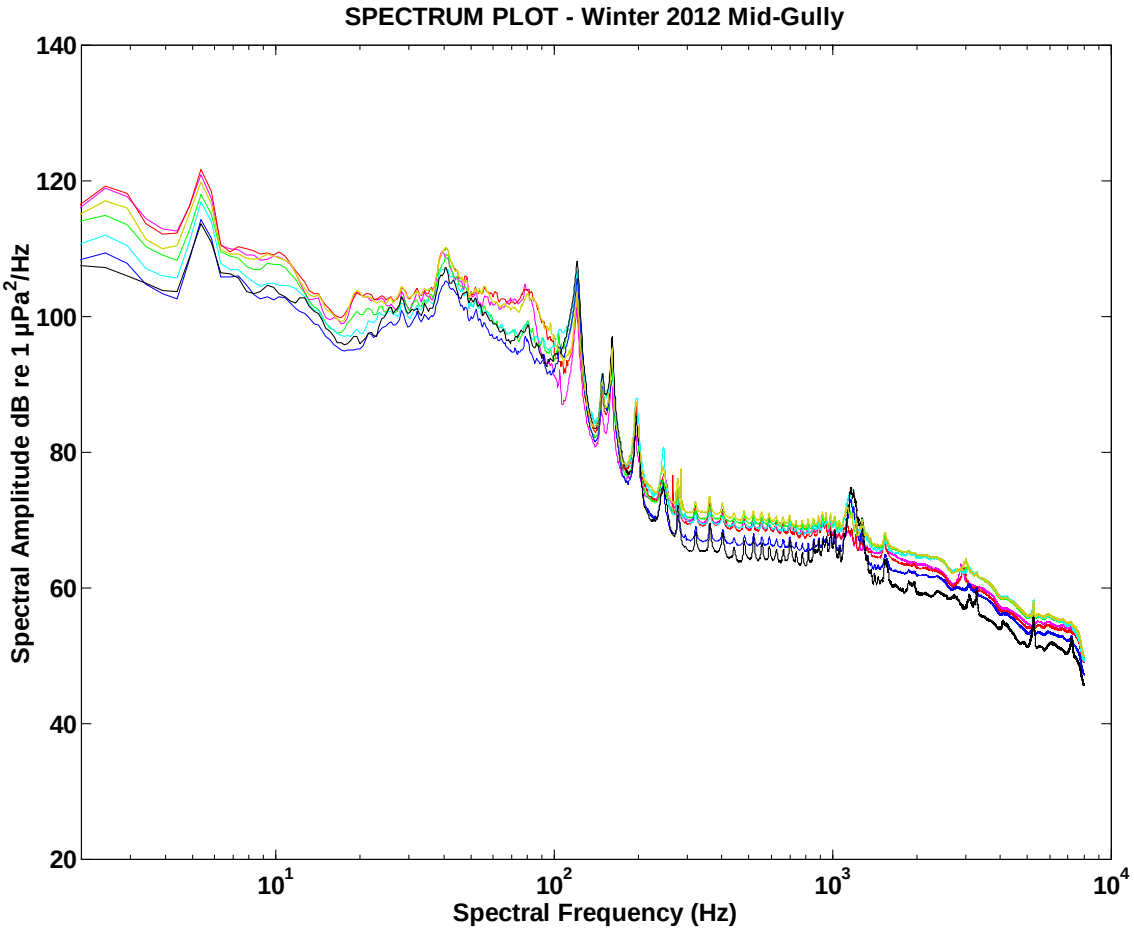


**Figure 29.** Multi-month spectral summary Winter 2012-13 MidGul.

Colour Key**:**
October – Magenta
November – Red
December – Yellow
January – Green
February – Cyan
March – Blue
April – Black

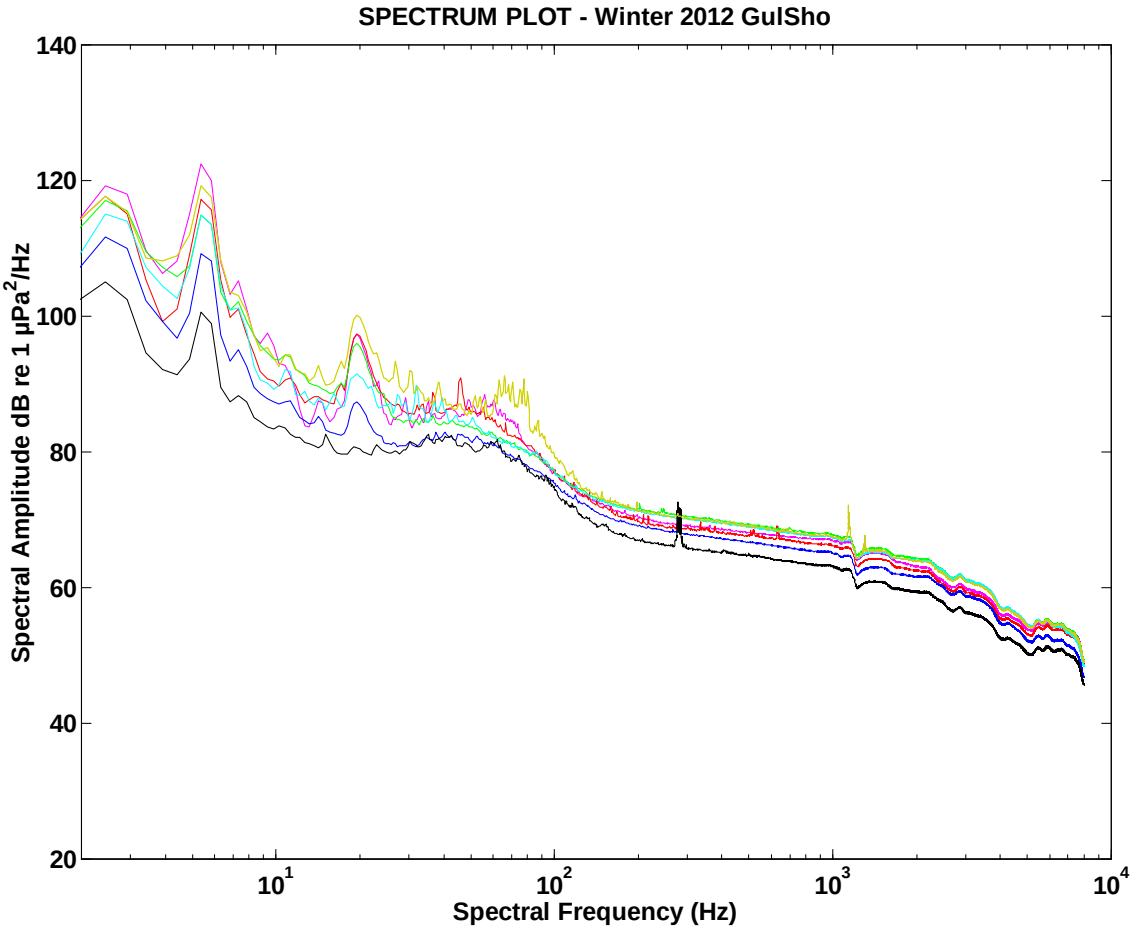


**Figure 30.** Multi-month spectral summary Winter 2012-13 GulSho. A strong noise event on 27–29 March 2013 has been eliminated by terminating the March analysis (GulSho only) at the end of March 26th.

Colour Key**:**
October – Magenta
November – Red
December – Yellow
January – Green
February – Cyan
March – Blue
April – Black

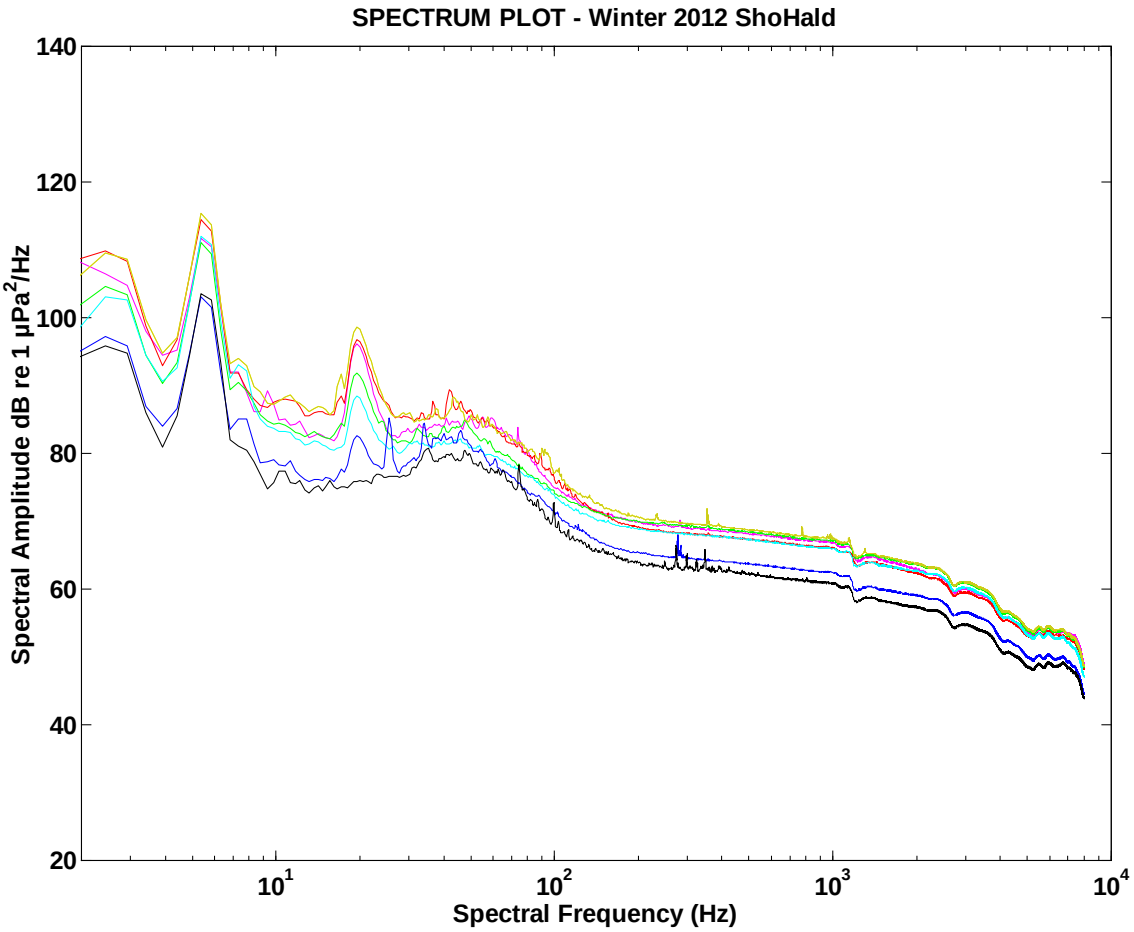


**Figure 31.** Multi-month spectral summary Winter 2012-13 ShoHald.

Colour Key**:**
October – Magenta
November – Red
December – Yellow
January – Green
February – Cyan
March – Blue
April – Black

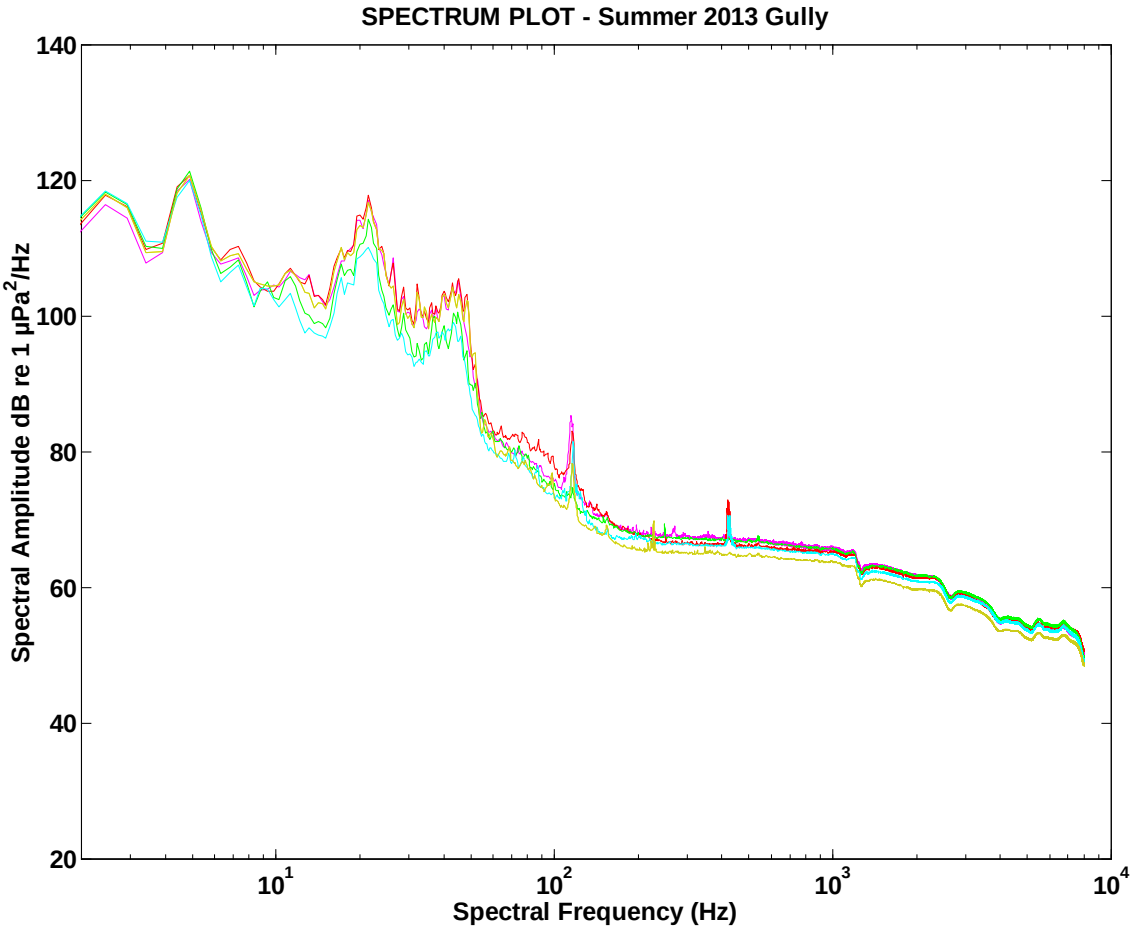


**Figure 32.** Multi-month spectral summary Summer 2013 MidGul.

Colour Key**:**
May – Magenta
June – Red
July – Yellow
August – Green
September – Cyan

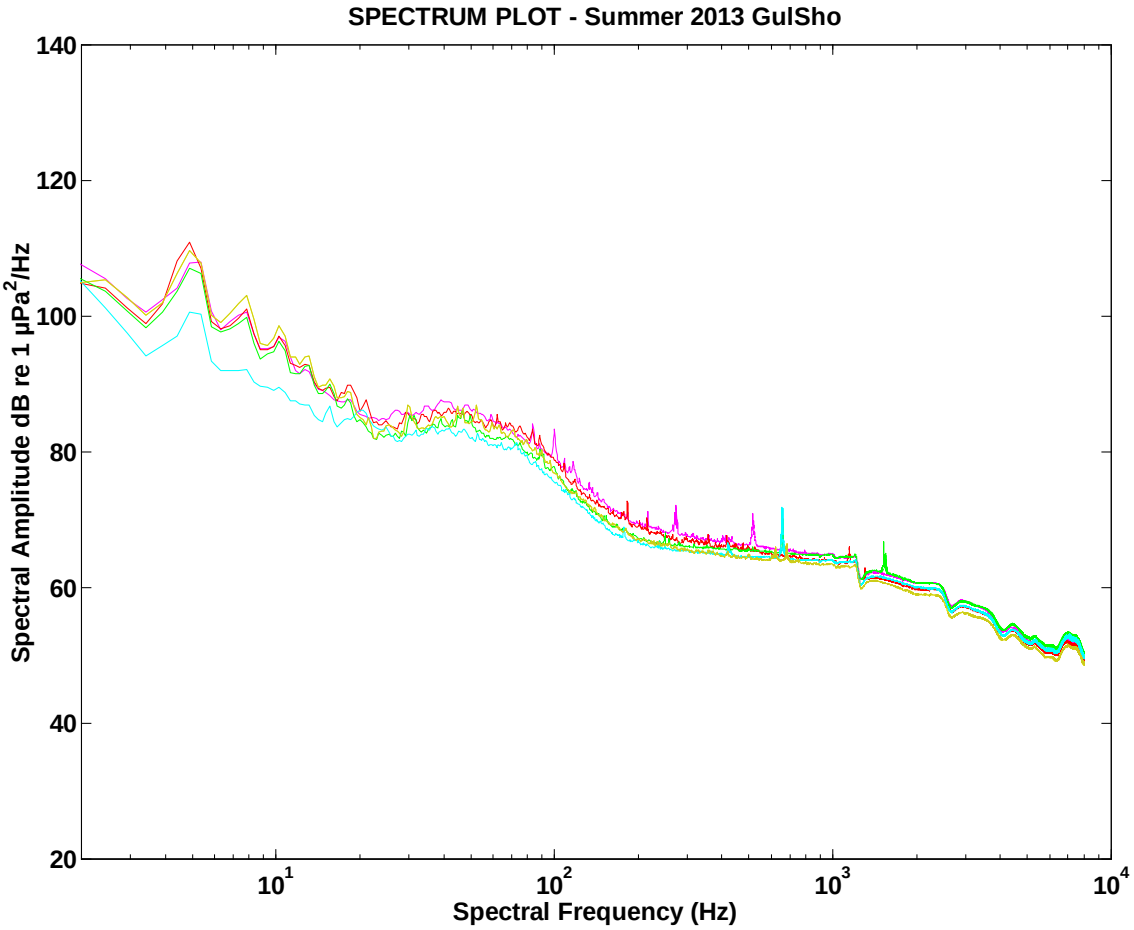


**Figure 33.** Multi-month spectral summary Summer 2013 GulSho.

Colour Key**:**
May – Magenta
June – Red
July – Yellow
August – Green
September – Cyan

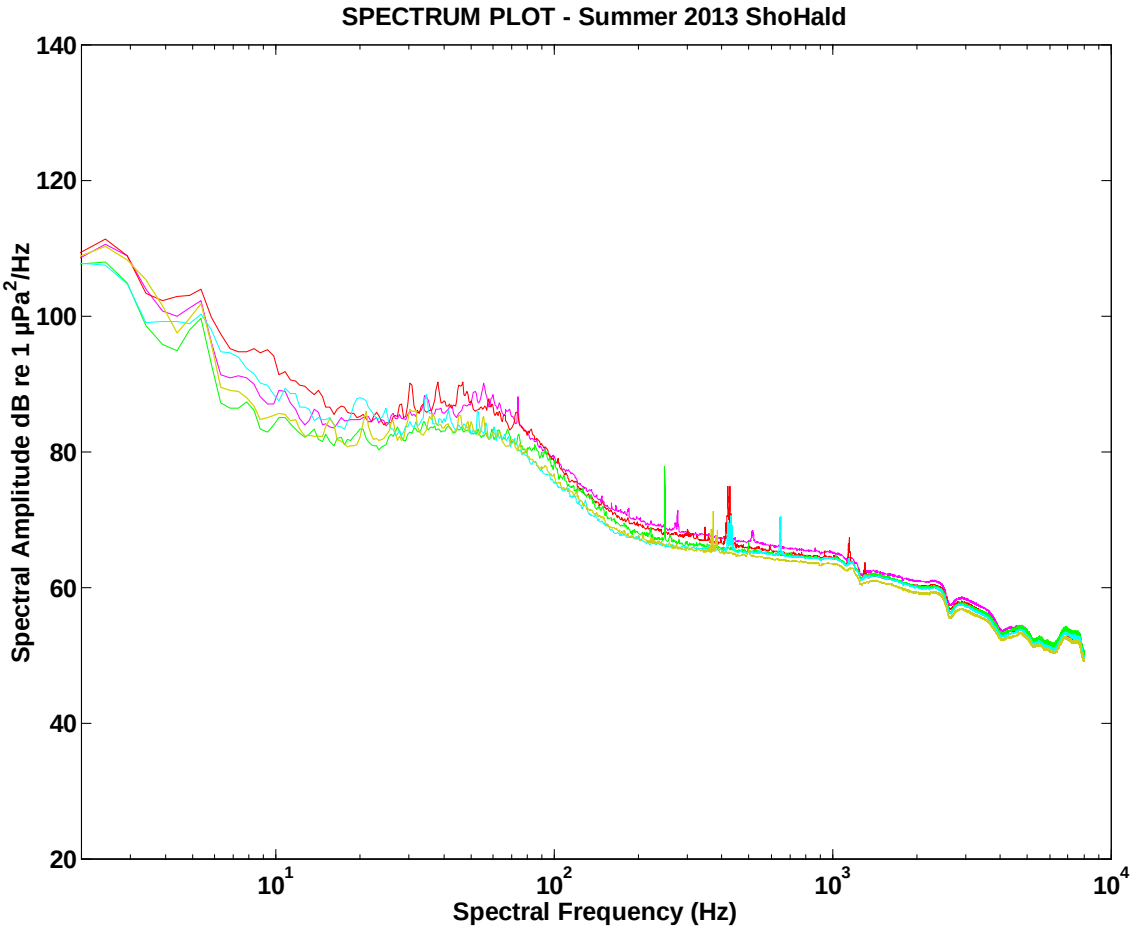


**Figure 34.** Multi-month spectral summary Summer 2013 ShoHald.
Strong ShoHald noise events on Aug. 24th and Aug. 28th (2013) have been eliminated by terminating the August analysis (ShoHald only) at end of Aug. 23rd (2013).

Colour Key**:**
May – Magenta
June – Red
July – Yellow
August – Green
September – Cyan

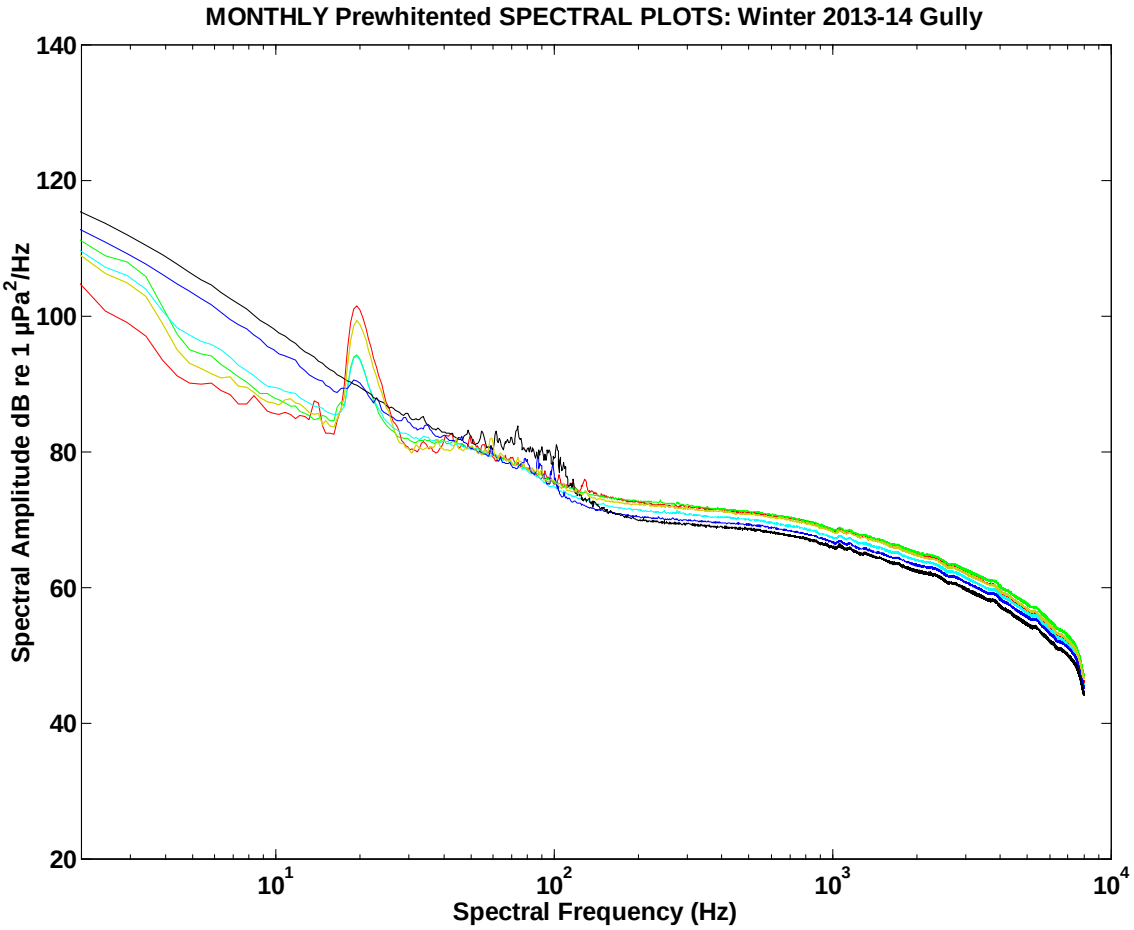


**Figure 35.** Multi-month spectral summary Winter 2013-14 MidGul.

Colour Key**:**
November – Red
December – Yellow
January – Green
February – Cyan
March – Blue
April - Black

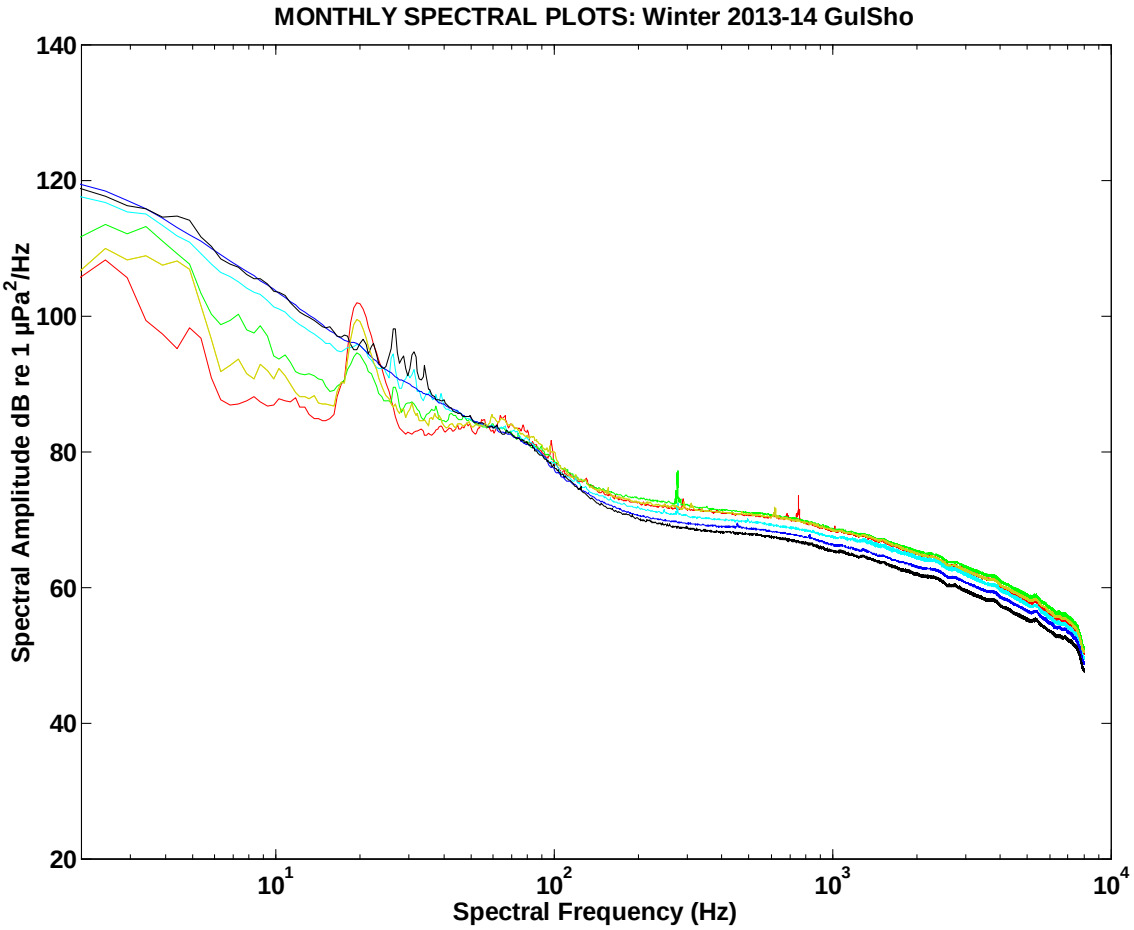


**Figure 36.** Multi-month spectral summary Winter 2013-14 GulSho.

Colour Key**:**
November – Red
December – Yellow
January – Green
February – Cyan
March – Blue
April - Black

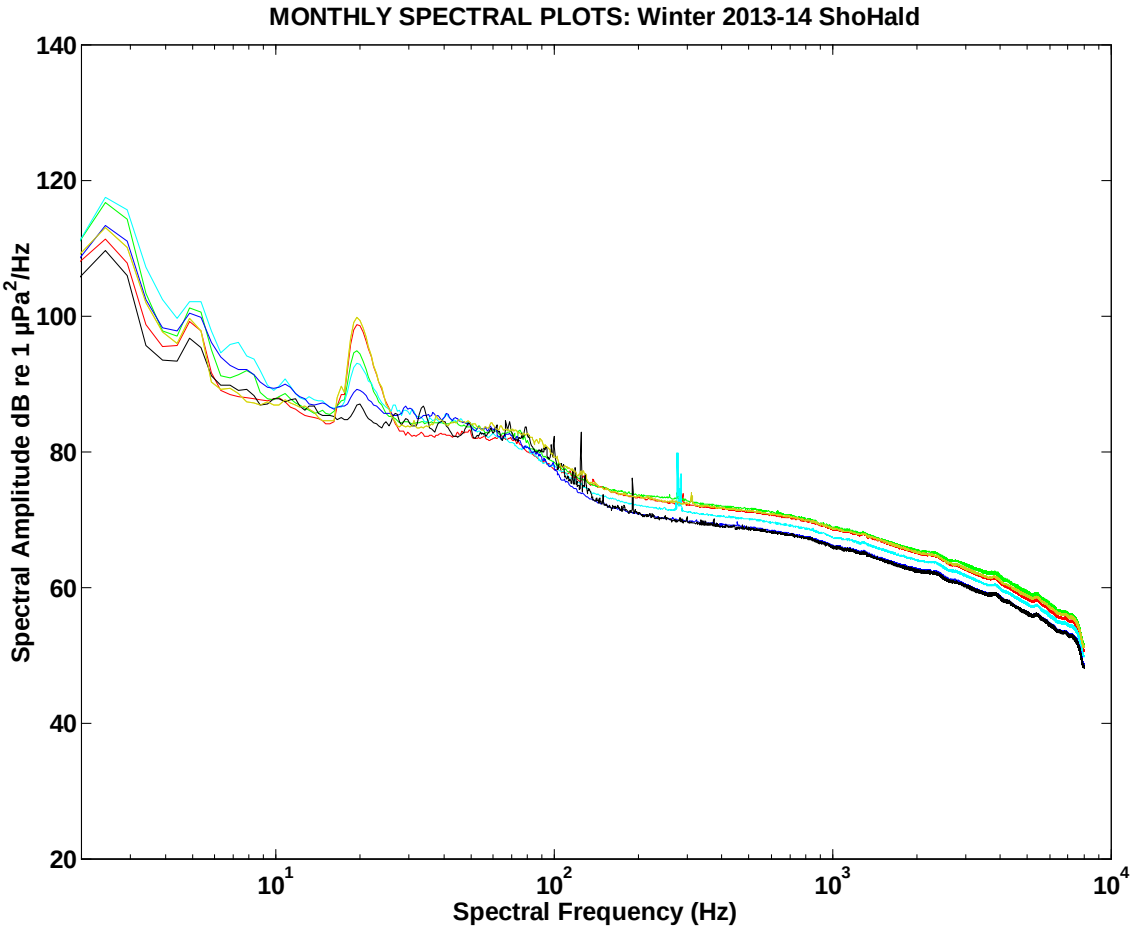


**Figure 37.** Multi-month spectral summary Winter 2013-14 ShoHald.

Colour Key**:**
November – Red
December – Yellow
January – Green
February – Cyan
March – Blue
April - Black

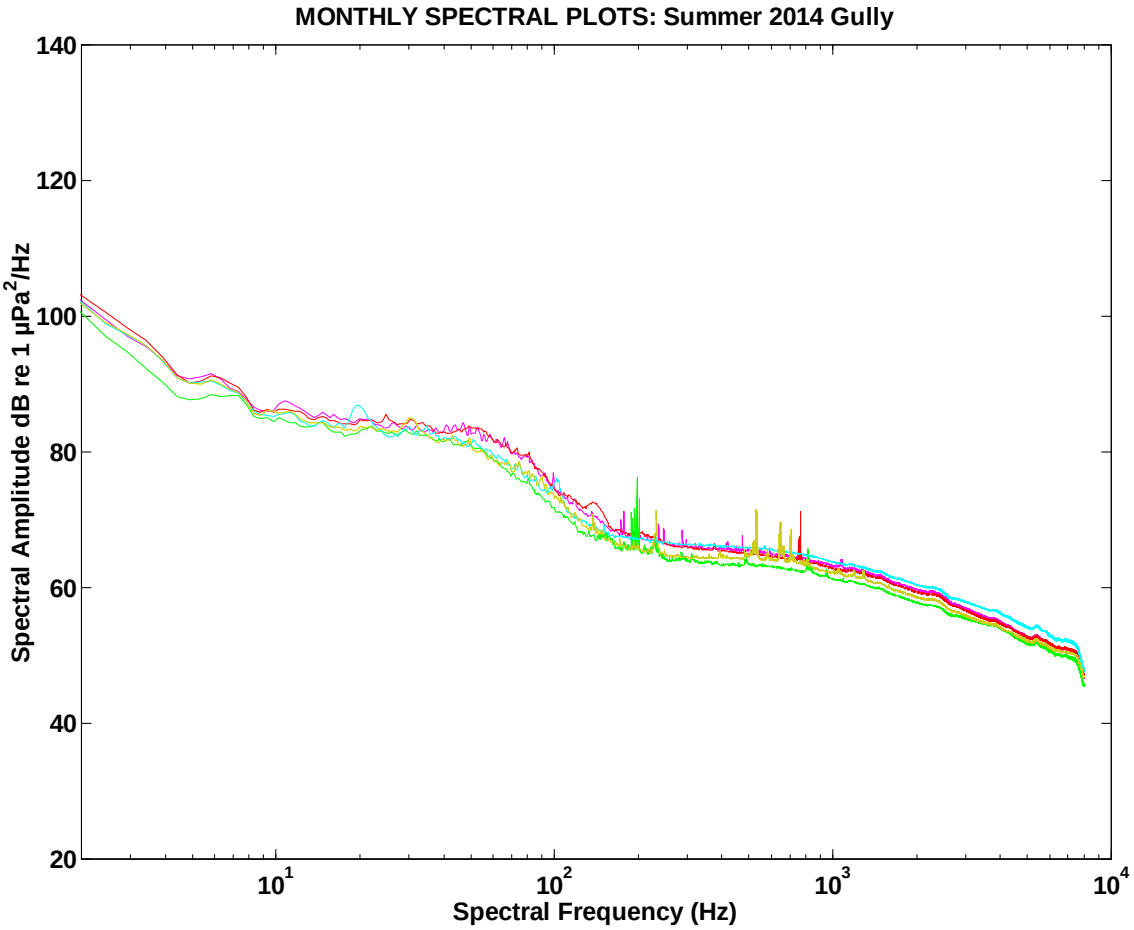


**Figure 38.** Multi-month spectral summary Summer 2014 MidGul.

Colour Key**:**
May – Magenta
June – Red
July – Yellow
August – Green
September – Cyan

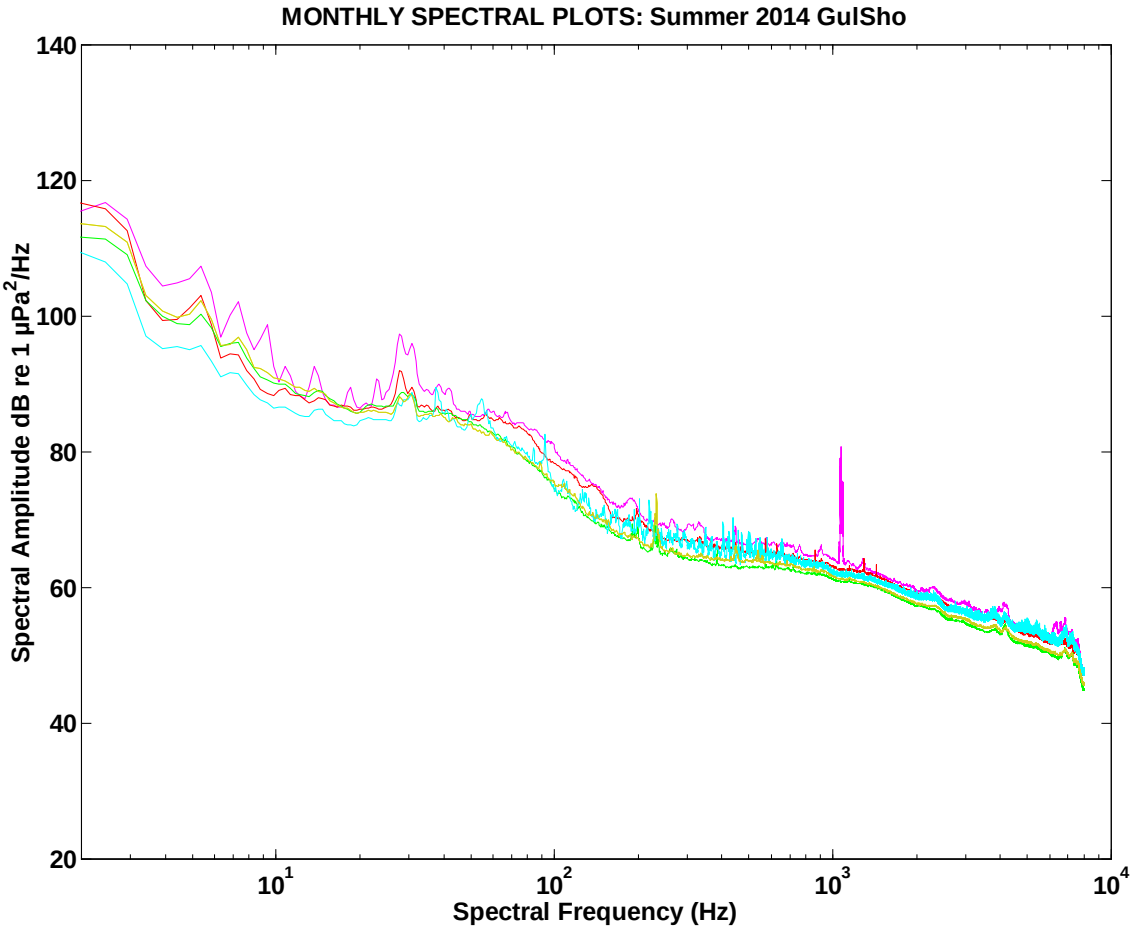


**Figure 39.** Multi-month spectral summary Summer 2014 GulSho.
A period of pronounced instrument instability after Sept. 18th has been eliminated by terminating the GulSho September analysis at end of Sept. 18th compared to the end of Sept. 25th at MidGul and ShoHald.

Colour Key**:**
May – Magenta
June – Red
July – Yellow
August – Green
September – Cyan

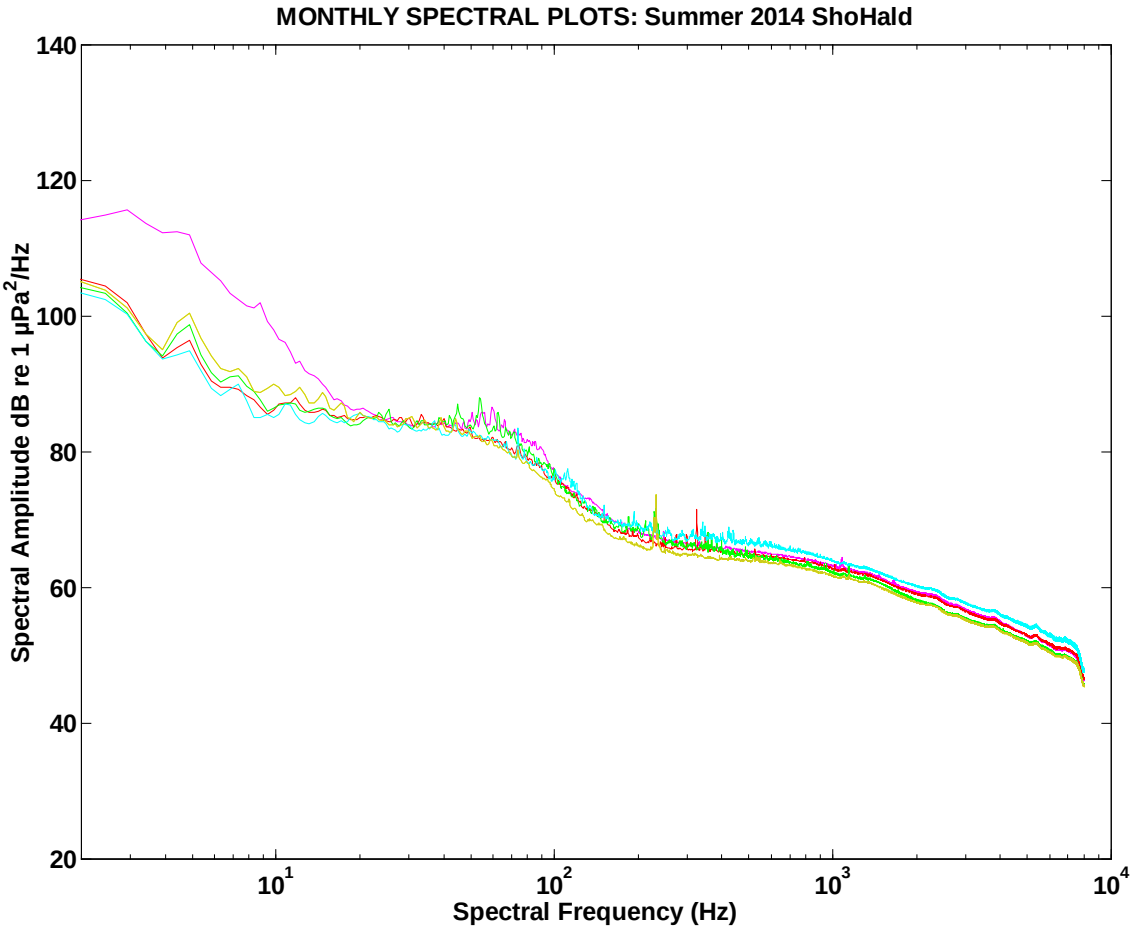


**Figure 40.** Multi-month spectral summary Summer 2014 ShoHald.

Colour Key**:**
May – Magenta
June – Red
July – Yellow
August – Green
September – Cyan

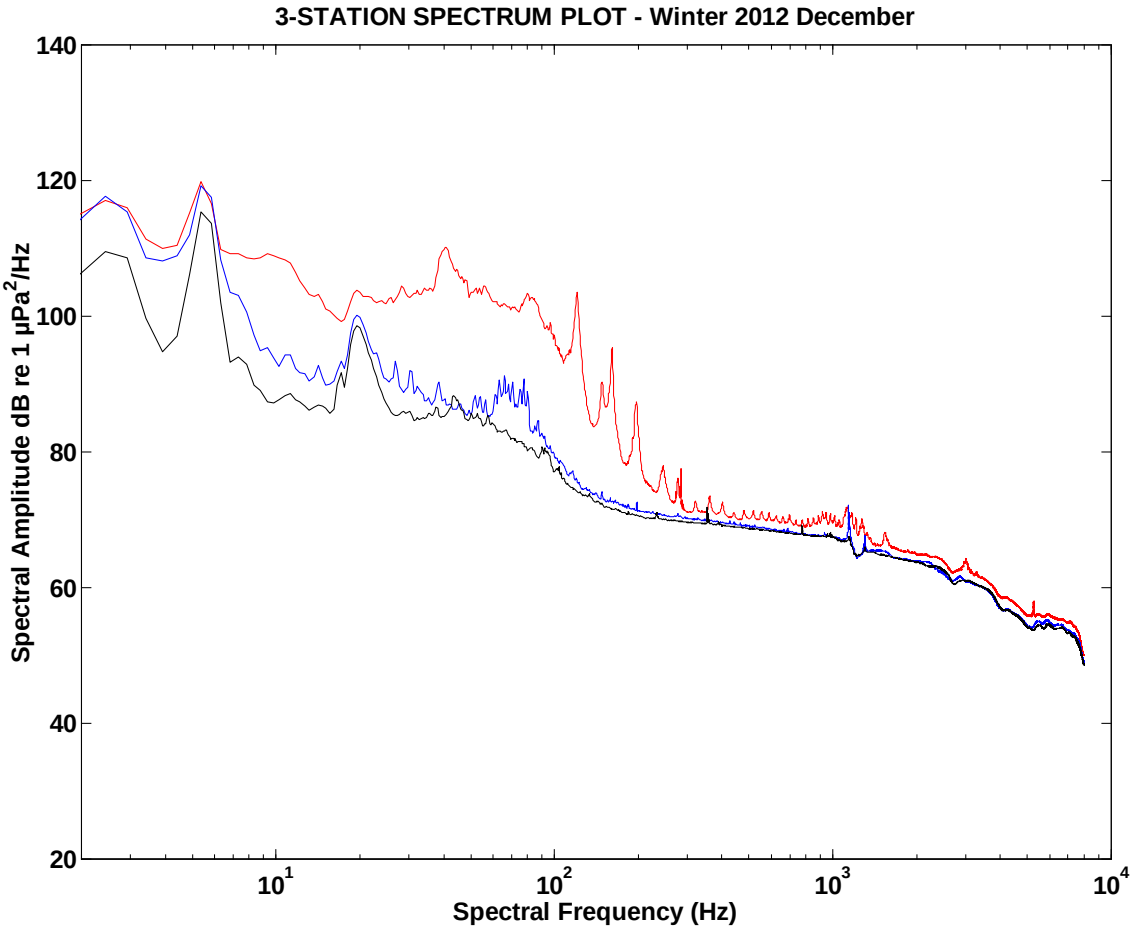


**Figure 41.** Overlay of power spectral densities vs. frequency for all three AMAR stations for Winter 2012-13, month of December.

Station Colour Key:
MidGul – Red
GulSho – Blue
ShoHald – Black

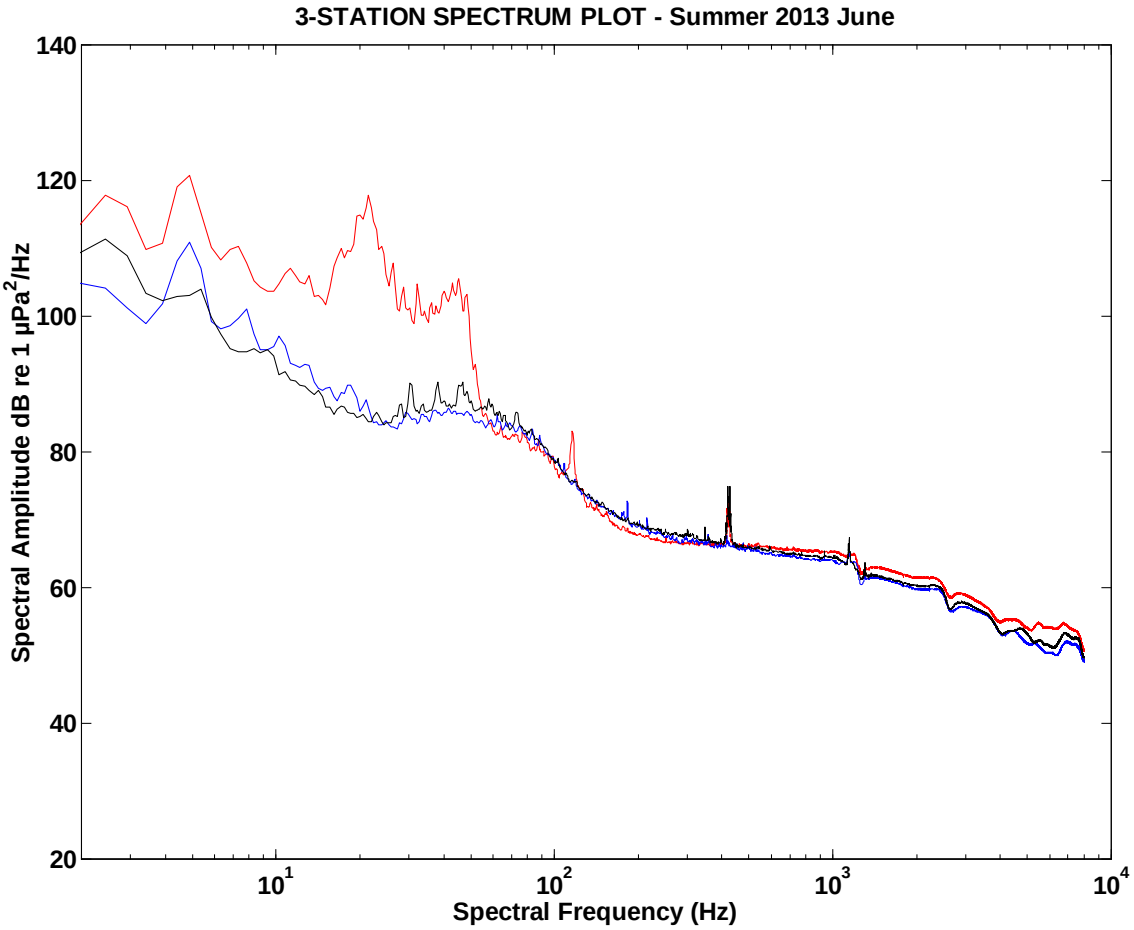


**Figure 42.** Overlay of power spectral densities vs. frequency for all three AMAR stations for Summer 2013, month of June.

Station Colour Key:
MidGul – Red
GulSho – Blue
ShoHald – Black

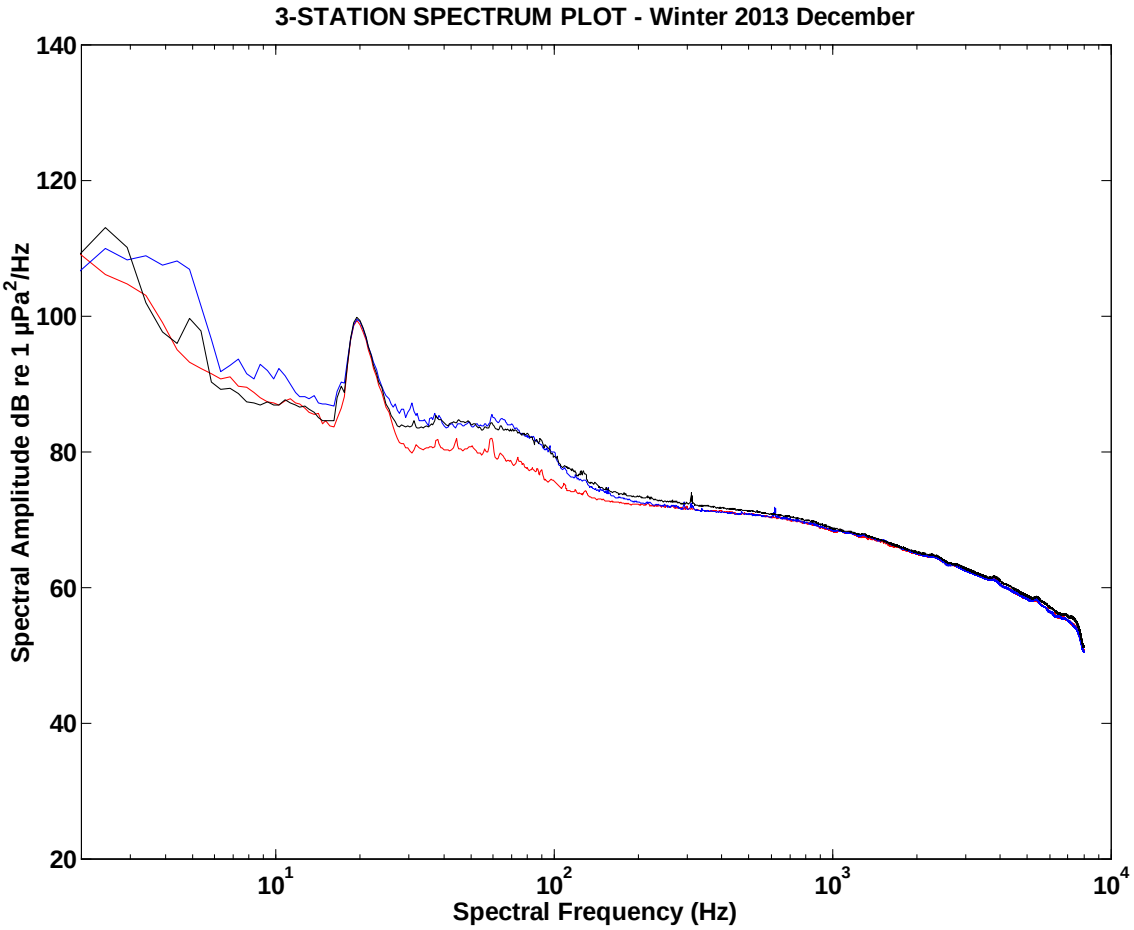


**Figure 43.** Overlay of power spectral densities vs. frequency for all three AMAR stations for Winter 2013-14, month of December.

Station Colour Key:
MidGul – Red
GulSho – Blue
ShoHald - Black

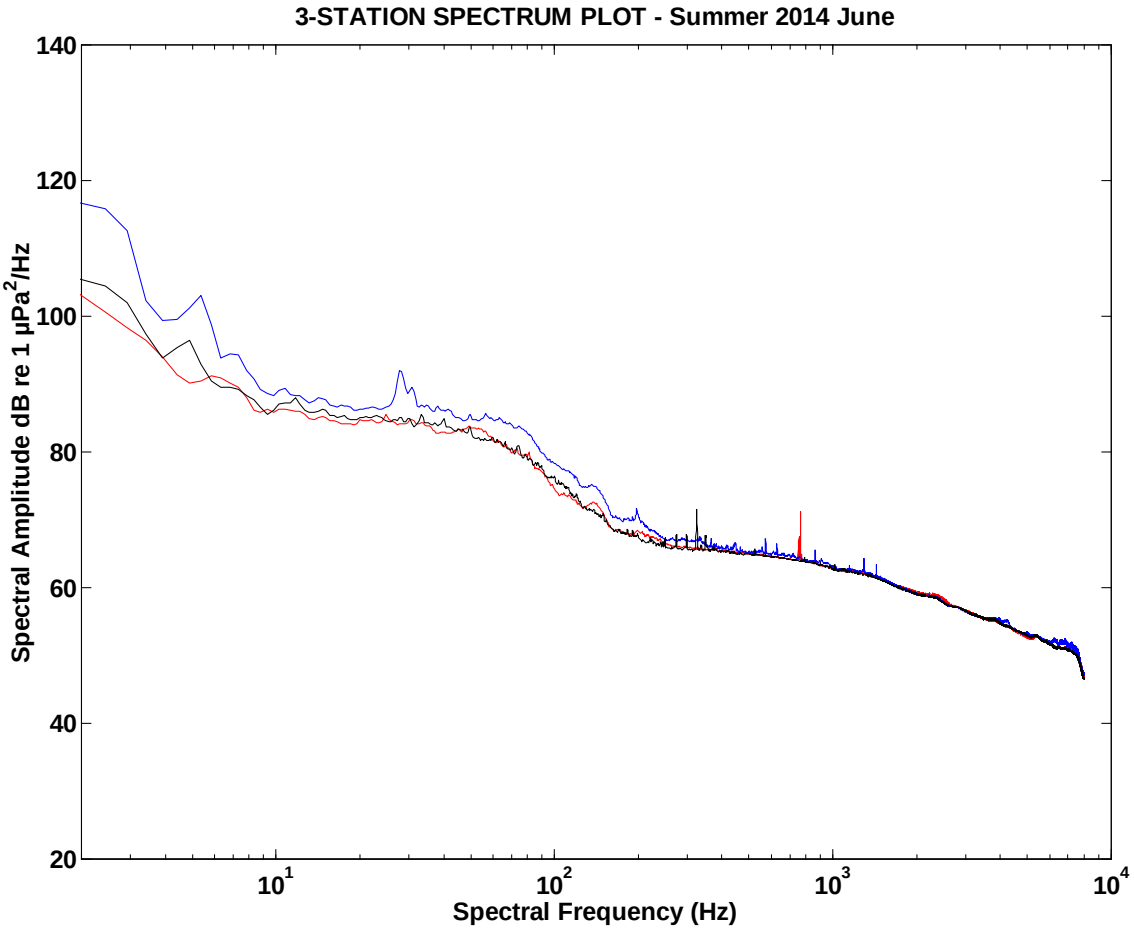


**Figure 44.** Overlay of power spectral densities vs. frequency for all three AMAR stations for Summer 2014, month of June.

Station Colour Key:
MidGul – Red
GulSho – Blue
ShoHald - Black

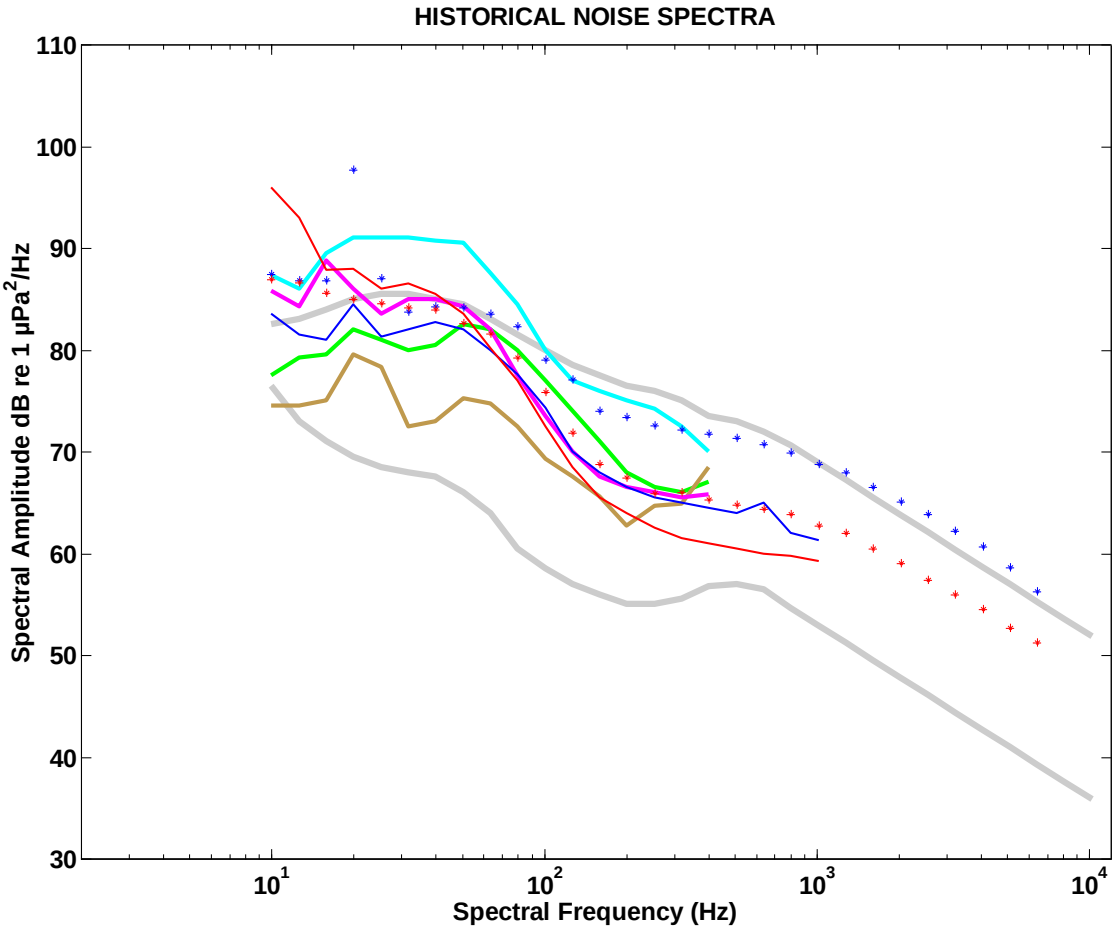


**Figure 45.** Comparison of selected AMAR spectral levels with historical deep water spectral measures:
Blue *asterisks* – ShoHald, month of Dec. 2013.
Red *asterisks* - ShoHald, month of June 2014.
Green *line* – Off Pt. Sur, California, 1963 – 1965 (Andrew et al. 2002; Wenz 1969).
Cyan *line* – Off Pt. Sur, California, 1994 – 2001 (Andrew et al. 2002).
Brown *line* – Off San Nicholas Is., California, 1964 - 1966 (McDonald et al. 2006; Wenz 1968a, 1968b)
Magenta *line* – Off San Nicholas Is. California, 2003- 2004 (McDonald et al. 2006).
Grey *lines* – Generalized deep ocean noise spectra scaled from Urick (1975), namely:
Upper: "Heavy shipping" and SS6 (winds 28 – 53 kts).
Lower: "Light shipping" and SS1 (winds 4 – 6 kts).
Blue *line (thin)*- Hatteras (Site 1), 2012-14 (Wiggins 2015)
Red *line (thin)* - Cherry Point Deep (Site 3), 2011-13 (Wiggins 2015)

# A1. APPENDIX 1: AMAR INTRUMENT ACOUSTIC FREQUENCY RESPONSE COMPENSATION

## A1.1. GENERAL

An efficient technique for correcting raw computed AMAR spectra for the frequency response characteristics of individual measurement instruments was needed in order to closely approximate true ambient pressure spectra. Correction required the construction and use of empirical instrument frequency response formulae sufficiently consistent with manufacturer-supplied tabulated discrete frequency instrumental responses to meet the accuracy requirements of our studies while allowing convenient single-formula computation of the required corrections over a continuous range of frequencies. In the absence of any current requirement to recover signal phase, only amplitude response corrections are treated. Several of our utilized empirical response formulations are defined below.

## A1.2. INSTRUMENT SPECIFICS

AMAR instruments were equipped with omnidirectional, spherical Geospectrum hydrophones, either models M8E-51 or M8Q-51. Employing either hydrophone, the AMAR systems were characterized by overall low frequency (LF) acoustic response roll-offs of about 20 dB/octave with -3 dB points around 20 Hz. An additional steeper roll-off commenced in the low single Hz range. At higher frequencies a very broad, near-level amplitude response was attained reaching a slight maximum in the vicinity of 1 kHz and extending upwards to about 5 - 8 kHz depending on hydrophone type. The nominal absolute calibration reference at 250 Hz was still essentially on the level portion of the response curve, only about 0.02 to 0.04 dB below the peak response level[9]. The difference between the 250 Hz and the 1 kHz responses was negligible in terms of the accuracies sought in this study and in comparison to other factors affecting calibration and frequency response in real field deployments.

## A1.3. RESULTS

### *A1.3.1. AMARs Equipped with Geospectrum M8E-51 Hydrophones*

All AMARs used in the Winter 2012-13 and Summer 2013 deployments were equipped with Geospectrum M8E-51 hydrophones. Only a single representative frequency response for the 16 kHz digitized acoustic channel was provided in the form of discrete frequency tabulated points which was plotted relative to the 1 kHz response maximum (Fig. A1-1).

[9] Our in-house analytical software assumes a calibration reference at the 1 kHz general response maximum so a slight adjustment is usually made to the 250 Hz calibration reference level but this is of little practical consequence.

By experiment, an empirical approximation to the above plotted response was derived and plotted in the form of a continuous curve in Fig. A1-1:

$$Response_{dB} = -10\log\left(1+\left(\frac{19.496}{f}\right)^2\right) - 10\log\left(1+\left(\frac{1.082}{f}\right)^2\right) - 10\log\left(1+\left(\frac{f}{41602}\right)^2\right) + 10\log\left(1+\left(\frac{f}{94665}\right)^4\right)$$

In the above formula *f* is in Hz and all logs are to base 10.

The first two terms establish the LF response and the latter two terms the HF response, the latter exhibiting only a very minor roll-off at the 8 kHz Nyquist frequency. For example, at 3.2 Hz the overall response computes to -16.28 dB while at 80 kHz (not used and well beyond the Nyquist for 16 kHz sampling) the response is -4.93 dB. The formula-derived response at 1 kHz computes to -0.004 dB, for all practical purposes zero.

Importantly, the above formula tracks the manufacturer-provided single reference response to within 0.05 dB in the currently utilized frequency range from 1.6 Hz to 8 kHz, the largest deviations confined to below 5 Hz. Since only a single reference response was provided it is unknown to what extent the frequency responses of specific units might deviate from the reference expectation.[10]

The above formula was used to correct data collected by all AMAR instruments on both the Winter 2012-13 and Summer 2013 deployments for the effects of instrumental frequency response.

### *A1.3.2. AMARs Equipped with Geospectrum M8Q-51 Hydrophones*

AMARS used for the Winter 2013-14 and Summer 2014 deployments were equipped with Geospectrum model M8Q-51 hydrophones. The same physical AMAR instruments equipped with the same serial # physical hydrophones were used at the identical stations on both deployments. The manufacturer supplied frequency responses at 3kHz and above for the 16 kHz digitized channel for each individual instrument. While the hydrophones were recalibrated at the 250 Hz reference frequency between the two field deployments total system frequency responses **relative to the response maxima** were assumed to remain unchanged between deployments. Below 3 kHz the same general response curve was provided as with the M8E-51 equipped units which contained the broad response peak at 1 kHz. The supplied high frequency responses differed considerably from those provided for the earlier M8E-51 units. AMAR frequency responses relative to the 1 kHz peak for the Winter 2013-14 and Summer 2014

[10] The frequency response should not be confused with the 250 Hz calibration reference which differed for every instrument.

deployments (assumed identical for the same instrument in both deployments) were plotted as discrete points in Fig. A1-2. Again, an experimentally derived empirical formula which closely approximates this frequency response was determined:

$$Response_{dB} = -10\log\left(1+\left(\frac{19.496}{f}\right)^2\right) - 10\log\left(1+\left(\frac{1.082}{f}\right)^2\right) - 10\log\left(1+\left(\frac{f}{9000}\right)^2\right) + 10\log\left(1+\left(\frac{f}{11600}\right)^2\right) - 10\log\left(1+\left(\frac{f}{68000}\right)^4\right) + 10\log\left(1+\left(\frac{f}{102000}\right)^8\right)$$

As with the previous formula, *f* is in Hz and all logs are to base 10. At 3.2 Hz, the response computes to the identical -16.28 dB of the earlier deployments while at 1 kHz the response computes to -0.02 dB, acceptably close to zero. The computed frequency response in the form of a continuous line is plotted in Fig. A1-2.

The immediate above formula was used to correct data collected by all AMAR instruments on both the Winter 2013-14 and Summer 2014 deployments for instrumental frequency response. The formulation main criteria was that a good match be obtained to the average instrument response and that acceptable matches be obtained to the detailed responses of each individual instrument in the 3 to 8 kHz range when such information was available.[11] The ≥ 3 kHz range produced the greatest known discrepancies with some specific instruments deviating up to 0.5 dB from the formula response up to 8 kHz (Fig. A1-2). These deviation magnitudes are of borderline significance for actual field applications but should be kept in mind during subsequent interpretations. However, in the absence of similar instrument-specific calibrations below 3 kHz for the last two deployments periods and for the entire frequency range for the first two deployments it was decided to simply proceed using the more appropriate of the above two proposed empirical relationships for all spectral frequency response corrections.

[11] Both proposed empirical formulas also attempt to fit the average response curve above 8 kHz but this is irrelevant for the current presented work.

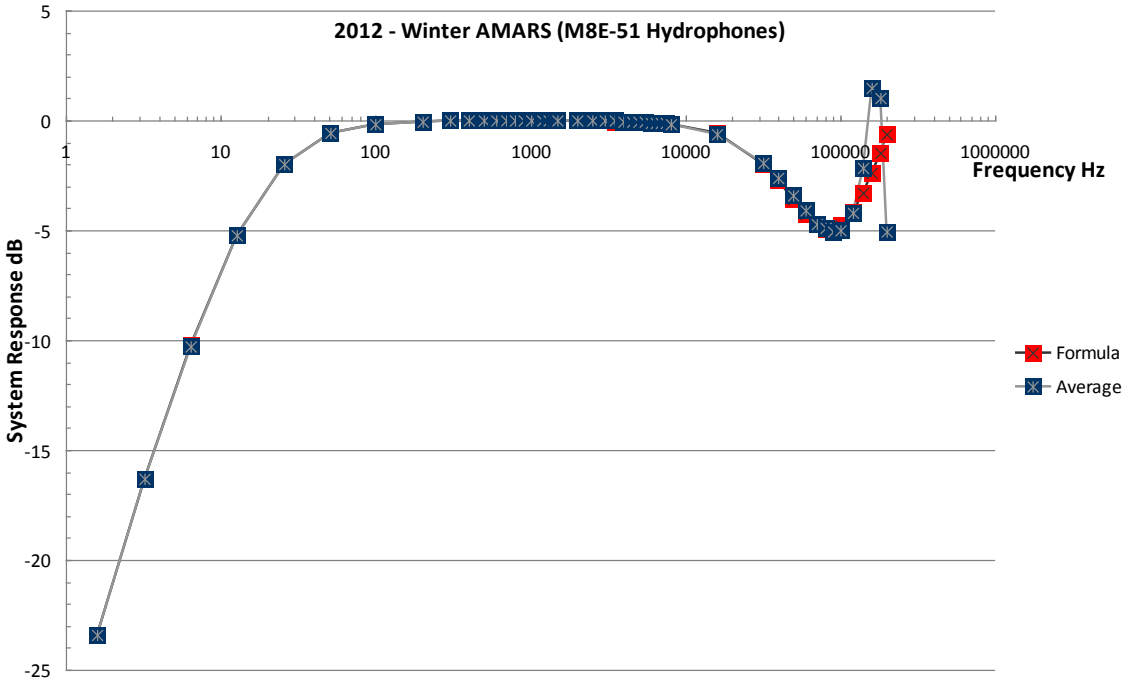


**Figure A1-1.** AMAR manufacturer-supplied acoustic frequency response (relative to maximum response at 1 kHz) and the formula approximation for the Winter 2012-13 and Summer 2013 deployments. The highest frequency currently utilized is 8 kHz.

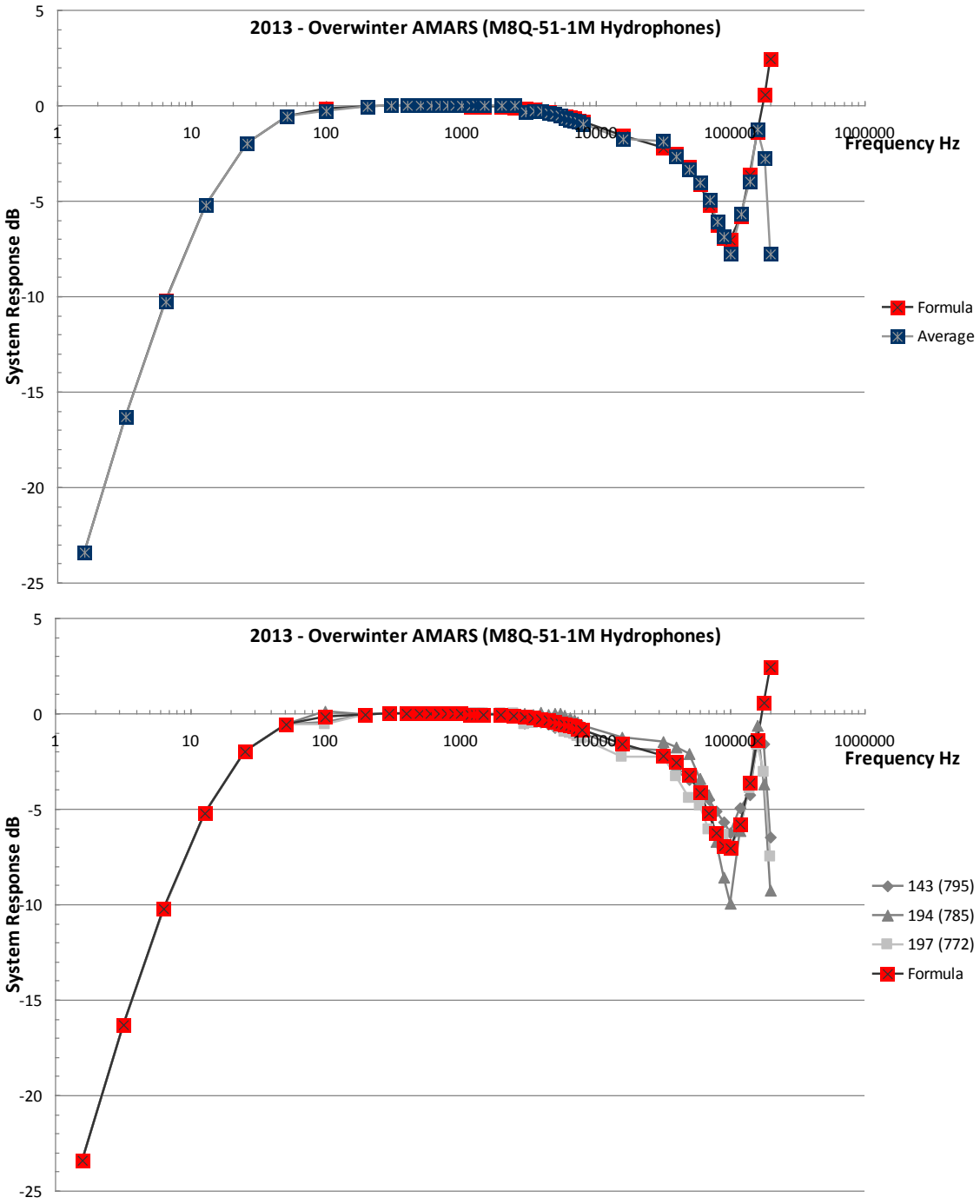


**Figure A1-2.** AMAR manufacturer-supplied acoustic frequency responses (relative to maximum response at 1 kHz) and the formula approximation for the Winter 2013-14 and Summer 2014 deployments (responses assumed identical for same instrument on both deployments). Average of three supplied instrument responses and formula approximation (top). Individual instrument responses and formula response (bottom). The highest frequency currently utilized is 8 kHz.

## A2. APPENDIX 2: SYSTEMATIC VARIATION OF AMAR SPECTRAL LEVELS OVER LONG TEMPORAL OBSERVATION SPANS

### A2.1. GENERAL

Acoustic sensitivity drift over long deployment times has been identified as issue with the AMAR recording instruments. Our AMAR deployment depths exceeded the hydrostatic pressure range for which the hydrophones and their electronics have been carefully tested. To address this issue, monthly spectral levels in the frequency range 150 Hz to 3 kHz were examined for systematic long term variations over the course of multi-month deployments.

### A2.2. PROCEDURE AND RESULTS

Our AMAR spectral levels below about 150 Hz were highly variable in both the temporal and frequency domains as noted in the main text. Sources of high variability include ship noise, mooring flow and strumming noise, fin whale vocalizations, and occasional very low frequency rumbles of an unknown origin. Real variability in low frequency ambient noise can produce misleading results on attempting to discern long term sensitivity drifts by simple examination of RMS signal levels. Instead, we choose to work from computed spectral levels $\geq$ 150 Hz where longer term time variability is more readily observed and where ambient levels appear to vary less strongly with frequency and perhaps with season.

Listed in Tables A2-1 and A2-2 below are deviations of monthly average spectral levels between 150 Hz and 3 kHz from initial spectral levels. Initial spectral levels were defined by averaging spectral levels over the calendar month of deployment. It was implicitly assumed that the levels for the calendar month of initial deployment constitute acceptable initial spectral reference levels, there appearing to be no clearly superior alternative methodology to define reference spectral levels characteristic of the actual deployment times. The "x d" reference in column 1 refers to the total number of days from deployment to the center of the specific temporal spectral averaging period. Averaging was performed by calendar month as this quantity was readily at hand and inherently incorporated the necessary degree of temporal smoothing. We arithmetically averaged spectral values over frequency in decibel form and then subtracted the similar frequency domain averaged initial reference level in dB. Mathematically, this is equivalent to differencing the monthly and initial decibel levels for each frequency bin and then averaging the decibel differences over the stated frequency range. The frequency response of the instrument can be ignored in this case since response corrections (in decibels) cancel in the differences at each frequency[12].

[12] Purists might (correctly) prefer arithmetic spectral averaging in the linear as opposed to the logarithmic decibel domain but then instrument frequency responses must be considered. Any real differences between averaging techniques in this normally fairly flat portion of the spectral frequency response are probably of little practical consequence.

Figure A2-1 shows comparative AMAR spectral levels vs. elapsed time from instrument deployment, the levels averaged over the frequency range 150 Hz to 3 kHz. This plot incorporates data from all four deployment periods - Winter 2012-13, Summer 2013, Winter 2013-14, and Summer 2014. Consequently, data obtained using both the Geospectrum M8E hydrophones (first two deployments) and the M8Q hydrophones (latter two deployments) are lumped. Each elapsed time point represents the arithmetic average of decibel spectral levels **over all three** simultaneously deployed instruments (it is assumed that for each deployment period, all three recording instruments are deployed simultaneously, a quite reasonable approximation)[13]. Each discrete point is common to only one instrument deployment period.

A noisy but seemingly systematic downward drift in spectral levels over time appears present in Fig. A2-1. This drift may reflect real temporal changes in hydrophone sensitivity, or, alternatively, arise from real systematic changes in ambient acoustic levels for example, from variations in forcing (i.e. wind) or changes in stratification-related acoustic propagation (or some combination of these effects). Figure A2-2 displays the same spectral levels with a **visually-fitted** combined data curve of the functional form:

$$Drift_{dB} = -10\log\left(1 + \left(\frac{t_{days}}{158.3}\right)^{4.577}\right)$$

Arguing for real changes in ambient acoustic levels is the fact that large spectral level drop-offs were observed in March and April near the ends of both the Winter 2012-13 and Winter 2013-14 deployments (see Figs. A2-3 to A2-6 displaying all four deployment periods in succession) even though differing model hydrophones were used over the course of the two deployments. The Summer 2013 deployment using M8E hydrophones lacks sufficient duration to critically compare with the preceding Winter 2012-13 deployment using similar M8E hydrophones - the rate of post deployment drift appears to accelerate with time and the summer deployment ends at about the elapsed time any such drift might be reliably discerned above the data scatter. The same is true of the Summer 2014 deployment compared to the preceding Winter 2013-14 deployment, both deployments using M8Q hydrophones. No attempt has been made (in this instance) to compensate for differing wind speeds during the two observation periods or to restrict comparisons to periods of comparable wind speed. Considered in aggregate (Fig. A2-2), the drift in spectral levels for the considered frequency range appears reasonably low over at least the first two months of most deployments. If the more marked downward drift in spectral levels observed at longer elapsed post-deployment times is actually a result of progressively declining hydrophone sensitivities, both the Geospectrum M8E

---

[13] For the Summer 2014 datasets for the month of September, the GulSho dataset was truncated early (end of day Sept. 18th vs. Sept 25 for both MidGul and ShoHald) due to an instrument stability problem. Nevertheless, we have averaged all three datasets and have assigned an average "center of deployment" time even though the three datasets do not exactly correspond in time.

and M8Q hydrophones would appear similarly affected (Figs. A2-7 and A2-8). Nevertheless, the degree of observation scatter is high in drawing this tentative conclusion.

Additional insights into the nature of the spectral fluctuations may be gleaned from inspecting individual station vs. elapsed deployment time plots. Figures A2-9 and A2-10 correspond to Figs. A2-1 and A2-2 respectively, except individual stations rather than 3-station deployment averages are plotted. Figures A2-11 and A2-12 repeat the contents of Figs. A2-9 and A2-10 respectively except now individual deployment periods are colour-coded. On observing specific deployments, early station spectral levels tend to cluster tightly in amplitude then, as time progresses, specific deployment station clusters move upward and downward in a coordinated manner relative to the proposed combined data fitting curve. These coordinated movements relative to the fitting curve may reflect real long term variations in ambient acoustic levels which for a specific deployment affect all three stations in a roughly similar manner. Later within deployments there is a general downward movement of the clusters combined with increased scatter within individual clusters. The downward movements could reflect real systematic changes in hydrophone sensitivity, actual changes in sensitivity varying from hydrophone to hydrophone and consequently giving rise to the increase in scatter or divergence within individual deployment clusters. This might be further explored by following the evolution for specific instruments.

If one accepts the existence of both real temporal fluctuations in ambient acoustic noise levels and artificial trends arising from anomalous changes in hydrophone sensitivity it is tempting to correct computed spectral levels for hydrophone sensitivity drift using the combined data relationship. Caution must be taken in any such attempt to do this as: 1) Sensitivity drifts may vary significantly from instrument to instrument – a fact suggested by the apparent systematic divergence of multi-instrument clusters over the course of deployments as noted above; and, 2) Imposing a drift correction also implicitly imposes an interpretation on the datasets – heavily averaged amplitude trends represent hydrophone drift, precluding the possibility that some portion of the averaged behaviour arises from true seasonal fluctuations in the ambient acoustic noise field. Exacerbating the problem is the fact that the strongest evidence for downward sensitivity drifts comes from the two long winter deployments (Fig. A2-13) that sample nearly identical seasonal time periods. If the two summer deployments (Fig. A2-14) were of slightly longer duration so as to provide unequivocal rather than merely suggestive evidence of similar downward trends, the sensitivity drift conjecture and its quantification would reside on a stronger footing.

We conclude that significant hydrophone sensitivity drifts were likely present in the present datasets, and present with a high degree of certainty in the Winter 2012-13 datasets. However, its quantification remains fairly uncertain. Unanswered, is whether the drift was identical for all instruments or for all hydrophone models, whether it was frequency independent, and even whether sensitivity drift constituted a process sufficiently regular and systematic in nature - as opposed to irregular or chaotic - to be adequately describable by simple continuous functional forms. It appears certain that any

sensitivity drift process accelerated over time, its effect remaining minimal over the initial few months of deployment. Therefore, any exacting quantitative conclusions drawn from these datasets should rely heavily on data gathered in the immediate post-deployment period.

**Table A2-1.** Deviations of monthly average spectral levels from those characterizing the initial post-deployment period for deployments and stations utilizing Geospectrum Model M8E hydrophones.

**Winter 2012-13 Deployment**

Hydrophone: Geospectrum M8E

| ***Station:*** | **MidGul** | **GulSho** | **ShoHald** |
|---|---|---|---|
| ***Deploy:*** | 12-Oct-12 | 12-Oct-12 | 12-Oct-12 |
| ***Start Analysis:*** | 13-Oct-12 incl. | 13-Oct-12 incl. | 13-Oct-12 incl. |
| **Month** | | | |
| Oct (10 d deploy) | * | * | * |
| Nov (35 d) | -0.2279 dB | -0.6174 | -0.6729 |
| Dec (65 d) | +1.4870 | +0.8057 | +0.7451 |
| Jan (96 d) | +1.1953 | +1.0994 | +0.5228 |
| Feb (126 d) | +1.0296 | +0.7775 | -0.5022 |
| Mar (155 d) | -1.4902 | -1.6519 | -4.0750 |
| Apr (175 d) | -2.9615 | -3.6699 | -5.7198 |
| ***End Analysis:*** | 09-Apr-13 incl. | 07-Apr-12 incl. | 09-Apr-12 incl. |
| ***Recover:*** | 09-Apr-13 | 10-Apr-13 | 10-Apr-13 |

**Summer 2013 Deployment**

Hydrophone: Geospectrum M8E

| ***Station:*** | **MidGul** | **GulSho** | **ShoHald** |
|---|---|---|---|
| ***Deploy:*** | 07-May-13 | 08-May-13 | 08-May-13 |
| ***Start Analysis:*** | 09-May-13 incl. | 09-May-13 incl. | 09-May-13 incl. |
| **Month** | | | |
| May (12 d deploy) | * | * | * |
| Jun (38 d) | -0.3327 dB | -0.8089 | -0.6368 |
| Jul (69 d) | -2.0198 | -1.6329 | -1.7581 |
| Aug (100 d) | -0.0174 | -0.2080 | -0.9047 |
| Sep (127 d) | -0.8299 | -0.9658 | -1.0914 |
| ***End Analysis:*** | 23-Sep-13 incl. | 23-Sep-13 incl. | 23-Sep-13 incl. |
| ***Recover:*** | 26-Sep-13 | 26-Sep-13 | 26-Sep-13 |

**Table A2-2.** Deviations of monthly average spectral levels from those characterizing the initial post-deployment period for deployments and stations utilizing Geospectrum Model M8Q hydrophones.

**Winter 2013-14 Deployment**

Hydrophone: Geospectrum M8Q

| ***Station:*** | **MidGul** | **GulSho** | **ShoHald** |
|---|---|---|---|
| ***Deploy:*** | 15-Nov-13 | 15-Nov-13 | 15-Nov-13 |
| ***Start Analysis:*** | 16-Nov-13 incl. | 16-Nov-13 incl. | 16-Nov-13 incl. |
| **Month** | | | |
| Nov (9 d deploy) | * | * | * |
| Dec (31 d) | -0.1979 dB | +0.0565 | +0.1195 |
| Jan (62 d) | +0.2272 | +0.3855 | +0.4221 |
| Feb (91 d) | -0.9576 | -0.7318 | -1.0544 |
| Mar (121 d) | -1.6987 | -1.9636 | -2.3570 |
| Apr (139 d) | -2.4929 | -2.9739 | -2.5777 |
| ***End Analysis:*** | 05-Apr-14 incl. | 05-Apr-14 incl. | 05-Apr-14 incl. |
| ***Recover:*** | 06-Apr-14 | 06-Apr-14 | 07-Apr-14 |

**Summer 2014 Deployment**

Hydrophone: Geospectrum M8Q

| ***Station:*** | **MidGul** | **GulSho** | **ShoHald** |
|---|---|---|---|
| ***Deploy:*** | 03-May-14 | 03-May-14 | 03-May-14 |
| ***Start Analysis:*** | 05-May-13 incl. | 05-May-14 incl. | 05-May-14 incl. |
| **Month** | | | |
| May (15 d deploy) | * | * | * |
| Jun (43 d) | -0.3101 dB | -1.0319 | -0.3399 |
| Jul (74 d) | -1.0561 | -2.5019 | -1.4902 |
| Aug (105 d) | -1.8856 | -2.9793 | -0.9819 |
| Sep (133 or 129 d) Assume (132) | +0.5875 | -1.4654 | +0.8675 |
| ***End Analysis:*** | 25-Sep-14 incl. | 18-Sep-13 incl. | 25-Sep-14 incl. |
| ***Recover:*** | 26-Sep-14 | 26-Sep-14 | 26-Sep-14 |

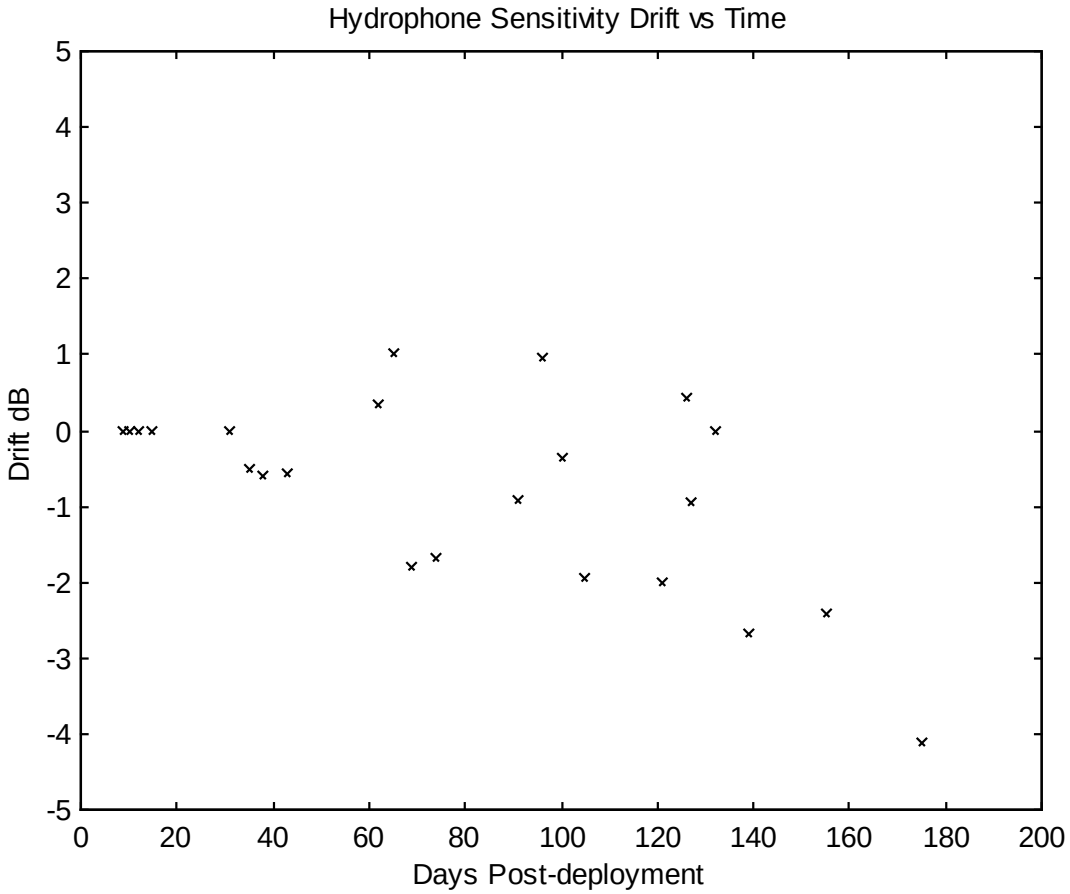


**Figure A2-1.** Average multi-station spectral level vs. time for all tabulated instrument deployments.

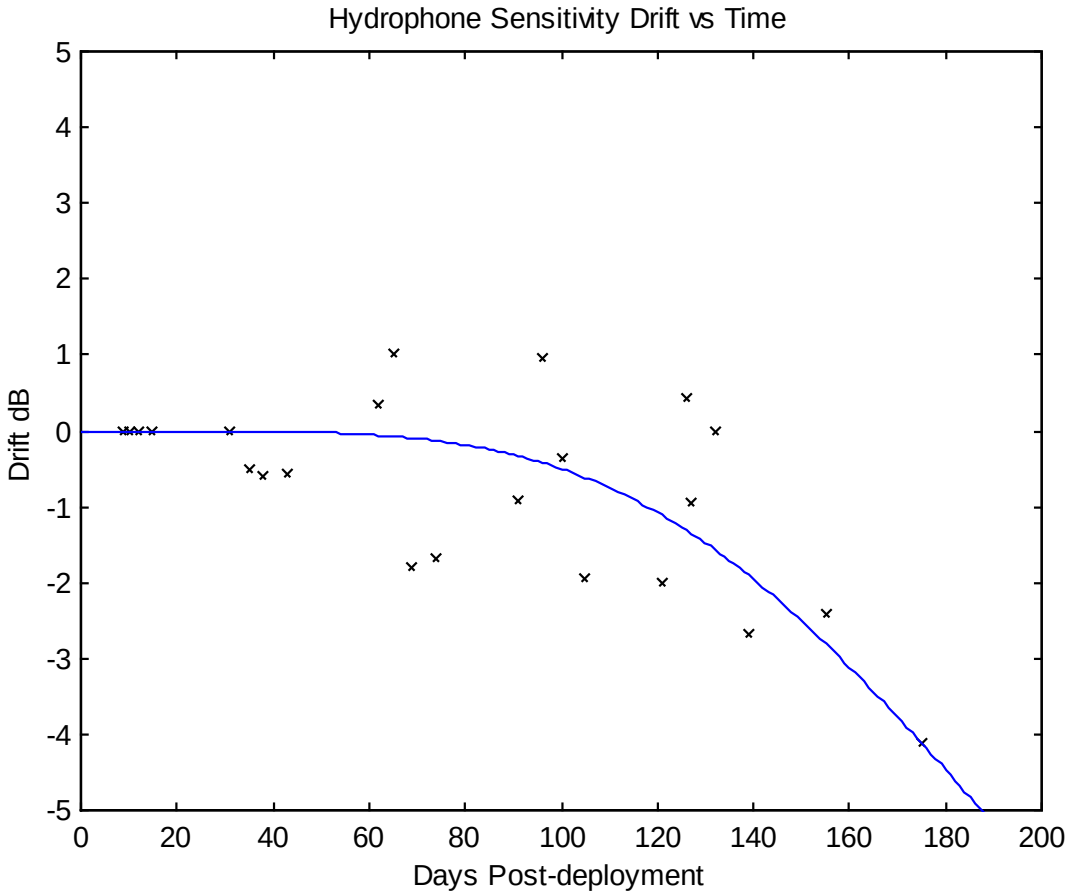


**Figure A2-2.** Average multi-station spectral level vs. time plotted for all deployments with proposed fitting curve.

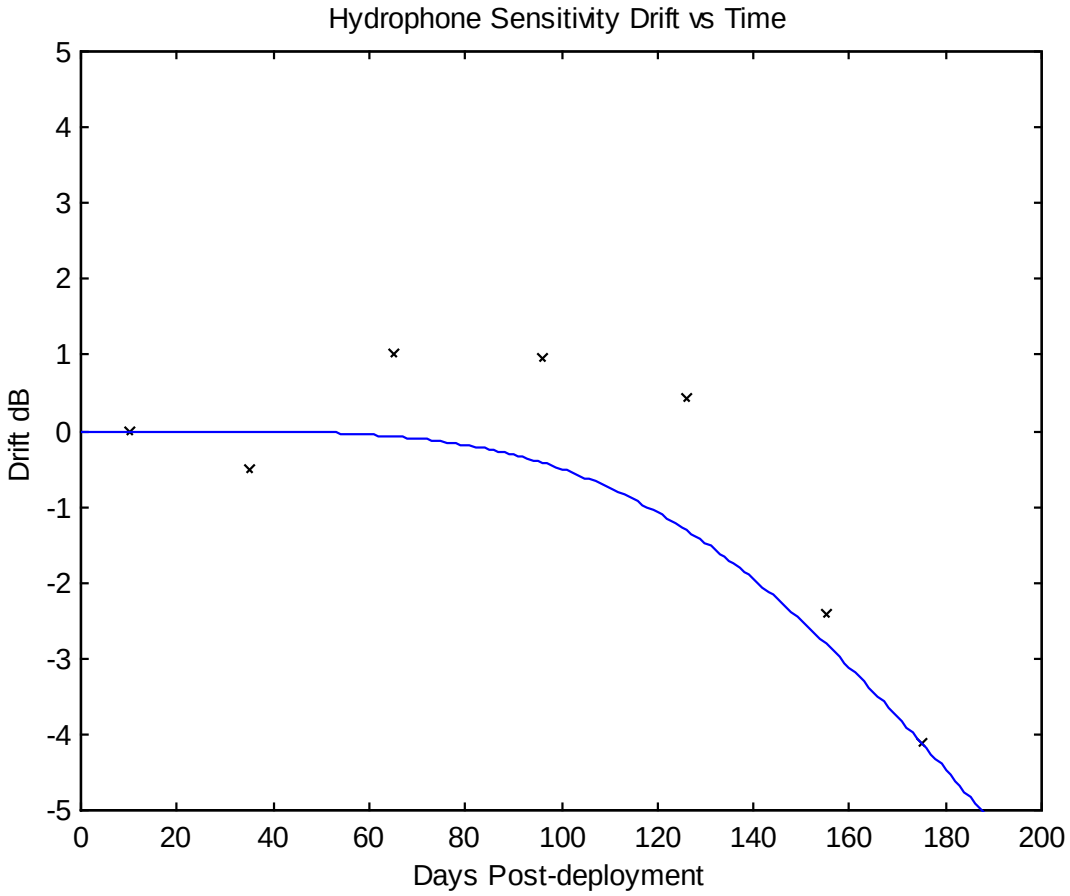


**Figure A2-3.** Average multi-station spectral level vs. time for the Winter 2012-13 deployment with the earlier shown "combined data" fitting curve.

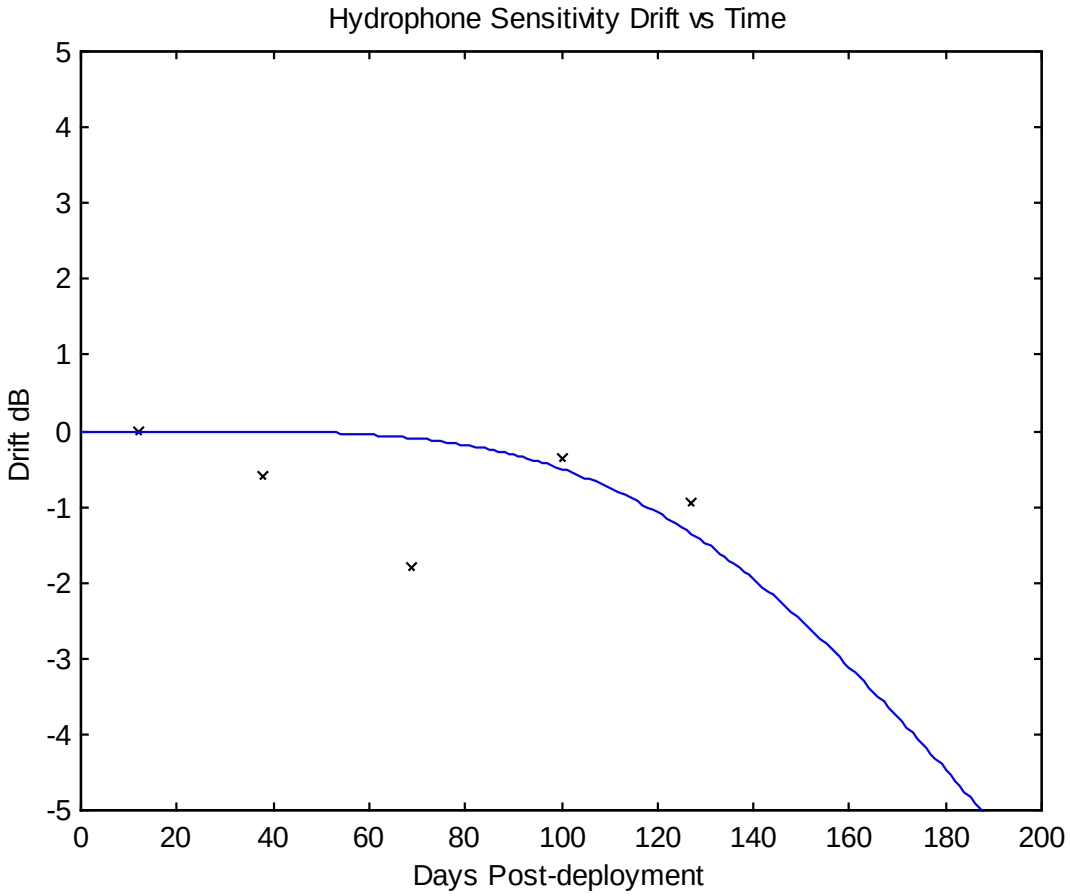


**Figure A2-4.** Average multi-station spectral level vs. time for the Summer 2013 deployment with the earlier shown "combined data" fitting curve.

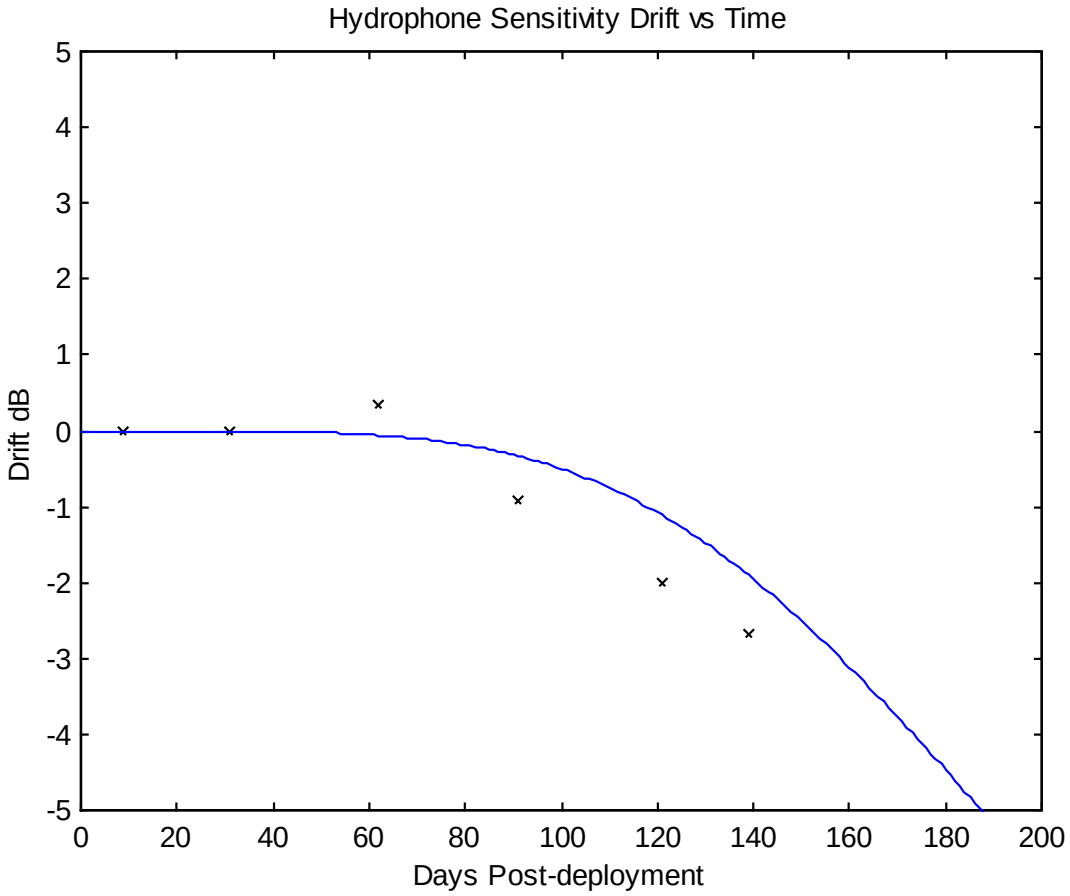


**Figure A2-5.** Average multi-station spectral level vs. time for the Winter 2013-14 deployment with the earlier shown "combined data" fitting curve.

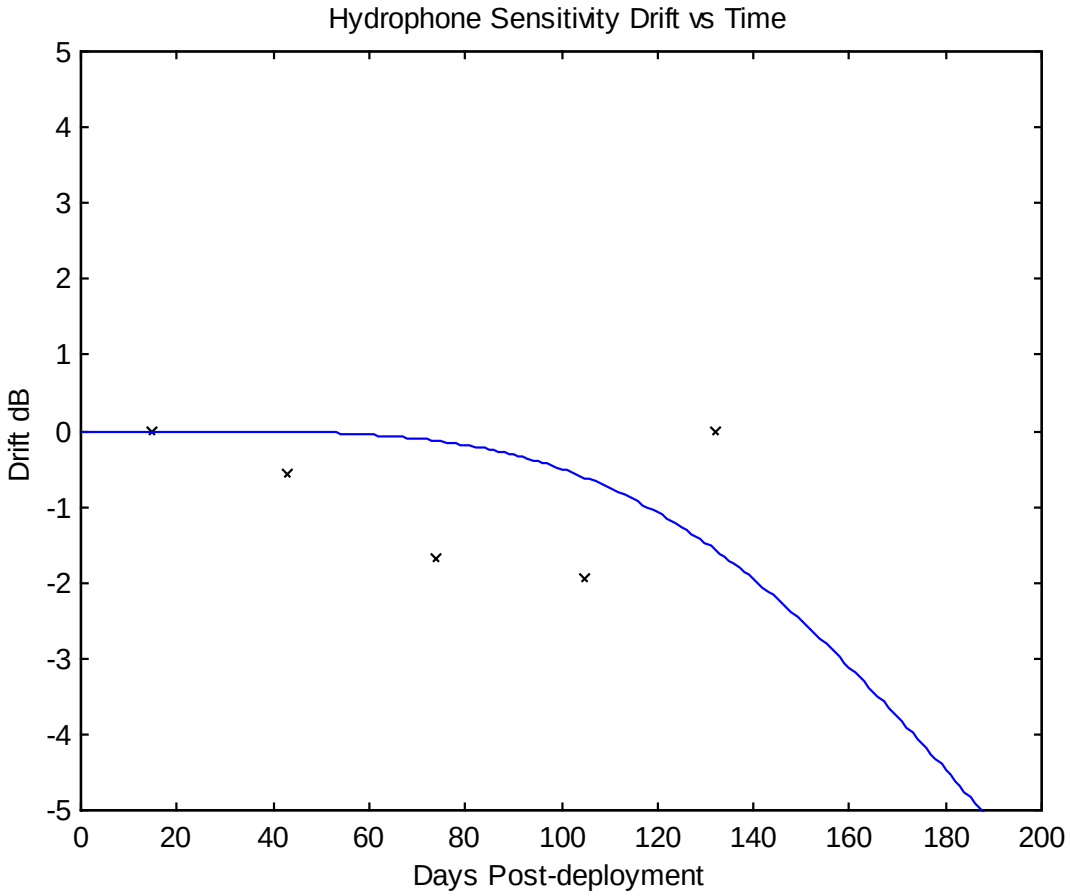


**Figure A2-6.** Average multi-station spectral level vs. time for the Summer 2014 deployment with the earlier shown "combined data" fitting curve.

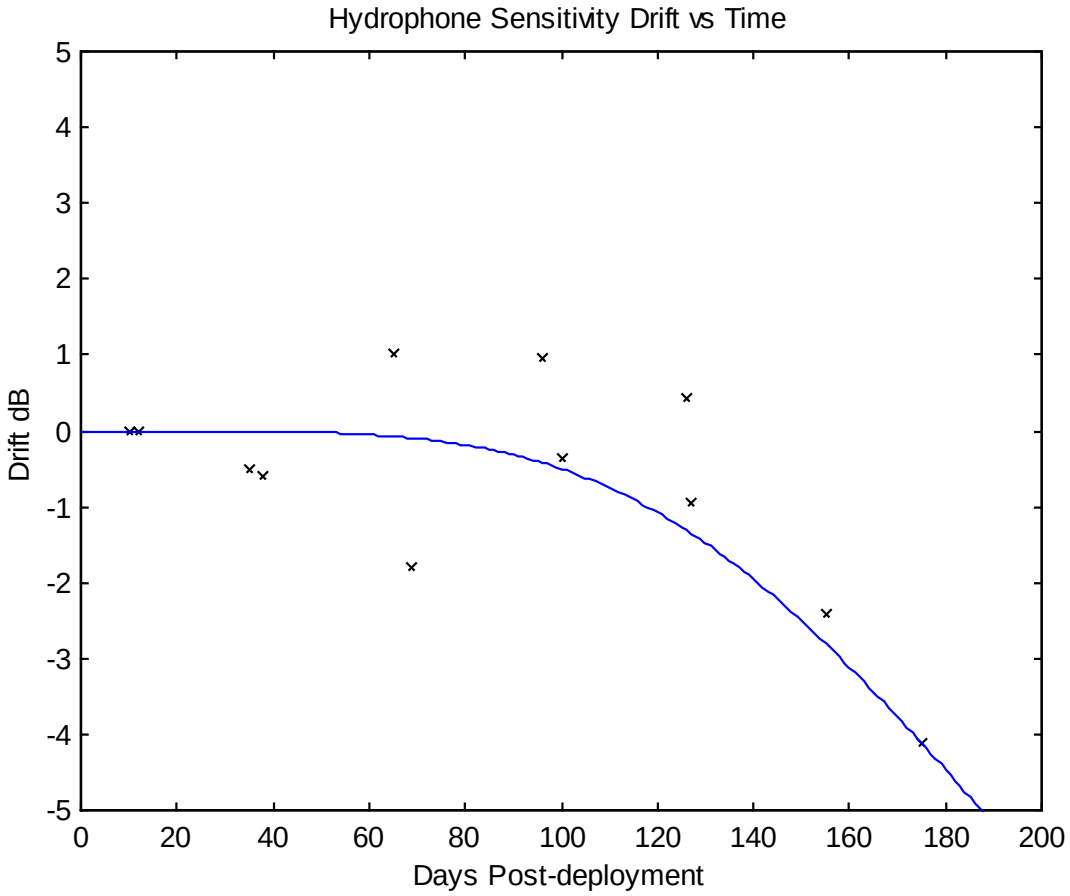


**Figure A2-7.** Average multi-station spectral level vs. time for all deployments using Geospectrum M8E hydrophones (i.e. Winter 2012-13 and Summer 2013 combined) with the earlier shown "combined data" fitting curve.

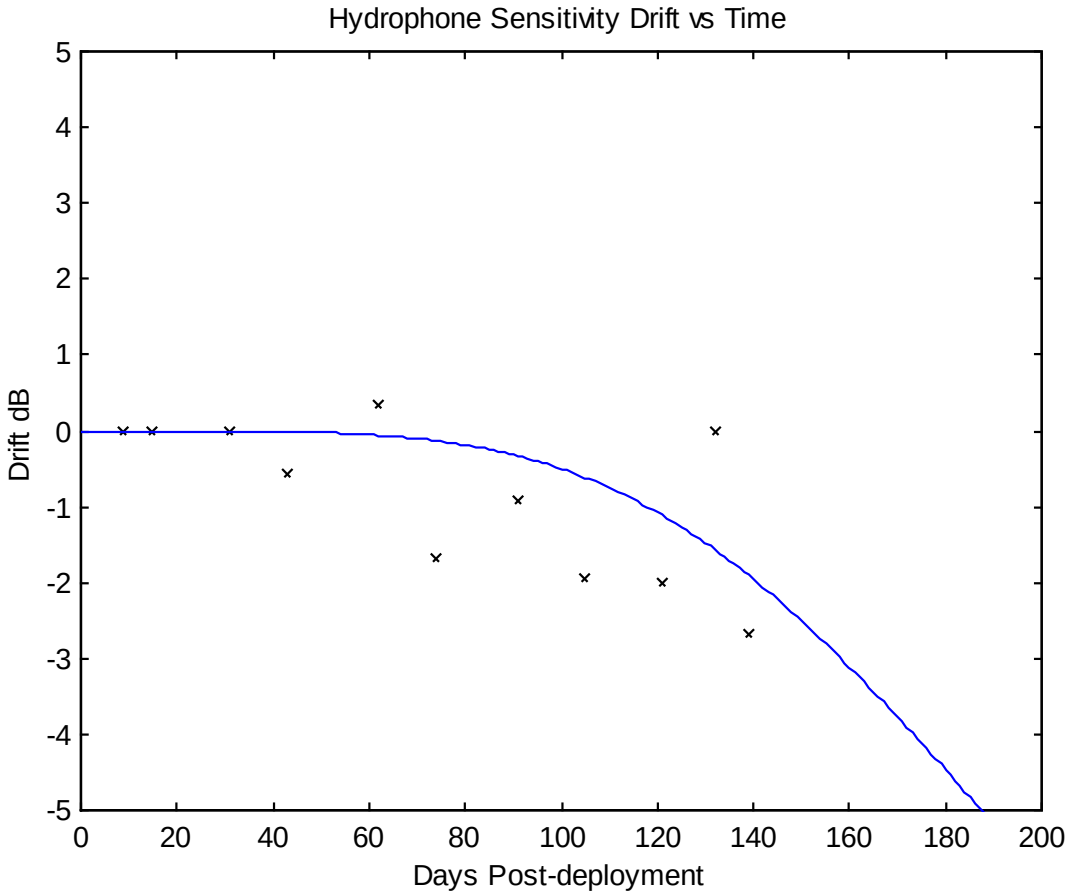


**Figure A2-8.** Average multi-station spectral level vs. time for all deployments using Geospectrum M8Q hydrophones (i.e. Winter 2013-14 alone) with the earlier shown "combined data" fitting curve (same data as in Fig. A2-5 in different context).

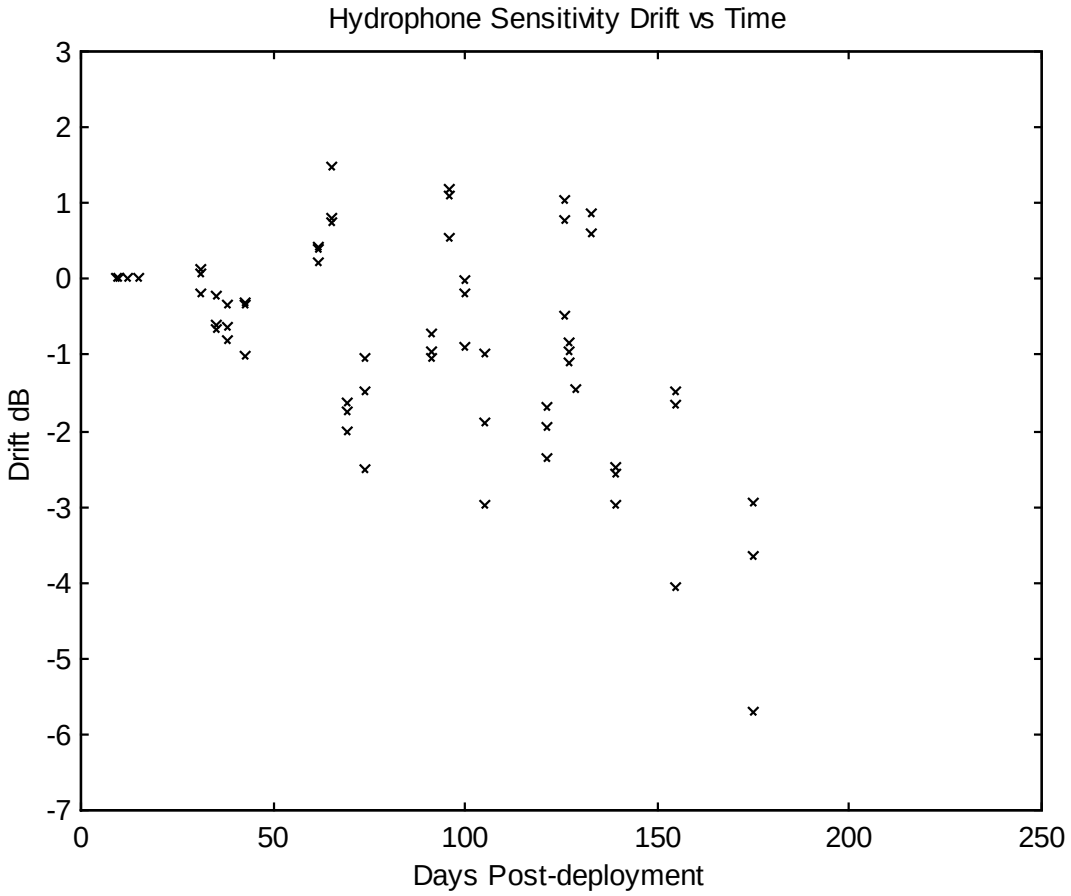


**Figure A2-9.** Spectral levels, station-by-station (non-averaged) vs. time from deployment.

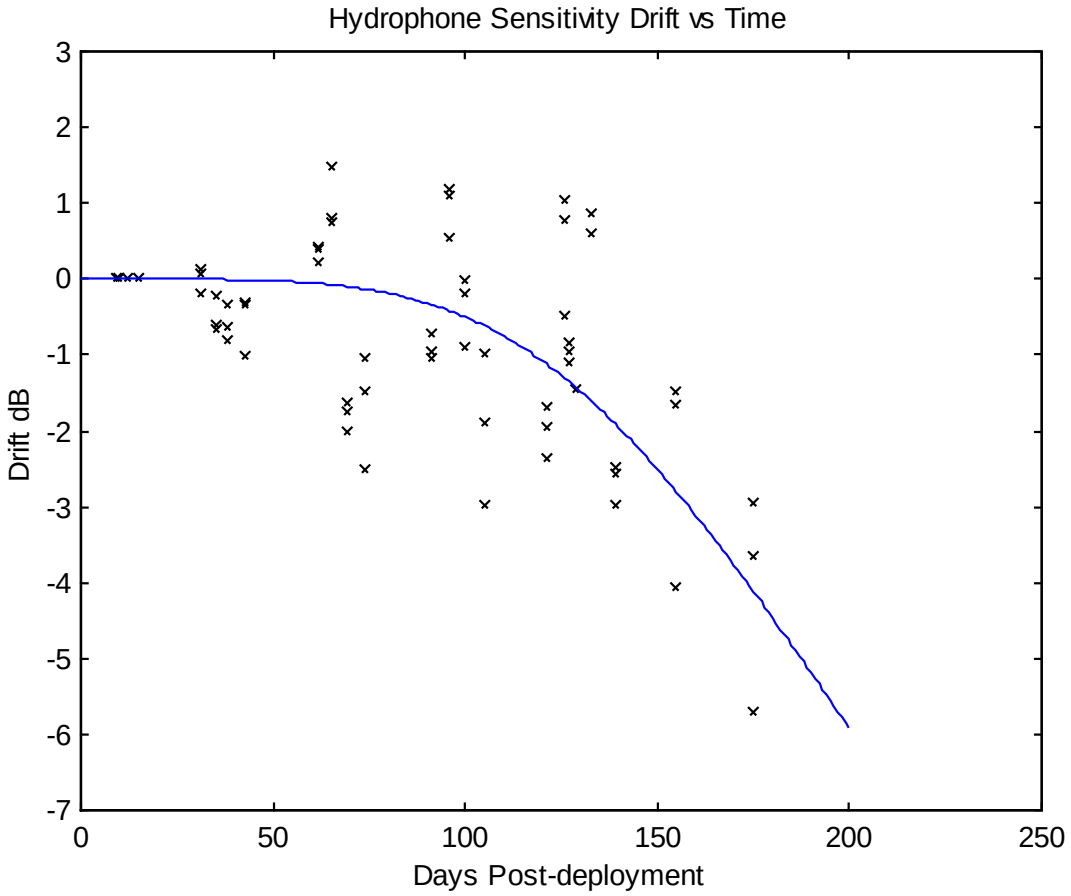


**Figure A2-10.** Same data as in Fig. A2-9 with "combined data" fitting curve as defined in main text.

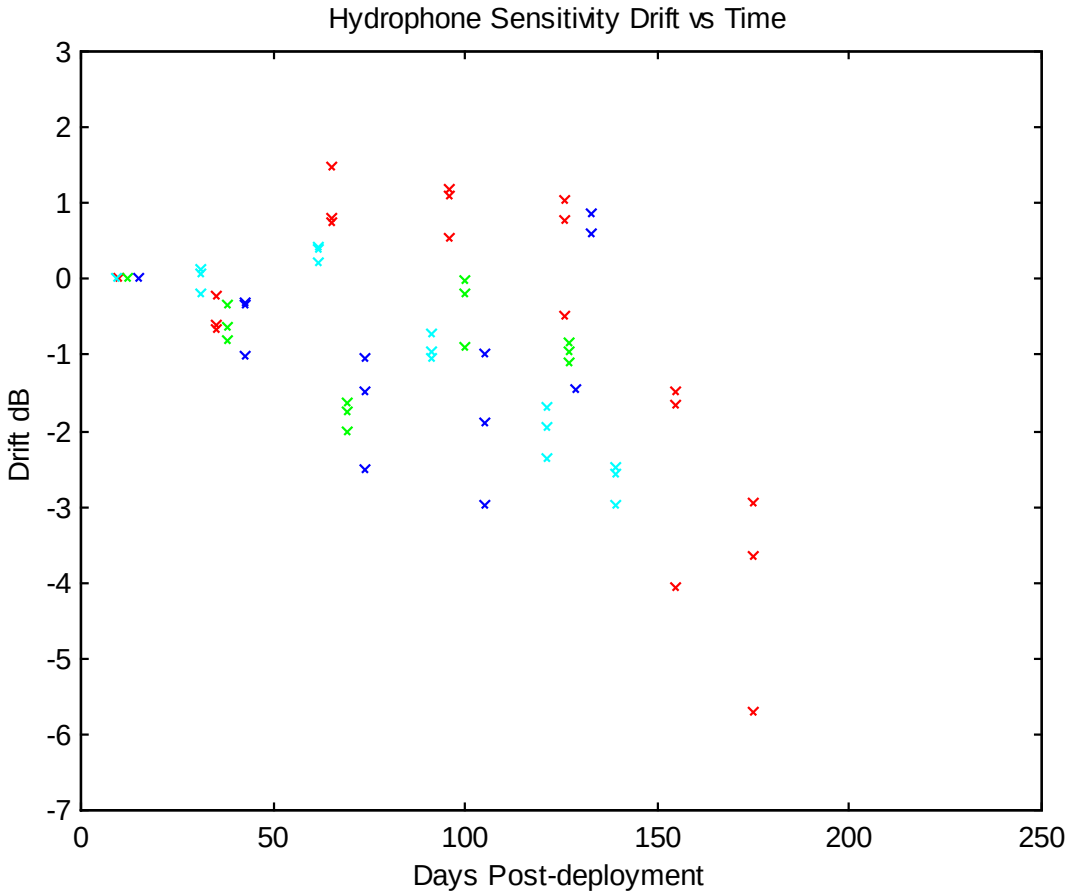


**Figure A2-11.** Same data as plotted in Fig. A2-9 with deployments colour-coded: Red – Winter 2012-13, Green – Summer 2013, Cyan – Winter 2013-14, Blue – Summer 2014

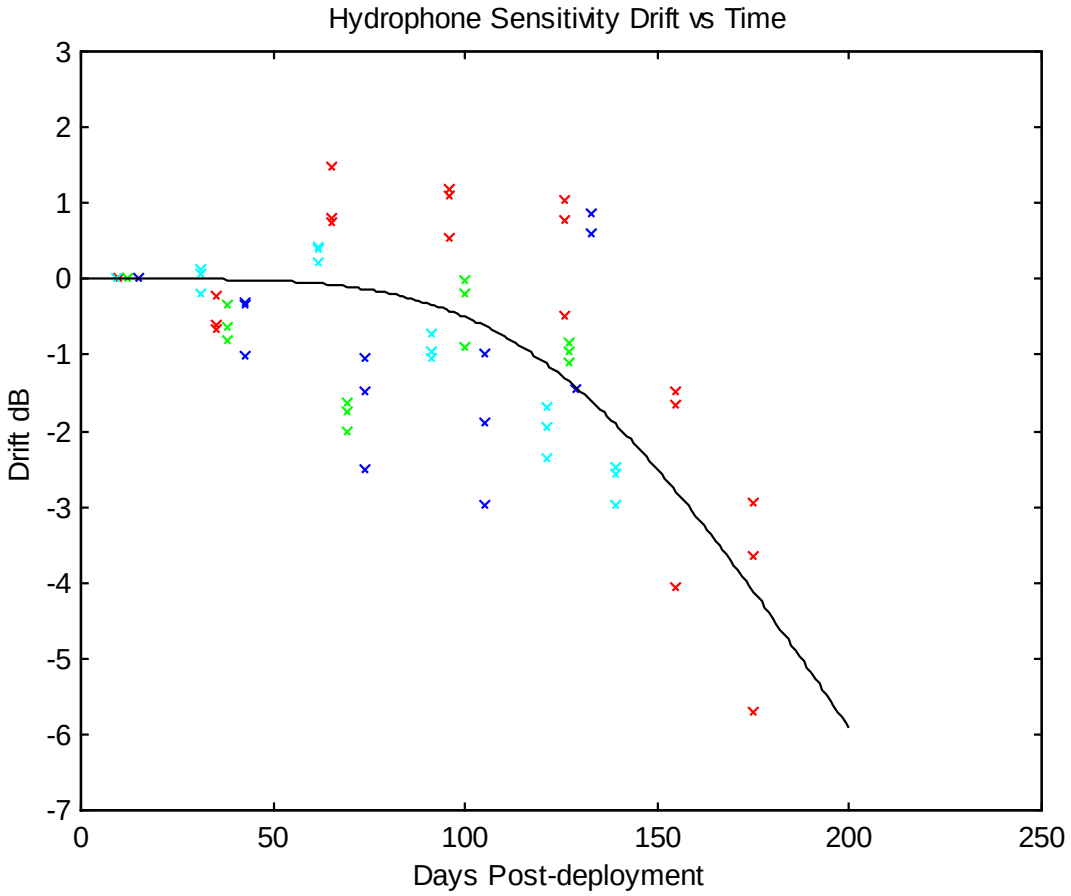


**Figure A2-12.** Same data as plotted in Fig. A2-9 with deployments colour-coded. The "combined data" fitting curve is superimposed. Codes: Red – Winter 2012-13, Green – Summer 2013, Cyan – Winter 2013-14, Blue – Summer 2014.

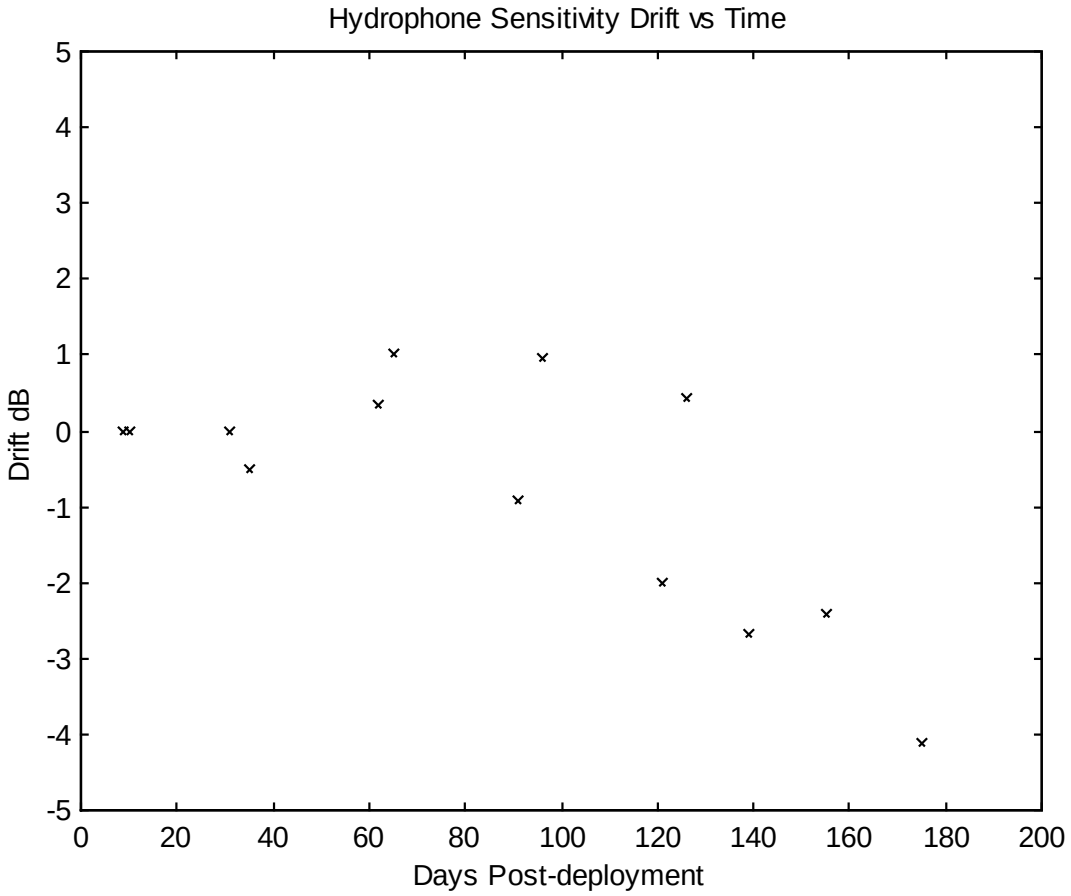


**Figure A2-13.** Average multi-station, winter-only spectral levels vs. time. The Winter 2012-13 and Winter 2013-14 datasets used differing model hydrophones.

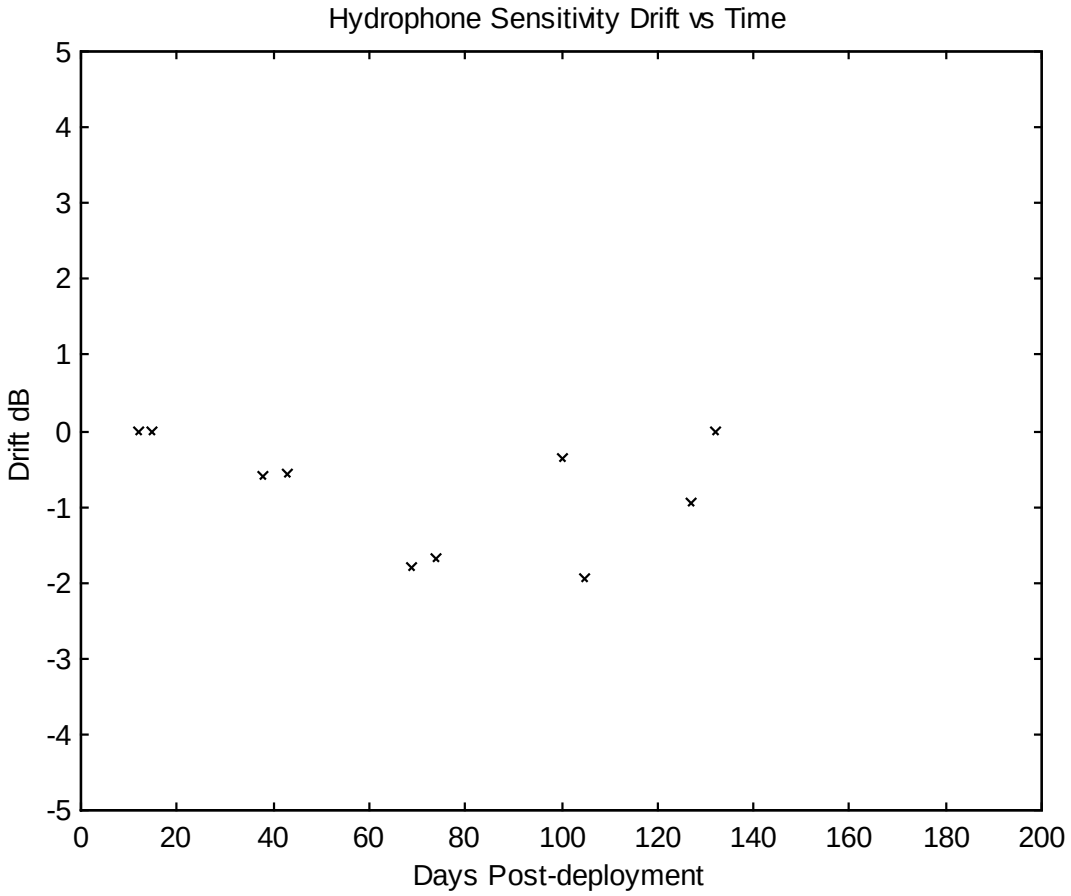


**Figure A2-14.** Average multi-station, summer-only spectral levels vs. time. The Summer 2013 and Summer 2014 datasets used differing model hydrophones.

# A3. APPENDIX 3: WIND AND METEOROLOGICAL ANALYSES

## A3.1. BACKGROUND

The close relationship between ocean ambient noise levels and prevailing sea states and atmospheric winds became quickly obvious with the extensive military use of ocean sound during World War II. Knudsen et al. (1948), summarising early work, noted strong correlations between ocean sound levels and both ocean sea state and the forcing atmospheric wind fields. Weather-related noise sources combined with biological and ship origin noise essentially defined the prevailing ocean ambient noise background from about 100 Hz to 25 kHz. Breaking waves were considered the primary sources of weather-related noise, the precise physical noise generation mechanisms remaining unclear. Rain was also known to increase ocean noise levels. Wenz (1962) elaborated on these mechanisms showing that ocean noise arising from wind dependent "bubbles and spray" was often dominant from about 50 Hz to 20 kHz. Noise levels below 100 Hz were strongly influenced by both ocean turbulence and by acoustic radiation from vessels, vessel related effects extending upwards to about 1 kHz. Wenz's conclusions, which still constitute a reasonably accurate summary of ocean noise generation mechanisms, are reproduced in Fig. A3-1.

In the frequency range 500 Hz - 20 kHz, in the absence of extraneous precipitation or strong anthropogenic or biological noise sources, the observed deep ocean noise spectral density for a given wind speed smoothly declines with increasing frequency at a rate of 5 – 6 dB/ octave or about 17 dB/decade (Urick 1975). Wenz (1962) observed that for fixed frequencies between 500 Hz and 5 kHz, spectral levels tended to rise about 5 dB for each doubling of wind speed over the range of 2.5 to 40 knots. Franz (1959), utilizing both theory and lab experiment, had earlier demonstrated that rain could contribute significantly to ambient noise levels from 1 to 10 kHz resulting in a distinctive, nearly white (i.e. level over frequency) spectral character with an amplitude determined by the rainfall rate. This rain-dominated spectral response contrasts with the steeply declining with frequency spectral character arising from wind alone. Shaw et al. (1978); building on the earlier studies of Wenz (1962), Piggott (1964), and Crouch and Burt (1972) - all of which had demonstrated essentially linear relationships between measured spectral levels and the log of wind speed, $v$, (~20 log $v$ dependence > several hundred Hz) - established the practicality of inferring local wind speed from deep ocean ambient sound levels at 5 kHz. However, non-wind origin noise from precipitation and from local vessel passages, placed limitations on single frequency methods. Evans et al. (1984) extended this work to 3 observed noise frequencies (4.3, 8.0 and 14.5 kHz) using an early version of the so-called WOTAN (**W**eather **O**bservations **T**hrough **A**mbient **N**oise) instrument package. Most study data were drawn from the equatorial Pacific but with some data from both sides of the North Atlantic with comparisons to select earlier studies. A 17 dB/ decade fall-off of spectral levels with frequency for fixed wind speeds was confirmed over the examined frequency range. More importantly, a fairly robust ability was demonstrated to predict local surface wind speeds to within ± 1 m/s from noise observations at depth.

Significantly, for a given noise frequency the critical linear relations between decibel spectral levels and log *v* required differing proportionality constants for winds speeds above and below about 5.5 m/s, the accepted threshold for the onset of ocean whitecapping.

A critical overview of the WOTAN technique together with a precise and systematic methodology or "universal algorithm" for its real world implementation was published by Vagle et al. (1990). Included were formulations for correcting acoustic spectral levels observed at depth to an equivalent source spectral level at the ocean surface. This involved corrections for geometric propagation from the measurement depth, non-bubble acoustic absorption, and water column refraction. Methodologies were set forth to reduce comparison wind speeds to a standardized measurement height (10 m), with relationships for deriving friction velocity and wind stress. FASINEX experimental data from the western North Atlantic yielded "Q" values, i.e. the slopes of decibel sound spectral level vs. log acoustic frequency, of close to -19.0 dB/decade between 4.3 and 19.5 kHz for wind speeds exceeding 2 m/s. This observation permitted spectral observations at multiple observation frequencies to be reduced to a single standard acoustic frequency for comparison. Q values deviating significantly from expectation (criteria supplied) allowed exclusion of data as contaminated by either precipitation or shipping noise.

While linear regressions of spectral source level vs. log of various wind speed measures can be used for wind speed inference, contrasts between the best fitting linear regression slopes for high and low wind speeds were flagged as problematic in the Vagle et al. studies. In reality, an overall quadratic fit, as opposed to a series of local linear fits, appeared advantageous. A 2$^{nd}$ alternative regression technique was proposed which significantly reduced the non-linearities otherwise encountered when working over wide ranges of wind speed. The alternative technique regressed absolute acoustic noise pressure (i.e. non-decibel pressure in Pascals) against linear wind speed - or pressure squared against linear wind stress (perfect linearity on employing the 2$^{nd}$ regression technique would also imply perfect linearity using the 1$^{st}$ regression technique with a regression slope of exactly 20 dB/decade provided that zero sound pressure level accompanies zero wind speed - which is never observed in reality). Application of the above methodologies permitted delineation of wind speeds in the range 4 – 15 m/s from field-measured noise levels with an uncertainty of about ± 0.5 m/s. Intervals of rapidly changing winds produced the greatest discrepancies. Predicted winds tended to be lower than measured during systematically rising winds and vice versa for decreasing winds. These discrepancies were probably a consequence of the time lags required for the surface wave field and its attendant sound generation mechanisms to equilibrate with the ambient wind.

## A3.2. DATA

The effects of **inferred** local wind fields on measured acoustic levels at all three deep-water AMAR sites (Table A3-1) were explored for the initial Winter 2012 deployment acoustic dataset. Since data was extracted from the 16 kHz sampled acoustic channel only, 8 kHz constituted the theoretical folding frequency. The months of November 2012

and March 2013, respectively near the beginning and the end of the same winter deployment were selected for study. The March acoustics from GulSho were truncated on the 26th inclusive to avoid some corrupted data.

In the absence of on-site wind sampling, standard (presumably 10 m height) wind speed data at 1 hr sample intervals was acquired from the Environment Canada Sable Island meteorological station which was located dominantly west of and at distances of 87.8, 113.5 and 156.4 km from MidGul, GulSho, and ShoHald respectively. The recorded Sable Island precipitation type was also utilized.

## A3.3. DATA REDUCTION

For each hourly meteorological observation, a corresponding acoustic file was selected with start time within 7.5 min (consecutive files spaced 15 min apart) of the nominal met observation time. Hourly sound level spectral estimates were computed from 100 consecutive, non-overlapping 32768 pt data series sampled at 16 kHz beginning at the start of the selected acoustic file. This resulted in a total effective averaging time of 205 s for each estimate. The normal compensated Hanning time domain window function was applied in spectral estimation. While the timing of specific spectral estimates may be slightly displaced from the actual time of wind sampling[14] any time displacements are assumed negligible compared to the 1 hr inter-sample time interval. After correction for the calibration and spectral responses of the AMAR instruments, the resultant spectral levels were **averaged** over 32, 1/3 octave bins with center frequencies ranging from 5 Hz to 6.451 kHz. Most relevant to our analysis are the 6 consecutive 1/3 octave estimates with center frequencies of 2.032, 2.560, 3.225, 4.064, 5.120, and 6.451 kHz. These 6 spectral bins lie within the frequency range anticipated to yield fairly linear acoustic decibel spectral level vs. log frequency "Wenz" curves for given wind speeds. Of the 6 discrete binned spectral estimates, special recourse will be had to the 5120 Hz level, simply referred to as the "5 kHz level" though the center frequency is slightly removed. Data reduction saw the generation of consecutive hourly combined parameter records, each record containing the date, UTC time, wind speed (km/hr), precipitation type, and the corresponding 32 acoustic spectral bin levels. The supplied 2012 Sable Island wind dataset was missing hourly values for Nov. 15th at both 1200 and 1300 UT and for the Nov. 27th at 2000 UT. These three hourly values were restored by interpolation. The March 2013 wind data was complete as supplied.

## A3.4. ANALYSIS

The wide geographic separations between the AMAR stations and the Sable Island meteorological station whose observations serve as local wind proxies, limits the rigour with which correlations between acoustic noise levels and inferred local winds can be explored. Much critical work elsewhere using superior quality data has been published. Consequently, we limit our investigation to demonstrating that the AMAR data is

[14] Time offsets originate both from the data selection methodology as outlined as well as any cumulative time base differences between the AMAR internal clocks and the independent met sampling times.

"typical", that is, it largely conforms to anticipated levels and patterns thereby confirming that the prevailing wind speed is dominant in determining acoustic levels in at least the explored 1 – 6 kHz spectral range. To begin, plots of wind speed and simultaneous 1/3 octave 5 kHz acoustic levels as functions of time for both monthly study periods at MidGul, GulSho, and ShoHald are shown in Figs. A3-2, A3-3, and A3-4 respectively. Wenz-type scatter plots of hourly power spectral amplitude averaged 1/3 octave vs. acoustic frequency (log scale) using contrasting colours to delineate simultaneously observed Sable Island wind ranges are shown in Figs. A3-5 to A3-7. These data are plotted without consideration of the simultaneous precipitation.

The average slopes of the hourly Wenz-type curves within the low kHz range have been explored in some detail for both monthly analysis periods. We proceeded by normalizing the 6 consecutive 1/3 octave spectral estimates with center frequencies of 2032, 2560, 3225, 4064, 5120, and 6451 Hz to the 2032 Hz estimate, hour-by-hour, by decibel subtraction. The resultant differences, i.e. "Relative Spectral Level", were plotted, hour-by-hour, against the relevant bin center acoustic frequencies on a log scale. The slope of the linear least squares regression fit to the Relative Spectral level (dB) vs. Log( Acoustic frequency) expressed in units of dB/decade defines the time averaged effective slope of the Wenz curves. Observe that the employed averaging process encompasses a natural ensemble of wind speeds. The linear fitting has been performed using two different data acceptance criteria:
1) The 1st fit simply accepts all data.
2) The 2nd fit employs "weather-filtering" i.e. elimination of all acoustic data points where **either** Sable Island winds speeds were < 20 km/hr or Sable Island rain or freezing rain were reported.

The working conjecture underlying the 2nd fitting procedure is that lighter wind fields are more likely to incorporate local influences and, therefore, are less likely to correlate well between Sable Island and the remote AMAR sites. Lighter winds also imply lower wind-generated acoustic levels, the latter being more prone to contamination from other noise sources either real ambient, such as precipitation-generated or biological noises, or extraneous non-ambient, such internally-generated instrumental noise or the higher frequency residuals of mooring generated pseudo-noise. A representative sample (GulSho station Nov. 2012) processed both with and without employing weather-filtering is shown in Fig. A3-8. A complete set of weather-filtered scatter plots with fitting linear regression lines appear in Figs. A3-9 to A3-11. Associated linear regression slopes and correlation coefficients on employing each of the data acceptance procedures appear in Table A3-2.

Regressions of acoustic level against wind speed have been examined for our AMAR datasets for a single chosen acoustic frequency. Specifically, plots of 1/3 octave averaged decibel spectral noise levels for the frequency bin centered at 5120 Hz vs. Sable Island wind speed plotted on a logarithmic horizontal axis[15] with linear regression lines

[15] Winds of 0 km/hr were assigned a nominal speed of 1km/hr for these plots only so all data points could be observed. This should not affect the subsequent analysis.

fitted to log(wind speed) for each of the three stations appear in Figs. A3-12 to A3-14. The 5120 Hz acoustic frequency was selected somewhat arbitrarily but is roughly consistent with that employed by Shaw et al. (1978). Alternative plots and regressions of 5120 Hz linear acoustic pressure vs. linear wind speed, more consistent with the preferred methodologies of Vagle et al. (1990) appear in Figs. A3-15 to A3-17. For both above regression approaches, all data points have been plotted but where weather-filtering was employed, regression lines are fitted only to the data points with wind speeds $\geq$ 20 km/hr. Data points corresponding to periods of rain or freezing rain (drizzle is not considered rain) observed at Sable Island, plotted in red, are also omitted from the weather-filtered regression calculations. Points corresponding to periods of snow, plotted in blue, are **not** eliminated from the regressions since there is little evidence that snowfall generates significant acoustic noise at 5 kHz (Scrimger et al. 1987). Linear regression parameters and correlation coefficients were computed and tabulated (Table A3-3) assuming, in the first case, zero time lags between Sable Island winds and the measured noise fields (plots displayed), and, secondly, time lags in integral whole hours that maximize the correlation coefficients between decibel spectral levels and the log of Sable wind speeds. Positive lags are defined by the notion that current AMAR acoustic levels correlate more highly with past Sable Island winds - as anticipated for weather systems moving generally west to east.

## A3.5. RESULTS AND DISCUSSION

### *A3.5.1. General*

Both study periods, November being early and March late in the same Winter 2012-13 deployment, were characterized by wide ranges of wind speed (Figs. A3-2 to A3-4). Because major uncertainties do exist regarding calibration (i.e. sensitivity) drift of the AMAR systems over extended deployments, critical evidence regarding this issue may be gained from the comparative study of acoustic levels for comparable wind speeds from early and from late within the same deployment. Any such clues regarding systematic sensitivity drifts will not be totally definitive since no attempt has been made to correct for seasonally variant acoustic absorption/propagation effects. In addition, since the moored AMARs were intended for multi-purpose acoustic studies over broad frequency ranges, their absolute calibrations and applied frequency response compensations in the low kHz range do leave something to be desired for critical wind noise studies, and are almost certainly less accurate than those of WOTAN systems specifically designed for wind speed measurement. For instance, the AMAR high resolution monthly spectral plots (section A4.1.HIGH RESOLUTION SPECTRA) reveal multiple dips between 1 and 8 kHz that for any given instrument appear both systematic and reproducible. These dips almost certainly arise from uncompensated instrumental response irregularities (origin uncertain, but possibly related to the proximate hydrophone placement relative to the AMAR pressure case) and therefore constitute one source of error. More positively, it should be noted that our highest utilized 1/3 octave bin centered at 6451 Hz does not incorporate frequency estimates affected by the known sharp dip in the AMAR response curves above 7500 Hz which appears related to the anti-aliasing characteristic of the instrument.

### *A3.5.2. Wenz Curves*

The Wenz-type curves for 10 km/hr increments of wind speed in Figs. A3-5 to A3-7 appear regular and well defined at GulSho and ShoHald above 100 – 150 Hz, and at MidGul above 200 – 300 Hz. Pseudo-noise levels at lower frequencies are especially high at MidGul and spill over into the otherwise anticipated lower frequency portions of the wind-dominated spectral space. However, the same pseudo-noise appears to damp out reasonably well before the anticipated "linear over log frequency" portions of the Wenz curves are reached at ≥2 kHz. Visually, there are strong suggestions that the curves are more consistent for Sable wind speeds ≥ 20 km/hr, an observation further explored below. The Wenz curves appear to flatten quite consistently for the last 1/3 octave frequency bin at 6451 Hz. This reduced slope is most likely an instrumental calibration effect as discussed above although precipitation origin sound could become significant near this frequency (Scrimger et al. 1987). It will be remembered that **all** existing data is plotted in Figs. A3-5 to A3-7 without regard to wind thresholds, simultaneous precipitation, or any consideration of possible systematic time delays between the AMAR acoustic levels and the remote Sable Island wind fields. In regard to time delays, the acoustic propagation analysis of Vagle et al. (1990) indicated that any mooring-observed acoustic field of wind origin is largely generated within a spatial radius of the same order as the mooring depth (this does vary somewhat with acoustic frequency). Consequently, AMAR recorders in the 1300 – 1900 m depth range (Table A3-1) should be mainly responsive to wind noise originating within several km of the mooring site. Since weather disturbances and their associated wind fields travel dominantly west-to-east along the Nova Scotia coast at characteristic speeds of 50 - 100 km/hr (a very rough estimate based on observations of successive weather charts) characteristic **average** delays of 1 – 2 hr, that is comparable to, to several times our 1 hr sampling interval, would seem not unreasonable. Delays associated with specific weather systems will deviate from any assumed characteristic average and therefore constitute a residual source of error even if compensation for an average delay is applied.

Wenz-curves for similar wind speeds and matching acoustic frequencies do appear to be characterised by lower ordinate values in March 2013 than in November 2012. From surficial visual examination of Figs. A3-5 to A3-7 the ordinate reduction would appear to be about 2½ dB for MidGul and GulSho and about 4 dB for ShoHald with uncertainties of about ± ½ dB. These ordinate reductions appear to further confirm the drops in system sensitivities over the deployment period previously reported in APPENDIX 2 based on less direct evidence – but again, alternative mechanisms arising from seasonal changes to the acoustic propagation environment have not been explored. These apparent sensitivity reductions are further examined below using more objective techniques.

The consistency of our estimated Wenz curve slopes is improved by elimination of data collected both at low wind speeds and during measurement periods potentially contaminated by precipitation noise as described earlier. This fact is demonstrated, for instance, for GulSho during Nov. 2012 in Fig. A3-8 and in Table A3-2 where the relevant correlation coefficient is observed to increase from 0.939 to 0.960 on the application of

weather-filtering. Similar improvements in correlation are noted at all other stations and datasets in Table A3-2. Linear regression slopes average -19.472 dB/decade for the weather-filtered data (Figs. A3-9 to A3-11 and Table A3-2), modestly higher than an average slope of -18.897 dB/decade on accepting all data. These slopes are in good agreement both with the roughly -20 dB/decade (-6 dB/octave) slopes for frequencies above 1 kHz as reported by Wenz (1962) at both deep and shallow water sites and the Q value of -19 dB/decade reported by Vagle et al. (1990) for the FASINEX dataset. Some caution is warranted for the comparisons with FASINEX Q values since standardization to a reference depth of 1 m corrects frequency dependent acoustic attenuation (among other things) so resultant Q slopes are nearly - but not exactly - comparable to the slopes for our non "standardized" AMAR data. Also, the close agreement of our computed slopes with those from previous studies may, in fact, be somewhat fortuitous since the frequency response characteristics of our AMAR instruments in the critical 2 – 6 kHz range are not compensated with extreme precision as discussed earlier. Uncompensated AMAR response irregularities are indeed hinted in Figs. A3-9 to A3-11; in particular, the final 6451 Hz estimate may well be biased high. It should be noted that our Wenz curve slopes explored in Figs. A3-9 to A3-11 are derived from the AMAR data alone with no utilization of the remote Sable Island weather data other than for the elimination of potentially unreliable data points. Also, the computed Wenz slopes should, at least to first order, be independent of any drifts in hydrophone sensitivities - provided such drifts do not involve amplitude non-linearities. Since our examination of Wenz curve slopes is in reality a study of the self-consistency of well defined, mainly local, noise generation processes it is not surprising that the correlation coefficients in Table A3-2 are quite high. Correlations do drop markedly when acoustic levels are regressed against non-locally measured wind speeds as will be seen in the next section.

### *A3.5.3. Regressions of Acoustic Level vs. Wind Speed*

The two differing linear regression approaches to relating acoustic levels to wind speeds were explored in Figs. A3-12 to A3-14 and Figs. A3-15 to A3-17 respectively. It will be remembered that the displayed regressions have been weather-filtered i.e. restricted to data points with winds $\geq$ 20 km/hr and with no simultaneously reported rain or freezing rain precipitation. Visual examination of relevant data scatter plots (points for all wind speeds are plotted) strongly suggests that a clear and obvious linear relationship rapidly breaks down below the employed 20 km/hr wind speed threshold (further confirmed by correlation analysis not shown). It is possible that pre-binning the regressed data by prior averaging of acoustic levels over a range of wind speeds, a technique used by some other investigators, might improve the linearity at lower wind speeds by removing an obvious bias in the distribution of data points toward lower wind speeds - an avenue we have not explored. Nevertheless, it seems reasonable that both the apparent breakdown of the linear relationships at low wind speeds as well as the relatively low correlations observed at higher wind speeds are primarily a consequence of the large spatial separations between the wind and acoustic sampling. Since wind speed fluctuations at lower wind speeds are more likely dominated by smaller spatial scale processes, such wind fields might be expected to correlate poorly over the long spatial scales employed in this analysis. Another potential problem is temporal aliasing since both our hourly wind

speed and acoustic level estimates use relatively short averaging times with no anti-aliasing filtering. However, the appearance of the time domain plots of Figs. A3-2, A3-3 and A3-4 suggests the frequency domain spectra of both wind speeds and 5 kHz sound level fluctuations are quite red. Assuming the red spectral character to also extend below the 0.5 cycle/hr Nyquist sampling frequency, adverse aliasing effects are probably minimal.

Removing the characteristic average time lags between the Sable Island wind fields and the corresponding, and presumably more locally generated, AMAR acoustic levels might partially compensate for the effects of their large, dominantly east-west spatial separations and, therefore, moderately improve both time series correlations and the quality of acoustic level regressions with wind speed. Figure A3-18 displays the correlation coefficients between 5 kHz decibel form sound spectral levels and Sable log (wind speed) at GulSho for both the Nov. 2012 and March 2013 datasets as functions of time lag in whole integer hours (the identical time lag assumed to characterize the entire month). Table A3-3 shows resultant acoustic vs. wind correlation coefficients and regression parameters for all stations and for both datasets using both lagged and non-lagged data. The identical specific time lags employed for both regressions were those maximizing the correlation coefficient between dB sound spectral level and log (wind speed). These lags varied between 0 and 2 hrs. Generally, employing wind data lagging improved correlations slightly. In one instance, GulSho March 2013, lagging the data so as to maximize the decibel sound x log wind speed correlation actually decreased the sound pressure x linear wind speed correlation. Lagging to maximize the numeric correlation coefficient generally decreased regression slopes - but only slightly.

The data of Figs. A3-12 to A3-14 with their related regressions provides insight regarding precise Wenz curve ordinates at 5120 Hz. Wenz curve ordinates might be expected to be comparatively more sensitive to site-dependent absorption and refraction effects (Vagle et al. 1990) than the Wenz curve slopes. Consequently, the ordinates are more difficult to compare numerically to field results elsewhere in the absence of these detailed corrections – which we have not attempted. Discrepancies of several dBs between AMAR noise level measurements conducted at 1300 – 1900 m depth compared to similar measurements conducted near-surface or mathematically extrapolated to the near-surface may be possible (discrepancies are further discussed below for the alternative regressions using linear wind speed). Nevertheless, our observed ordinate values appear to be of the right order: For instance Vagle et al. (1990) display a regression line to their FASINEX data (their Fig. 4 and Table 2) which predicts a sound spectral level of 55.22 dB re $1\mu Pa^2$/Hz at an assigned frequency of 5120 Hz for winds (their "$U_N 10$" which we assume to correspond to our Sable measured wind) in the range of 8 – 10 m/s. Our own (lagged and weather-filtered) regressions at the identical 5120 Hz frequency and center-of-range wind speed of 9 m/s (32.4 km/hr) yield 54.91, 53.94, 53.72 dB re $1\mu Pa^2$/Hz at MidGul, GulSho, and ShoHald respectively using our November 2012 AMAR data, gathered sufficiently early in the deployment to unlikely be strongly affected by calibration drifts. We believe that these regression acoustic levels for a given wind speed compare quite reasonably to those of the Vagle et al. considering the absence of detailed acoustic absorption and refraction corrections.

Regressions slopes at all three AMAR stations in Figs. A3-12 to A3-14 and Table A3-3 (upper half) are markedly shallower for the month of Nov. 2012 than for Mar. 2013 (average 21.90 vs. 26.93 dB/decade respectively). Since average winds speeds were generally higher at Sable Island in March 2013 than in November 2012 (Fig. A3-2) the behaviour of the regression slopes may appear at variance with Vagle et al.'s observation of higher wind speed ranges being associated with lower (piecewise) regression slopes i.e. non-linearity. A typical overall regression slope from Vagle et al. is 28.39 ("*B*" value from their Table 3 on their utilization of log "$U_N$ 10" as the wind speed measure), close to our March 2013 slopes but considerable higher than our slopes for Nov. 2012. Perhaps pre-binning our data points for fixed increments in log wind speed before computing the regressions might yield more consistent results? Note that our regression slopes should not be influenced to first order by any systematic drifts in hydrophone sensitivities.

We now consider the alternative linear regression fits to sound spectral pressure level vs. linear wind speed displayed in Figs. A3-15 to A3-17 and Table A3-3 (lower half). It is observed that the regression slopes on average are fairly consistent between Nov. 2012 and March 2013 (15.79 vs. 14.64 μPa/(km/hr)) respectively. Comparing these regression fits to those of Vagle et al., especially their Table 4, introduces the complexity of their spectral sound levels and accompanying regressions having been plotted after frequency shifting to a standard reference frequency of 8 kHz. For the earlier considered regressions of dB spectral sound levels vs. log (wind speed), frequency shifting for a specified frequency reduced to a simple decibel Y-axis constant offset leaving regressions slopes unaltered. When plotting data points with spectral acoustic pressure as the ordinate, frequency shifting reduces to the application of a fixed multiplicative factor to the ordinate value. After frequency shifted data is regressed, the relevant multiplicative factor must be properly utilized to correct both the regression slopes and intercepts to the corresponding slopes and intercepts for specific acoustic frequencies. Using the Vagle et al. (1990) notation and their relations (5) and (18) and assuming frequency shifting for Wenz curves having a constant slope of -19 dB/decade:

$$\begin{aligned} \mathrm{SSL}_0(f_0) &= \mathrm{SSL}_0(f_j) - 19.0\ \log(f_0/f_j) \\ &= \mathrm{SSL}(h, f_j) + \beta(h, f) - 19.0\ \log(f_0/f_j) \end{aligned}$$

Translating from decibel sound spectral levels to spectral sound pressure levels $P_0$:

$$\begin{aligned} \mathrm{P}(h, f_j) &= 10^{(\mathrm{SSL}_0(f_0) + 19\log(f_0/f_j) - \beta(h, f))/20} \\ &= \mathrm{P}_0(f_0) \cdot \left(f_0/f_j\right)^{19/20} \cdot 10^{-\beta(h, f)/20} \end{aligned}$$

Re-writing the relation immediate above in terms of regression slopes for our plotted non-shifted and non-refraction/absorption corrected sound pressure level measured at depth h:

$$\frac{\Delta \mathrm{P}(h, f_j)}{\Delta v} = \frac{\Delta \mathrm{P}_0(f_0)}{\Delta v} \cdot \left( f_0 \big/ f_j \right)^{19/20} \cdot 10^{-\beta(h, f)/20}$$

It is observed that our regression slope is related to the regression slopes of Vagle et al. by two separate multiplicative terms, the 1st term dependent on the degree of frequency shifting employed, and the 2nd dependent on the magnitude of the refraction and absorption corrections. Ignoring for the moment the refraction/absorption term, Table 4 of Vagle et al. suggests a frequency shifted regression slope of 53.91 μPa/(m/s) or 14.98 μPa/(km/hr) on translating from their m/s to our km/hr units. The frequency shift correction factor from their 8000 Hz reference frequency to our 5120 Hz computes to 1.528 resulting in a predicted regression slope at 5120 Hz of 22.89 μPa/(km/hr). This predicted slope is approximately 50% higher than our observed slopes. Might the multiplicative absorption/refraction correction factor, which we have not yet considered, explain the difference? Without extensive computations some hand-waving arguments are possible: The acoustic absorptions in isolation from the ocean surface to the Mid Gully, GulSho, and ShoHald instruments at 5120 Hz compute to about 0.62, 0.47, and 0.58 dB respectively (using a representative 16 April 2003 *HUDSON* CTD profile at 43° 46.71' N 57° 50.23' W south of Haldimand Canyon). At 5120 Hz the "listening radius" for our AMAR systems is probably modestly greater than their deployment depths, perhaps 20% more (see Fig. 2 of Vagle et al.). Therefore, it seems reasonable that the effective attenuation will be about equivalent to that characterizing an acoustic propagation path from AMAR recorder to surface at the effective listening radii of between 2 and 3 km length. The resultant total absorption corrections for MidGul, GulSho, and ShoHald should compute to around 1.0, 0.7, and 0.9 dB respectively. A β value of 0.9 dB translates to a regression slope multiplicative factor of 0.90, still not too far from unity, but when applied reduces the Vagle et al. 5120 Hz predicted regression slope to about 20.6 μPa/(km/hr) - the right order of magnitude but still higher than our observed 5120 Hz regression slopes. Might additional refractive attenuation associated with the persisting shallow sound channel in November and an uncapped surface low speed winter surface sound channel in March explain the remaining difference (a β value of just over 3 dB would bring the slopes into rough agreement)?.

Our linear regression Y-intercepts (the Y-axis passing though X-axis 0 wind speed) are small, averaging to only 14.8 μPa for Nov. 2012 and -118.7 μPa for March 2013. The relevant Vagle et al. Y-intercept is -104.5 μPa (their Table 4) which using the arguments above translates to roughly -104.5 μPa x 1.528 x 0.90 = -143.7 μPa for a hypothetical regression at 5120 Hz. Interestingly, if our AMAR systems drift in sensitivity over the course of the deployment, this drift will manifest to first order in both the slope and intercept on employing the 2nd type regression (i.e. linear in wind speed) but in intercept only on employing the 1st type regression (i.e. linear in log (wind speed)).

### *A3.5.4. AMAR Sensitivity Drifts*

Exploration of the contrasting AMAR sound level vs. wind speed regressions for acoustic data recorded early and late in the Winter 2012 deployment may afford quite critical tests for hydrophone sensitivity drifts over time. The November 2012 and March 2013 monthly datasets were centered about 34 and 154 days respectively into the same deployment. In Table A3-4 we have tabulated for each of the two observation months the predicted 5120 Hz decibel sound spectral levels for a hypothetical 40 km/hr wind using the regression parameter set appropriate to each AMAR station. On comparison of the resultant predicted decibel spectral levels, one infers that the AMAR recorders at MidGul, GulSho, and ShoHald dropped about 2.1, 2.2, and 4.5 dB respectively in overall sensitivity between the two analysed recording periods (on averaging the results of the two differing regression approaches). These values seem roughly consistent with the sensitivity drifts inferred above from visual inspection of monthly Wenz-type plots earlier in this section as well as the sensitivity drifts inferred from the less direct, non-wind constrained evidence presented in the Main Report. Again, seasonally variable acoustic absorption and refraction effects were not considered in arriving at these numeric values.

### *A3.5.5. Lower Frequency Wenz Curve Behaviour*

Our Wenz curves for November 2012 (Figs. A3-5 to A3-7) in the somewhat lower 100 – 1000 Hz frequency range for > 30 – 40 km/hr winds, appear to be in reasonably good agreement with the Scotian Shelf measurements of Zakarauskas et al. (1990) (see their Fig. 4 for 20 knot (37 km/hr) winds, the Zakarauskas et al. figure also including earlier measurements by Piggott) even though their work was restricted to shallower shelf environments. Mooring pseudo-noise in our MidGul data precludes reliable low frequency comparisons at this one site - at least without data selection to specifically exclude the noisy sections.

## A3.6. CONCLUSIONS

1) Display, analysis, and study of passive acoustic data collected at all three AMAR sites for two 1-month duration study periods within the Winter 2012 deployment with reference to concurrent meteorological data from Sable Island, show that the spectral properties of collected AMAR data in the wind-dominated portion of the acoustic spectrum above 500 Hz generally conform to the accepted spectral noise characteristics of deep ocean environments. Especially the case, were observed slopes of nearly 20 dB/decade that characterized instantaneous decibel sound spectral level vs. log (acoustic freq.) Wenz curves computed over the frequency range 2 – 6 kHz for a natural ensemble of wind speeds.

2) At fixed acoustic frequencies, AMAR acoustic noise levels were closely related to wind speed as discerned from remote wind measurements on Sable Island. Comparisons of AMAR data derived results at 5120 Hz with the widely accepted WOTAN study results of Vagle et al. (1990) show reasonable agreement for linear regressions of decibel

sound spectral level vs. log (wind speed) and rough but, at least on superficial examination, less exact agreement for sound pressure level vs. linear wind speed. Limitations to our study included no detailed corrections of the AMAR results for acoustic absorption and refraction effects in spite of an unusually deep deployment depth, uncertainties in the precise frequency responses of our instruments, probably drifts in AMAR hydrophone sensitivities over the multi-month deployments, and the use of Sable Island winds as a proxy to local wind fields at AMAR stations displaced hundreds of kilometres to the east. Visual inspection of regression plots suggests that the latter effect limits meaningful correlation studies to wind speeds exceeding 20 km/hr (~5.6 m/s). Time lagging Sable winds up to 2 hours relative to AMAR observed acoustic levels to crudely compensate for the general west to east propagation time of regional wind fields frequently resulted in modest improvements in linear correlations.

3) Predicted acoustic levels for a given wind speed at all three stations, using the best derived regression relationships, were lower for late in the Winter 2012-13 deployments than for near the deployment initiations. This fact argues strongly for the reality of systematic downward drifts in AMAR instrumental sensitivities during the course of the extended deployments. The magnitude of these drifts appear to differ significantly from instrument-to-instrument but total deployment drifts are of the same order as suggested by alternative investigations using no constraints on wind (APPENDIX 2).

## A3.7. REFERENCES (APPENDIX 3)


Crouch, W.W., and Burt, P.J. 1972. The logarithmic dependence of surface-generated ambient-sea-noise spectrum level on wind speed. J. Acoust. Soc. Am. 51(3): 1066 – 1072.

Evans, D.L., Watts, D.R., Halpern, D., and Bourassa, S. 1984. Oceanic winds measured from the seafloor. J. Geophys. Res. 89(C3): 3457 – 3461.

Franz, G.J. 1959. Splashes as sources of sound in liquids. J. Acoust. Soc. Am. 31(8): 1080 - 1096.

Knudsen, V.O., Alford, R.S., and Emling, J.W. 1948. Underwater ambient noise. J. Mar. Res. 7: 410 – 429.

Piggott, C.L. 1964. Ambient sea noise at low frequencies in shallow water of the Scotian Shelf. J. Acoust. Soc. Am. 36(11): 2152 – 2163.

Scrimger, J.A., Evans, D.L., McBean, G.A., Farmer, D.M., and Kerman, B.R. 1987. Underwater noise due to rain, hail, and snow. J. Acoust. Soc. Am. 81(1): 79 – 86.

Shaw, P.T., Watts, D.R., and Rossby, H.T. 1978. On the estimation of oceanic wind speed and stress from ambient noise measurements. Deep-Sea Res. 25: 1225 – 1233.

Urick, R.J. 1975. Principles of underwater sound. McGraw-Hill, New York. 384 p.

Vagle, S., Large, W.G., and Farmer, D.M. 1990. An evaluation of the WOTAN technique of inferring oceanic winds from underwater ambient sound. J. Atmos. Oceanic Technol. 7: 576 – 595.

Wenz, G.M. 1962. Acoustic ambient noise in the ocean: Spectra and sources. J. Acoust. Soc. Am. 34(12): 1936 – 1956.

Zakarauskas, P., Chapman, D.M.F., and Staal, P.R. 1990. Underwater acoustic ambient noise levels on the eastern Canadian continental shelf. J. Acoust. Soc. Am. 87(5): 2064 -2071.

**Table A3-1.** Water depths and AMAR measurement depths for the three Winter 2012 stations: "Depth Deploy" is the echosounder water depth observed on mooring free-drop release. "Depth AMAR (nominal)" is the inferred depth of the AMAR hydrophone assumed located 60 m above bottom as defined by the above sounding. "Depth BENTHOS" is an acoustic pinger triangulated depth to the BENTHOS acoustic release hydrophone (abt. 2 m above bottom) obtained post-deployment. "Depth AMAR from BENTHOS" is the resultant depth of the AMAR hydrophone assuming the same to be located about 58 m above the BENTHOS release hydrophone[16].

| Station | Depth Deploy | Depth AMAR (nominal) | Depth BENTHOS | Depth AMAR from BENTHOS |
|---|---|---|---|---|
| | m | m | M | m |
| ***MidGul*** | 1780 | 1720 | 1914 | 1856 |
| ***GulSho*** | 1516 | 1456 | 1435 | 1377 |
| ***ShoHald*** | 1700 | 1640 | 1789 | 1731 |

[16] The post-deployment BENTHOS inferred AMAR depth (final column) is believed to be the most accurate. Small lateral drifts of the AMAR units during the free-drop deployment or misinterpretation of echosounder diffraction fringes in regions of strong bottom bathymetry can result in substantial deployment depth errors in the absence of more direct post-deployment measurements.

**Table A3-2.** Correlation coefficients and slopes of linear regression fits to normalized 1/3 octave average sound spectral levels vs. acoustic frequency for bin center frequencies of 2.032 to 6.451 kHz. "Accepted" data have been subjected to weather-filtering.

| Station | Hourly Estimates | | Corr. Coeff. | | Slope dB/decade | |
|---|---|---|---|---|---|---|
| | *All Data* | *Accepted* | *All Data* | *Accepted* | *All Data* | *Accepted* |
| ***2012 Nov*** | | | | | | |
| MidGul | 720 | 391 | -0.926 | -0.953 | -18.957 | -19.615 |
| GulSho | 720 | 391 | -0.939 | -0.960 | -18.289 | -18.970 |
| ShoHald | 720 | 391 | -0.940 | -0.960 | -18.650 | -19.230 |
| ***2013 Mar*** | | | | | | |
| MidGul | 744 | 467 | -0.951 | -0.972 | -18.334 | -19.115 |
| GulSho | 624 | 392 | -0.963 | -0.975 | -20.027 | -20.251 |
| ShoHald | 744 | 467 | -0.961 | -0.974 | -19.122 | -19.649 |

**Table A3-3.** Correlation and regression properties of AMAR acoustic levels vs. Sable Island for wind speeds ≥ 20 km/hr and in the absence of Sable Island reported rain and freezing rain. For log scale wind speed plots, Y – axis passes through X-axis at wind speed = 1 km/hr so log (wind speed) = 0. For linear wind speed plots, Y- axis passes through X- axis at wind speed = 0 km/hr.

### Decibel Spectral Level @ 5 kHz vs. Log(Wind Speed km/hr)

| Station | Hourly Estimates | | | Corr. Coeff. | | Slope dB/decade | | Y – Intercept dB | |
|---|---|---|---|---|---|---|---|---|---|
| | *All Data* | *Weather Accepted* | *Lag hrs* | *No Lag* | *Lagged* | *No Lag* | *Lagged* | *No Lag* | *Lagged* |
| **2012 Nov.** | | | | | | | | | |
| MidGul | 720 | 391 | 0 | 0.688 | 0.688 | 22.381 | 22.381 | 21.107 | 21.107 |
| GulSho | 720 | 391 | 1 | 0.707 | 0.726 | 21.178 | 20.975 | 21.909 | 22.261 |
| ShoHald | 720 | 391 | 2 | 0.655 | 0.698 | 22.954 | 22.344 | 18.880 | 19.973 |
| **2013 Mar.** | | | | | | | | | |
| MidGul | 744 | 467 | 2 | 0.781 | 0.784 | 28.356 | 26.687 | 9.219 | 11.953 |
| GulSho | 624 | 392 | 1 | 0.781 | 0.781 | 28.032 | 27.033 | 8.478 | 10.126 |
| ShoHald | 744 | 467 | 1 | 0.728 | 0.734 | 27.836 | 27.056 | 6.444 | 7.747 |

### Sound Pressure Level @ 5 kHz vs. Wind Speed km/hr

| Station | Hourly Estimates | | | Corr. Coeff. | | Slope µPa/km/hr | | Y – Intercept µPa | |
|---|---|---|---|---|---|---|---|---|---|
| | *All Data* | *Weather Accepted* | *Lag hrs* | *No Lag* | *Lagged* | *No Lag* | *Lagged* | *No Lag* | *Lagged* |
| **2012 Nov.** | | | | | | | | | |
| MidGul | 720 | 391 | 0 | 0.680 | 0.680 | 17.023 | 17.023 | 26.815 | 26.815 |
| GulSho | 720 | 391 | 1 | 0.734 | 0.756 | 14.933 | 14.835 | 27.113 | 30.467 |
| ShoHald | 720 | 391 | 2 | 0.690 | 0.736 | 15.793 | 15.523 | -9.494 | 1.536 |
| **2013 Mar.** | | | | | | | | | |
| MidGul | 744 | 467 | 2 | 0.821 | 0.798 | 18.045 | 17.266 | -149.957 | -118.777 |
| GulSho | 624 | 392 | 1 | 0.846 | 0.848 | 15.417 | 15.251 | -122.621 | -114.799 |
| ShoHald | 744 | 467 | 1 | 0.786 | 0.795 | 11.614 | 11.403 | -83.421 | -75.272 |

**Table A3-4.** Predicted 5 kHz decibel sound sepectral levels at each of the three AMAR stations for a hypothetical 40 km/hr Sable Island wind speed for the two separate analysis periods November 2012 and March 2013.

**Predicted 5 kHz Decibel Sound Spectral Level for 40 km/hr wind**
**Utilizing Lagged Regression: Decibel Spectral Level @ 5 kHz vs. Log(Wind Speed km/hr)**

| Station | MidGul | GulSho | ShoHald |
|---|---|---|---|
| 2012 Nov. | 56.96 | 55.86 | 55.77 |
| 2013 Mar. | 54.71 | 53.43 | 51.09 |
| **Difference** | 2.25 | 2.43 | 4.68 |

**Predicted 5 kHz Decibel Sound Spectral Level for 40 km/hr wind**
**Utilizing Lagged Regression: Sound Pressure Level @ 5 kHz vs. Wind Speed km/hr**

| Station | MidGul | GulSho | ShoHald |
|---|---|---|---|
| 2012 Nov. | 57.00 | 55.90 | 55.88 |
| 2013 Mar. | 55.15 | 53.90 | 51.62 |
| **Difference** | 1.85 | 2.00 | 4.26 |

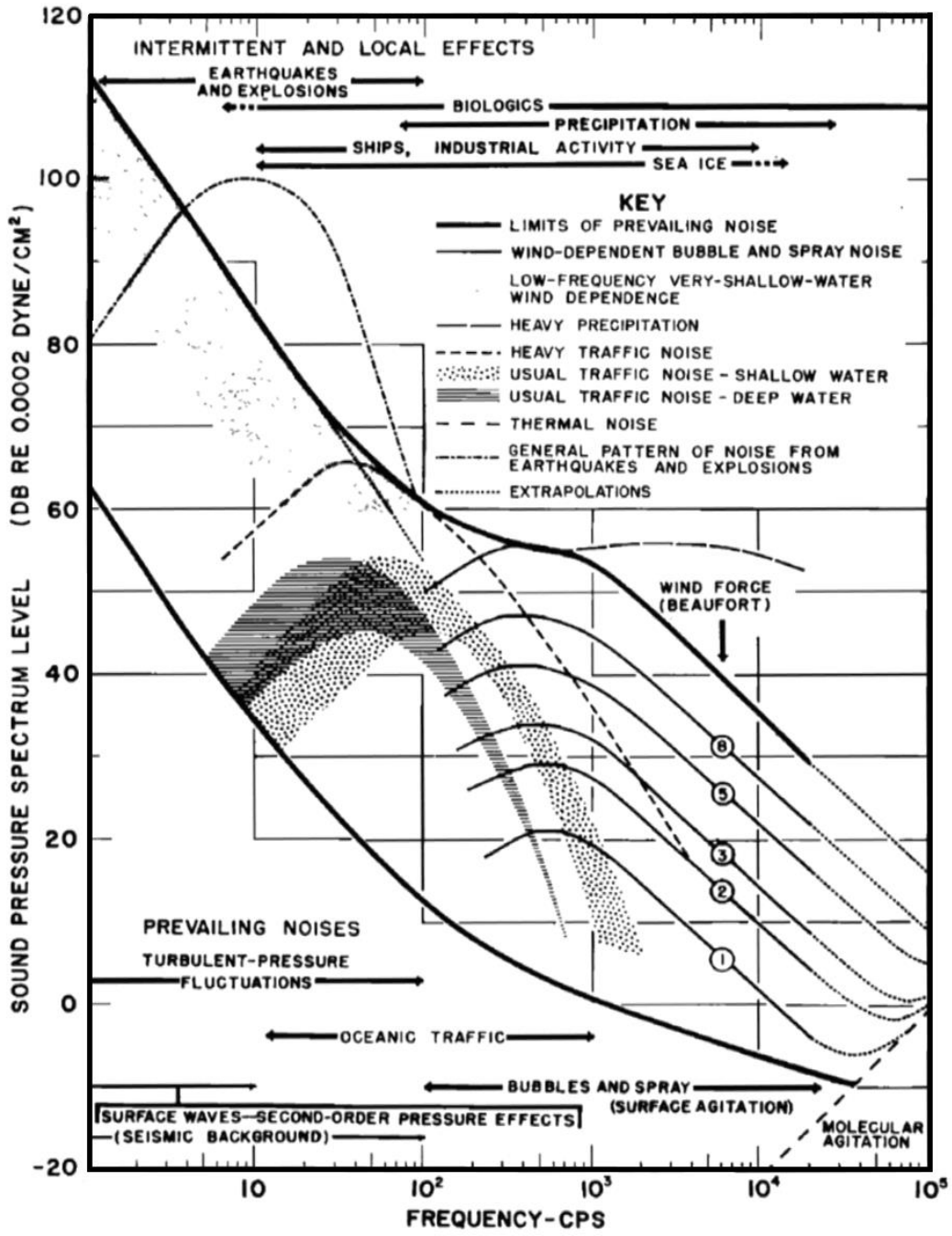


**Figure A3-1.** Typical oceanic noise spectra with inferred noise sources from Wenz (1962). To convert Sound Pressure Spectrum Levels in dB re 0.0002 dyne/(cm$^2$ Hz) to modern units of dB re 1μPa$^2$/Hz, add 26 dB. Winds are labelled on the Beaufort scale (***B***) which can be converted to wind speeds in m/s at 10 m above the sea surface by the relationship $v = 0.836\ B^{1.5}$ or to km/hr using $3.01\ B^{1.5}$. These curves are averaged over shallow and deep water observations. For the case of deep water onservations in isolation, ordinate values should be decreased 2 – 3 dB; for shallow water they should be increased by 2 – 3 dB.

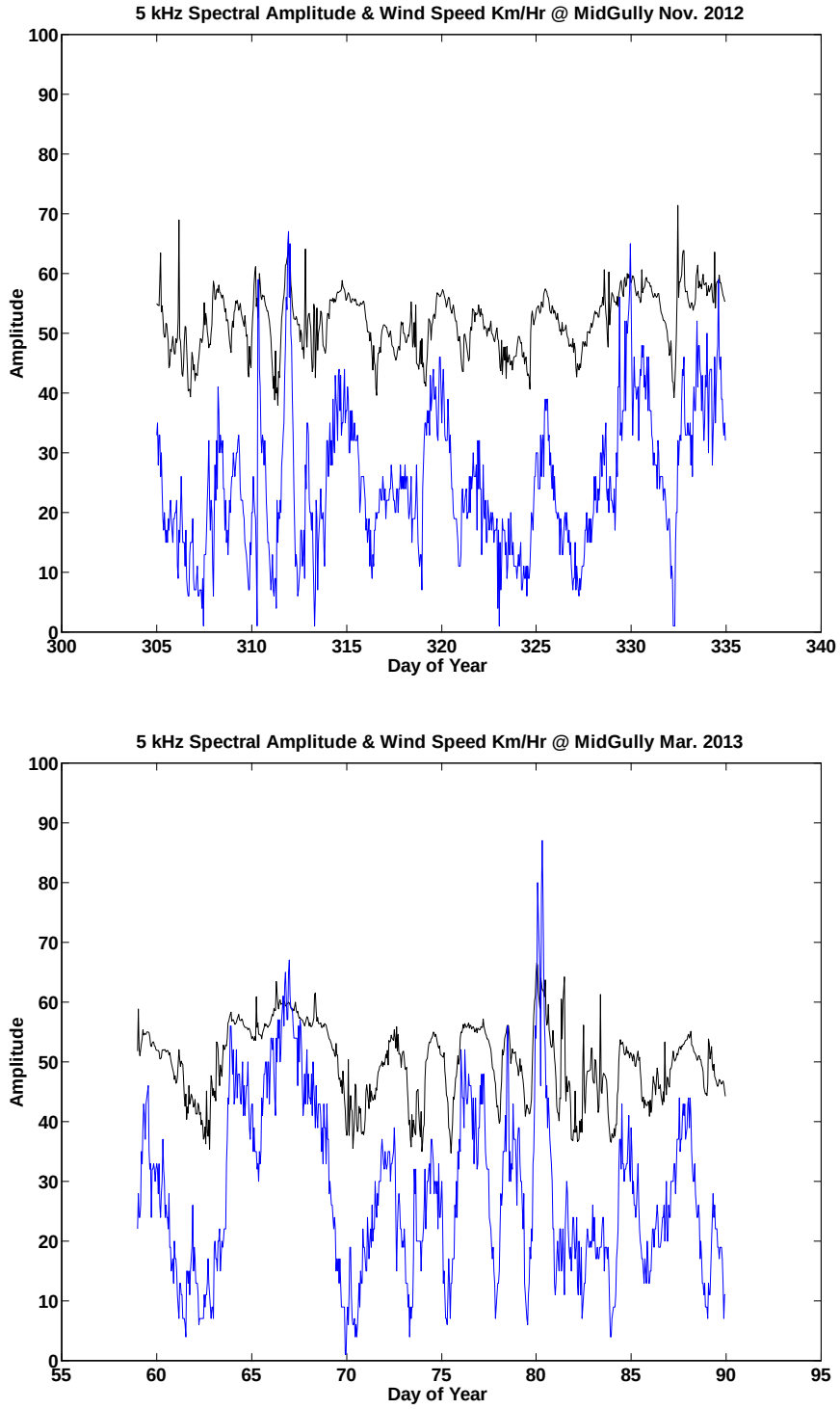


**Figure A3-2.** Plots of MidGul hourly 1/3 octave averaged 5 kHz acoustic spectral levels in dB re 1μPa$^2$/Hz (black) and Sable Island wind speeds in km/hr (blue) vs. Day of Year for November 2012 (top) and March 2013 (bottom).

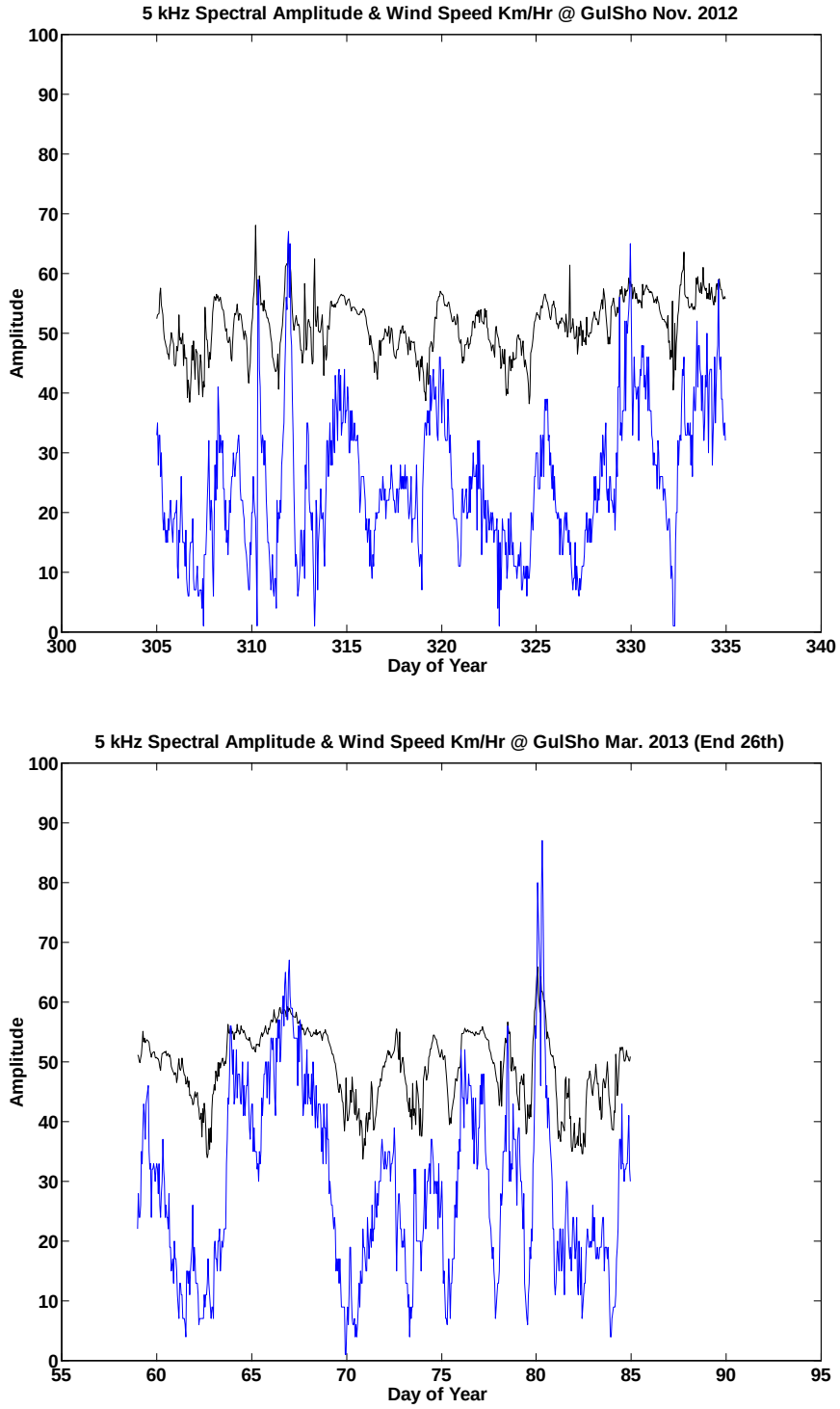


**Figure A3-3.** Plots of GulSho hourly 1/3 octave averaged 5 kHz acoustic spectral levels in dB re 1μPa$^2$/Hz (black) and Sable Island wind speeds in km/hr (blue) vs. Day of Year for November 2012 (top) and March 2013 (bottom).

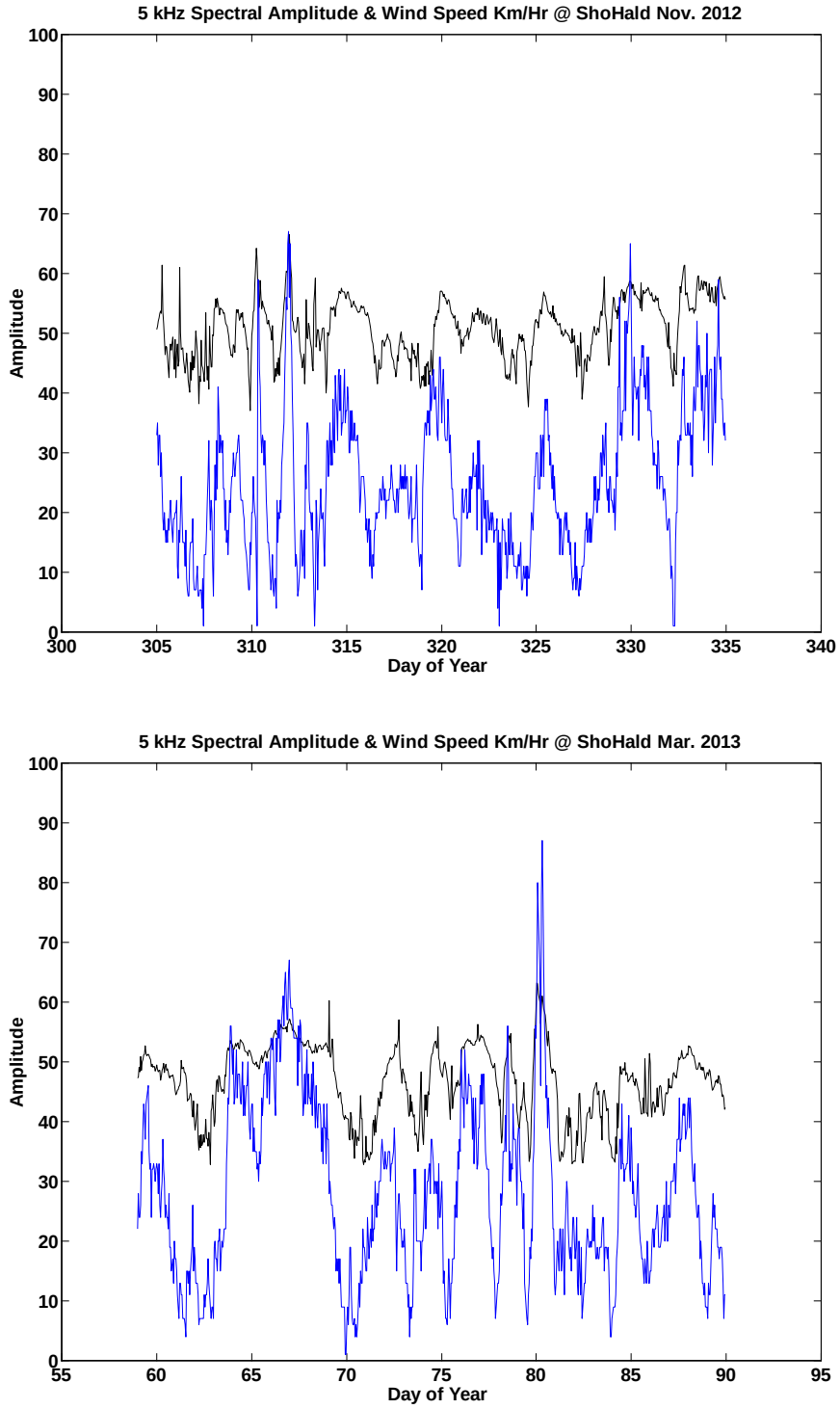


**Figure A3-4.** Plots of ShoHald hourly 1/3 octave averaged 5 kHz acoustic spectral levels in dB re 1μPa$^2$/Hz (black) and Sable Island wind speeds in km/hr (blue) vs. Day of Year for November 2012 (top) and March 2013 (bottom).

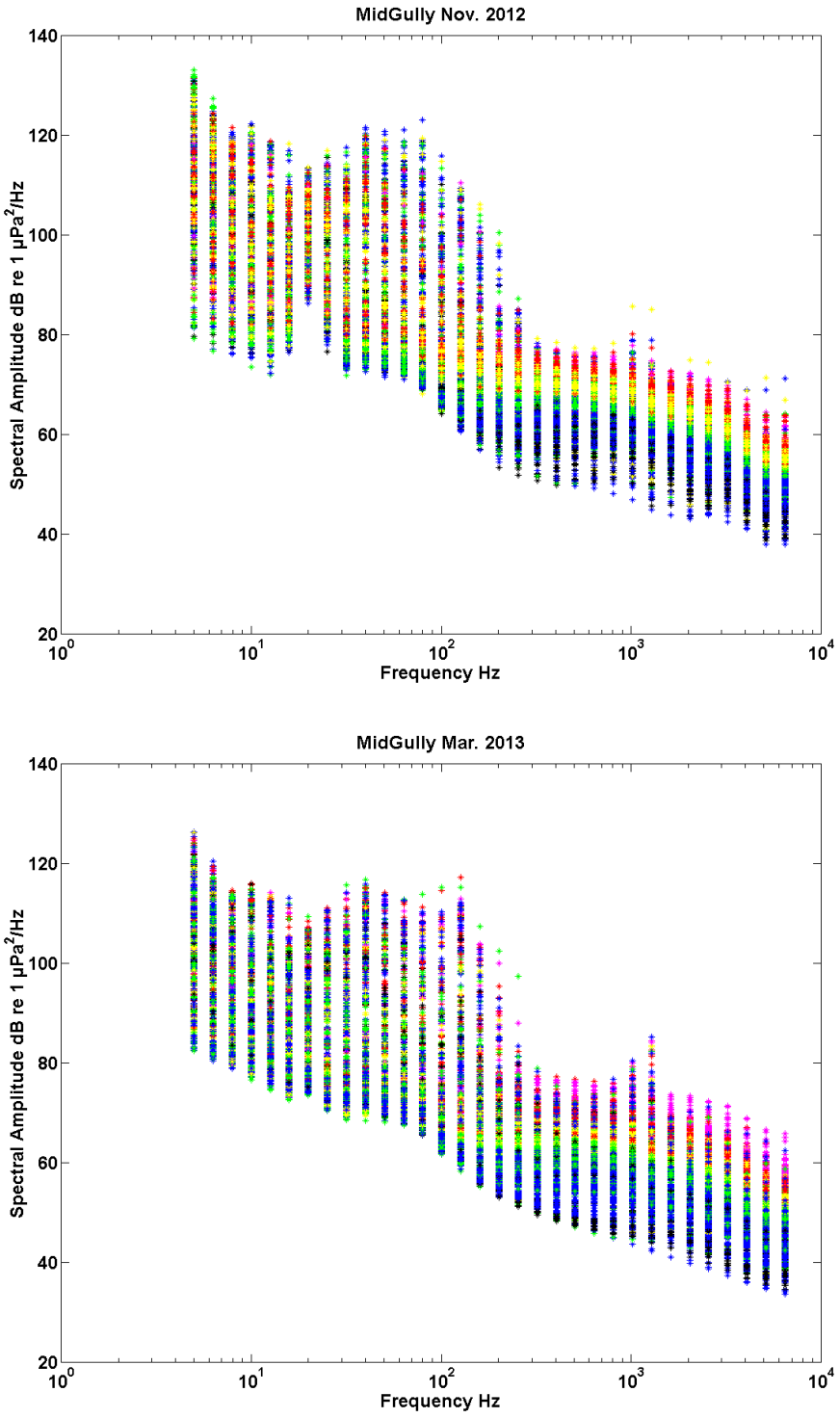


**Figure A3-5.** Plots of MidGul hourly, 1/3 octave averaged, acoustic power spectral densities vs. frequency. Data points are colour-coded in accord with simultaneously observed Sable Island wind ranges: Black 0 – 10, blue > 10 – 20, green > 20 – 30, yellow > 30 – 40, red > 40 – 50, and magenta > 50 km/hr. Data for March 2012 (top) and November 2013 (bottom).

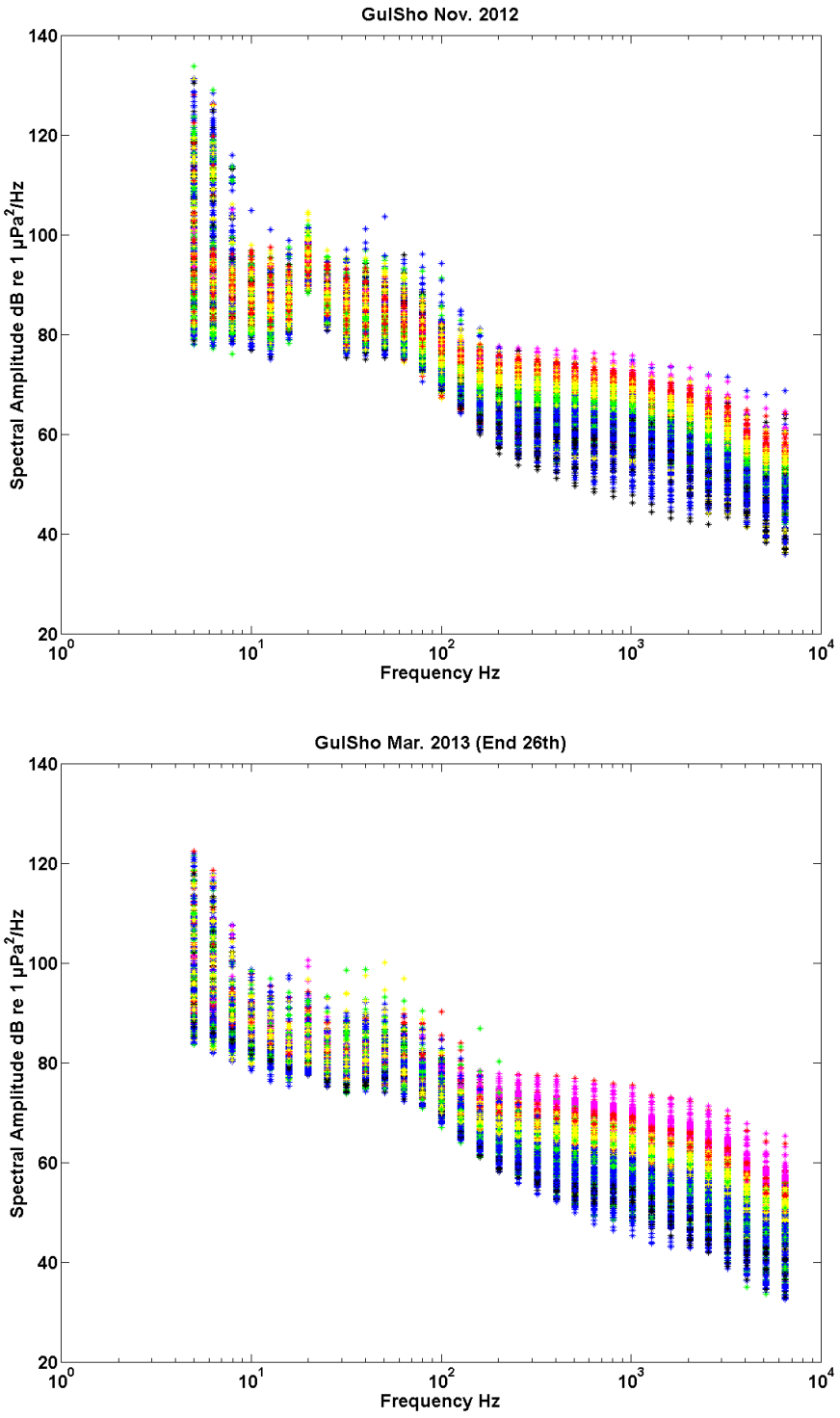


**Figure A3-6.** Plots of GulSho hourly, 1/3 octave averaged, acoustic power spectral densities vs. frequency. Data points are colour-coded in accord with simultaneously observed Sable Island wind ranges: Black 0 – 10, blue > 10 – 20, green > 20 – 30, yellow > 30 – 40, red > 40 – 50, and magenta > 50 km/hr. Data for March 2012 (top) and November 2013 (bottom).

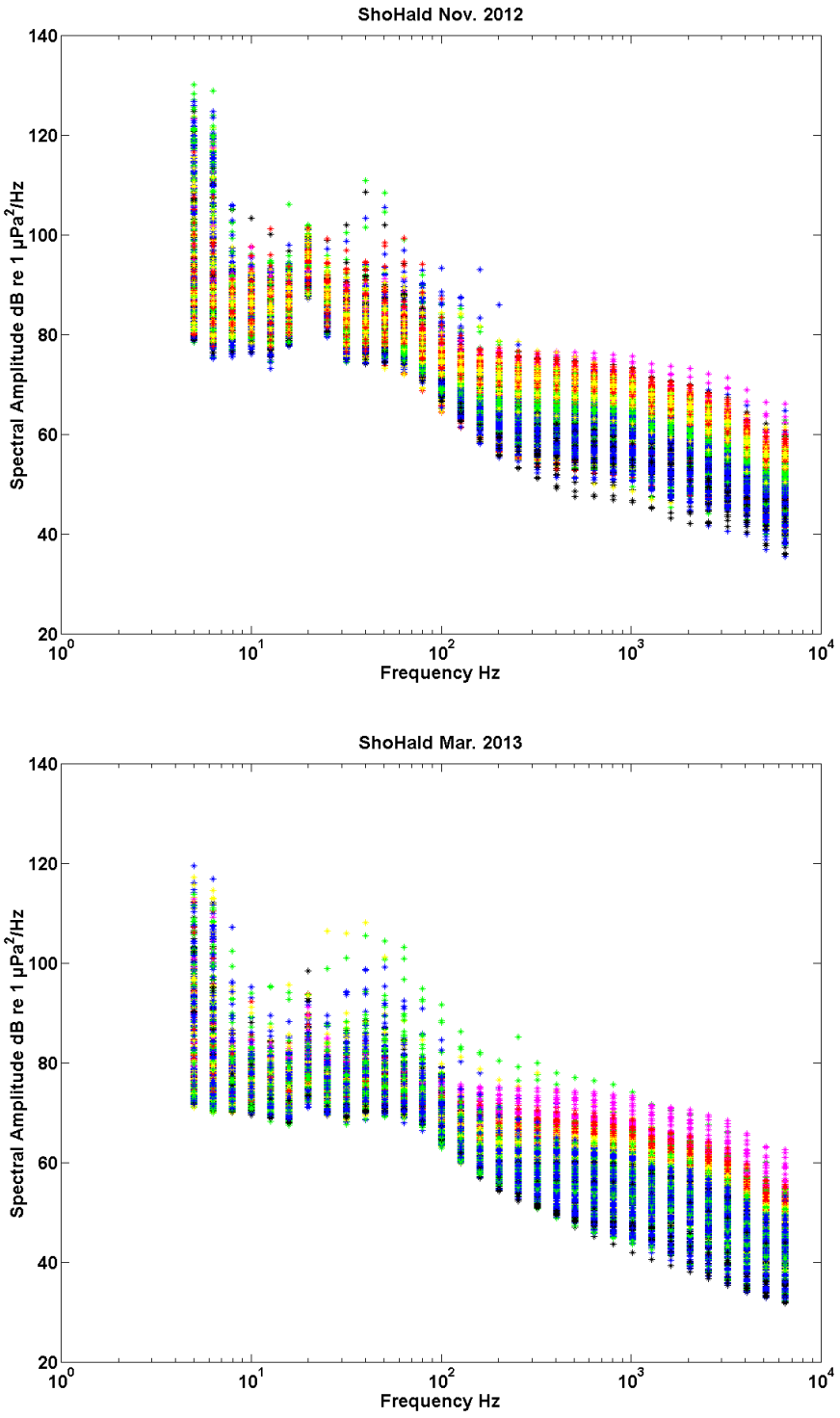


**Figure A3-7.** Plots of ShoHald hourly, 1/3 octave averaged, acoustic power spectral densities vs. frequency. Data points are colour-coded in accord with simultaneously observed Sable Island wind ranges: Black 0 – 10, blue > 10 – 20, green > 20 – 30, yellow > 30 – 40, red > 40 – 50, and magenta > 50 km/hr. Data for March 2012 (top) and November 2013 (bottom).

**All data**

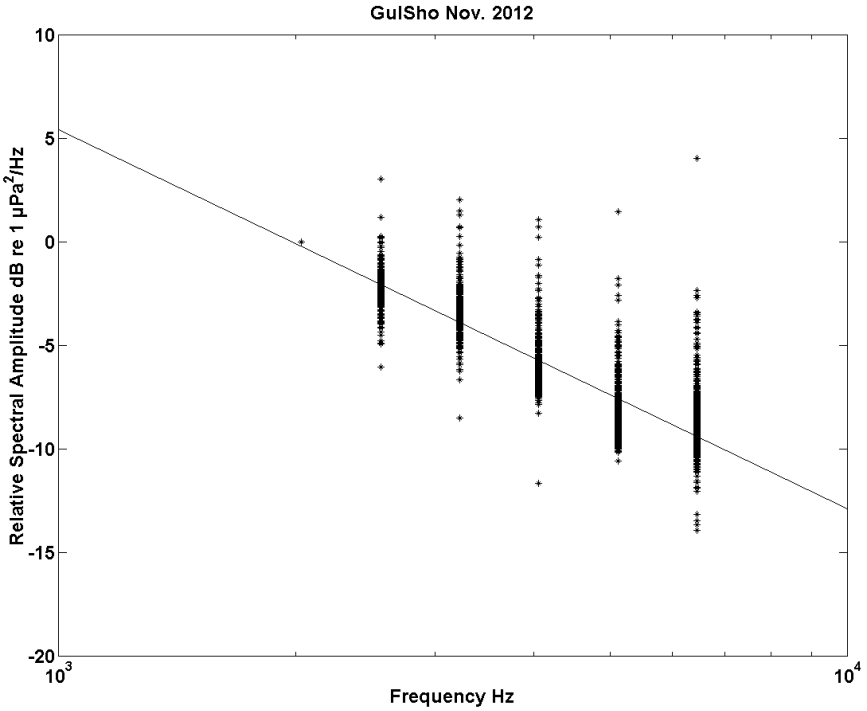


**Weather-filtered data**

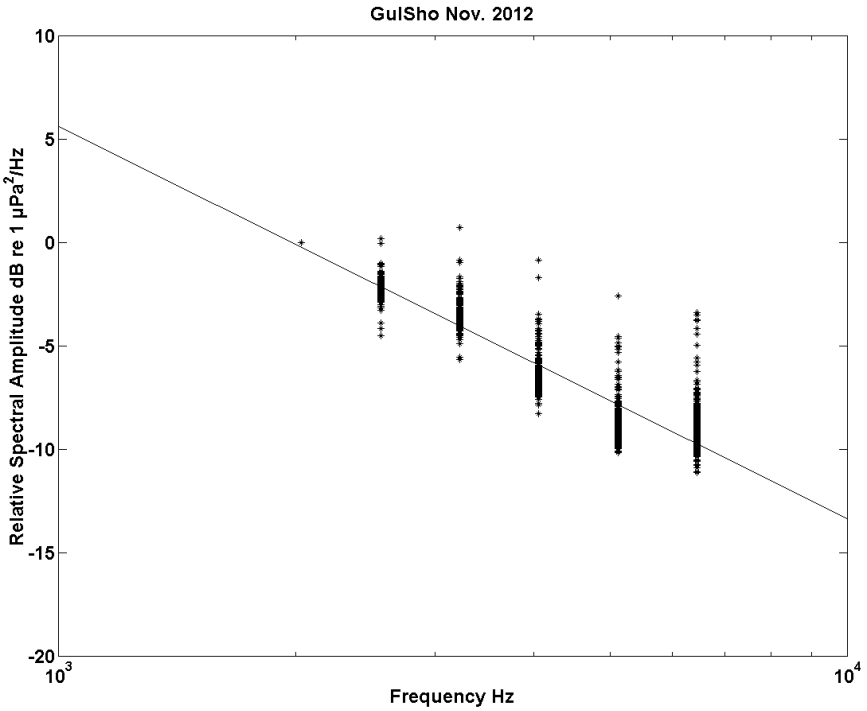


**Figure A3-8.** Relative 1/3 octave average spectral amplitude vs. Acoustic frequency (log scale) with least squares regression line for GulSho Nov. 2012. Top plot – All hourly estimates plotted. Bottom plot – Only hourly estimates corresponding to Sable Island winds ≥ 20 km/hr and with no rain or freezing rain reported.

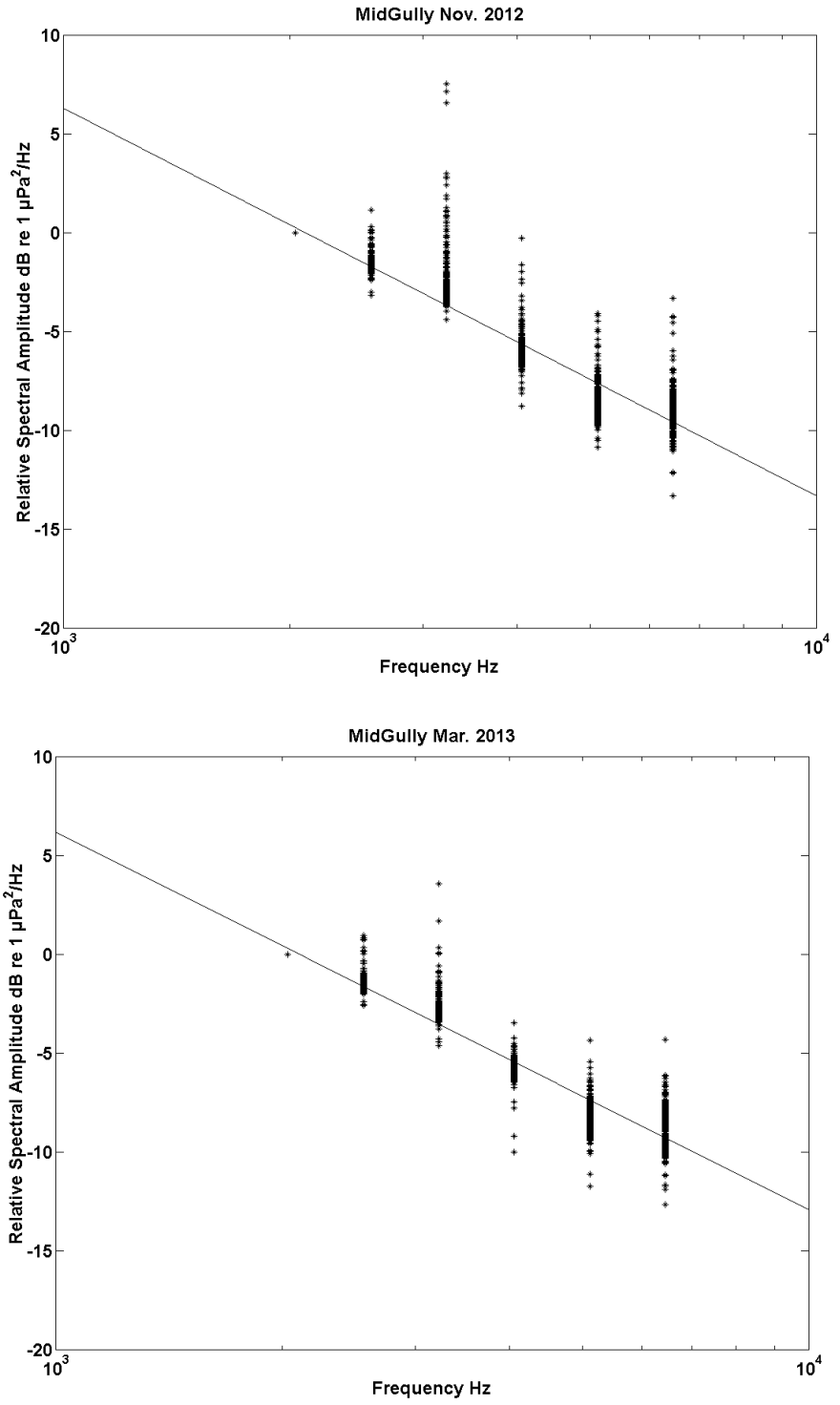


**Figure A3-9.** Plots of MidGul hourly relative 1/3 octave average spectral amplitude vs. Acoustic frequency (log scale) with least squares regression line. Data for March 2012 (top) and November 2013 (bottom). Weather-filtering has been applied.

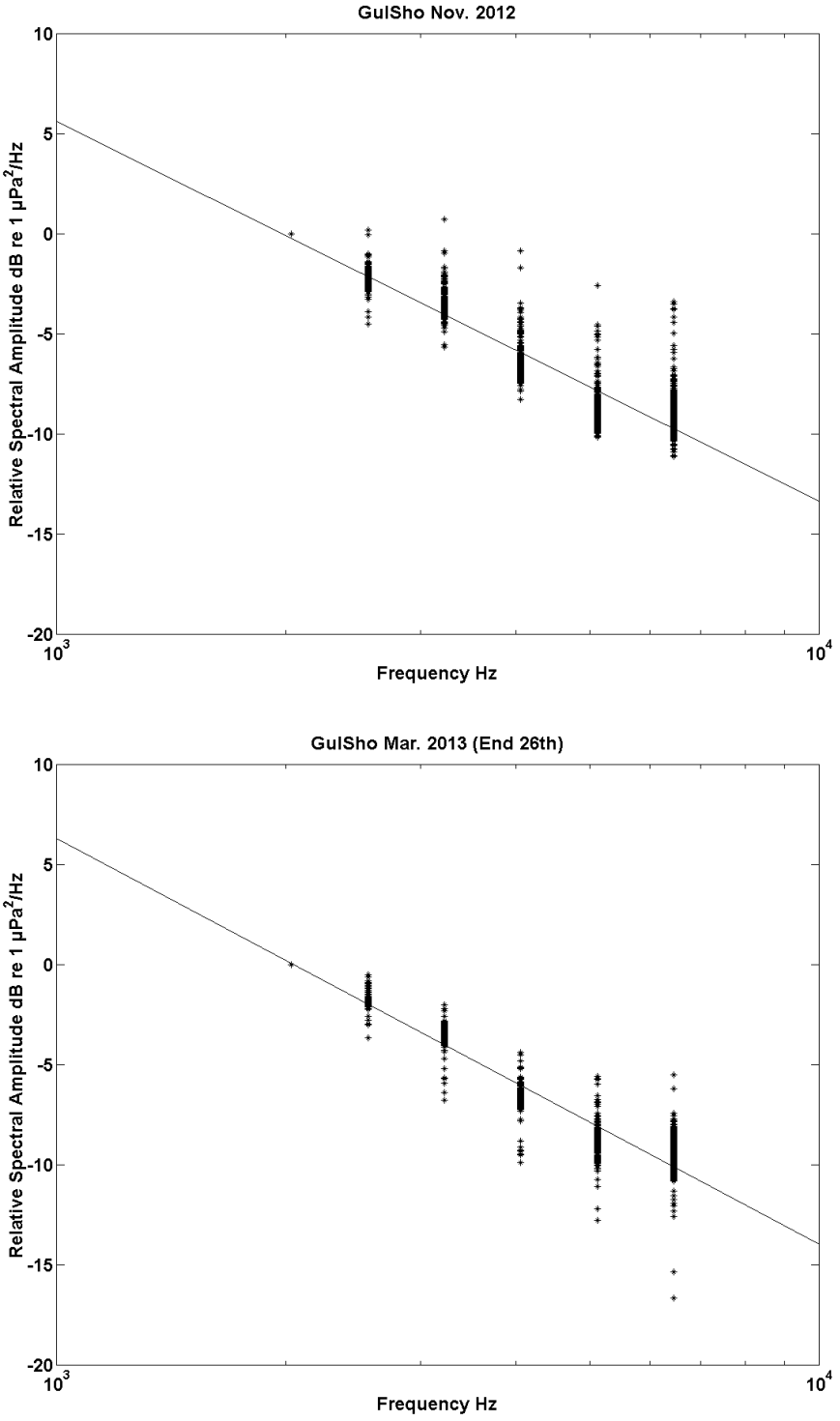


**Figure A3-10.** Plots of GulSho hourly relative 1/3 octave average spectral amplitude vs. Acoustic frequency (log scale) with least squares regression line. Data for March 2012 (top) and November 2013 (bottom). Weather-filtering has been applied.

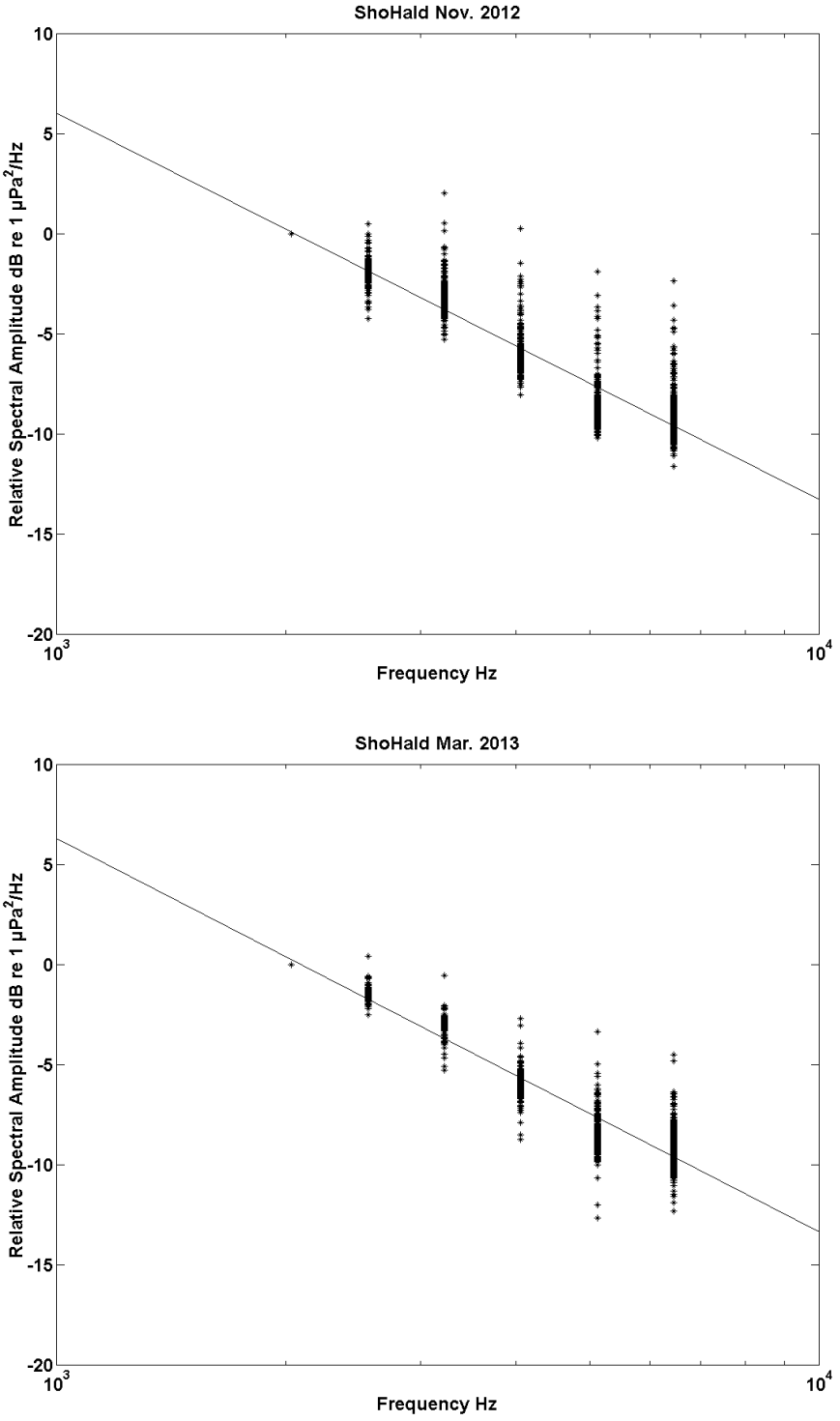


**Figure A3-11.** Plots of ShoHald hourly relative 1/3 octave average spectral amplitude vs. Acoustic frequency (log scale) with least squares regression line. Data for March 2012 (top) and November 2013 (bottom). Weather-filtering has been applied.

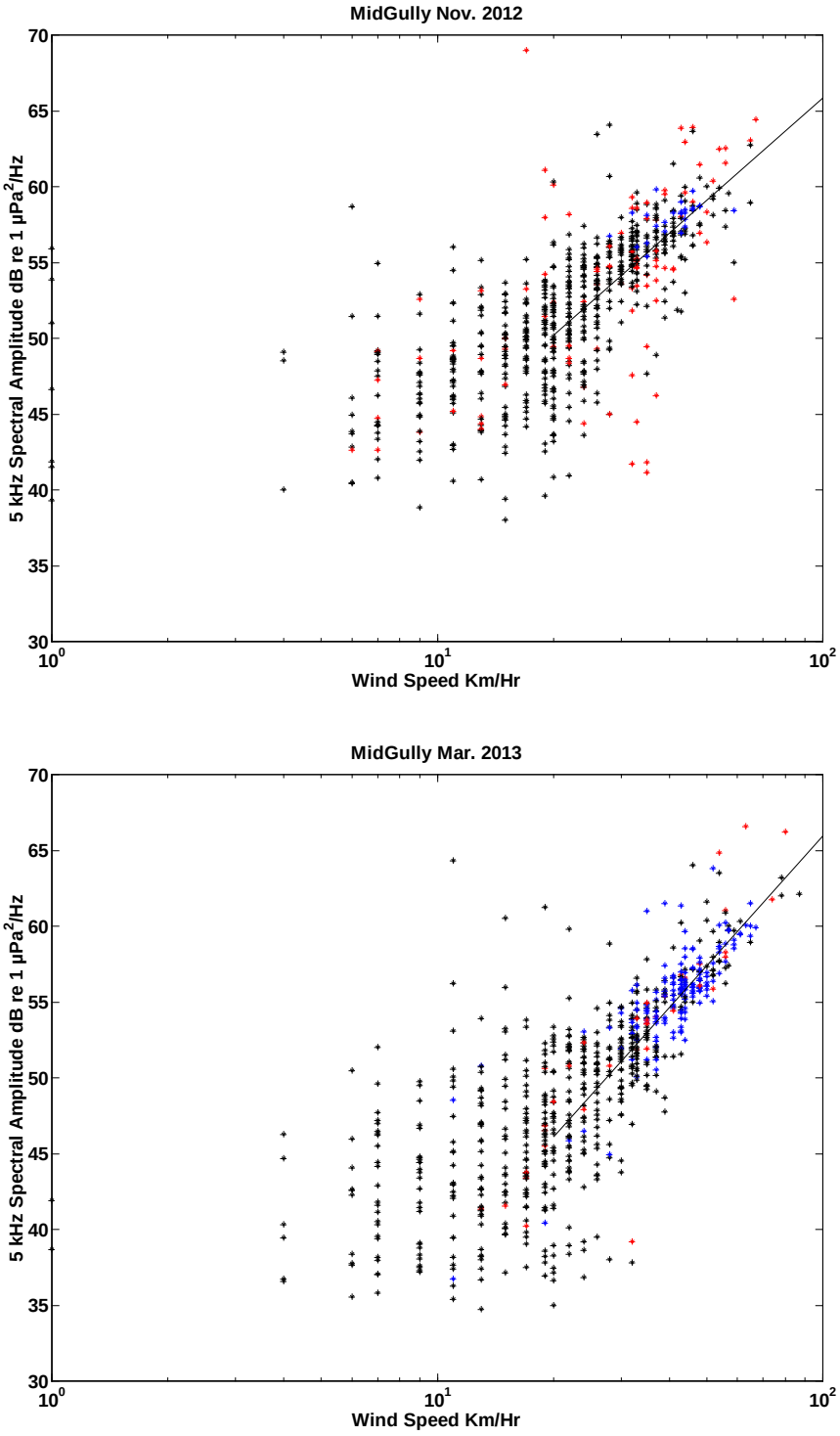


**Figure A3-12.** Plots of MidGul hourly 1/3 octave averaged spectral levels for 5120 Hz bin vs. Wind Speed (log scale) from Sable Island. Linear regression lines plotted using winds speeds ≥ 20 km/hr while omitting data points corresponding to reported rain or freezing rain (plotted in red). Data from March 2012 (top) and from November 2013 (bottom).

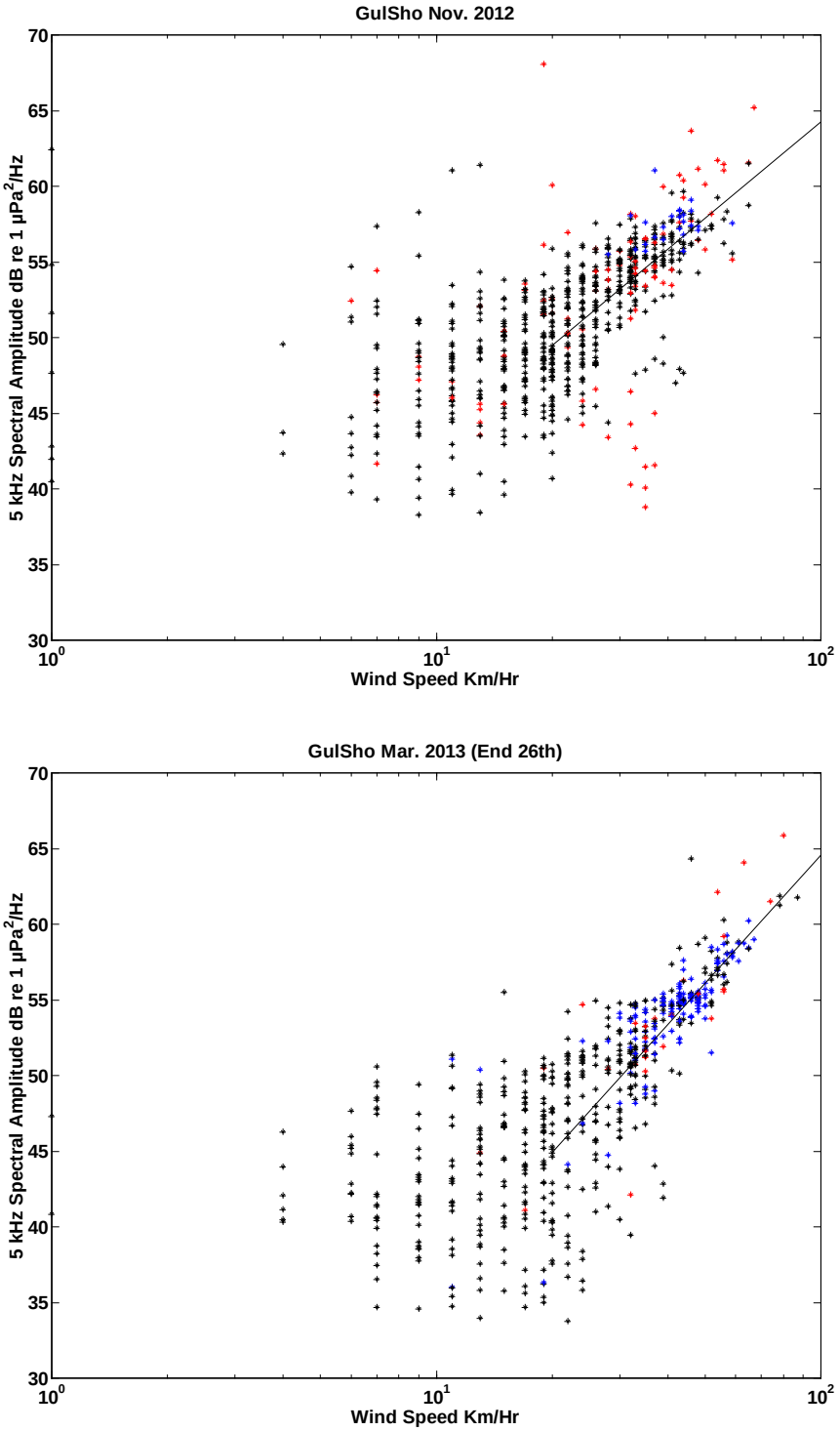


**Figure A3-13.** Plots of GulSho hourly 1/3 octave averaged spectral levels for 5120 Hz bin vs. Wind Speed (log scale) from Sable Island. Linear regression lines plotted using winds speeds ≥ 20 km/hr while omitting data points corresponding to reported rain or freezing rain (plotted in red). Data from March 2012 (top) and from November 2013 (bottom).

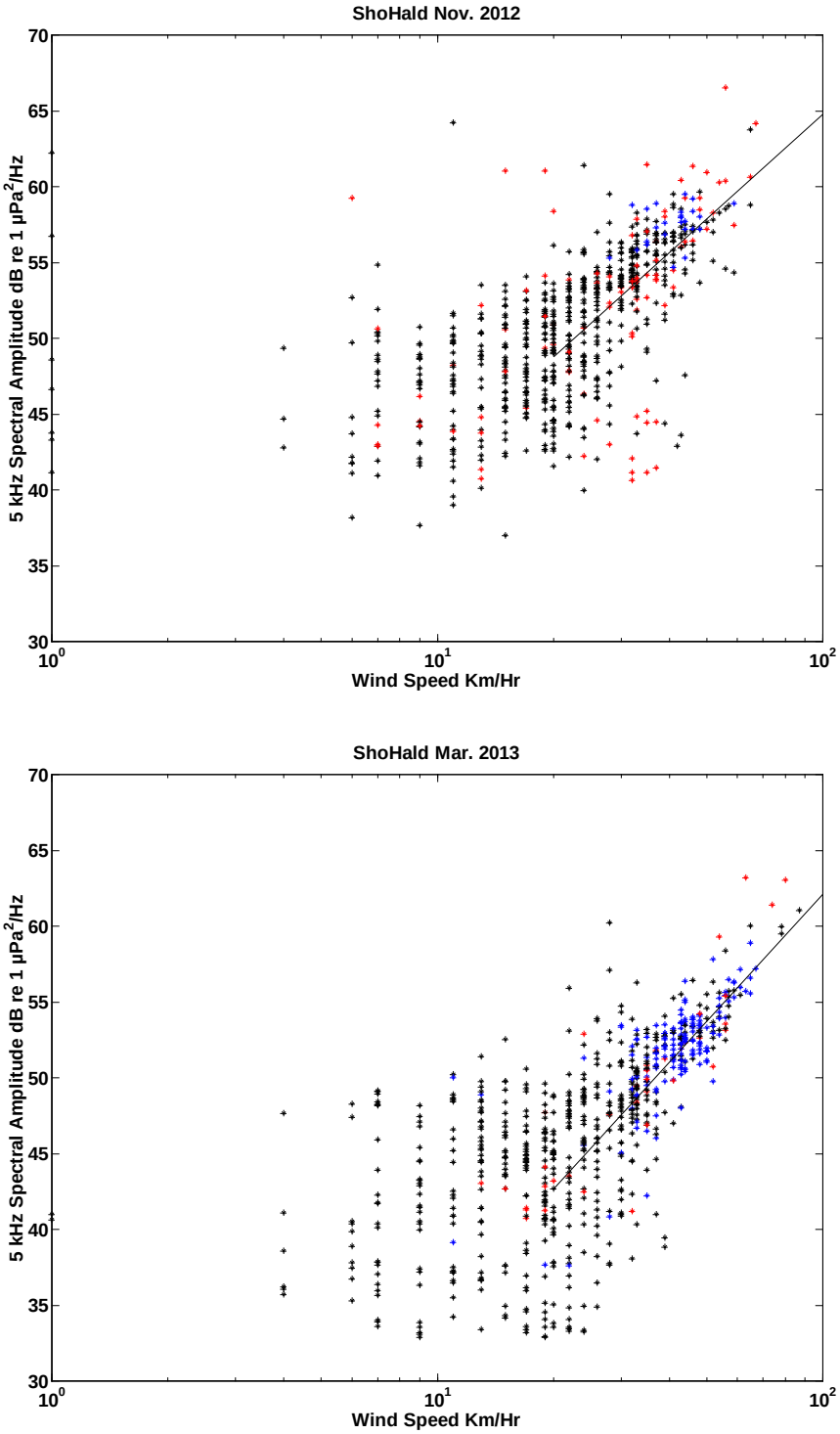


**Figure A3-14.** Plots of ShoHald hourly 1/3 octave averaged spectral levels for 5120 Hz bin vs. Wind Speed (log scale) from Sable Island. Linear regression lines plotted using winds speeds ≥ 20 km/hr while omitting data points corresponding to reported rain or freezing rain (plotted in red). Data from March 2012 (top) and from November 2013 (bottom).

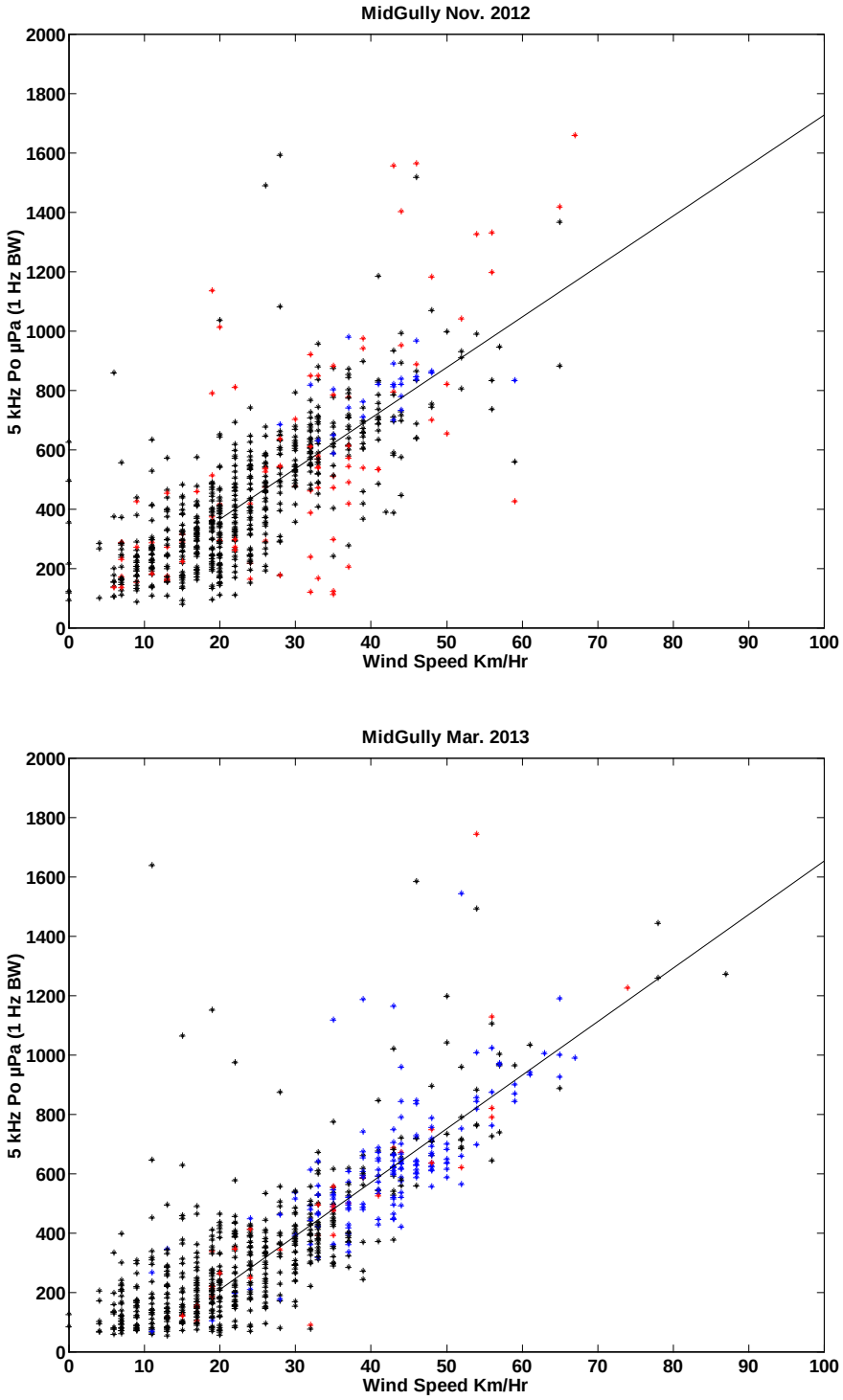


**Figure A3-15.** Plots of MidGul hourly acoustic pressure levels computed from 1/3 octave averaged spectral levels for 5120 Hz bin vs. Wind Speed from Sable Island. Linear regression lines plotted using winds speeds ≥ 20 km/hr while omitting data points corresponding to reported rain or freezing rain (plotted in red). Data from March 2012 (top) and from November 2013 (bottom).

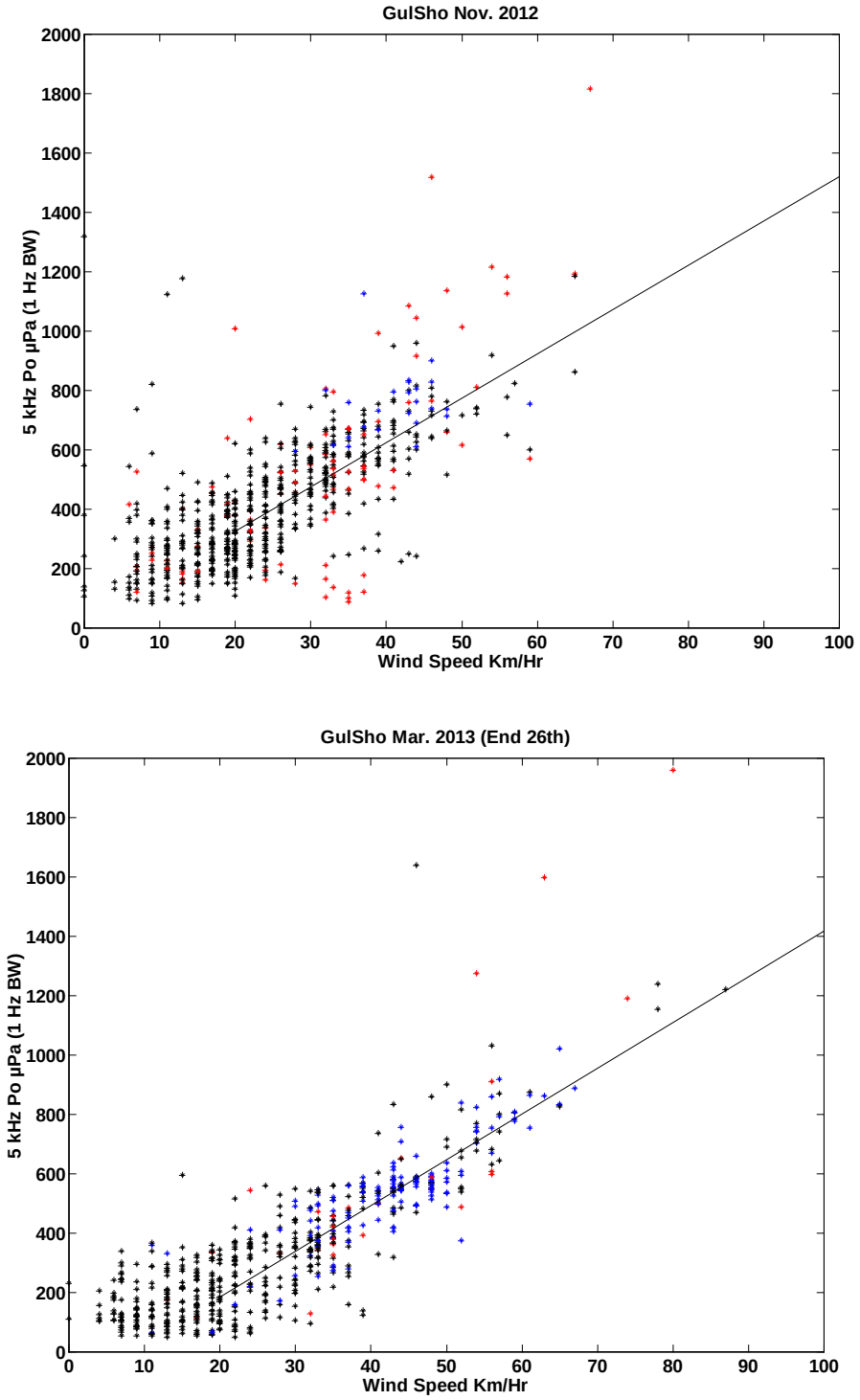


**Figure A3-16.** Plots of GulSho hourly acoustic pressure levels computed from 1/3 octave averaged spectral levels for 5120 Hz bin vs. Wind Speed from Sable Island. Linear regression lines plotted using winds speeds ≥ 20 km/hr while omitting data points corresponding to reported rain or freezing rain (plotted in red). Data from March 2012 (top) and from November 2013 (bottom).

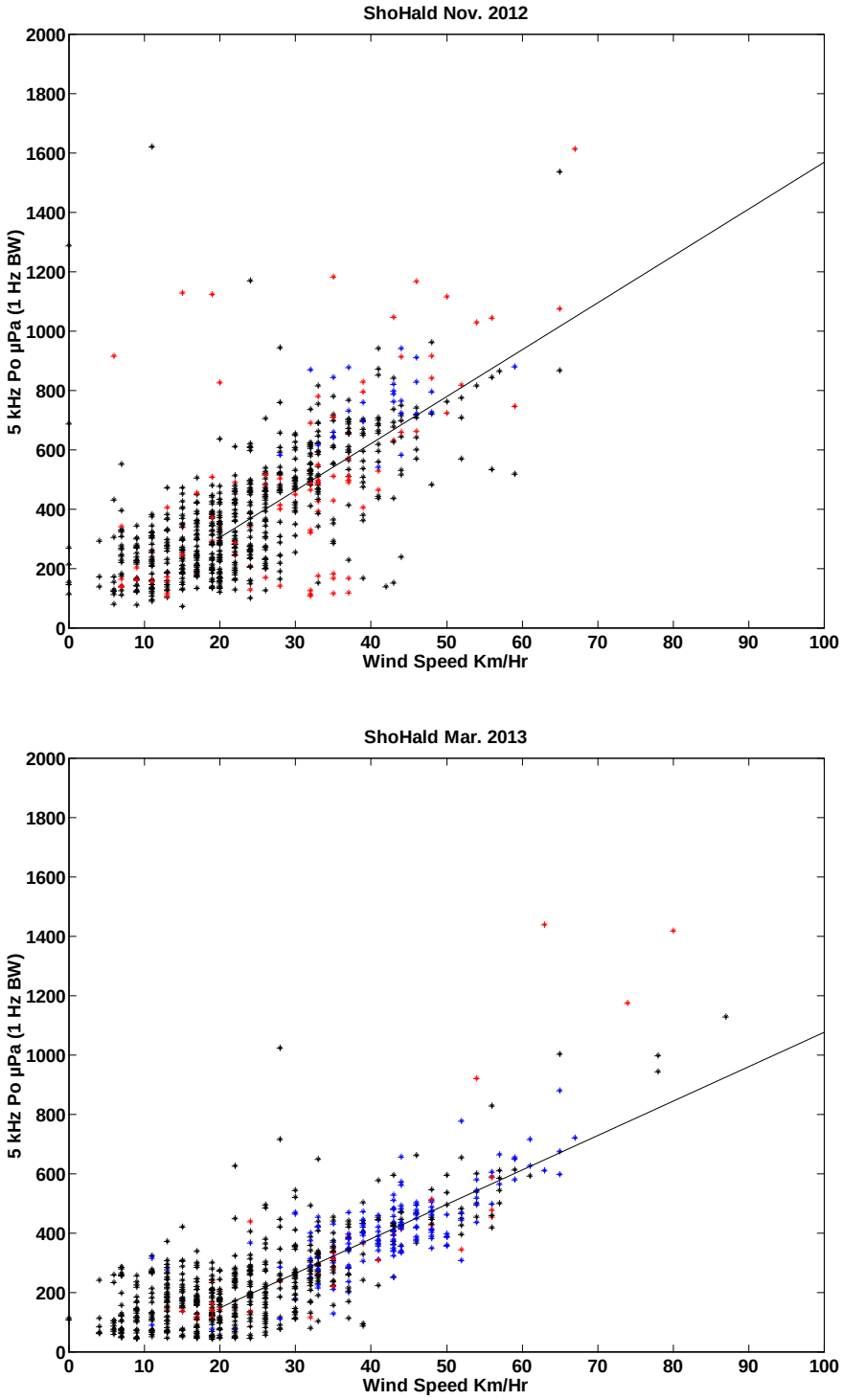


**Figure A3-17.** Plots of ShoHald hourly acoustic pressure levels computed from 1/3 octave averaged spectral levels for 5120 Hz bin vs. Wind Speed from Sable Island. Linear regression lines plotted using winds speeds ≥ 20 km/hr while omitting data points corresponding to reported rain or freezing rain (plotted in red). Data from March 2012 (top) and from November 2013 (bottom).

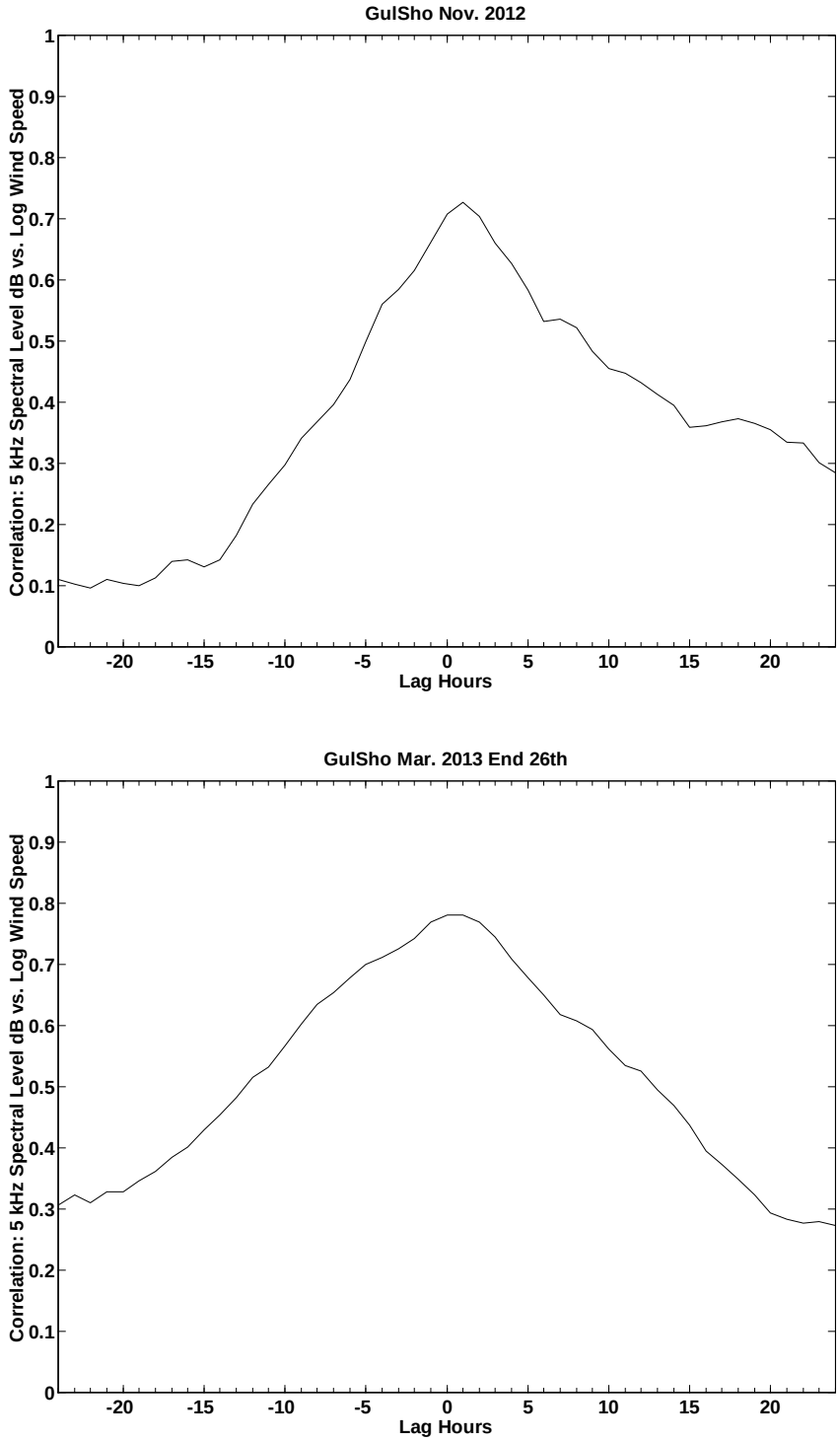


**Figure A3-18.** Correlation coefficients between AMAR 5 kHz 1/3 octave averaged spectral levels and log (wind speed) at Sable Island computed as functions of lag time for GulSho Nov. 2012 and March 2013 datasets. Weather-filtering has been employed.

# A4. APPENDIX 4: SPECTRAL DATA PLOTS

## A4.1. HIGH RESOLUTION SPECTRA

### *A4.1.1. Winter 2012-13 Deployments*

**Figure (series) A4-1-Winter 2012-13 Deployments** – Plots of high resolution power spectral density and power spectral density + 1 standard deviation (S.D.) of sub-series spectral densities.

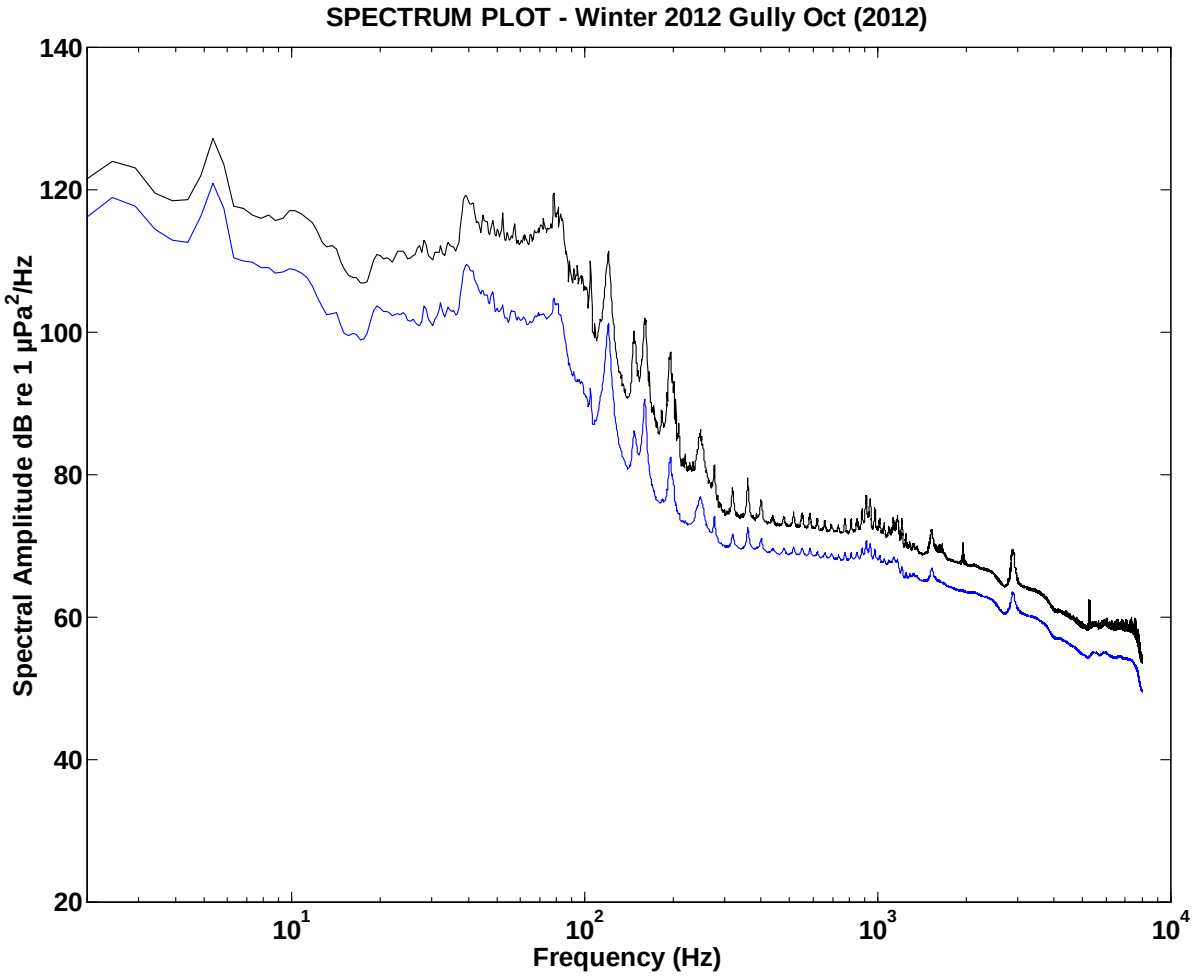


**Figure A4-1-MidGul-2012-Oct.** Plot of high resolution power spectral density (blue curve) and power spectral density + 1 S.D. of sub-series spectral densities (black curve).

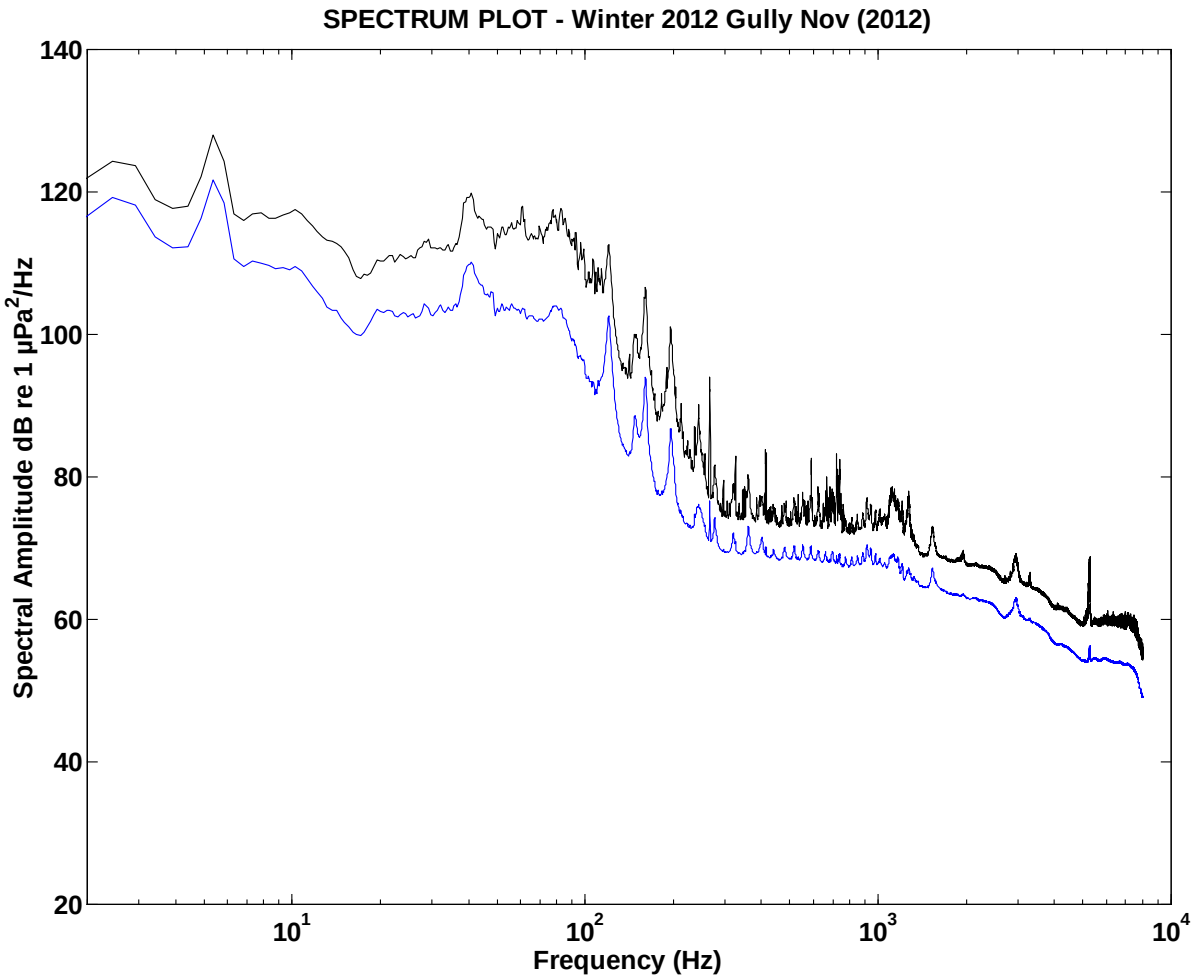


**Figure A4-1-MidGul-2012-Nov.** Plot of high resolution power spectral density (blue curve) and power spectral density + 1 S.D. of sub-series spectral densities (black curve).

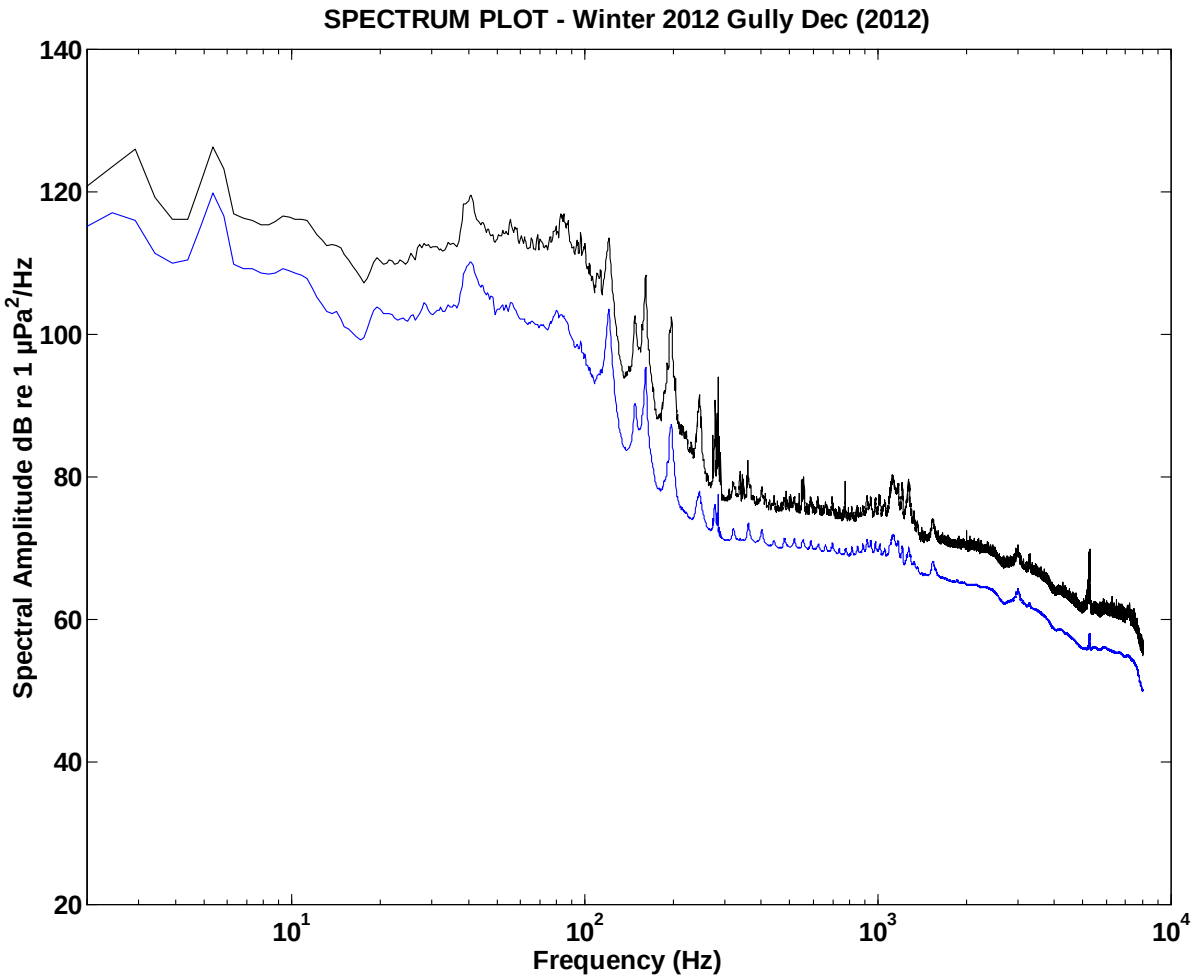


**Figure A4-1-MidGul-2012-Dec.** Plot of high resolution power spectral density (blue curve) and power spectral density + 1 S.D. of sub-series spectral densities (black curve).

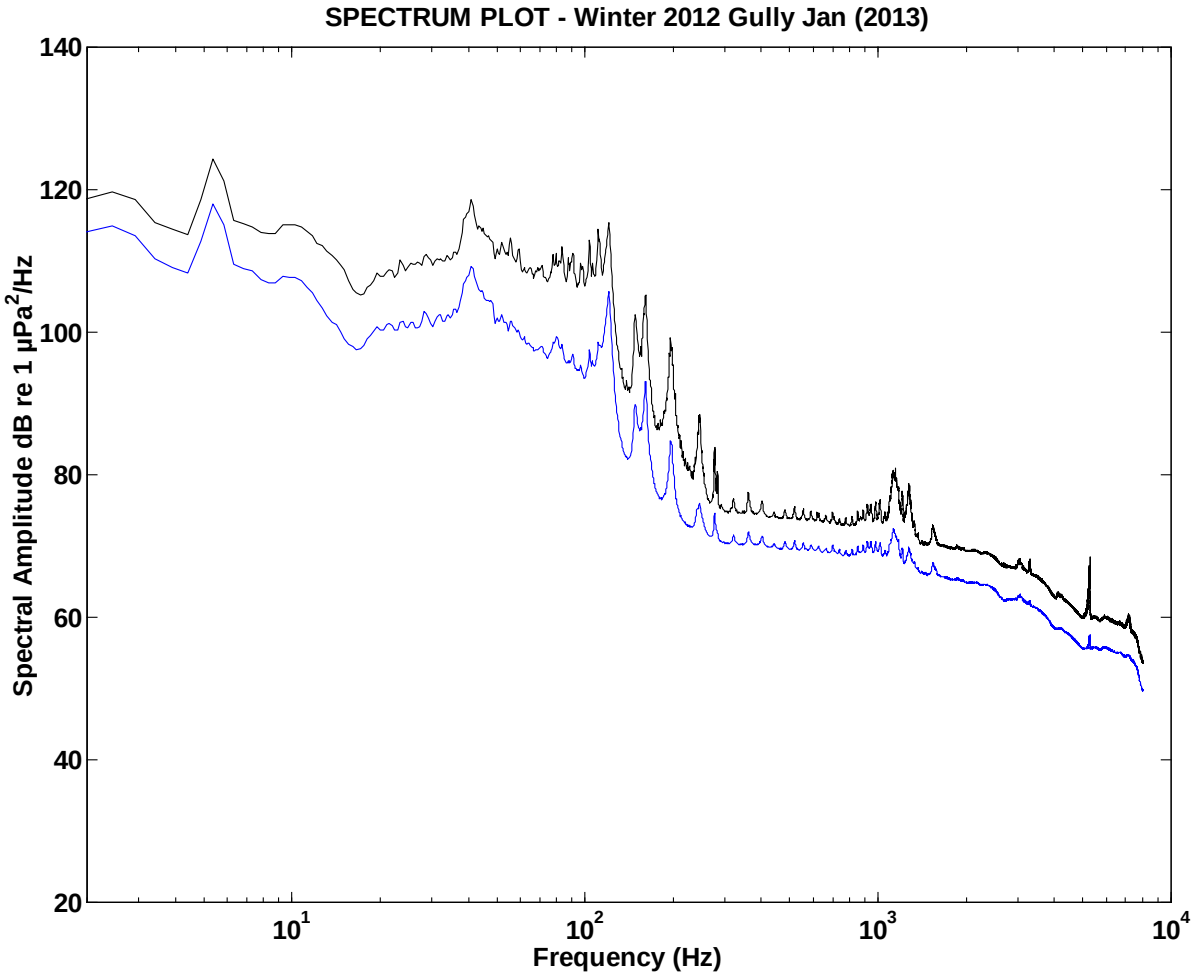


**Figure A4-1-MidGul-2013-Jan.** Plot of high resolution power spectral density (blue curve) and power spectral density + 1 S.D. of sub-series spectral densities (black curve).

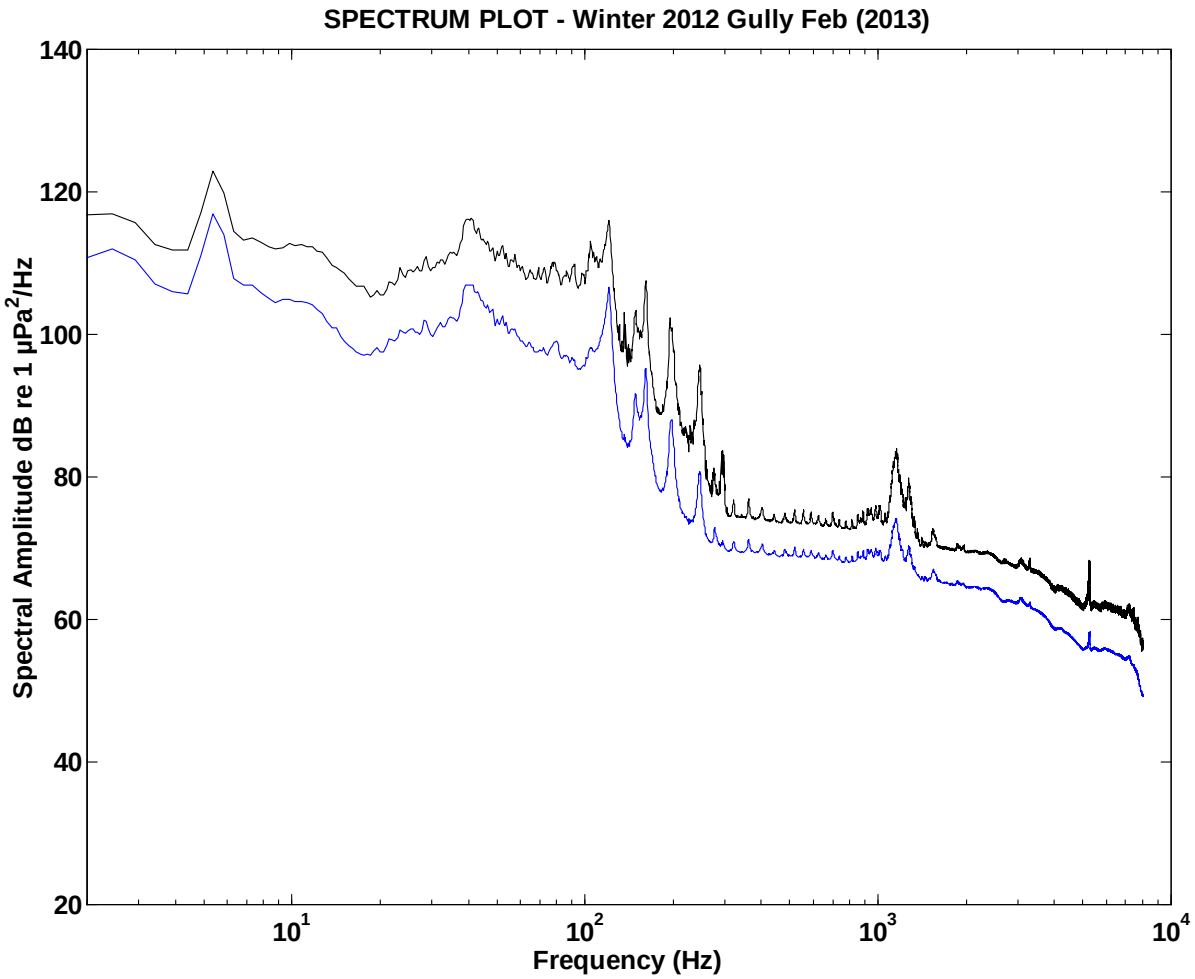


**Figure A4-1-MidGul-2013-Feb.** Plot of high resolution power spectral density (blue curve) and power spectral density + 1 S.D. of sub-series spectral densities (black curve).

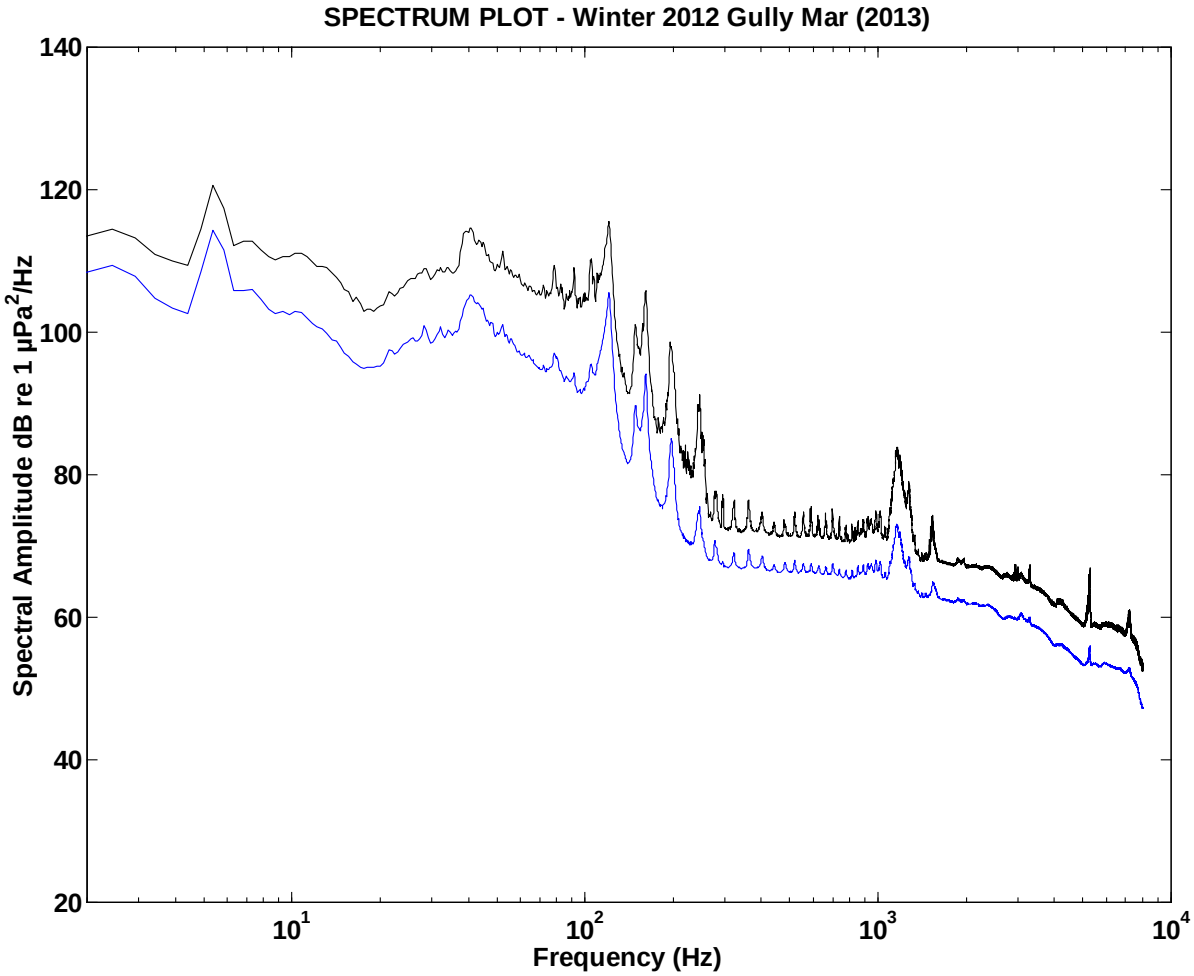


**Figure A4-1-MidGul-2013-Mar.** Plot of high resolution power spectral density (blue curve) and power spectral density + 1 S.D. of sub-series spectral densities (black curve).

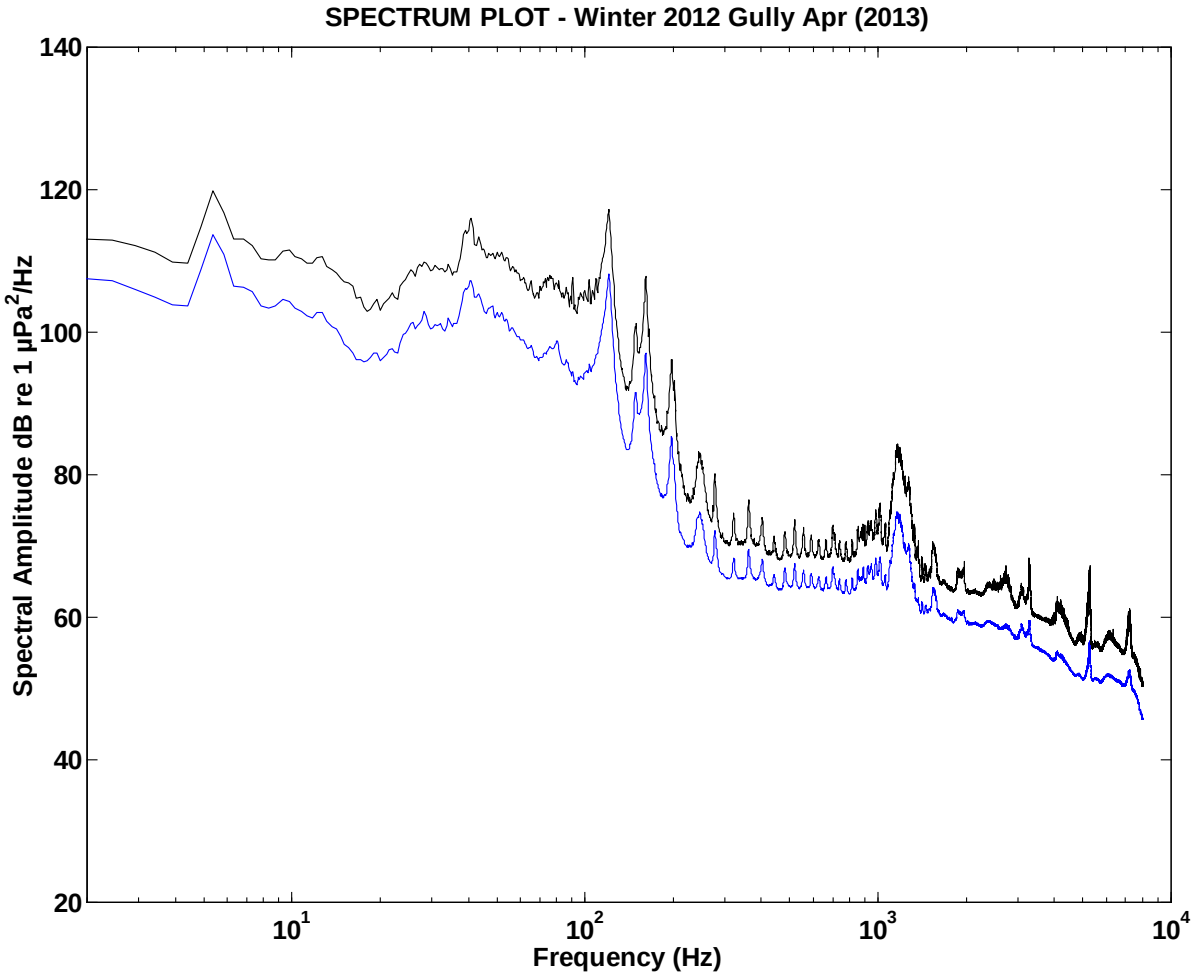


**Figure A4-1-MidGul-2013-Apr.** Plot of high resolution power spectral density (blue curve) and power spectral density + 1 S.D. of sub-series spectral densities (black curve).

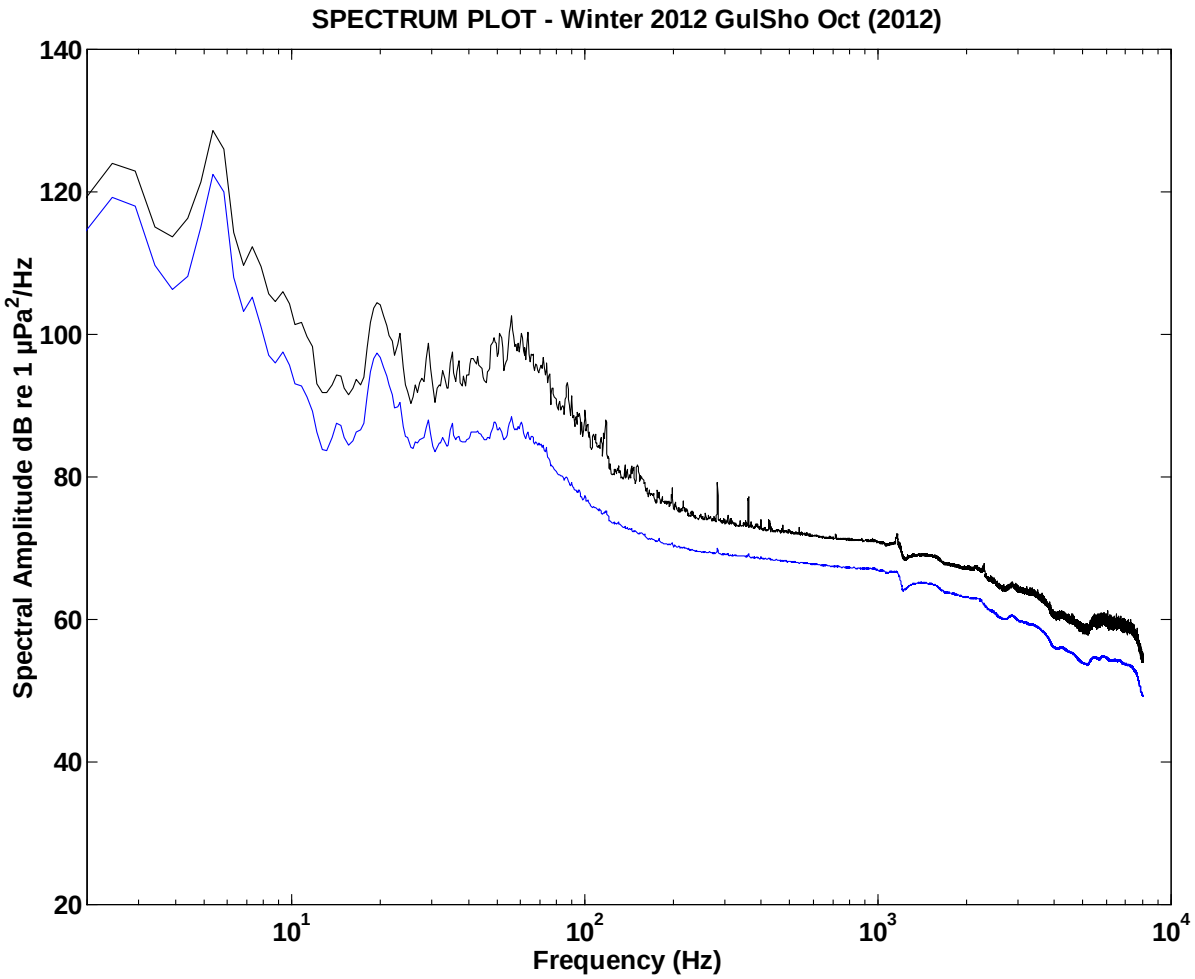


**Figure A4-1-GulSho-2012-Oct.** Plot of high resolution power spectral density (blue curve) and power spectral density + 1 S.D. of sub-series spectral densities (black curve).

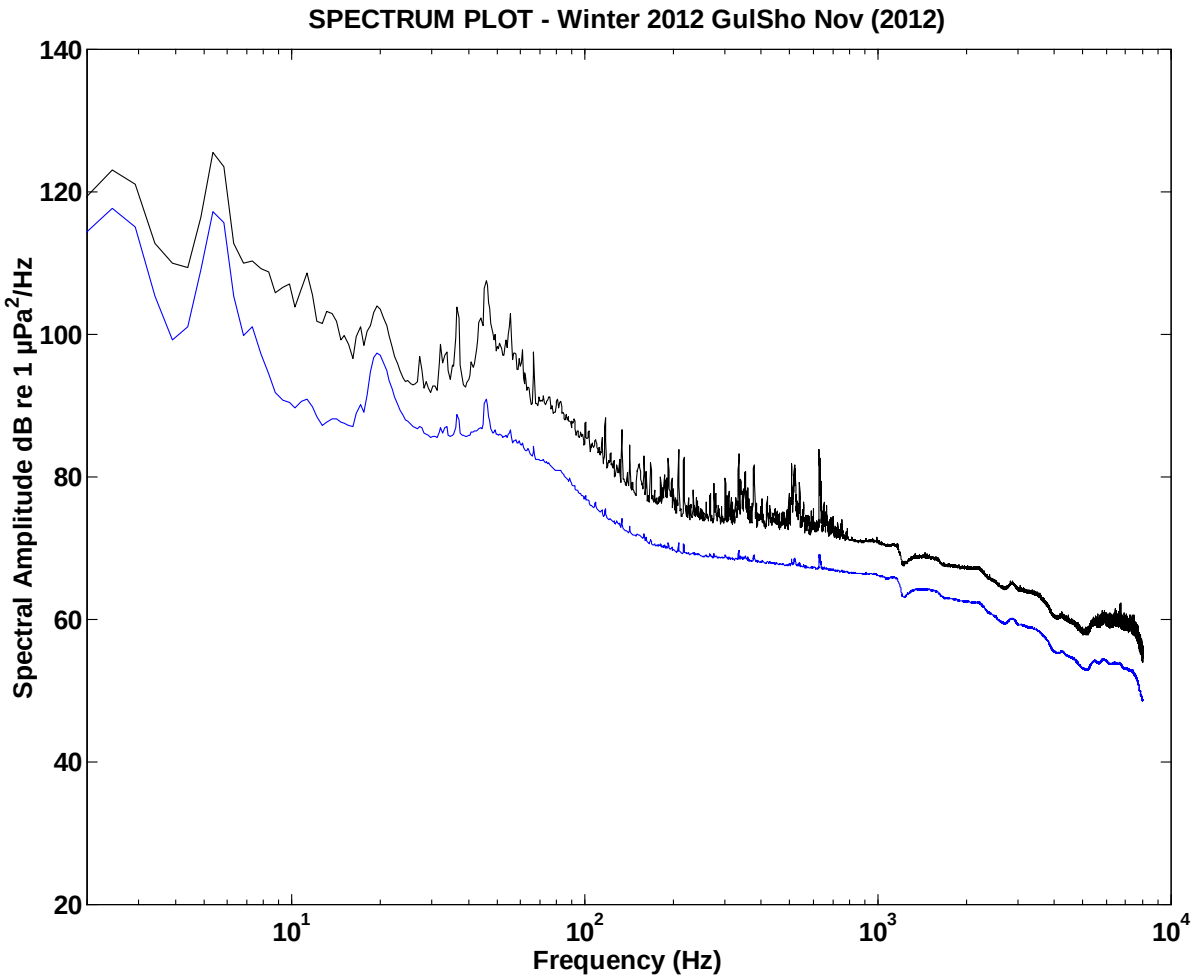


**Figure A4-1-GulSho-2012-Nov.** Plot of high resolution power spectral density (blue curve) and power spectral density + 1 S.D. of sub-series spectral densities (black curve).

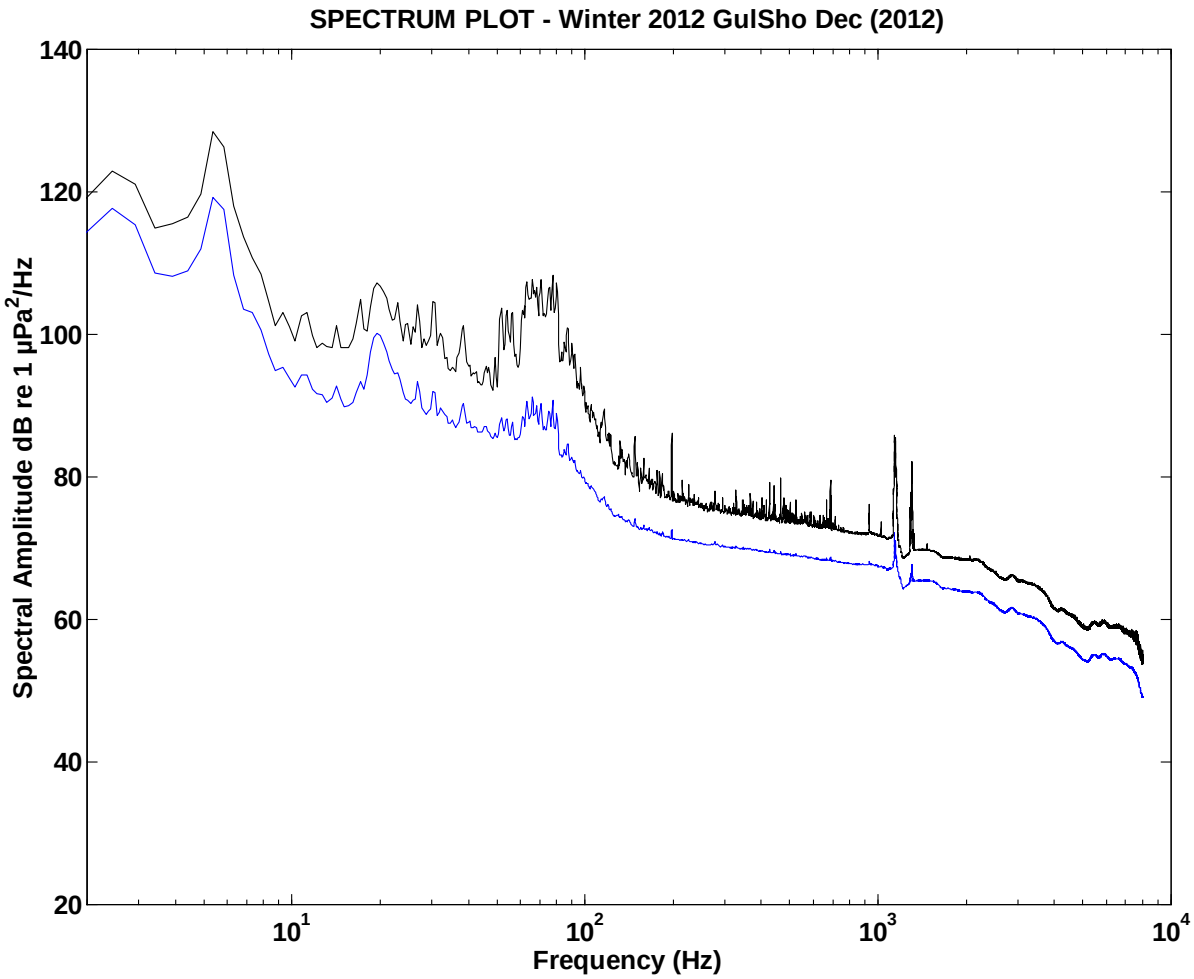


**Figure A4-1-GulSho-2012-Dec.** Plot of high resolution power spectral density (blue curve) and power spectral density + 1 S.D. of sub-series spectral densities (black curve).

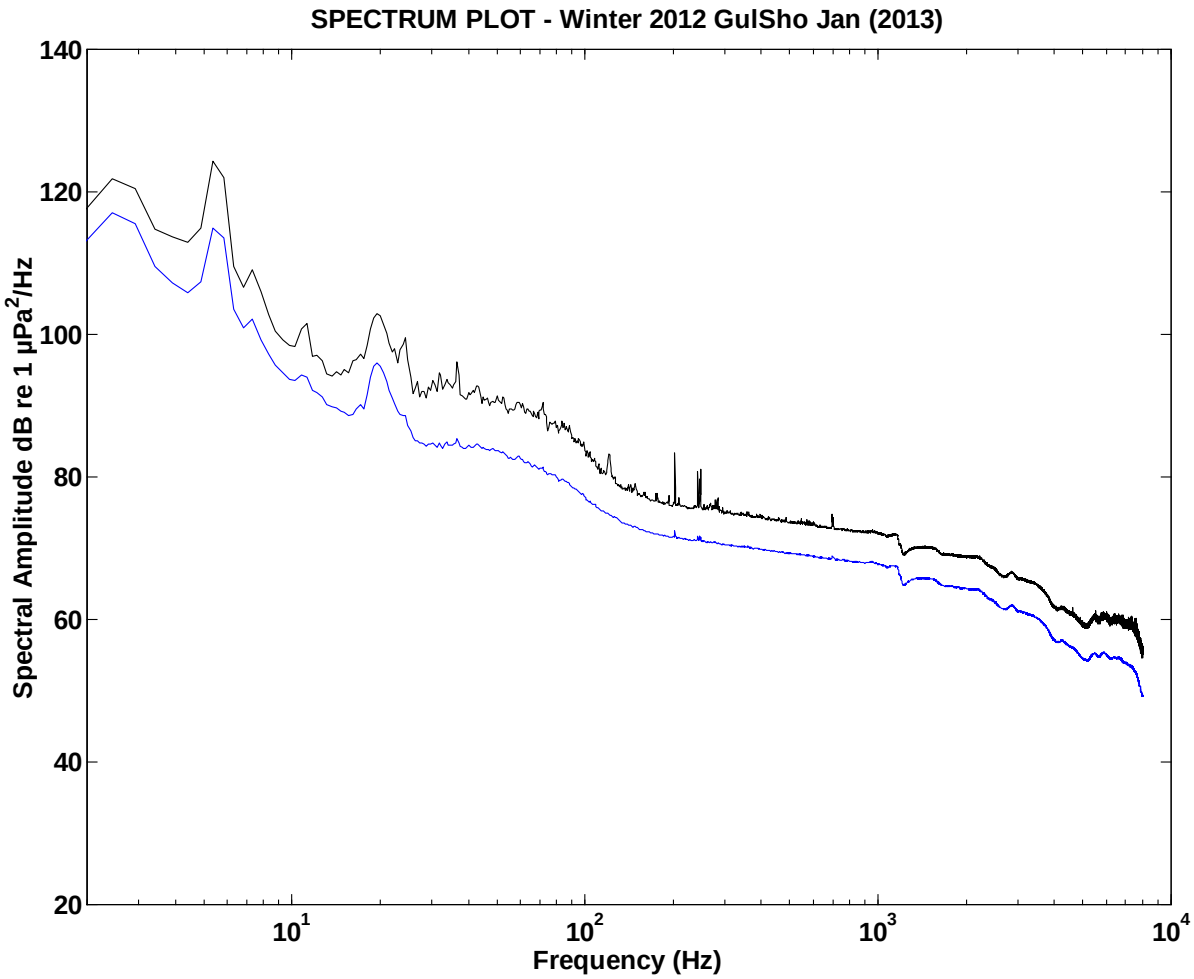


**Figure A4-1-GulSho-2013-Jan.** Plot of high resolution power spectral density (blue curve) and power spectral density + 1 S.D. of sub-series spectral densities (black curve).

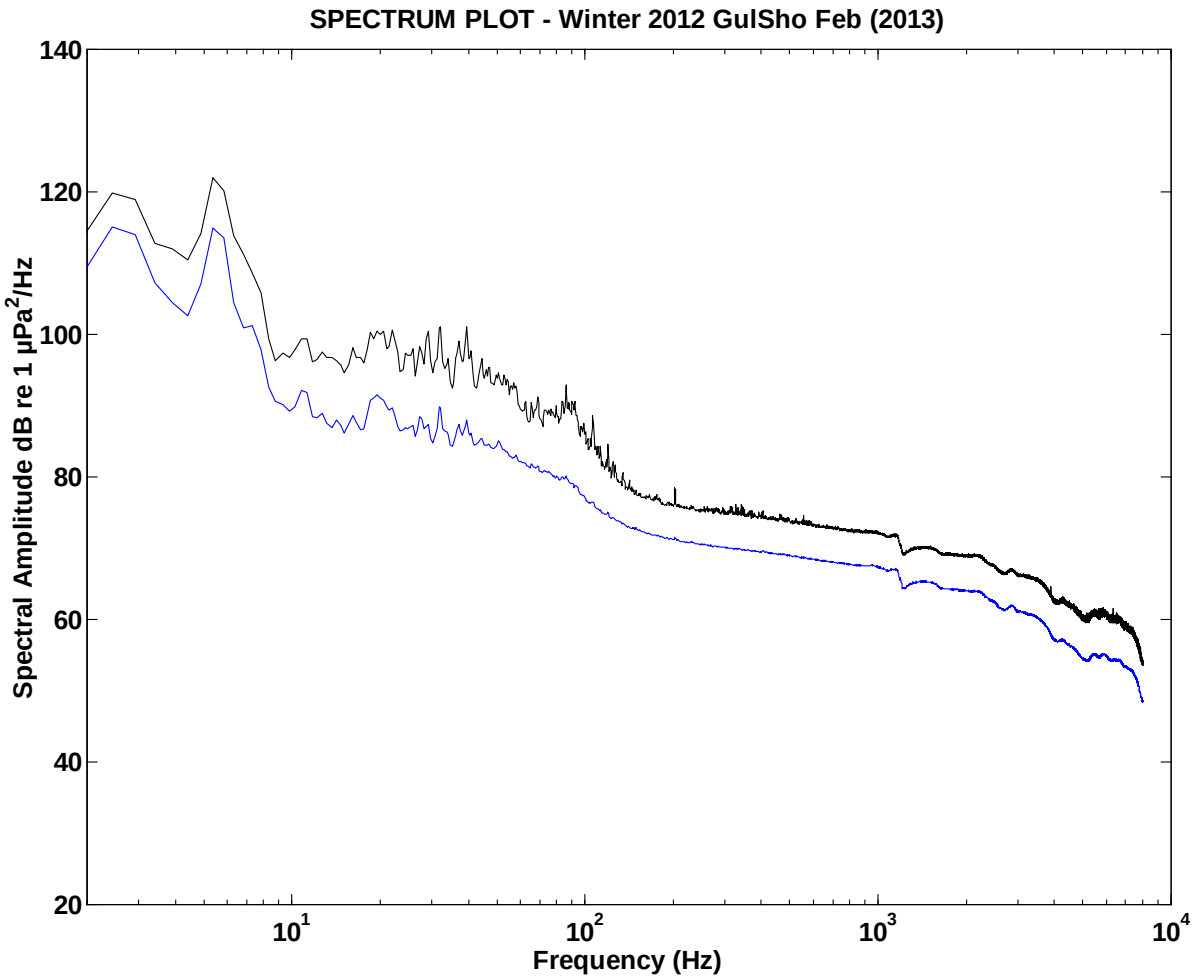


**Figure A4-1-GulSho-2013-Feb.** Plot of high resolution power spectral density (blue curve) and power spectral density + 1 S.D. of sub-series spectral densities (black curve).

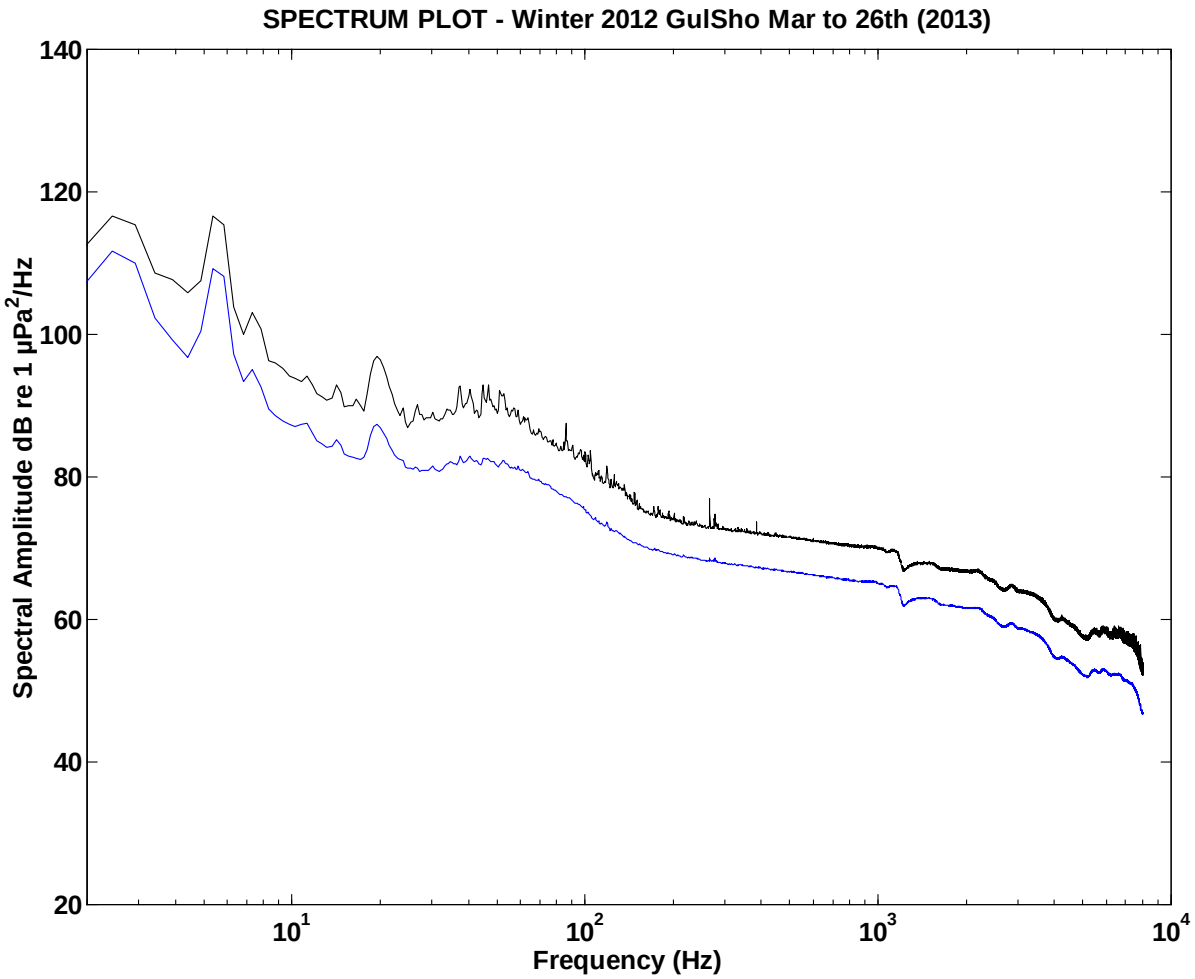


**Figure A4-1-GulSho-2013-Mar.** Plot of high resolution power spectral density (blue curve) and power spectral density + 1 S.D. of sub-series spectral densities (black curve). Series terminated on March 26th incl. to eliminated corrupted data.

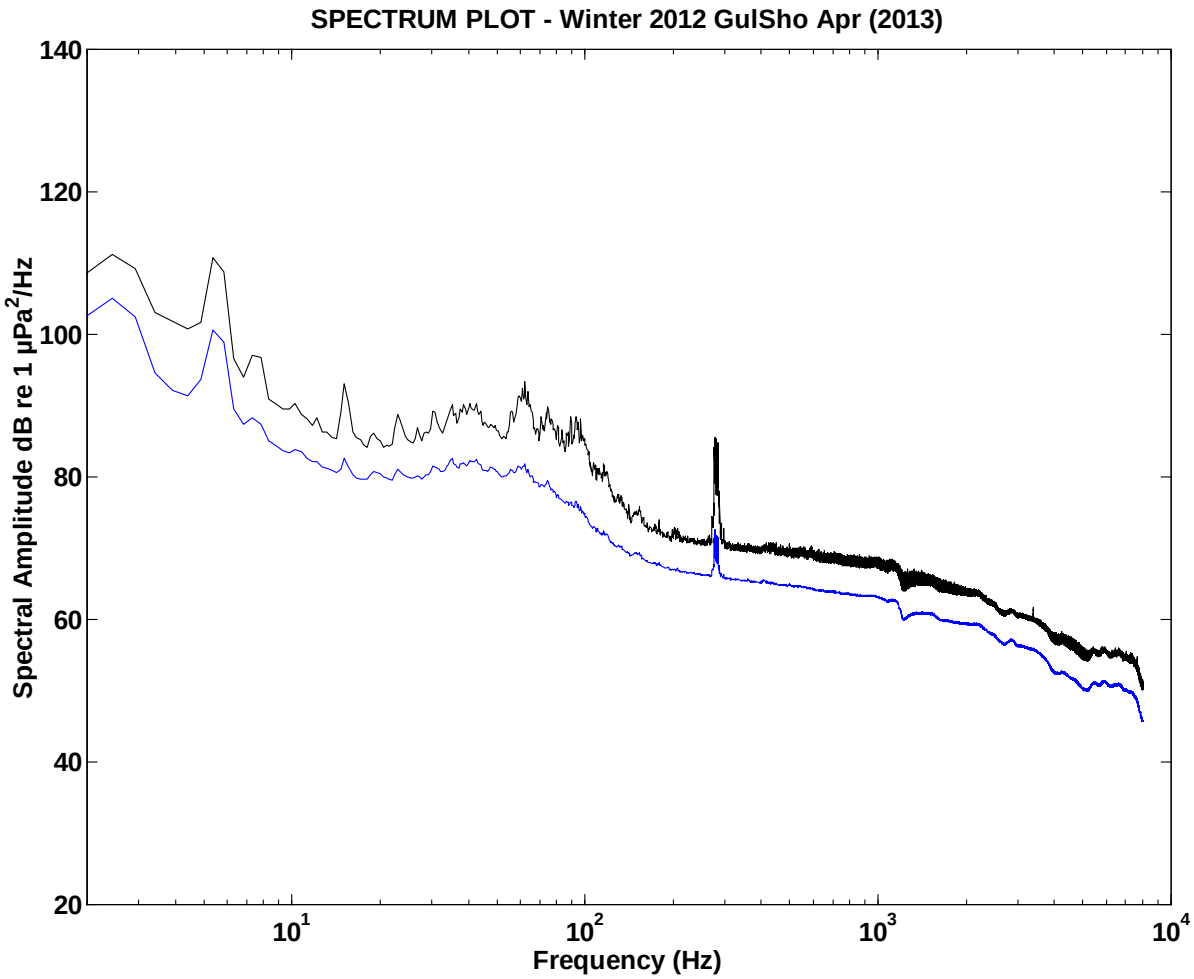


**Figure A4-1-GulSho-2013-Apr.** Plot of high resolution power spectral density (blue curve) and power spectral density + 1 S.D. of sub-series spectral densities (black curve).

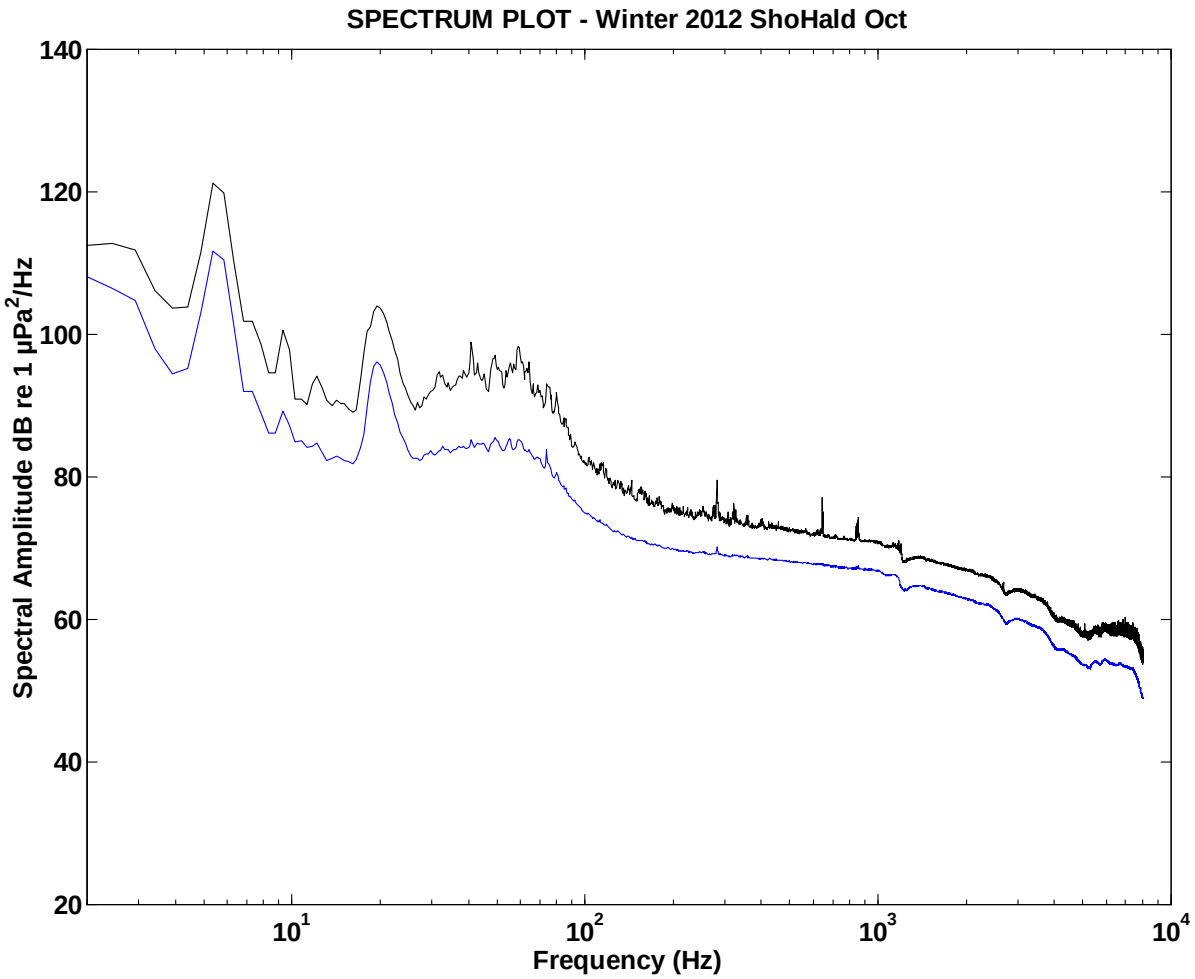


**Figure A4-1-ShoHald-2012-Oct.** Plot of high resolution power spectral density (blue curve) and power spectral density + 1 S.D. of sub-series spectral densities (black curve).

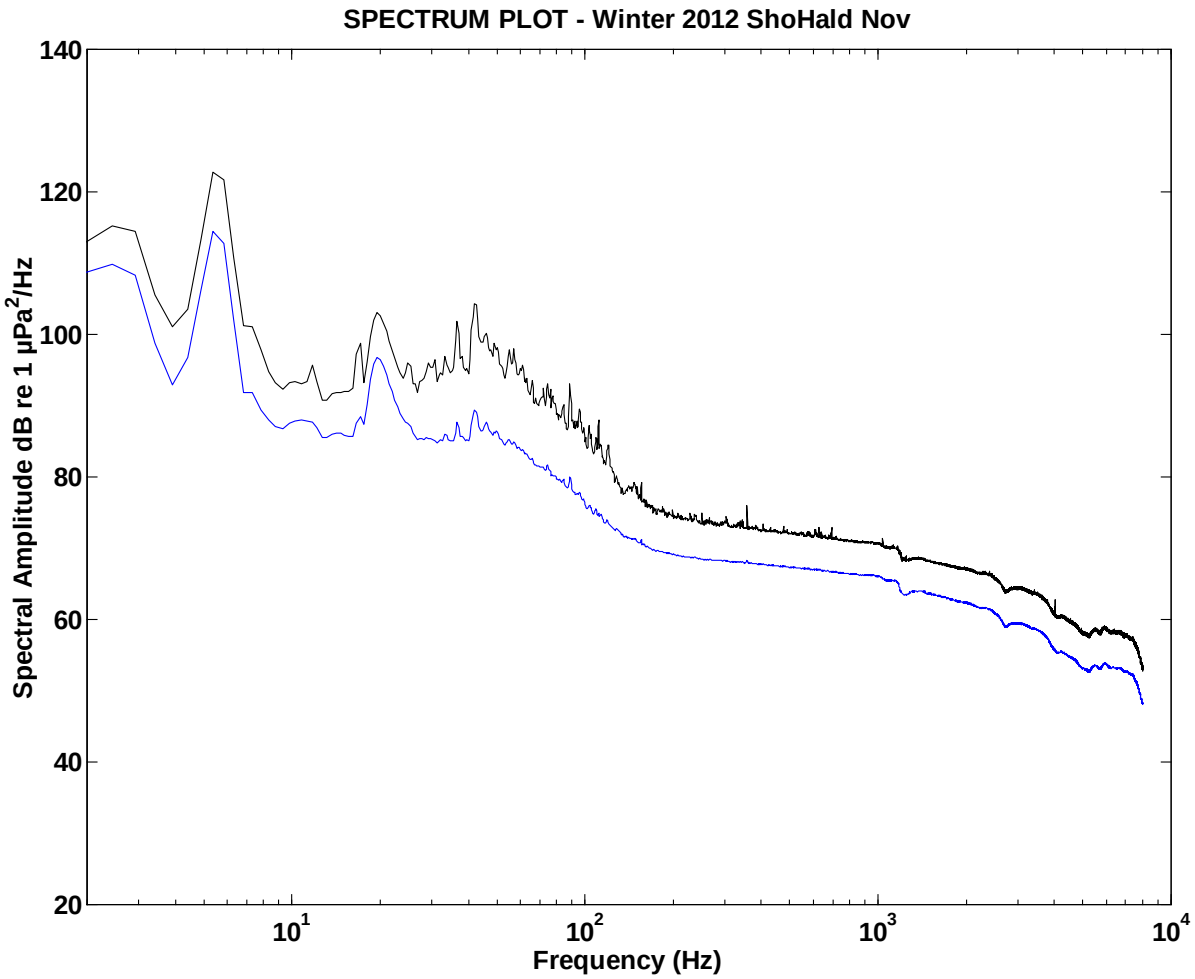


**Figure A4-1-ShoHald-2012-Nov.** Plot of high resolution power spectral density (blue curve) and power spectral density + 1 S.D. of sub-series spectral densities (black curve).

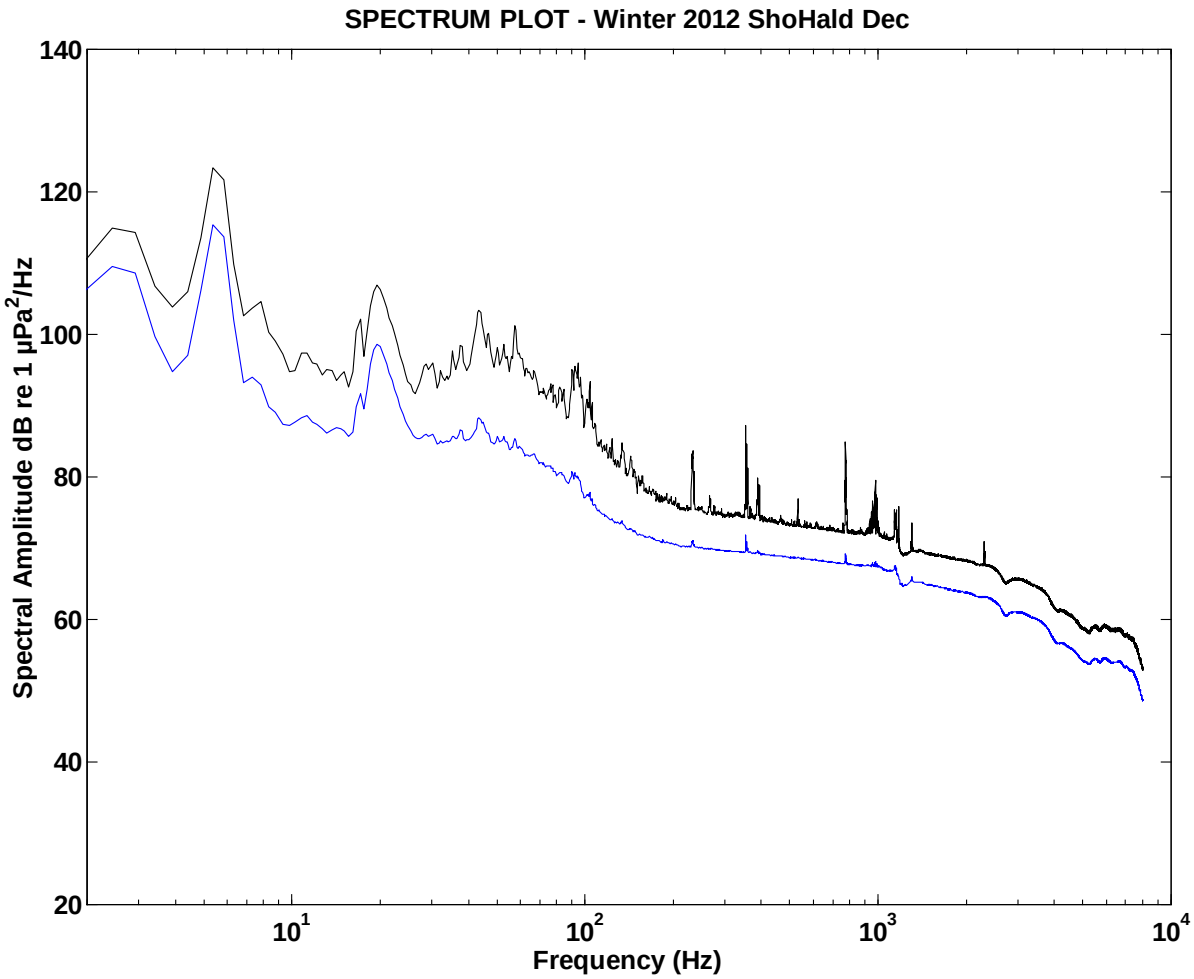


**Figure A4-1-ShoHald-2012-Dec.** Plot of high resolution power spectral density (blue curve) and power spectral density + 1 S.D. of sub-series spectral densities (black curve).

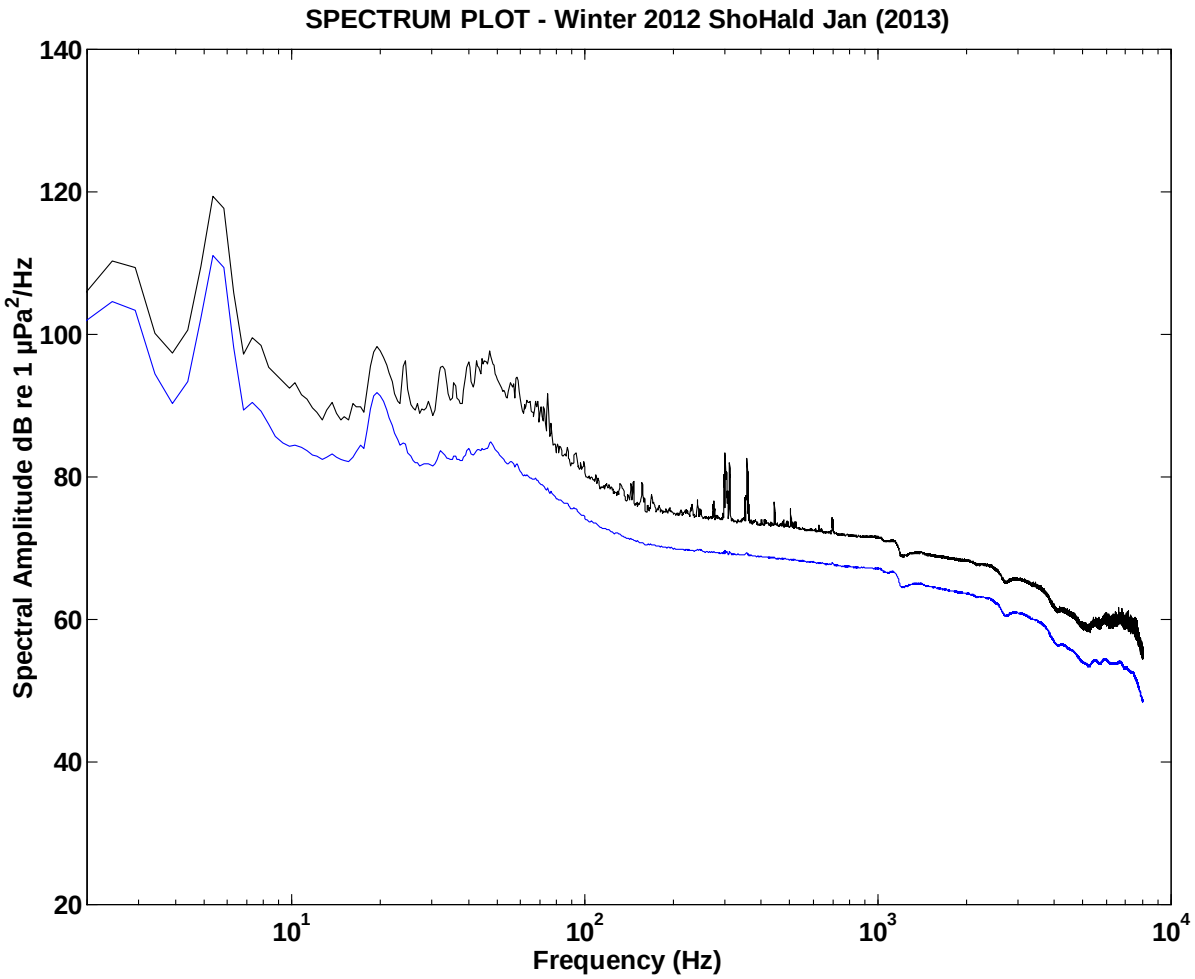


**Figure A4-1-ShoHald-2013-Jan.** Plot of high resolution power spectral density (blue curve) and power spectral density + 1 S.D. of sub-series spectral densities (black curve).

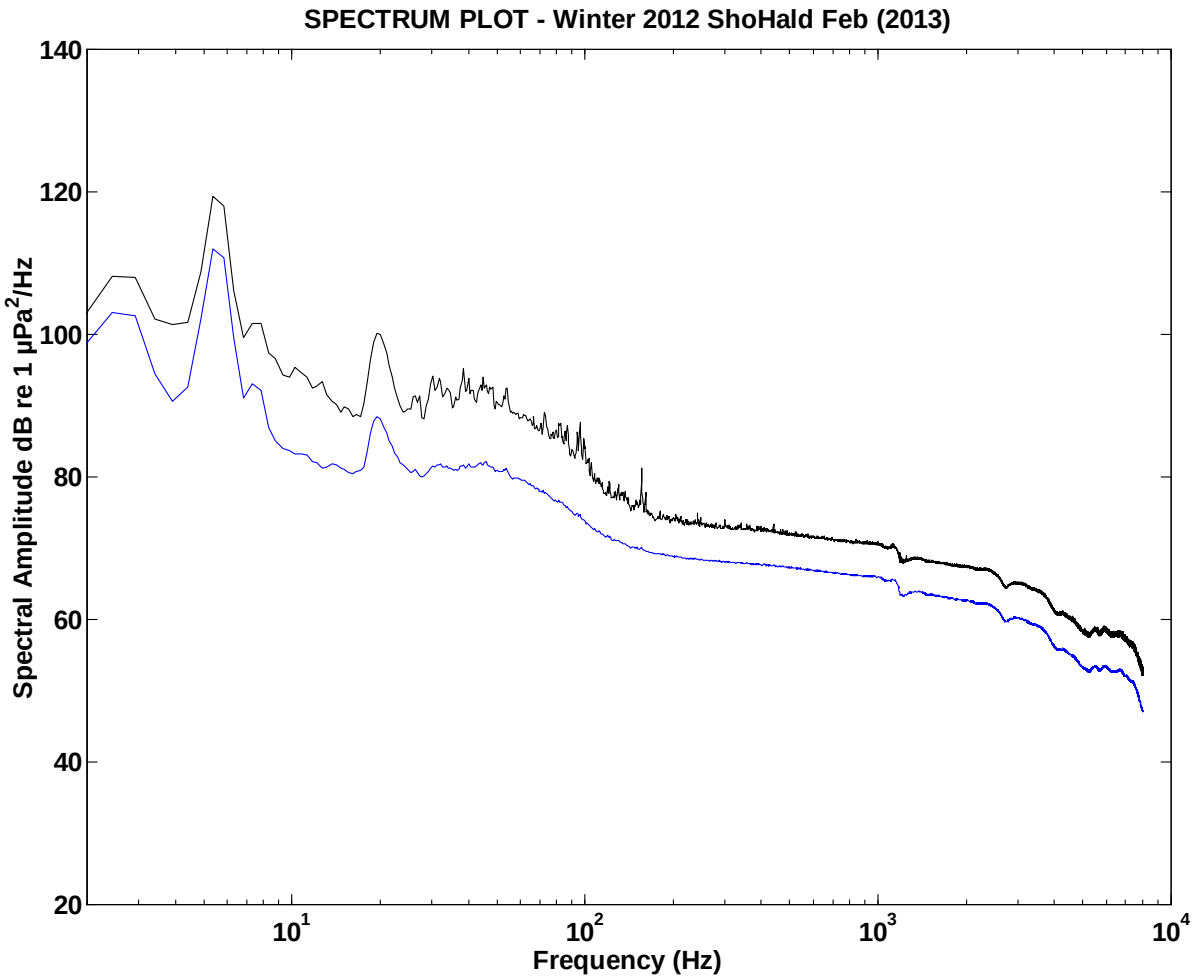


**Figure A4-1-ShoHald-2013-Feb.** Plot of high resolution power spectral density (blue curve) and power spectral density + 1 S.D. of sub-series spectral densities (black curve).

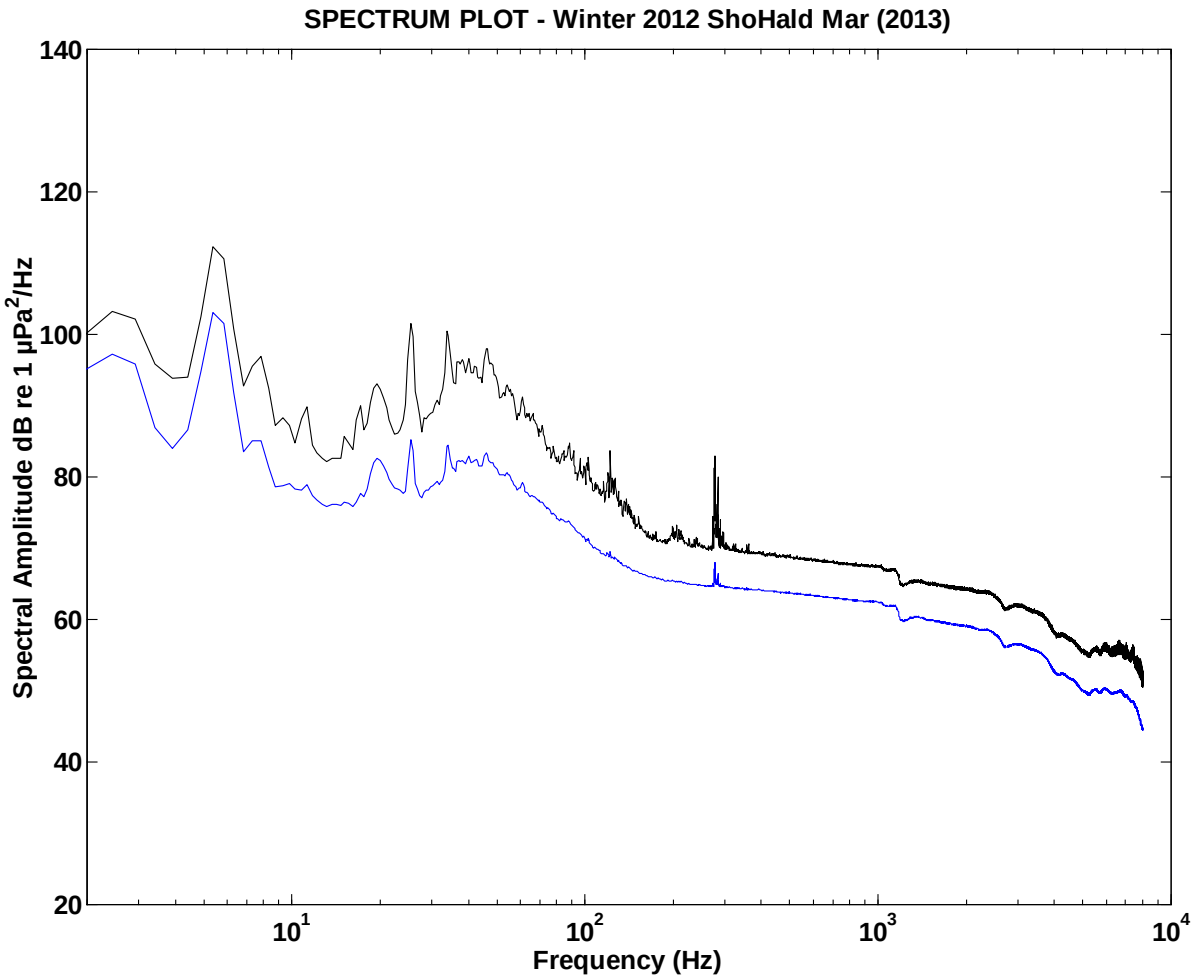


**Figure A4-1-ShoHald-2013-Mar.** Plot of high resolution power spectral density (blue curve) and power spectral density + 1 S.D. of sub-series spectral densities (black curve).

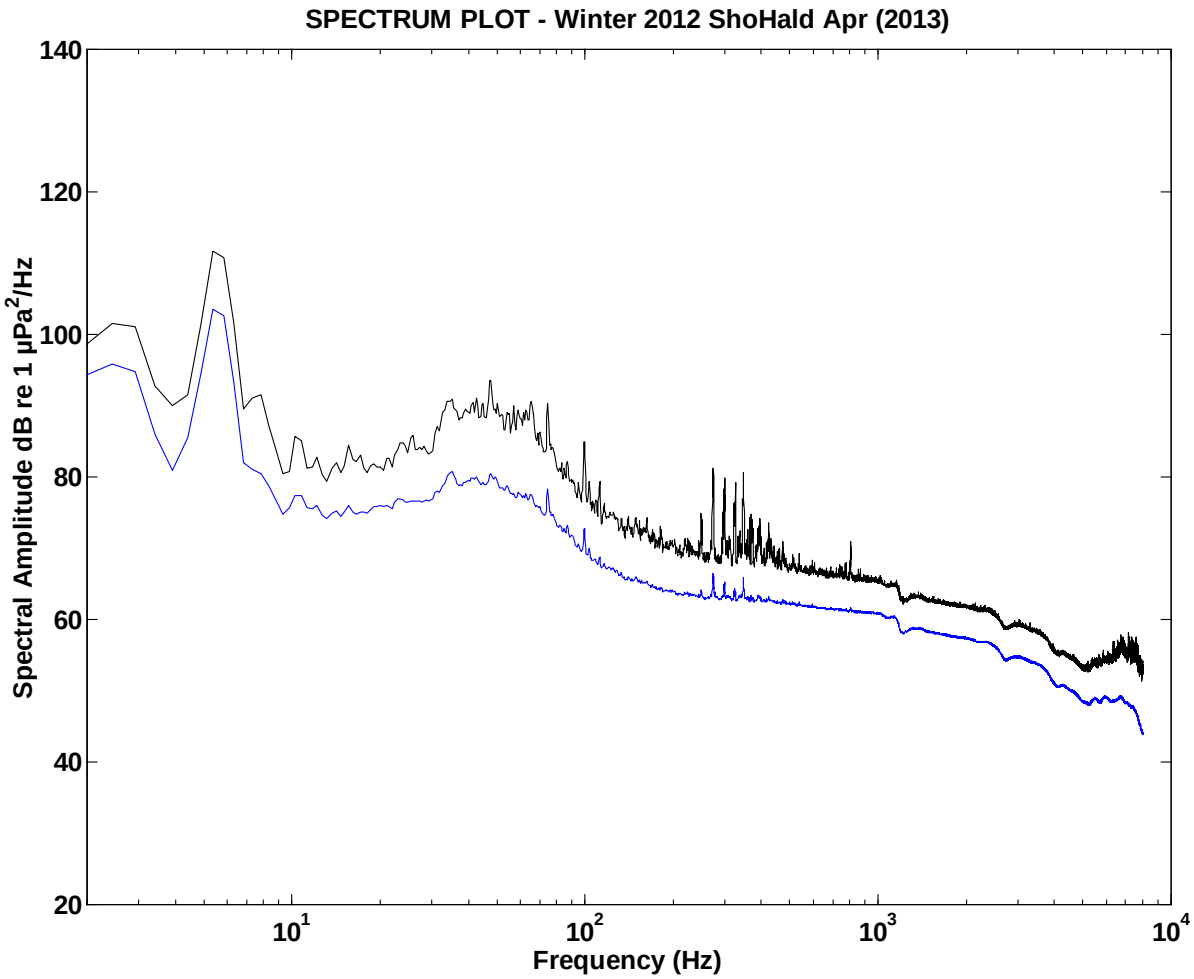


**Figure A4-1-ShoHald-2013-Apr.** Plot of high resolution power spectral density (blue curve) and power spectral density + 1 S.D. of sub-series spectral densities (black curve).

### *A4.1.2. Summer 2013 Deployments*

**Figure (series) A4-1–Summer 2013 Deployments** - Plots of high resolution power spectral density and power spectral density + 1 standard deviation (S.D.) of sub-series spectral densities.

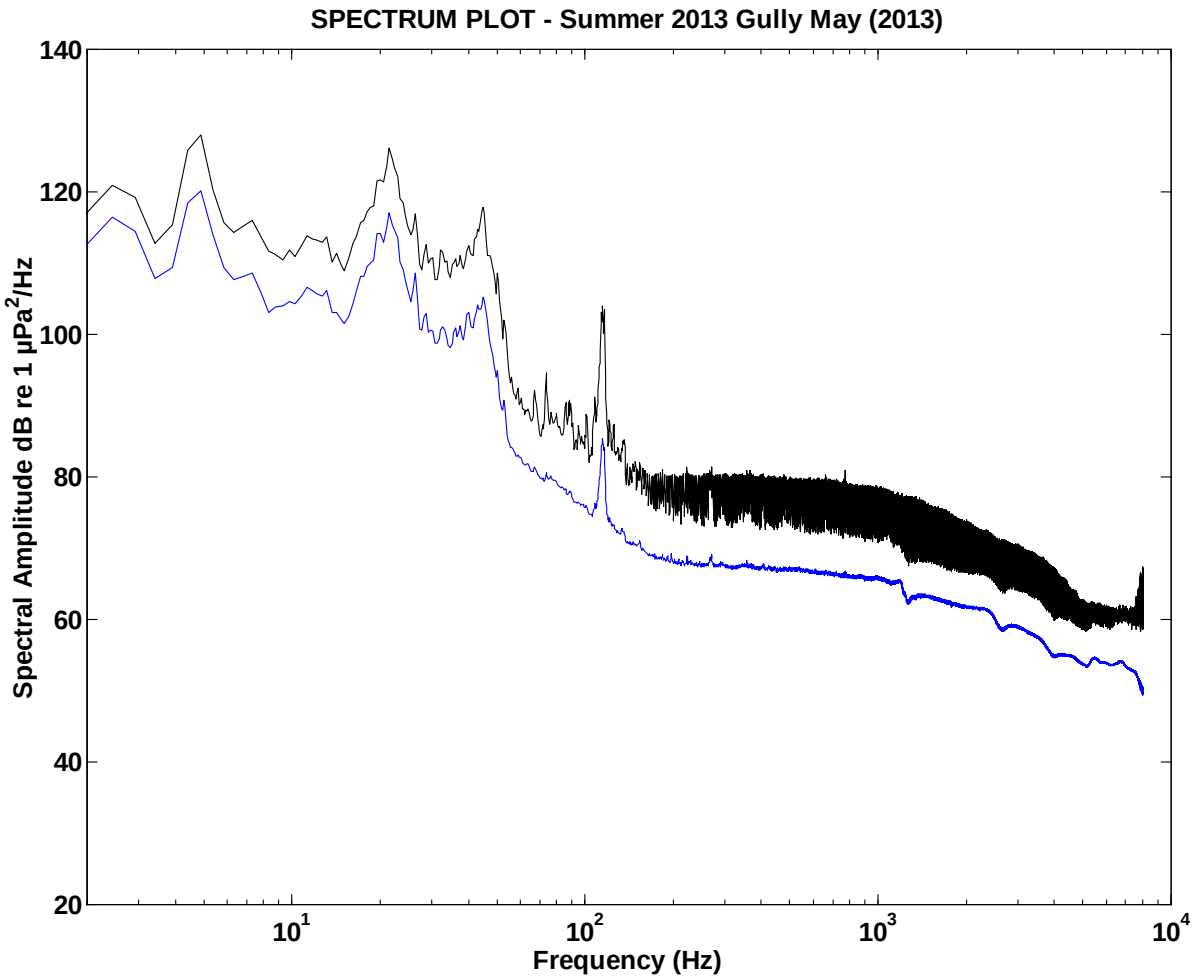


**Figure A4-1-MidGul-2013-May.** Plot of high resolution power spectral density (blue curve) and power spectral density + 1 S.D. of sub-series spectral densities (black curve).

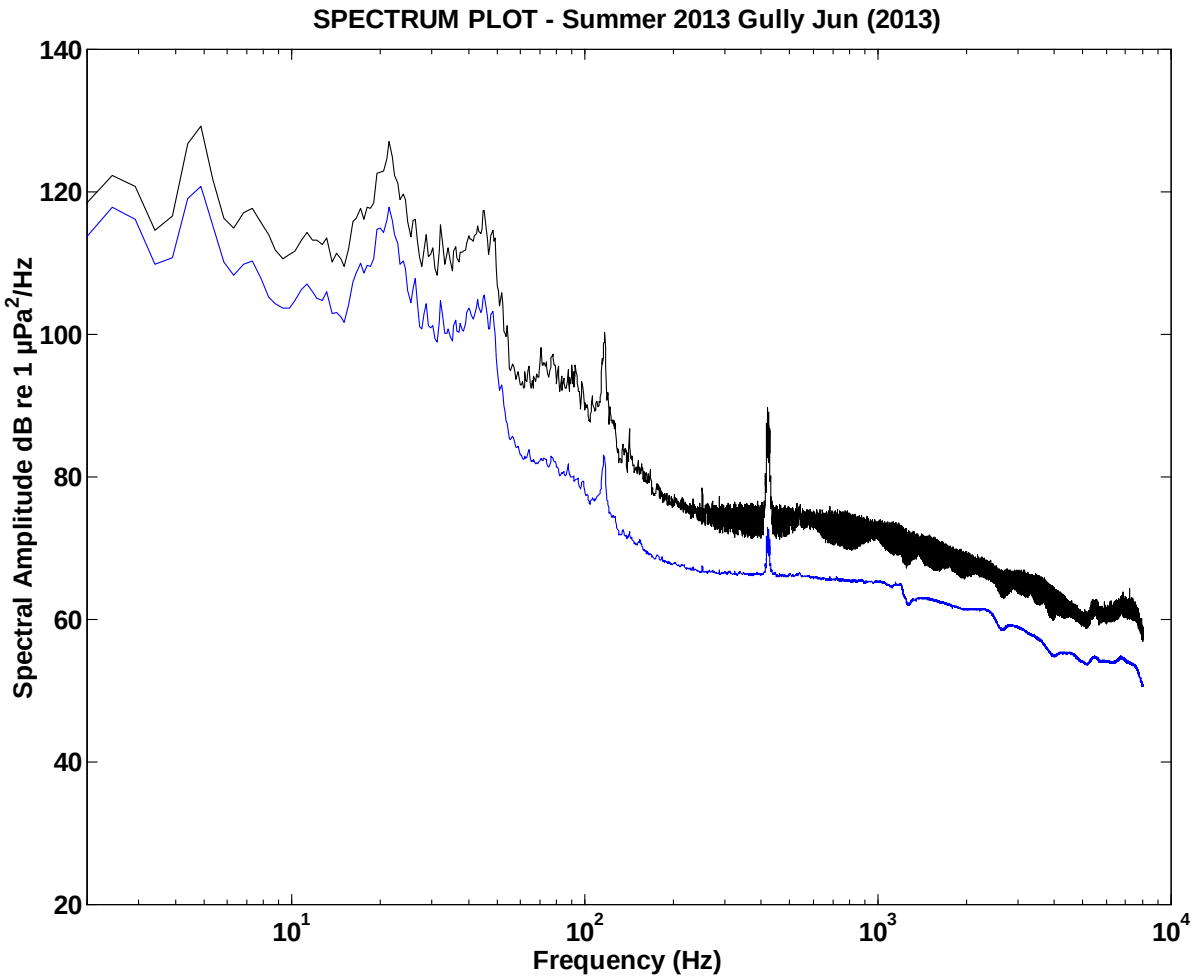


**Figure A4-1-MidGul-2013-Jun.** Plot of high resolution power spectral density (blue curve) and power spectral density + 1 S.D. of sub-series spectral densities (black curve).

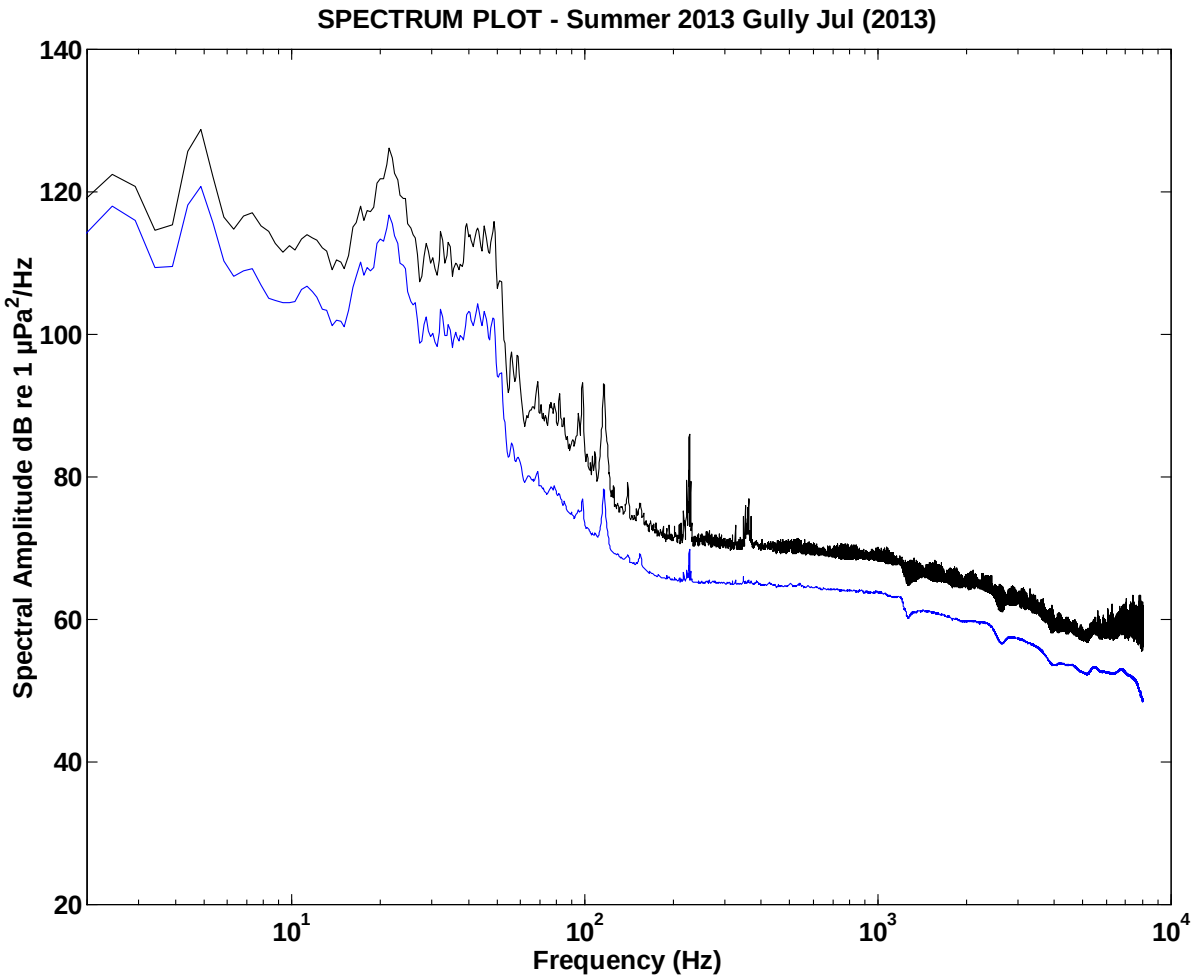


**Figure A4-1-MidGul-2013-Jul.** Plot of high resolution power spectral density (blue curve) and power spectral density + 1 S.D. of sub-series spectral densities (black curve).

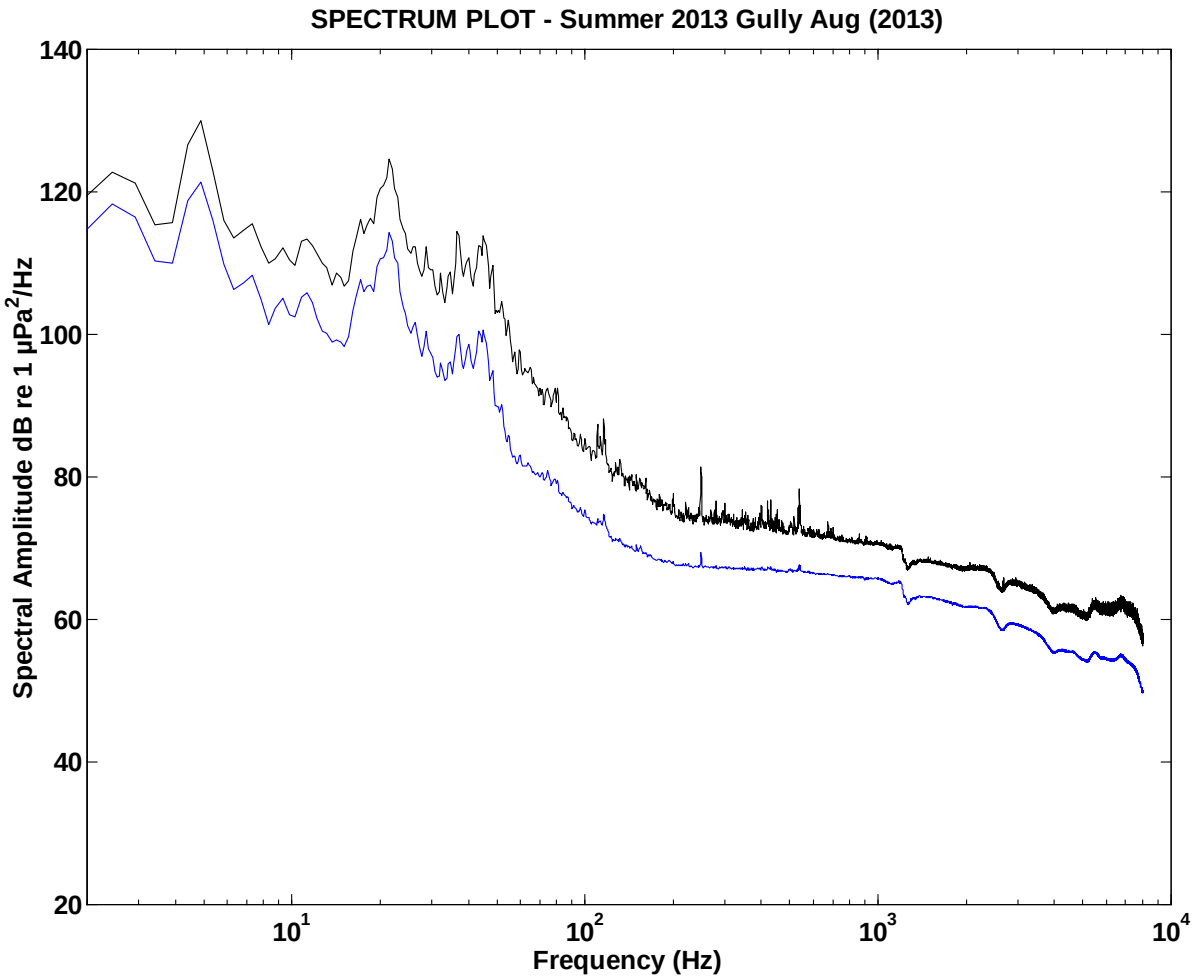


**Figure A4-1-MidGul-2013-Aug.** Plot of high resolution power spectral density (blue curve) and power spectral density + 1 S.D. of sub-series spectral densities (black curve).

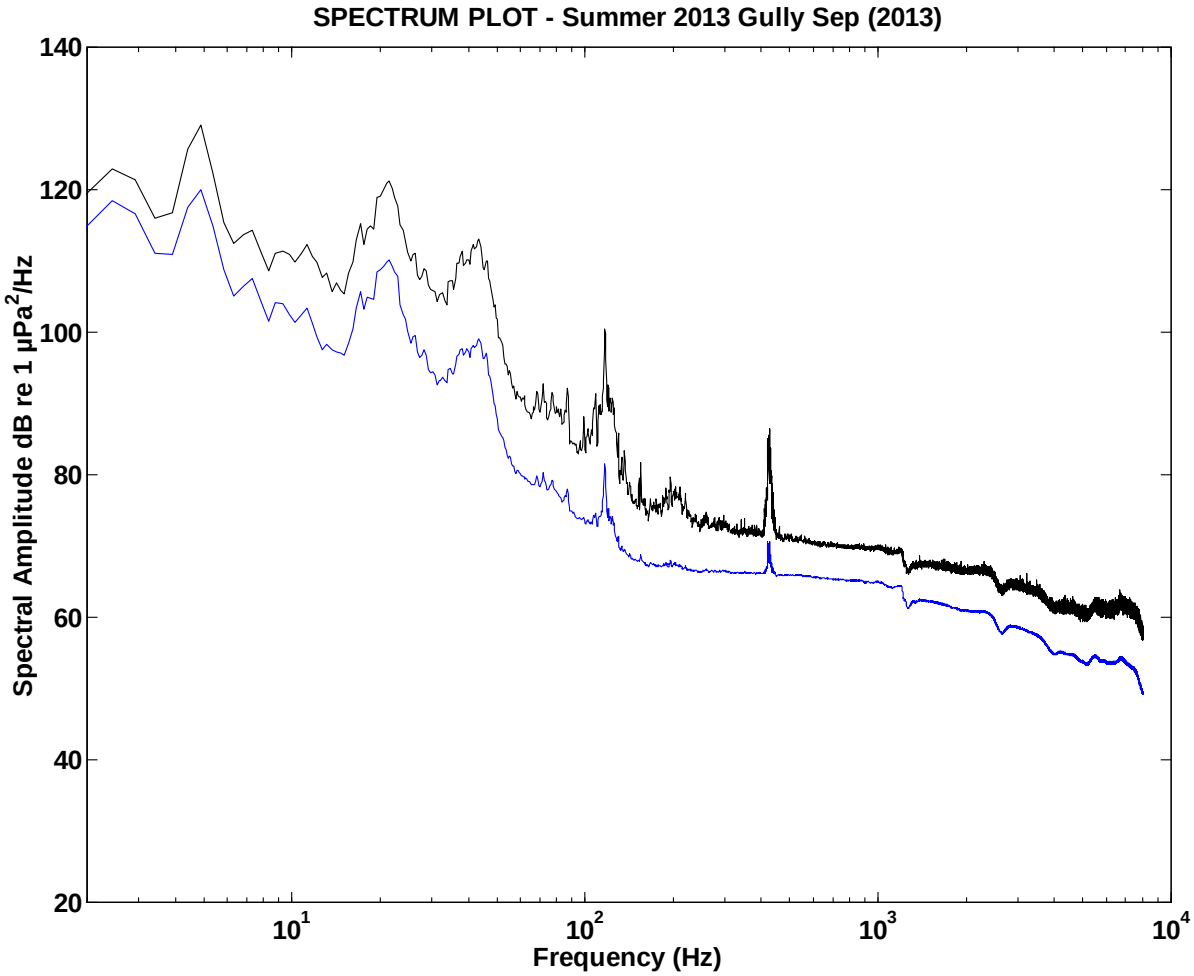


**Figure A4-1-MidGul-2013-Sep.** Plot of high resolution power spectral density (blue curve) and power spectral density + 1 S.D. of sub-series spectral densities (black curve).

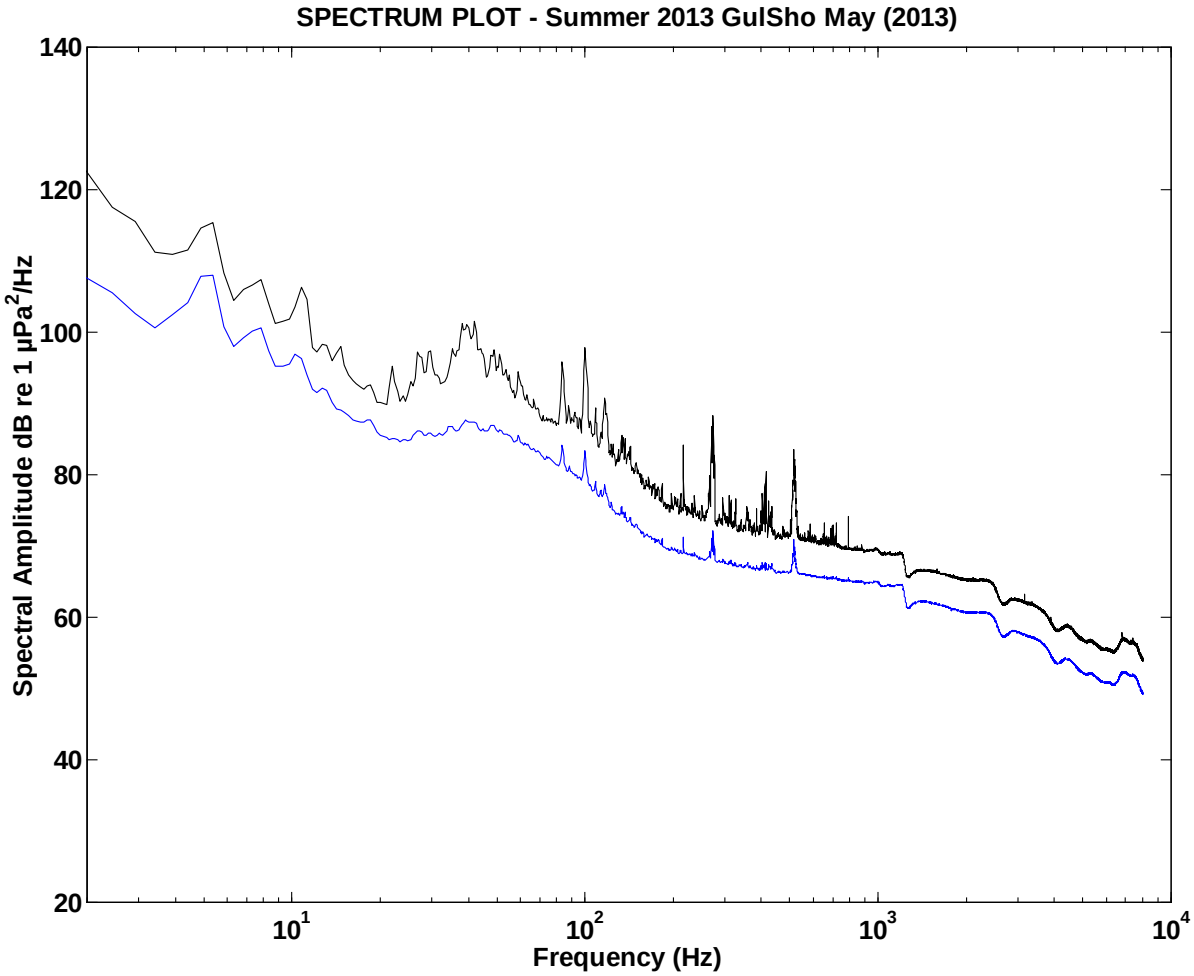


**Figure A4-1-GulSho-2013-May.** Plot of high resolution power spectral density (blue curve) and power spectral density + 1 S.D. of sub-series spectral densities (black curve).

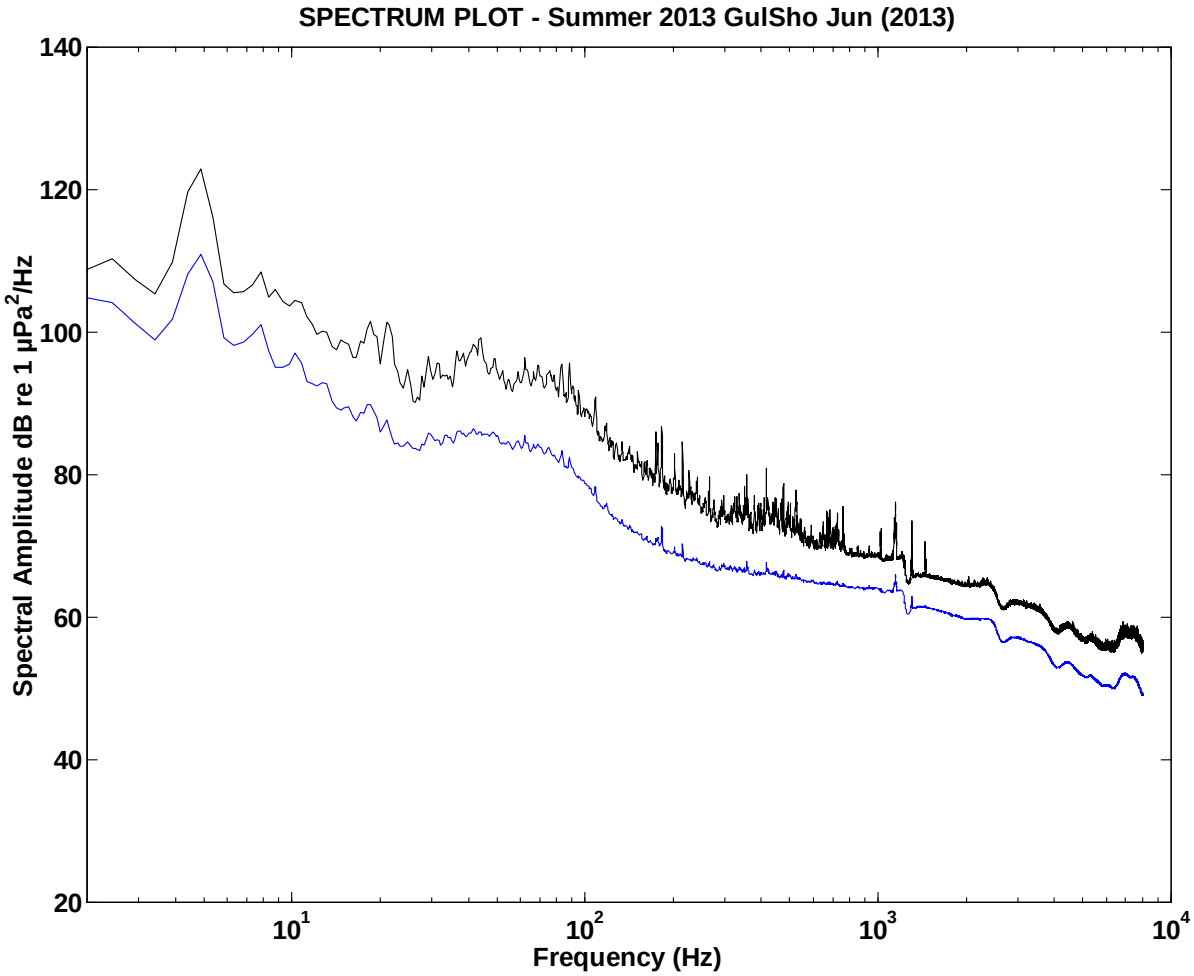


**Figure A4-1-GulSho-2013-Jun.** Plot of high resolution power spectral density (blue curve) and power spectral density + 1 S.D. of sub-series spectral densities (black curve).

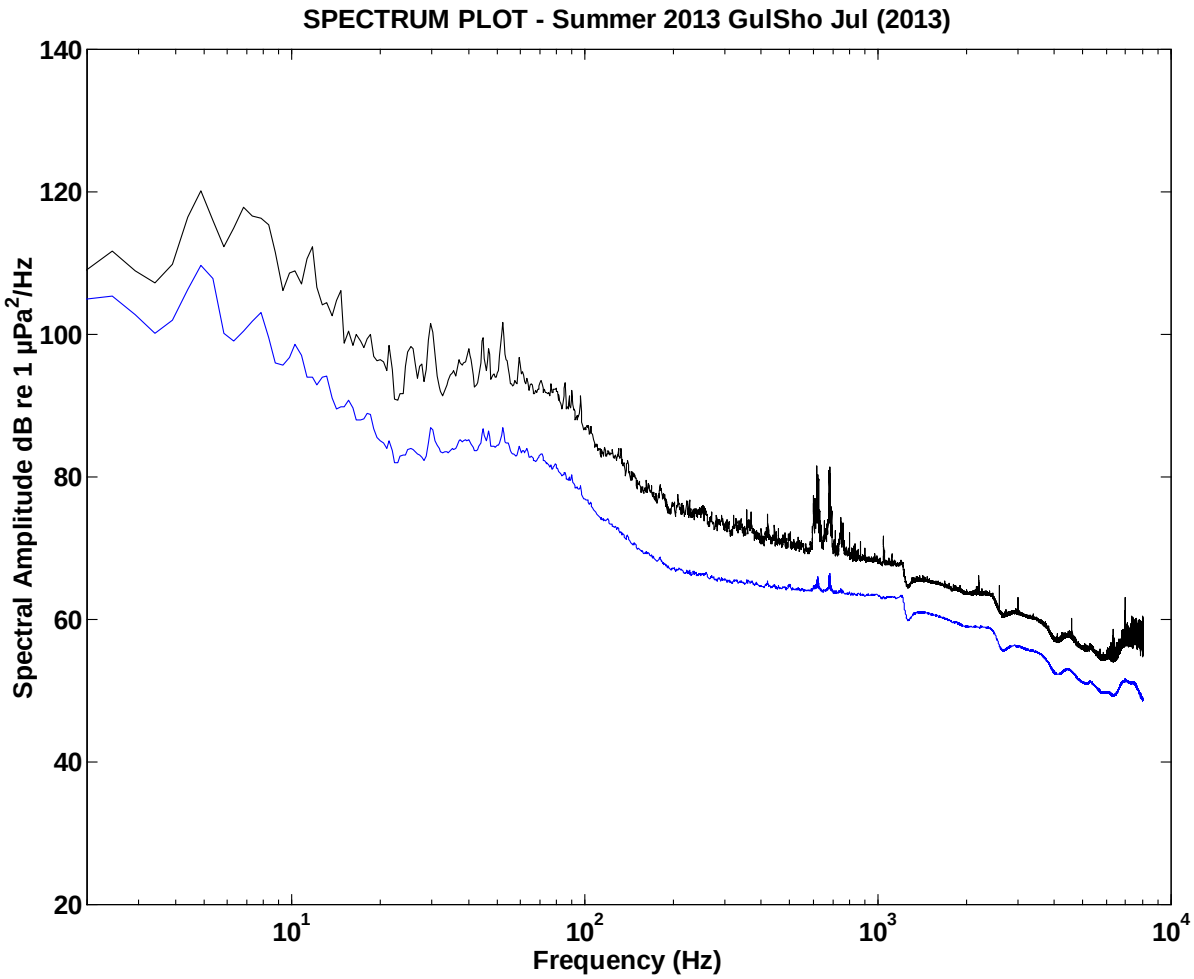


**Figure A4-1-GulSho-2013-Jul.** Plot of high resolution power spectral density (blue curve) and power spectral density + 1 S.D. of sub-series spectral densities (black curve).

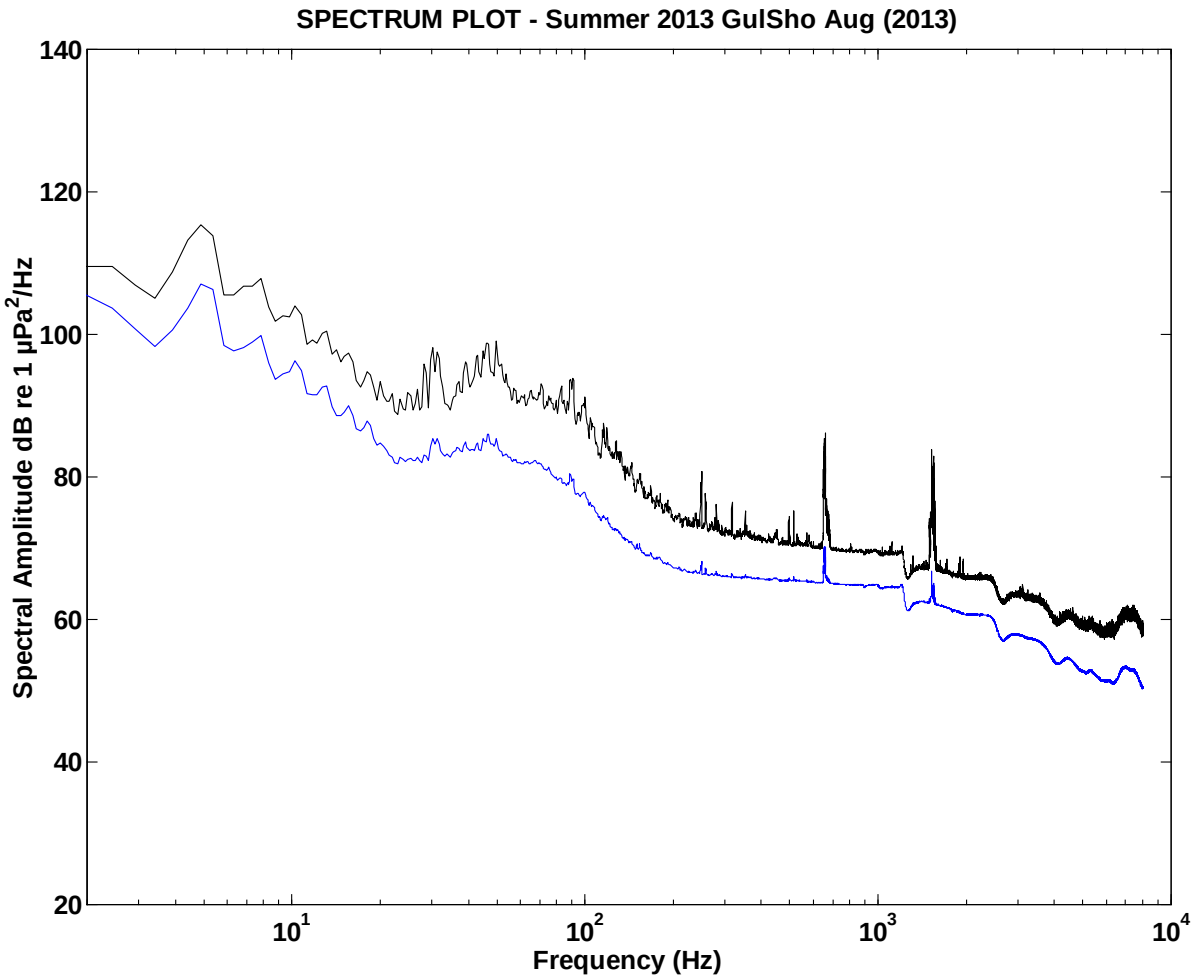


**Figure A4-1-GulSho-2013-Aug.** Plot of high resolution power spectral density (blue curve) and power spectral density + 1 S.D. of sub-series spectral densities (black curve).

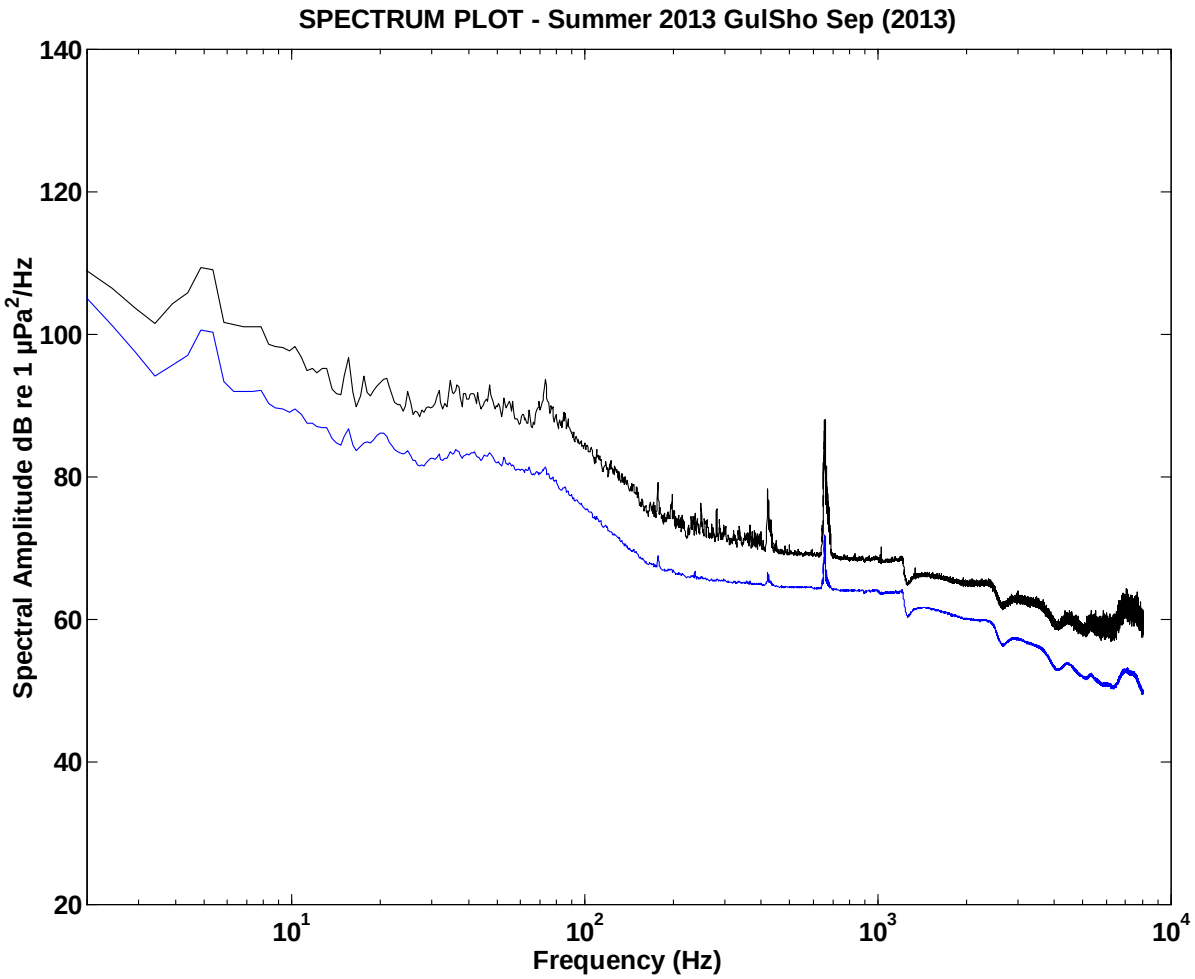


**Figure A4-1-GulSho-2013-Sep.** Plot of high resolution power spectral density (blue curve) and power spectral density + 1 S.D. of sub-series spectral densities (black curve).

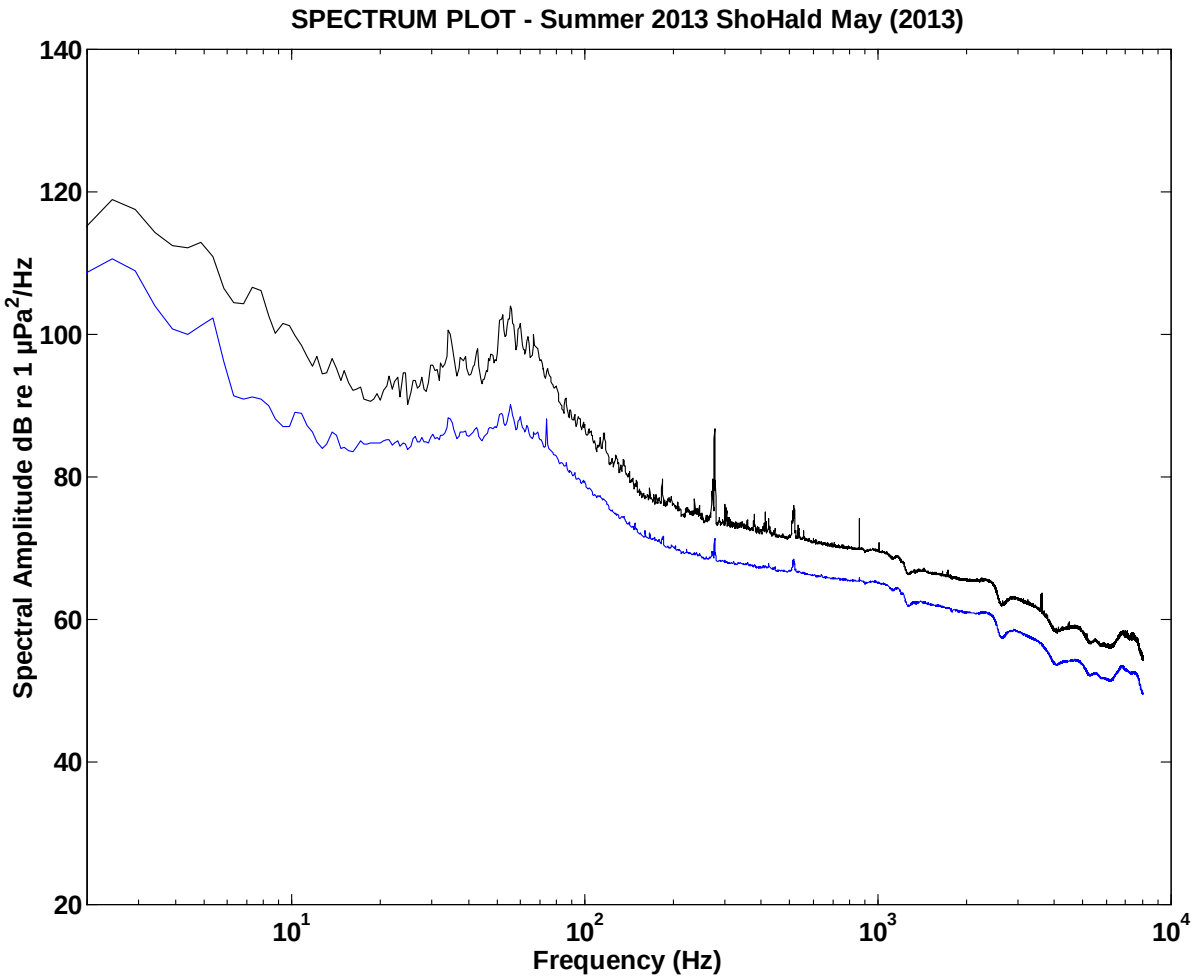


**Figure A4-1-ShoHald-2013-May.** Plot of high resolution power spectral density (blue curve) and power spectral density + 1 S.D. of sub-series spectral densities (black curve).

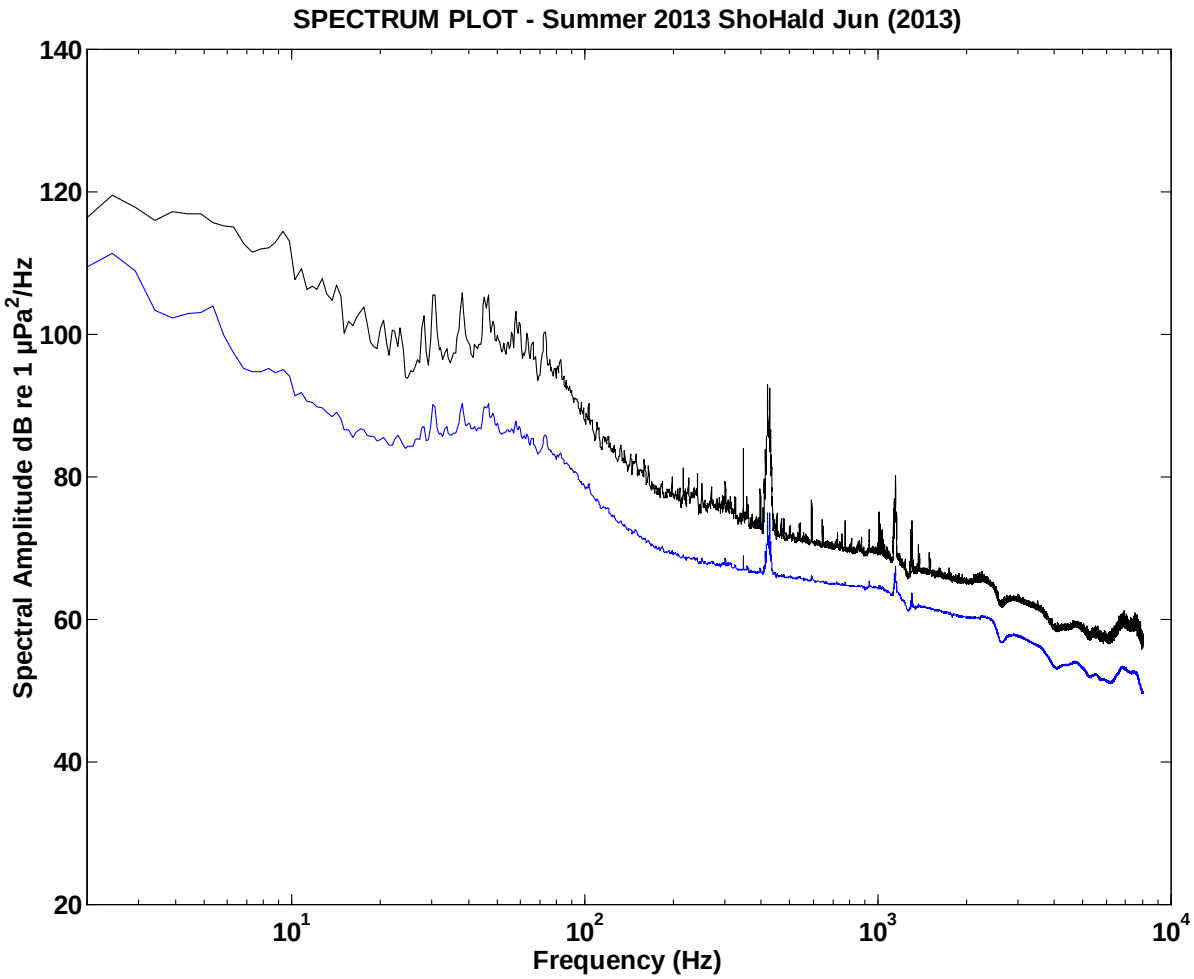


**Figure A4-1-ShoHald-2013-Jun.** Plot of high resolution power spectral density (blue curve) and power spectral density + 1 S.D. of sub-series spectral densities (black curve).

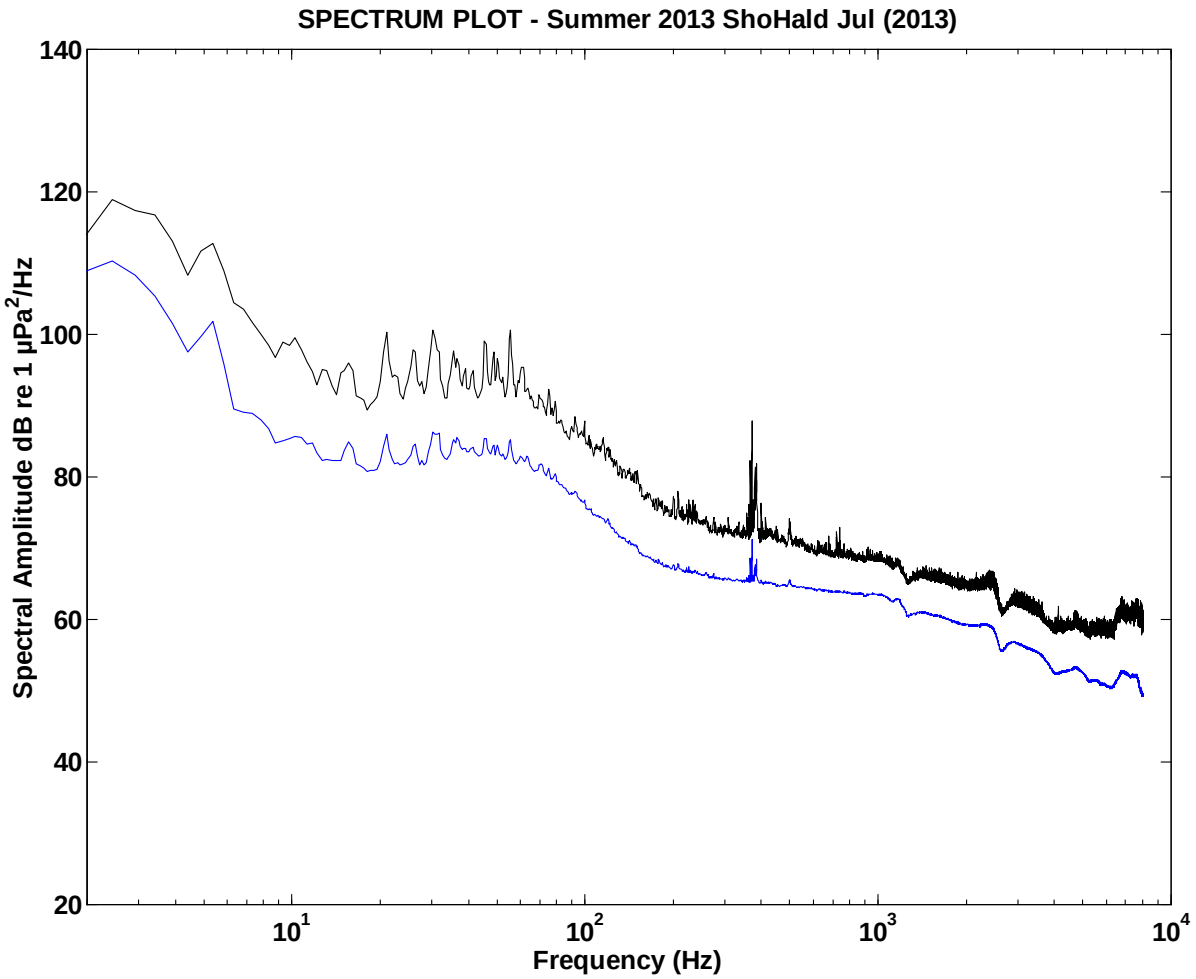


**Figure A4-1-ShoHald-2013-Jul.** Plot of high resolution power spectral density (blue curve) and power spectral density + 1 S.D. of sub-series spectral densities (black curve).

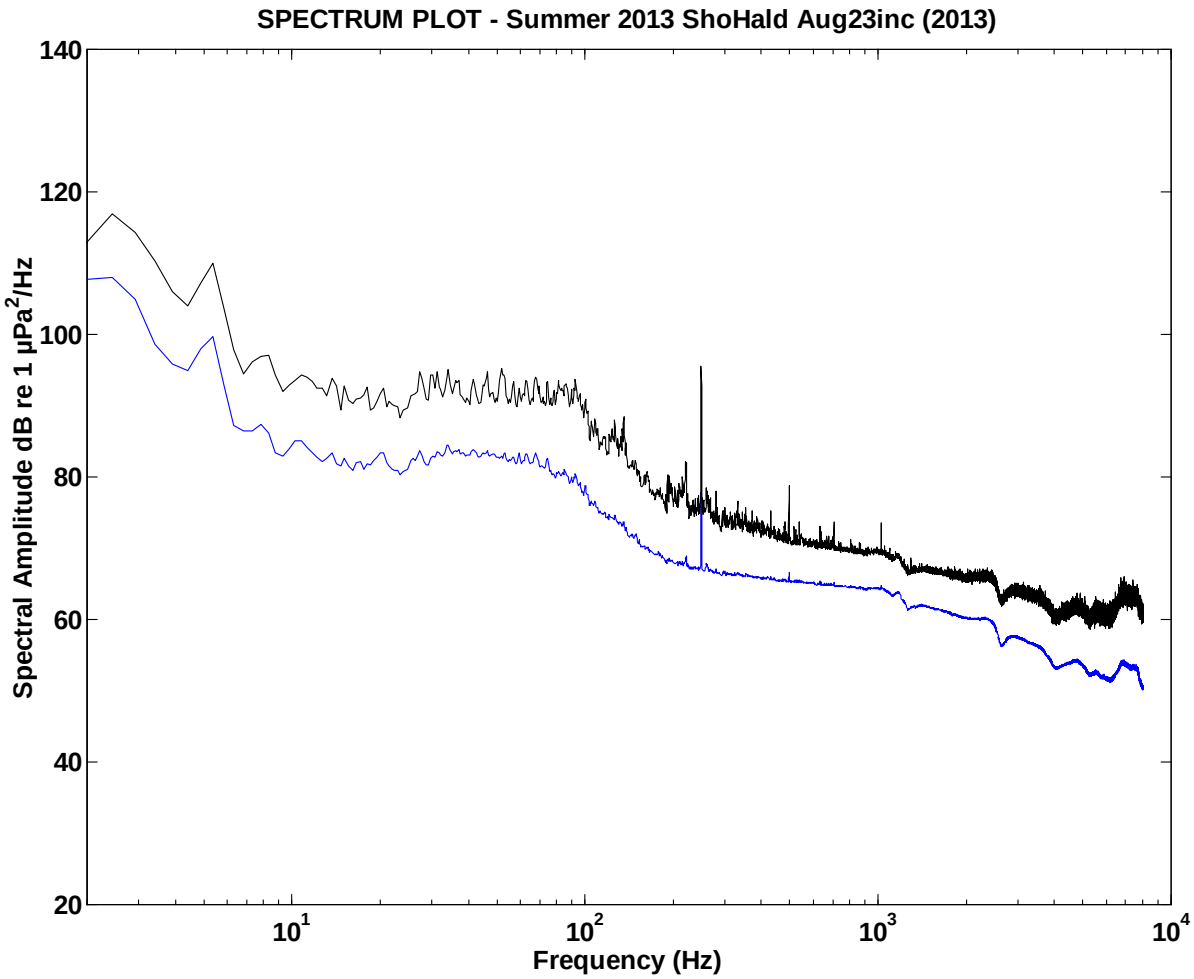


**Figure A4-1-ShoHald-2013-Aug.** Plot of high resolution power spectral density (blue curve) and power spectral density + 1 S.D. of sub-series spectral densities (black curve). Data series truncation after Aug. 23rd incl. to eliminate corrupted data.

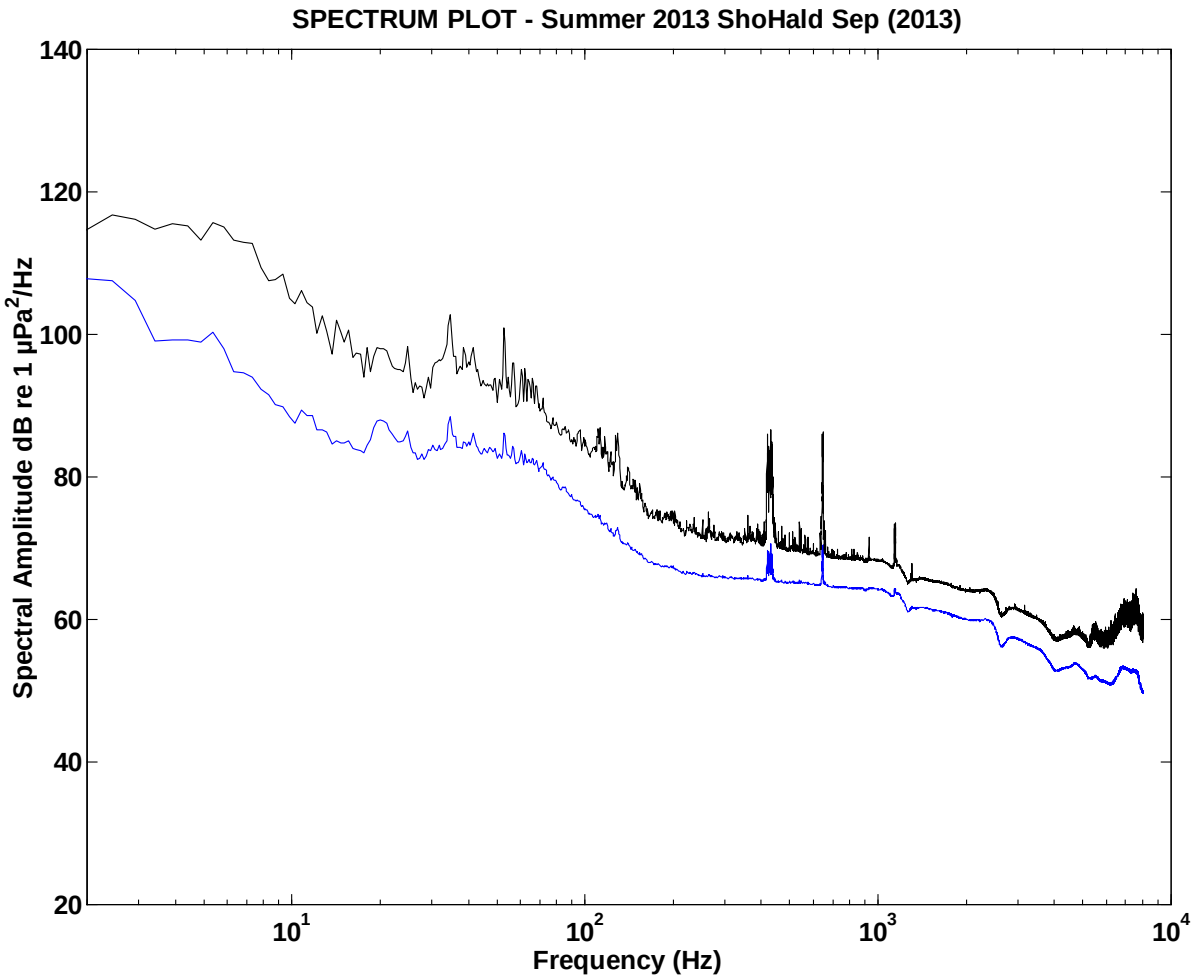


**Figure A4-1-ShoHald-2013-Sep.** Plot of high resolution power spectral density (blue curve) and power spectral density + 1 S.D. of sub-series spectral densities (black curve).

### *A4.1.3. Winter 2013-14 Deployments*

**Figure (series) A4-1-Winter 2013-14 Deployments** - Plots of high resolution power spectral density and power spectral density + 1 standard deviation (S.D.) of sub-series spectral densities.

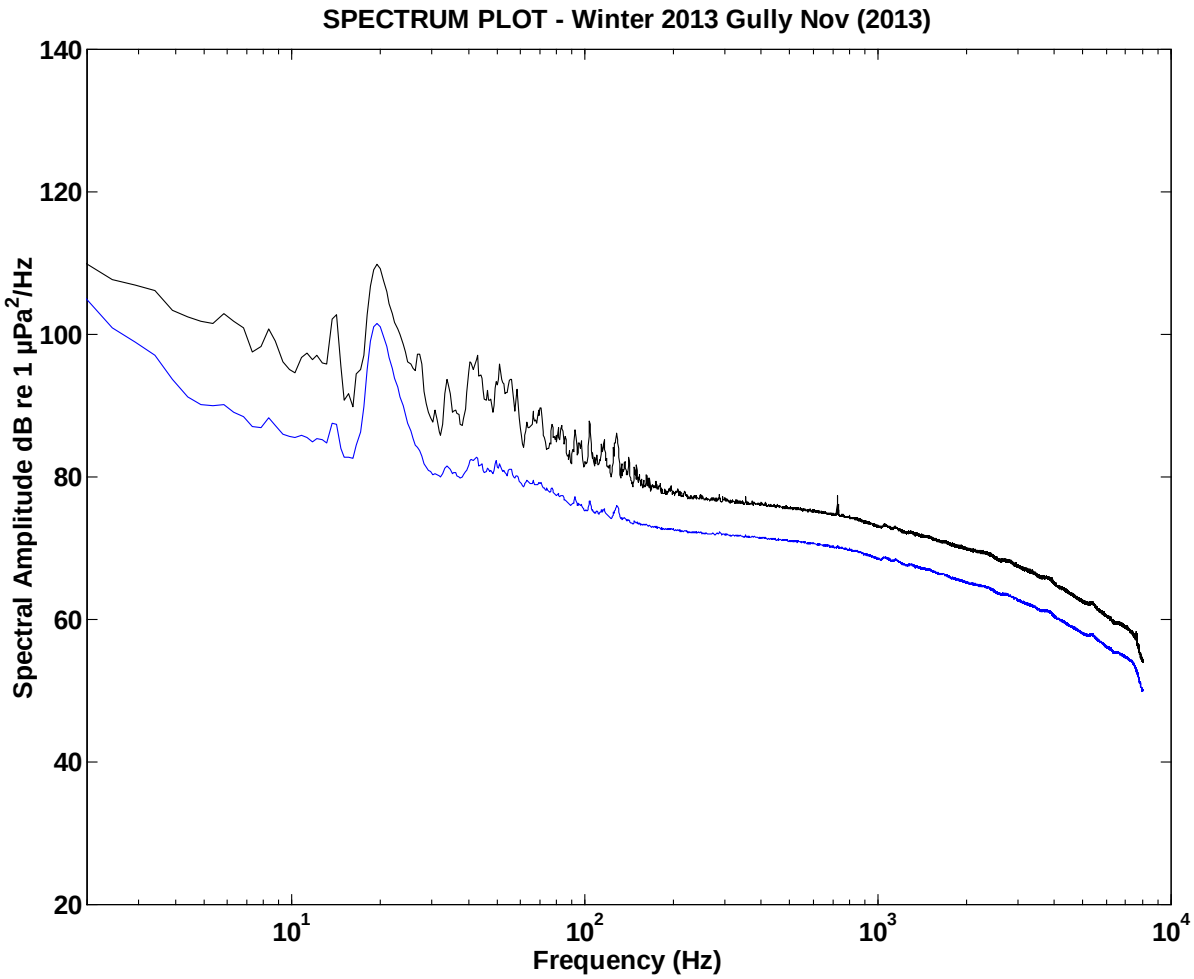


**Figure A4-1-MidGul-2013-Nov.** Plot of high resolution power spectral density (blue curve) and power spectral density + 1 S.D. of sub-series spectral densities (black curve).

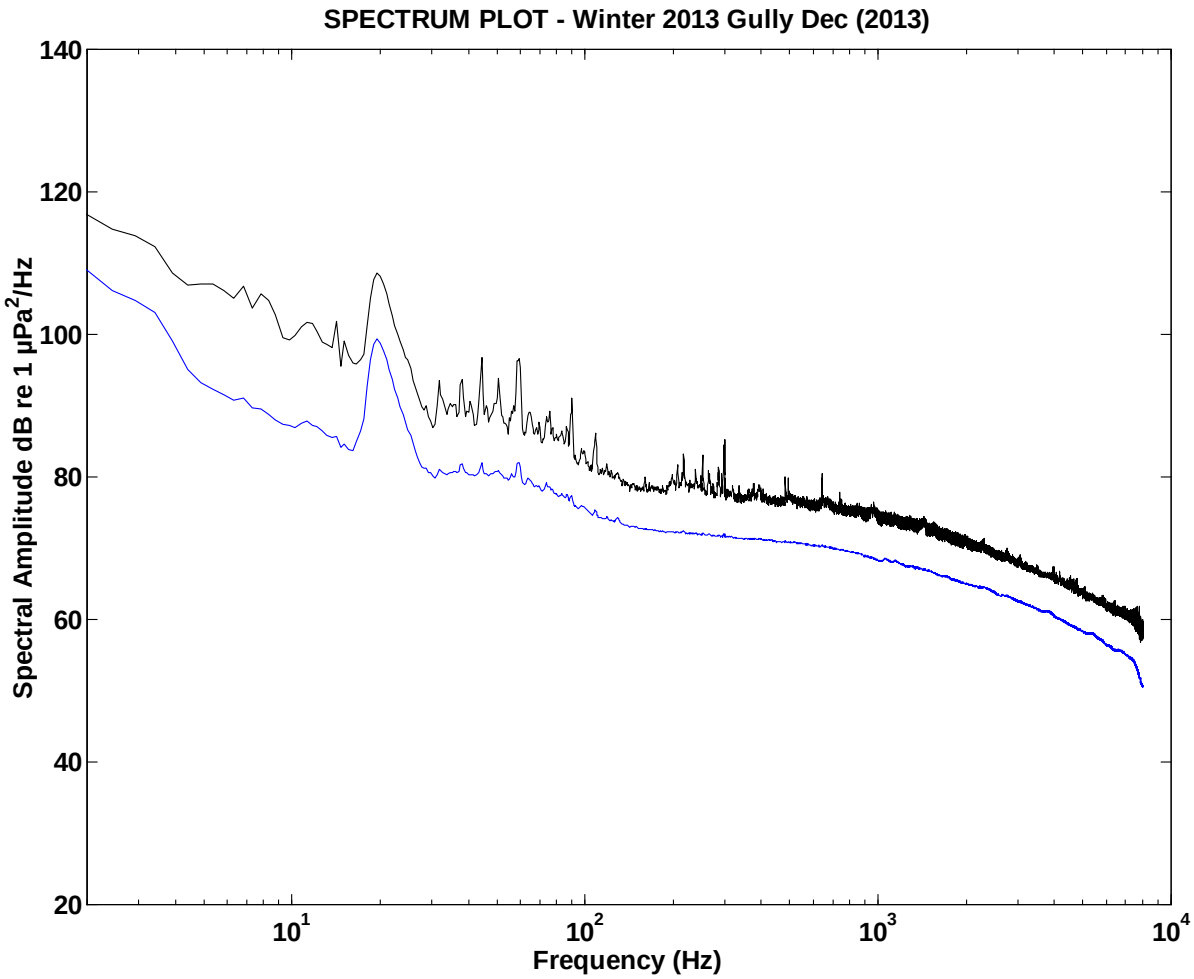


**Figure A4-1-MidGul-2013-Dec.** Plot of high resolution power spectral density (blue curve) and power spectral density + 1 S.D. of sub-series spectral densities (black curve).

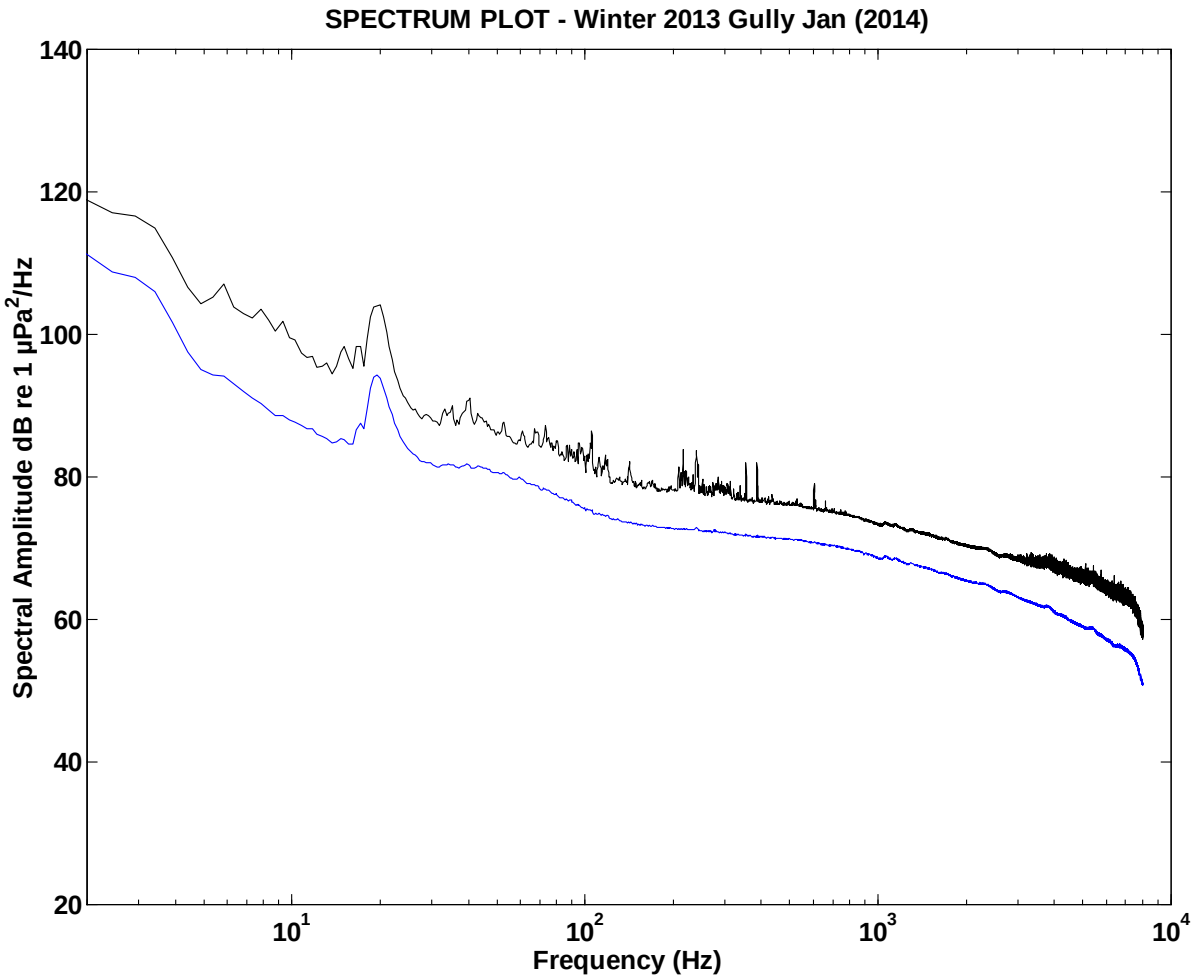


**Figure A4-1-MidGul-2013-Jan.** Plot of high resolution power spectral density (blue curve) and power spectral density + 1 S.D. of sub-series spectral densities (black curve).

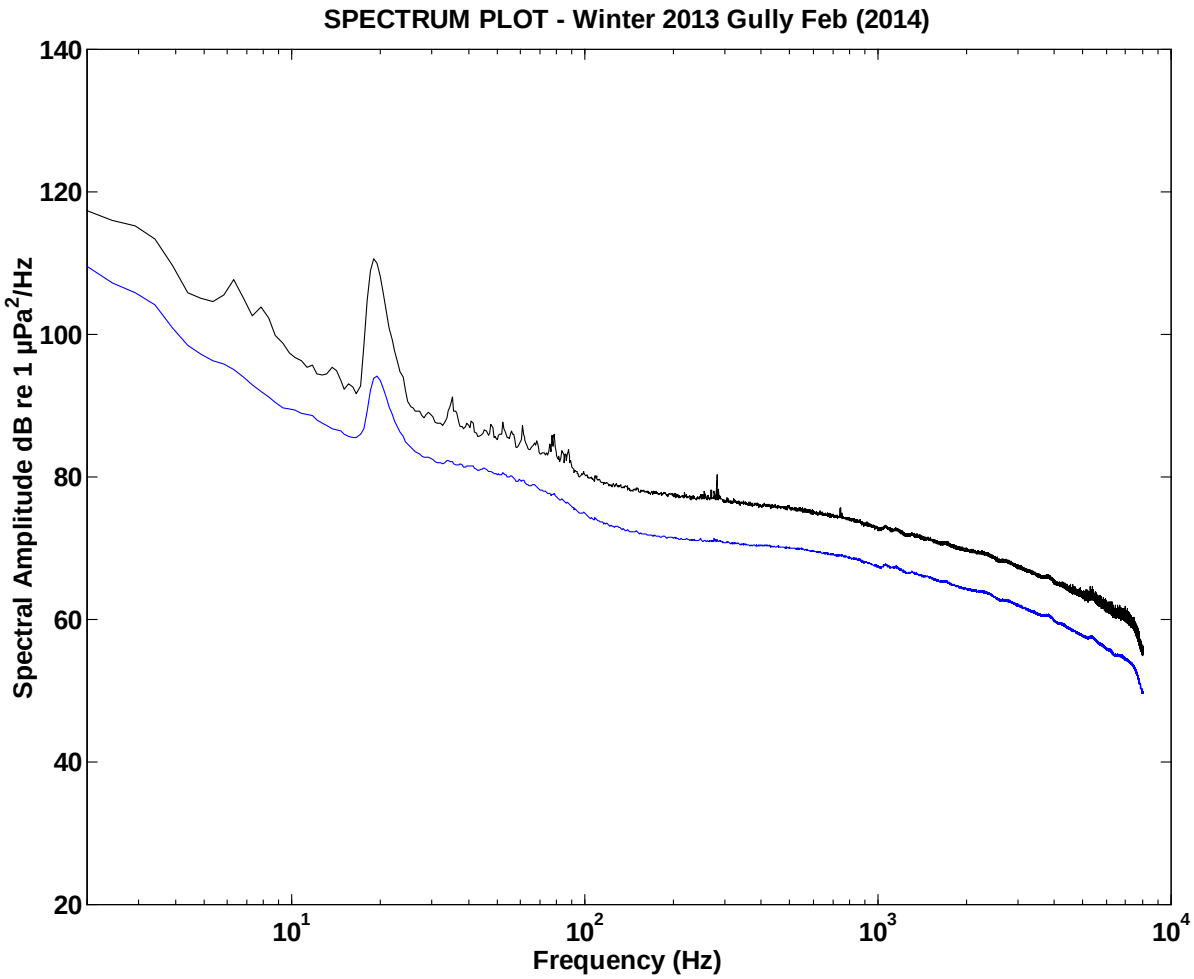


**Figure A4-1-MidGul-2014-Feb.** Plot of high resolution power spectral density (blue curve) and power spectral density + 1 S.D. of sub-series spectral densities (black curve).

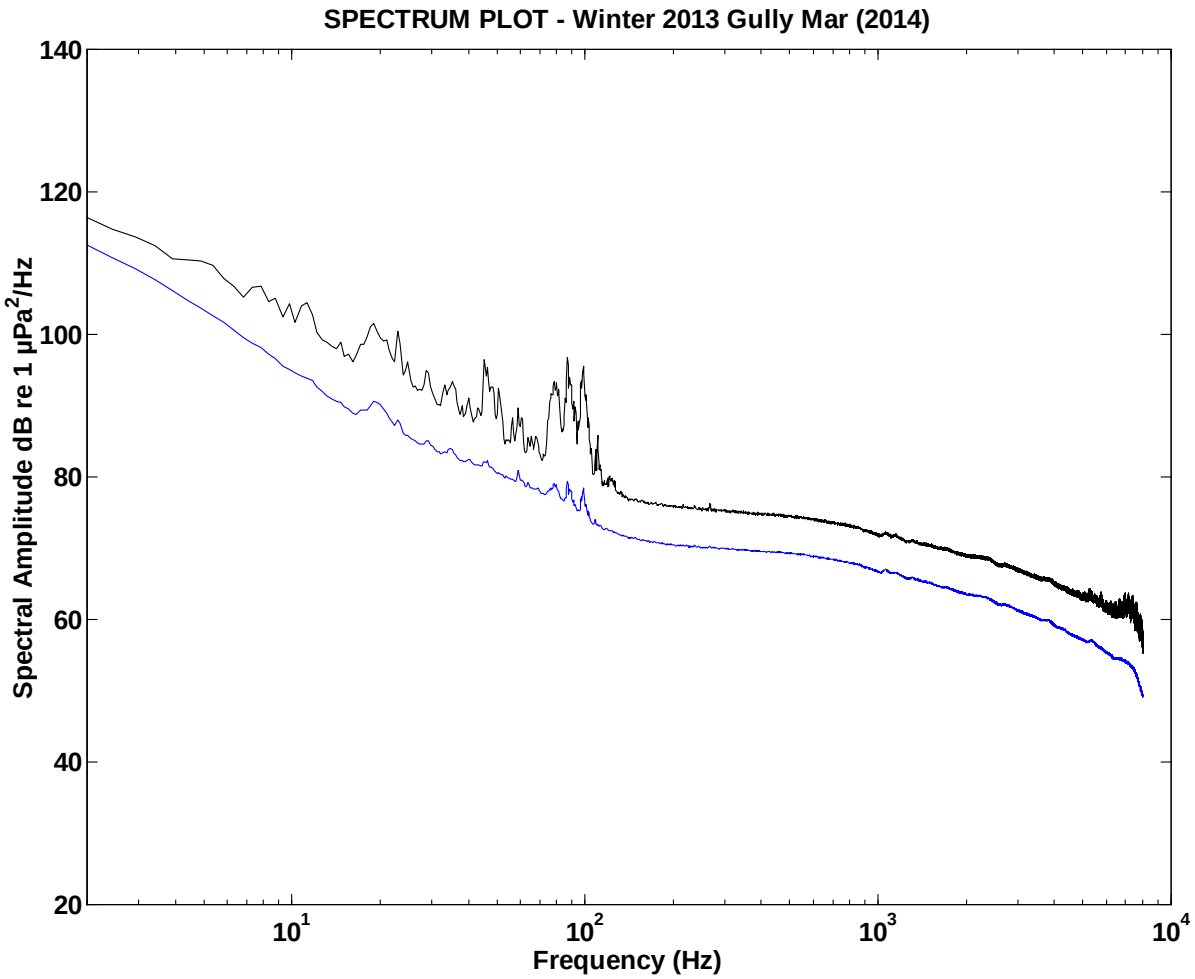


**Figure A4-1-MidGul-2014-Mar.** Plot of high resolution power spectral density (blue curve) and power spectral density + 1 S.D. of sub-series spectral densities (black curve).

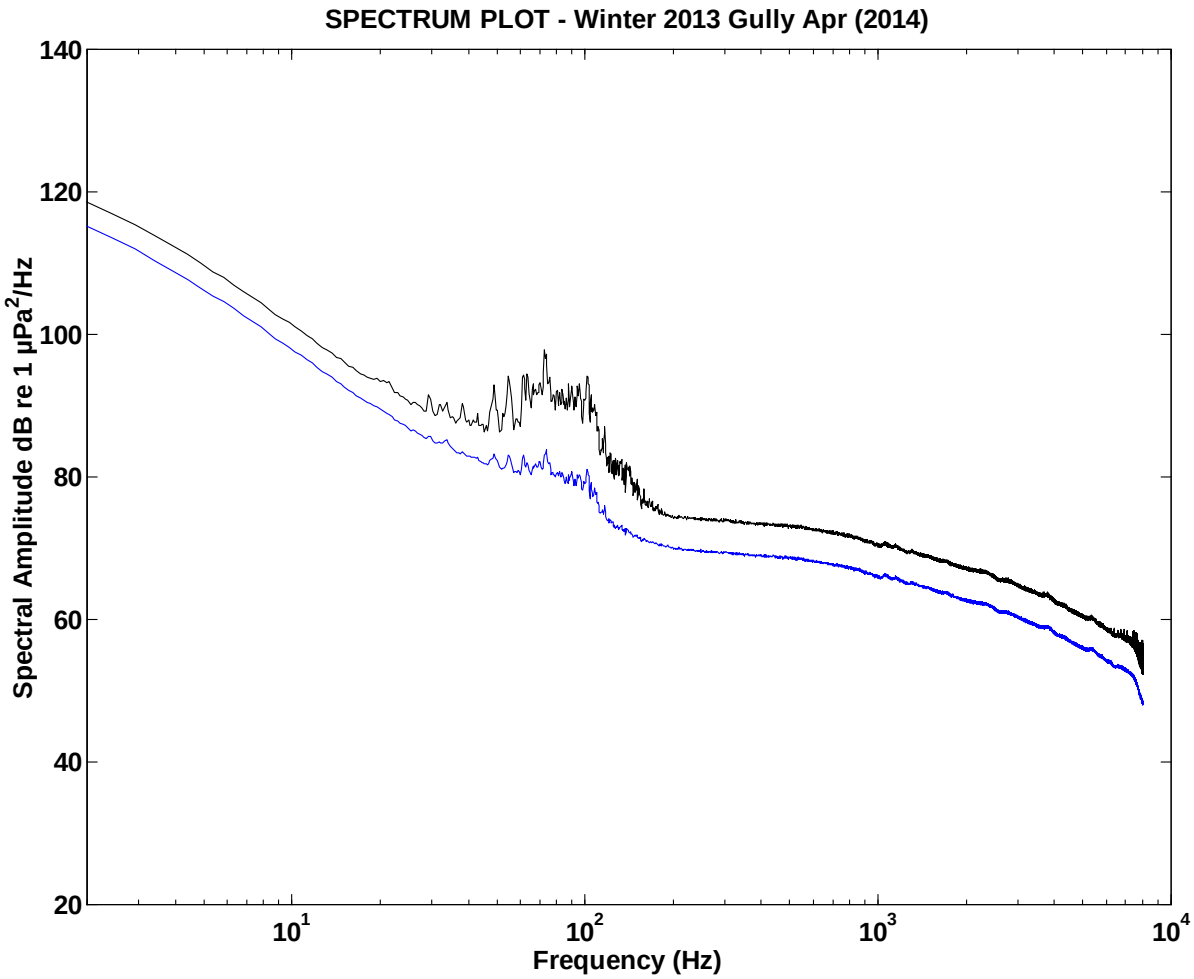


**Figure A4-1-MidGul-2014-Apr.** Plot of high resolution power spectral density (blue curve) and power spectral density + 1 S.D. of sub-series spectral densities (black curve).

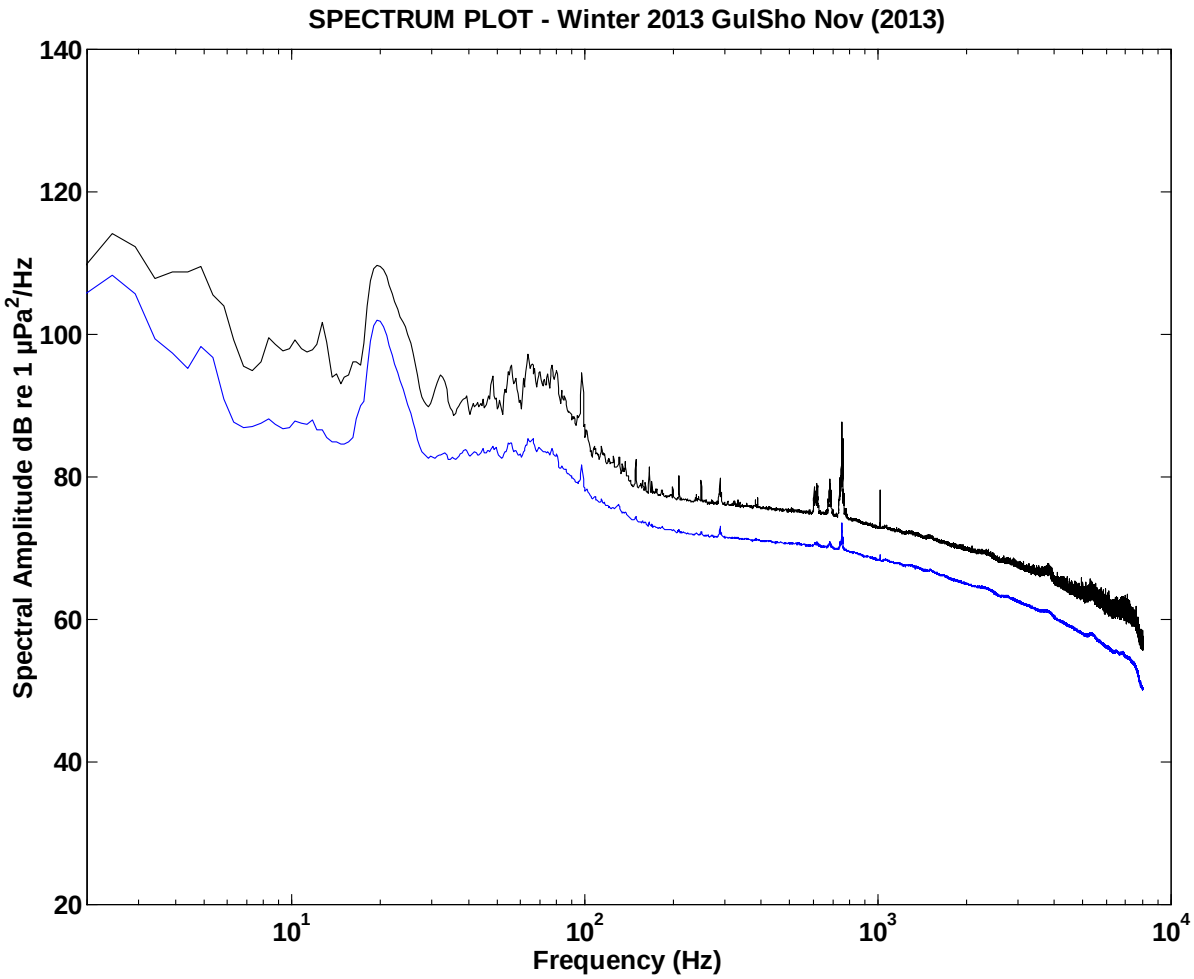


**Figure A4-1-GulSho-2013-Nov.** Plot of high resolution power spectral density (blue curve) and power spectral density + 1 S.D. of sub-series spectral densities (black curve).

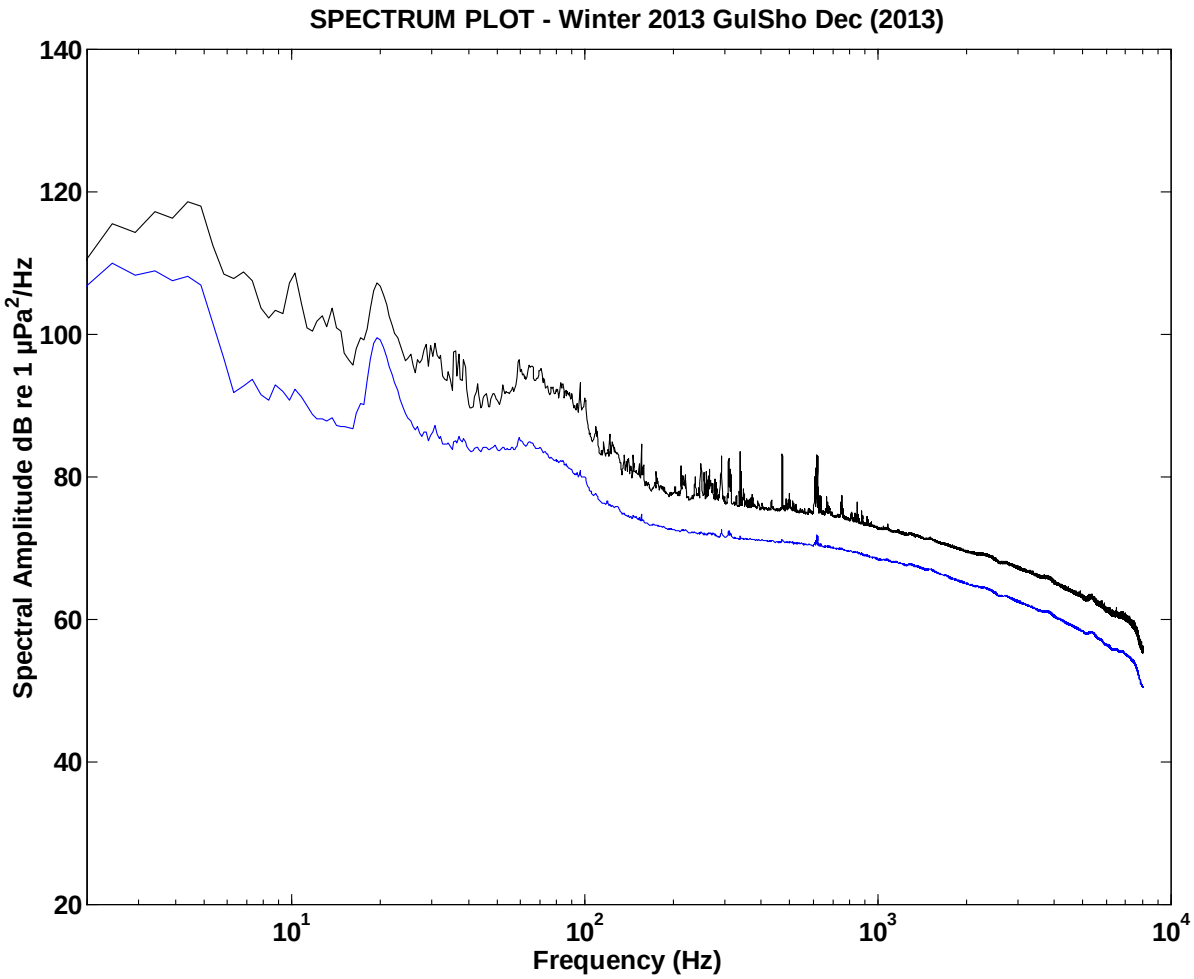


**Figure A4-1-GulSho-2013-Dec.** Plot of high resolution power spectral density (blue curve) and power spectral density + 1 S.D. of sub-series spectral densities (black curve).

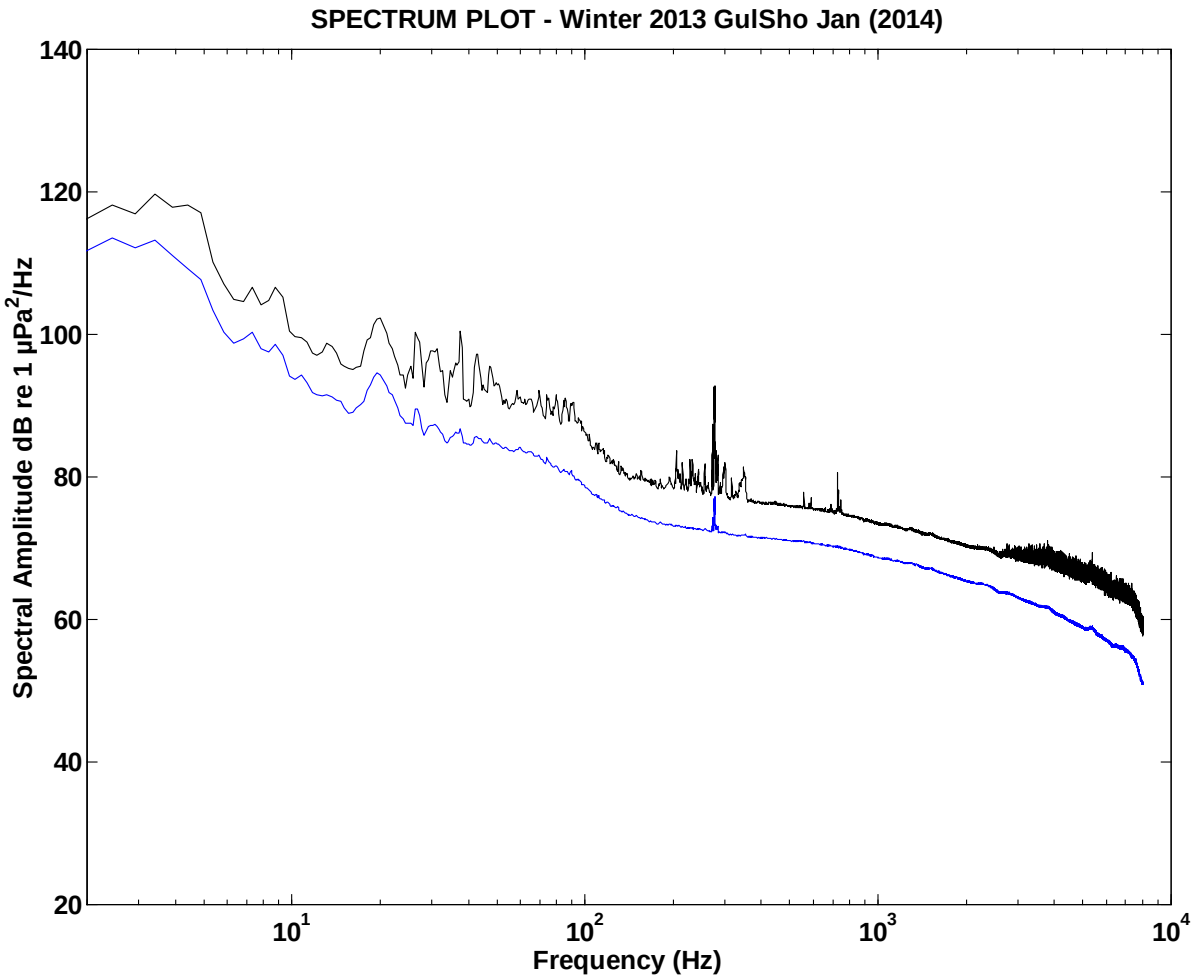


**Figure A4-1-GulSho-2014-Jan.** Plot of high resolution power spectral density (blue curve) and power spectral density + 1 S.D. of sub-series spectral densities (black curve).

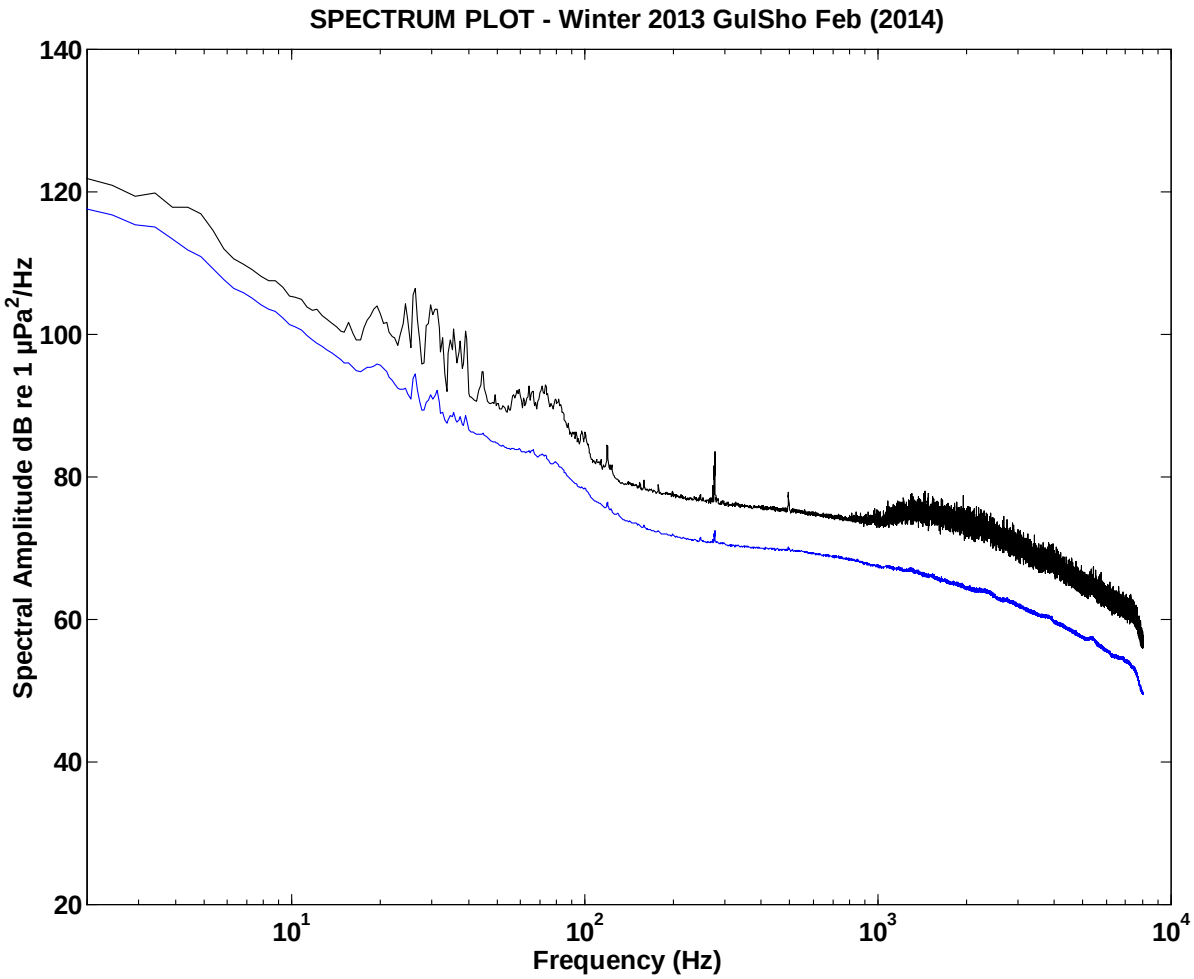


**Figure A4-1-GulSho-2014-Feb.** Plot of high resolution power spectral density (blue curve) and power spectral density + 1 S.D. of sub-series spectral densities (black curve).

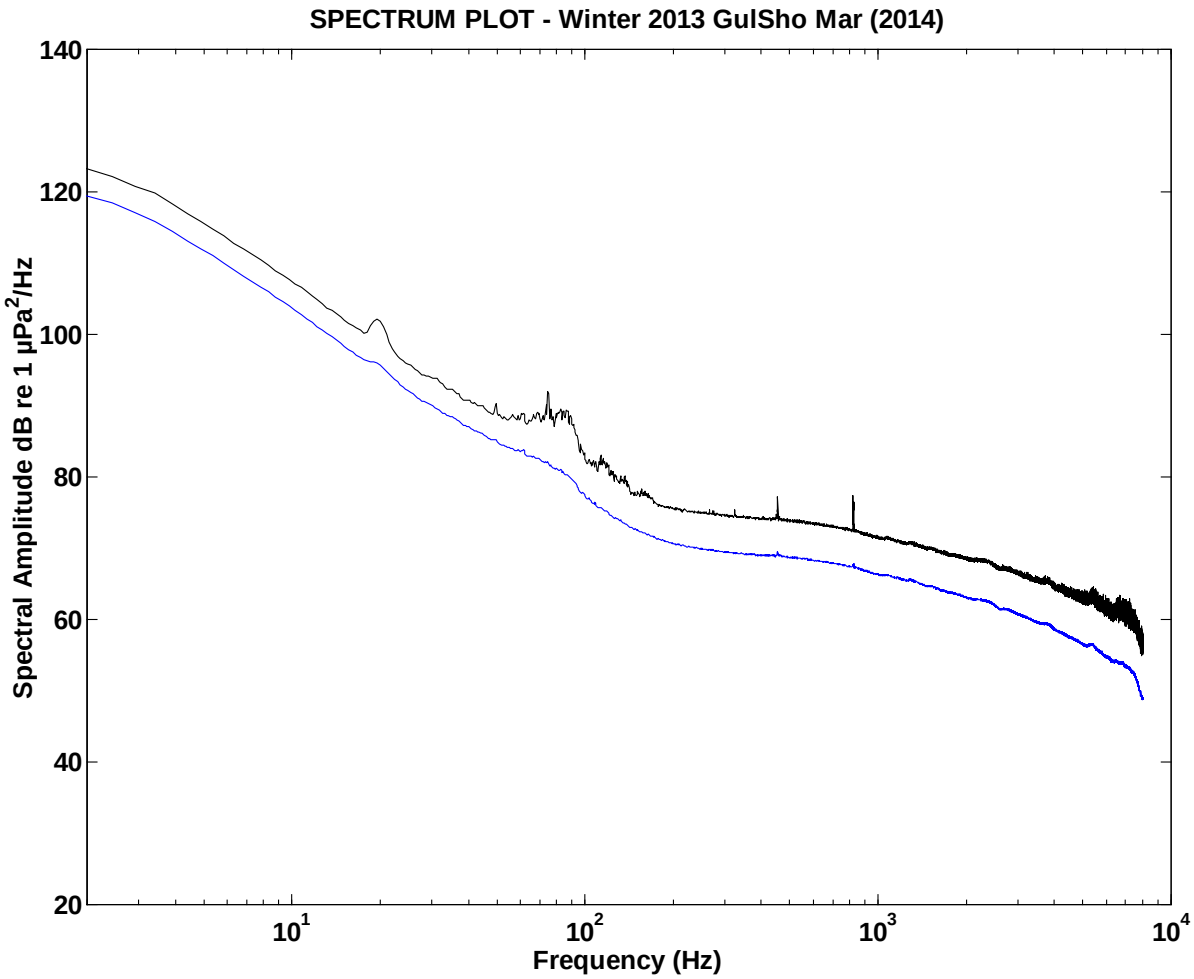


**Figure A4-1-GulSho-2014-Mar.** Plot of high resolution power spectral density (blue curve) and power spectral density + 1 S.D. of sub-series spectral densities (black curve).

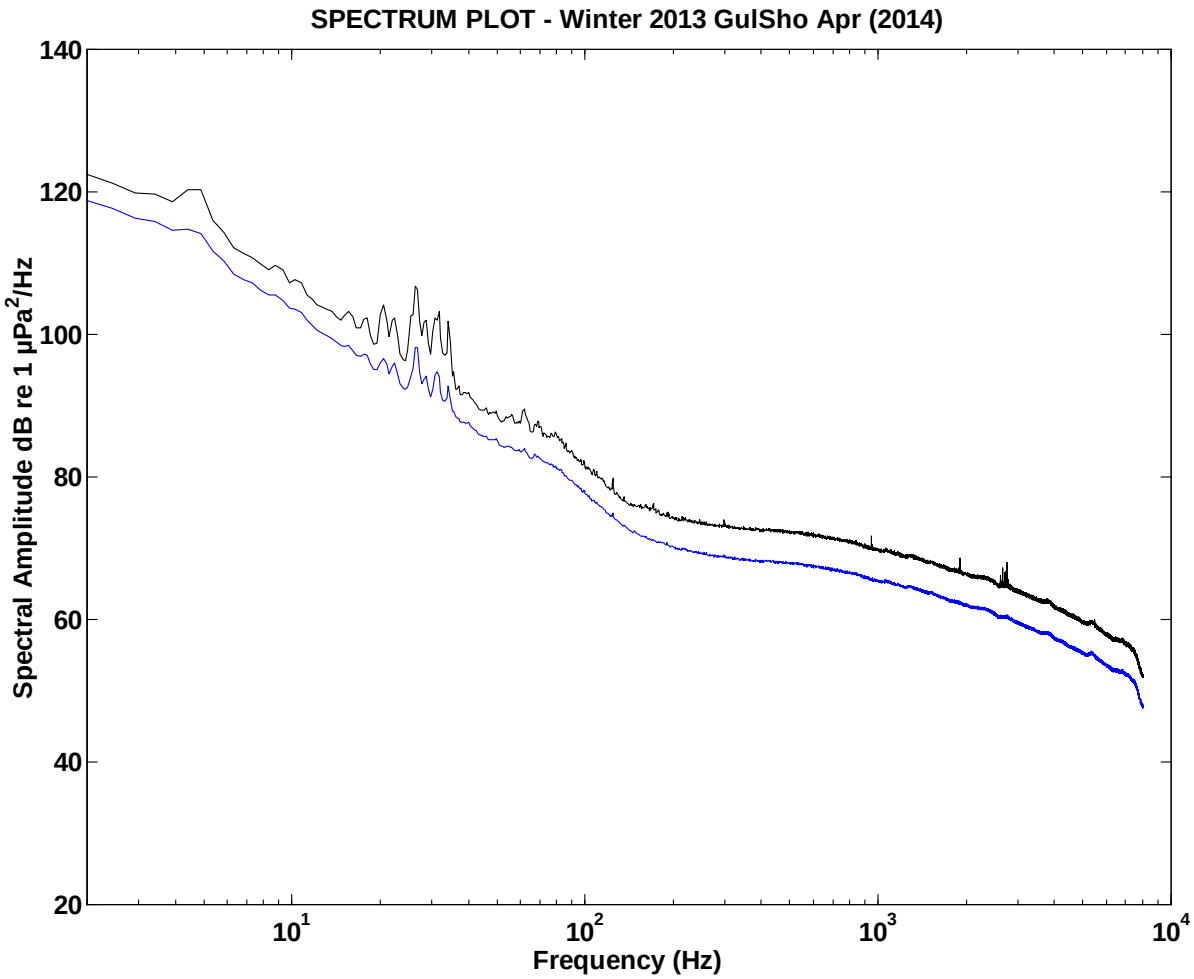


**Figure A4-1-GulSho-2014-Apr.** Plot of high resolution power spectral density (blue curve) and power spectral density + 1 S.D. of sub-series spectral densities (black curve).

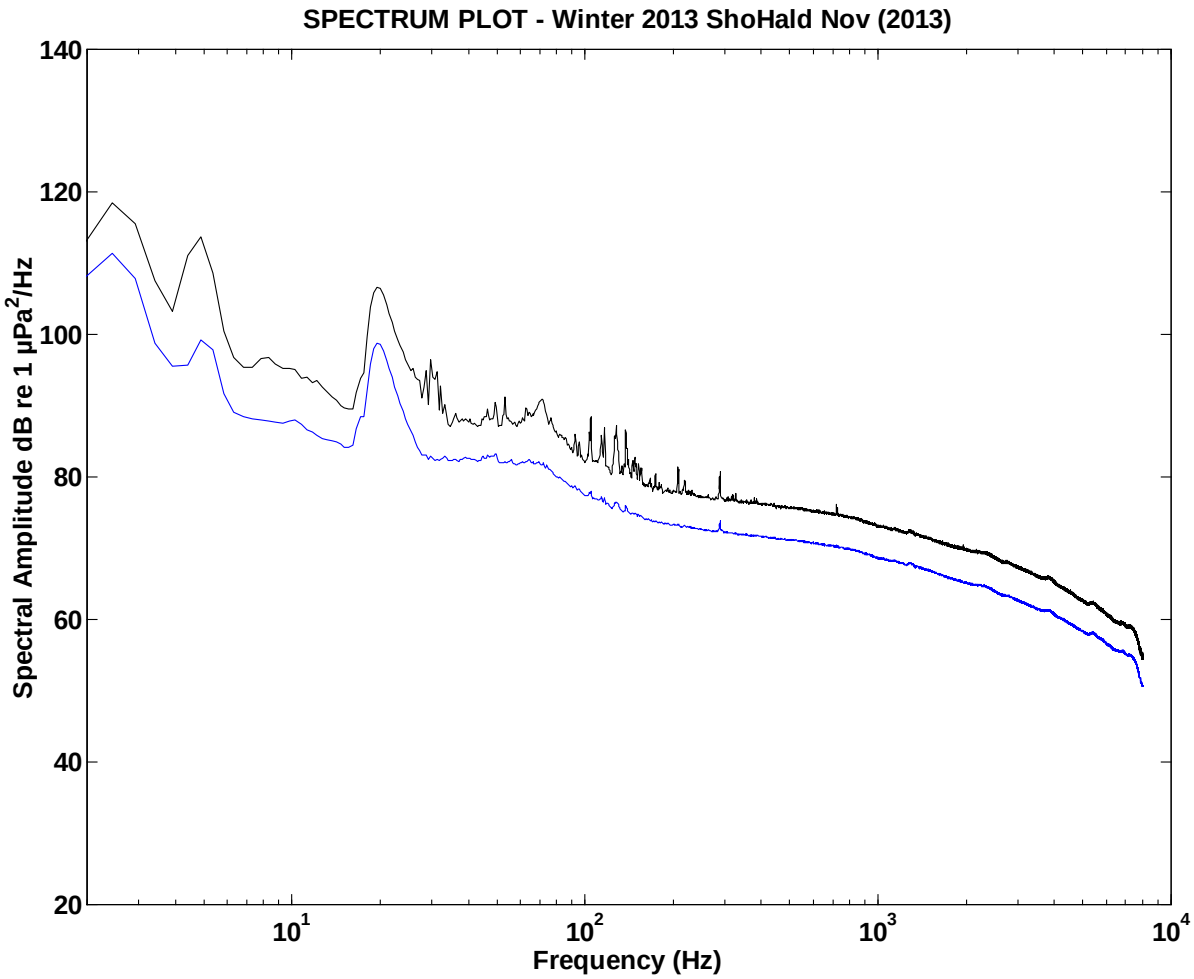


**Figure A4-1-ShoHald-2013-Nov.** Plot of high resolution power spectral density (blue curve) and power spectral density + 1 S.D. of sub-series spectral densities (black curve).

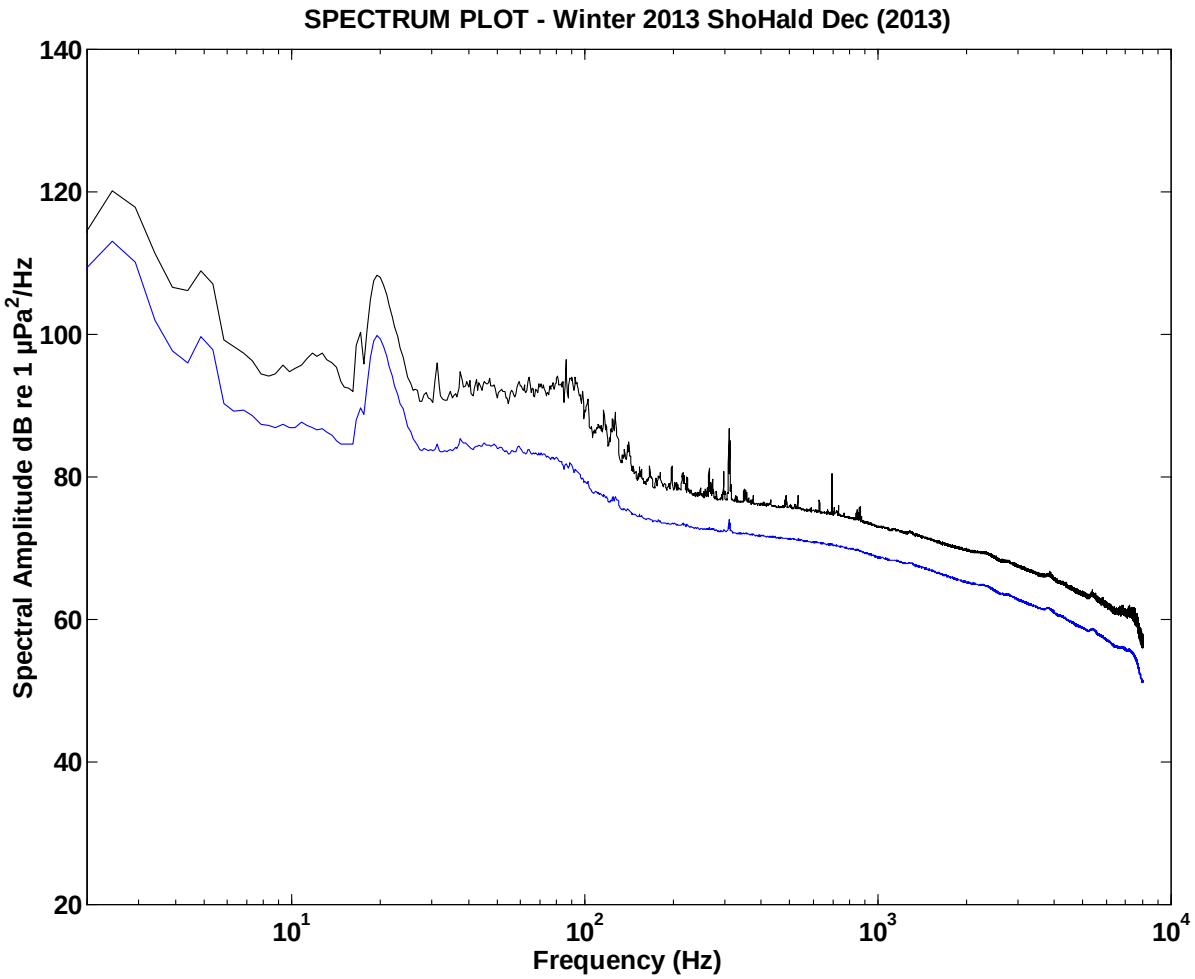


**Figure A4-1-ShoHald-2013-Dec.** Plot of high resolution power spectral density (blue curve) and power spectral density + 1 S.D. of sub-series spectral densities (black curve).

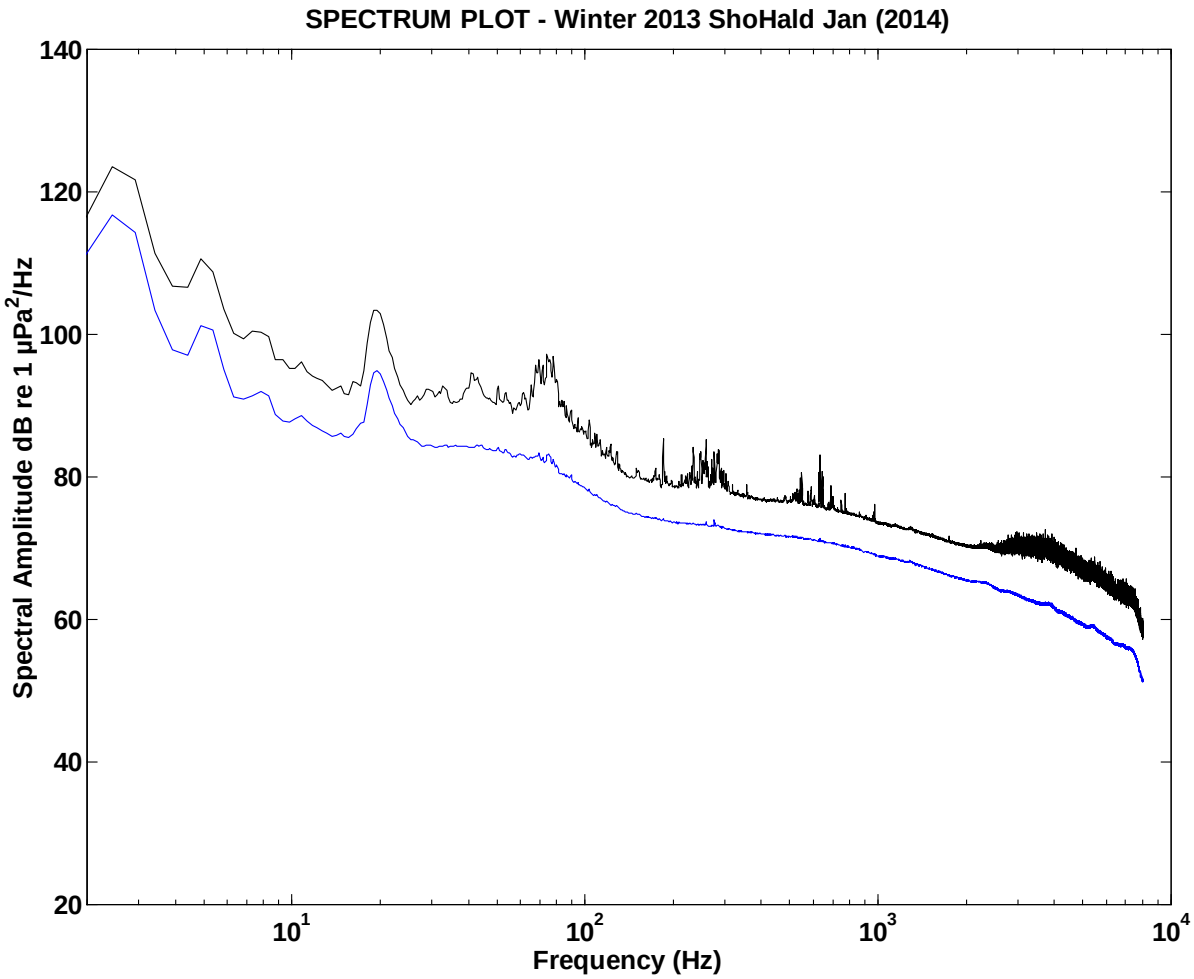


**Figure A4-1-ShoHald-2014-Jan.** Plot of high resolution power spectral density (blue curve) and power spectral density + 1 S.D. of sub-series spectral densities (black curve).

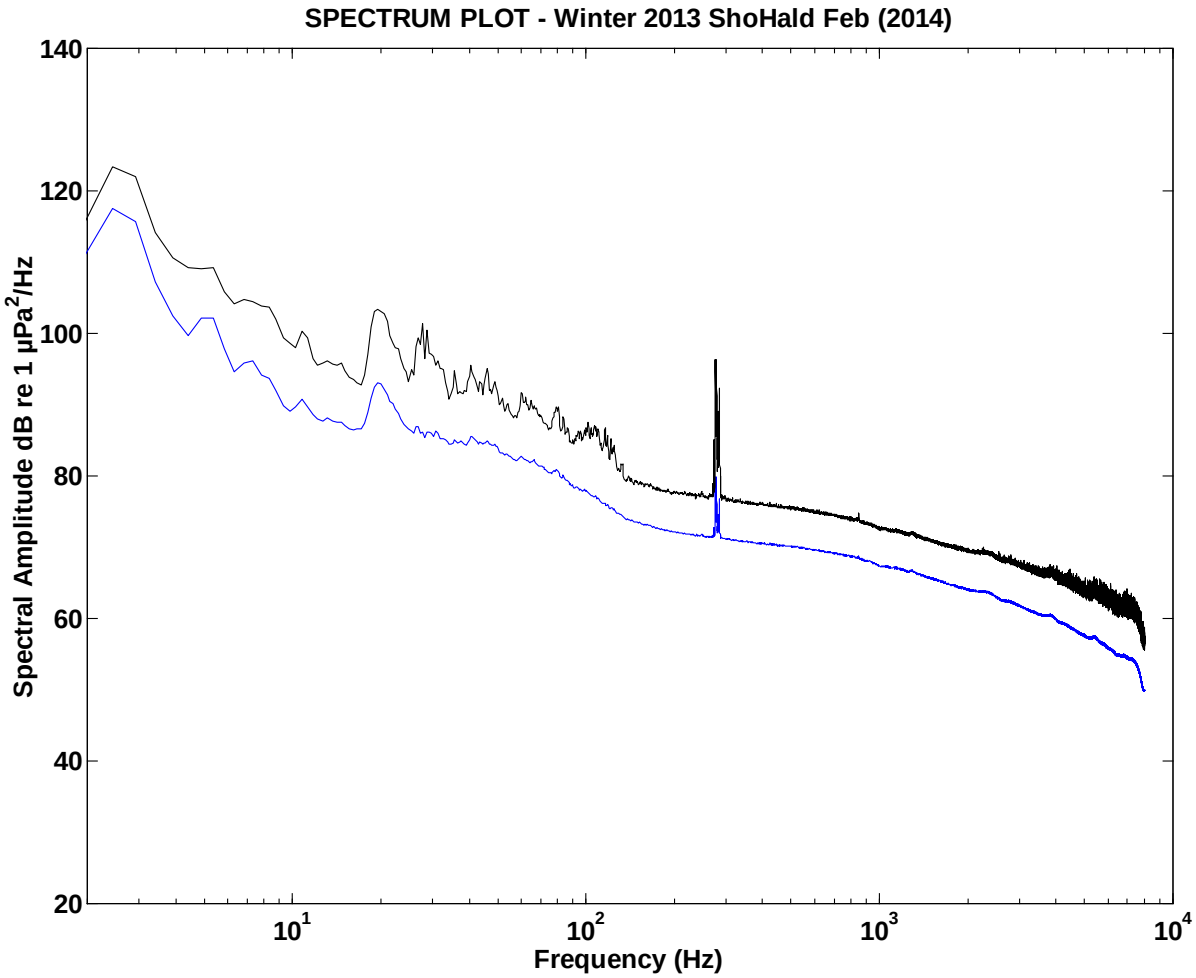


**Figure A4-1-ShoHald-2014-Feb.** Plot of high resolution power spectral density (blue curve) and power spectral density + 1 S.D. of sub-series spectral densities (black curve).

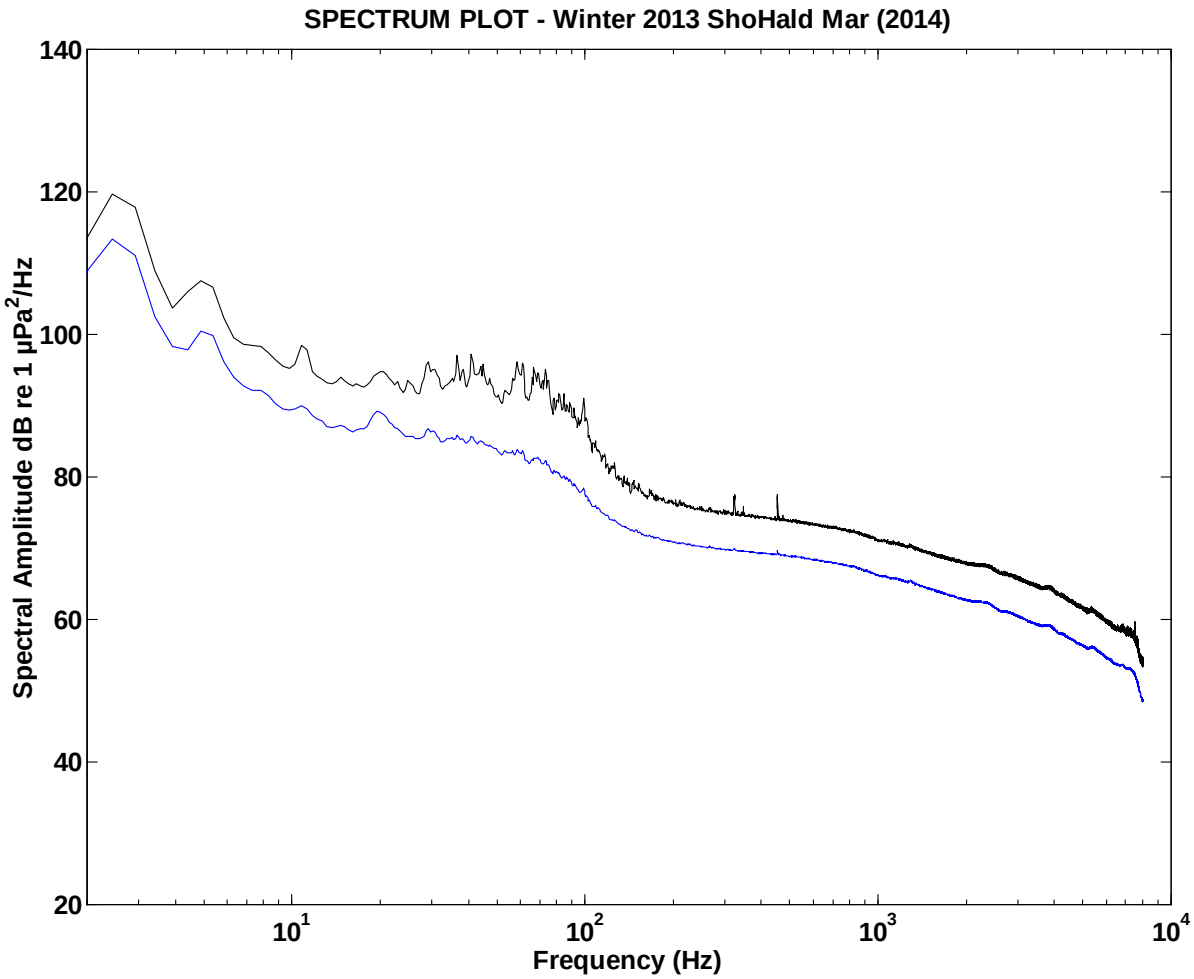


**Figure A4-1-ShoHald-2014-Mar.** Plot of high resolution power spectral density (blue curve) and power spectral density + 1 S.D. of sub-series spectral densities (black curve).

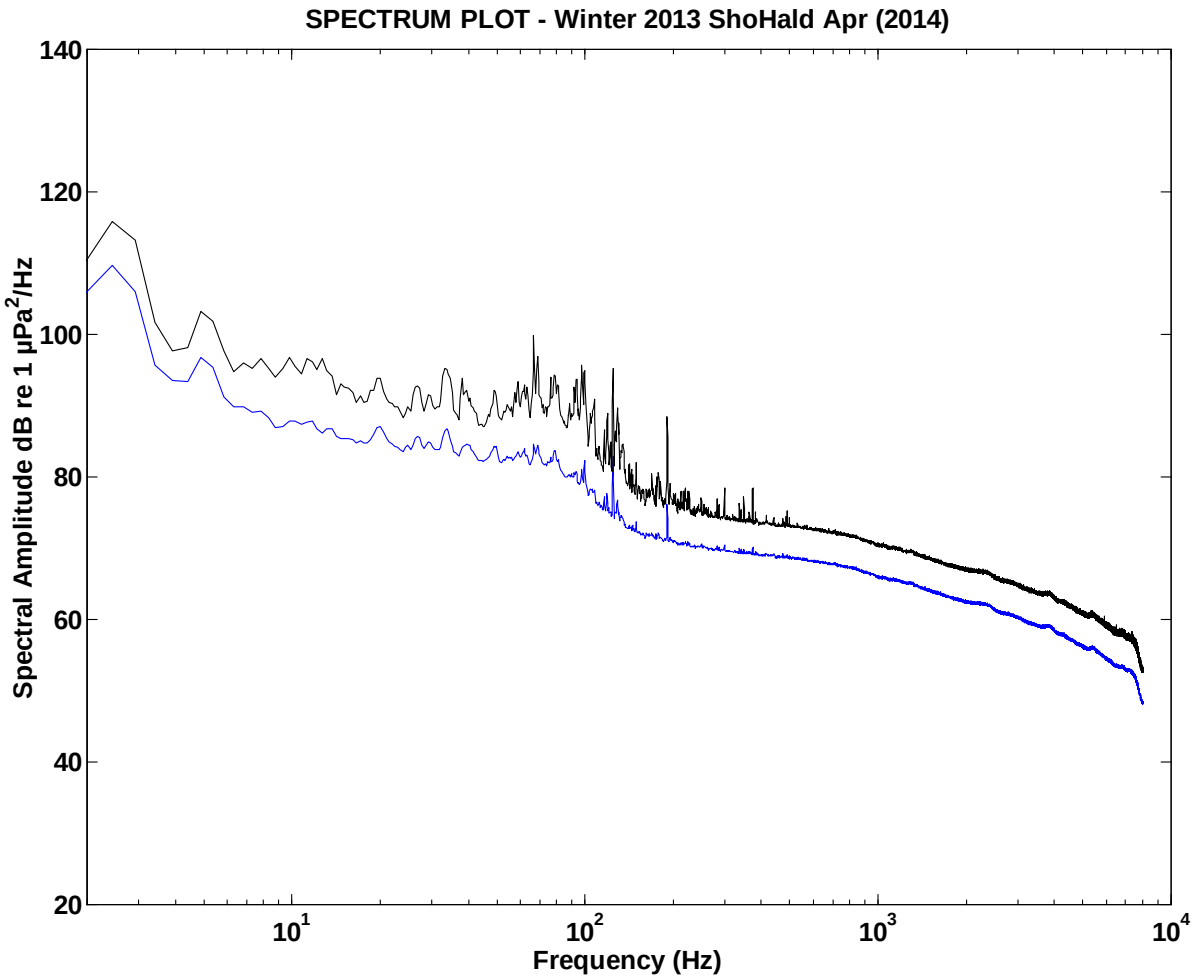


**Figure A4-1-ShoHald-2014-Apr.** Plot of high resolution power spectral density (blue curve) and power spectral density + 1 S.D. of sub-series spectral densities (black curve).

### *A4.1.4. Summer 2014 Deployments*

**Figure (series) A4-1-Summer 2014 Deployments** - Plots of high resolution power spectral density and power spectral density + 1 standard deviation (S.D.) of sub-series spectral densities.

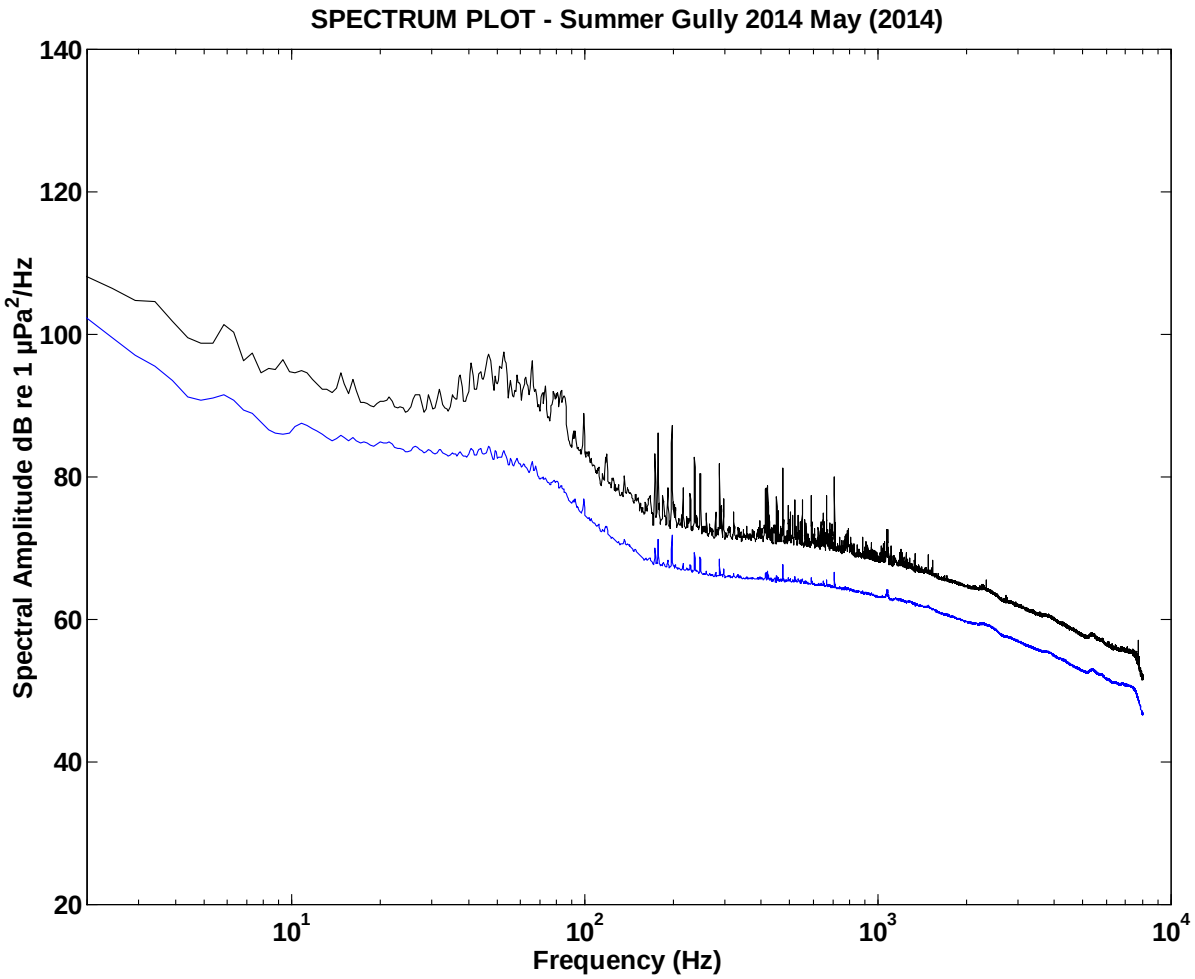


**Figure A4-1-MidGul-2014-May.** Plot of high resolution power spectral density (blue curve) and power spectral density + 1 S.D. of sub-series spectral densities (black curve).

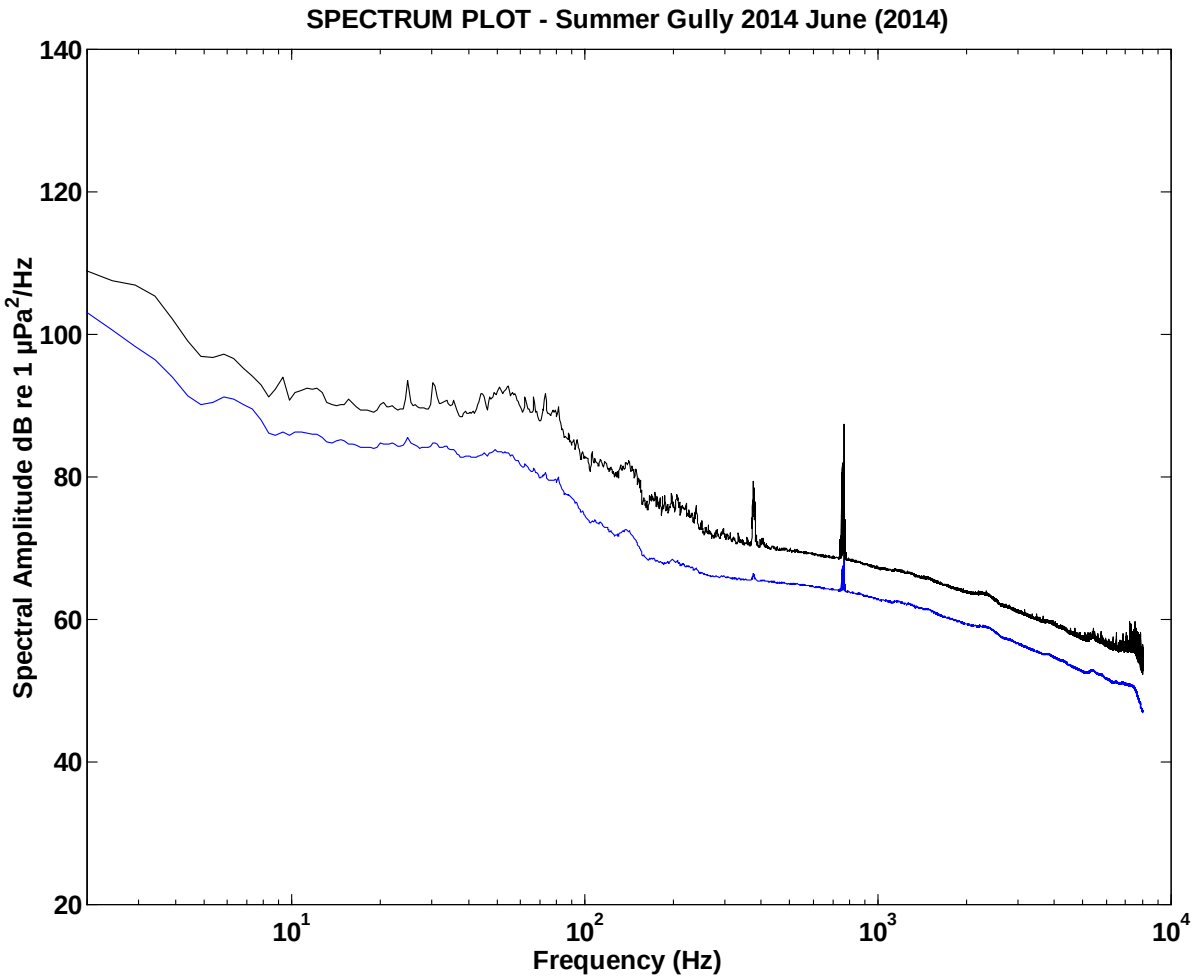


**Figure A4-1-MidGul-2014-Jun.** Plot of high resolution power spectral density (blue curve) and power spectral density + 1 S.D. of sub-series spectral densities (black curve).

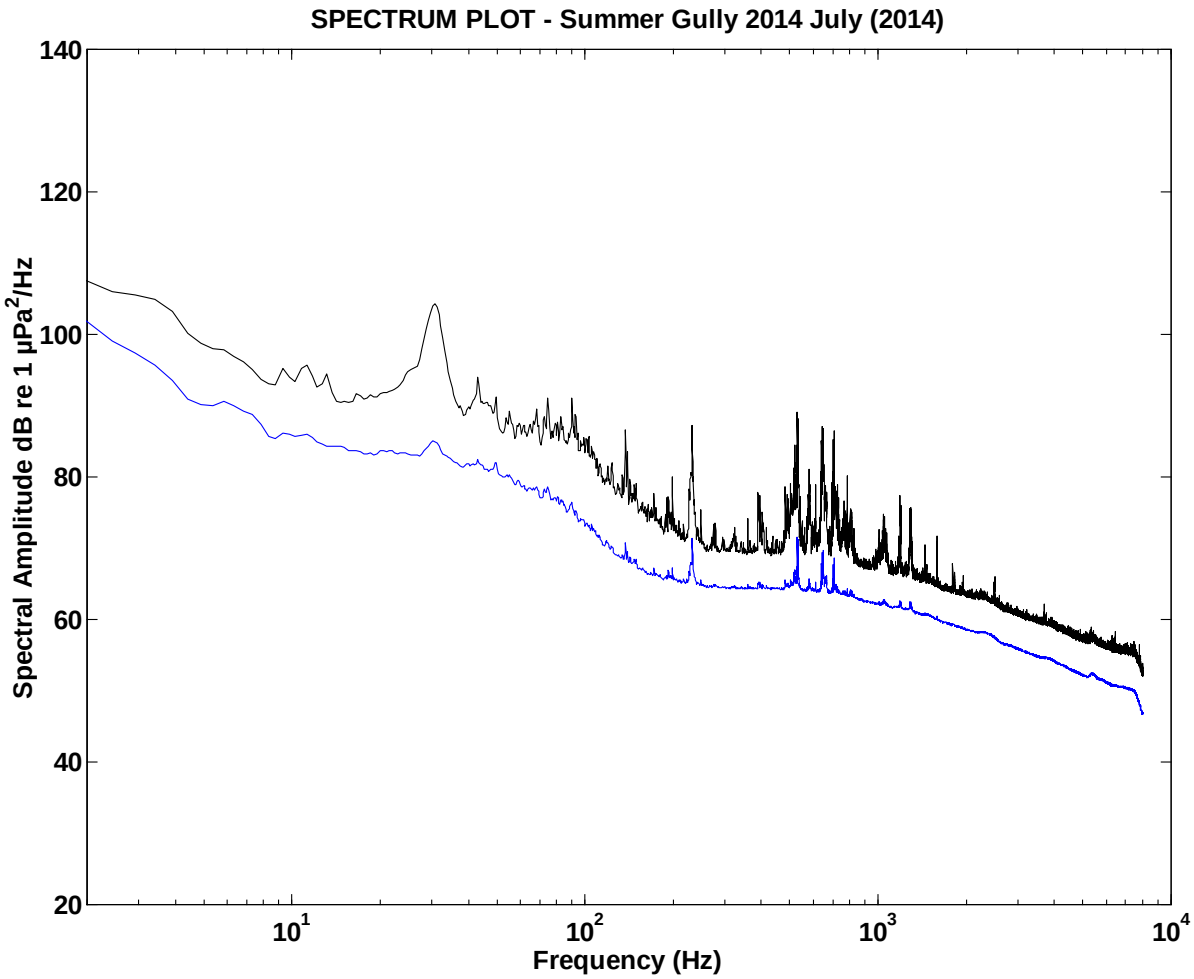


**Figure A4-1-MidGul-2014-Jul.** Plot of high resolution power spectral density (blue curve) and power spectral density + 1 S.D. of sub-series spectral densities (black curve).

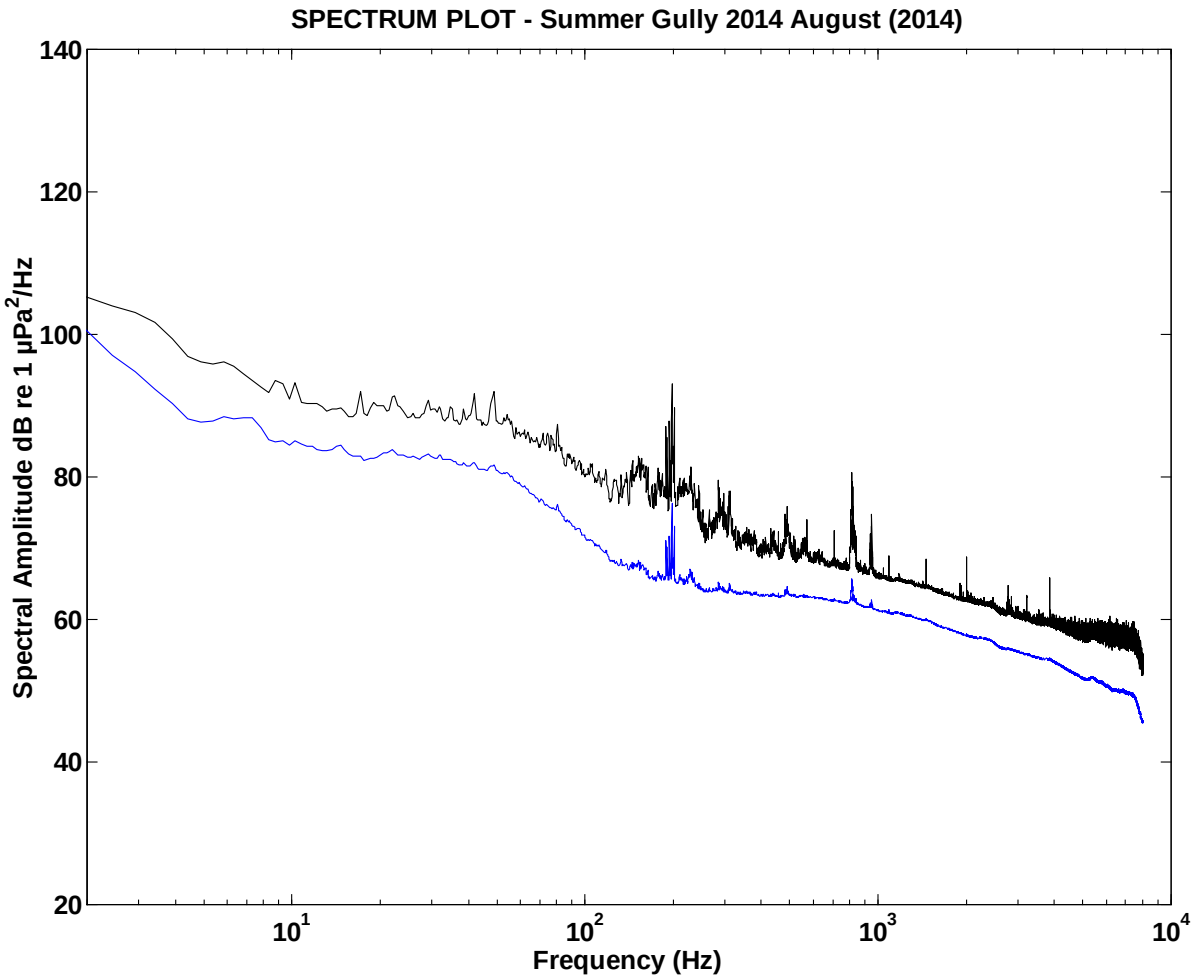


**Figure A4-1-MidGul-2014-Aug.** Plot of high resolution power spectral density (blue curve) and power spectral density + 1 S.D. of sub-series spectral densities (black curve).

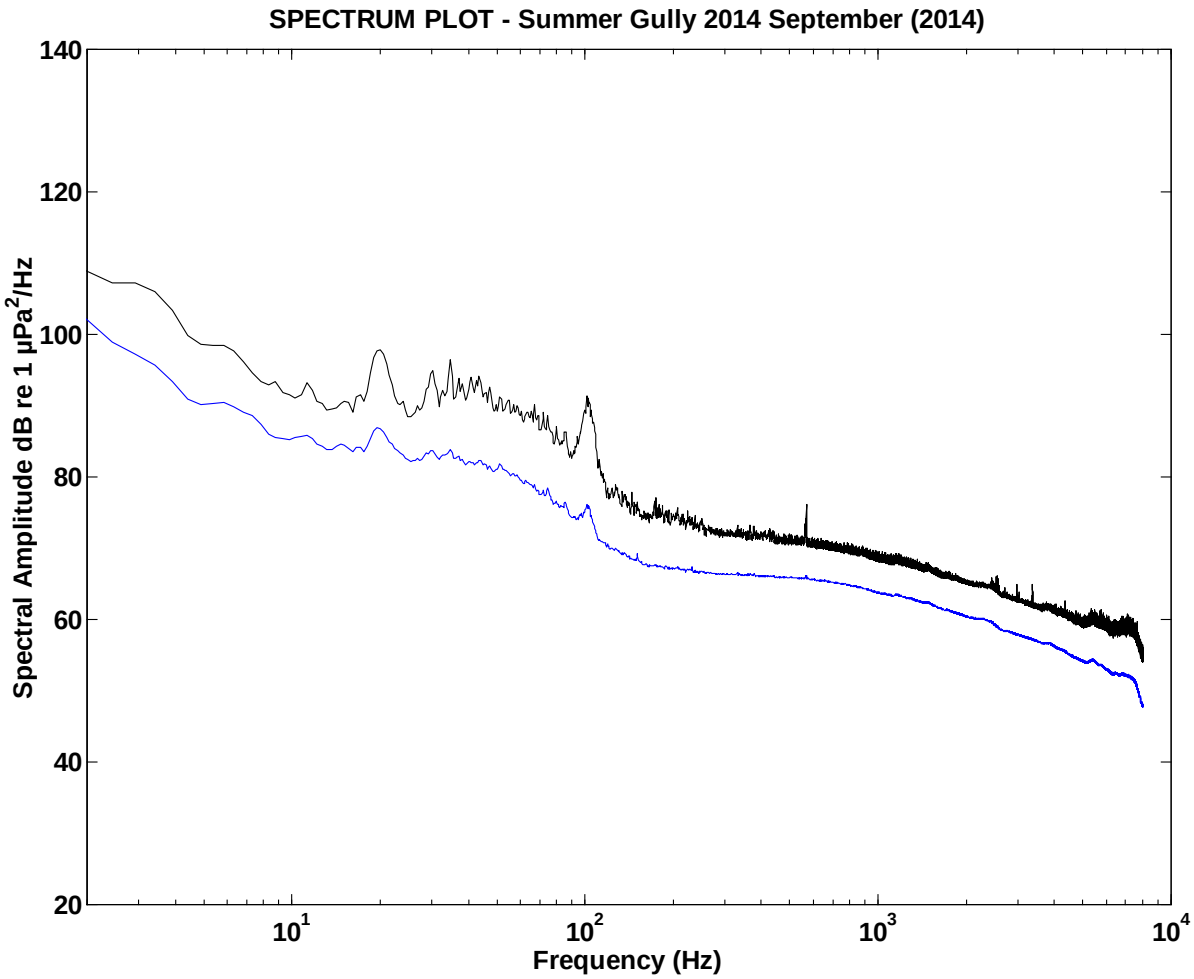


**Figure A4-1-MidGul-2014-Sep.** Plot of high resolution power spectral density (blue curve) and power spectral density + 1 S.D. of sub-series spectral densities (black curve).

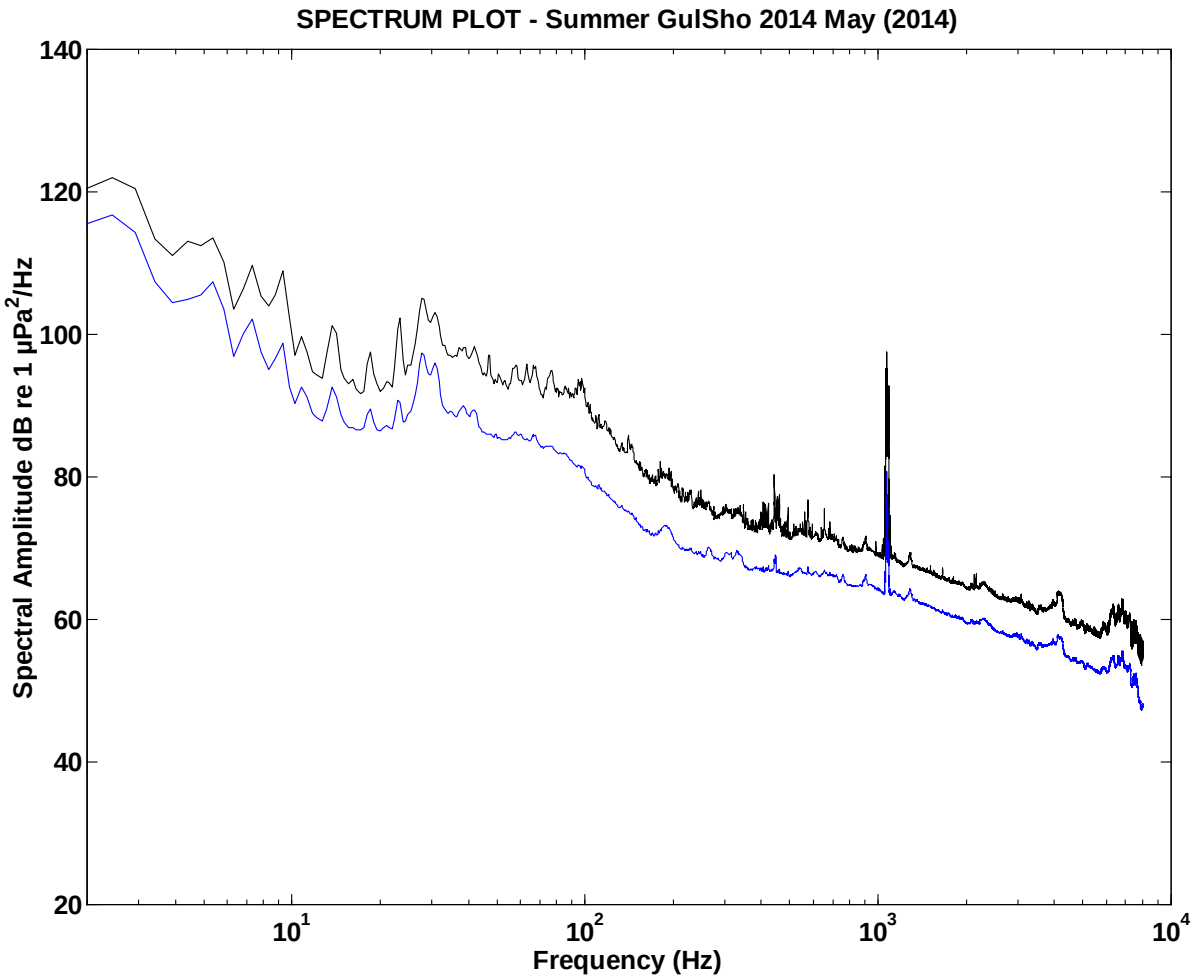


**Figure A4-1-GulSho-2014-May.** Plot of high resolution power spectral density (blue curve) and power spectral density + 1 S.D. of sub-series spectral densities (black curve).

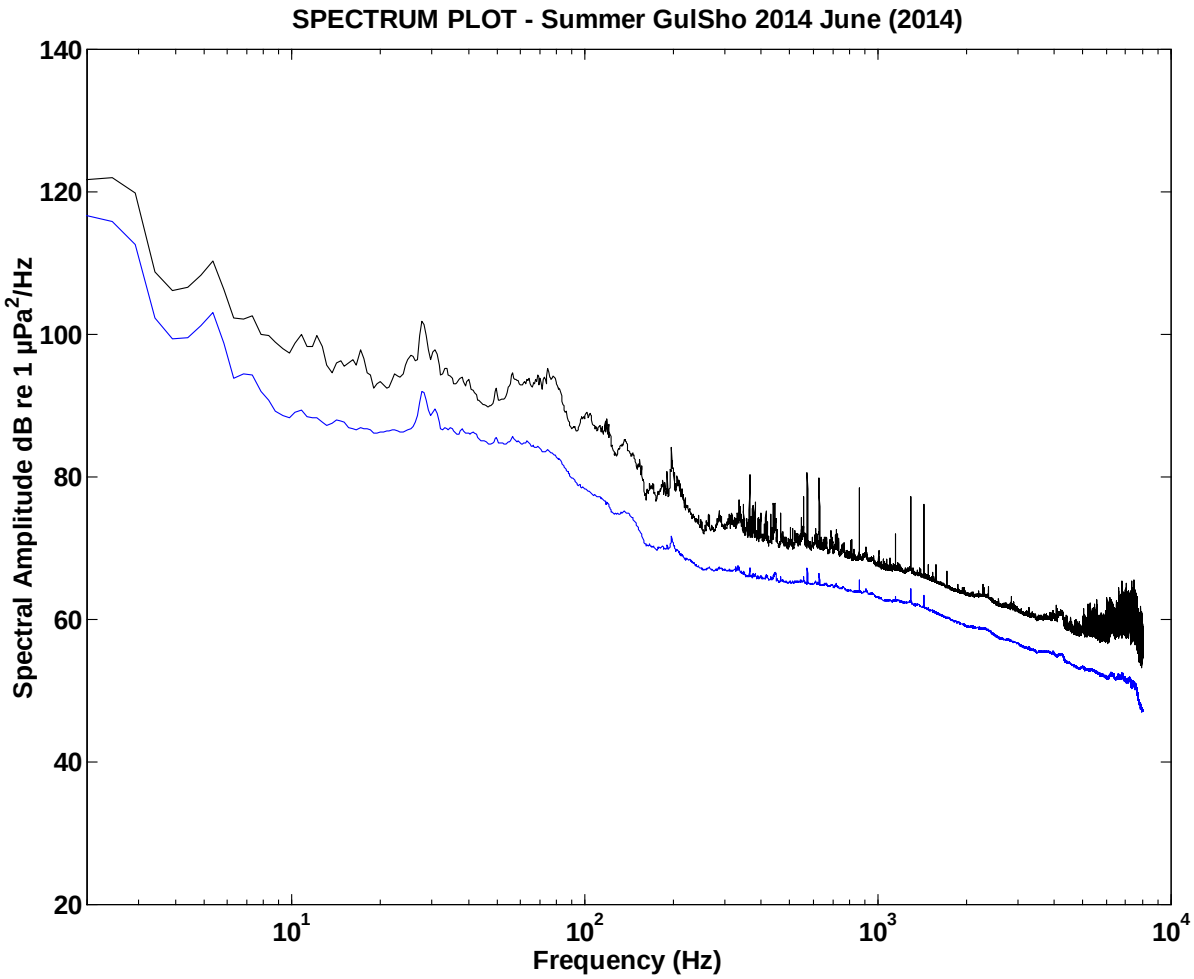


**Figure A4-1-GulSho-2014-Jun.** Plot of high resolution power spectral density (blue curve) and power spectral density + 1 S.D. of sub-series spectral densities (black curve).

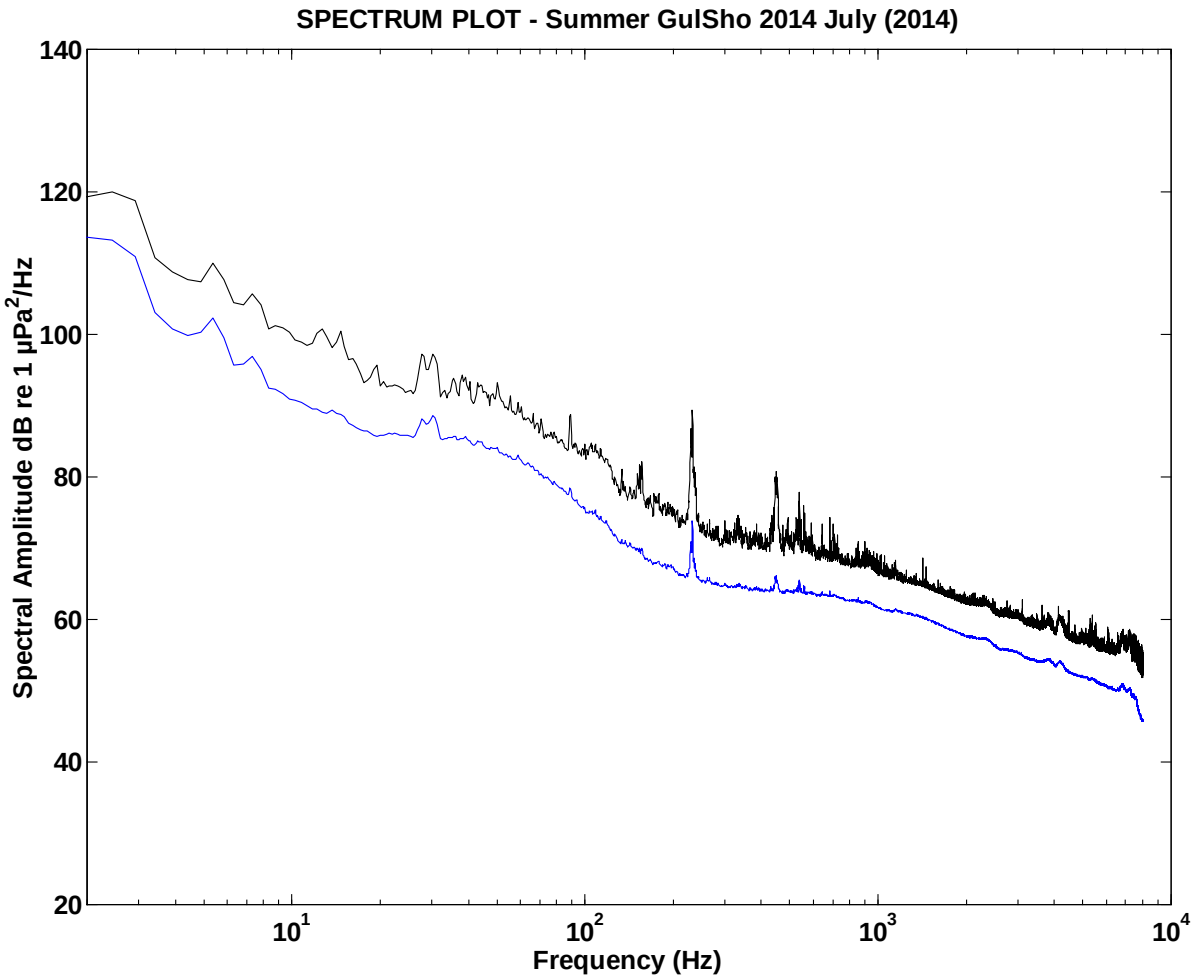


**Figure A4-1-GulSho-2014-Jul.** Plot of high resolution power spectral density (blue curve) and power spectral density + 1 S.D. of sub-series spectral densities (black curve).

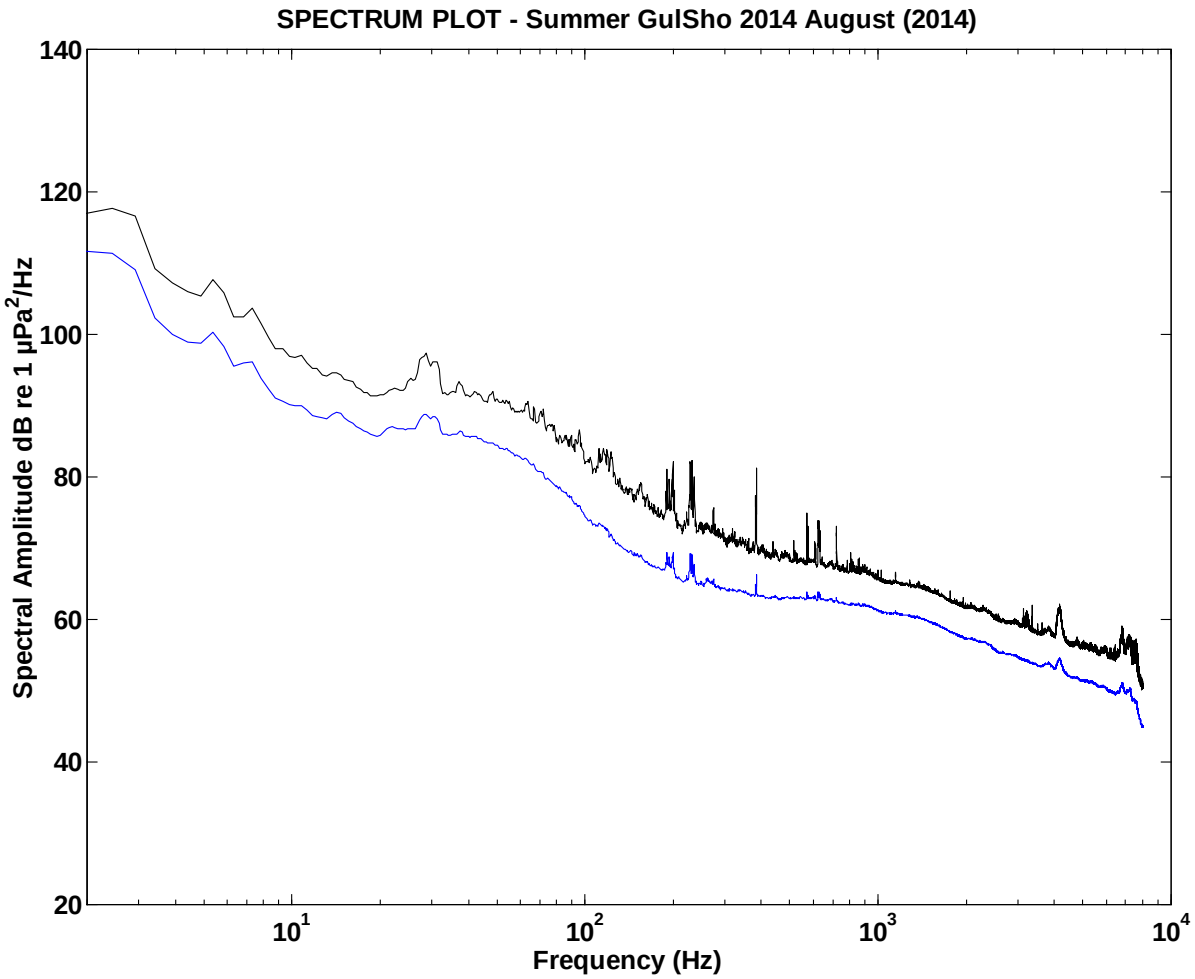


**Figure A4-1-GulSho-2014-Aug.** Plot of high resolution power spectral density (blue curve) and power spectral density + 1 S.D. of sub-series spectral densities (black curve).

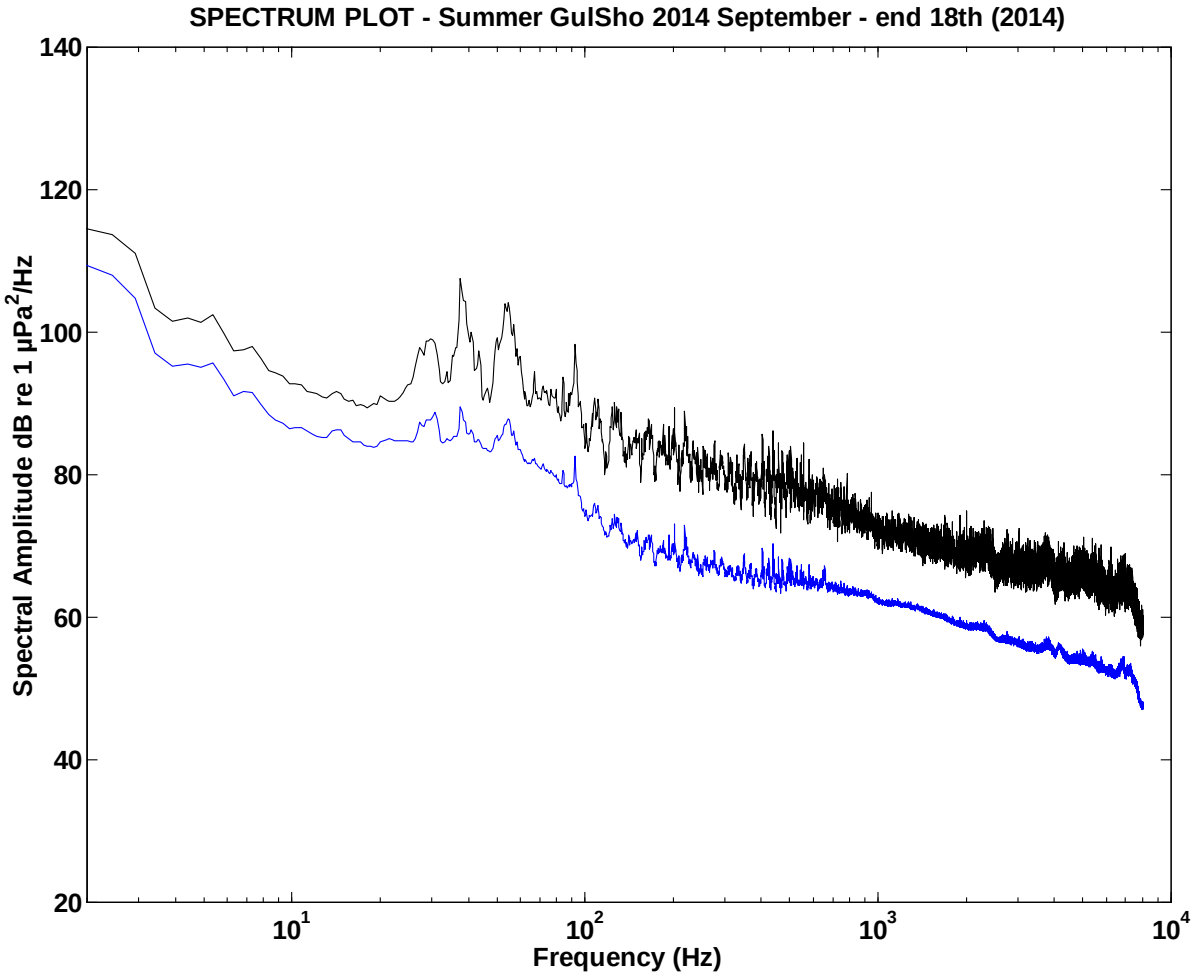


**Figure A4-1-GulSho-2014-Sep.** Plot of high resolution power spectral density (blue curve) and power spectral density + 1 S.D. of sub-series spectral densities (black curve). Data series truncated at end of Sept. 18th incl. because of equipment malfunction.

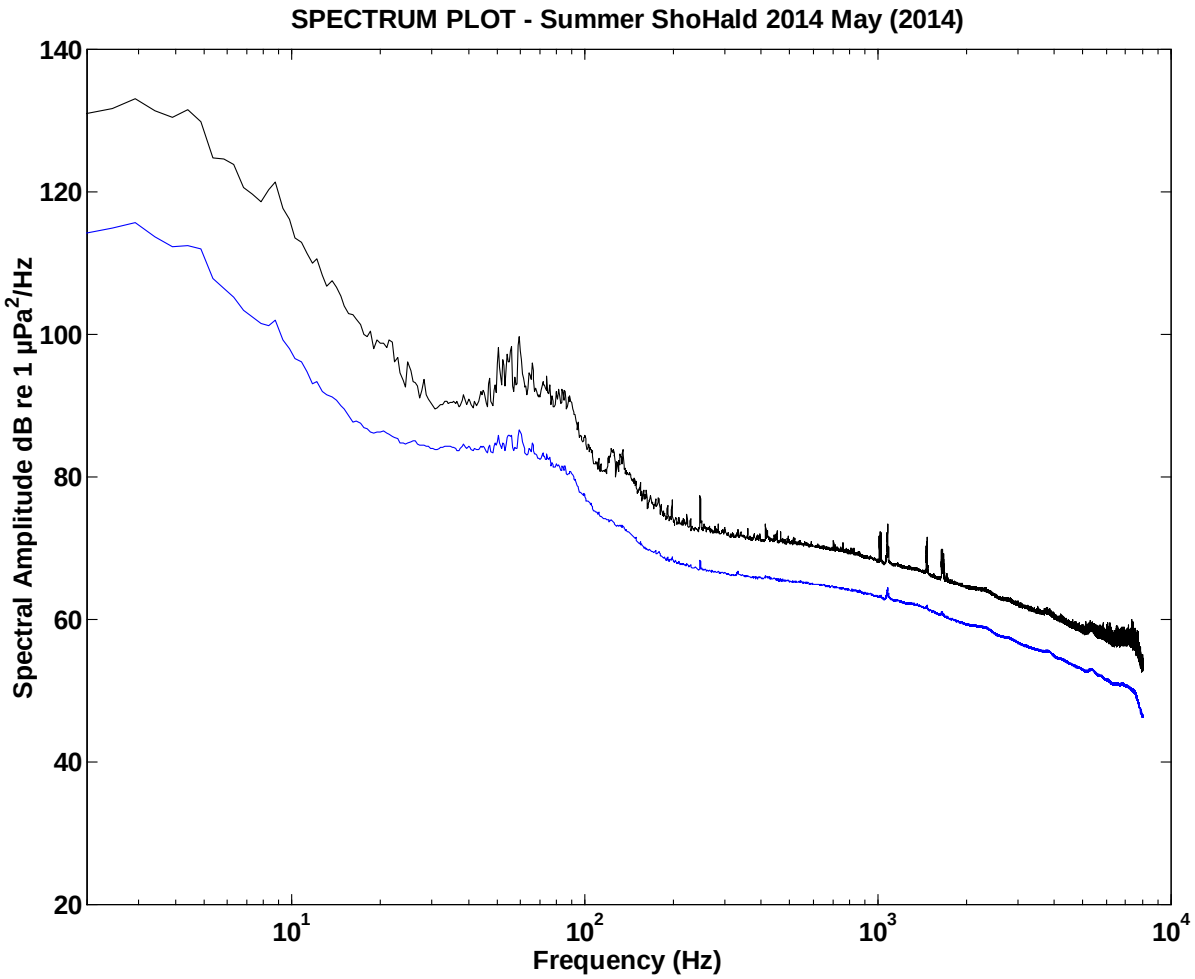


**Figure A4-1-ShoHald-2014-May.** Plot of high resolution power spectral density (blue curve) and power spectral density + 1 S.D. of sub-series spectral densities (black curve).

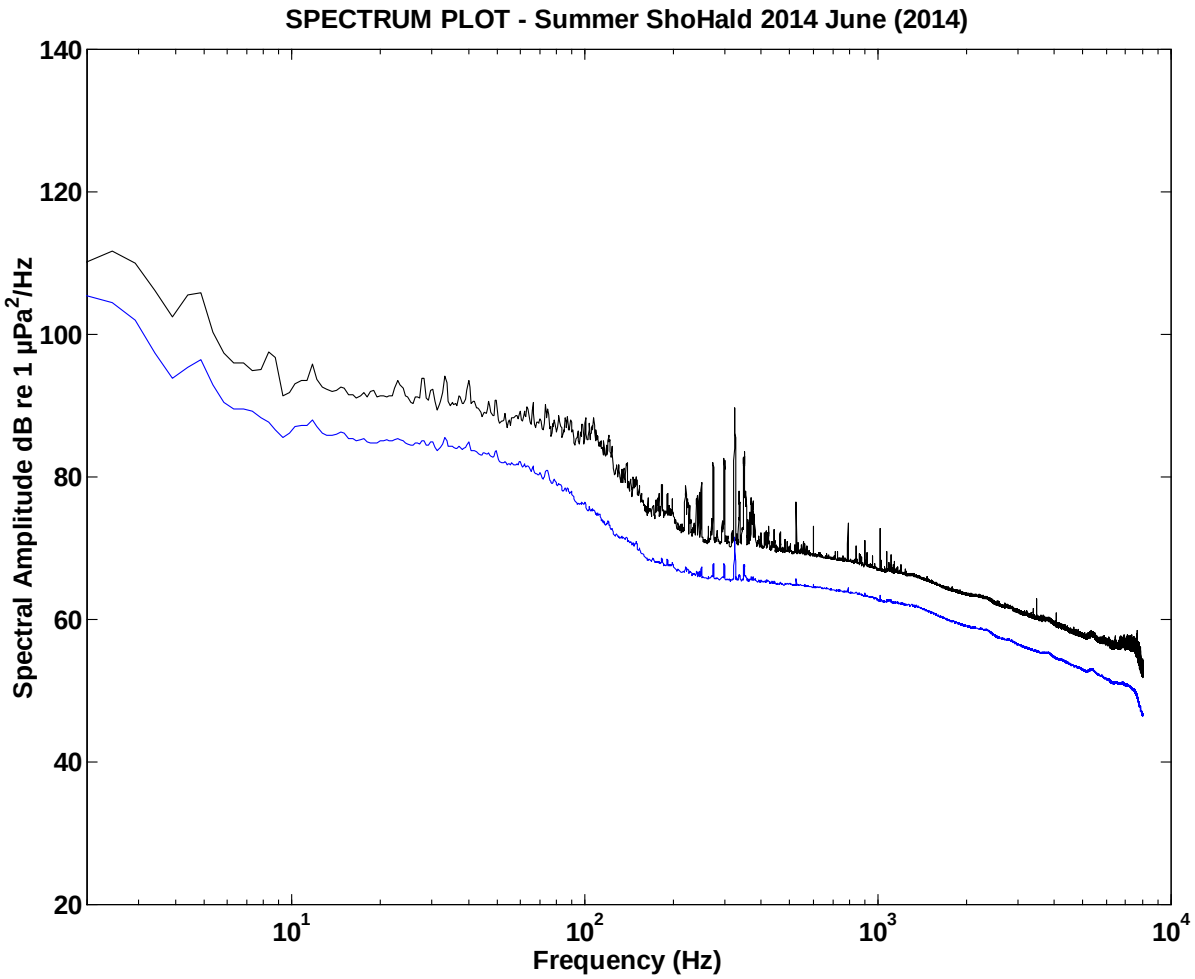


**Figure A4-1-ShoHald-2014-Jun.** Plot of high resolution power spectral density (blue curve) and power spectral density + 1 S.D. of sub-series spectral densities (black curve).

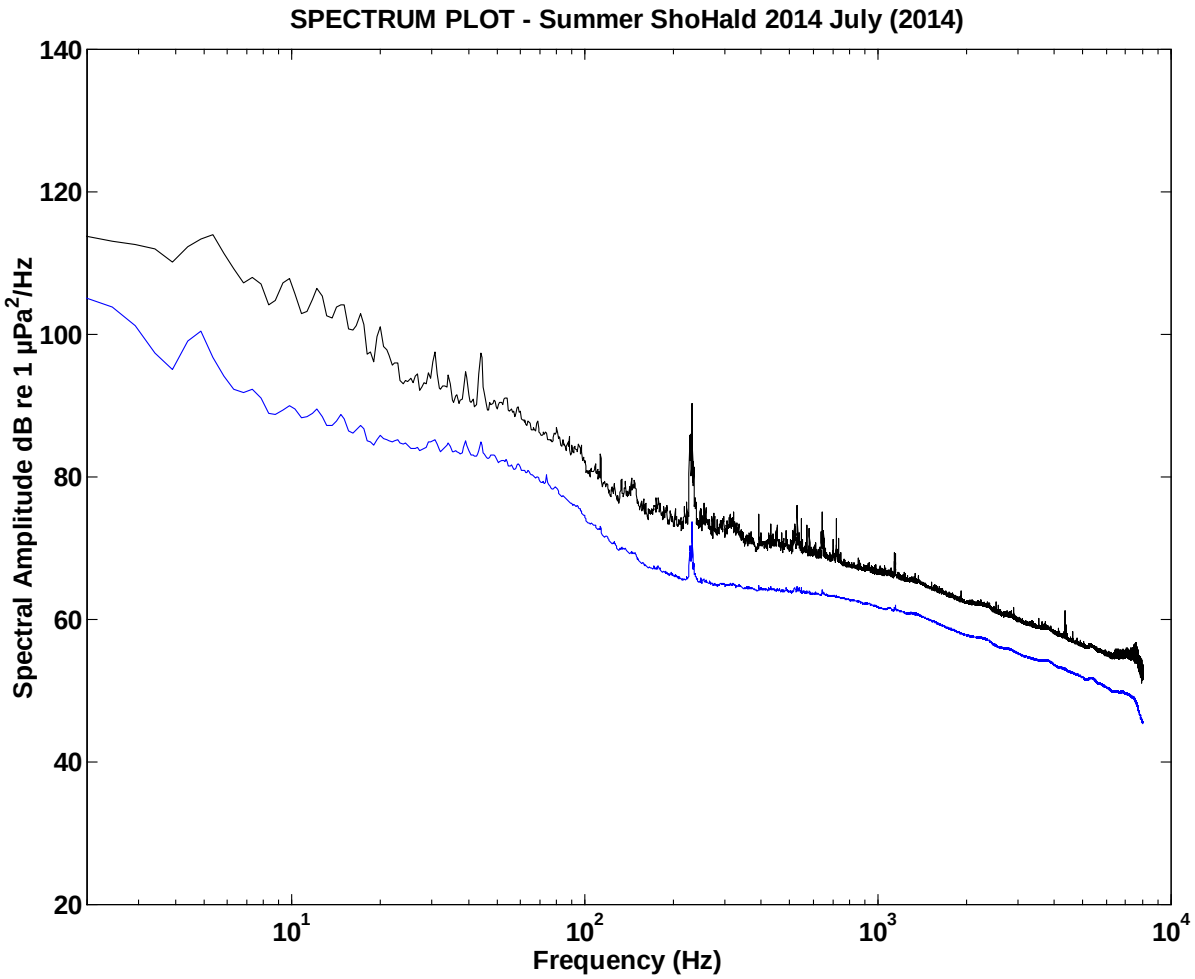


**Figure A4-1-ShoHald-2014-Jul.** Plot of high resolution power spectral density (blue curve) and power spectral density + 1 S.D. of sub-series spectral densities (black curve).

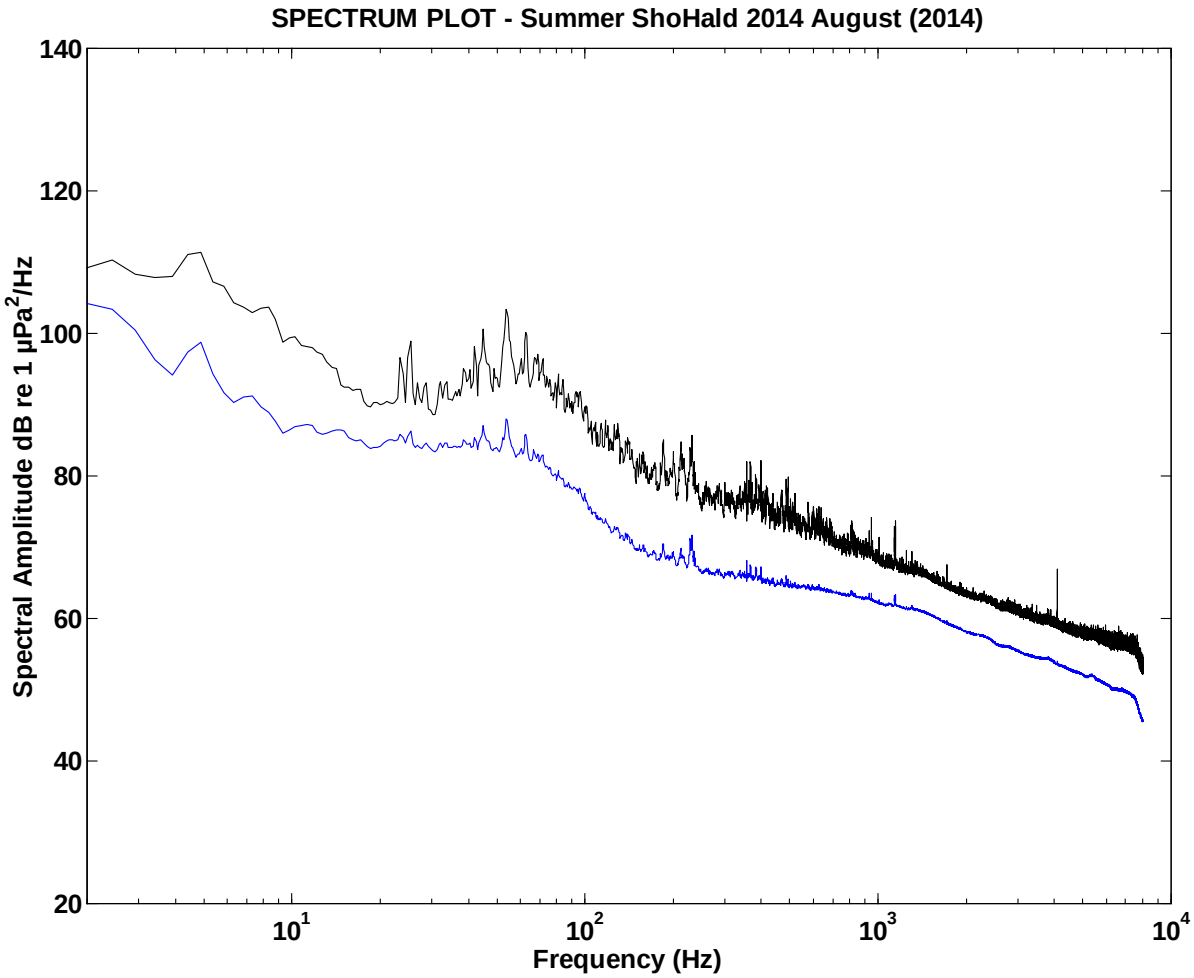


**Figure A4-1-ShoHald-2014-Aug.** Plot of high resolution power spectral density (blue curve) and power spectral density + 1 S.D. of sub-series spectral densities (black curve).

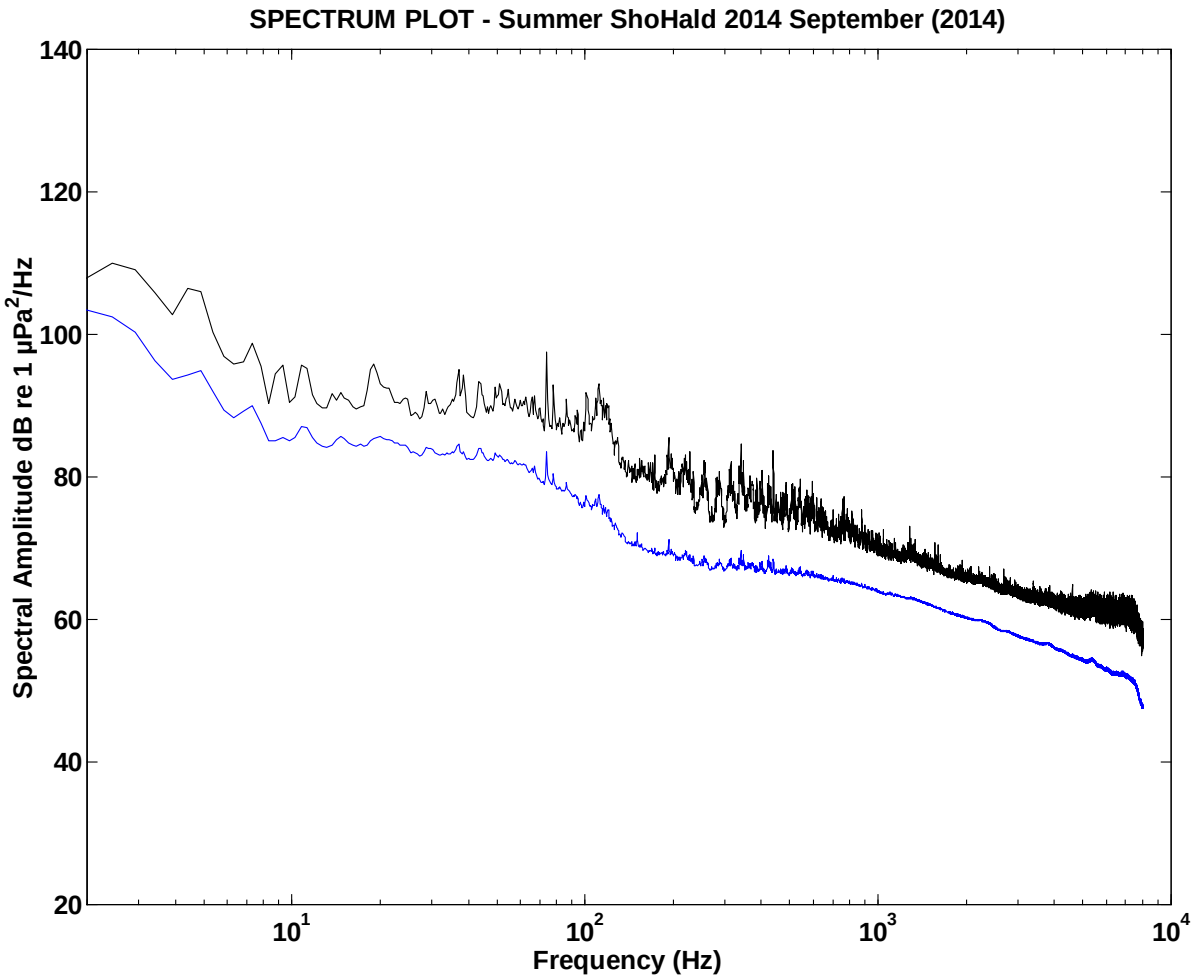


**Figure A4-1-ShoHald-2014-Sep.** Plot of high resolution power spectral density (blue curve) and power spectral density + 1 S.D. of sub-series spectral densities (black curve).

## A4.2. MEDIUM RESOLUTION SPECTRA WITH STATS

### *A4.2.1. Winter 2012-13 Deployments*

**Figure (series) A4-2-Winter 2012-13 Deployments** - Medium resolution power spectral density with stats: Standard power spectral density, cumulative percentile curves for spectral sub-estimates, and PDF distribution of spectral sub-estimates.

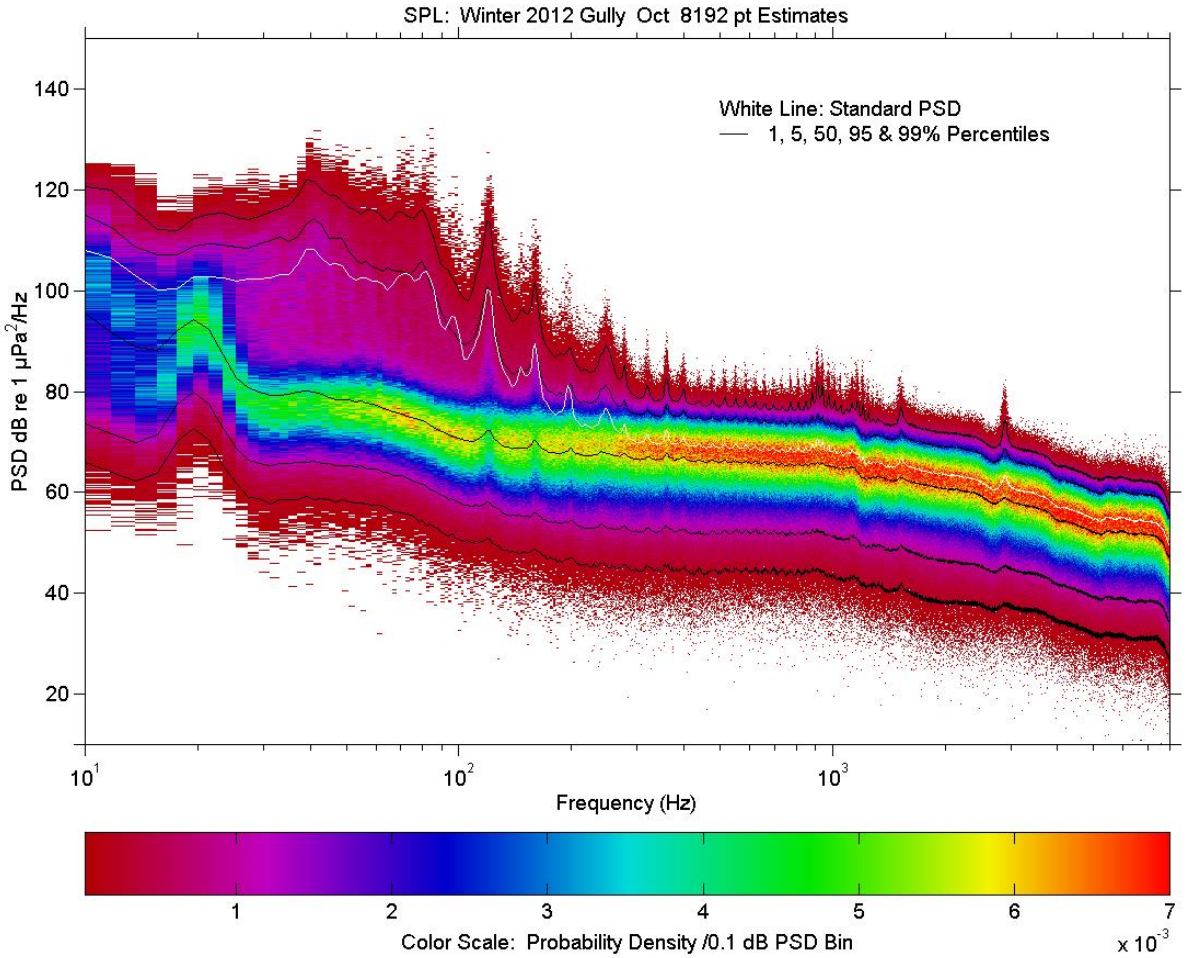


**Figure A4-2-MidGul-2012-Oct.** Medium resolution power spectral density with stats: Standard power spectral density (white), cumulative percentile curves for spectral sub-estimates (black), and PDF distribution of spectral sub-estimates (solid colour).

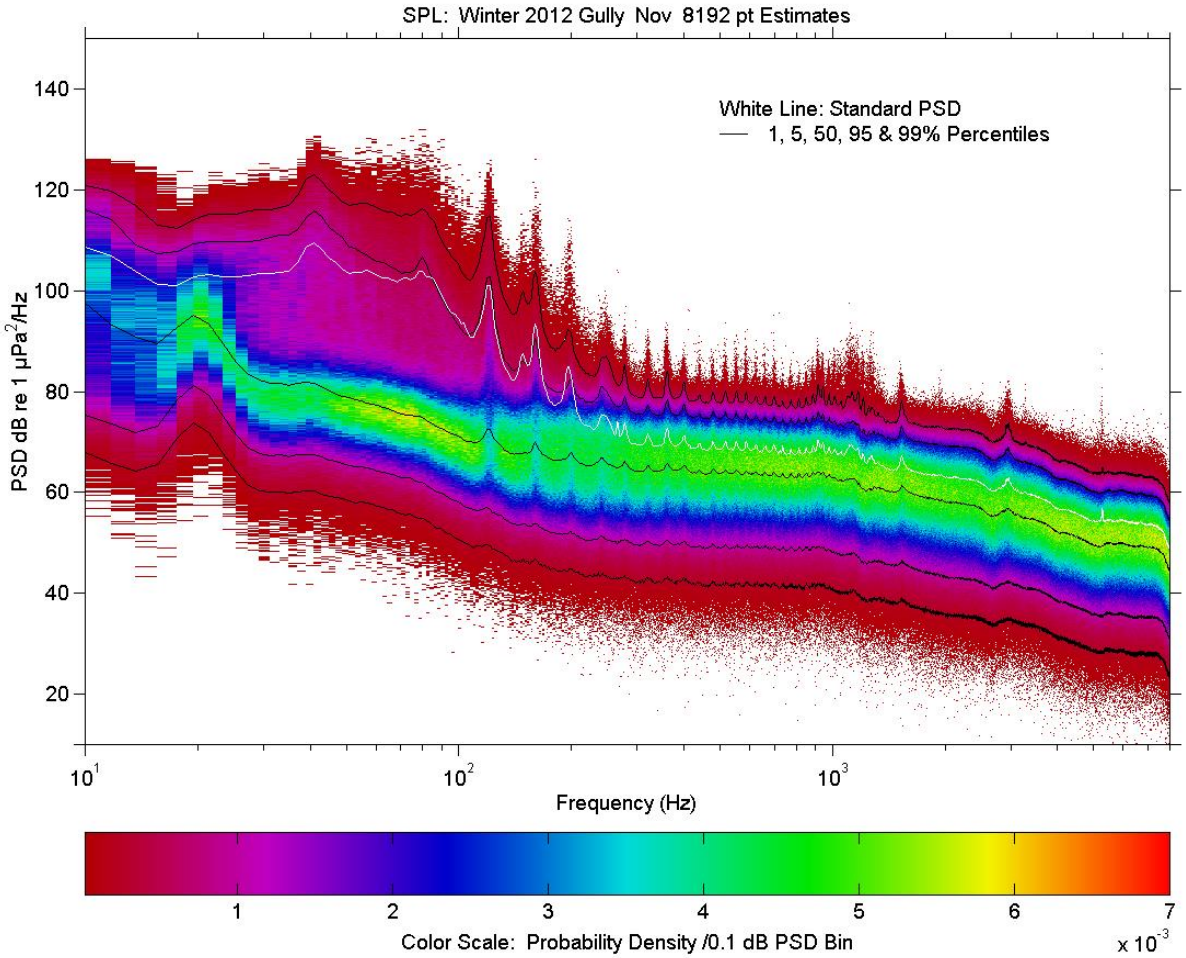


**Figure A4-2-MidGul-2012-Nov.** Medium resolution power spectral density with stats: Standard power spectral density (white), cumulative percentile curves for spectral sub-estimates (black), and PDF distribution of spectral sub-estimates (solid colour).

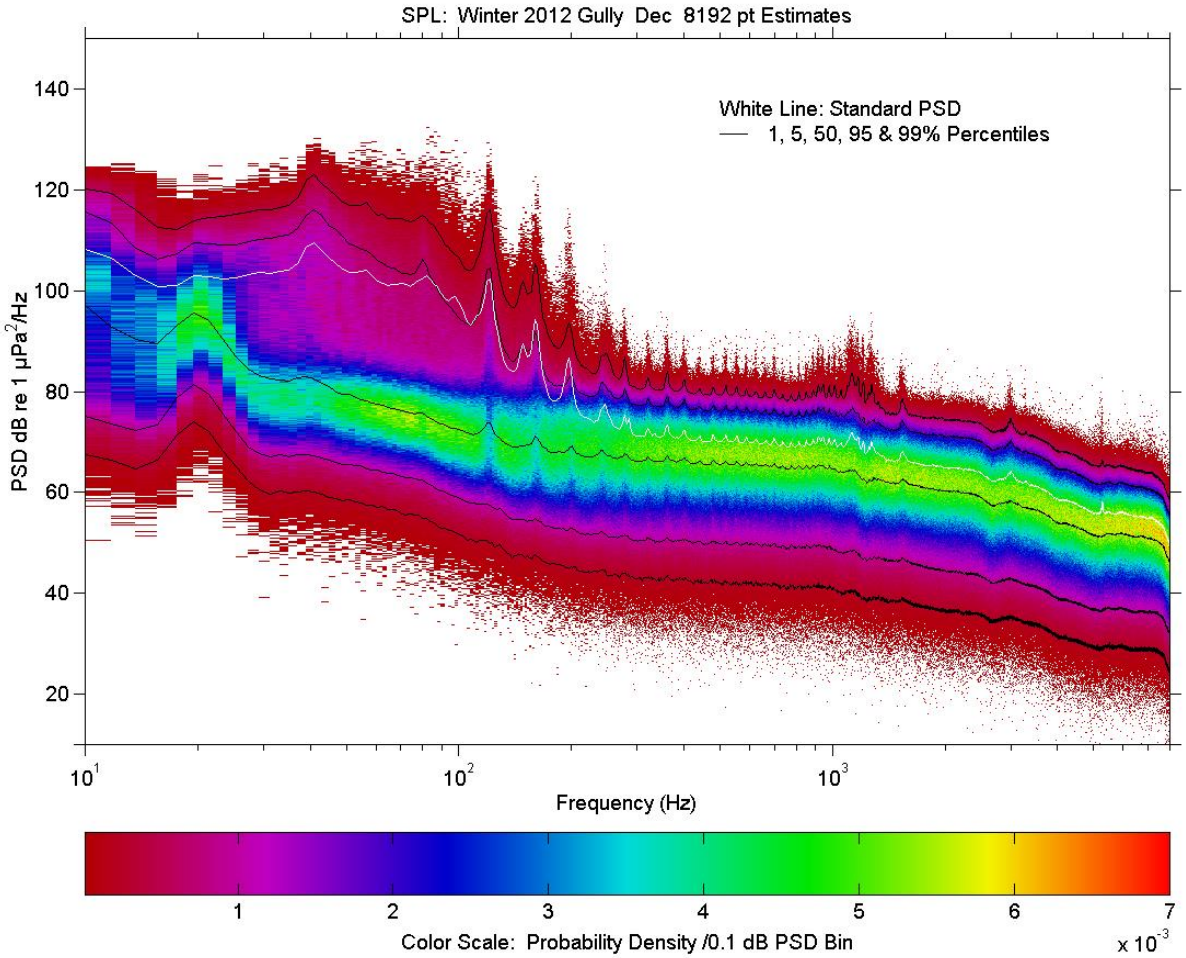


**Figure A4-2-MidGul-2012-Dec.** Medium resolution power spectral density with stats: Standard power spectral density (white), cumulative percentile curves for spectral sub-estimates (black), and PDF distribution of spectral sub-estimates (solid colour).

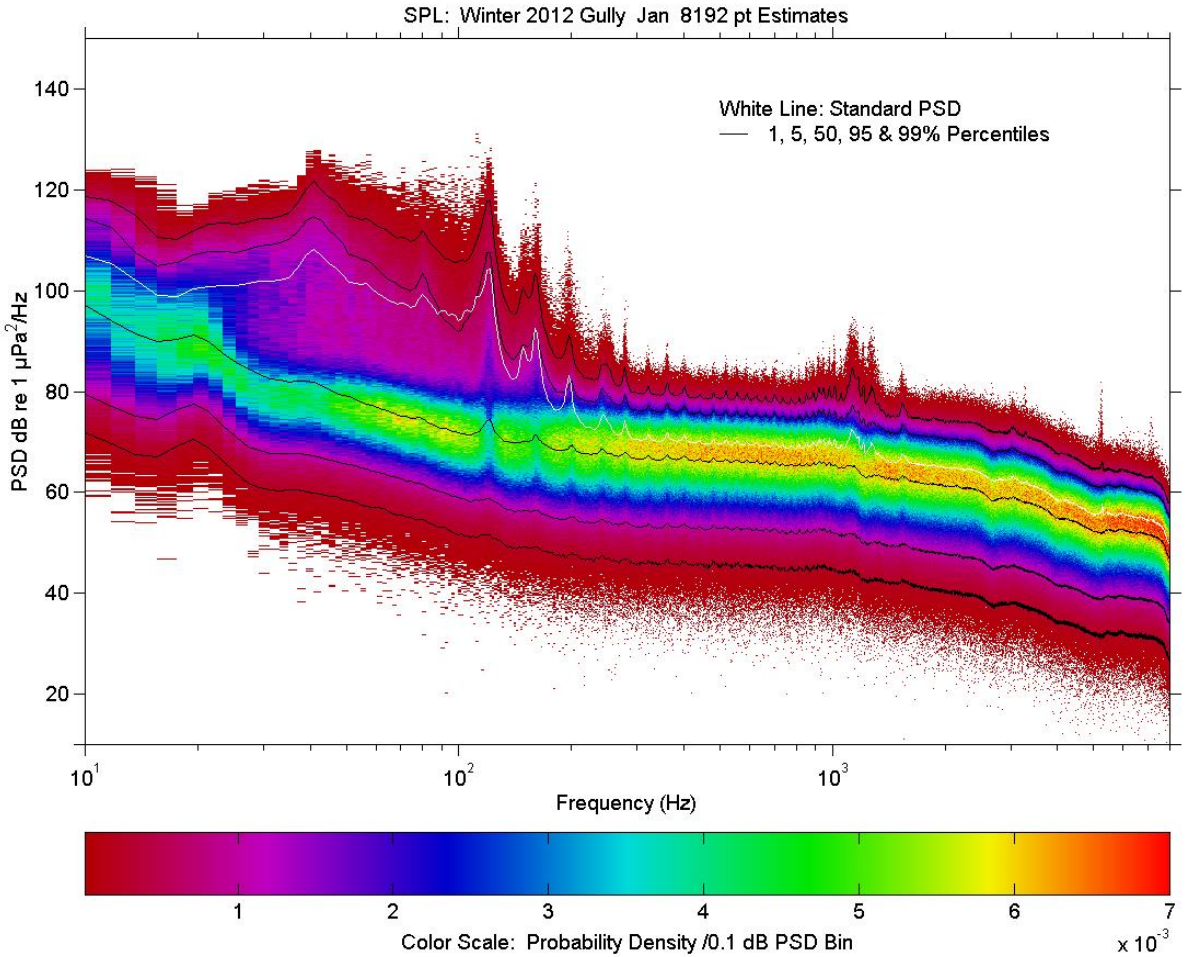


**Figure A4-2-MidGul-2013-Jan.** Medium resolution power spectral density with stats: Standard power spectral density (white), cumulative percentile curves for spectral sub-estimates (black), and PDF distribution of spectral sub-estimates (solid colour).

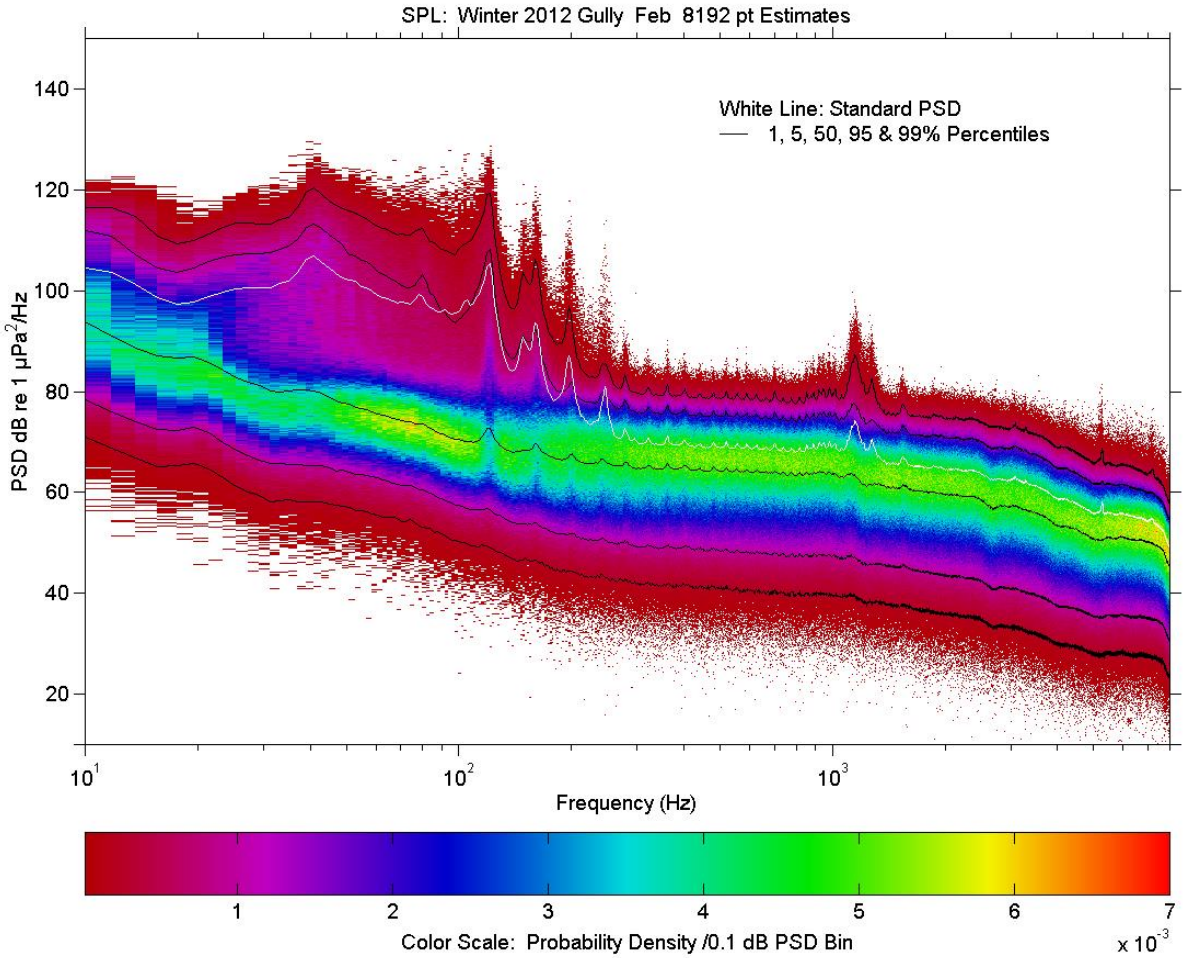


**Figure A4-2-MidGul-2013-Feb.** Medium resolution power spectral density with stats: Standard power spectral density (white), cumulative percentile curves for spectral sub-estimates (black), and PDF distribution of spectral sub-estimates (solid colour).

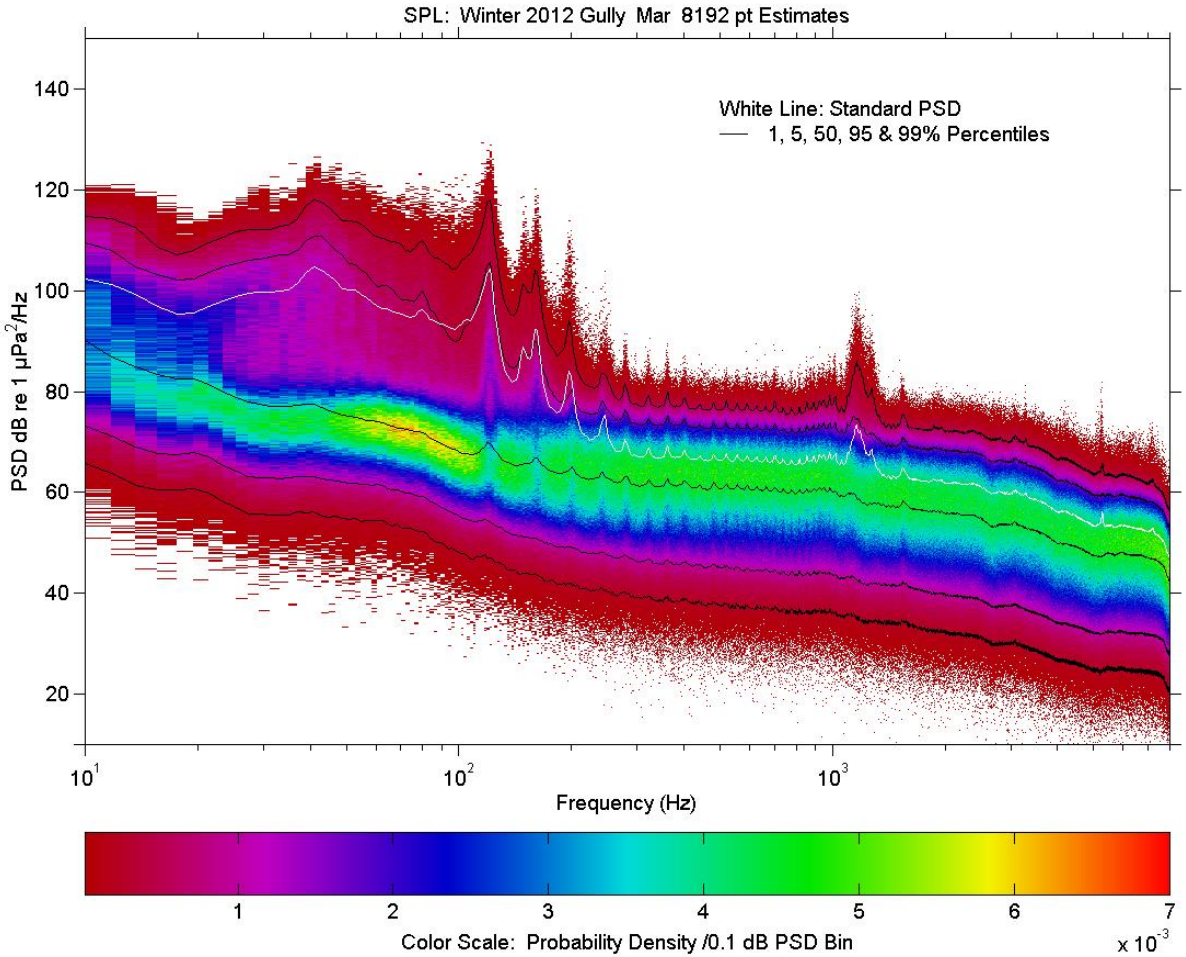


**Figure A4-2-MidGul-2013-Mar.** Medium resolution power spectral density with stats: Standard power spectral density (white), cumulative percentile curves for spectral sub-estimates (black), and PDF distribution of spectral sub-estimates (solid colour).

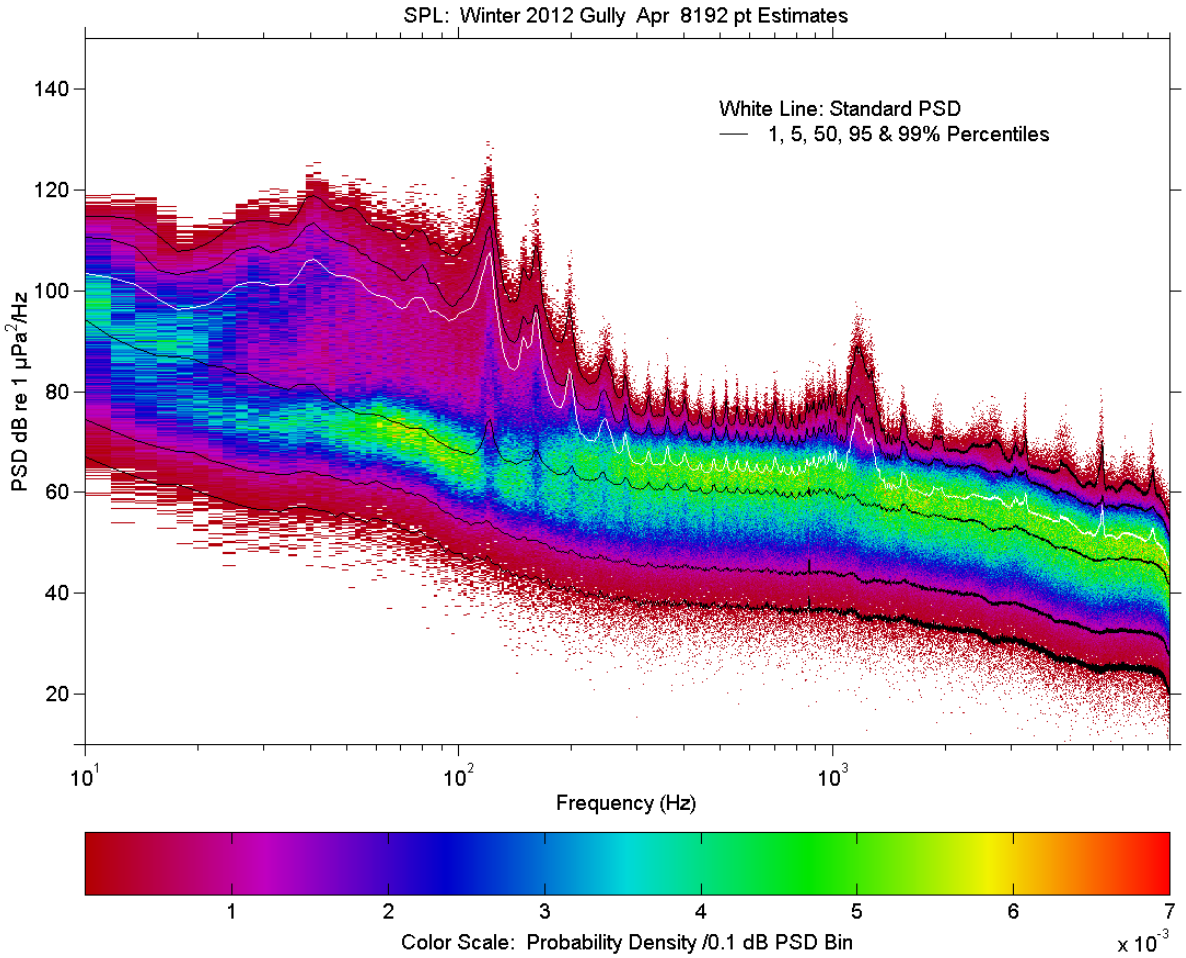


**Figure A4-2-MidGul-2013-Apr.** Medium resolution power spectral density with stats: Standard power spectral density (white), cumulative percentile curves for spectral sub-estimates (black), and PDF distribution of spectral sub-estimates (solid colour).

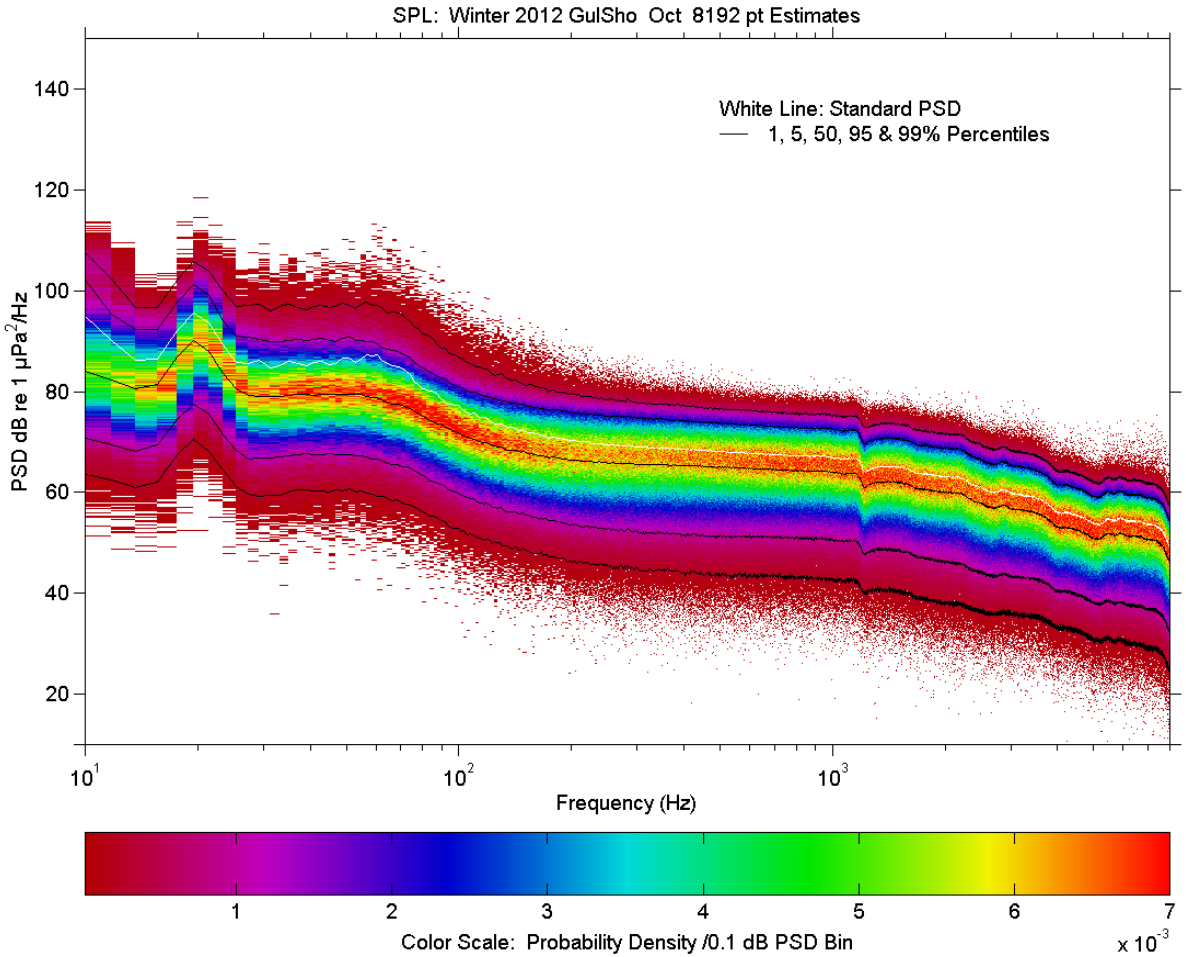


**Figure A4-2-GulSho-2012-Oct.** Medium resolution power spectral density with stats: Standard power spectral density (white), cumulative percentile curves for spectral sub-estimates (black), and PDF distribution of spectral sub-estimates (solid colour).

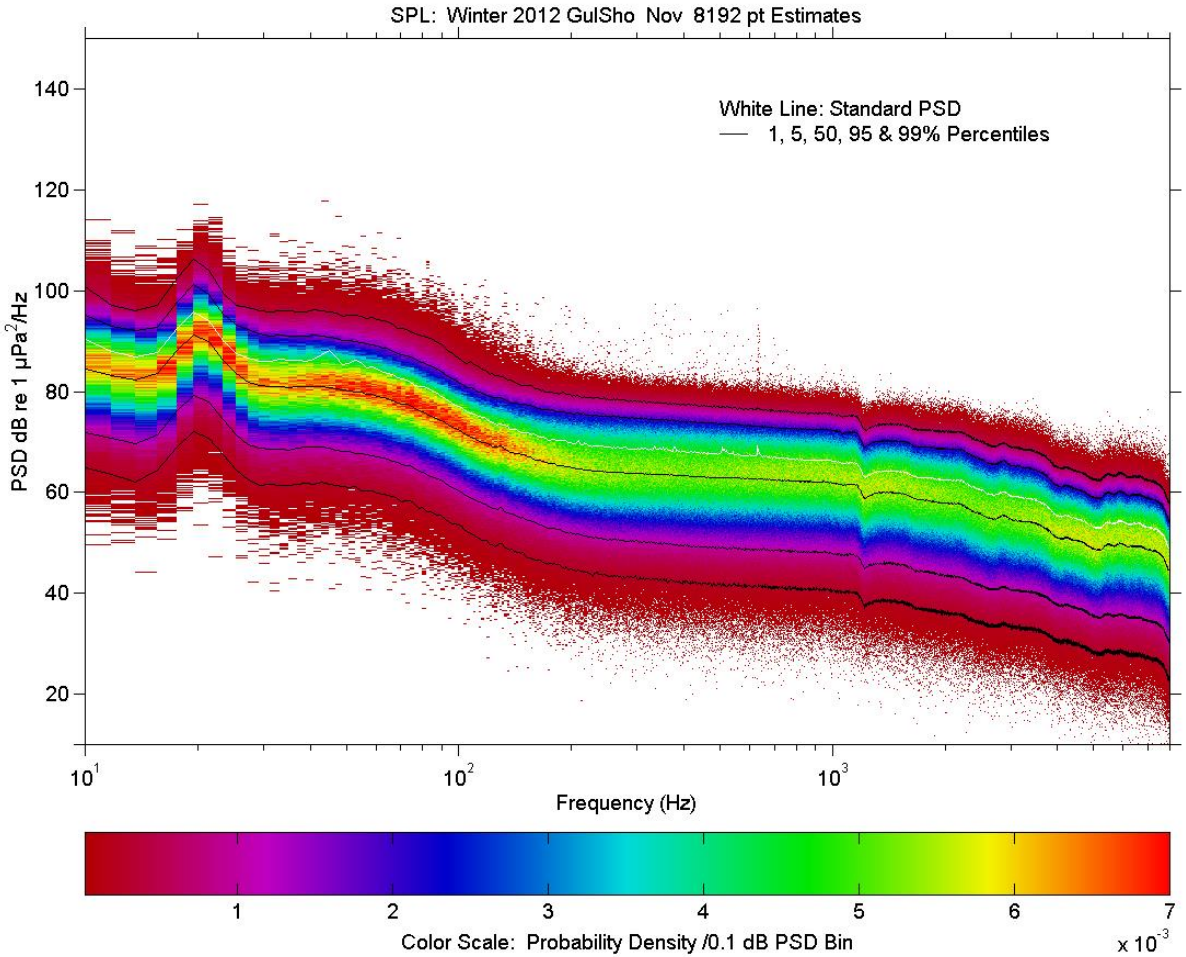


**Figure A4-2-GulSho-2012-Nov.** Medium resolution power spectral density with stats: Standard power spectral density (white), cumulative percentile curves for spectral sub-estimates (black), and PDF distribution of spectral sub-estimates (solid colour).

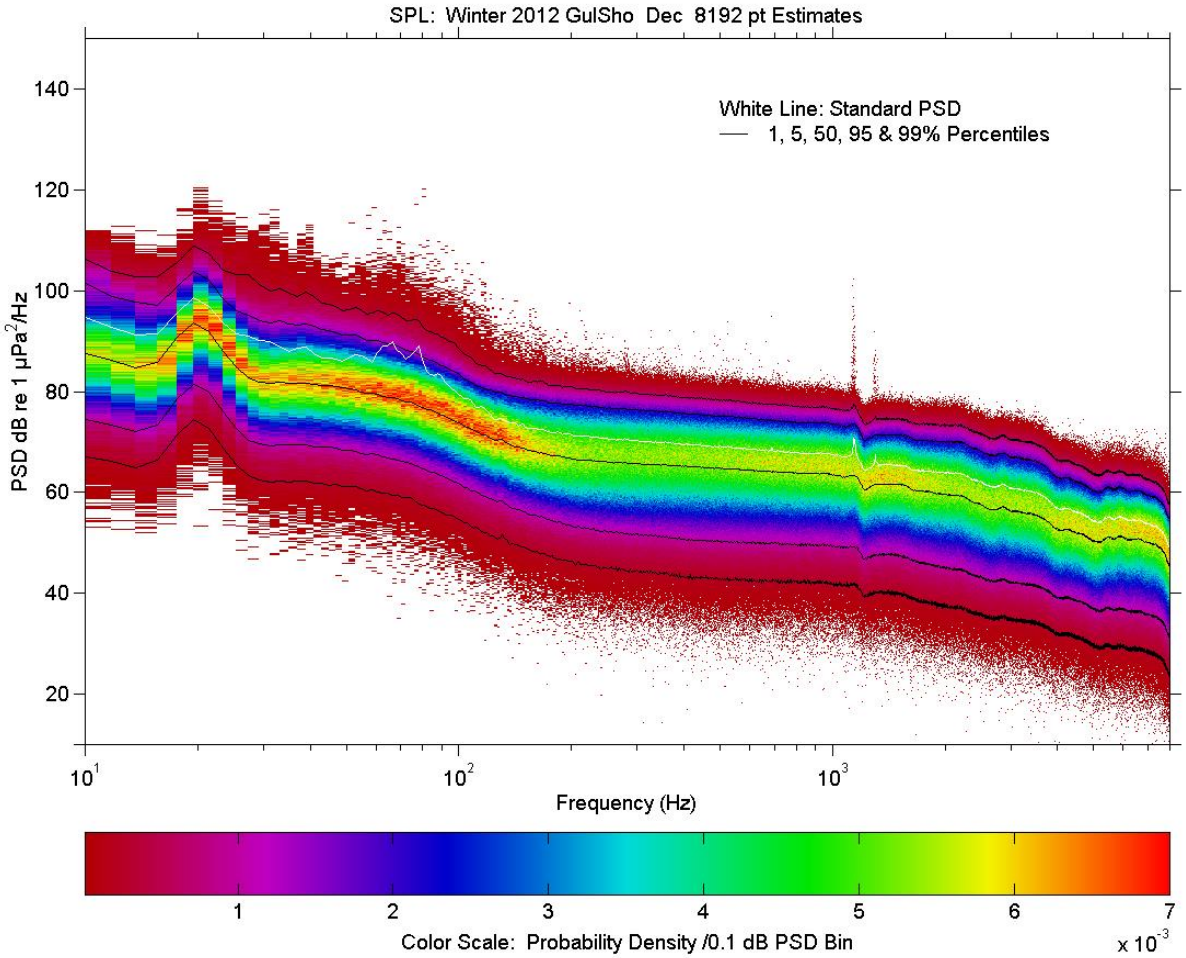


**Figure A4-2-GulSho-2012-Dec.** Medium resolution power spectral density with stats: Standard power spectral density (white), cumulative percentile curves for spectral sub-estimates (black), and PDF distribution of spectral sub-estimates (solid colour).

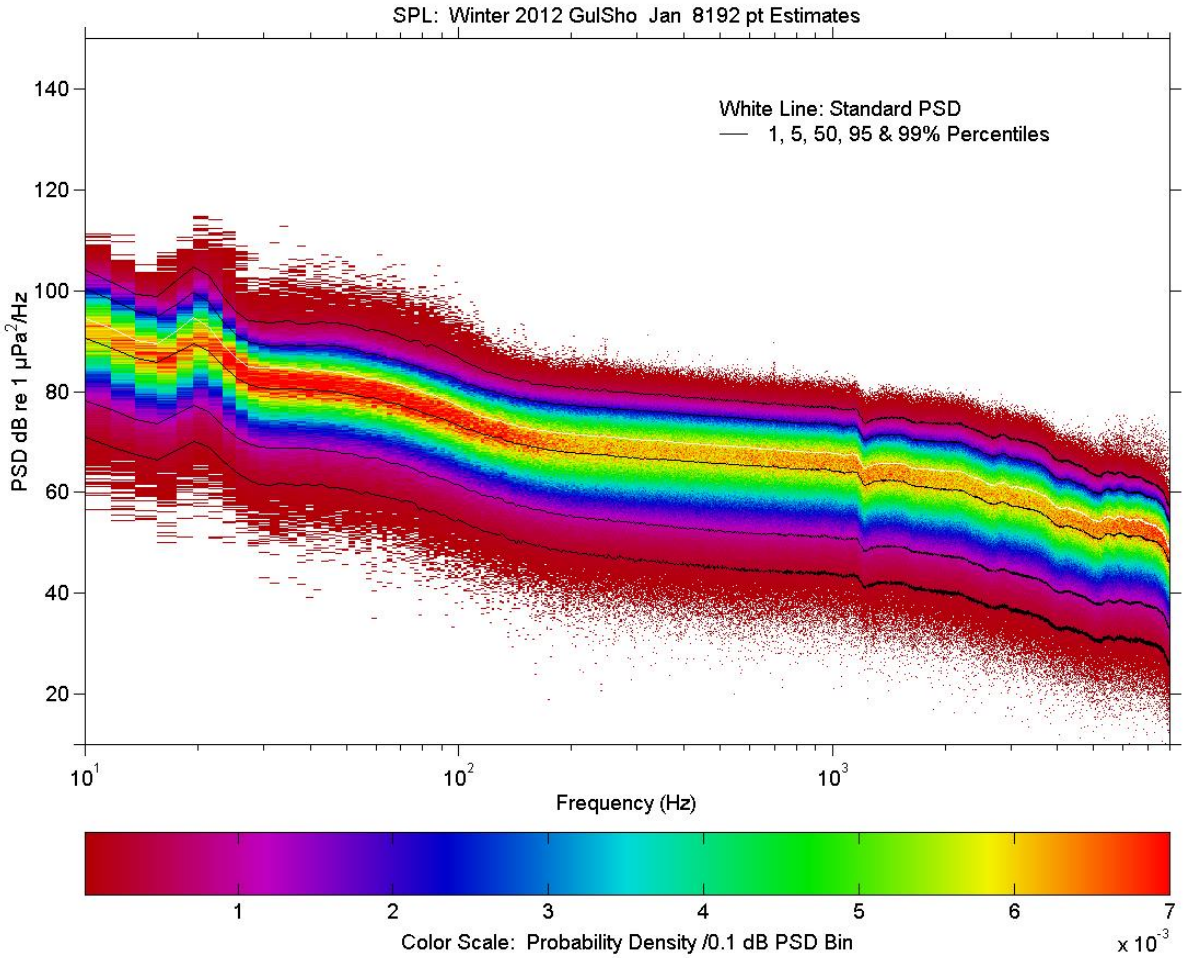


**Figure A4-2-GulSho-2013-Jan.** Medium resolution power spectral density with stats: Standard power spectral density (white), cumulative percentile curves for spectral sub-estimates (black), and PDF distribution of spectral sub-estimates (solid colour).

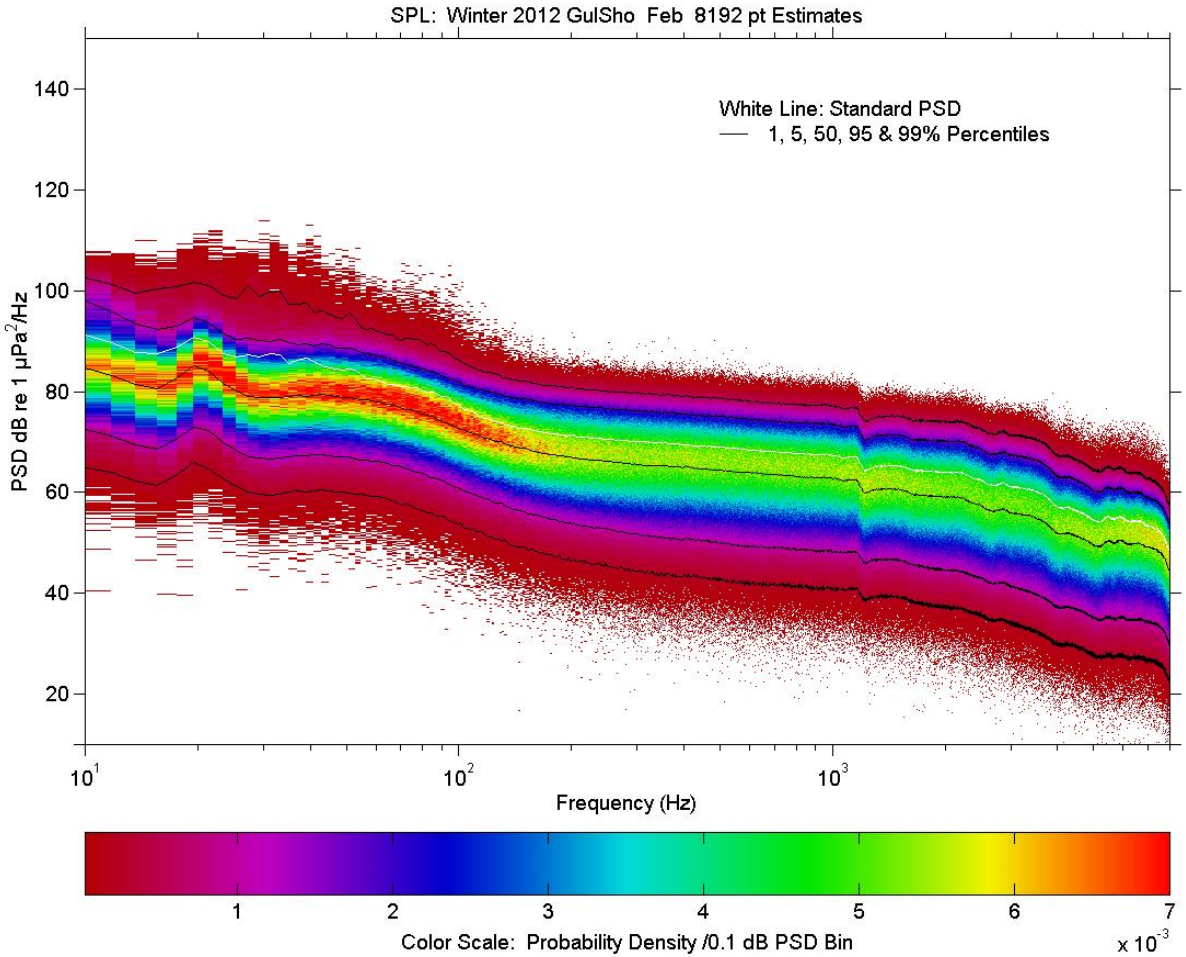


**Figure A4-2-GulSho-2013-Feb.** Medium resolution power spectral density with stats: Standard power spectral density (white), cumulative percentile curves for spectral sub-estimates (black), and PDF distribution of spectral sub-estimates (solid colour).

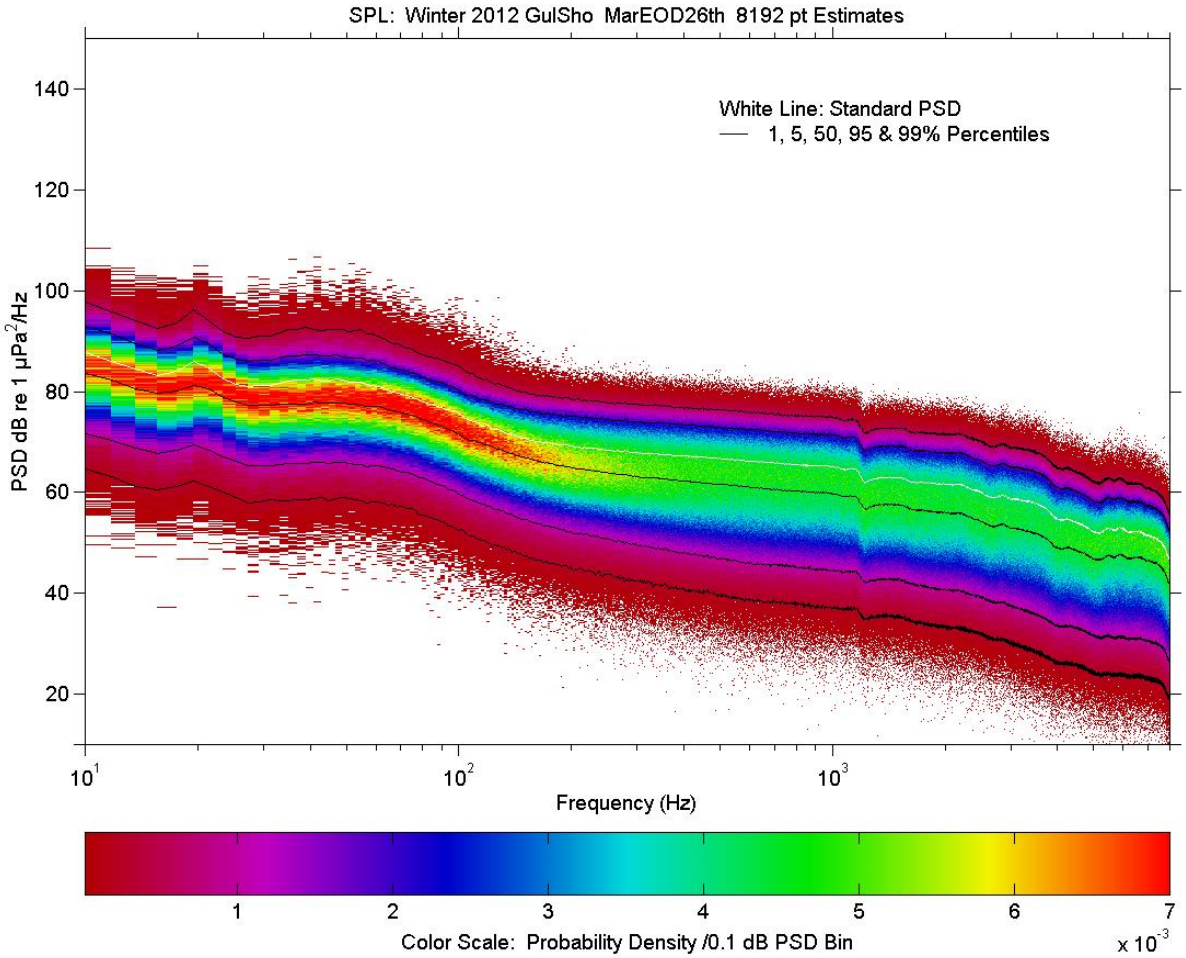


**Figure A4-2-GulSho-2013-Mar.** Medium resolution power spectral density with stats: Standard power spectral density (white), cumulative percentile curves for spectral sub-estimates (black), and PDF distribution of spectral sub-estimates (solid colour). Data extends to 26th incl. On March 27, 28 and 29th a shift in noise baseline occurs, an apparent instrumental or mooring problem.

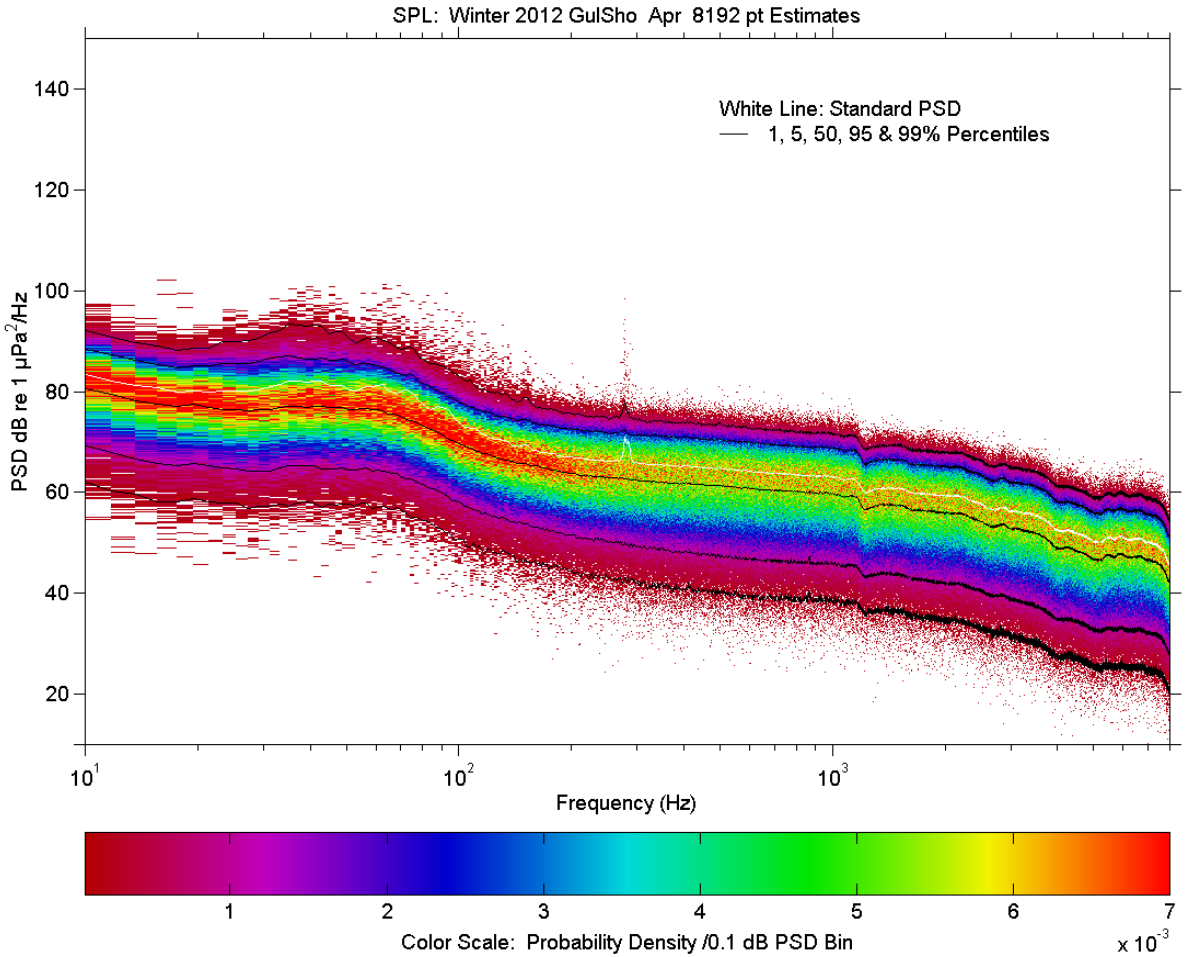


**Figure A4-2-GulSho-2013-Apr.** Medium resolution power spectral density with stats: Standard power spectral density (white), cumulative percentile curves for spectral sub-estimates (black), and PDF distribution of spectral sub-estimates (solid colour).

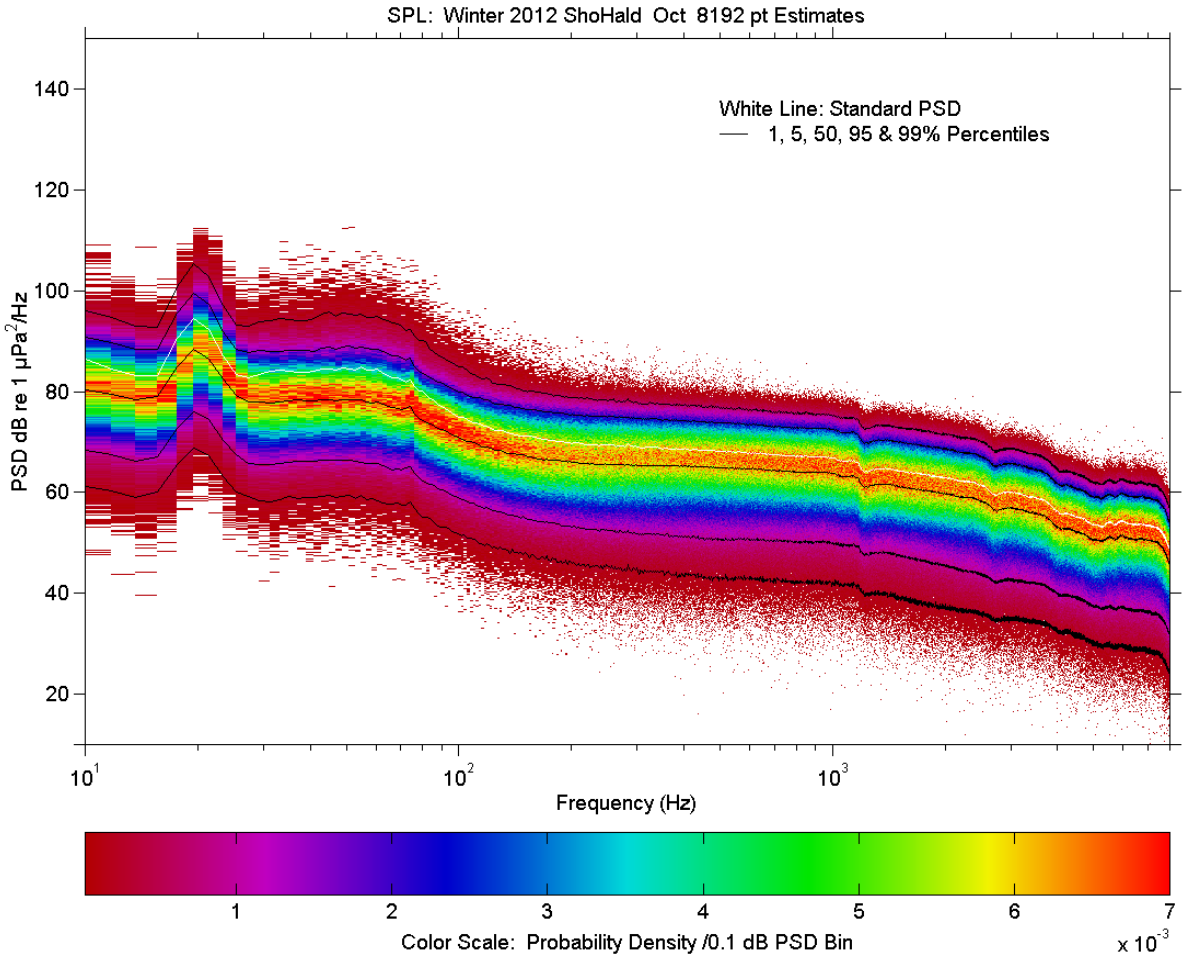


**Figure A4-2-ShoHald-2012-Oct.** Medium resolution power spectral density with stats: Standard power spectral density (white), cumulative percentile curves for spectral sub-estimates (black), and PDF distribution of spectral sub-estimates (solid colour).

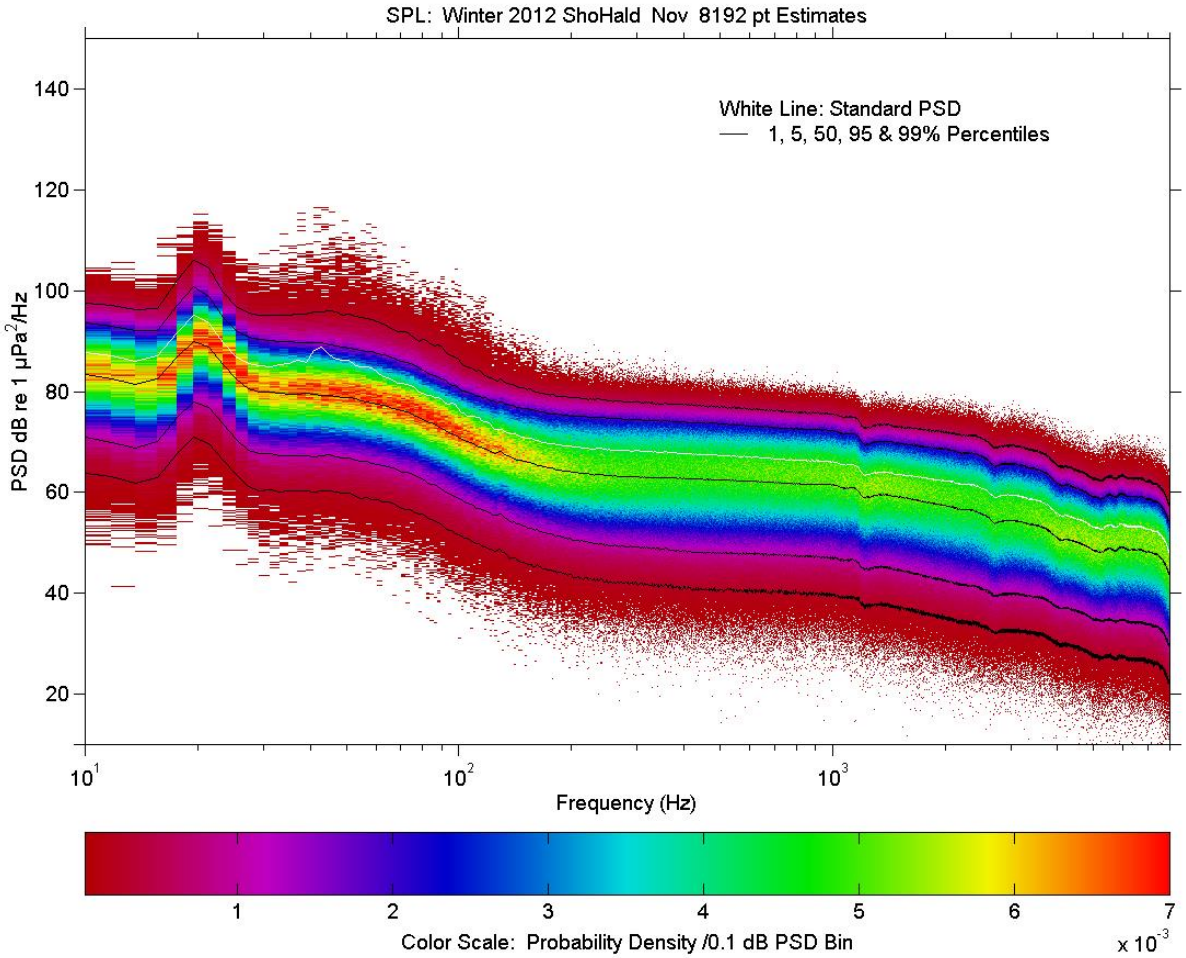


**Figure A4-2-ShoHald-2012-Nov.** Medium resolution power spectral density with stats: Standard power spectral density (white), cumulative percentile curves for spectral sub-estimates (black), and PDF distribution of spectral sub-estimates (solid colour).

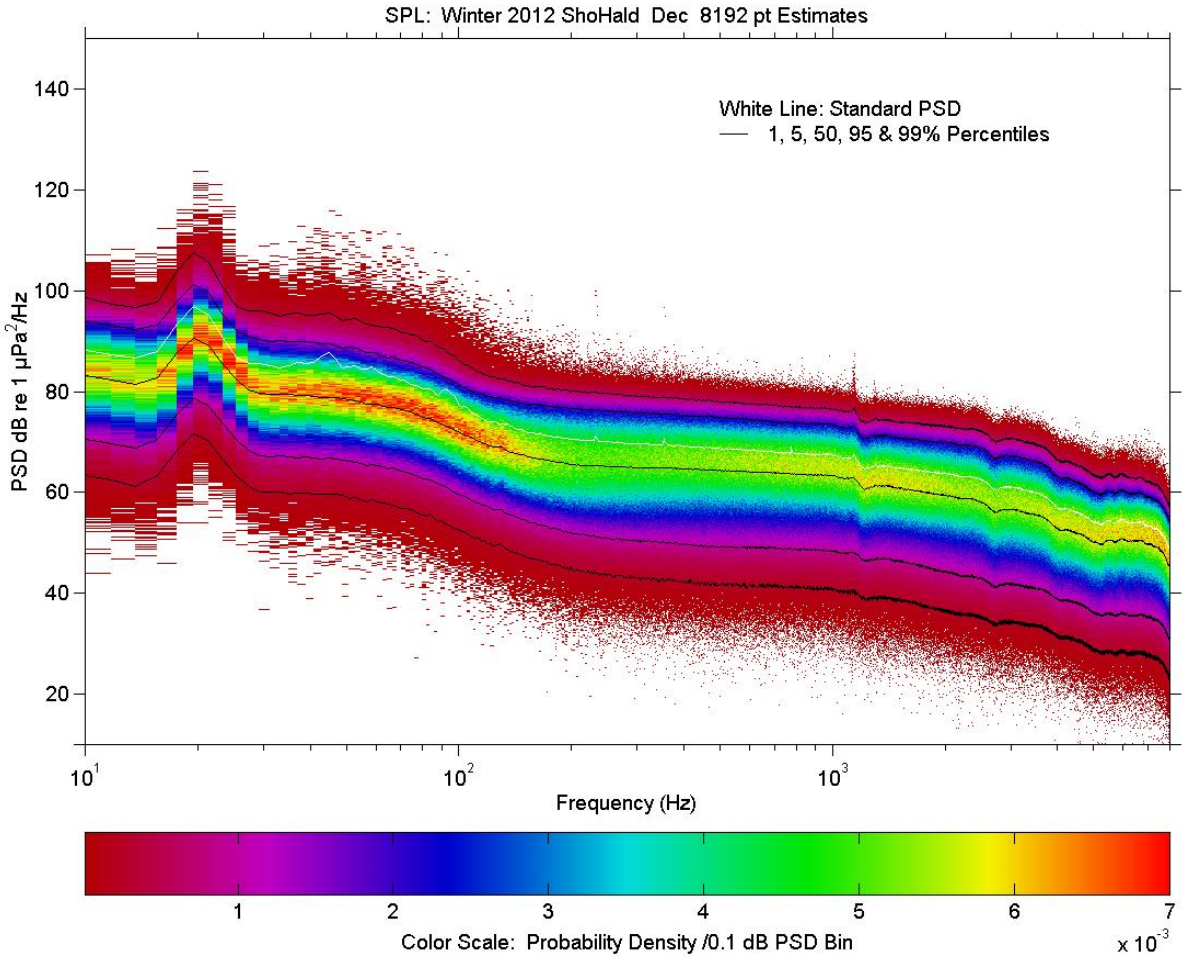


**Figure A4-2-ShoHald-2012-Dec.** Medium resolution power spectral density with stats: Standard power spectral density (white), cumulative percentile curves for spectral sub-estimates (black), and PDF distribution of spectral sub-estimates (solid colour).

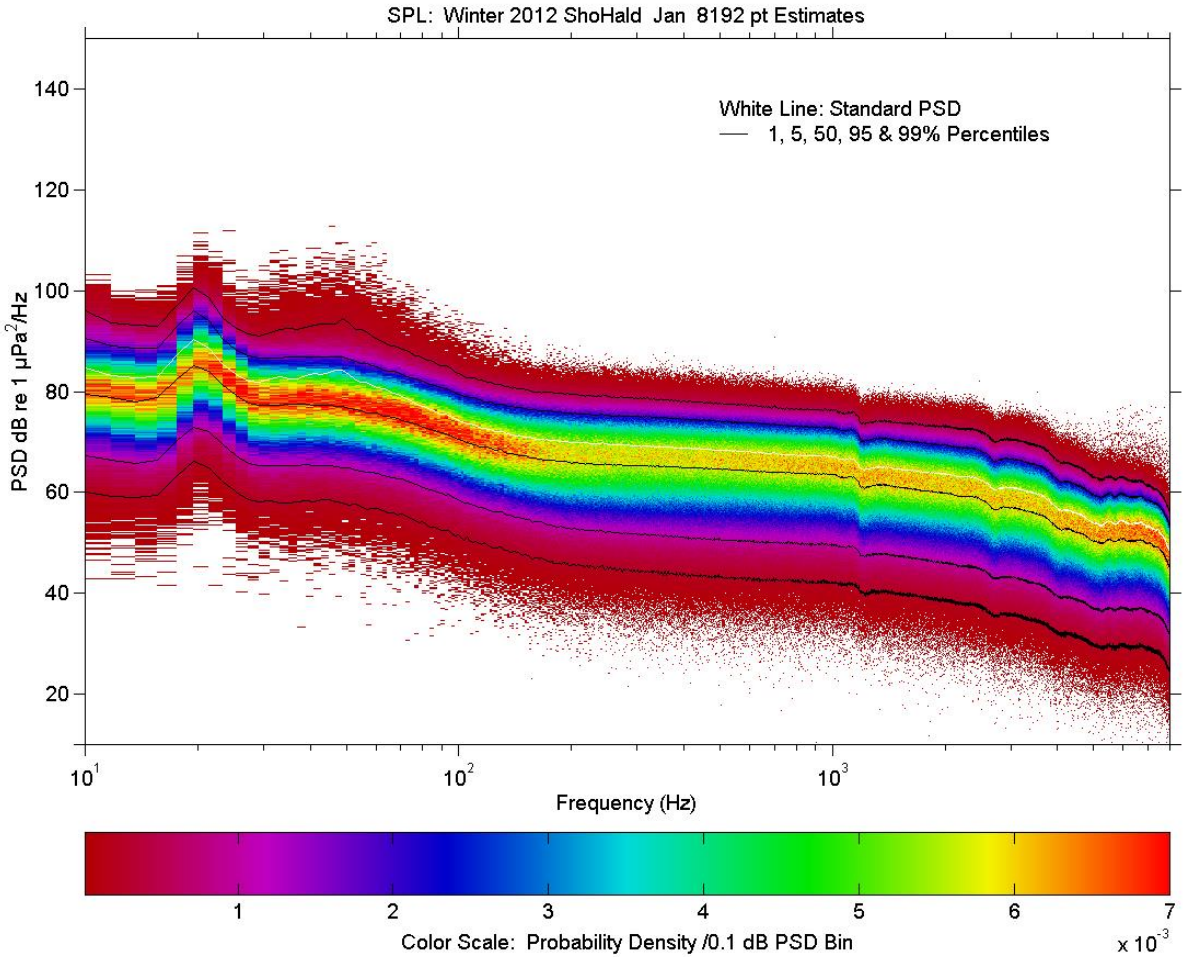


**Figure A4-2-ShoHald-2013-Jan.** Medium resolution power spectral density with stats: Standard power spectral density (white), cumulative percentile curves for spectral sub-estimates (black), and PDF distribution of spectral sub-estimates (solid colour).

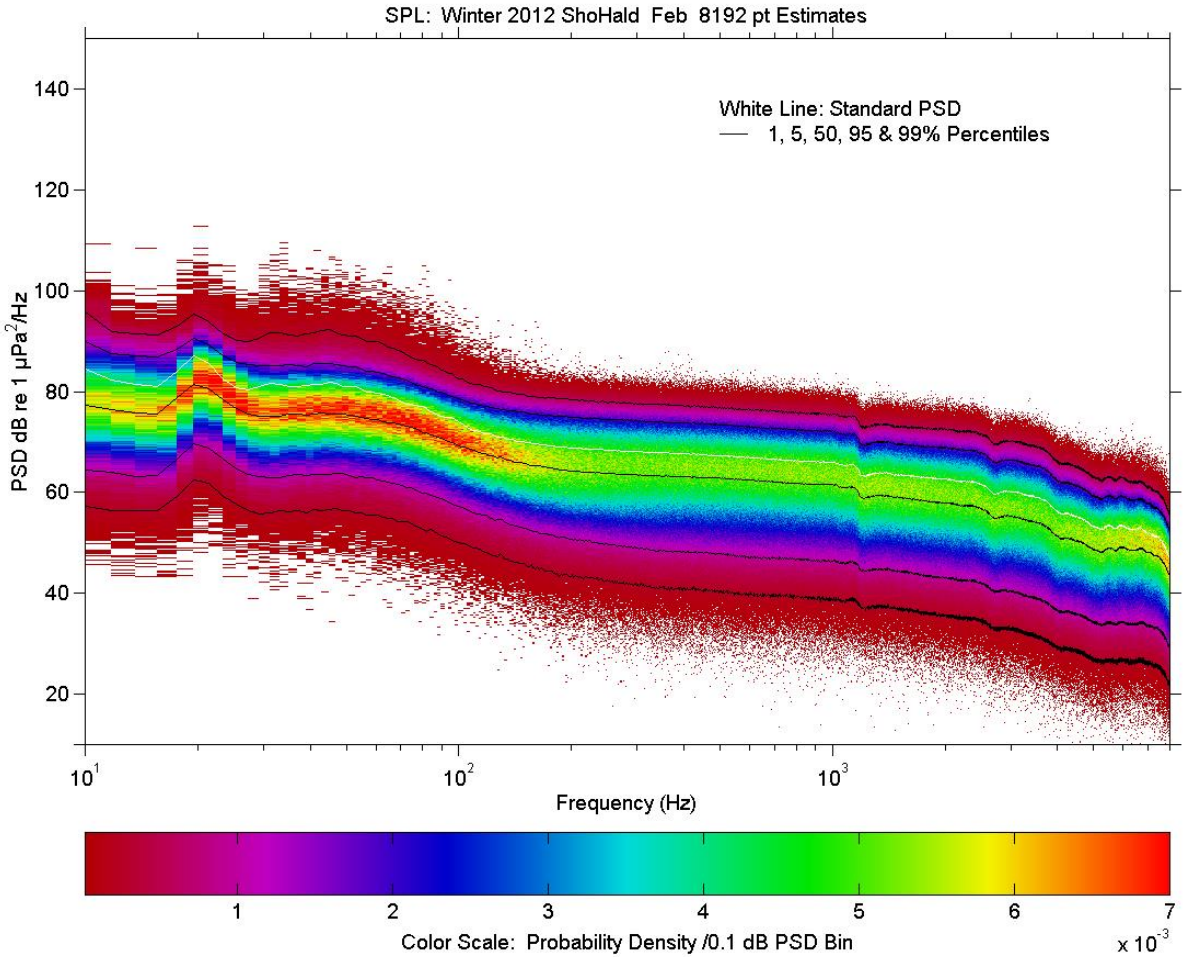


**Figure A4-2-ShoHald-2013-Feb.** Medium resolution power spectral density with stats: Standard power spectral density (white), cumulative percentile curves for spectral sub-estimates (black), and PDF distribution of spectral sub-estimates (solid colour).

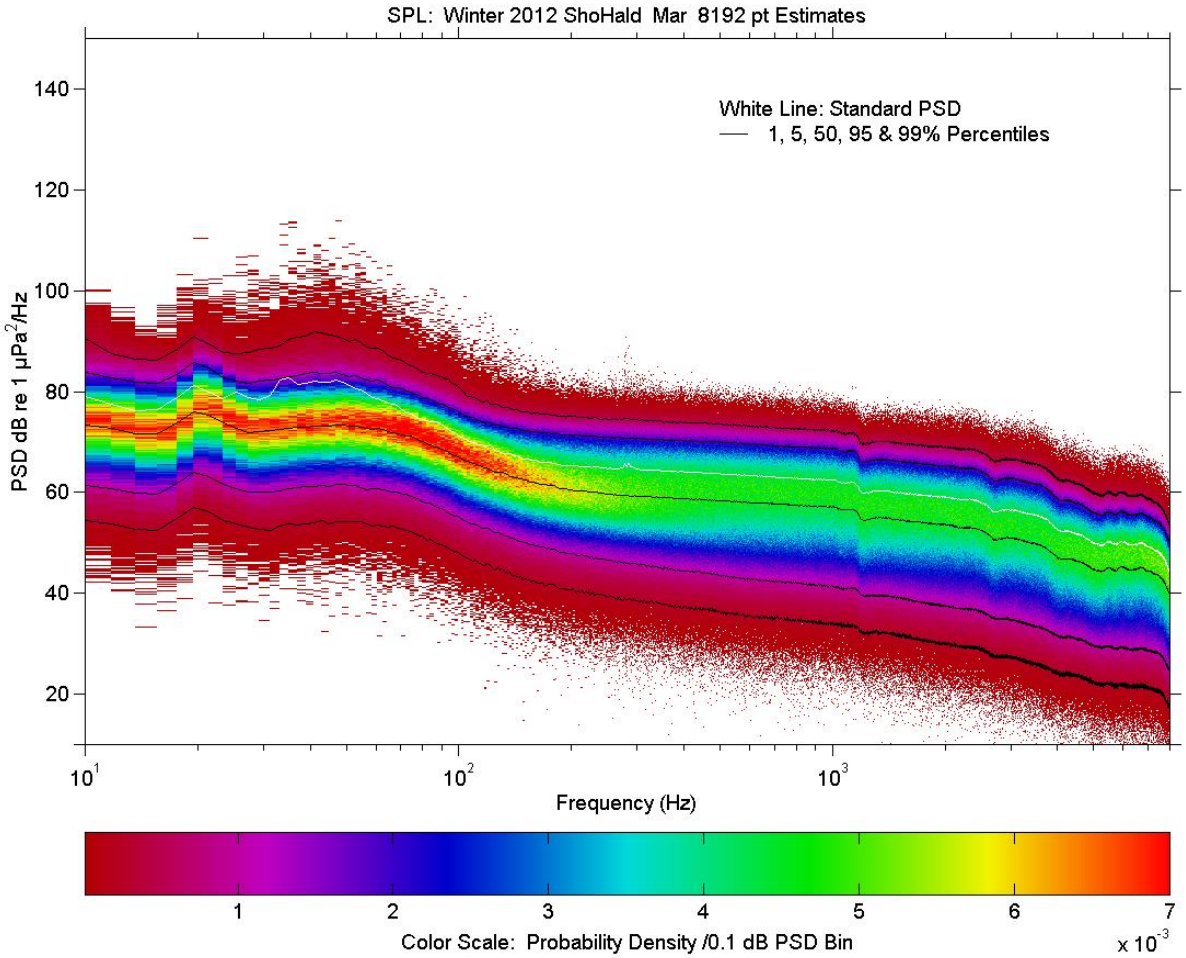


**Figure A4-2-ShoHald-2013-Mar.** Medium resolution power spectral density with stats: Standard power spectral density (white), cumulative percentile curves for spectral sub-estimates (black), and PDF distribution of spectral sub-estimates (solid colour).

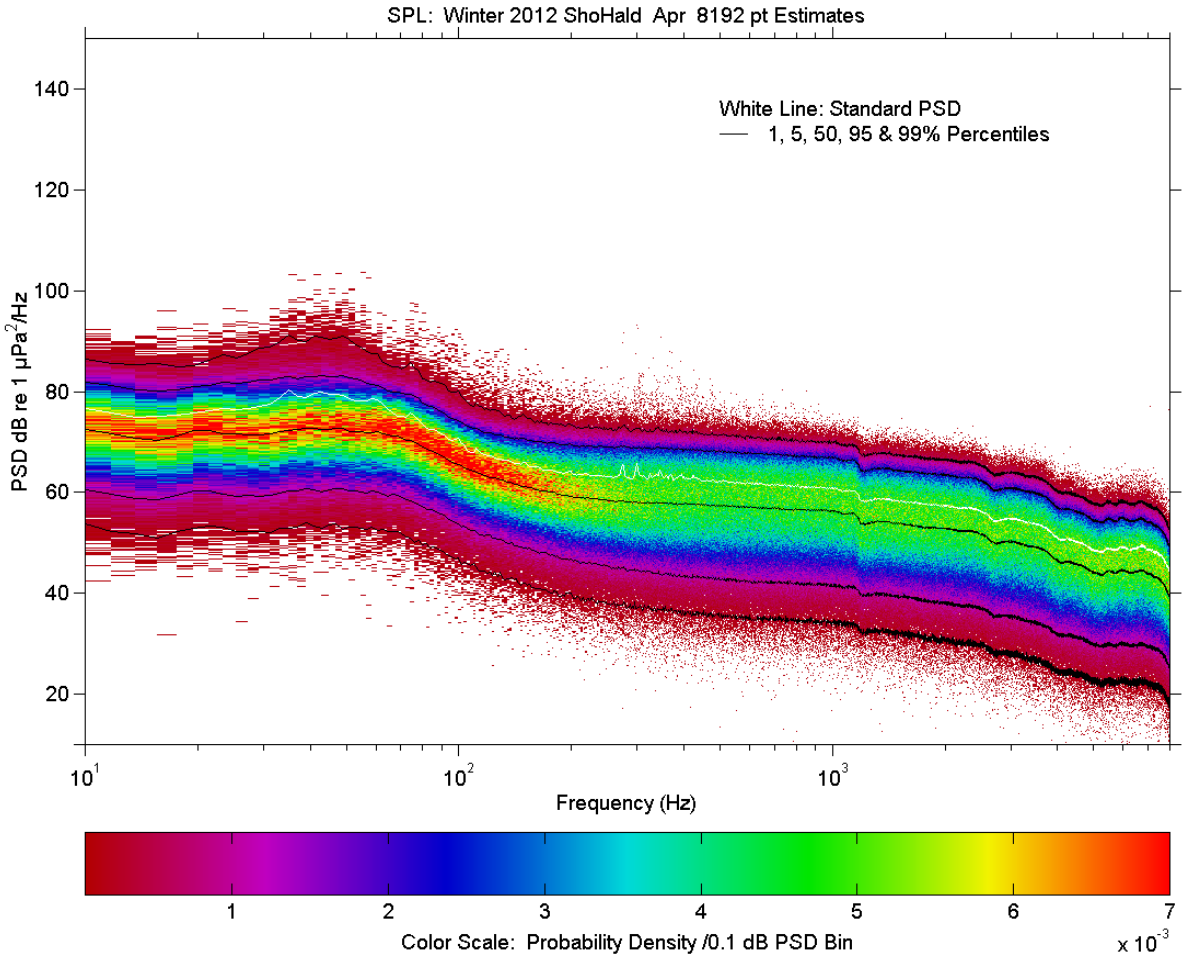


**Figure A4-2-ShoHald-2013-Apr.** Medium resolution power spectral density with stats: Standard power spectral density (white), cumulative percentile curves for spectral sub-estimates (black), and PDF distribution of spectral sub-estimates (solid colour).

### *A4.2.2. Summer 2013 Deployments*

**Figure (series) A4-2-Summer 2013 Deployments** - Medium resolution power spectral densities with stats: Standard power spectral density, cumulative percentile curves for spectral sub-estimates, and PDF distribution of spectral sub-estimates.

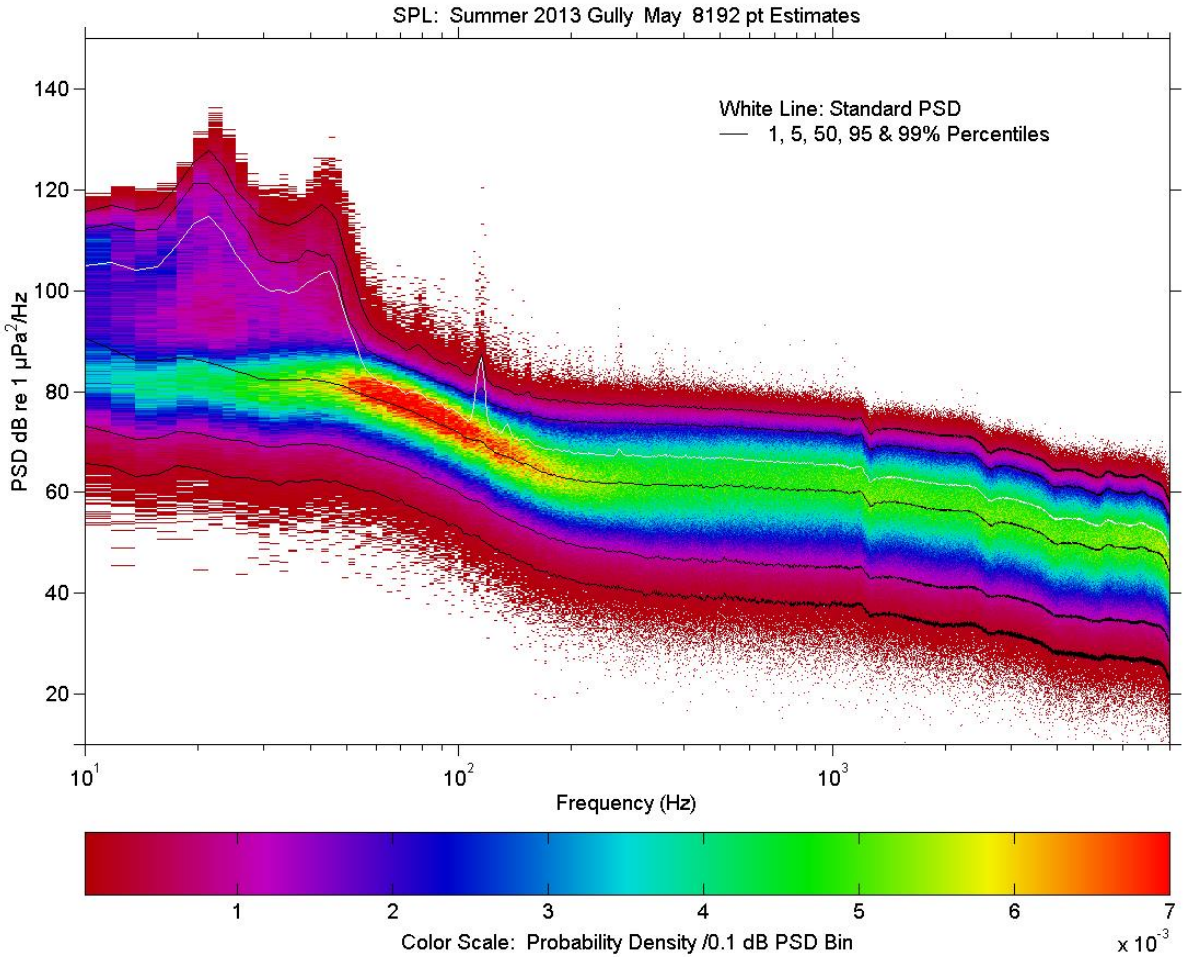


**Figure A4-2-MidGul-2013-May.** Medium resolution power spectral density with stats: Standard power spectral density (white), cumulative percentile curves for spectral sub-estimates (black), and PDF distribution of spectral sub-estimates (solid colour).

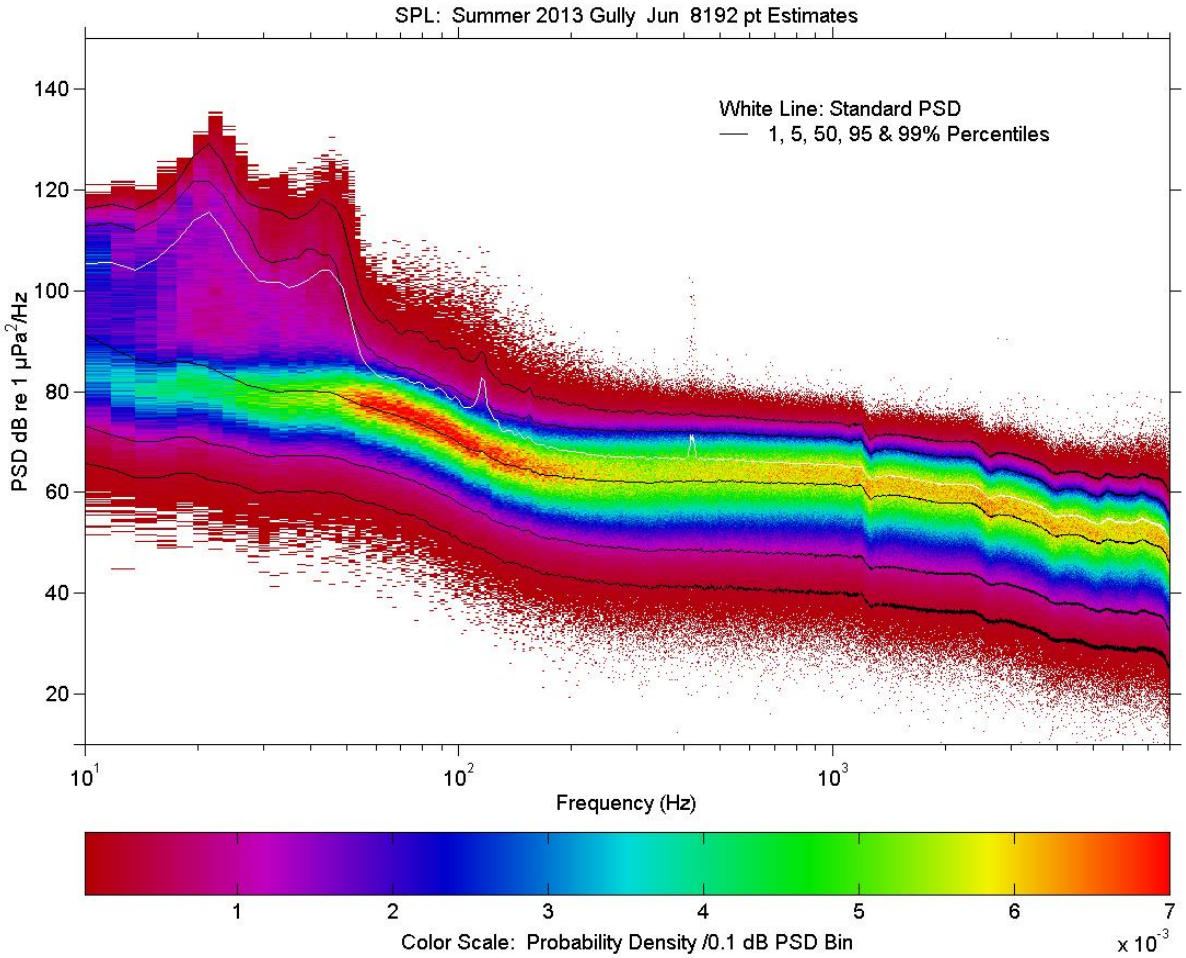


**Figure A4-2-MidGul-2013-Jun.** Medium resolution power spectral density with stats: Standard power spectral density (white), cumulative percentile curves for spectral sub-estimates (black), and PDF distribution of spectral sub-estimates (solid colour).

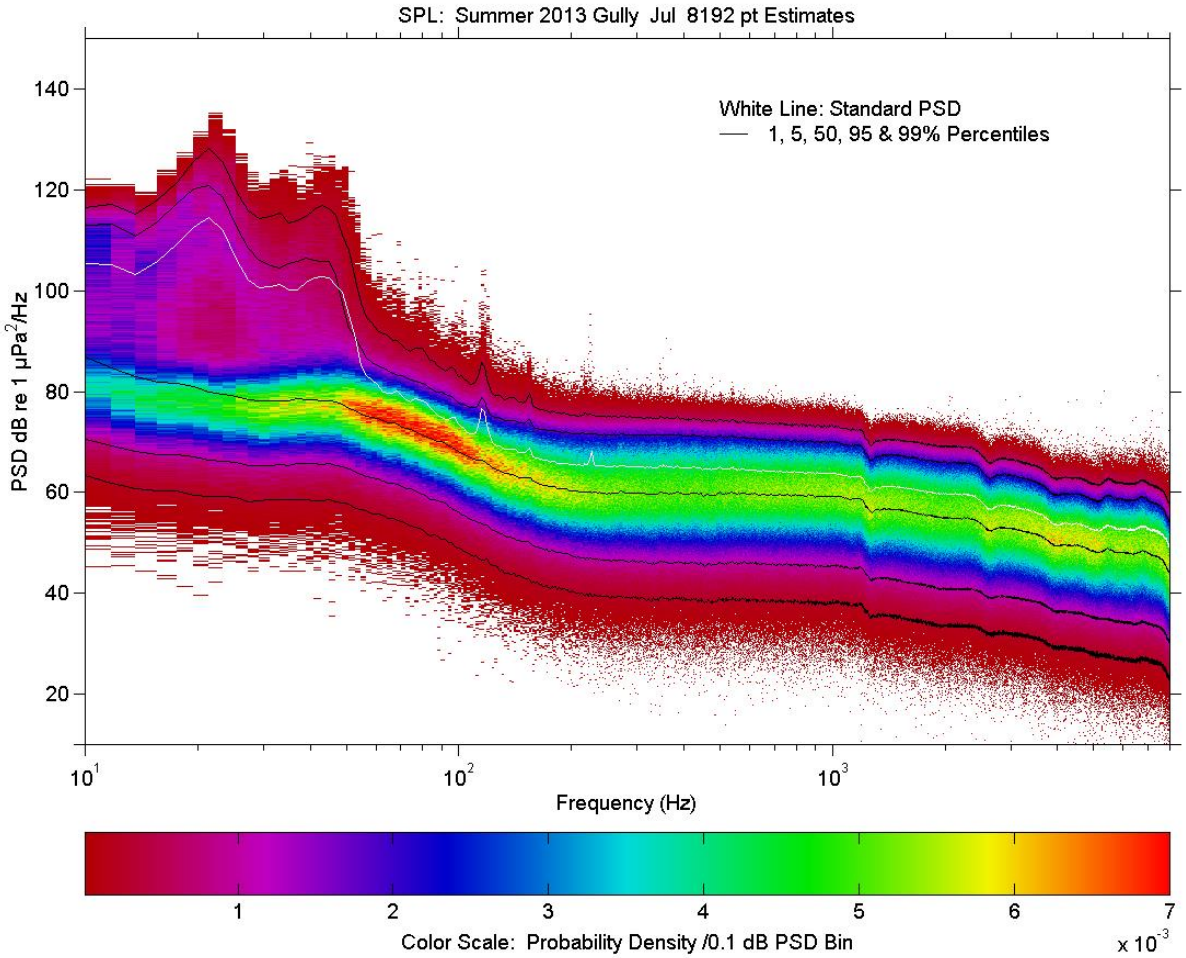


**Figure A4-2-MidGul-2013-Jul.** Medium resolution power spectral density with stats: Standard power spectral density (white), cumulative percentile curves for spectral sub-estimates (black), and PDF distribution of spectral sub-estimates (solid colour).

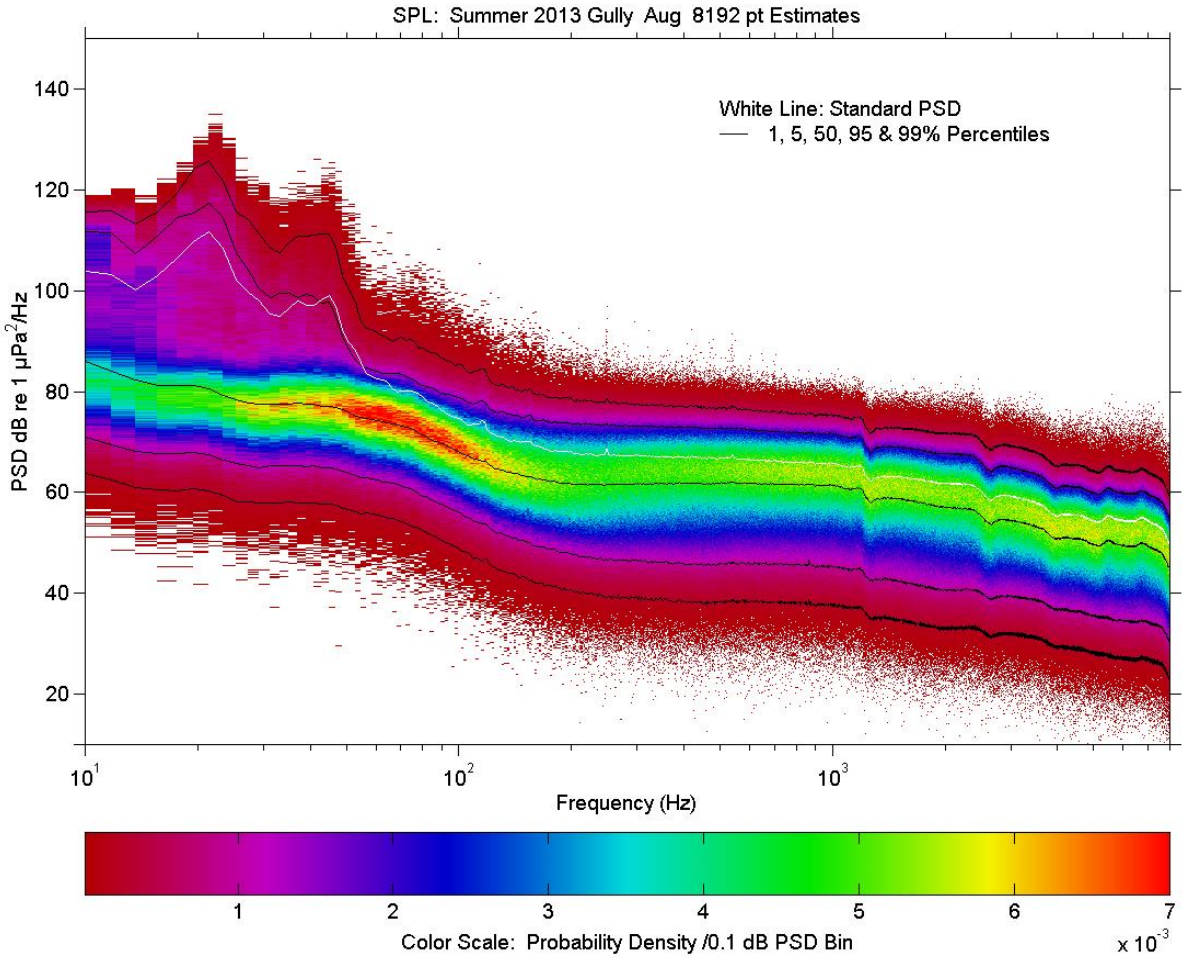


**Figure A4-2-MidGul-2013-Aug.** Medium resolution power spectral density with stats: Standard power spectral density (white), cumulative percentile curves for spectral sub-estimates (black), and PDF distribution of spectral sub-estimates (solid colour).

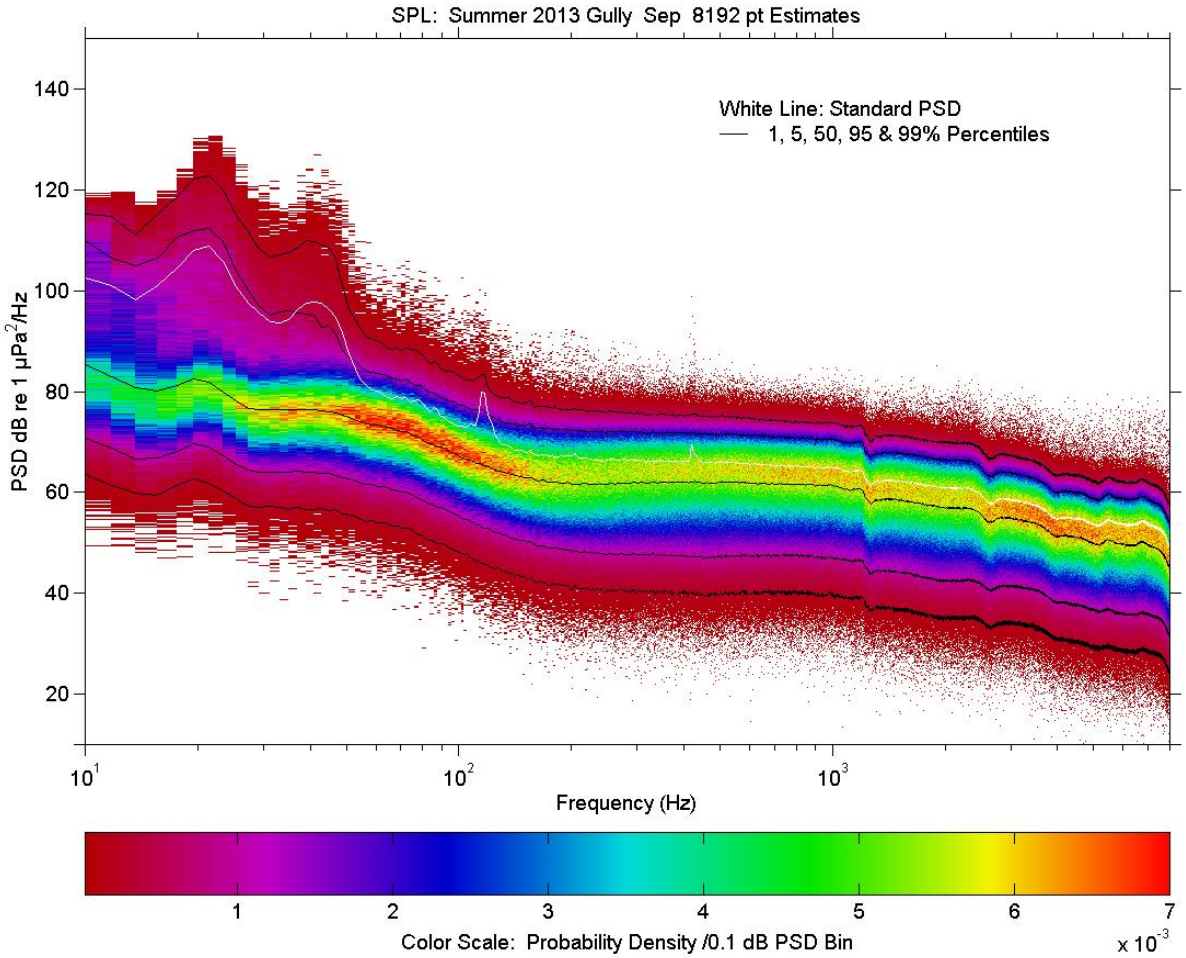


**Figure A4-2-MidGul-2013-Sep.** Medium resolution power spectral density with stats: Standard power spectral density (white), cumulative percentile curves for spectral sub-estimates (black), and PDF distribution of spectral sub-estimates (solid colour).

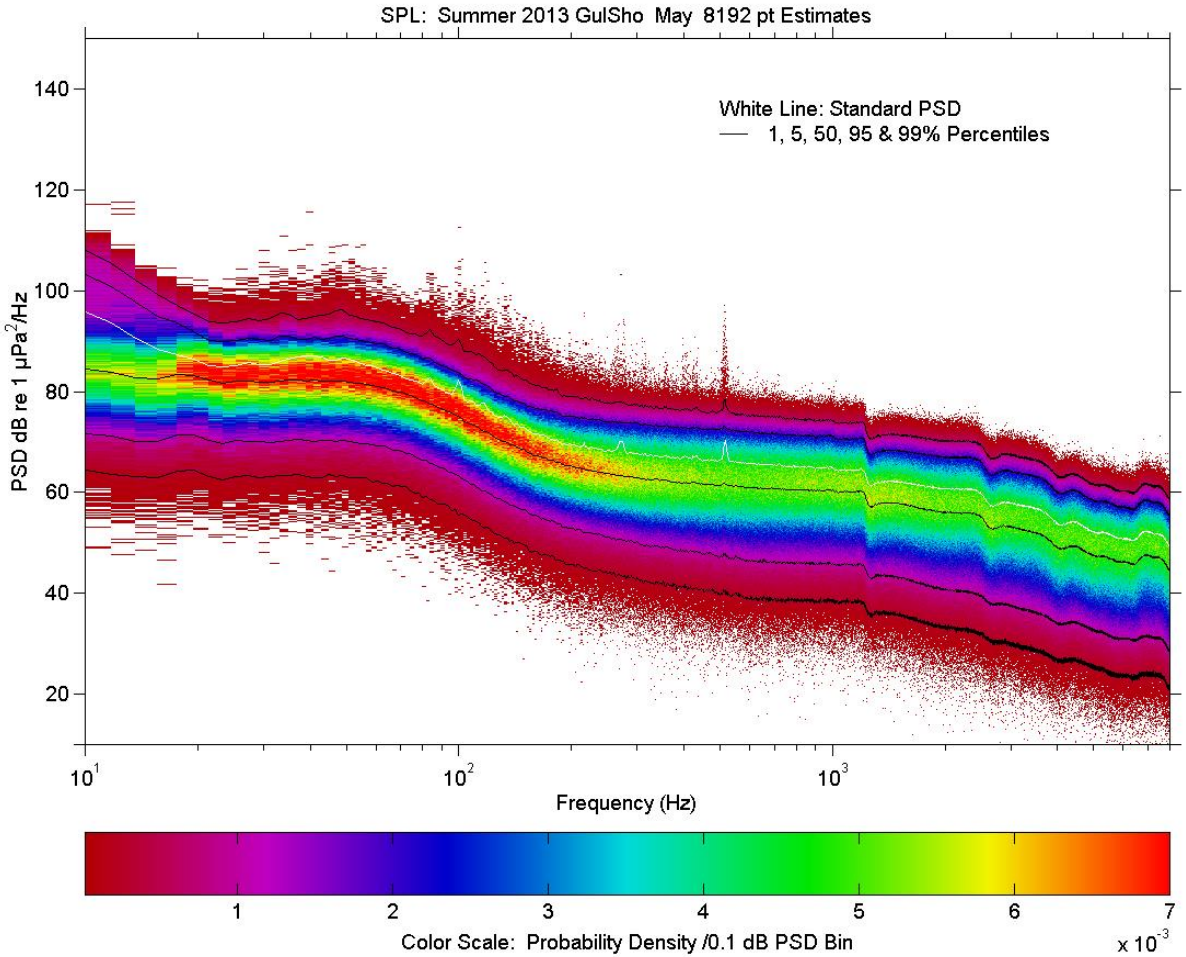


**Figure A4-2-GulSho-2013-May.** Medium resolution power spectral density with stats: Standard power spectral density (white), cumulative percentile curves for spectral sub-estimates (black), and PDF distribution of spectral sub-estimates (solid colour).

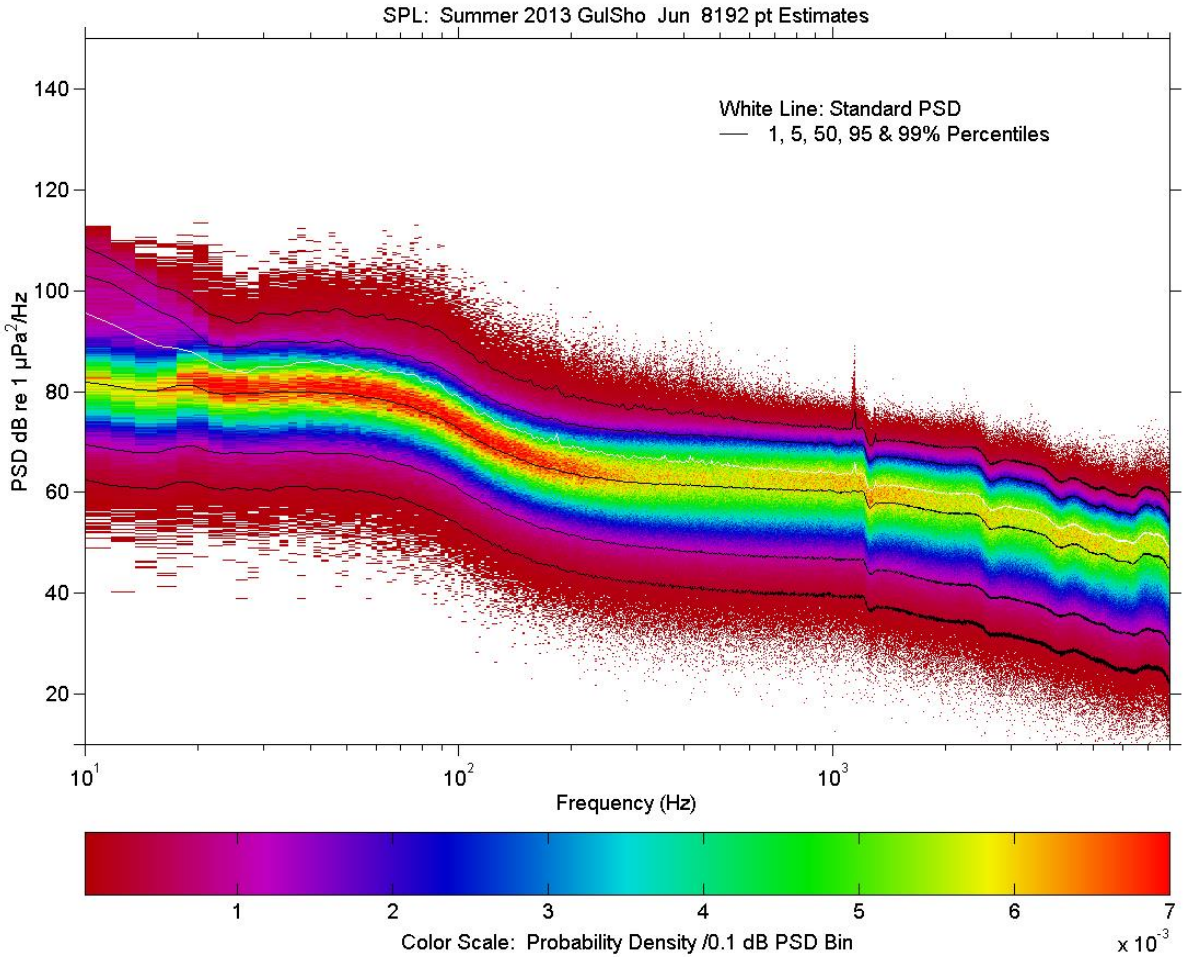


**Figure A4-2-GulSho-2013-Jun.** Medium resolution power spectral density with stats: Standard power spectral density (white), cumulative percentile curves for spectral sub-estimates (black), and PDF distribution of spectral sub-estimates (solid colour).

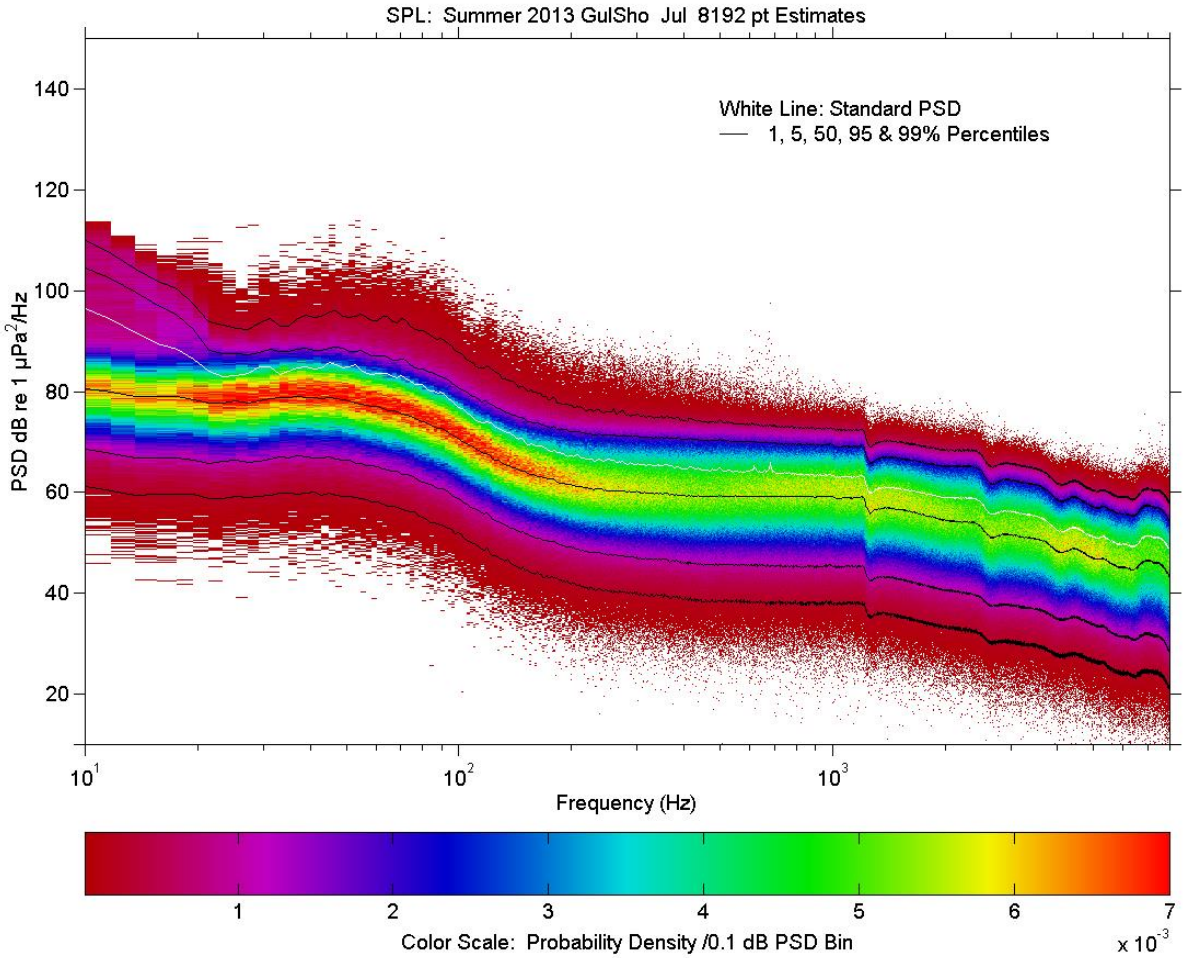


**Figure A4-2-GulSho-2013-Jul.** Medium resolution power spectral density with stats: Standard power spectral density (white), cumulative percentile curves for spectral sub-estimates (black), and PDF distribution of spectral sub-estimates (solid colour).

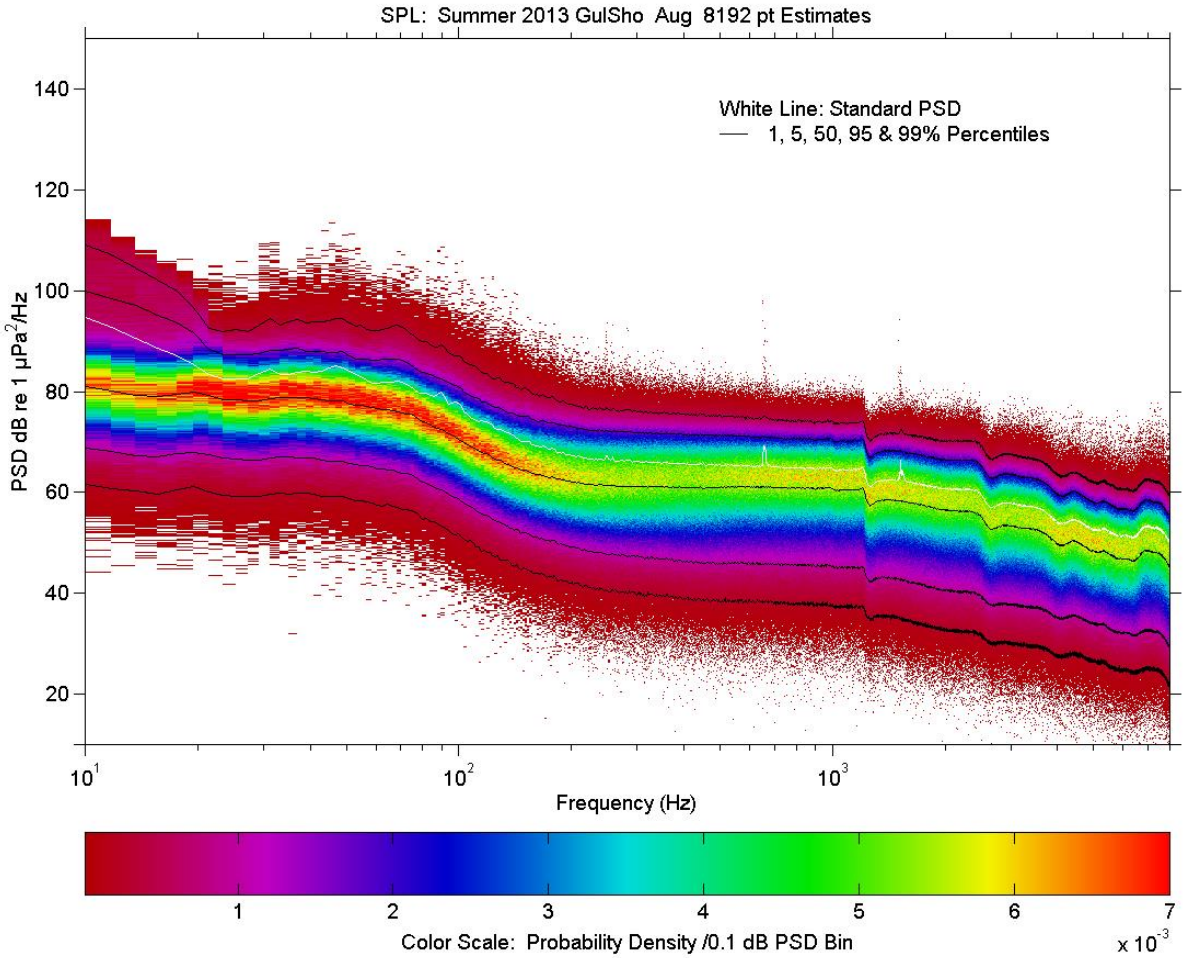


**Figure A4-2-GulSho-2013-Aug.** Medium resolution power spectral density with stats: Standard power spectral density (white), cumulative percentile curves for spectral sub-estimates (black), and PDF distribution of spectral sub-estimates (solid colour).

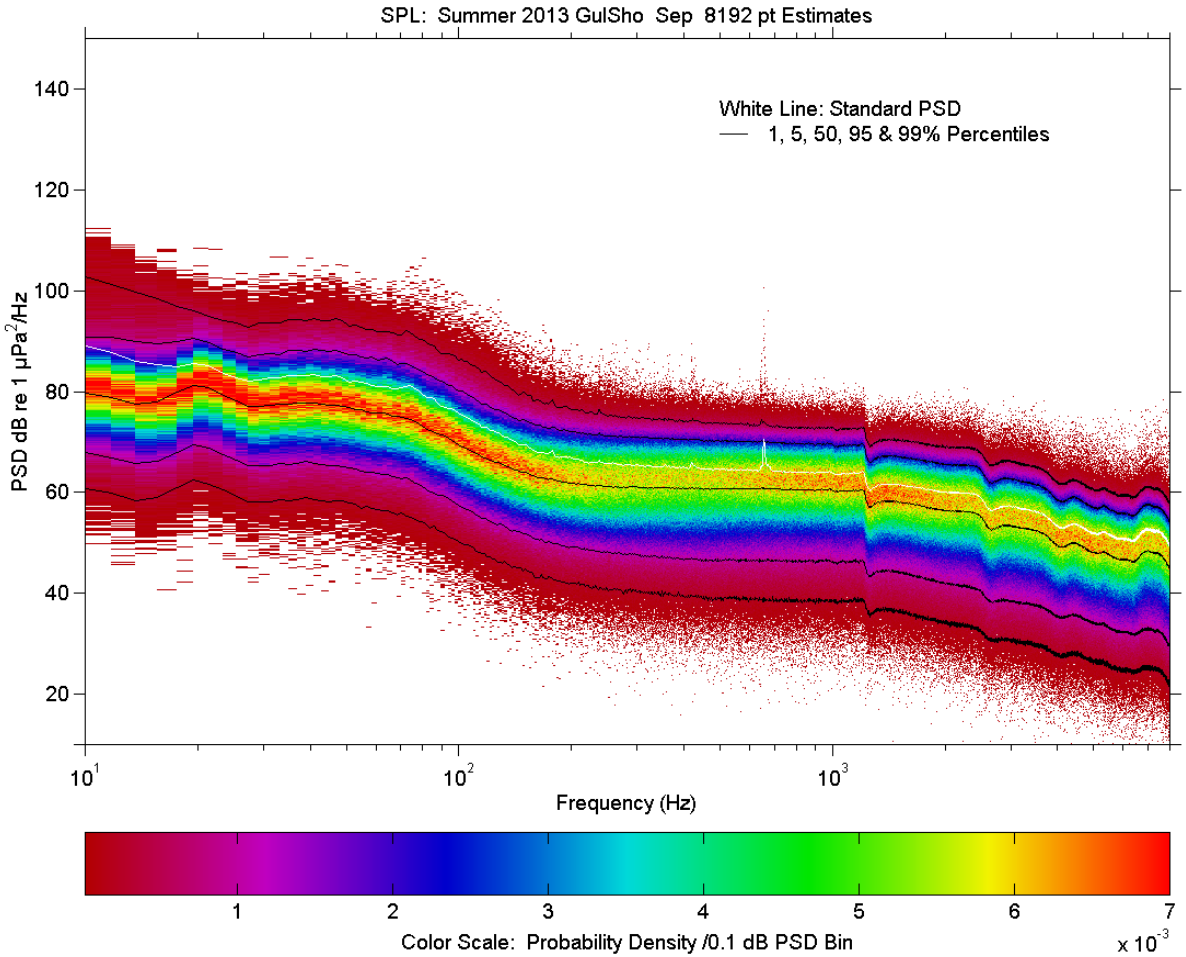


**Figure A4-2-GulSho-2013-Sep.** Medium resolution power spectral density with stats: Standard power spectral density (white), cumulative percentile curves for spectral sub-estimates (black), and PDF distribution of spectral sub-estimates (solid colour).

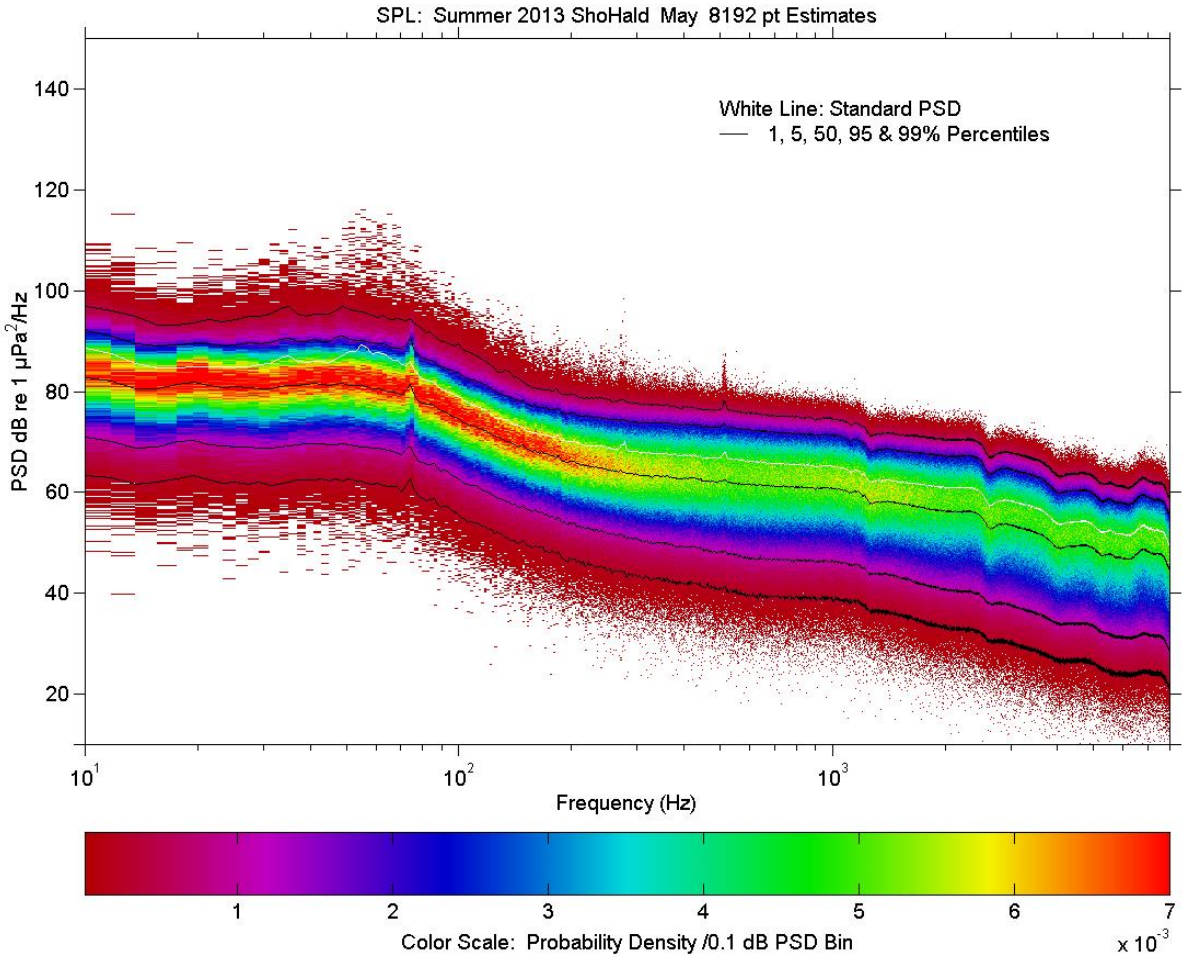


**Figure A4-2-ShoHald-2013-May.** Medium resolution power spectral density with stats: Standard power spectral density (white), cumulative percentile curves for spectral sub-estimates (black), and PDF distribution of spectral sub-estimates (solid colour).

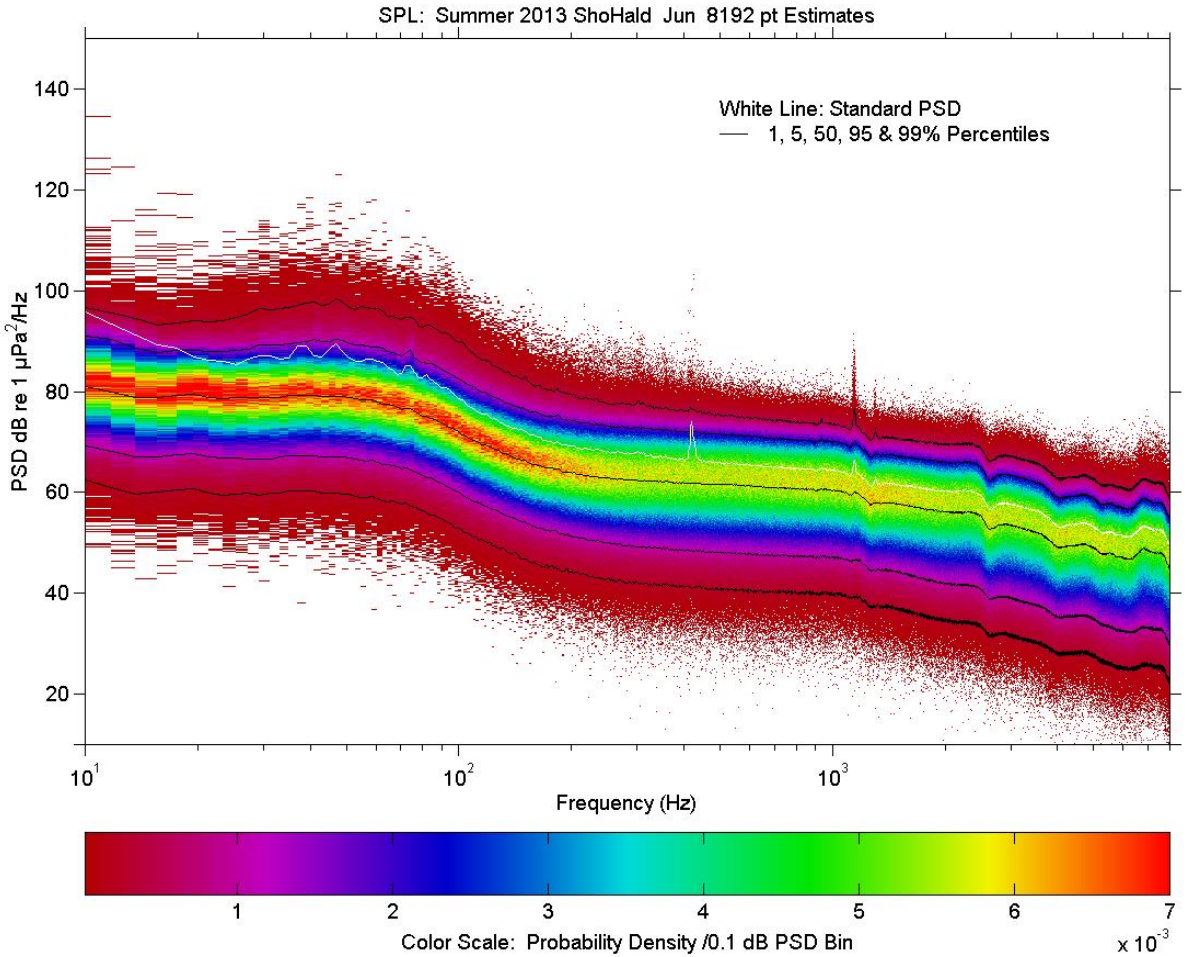


**Figure A4-2-ShoHald-2013-Jun.** Medium resolution power spectral density with stats: Standard power spectral density (white), cumulative percentile curves for spectral sub-estimates (black), and PDF distribution of spectral sub-estimates (solid colour).

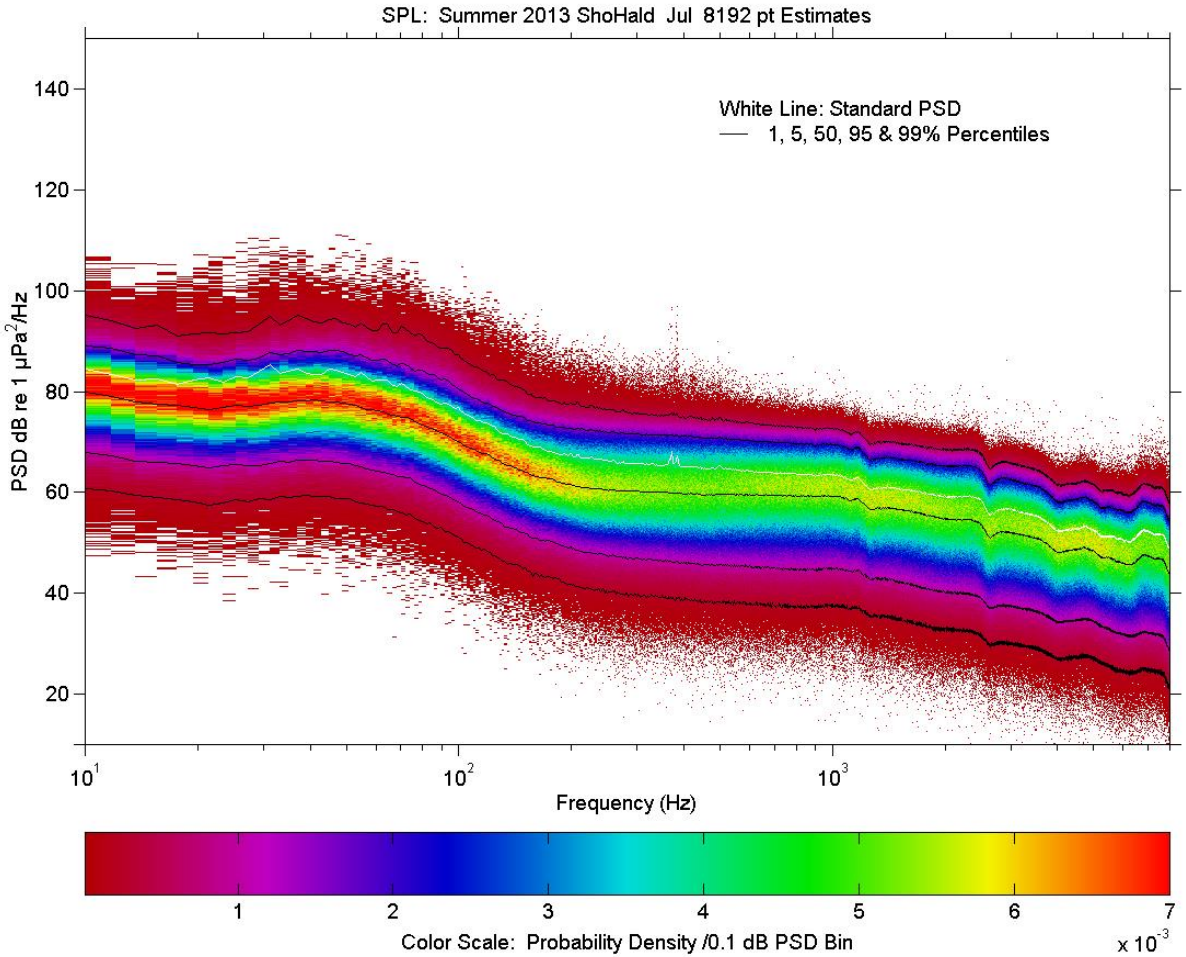


**Figure A4-2-ShoHald-2013-Jul.** Medium resolution power spectral density with stats: Standard power spectral density (white), cumulative percentile curves for spectral sub-estimates (black), and PDF distribution of spectral sub-estimates (solid colour).

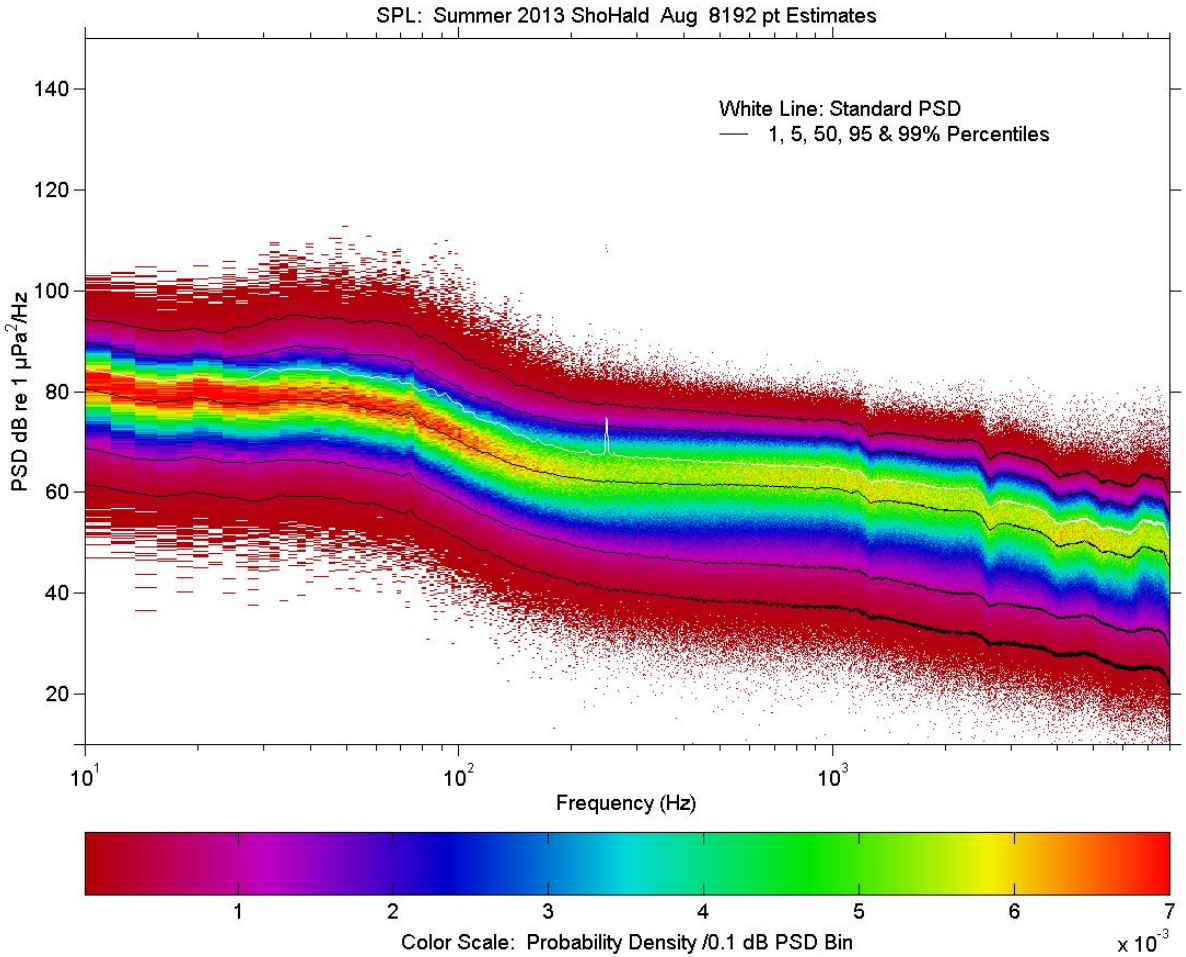


**Figure A4-2-ShoHald-2013-Aug.** Medium resolution power spectral density with stats: Standard power spectral density (white), cumulative percentile curves for spectral sub-estimates (black), and PDF distribution of spectral sub-estimates (solid colour).

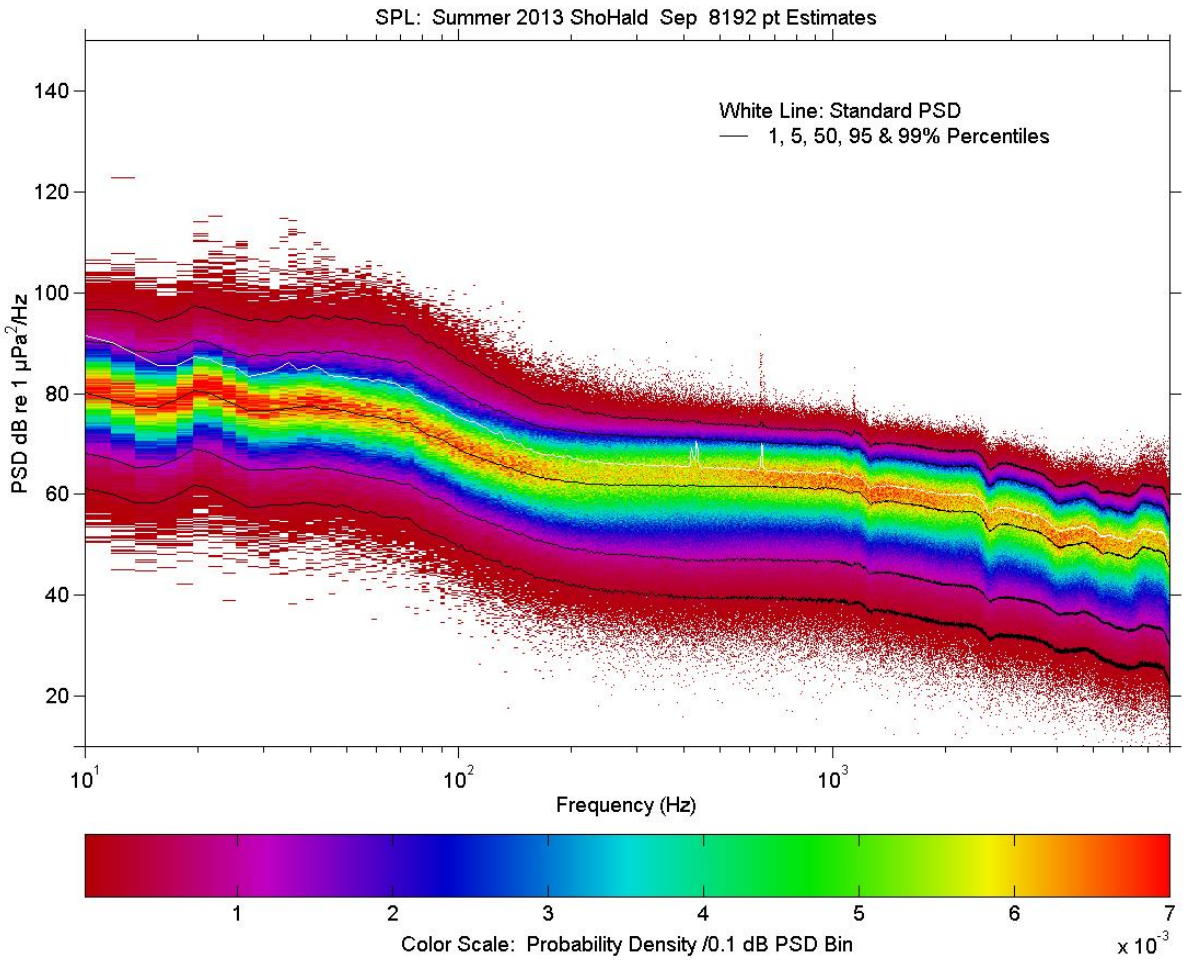


**Figure A4-2-ShoHald-2013-Sep.** Medium resolution power spectral density with stats: Standard power spectral density (white), cumulative percentile curves for spectral sub-estimates (black), and PDF distribution of spectral sub-estimates (solid colour).

### *A4.2.3. Winter 2013-14 Deployments*

**Figure (series) A4-2-Winter 2013-14 Deployments** - Medium resolution power spectral densities with stats: Standard power spectral density, cumulative percentile curves for spectral sub-estimates, and PDF distribution of spectral sub-estimates.

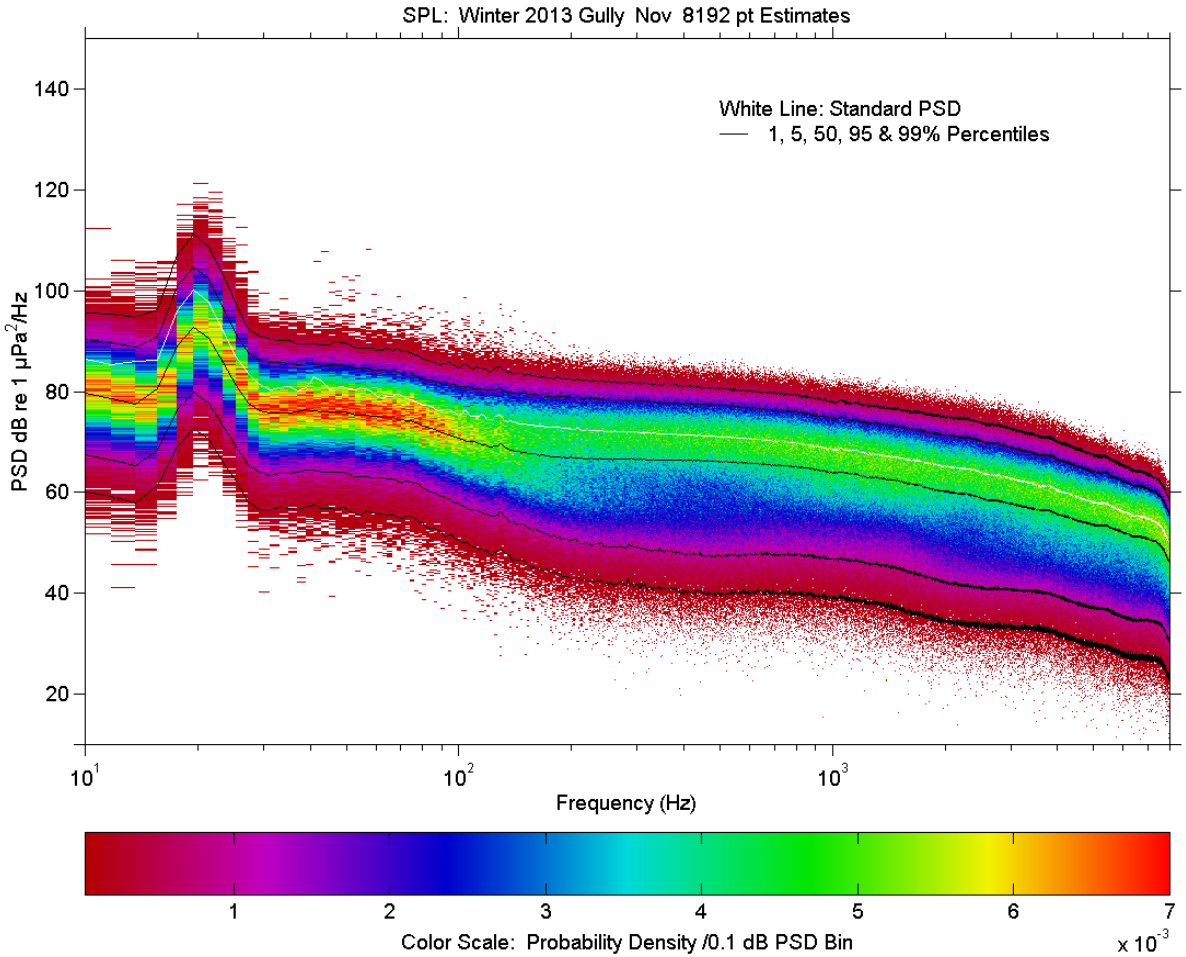


**Figure A4-2-MidGul-2013-Nov.** Medium resolution power spectral density with stats: Standard power spectral density (white), cumulative percentile curves for spectral sub-estimates (black), and PDF distribution of spectral sub-estimates (solid colour).

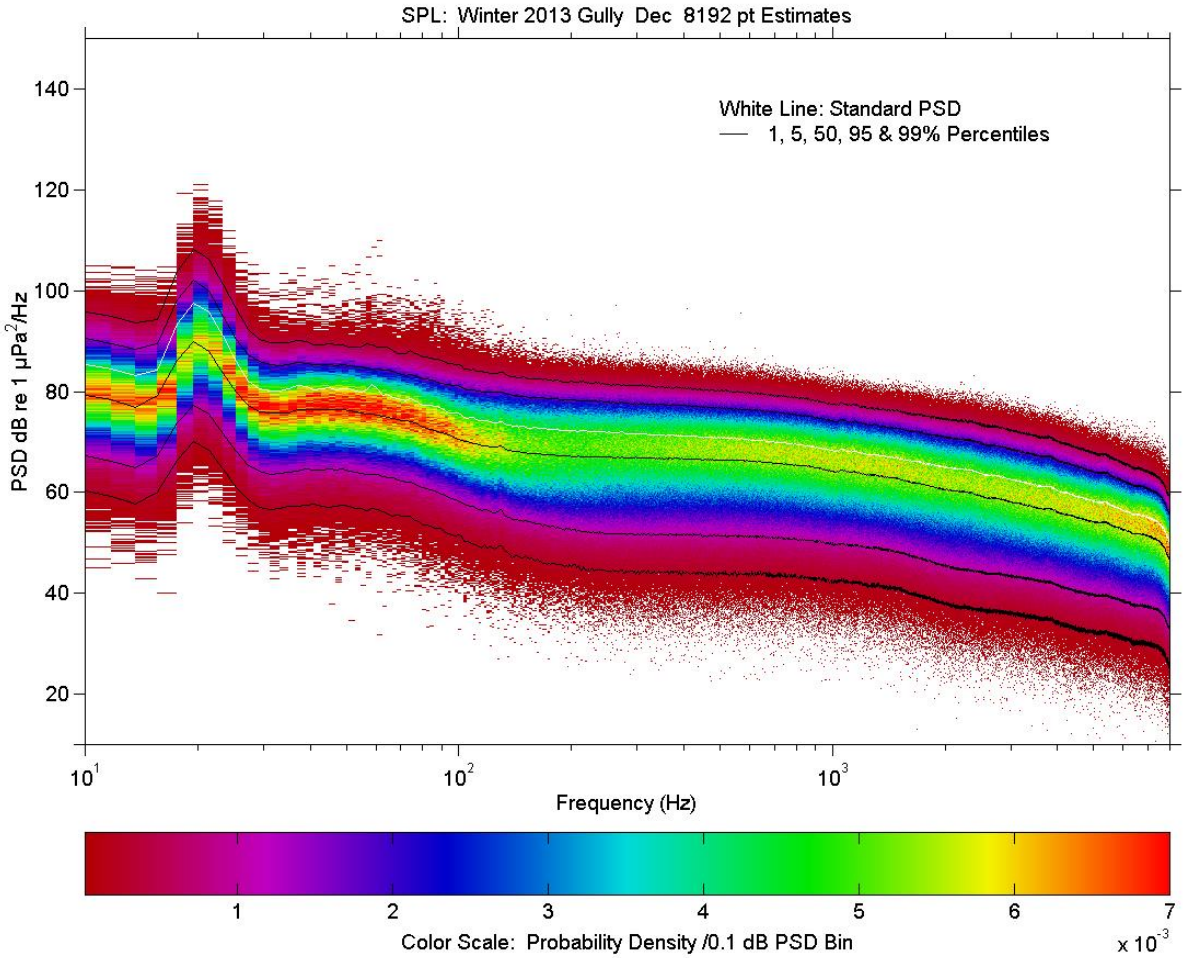


**Figure A4-2-MidGul-2013-Dec.** Medium resolution power spectral density with stats: Standard power spectral density (white), cumulative percentile curves for spectral sub-estimates (black), and PDF distribution of spectral sub-estimates (solid colour).

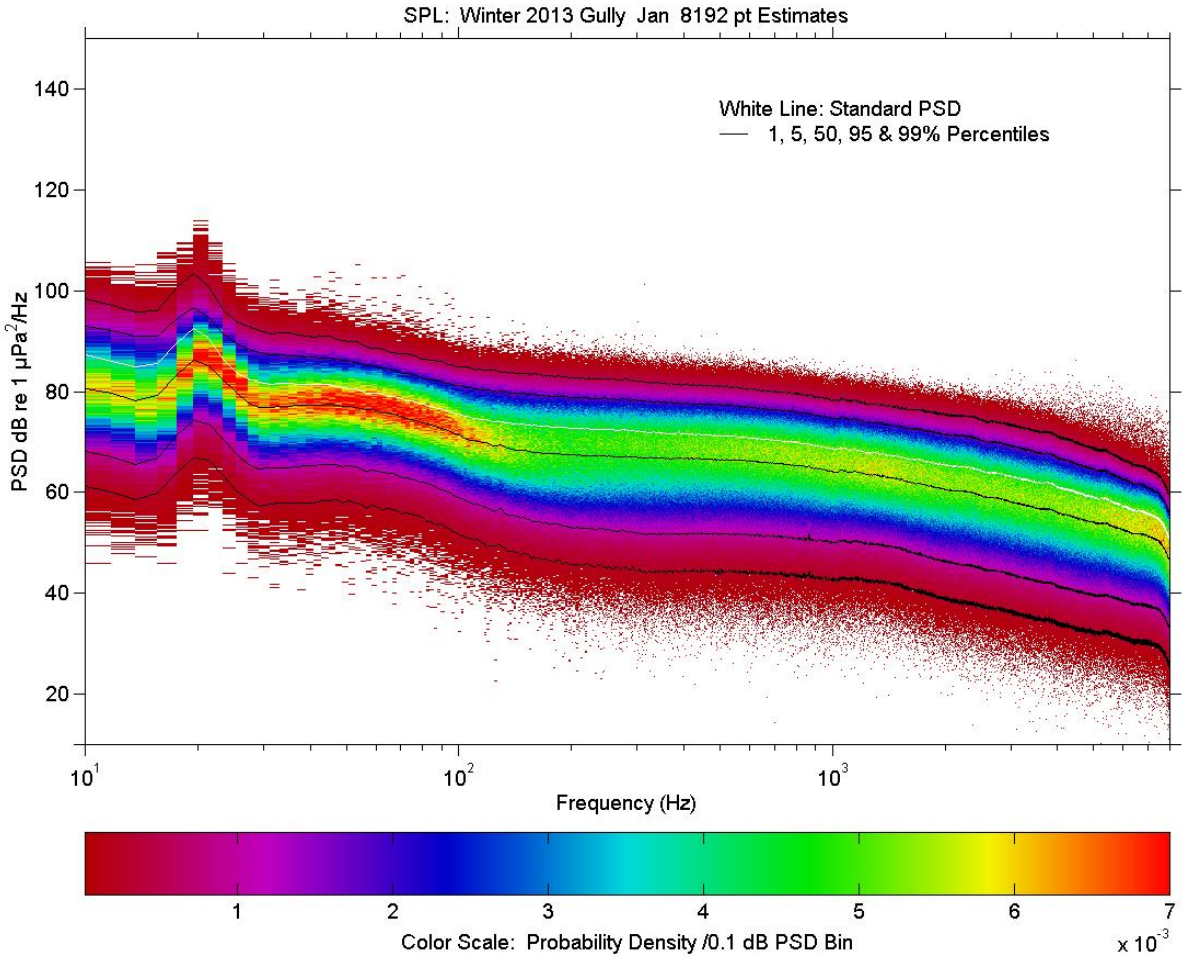


**Figure A4-2-MidGul-2014-Jan.** Medium resolution power spectral density with stats: Standard power spectral density (white), cumulative percentile curves for spectral sub-estimates (black), and PDF distribution of spectral sub-estimates (solid colour).

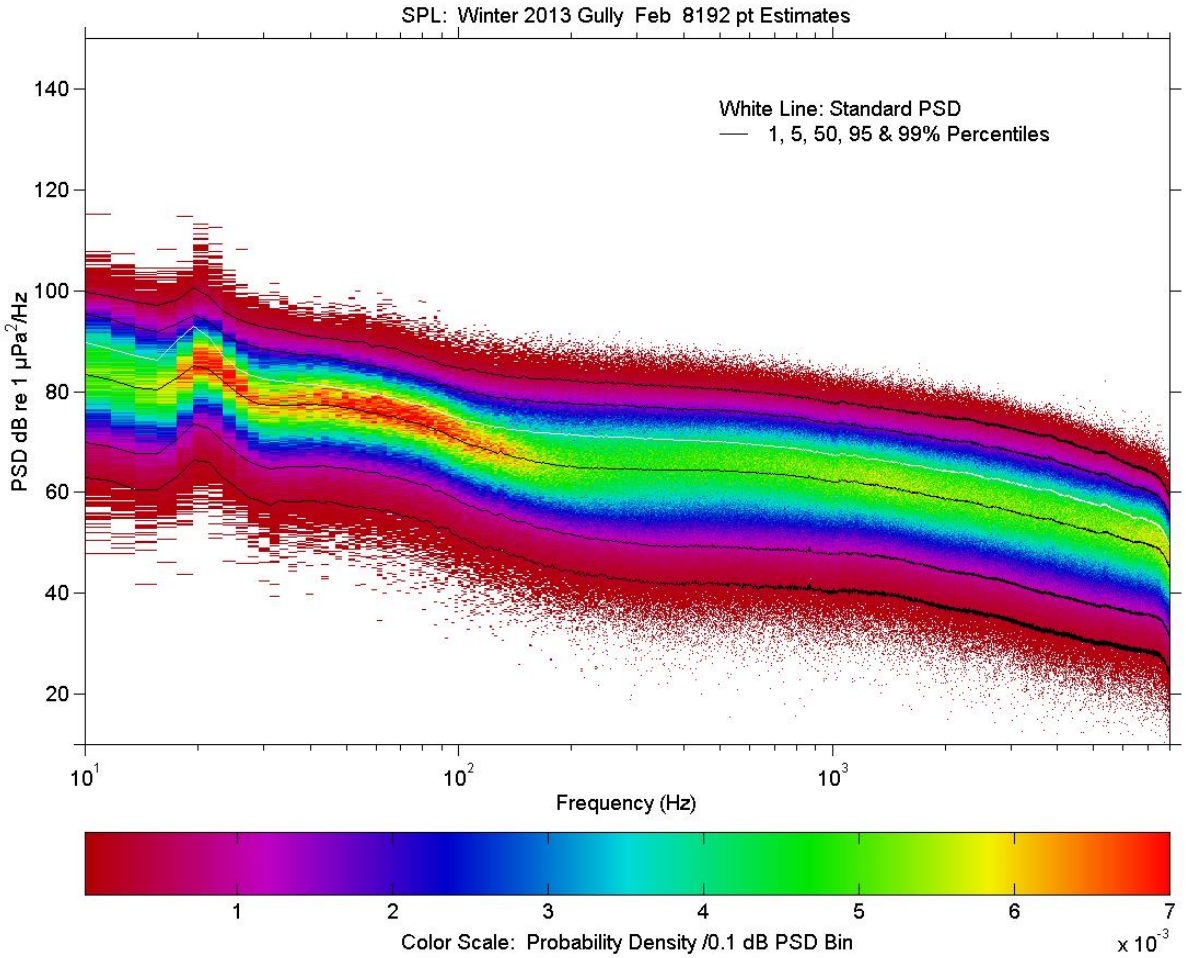


**Figure A4-2-MidGul-2014-Feb.** Medium resolution power spectral density with stats: Standard power spectral density (white), cumulative percentile curves for spectral sub-estimates (black), and PDF distribution of spectral sub-estimates (solid colour).

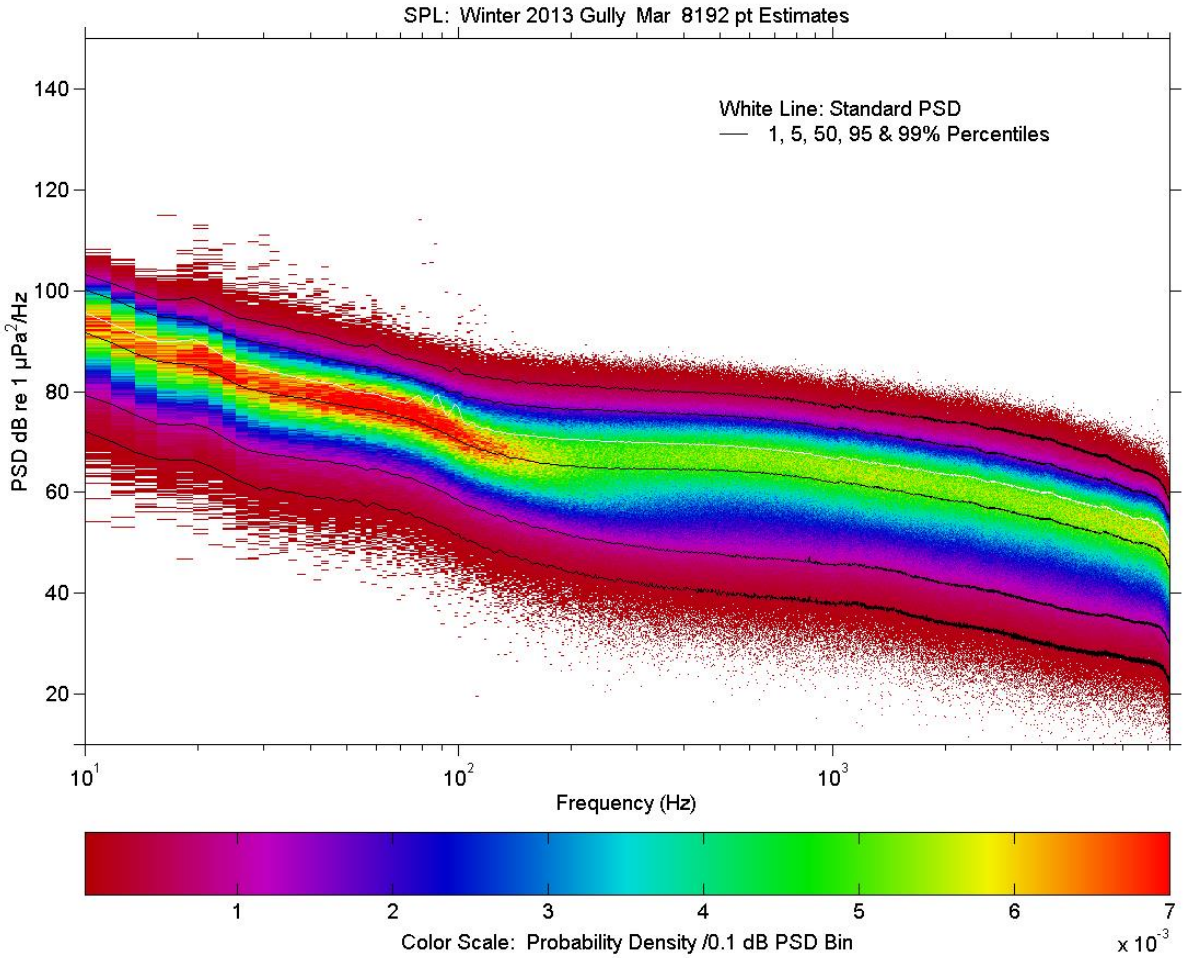


**Figure A4-2-MidGul-2014-Mar.** Medium resolution power spectral density with stats: Standard power spectral density (white), cumulative percentile curves for spectral sub-estimates (black), and PDF distribution of spectral sub-estimates (solid colour).

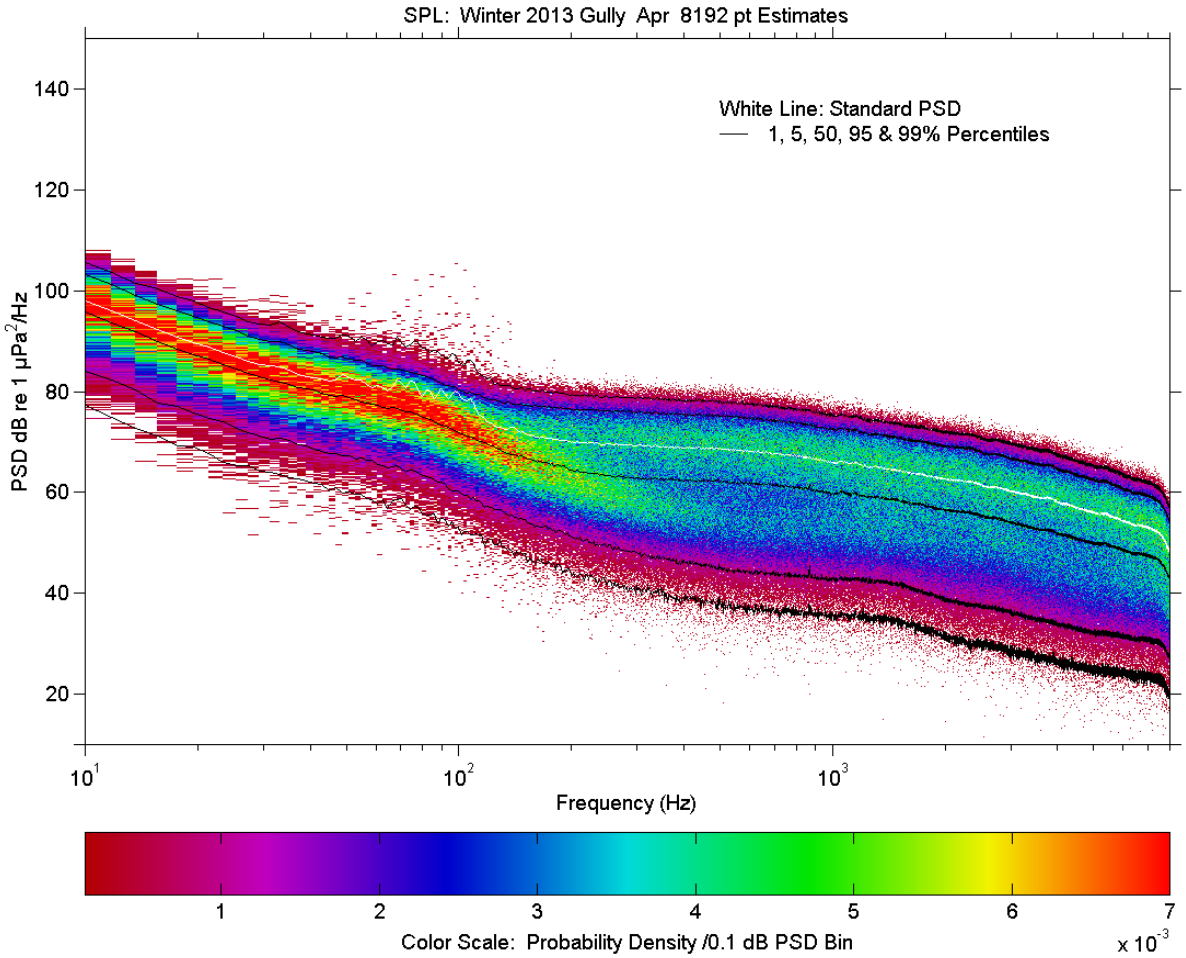


**Figure A4-2-MidGul-2014-Apr.** Medium resolution power spectral density with stats: Standard power spectral density (white), cumulative percentile curves for spectral sub-estimates (black), and PDF distribution of spectral sub-estimates (solid colour).

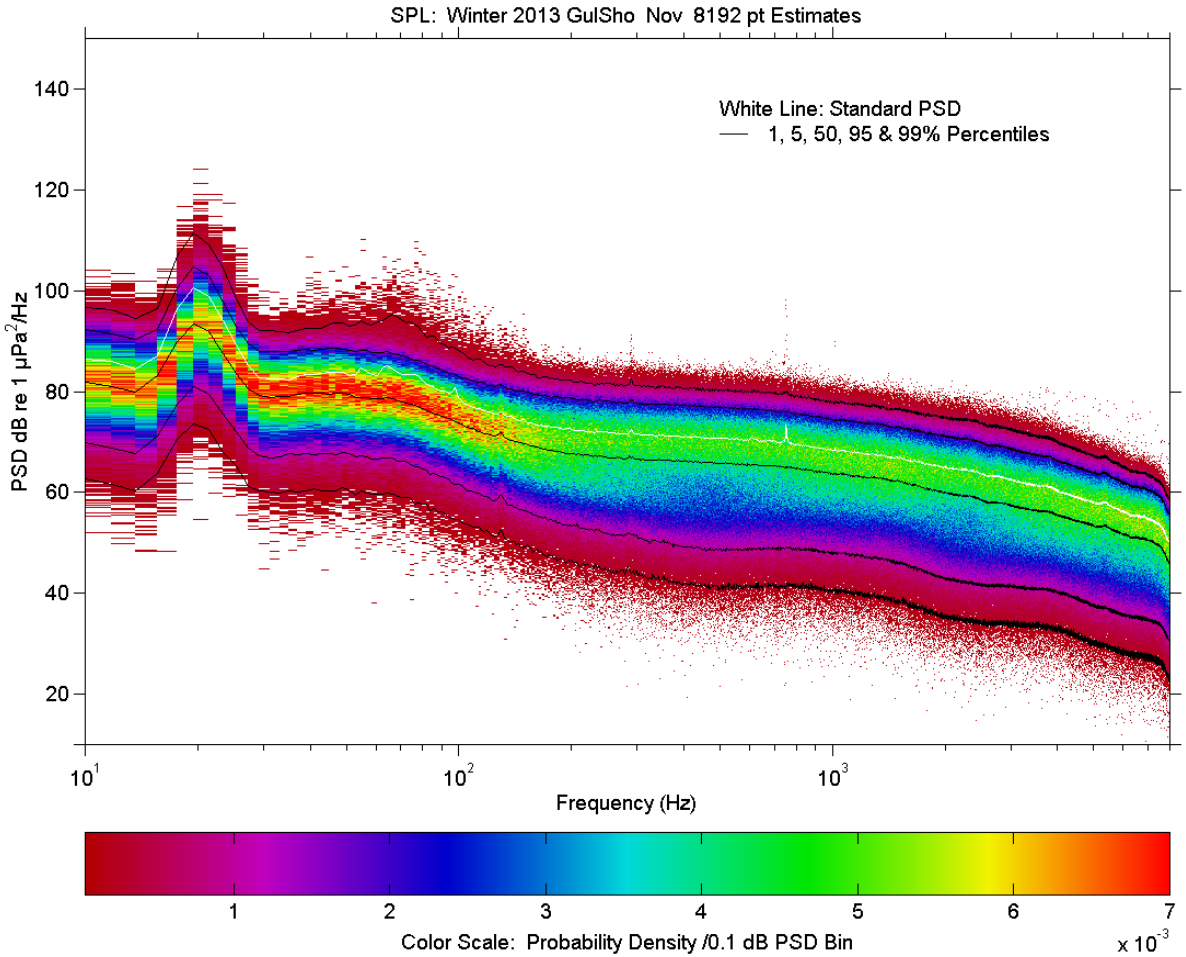


**Figure A4-2-GulSho-2013-Nov.** Medium resolution power spectral density with stats: Standard power spectral density (white), cumulative percentile curves for spectral sub-estimates (black), and PDF distribution of spectral sub-estimates (solid colour).

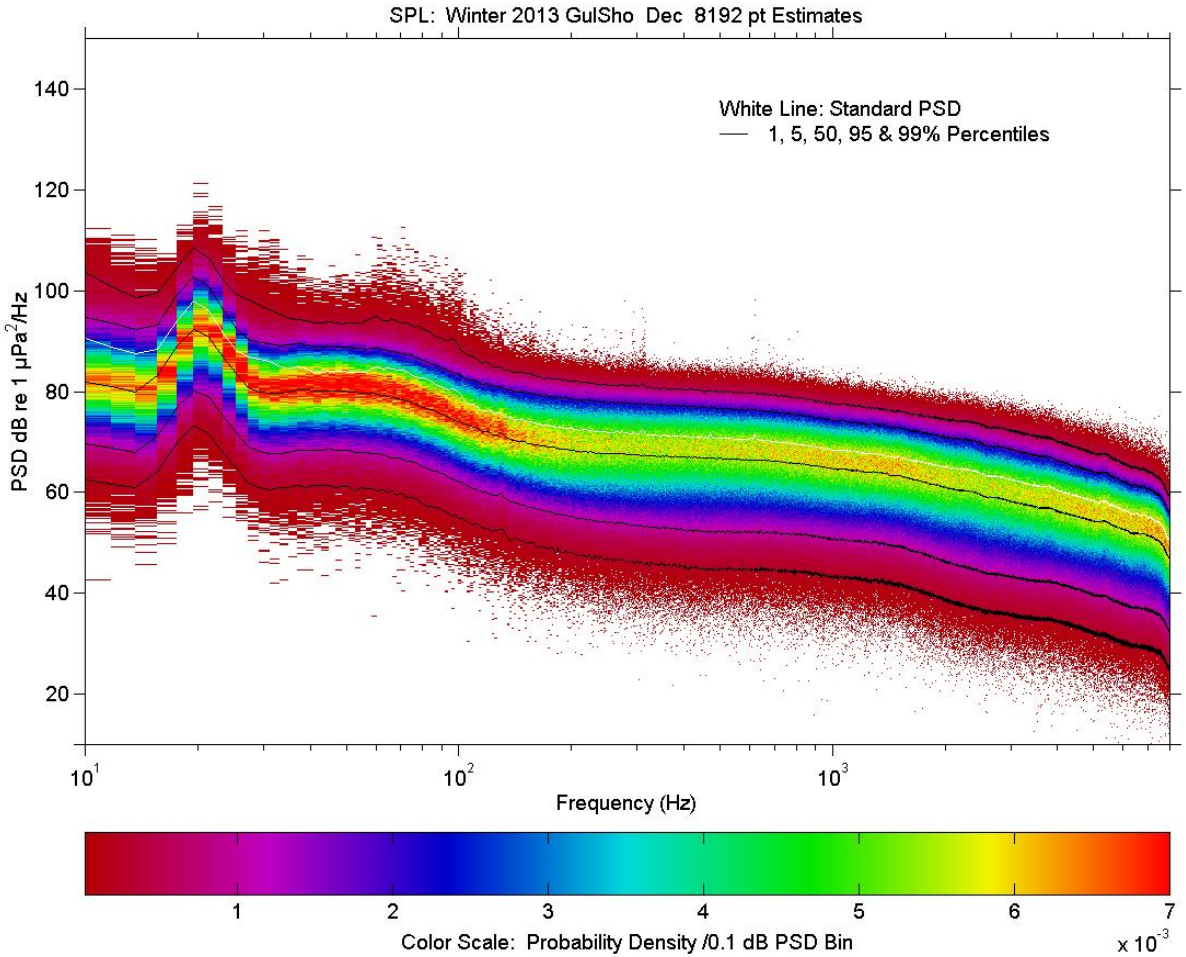


**Figure A4-2-GulSho-2013-Dec.** Medium resolution power spectral density with stats: Standard power spectral density (white), cumulative percentile curves for spectral sub-estimates (black), and PDF distribution of spectral sub-estimates (solid colour).

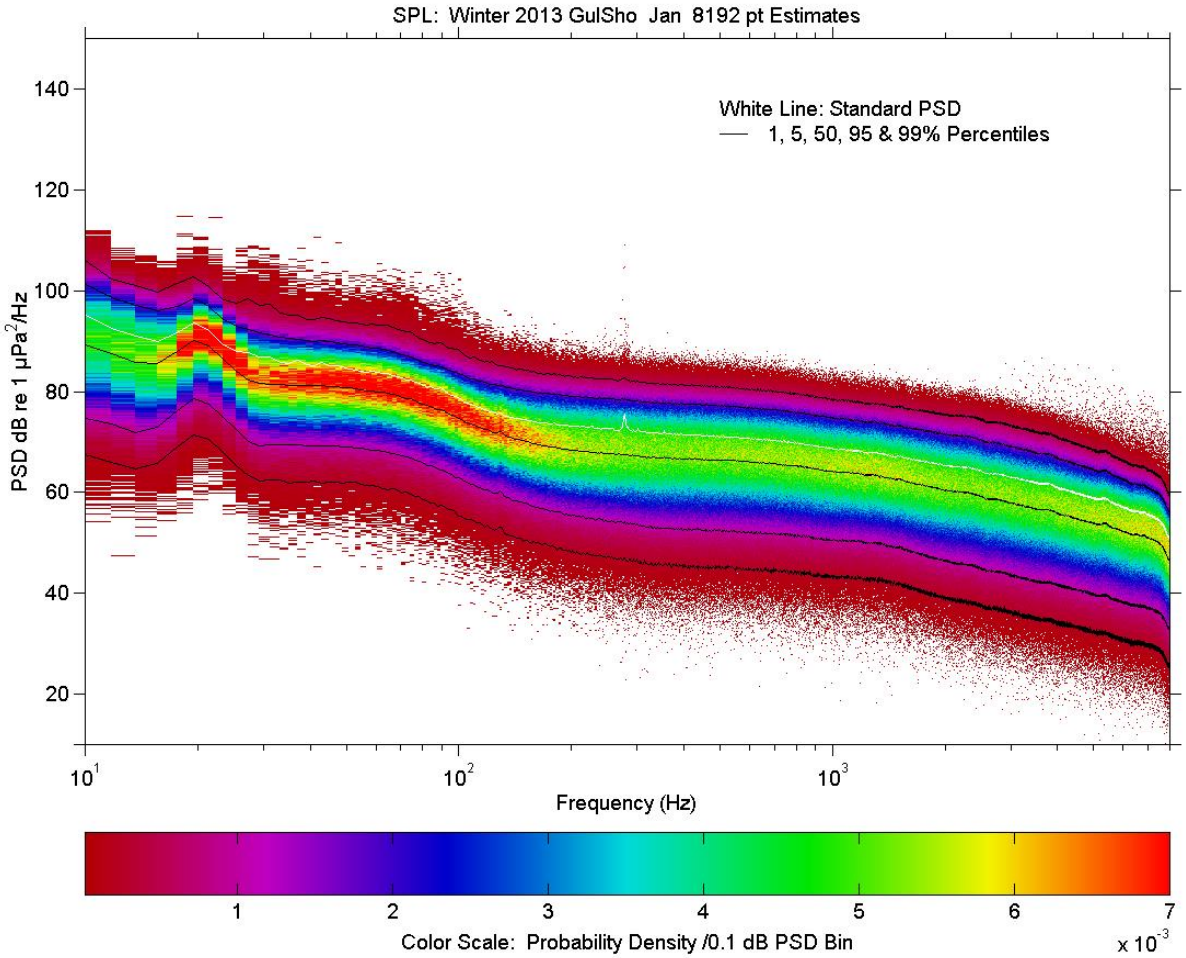


**Figure A4-2-GulSho-2014-Jan.** Medium resolution power spectral density with stats: Standard power spectral density (white), cumulative percentile curves for spectral sub-estimates (black), and PDF distribution of spectral sub-estimates (solid colour).

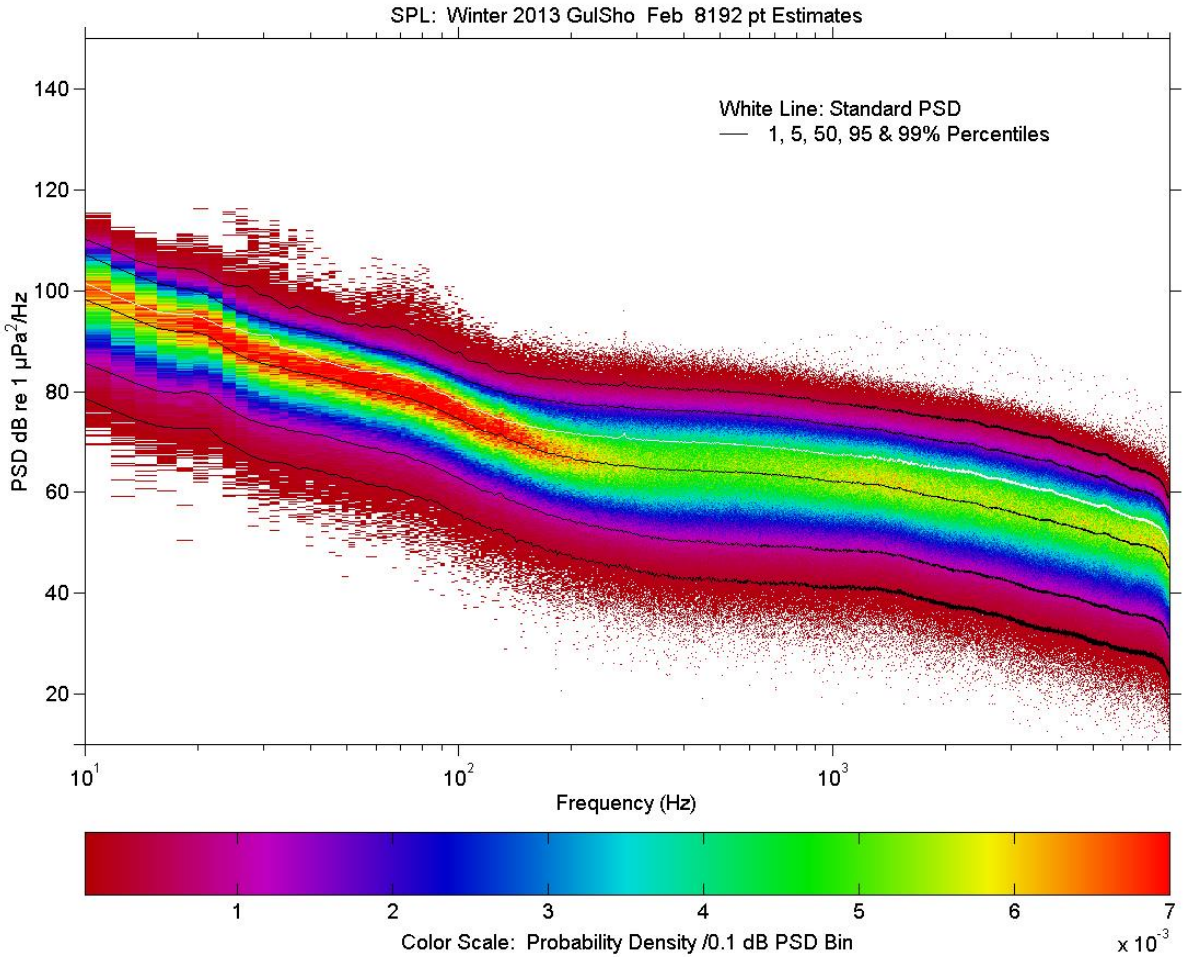


**Figure A4-2-GulSho-2014-Feb.** Medium resolution power spectral density with stats: Standard power spectral density (white), cumulative percentile curves for spectral sub-estimates (black), and PDF distribution of spectral sub-estimates (solid colour).

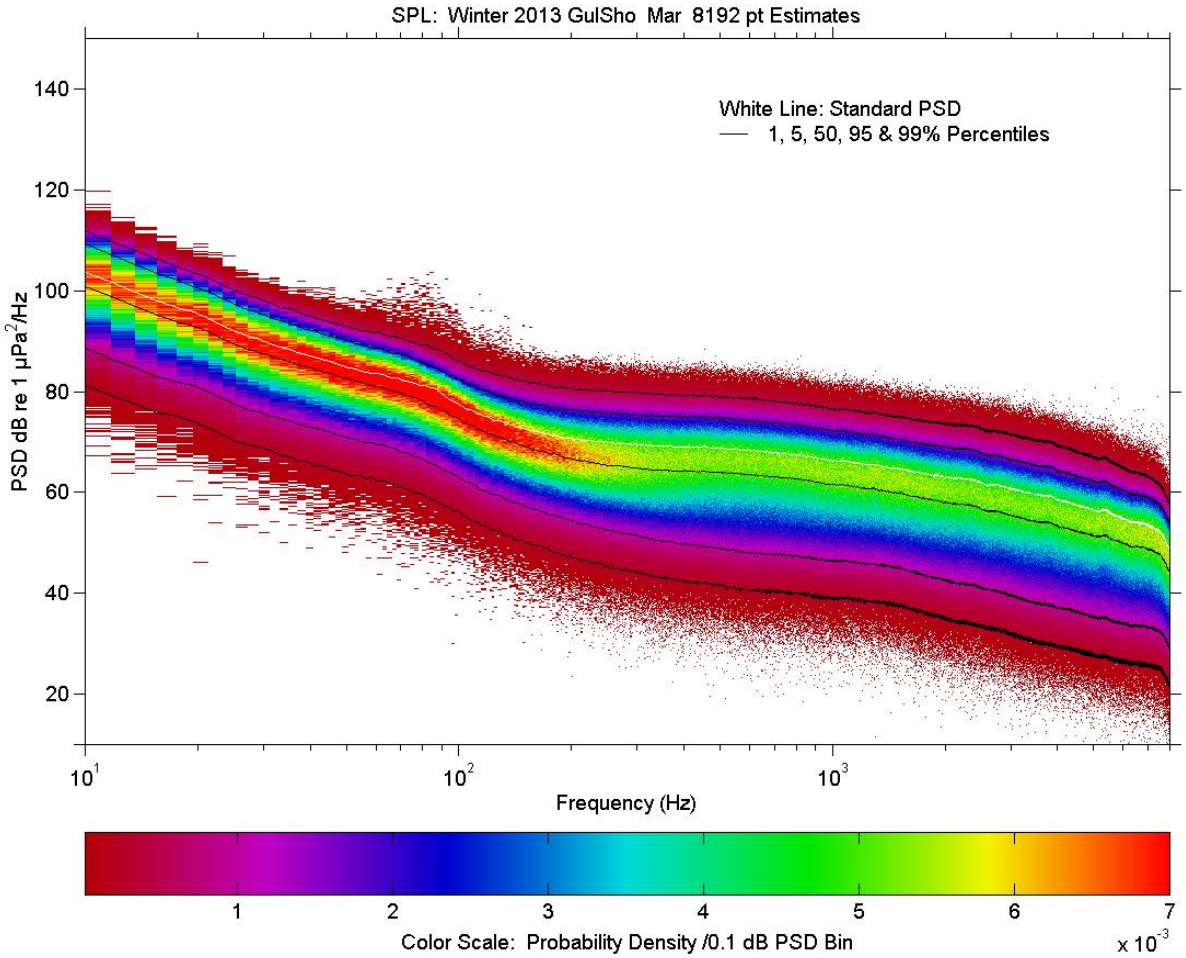


**Figure A4-2-GulSho-2014-Mar.** Medium resolution power spectral density with stats: Standard power spectral density (white), cumulative percentile curves for spectral sub-estimates (black), and PDF distribution of spectral sub-estimates (solid colour).

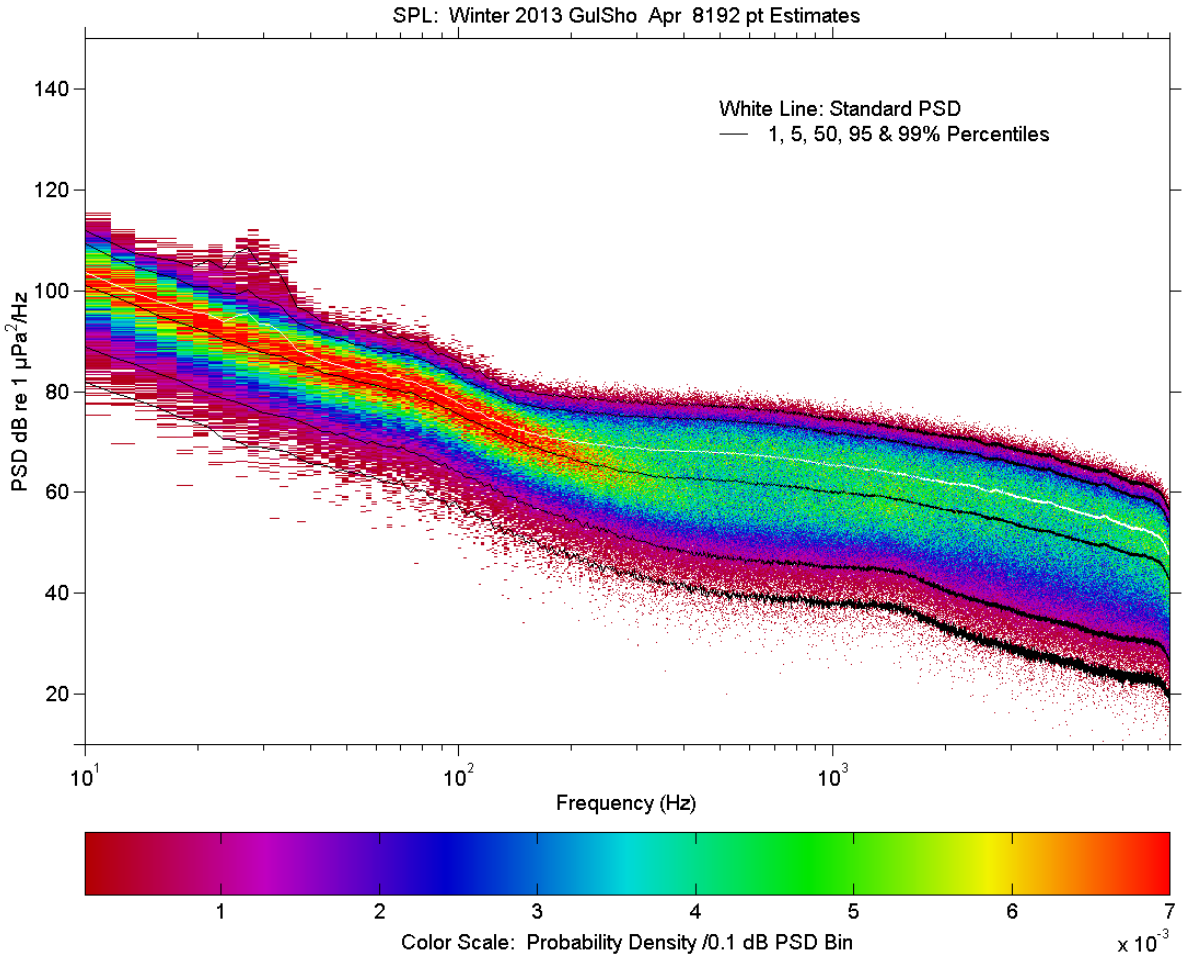


**Figure A4-2-GulSho-2014-Apr.** Medium resolution power spectral density with stats: Standard power spectral density (white), cumulative percentile curves for spectral sub-estimates (black), and PDF distribution of spectral sub-estimates (solid colour).

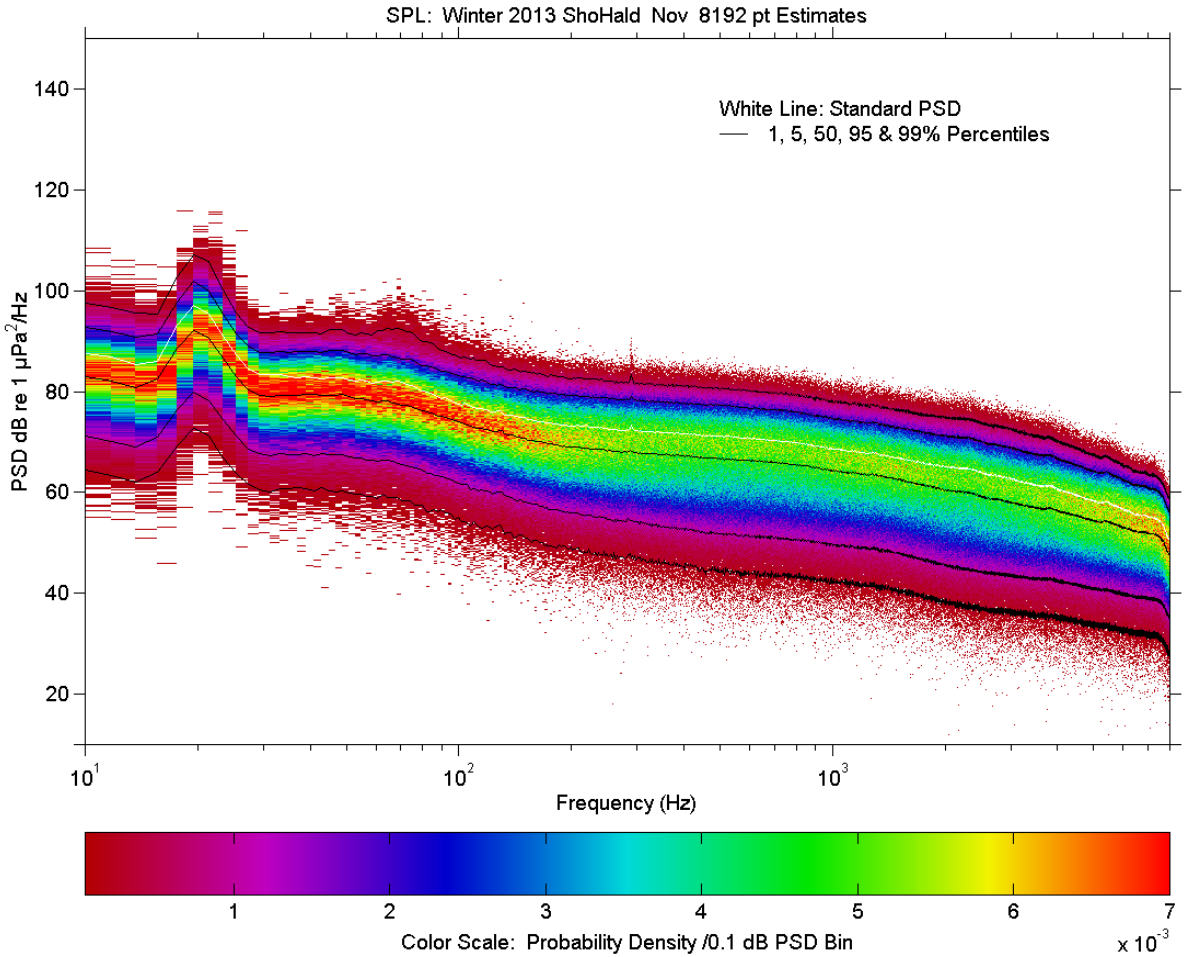


**Figure A4-2-ShoHald-2013-Nov.** Medium resolution power spectral density with stats: Standard power spectral density (white), cumulative percentile curves for spectral sub-estimates (black), and PDF distribution of spectral sub-estimates (solid colour).

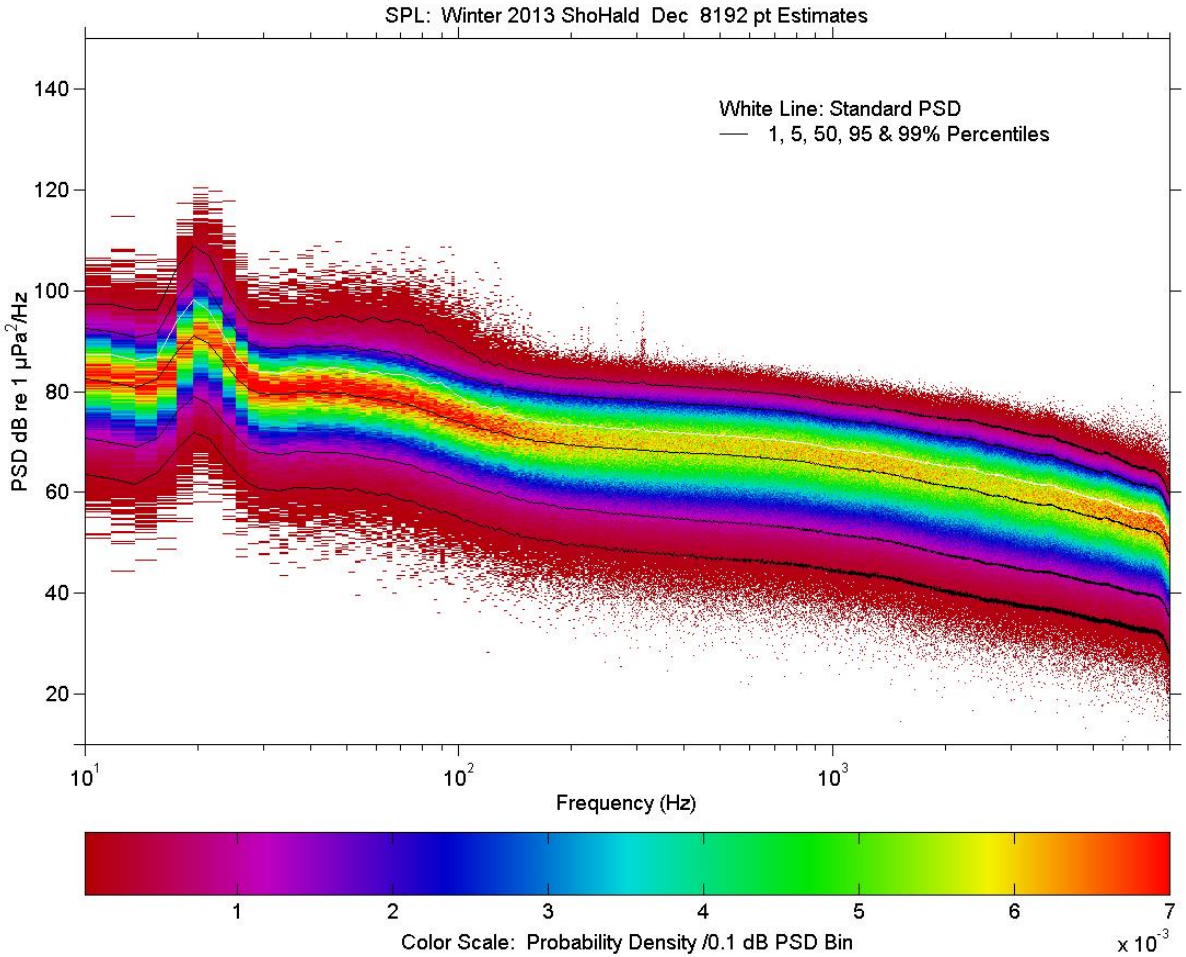


**Figure A4-2-ShoHald-2013-Dec.** Medium resolution power spectral density with stats: Standard power spectral density (white), cumulative percentile curves for spectral sub-estimates (black), and PDF distribution of spectral sub-estimates (solid colour).

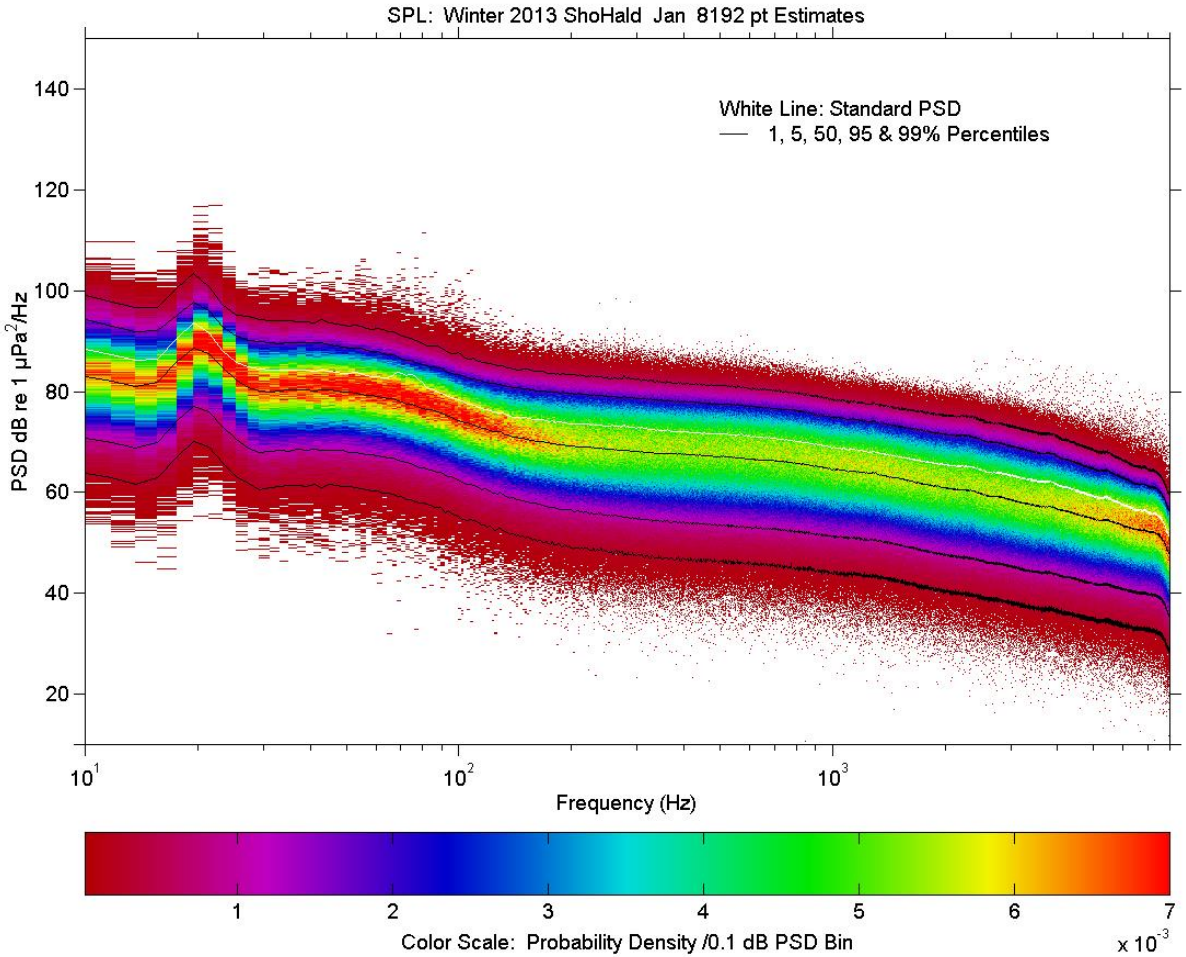


**Figure A4-2-ShoHald-2014-Jan.** Medium resolution power spectral density with stats: Standard power spectral density (white), cumulative percentile curves for spectral sub-estimates (black), and PDF distribution of spectral sub-estimates (solid colour).

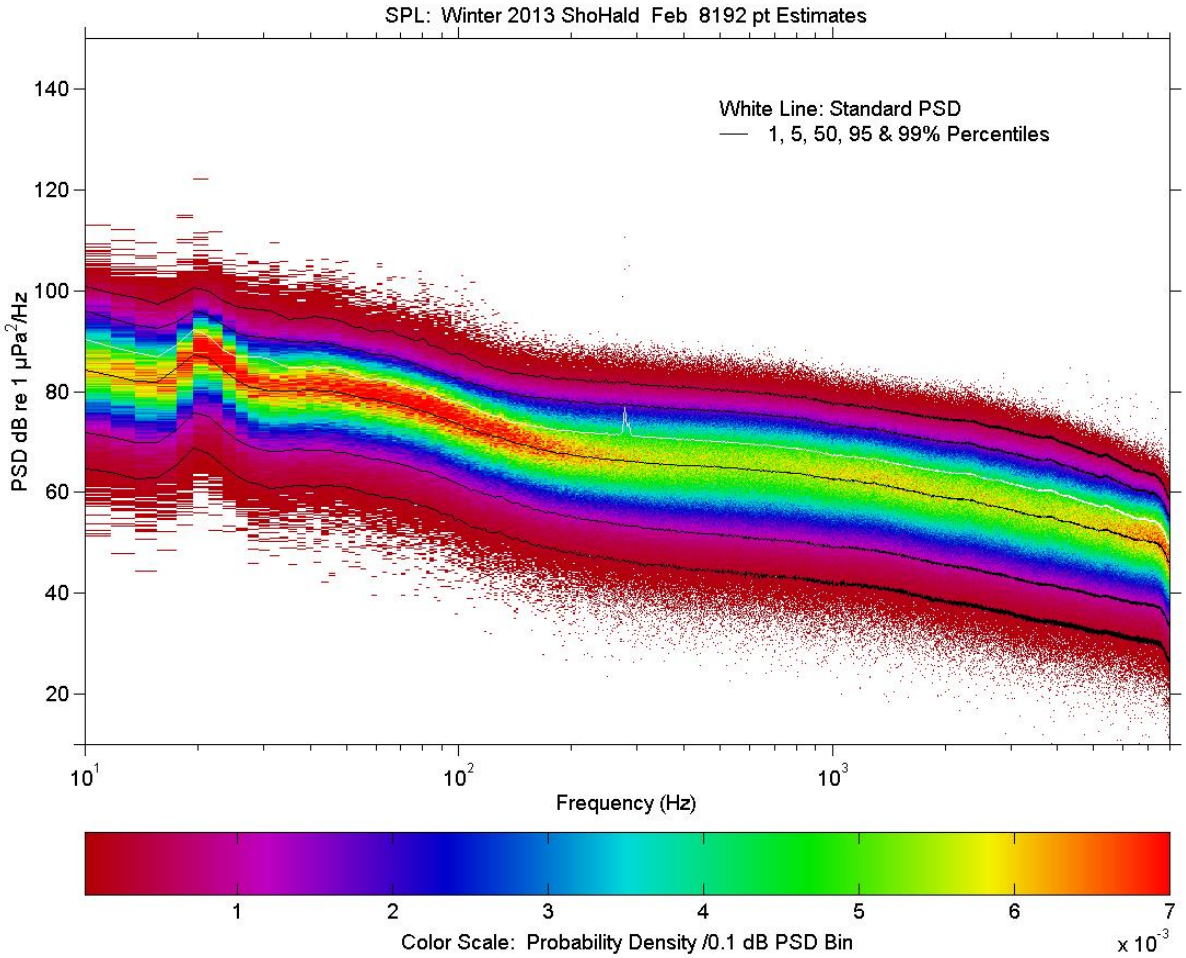


**Figure A4-2-ShoHald-2014-Feb.** Medium resolution power spectral density with stats: Standard power spectral density (white), cumulative percentile curves for spectral sub-estimates (black), and PDF distribution of spectral sub-estimates (solid colour).

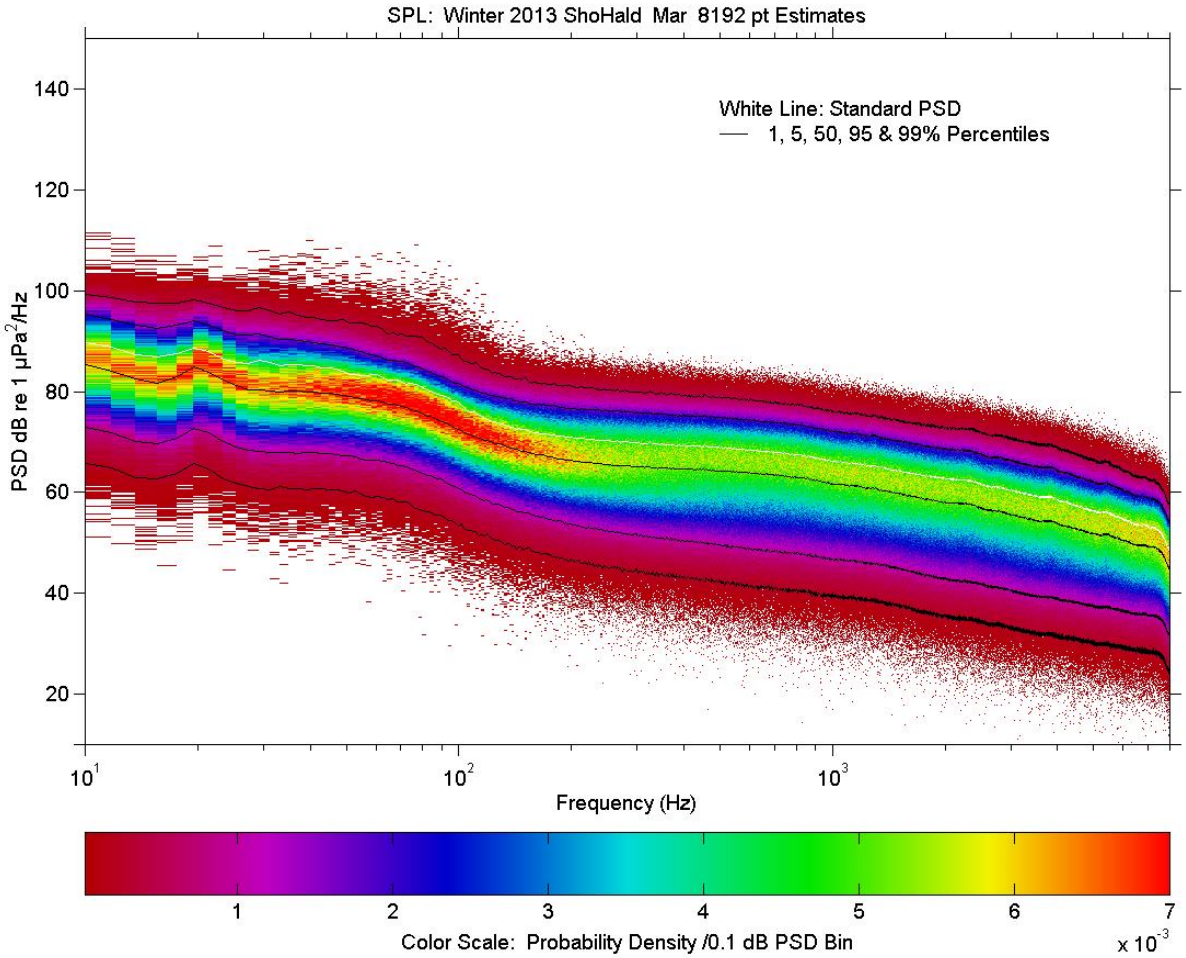


**Figure A4-2-ShoHald-2014-Mar.** Medium resolution power spectral density with stats: Standard power spectral density (white), cumulative percentile curves for spectral sub-estimates (black), and PDF distribution of spectral sub-estimates (solid colour).

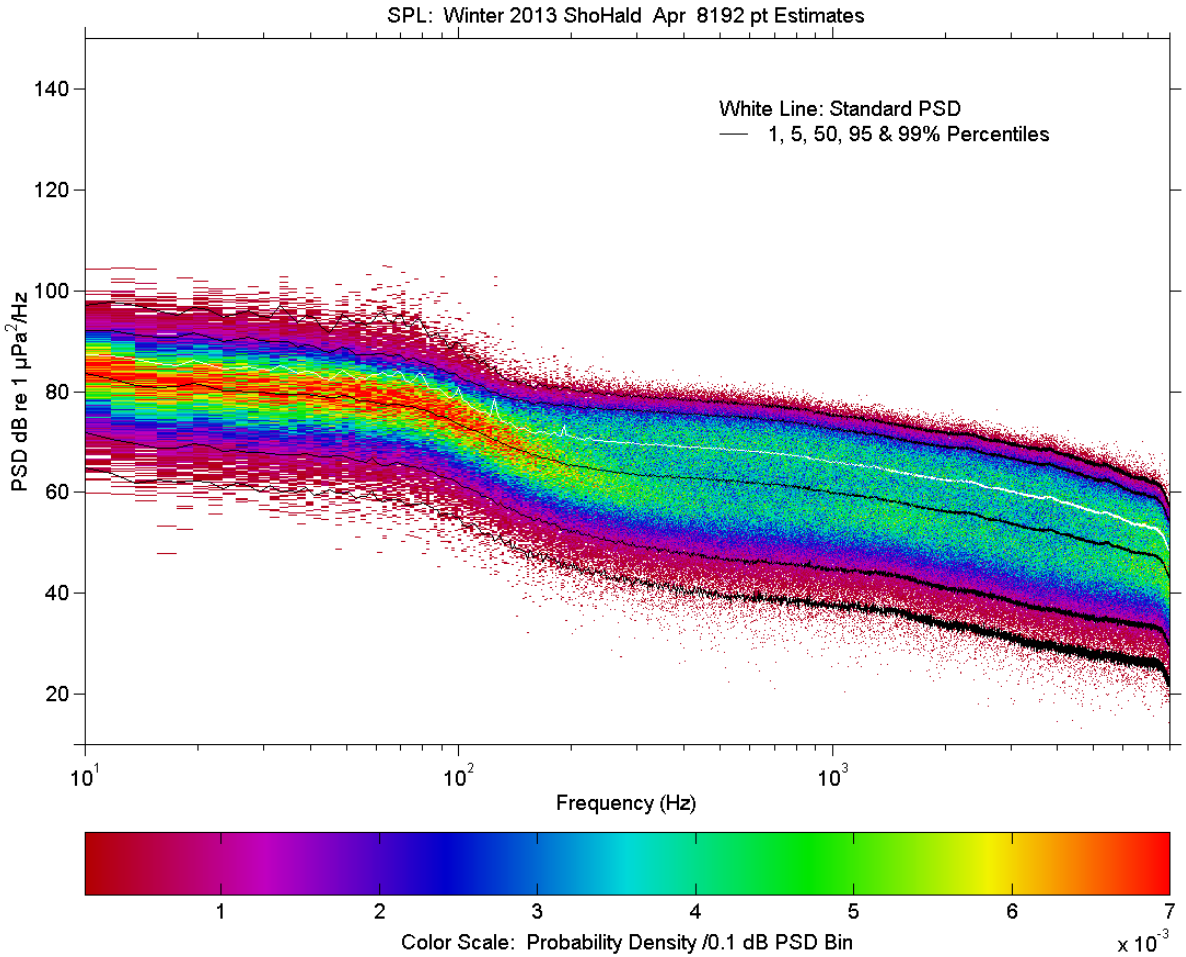


**Figure A4-2-ShoHald-2014-Apr.** Medium resolution power spectral density with stats: Standard power spectral density (white), cumulative percentile curves for spectral sub-estimates (black), and PDF distribution of spectral sub-estimates (solid colour).

### *A4.2.4. Summer 2014 Deployments*

**Figure (series) A4-2–Summer 2014 Deployments** - Medium resolution power spectral densities with stats: Standard power spectral density, cumulative percentile curves for spectral sub-estimates, and PDF distribution of spectral sub-estimates.

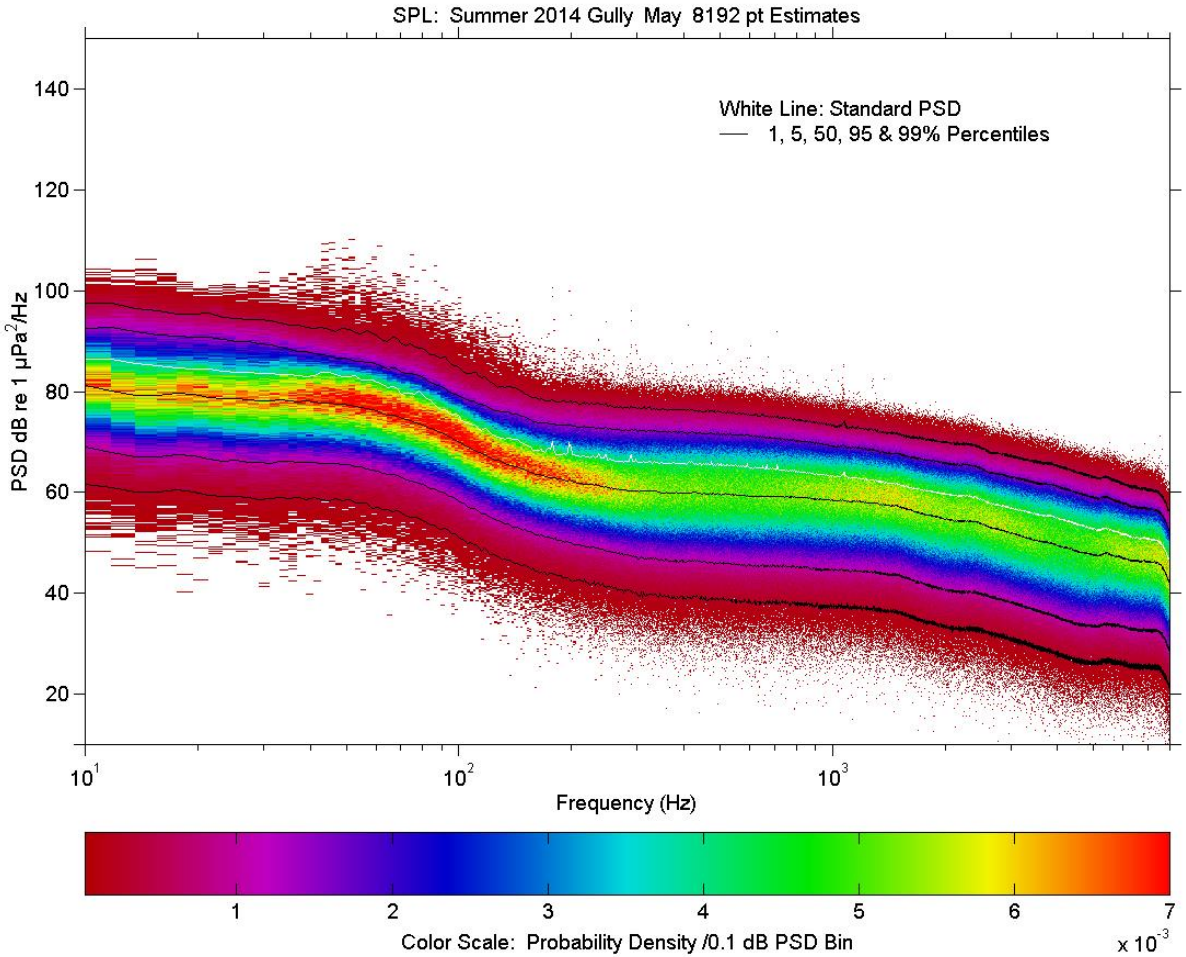


**Figure A4-2-MidGul-2014-May.** Medium resolution power spectral density with stats: Standard power spectral density (white), cumulative percentile curves for spectral sub-estimates (black), and PDF distribution of spectral sub-estimates (solid colour).

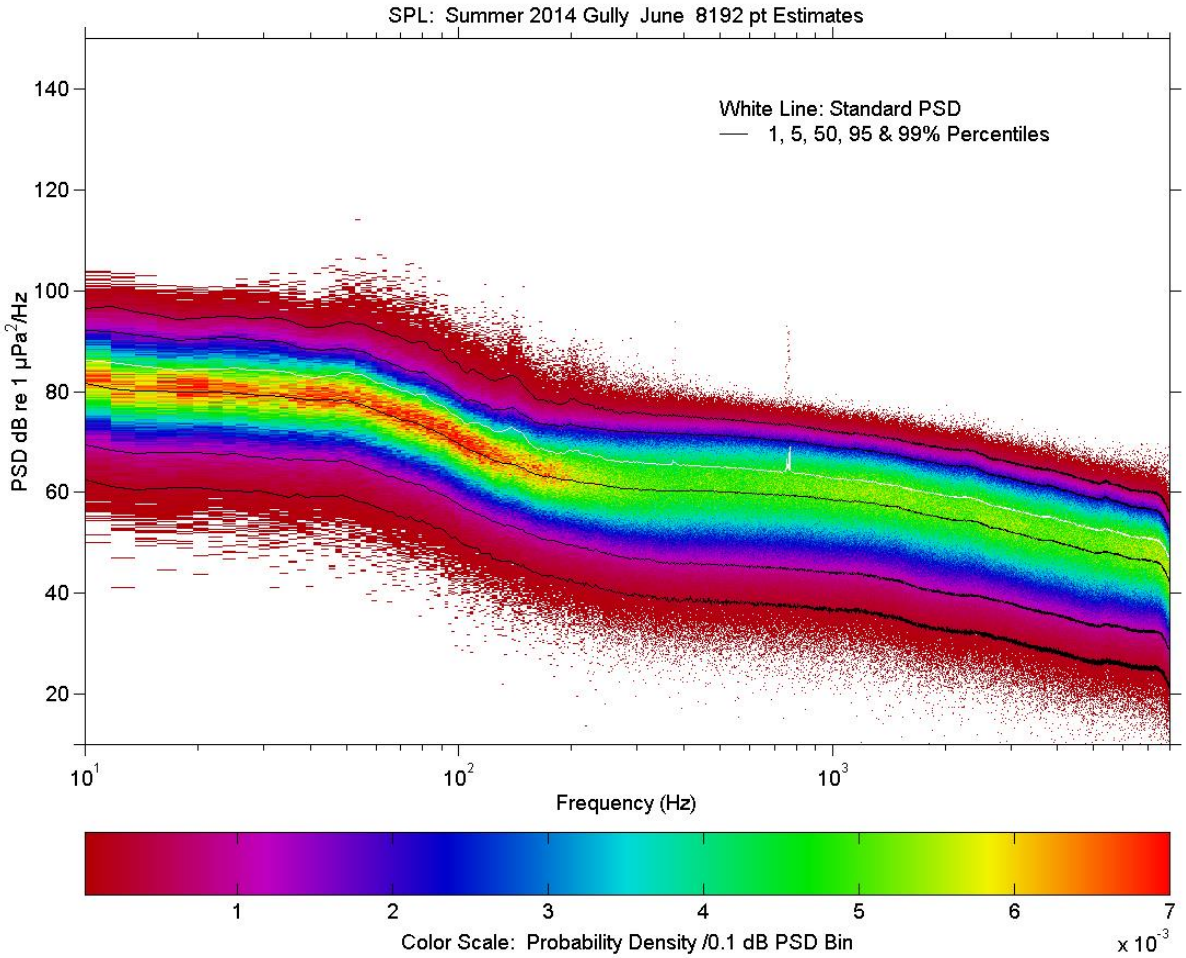


**Figure A4-2-MidGul-2014-Jun.** Medium resolution power spectral density with stats: Standard power spectral density (white), cumulative percentile curves for spectral sub-estimates (black), and PDF distribution of spectral sub-estimates (solid colour).

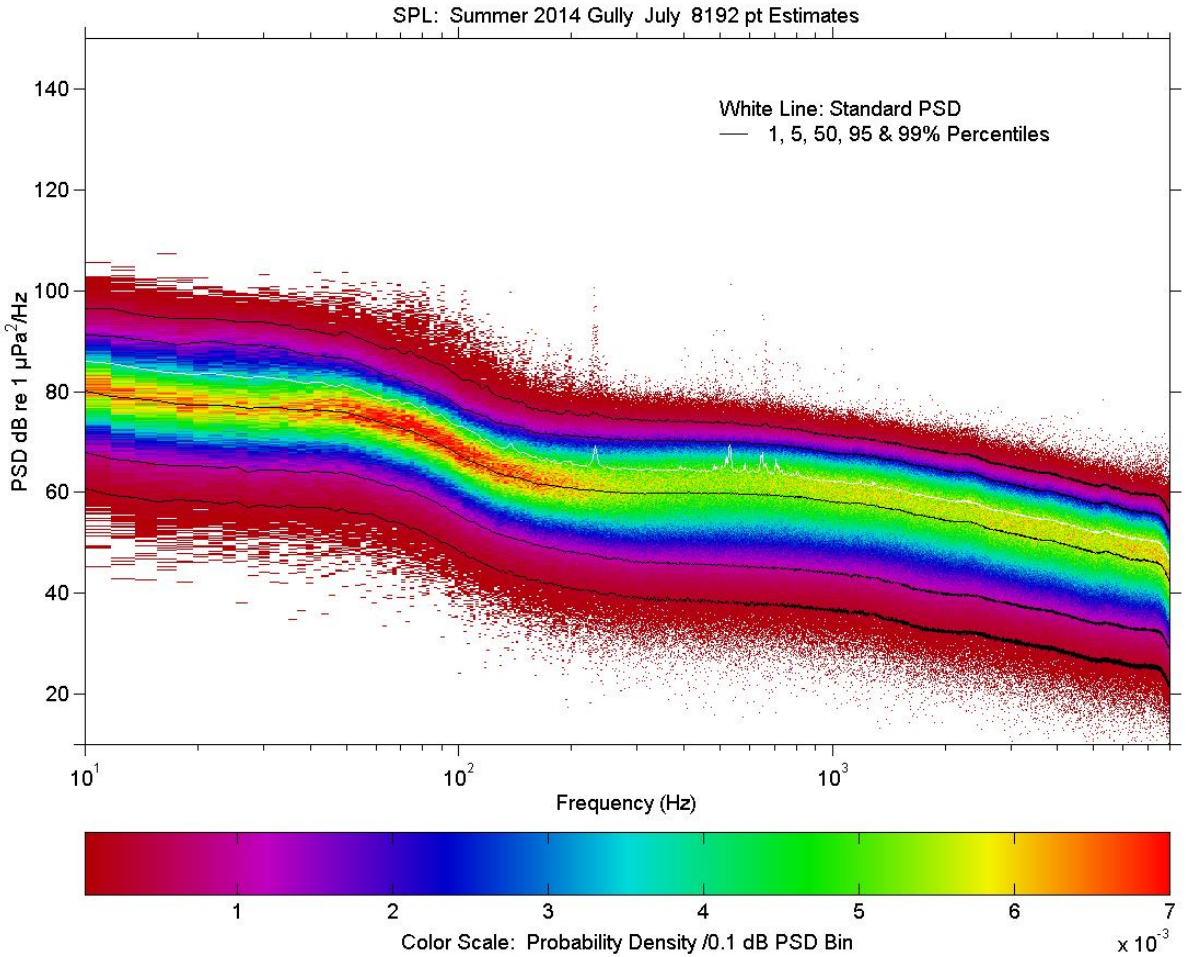


**Figure A4-2-MidGul-2014-Jul.** Medium resolution power spectral density with stats: Standard power spectral density (white), cumulative percentile curves for spectral sub-estimates (black), and PDF distribution of spectral sub-estimates (solid colour).

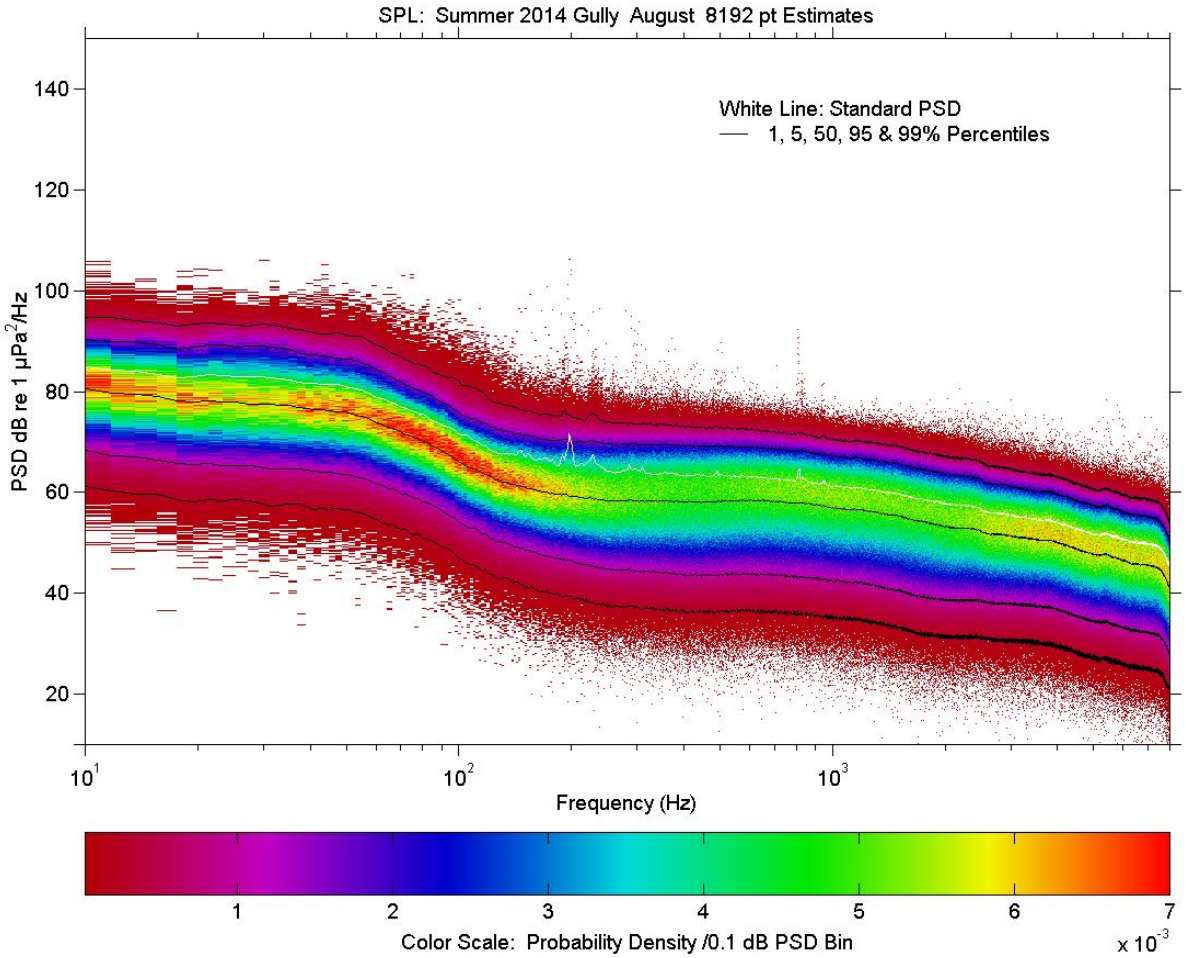


**Figure A4-2-MidGul-2014-Aug.** Medium resolution power spectral density with stats: Standard power spectral density (white), cumulative percentile curves for spectral sub-estimates (black), and PDF distribution of spectral sub-estimates (solid colour).

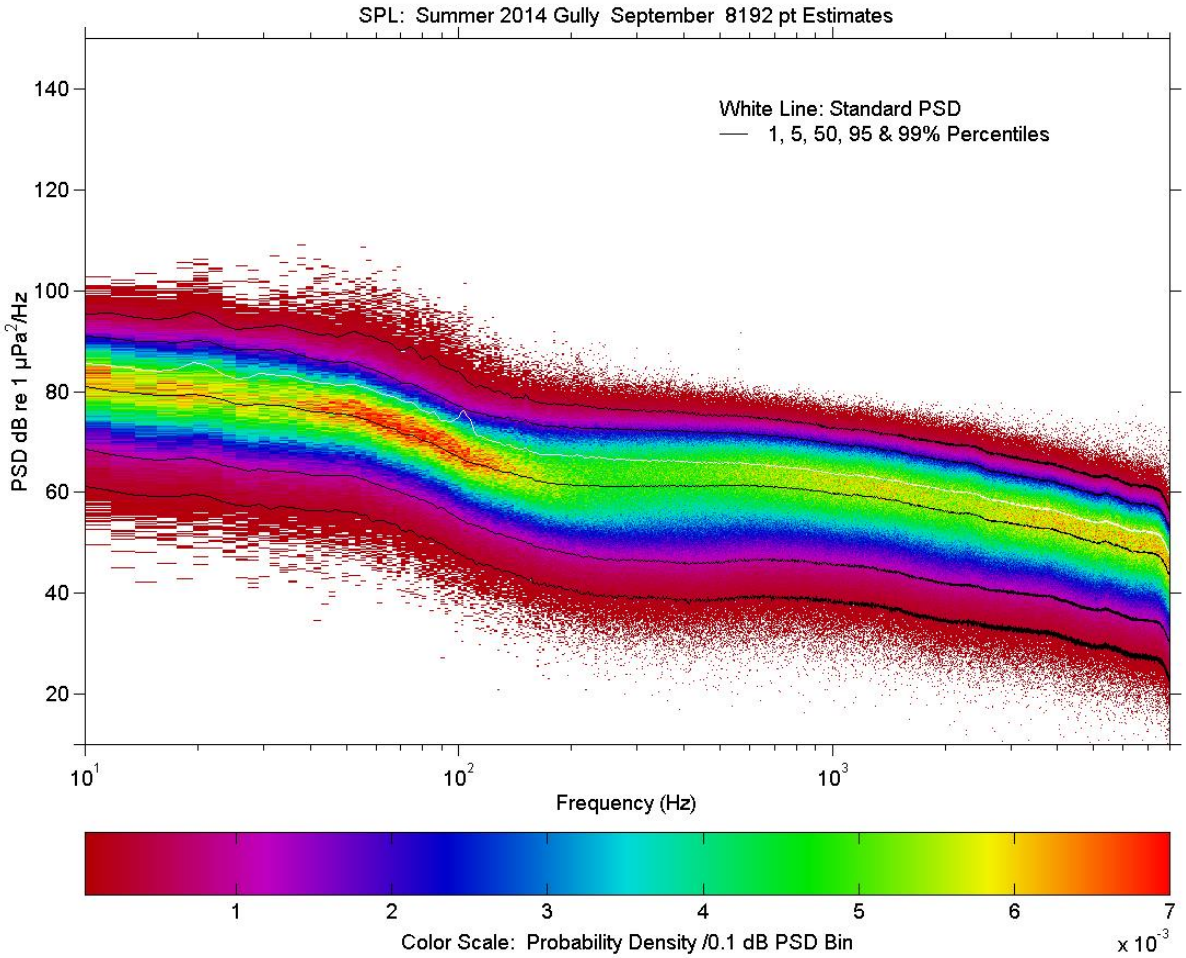


**Figure A4-2-MidGul-2014-Sep.** Medium resolution power spectral density with stats: Standard power spectral density (white), cumulative percentile curves for spectral sub-estimates (black), and PDF distribution of spectral sub-estimates (solid colour).

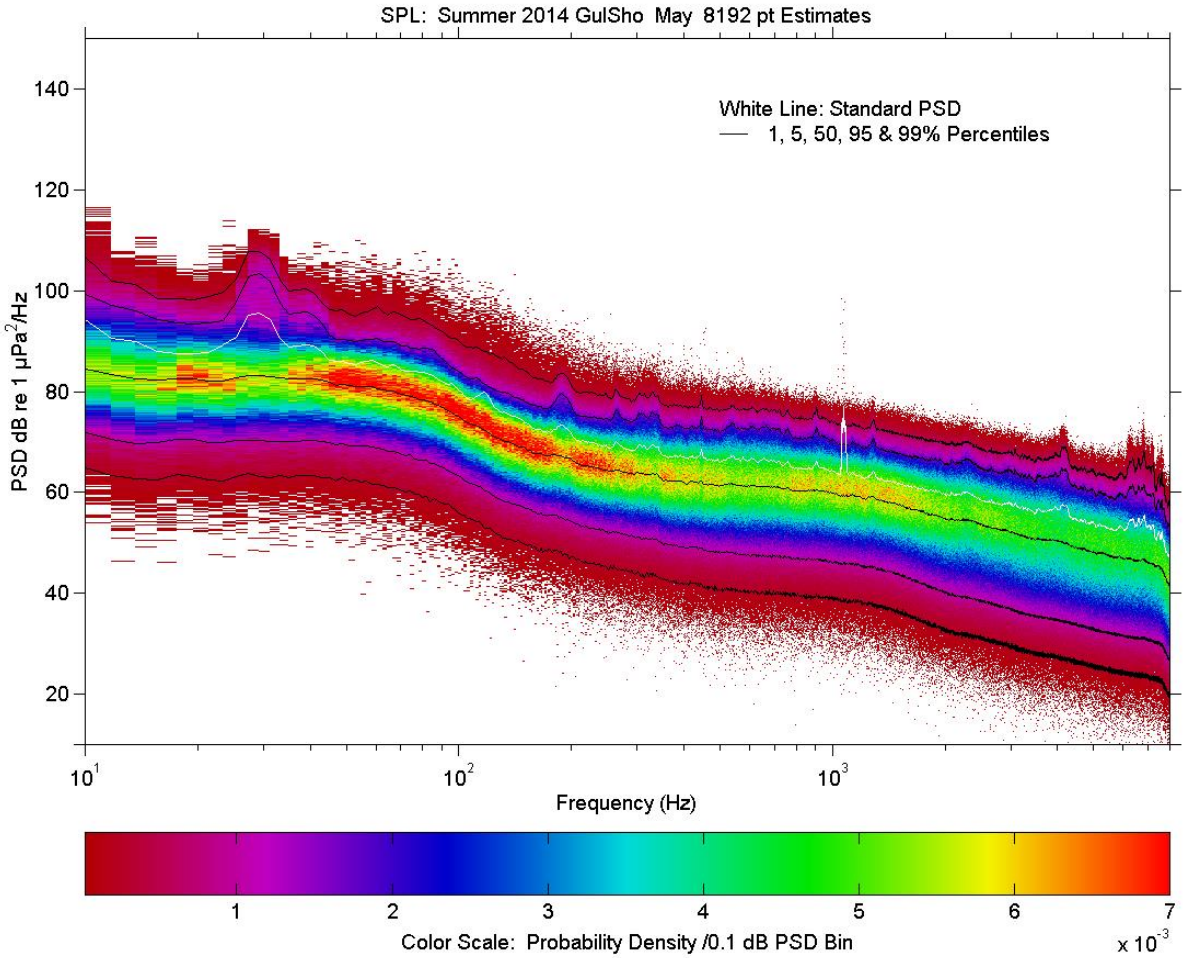


**Figure A4-2-GulSho-2014-May.** Medium resolution power spectral density with stats: Standard power spectral density (white), cumulative percentile curves for spectral sub-estimates (black), and PDF distribution of spectral sub-estimates (solid colour).

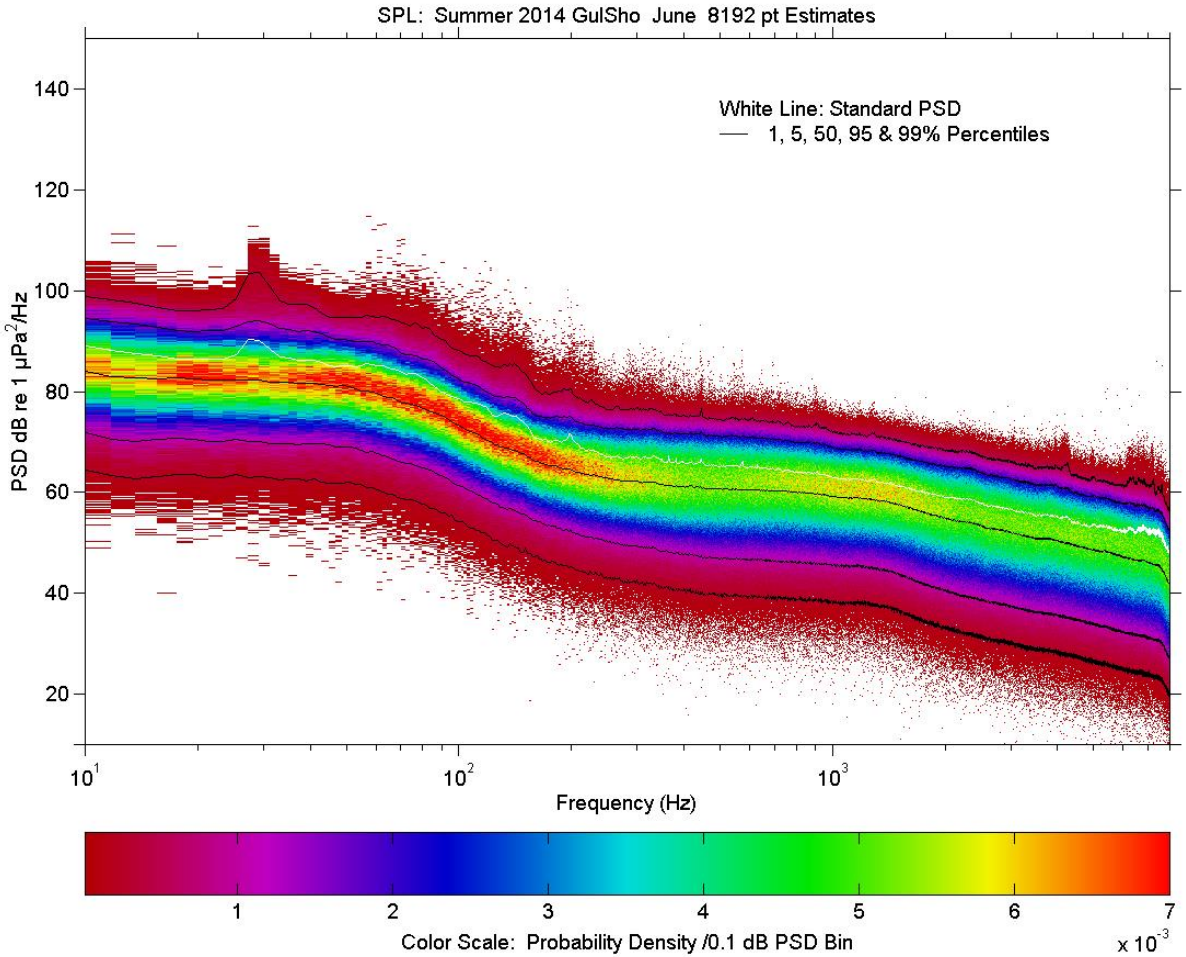


**Figure A4-2-GulSho-2014-Jun.** Medium resolution power spectral density with stats: Standard power spectral density (white), cumulative percentile curves for spectral sub-estimates (black), and PDF distribution of spectral sub-estimates (solid colour).

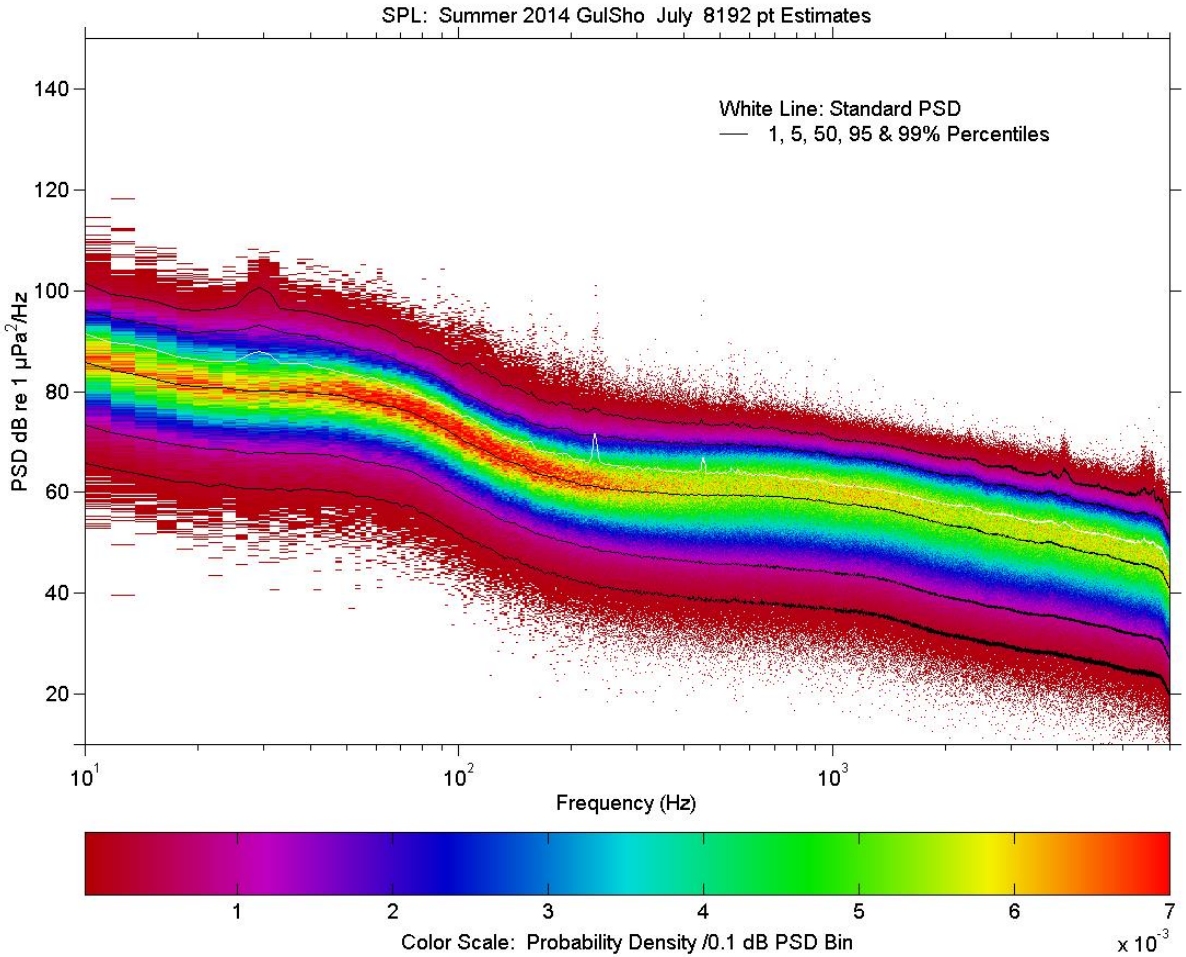


**Figure A4-2-GulSho-2014-Jul.** Medium resolution power spectral density with stats: Standard power spectral density (white), cumulative percentile curves for spectral sub-estimates (black), and PDF distribution of spectral sub-estimates (solid colour).

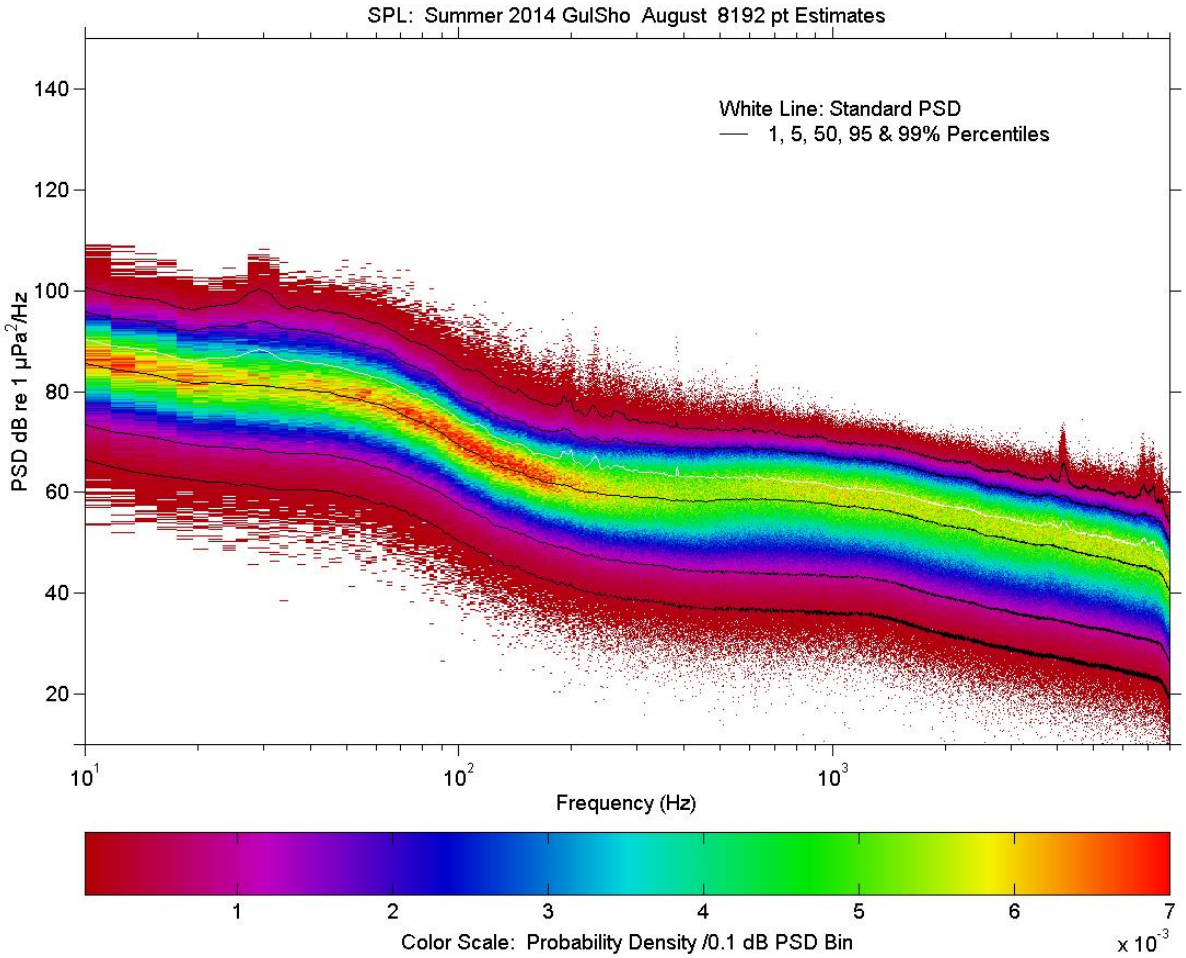


**Figure A4-2-GulSho-2014-Aug.** Medium resolution power spectral density with stats: Standard power spectral density (white), cumulative percentile curves for spectral sub-estimates (black), and PDF distribution of spectral sub-estimates (solid colour).

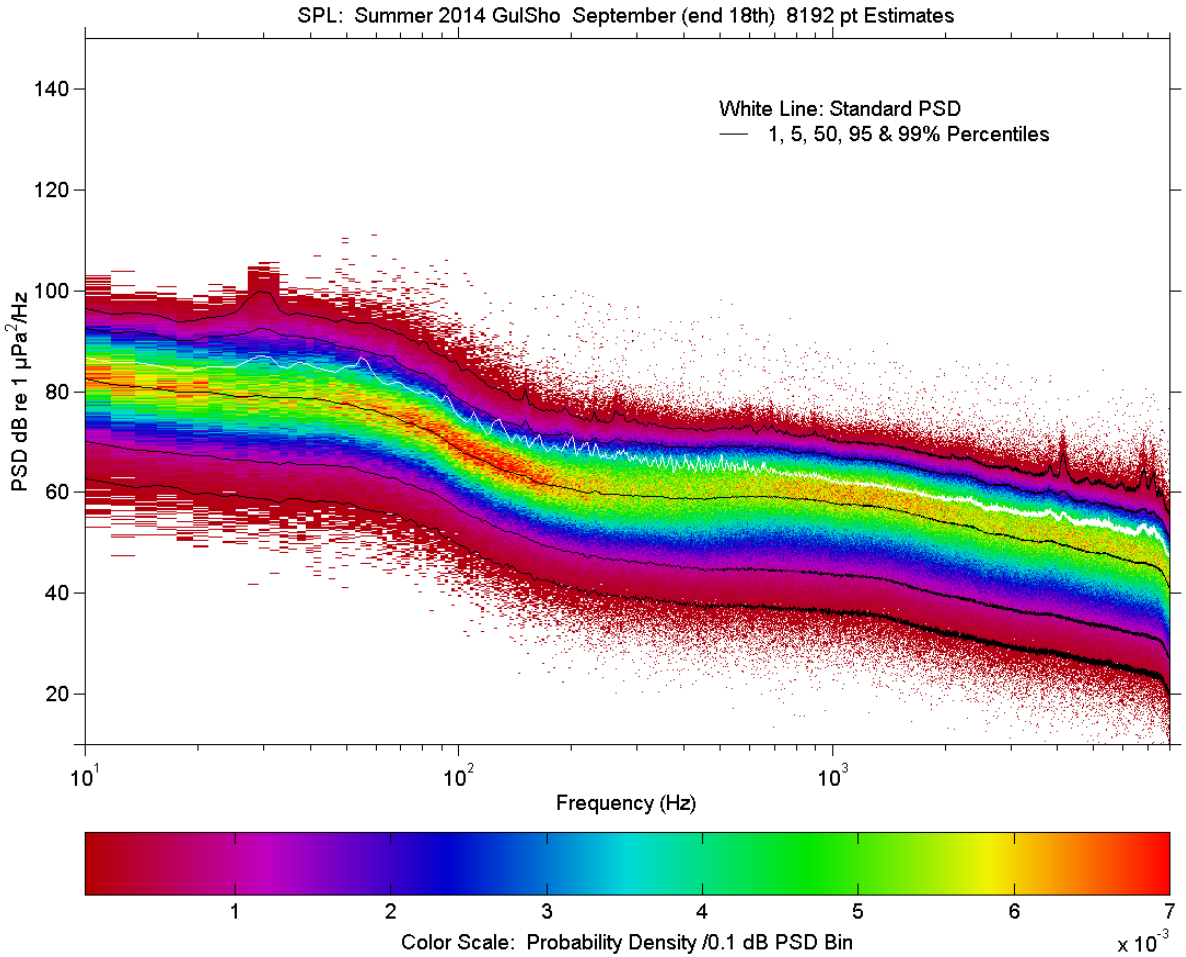


**Figure A4-2-GulSho-2014-Sep.** Medium resolution power spectral density with stats: Standard power spectral density (white), cumulative percentile curves for spectral sub-estimates (black), and PDF distribution of spectral sub-estimates (solid colour). Data extends to Sept. 18th incl.

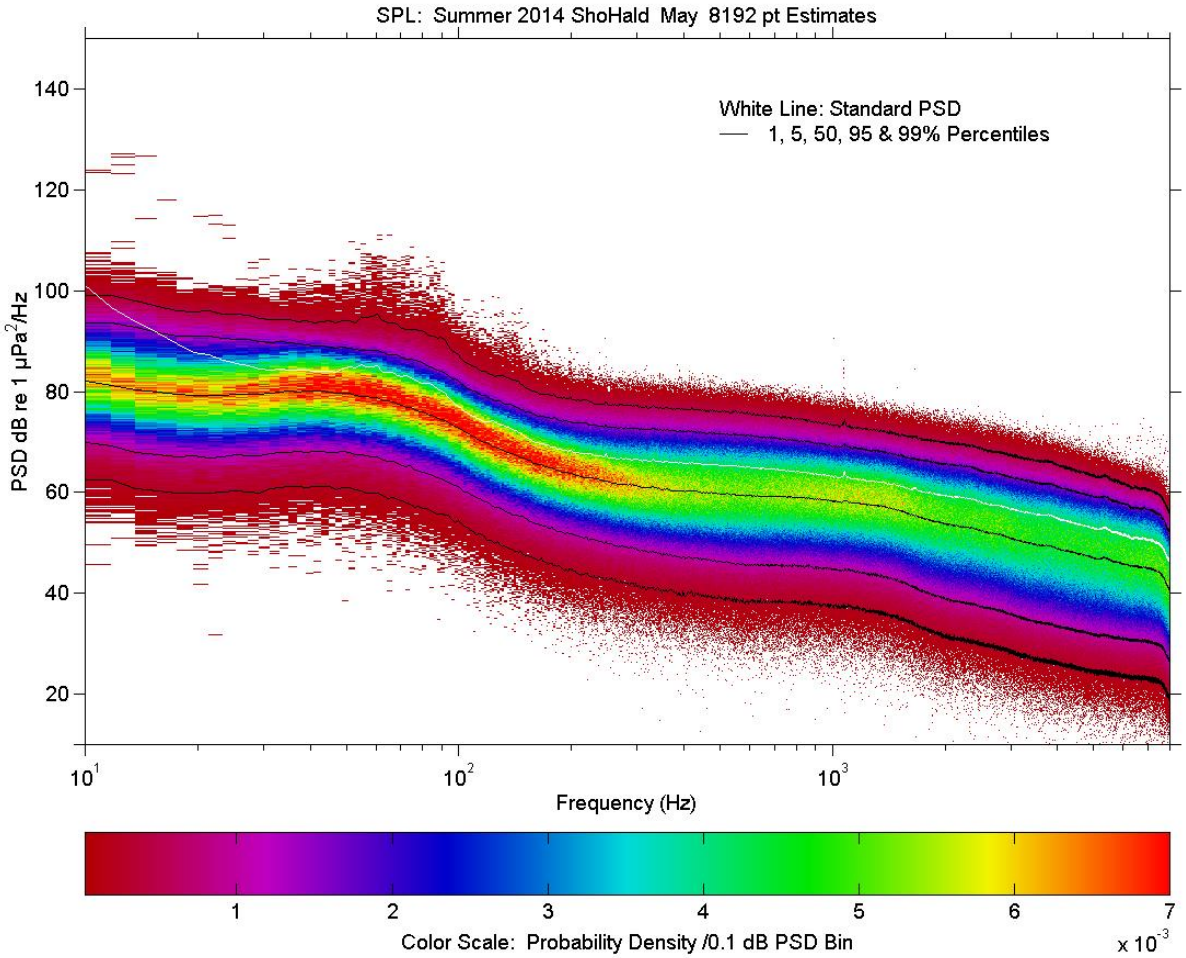


**Figure A4-2-ShoHald-2014-May.** Medium resolution power spectral density with stats: Standard power spectral density (white), cumulative percentile curves for spectral sub-estimates (black), and PDF distribution of spectral sub-estimates (solid colour).

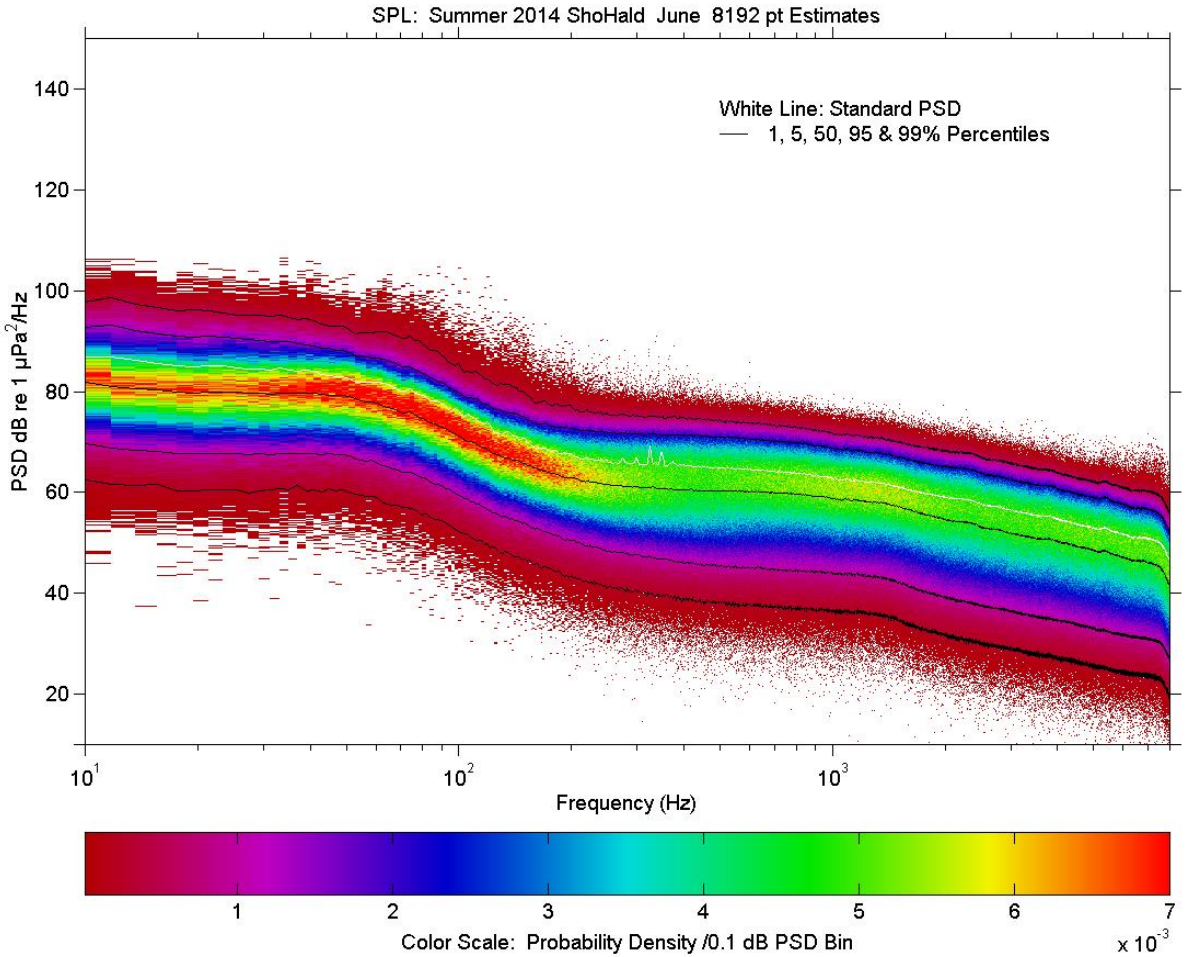


**Figure A4-2-ShoHald-2014-Jun.** Medium resolution power spectral density with stats: Standard power spectral density (white), cumulative percentile curves for spectral sub-estimates (black), and PDF distribution of spectral sub-estimates (solid colour).

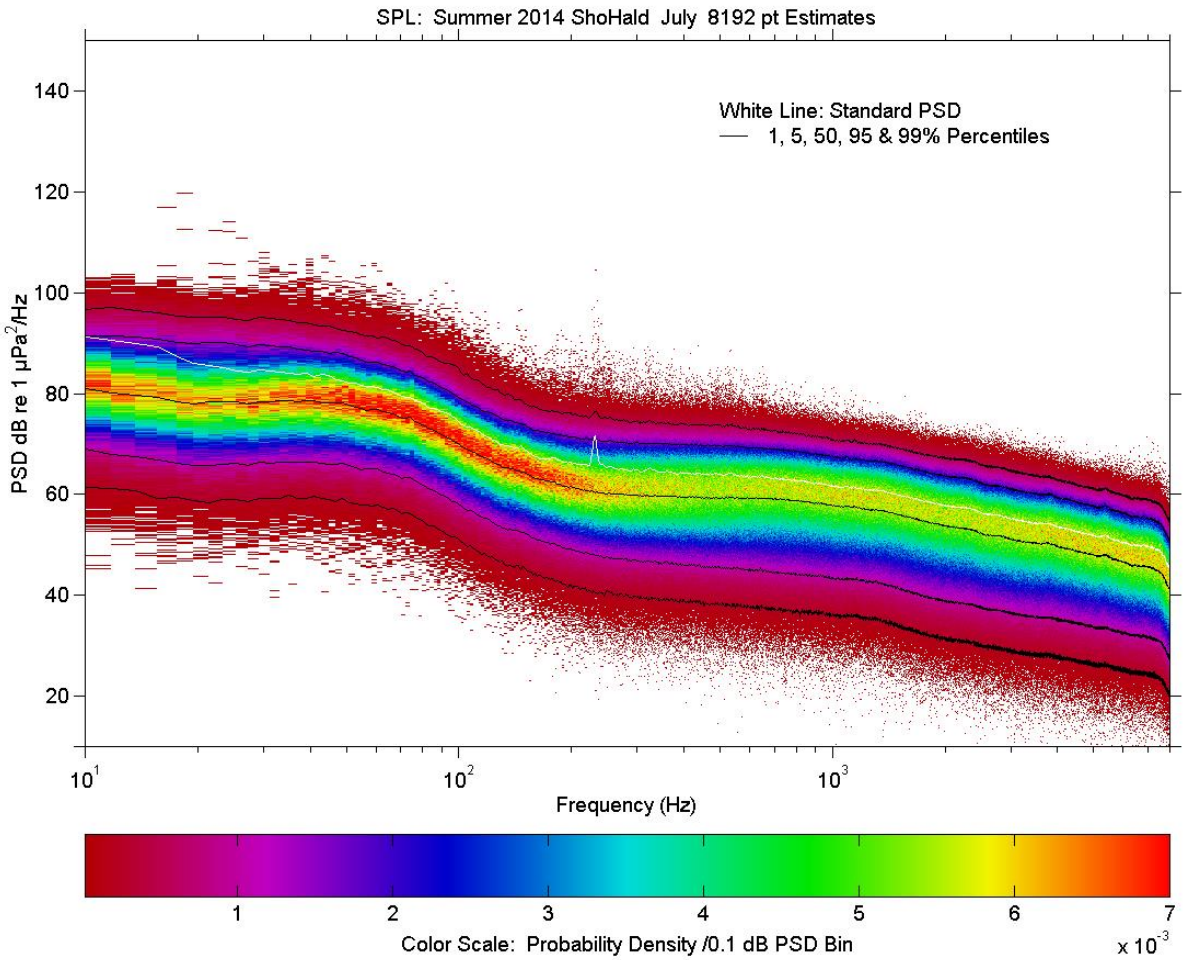


**Figure A4-2-ShoHald-2014-Jul.** Medium resolution power spectral density with stats: Standard power spectral density (white), cumulative percentile curves for spectral sub-estimates (black), and PDF distribution of spectral sub-estimates (solid colour).

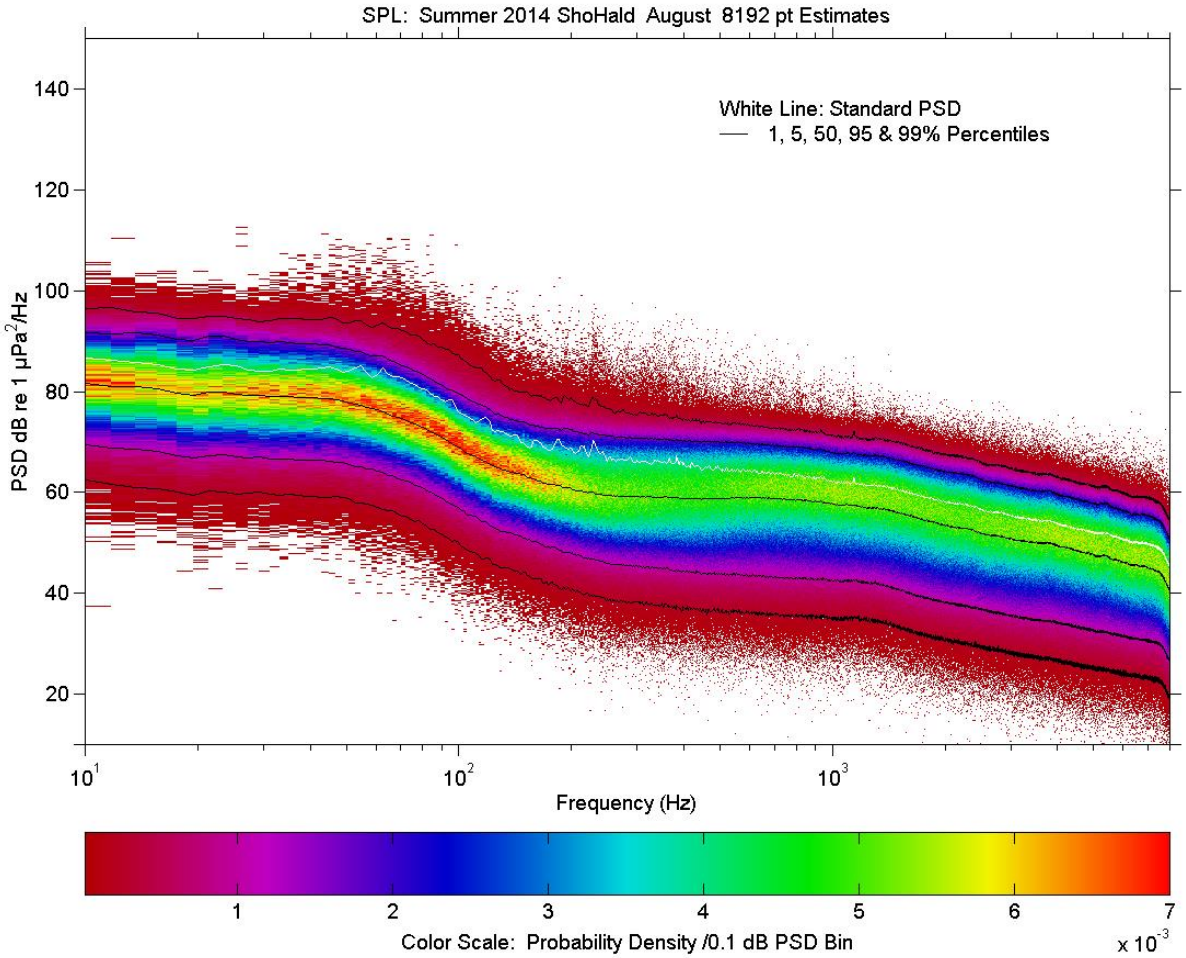


**Figure A4-2-ShoHald-2014-Aug.** Medium resolution power spectral density with stats: Standard power spectral density (white), cumulative percentile curves for spectral sub-estimates (black), and PDF distribution of spectral sub-estimates (solid colour).

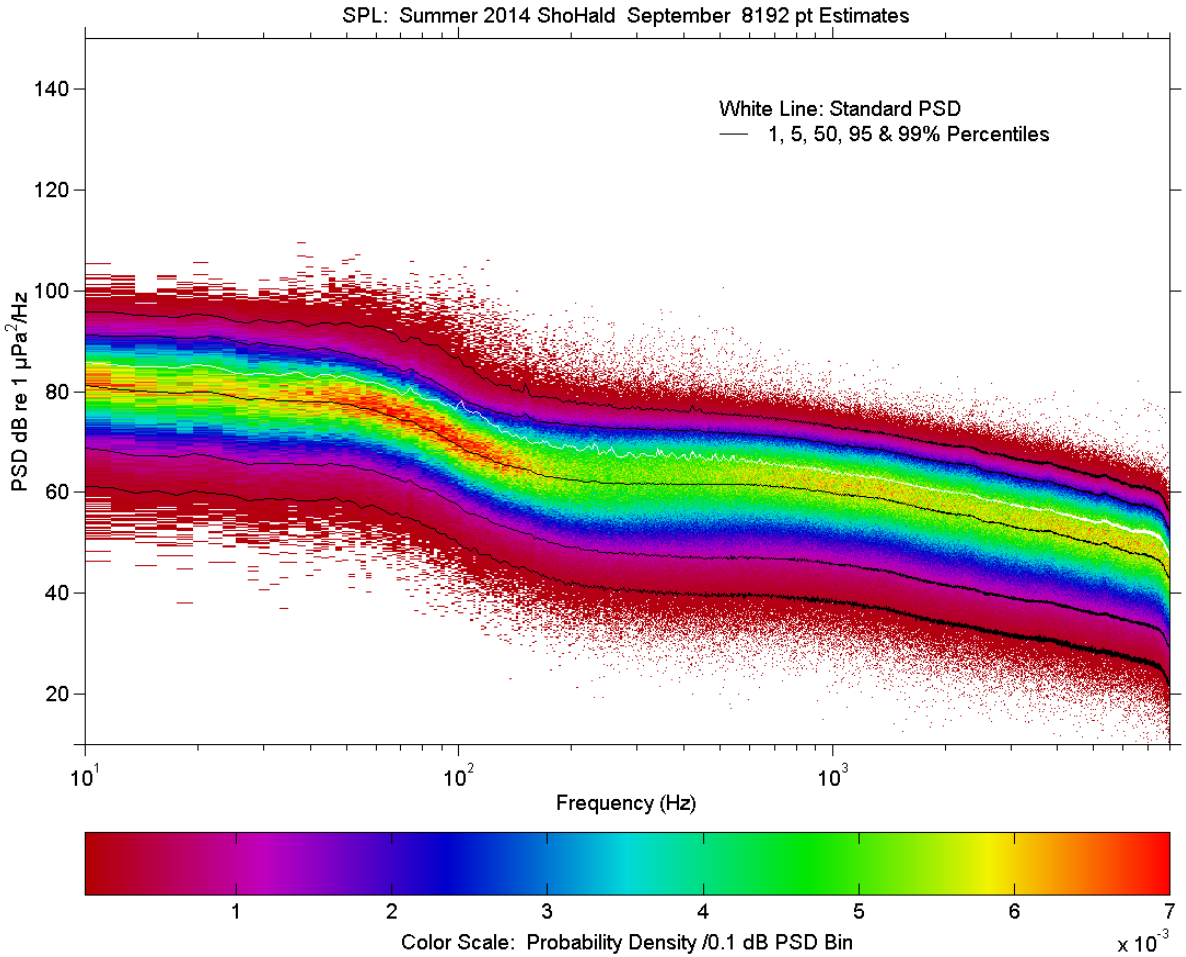


**Figure A4-2-ShoHald-2014-Sep.** Medium resolution power spectral density with stats: Standard power spectral density (white), cumulative percentile curves for spectral sub-estimates (black), and PDF distribution of spectral sub-estimates (solid colour).

## A4.3. SPECTRAL SECTIONS

### *A4.3.1. Winter 2012-13 Deployments*

**Figure (series) A4-3-Winter 2012-13 Deployments** - Power spectral density sections in time x frequency space.

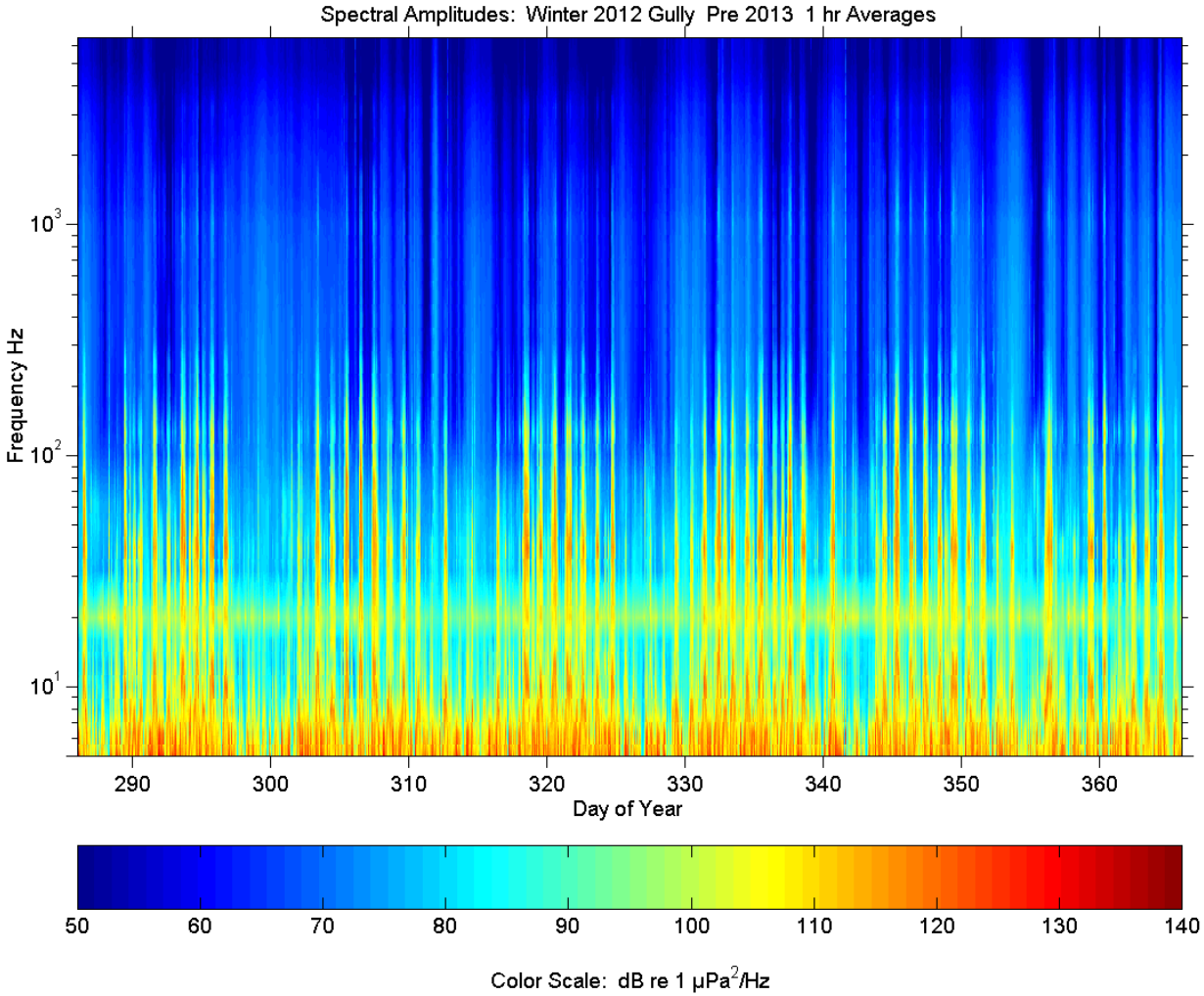


**Figure A4-3-MidGul-W2012-1.** Power spectral density sections in time x frequency space for **pre** New Year deployment period, Power spectral amplitudes averaged over 1/3 octave in frequency and 1 hour in time and plotted in colour-encoded format in accordance with the displayed scale.

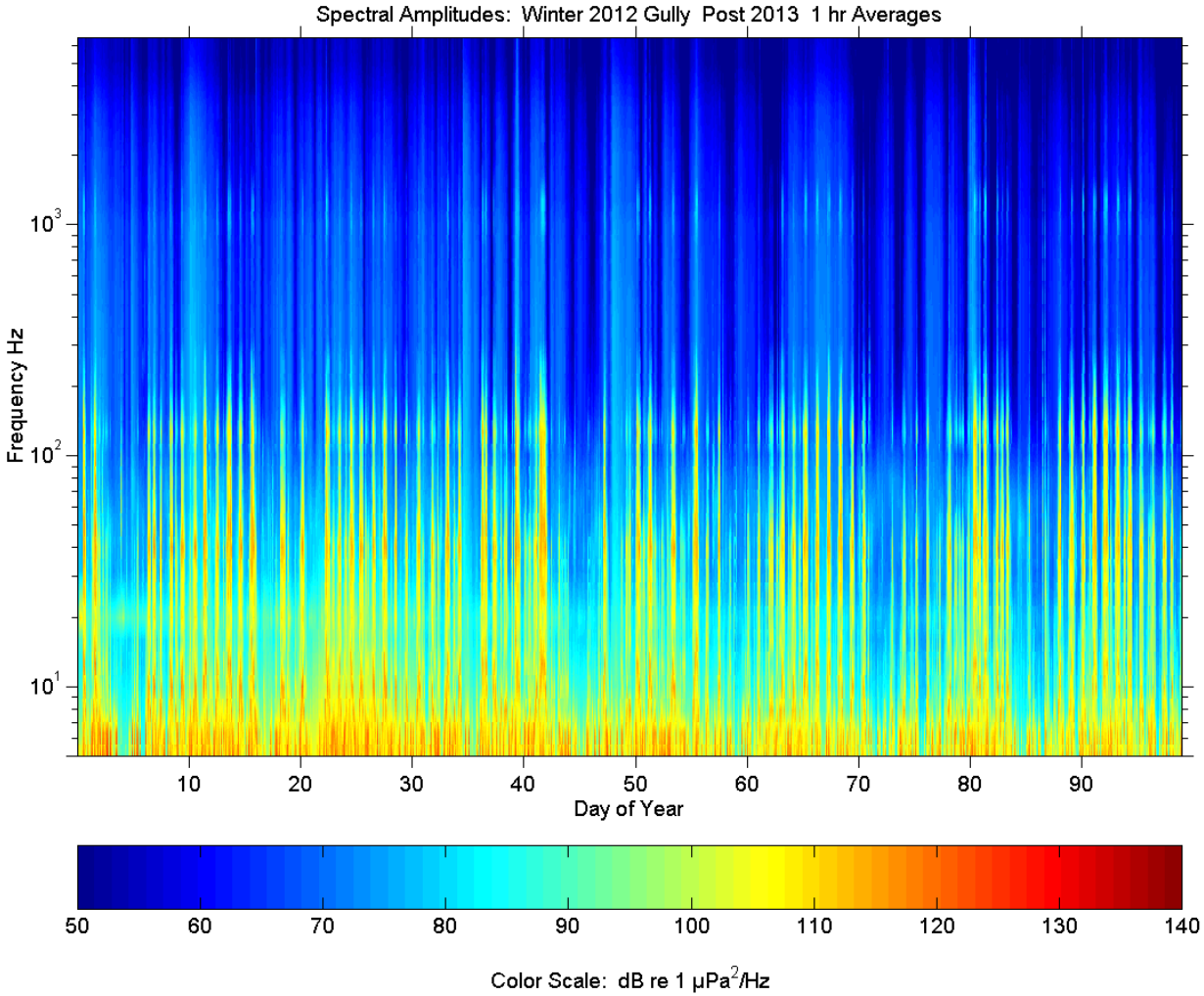


**Figure A4-3-MidGul-W2012-2.** Power spectral density section in time x frequency space for **post** New Year deployment period, Power spectral amplitudes averaged over 1/3 octave in frequency and 1 hour in time and plotted in colour-encoded format according to the displayed scale.

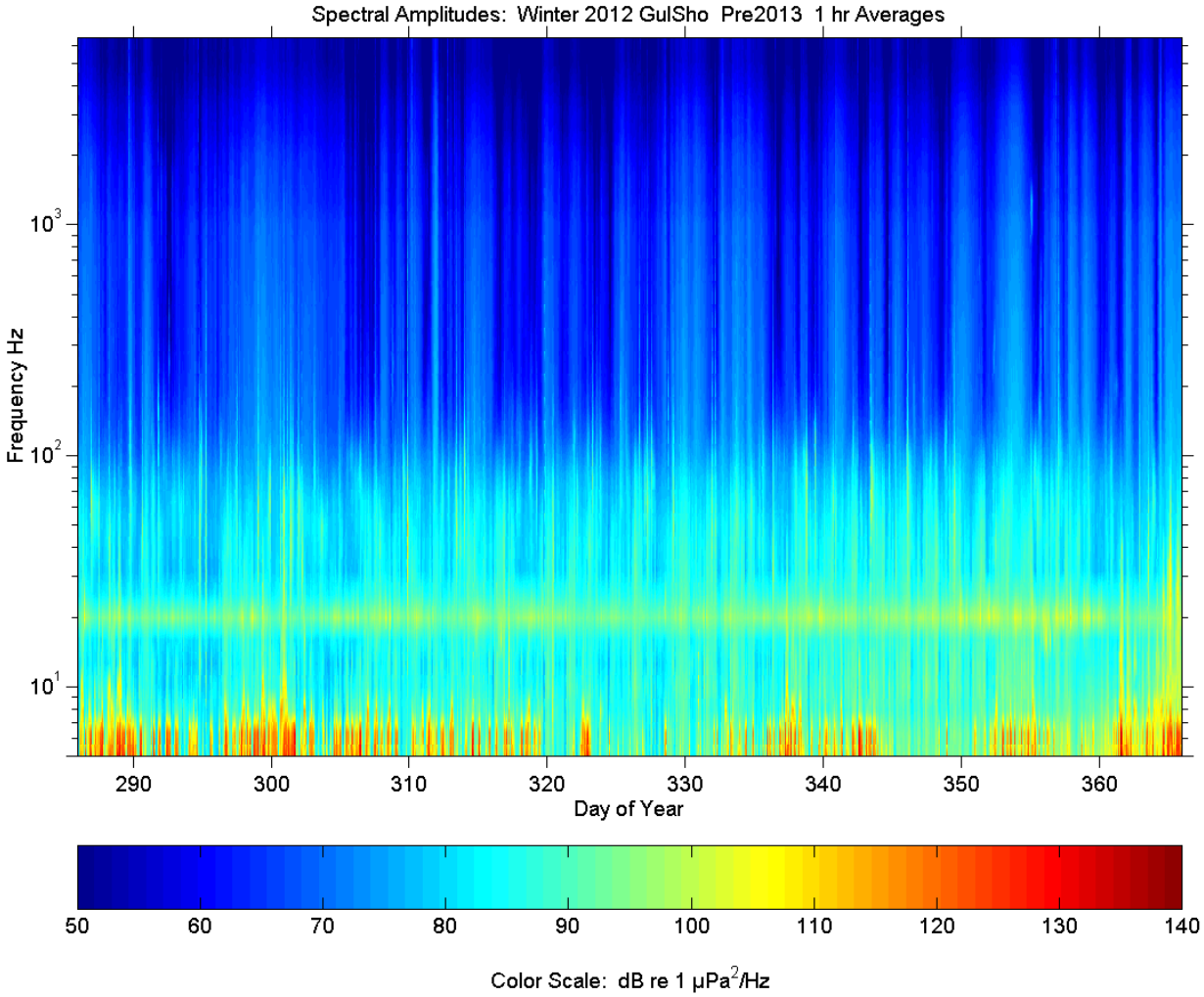


**Figure A4-3-GulSho-W2012-1.** Power spectral density section in time x frequency space for **pre** New Year deployment period, Power spectral amplitudes averaged over 1/3 octave in frequency and 1 hour in time and plotted in colour-encoded format in accordance with the displayed scale.

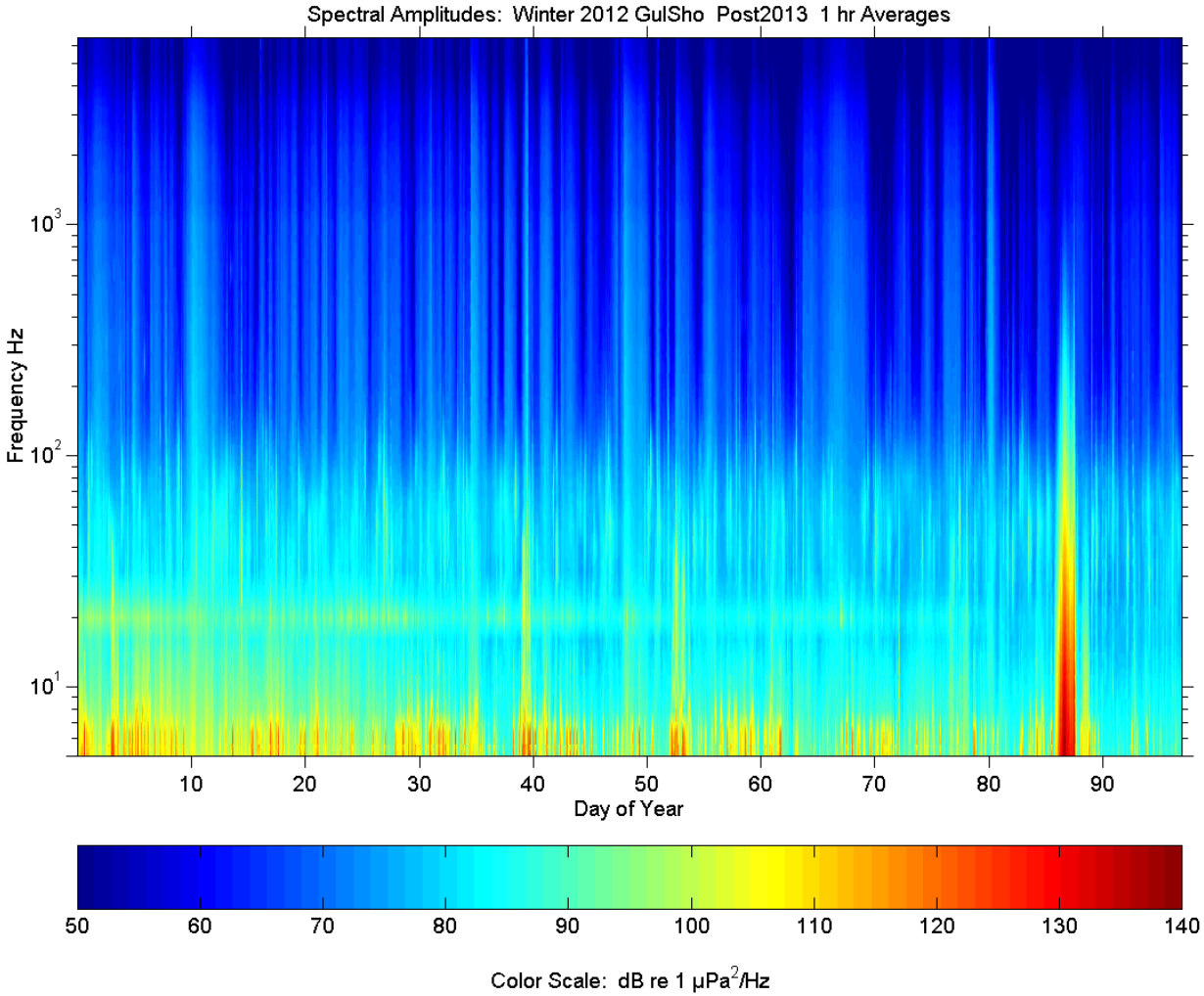


**Figure A4-3-GulSho-W2012-2.** Power spectral density section in time x frequency space for **post** New Year deployment period. Power spectral amplitudes averaged over 1/3 octave in frequency and 1 hour in time and plotted in colour-encoded format in accordance with the displayed scale.

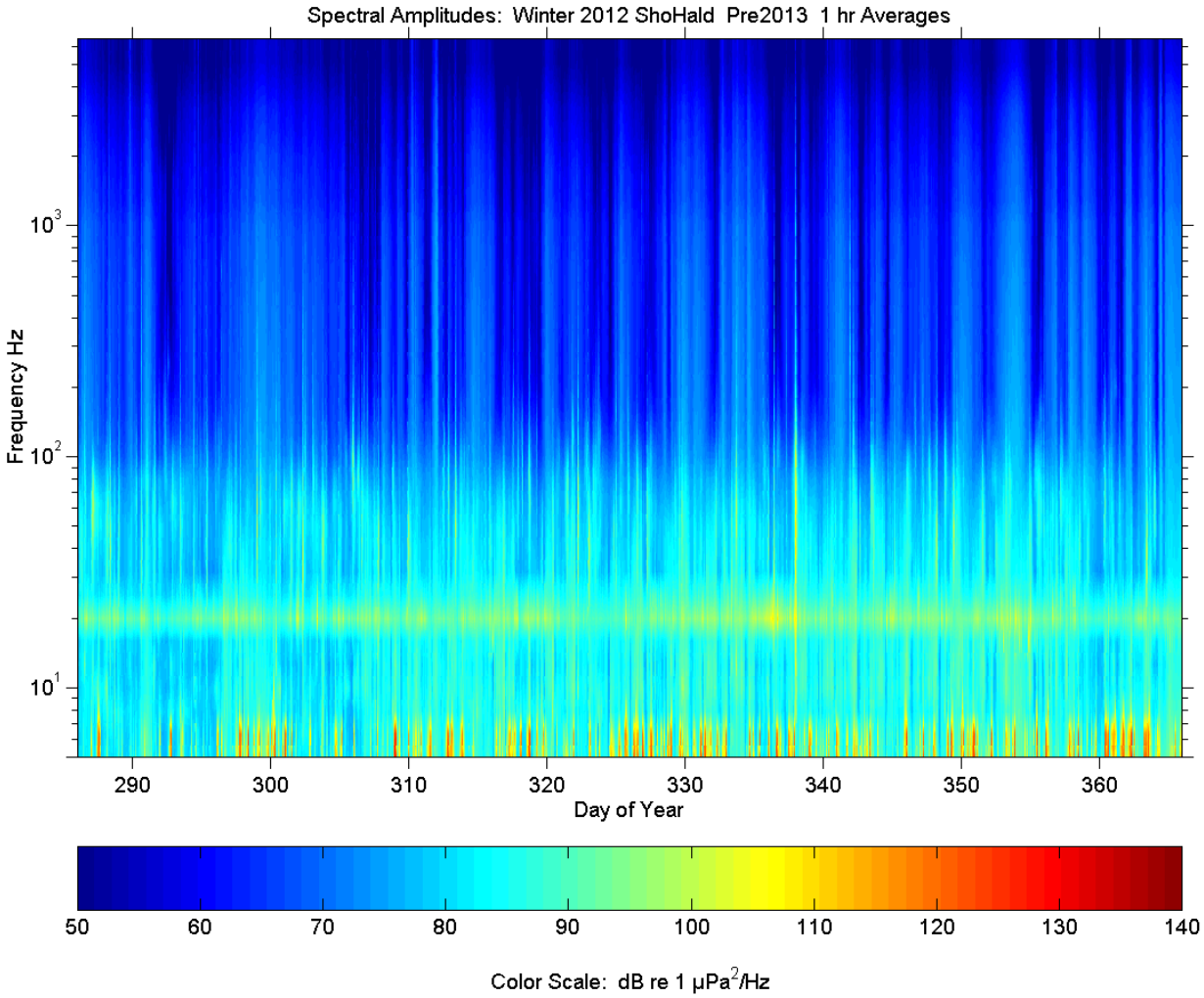


**Figure A4-3-ShoHald-W2012-1.** Power spectral density section in time x frequency space for **pre** New Year deployment period. Power spectral amplitudes averaged over 1/3 octave in frequency and 1 hour in time and plotted in colour-encoded format in accordance with the displayed scale.

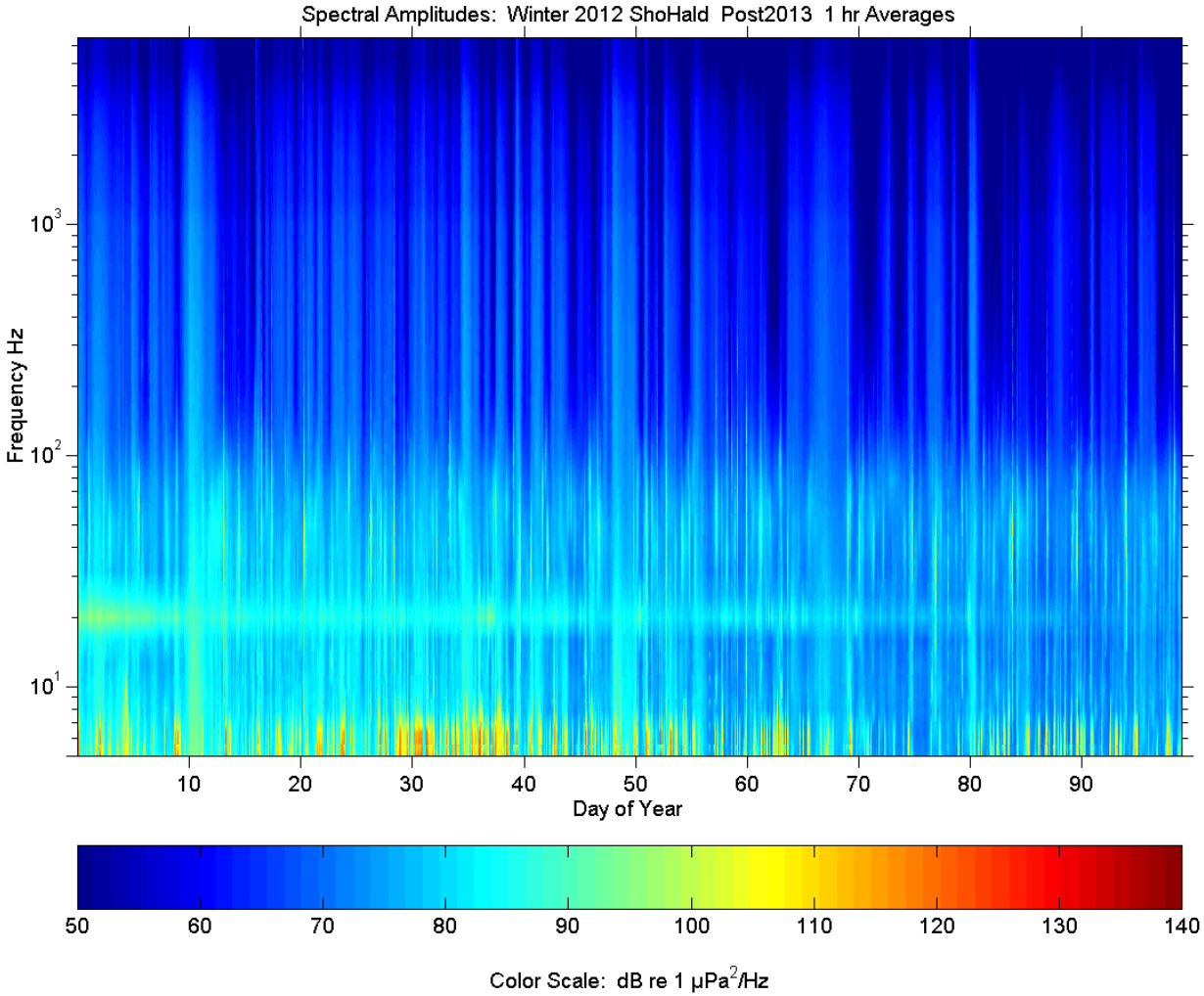


**Figure A4-3-ShoHald-W2012-2.** Power spectral density section in time x frequency space for **post** New Year deployment period. Power spectral amplitudes averaged over 1/3 octave in frequency and 1 hour in time and plotted in colour-encoded format in accordance with the displayed scale.

### *A4.3.2. Summer 2013 Deployments*

**Figure (series) A4-3-Summer 2013 Deployments** - Power spectral density sections in time x frequency space.

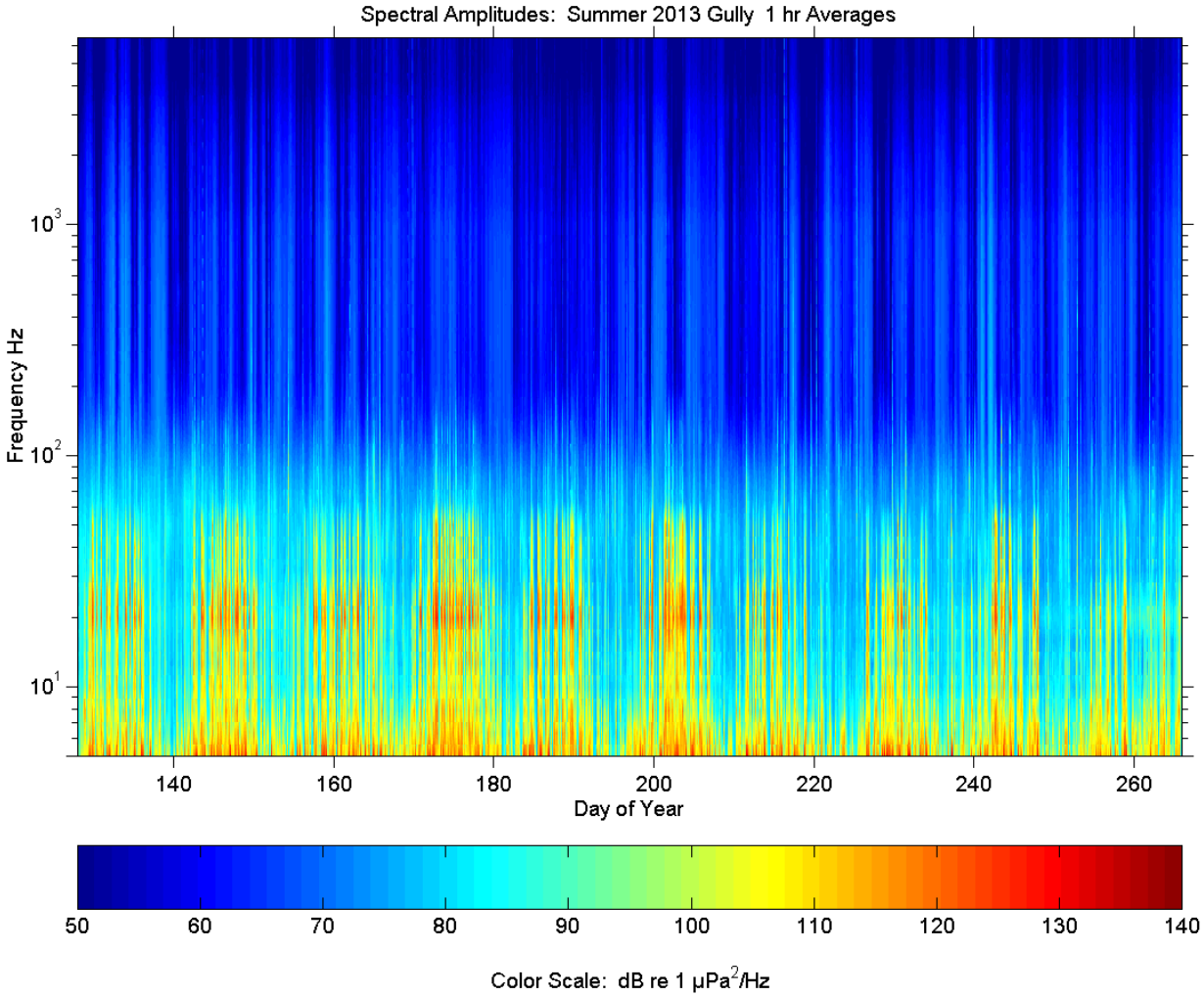


**Figure A4-3-MidGul-S2013.** Power spectral density section in time x frequency space. Power spectral amplitudes averaged over 1/3 octave in frequency and 1 hour in time and plotted in colour-encoded format in accordance with the displayed scale.

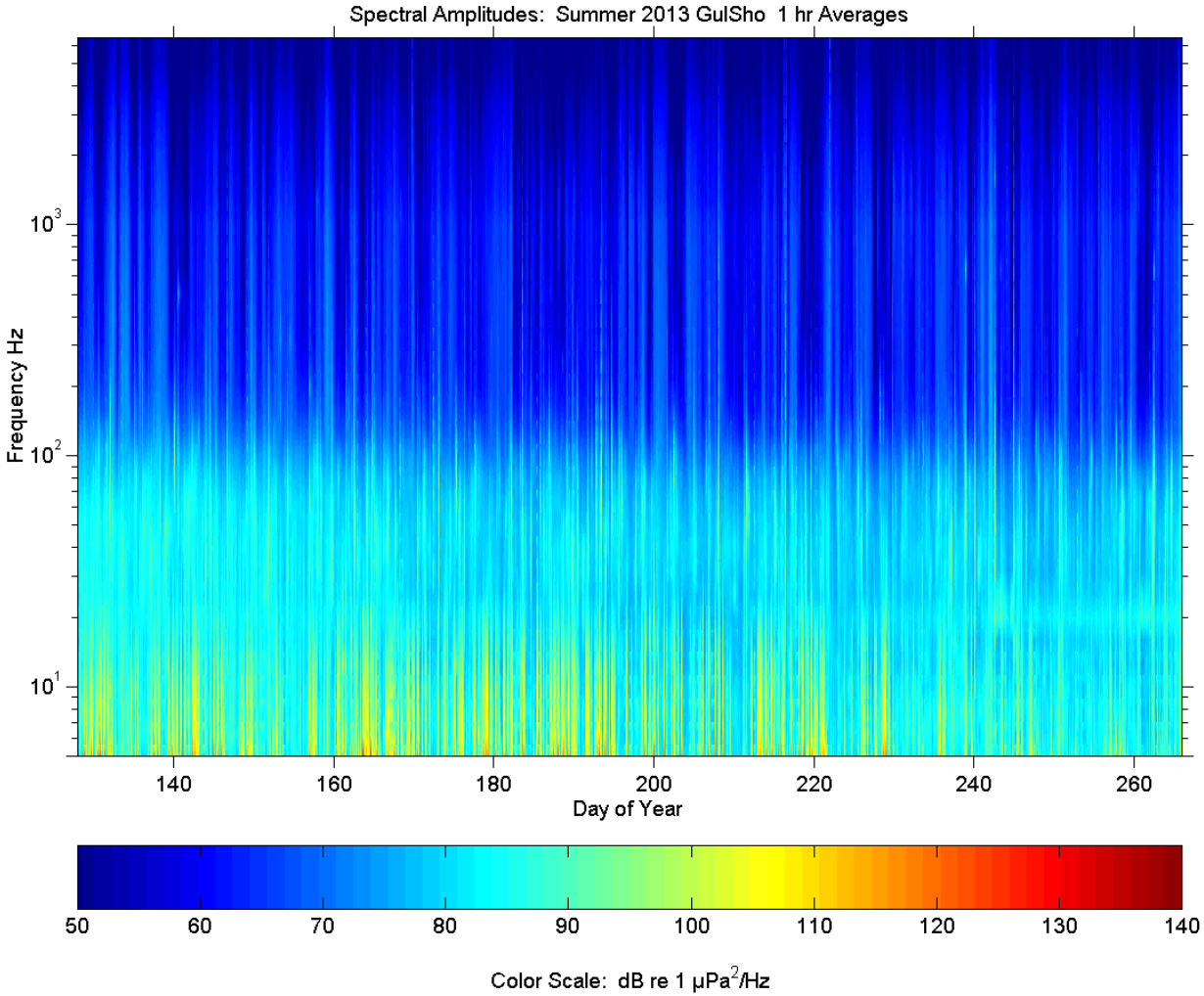


**Figure A4-3-GulSho-S2013.** Power spectral density section in time x frequency space. Power spectral amplitudes averaged over 1/3 octave in frequency and 1 hour in time and plotted in colour-encoded format in accordance with the displayed scale.

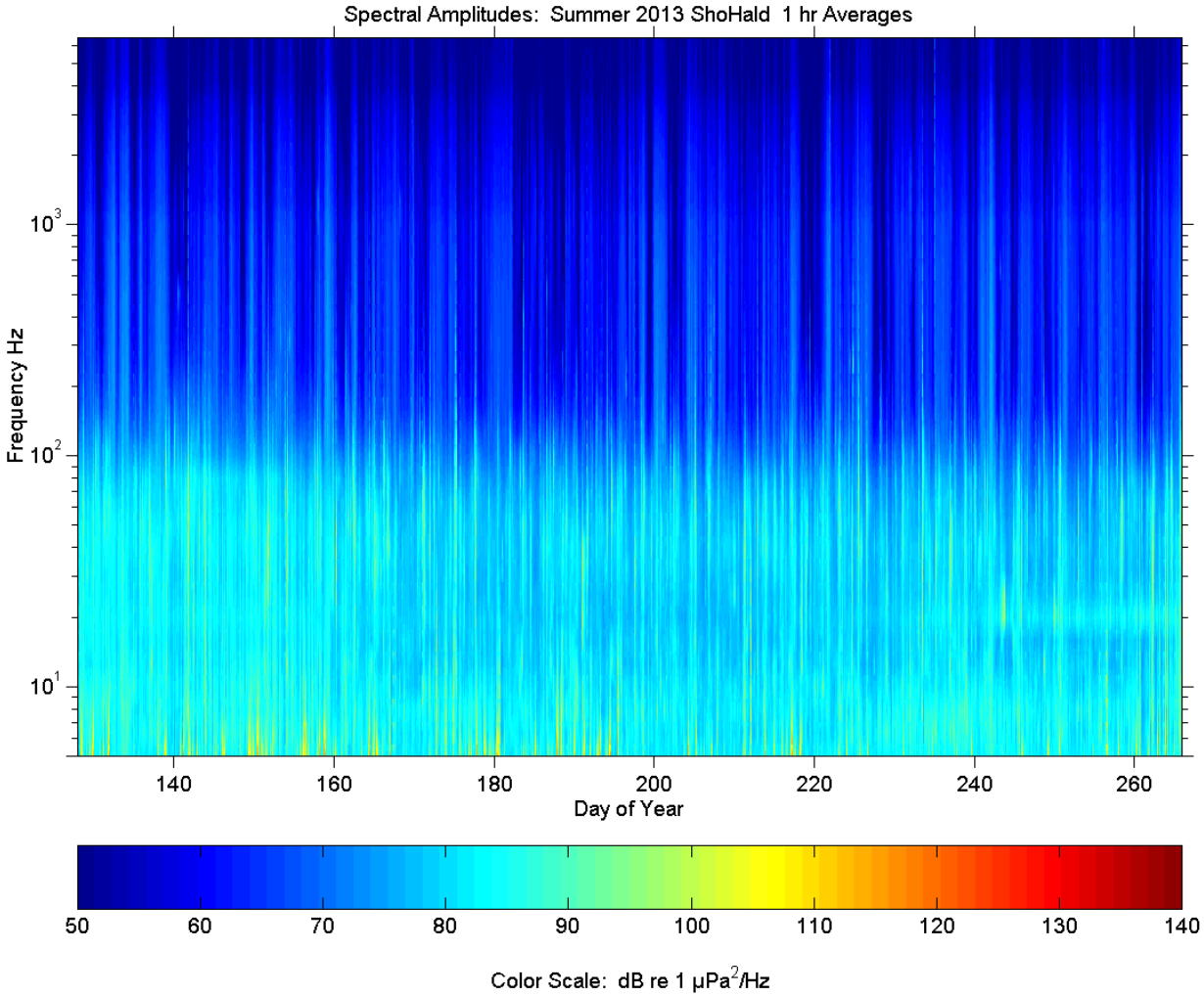


**Figure A4-3-ShoHald-S2013.** Power spectral density section in time x frequency space. Power spectral amplitudes averaged over 1/3 octave in frequency and 1 hour in time and plotted in colour-encoded format in accordance with the displayed scale.

### *A4.3.3. Winter 2013-14 Deployments*

**Figure (series) A4-3-Winter 2013-14 Deployments** - Power spectral density sections in time x frequency space.

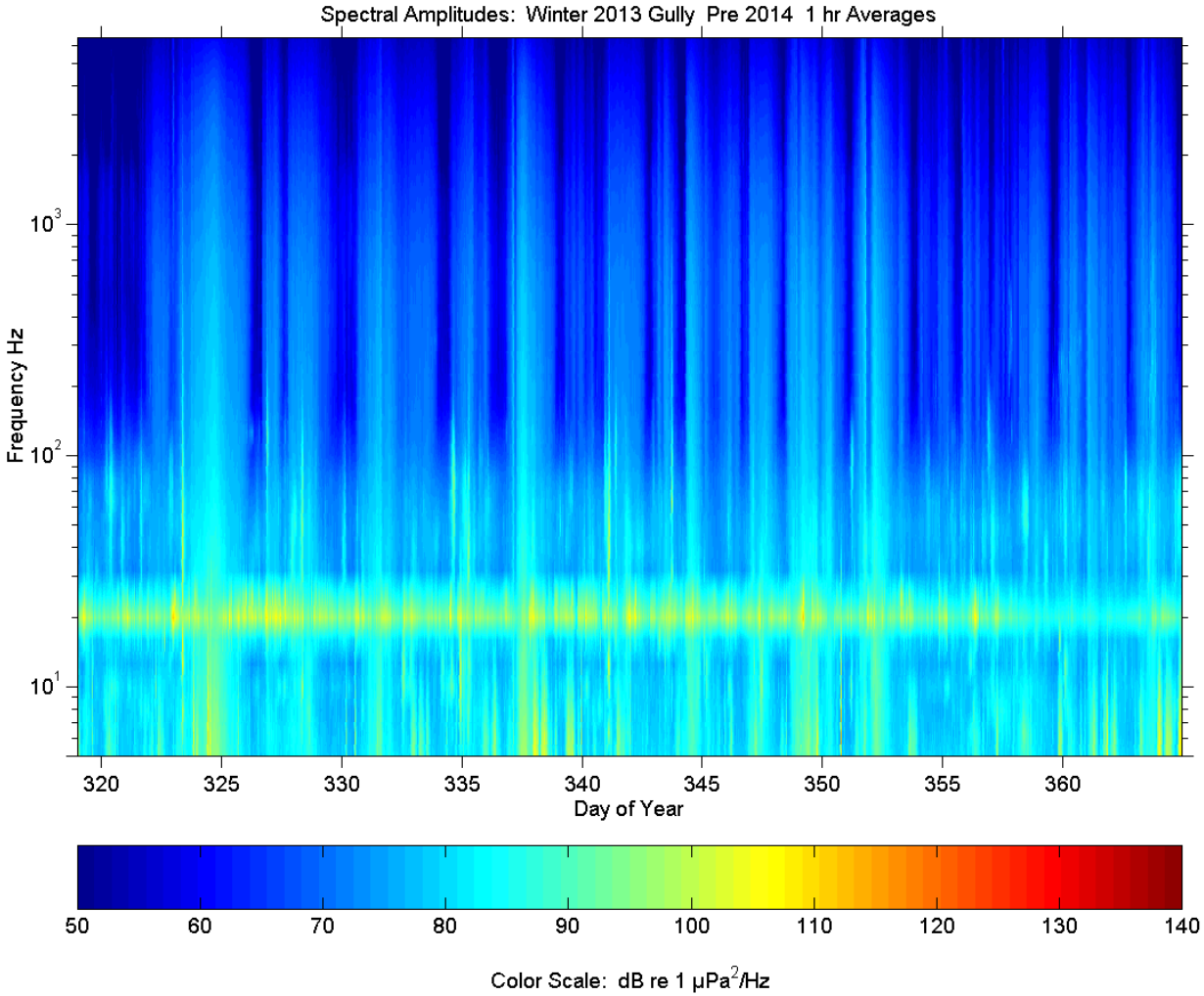


**Figure A4-3-MidGul-W2013-1.** Power spectral density sections in time x frequency space for **pre** New Year deployment period. Power spectral amplitudes averaged over 1/3 octave in frequency and 1 hour in time and plotted in colour-encoded format in accordance with the displayed scale.

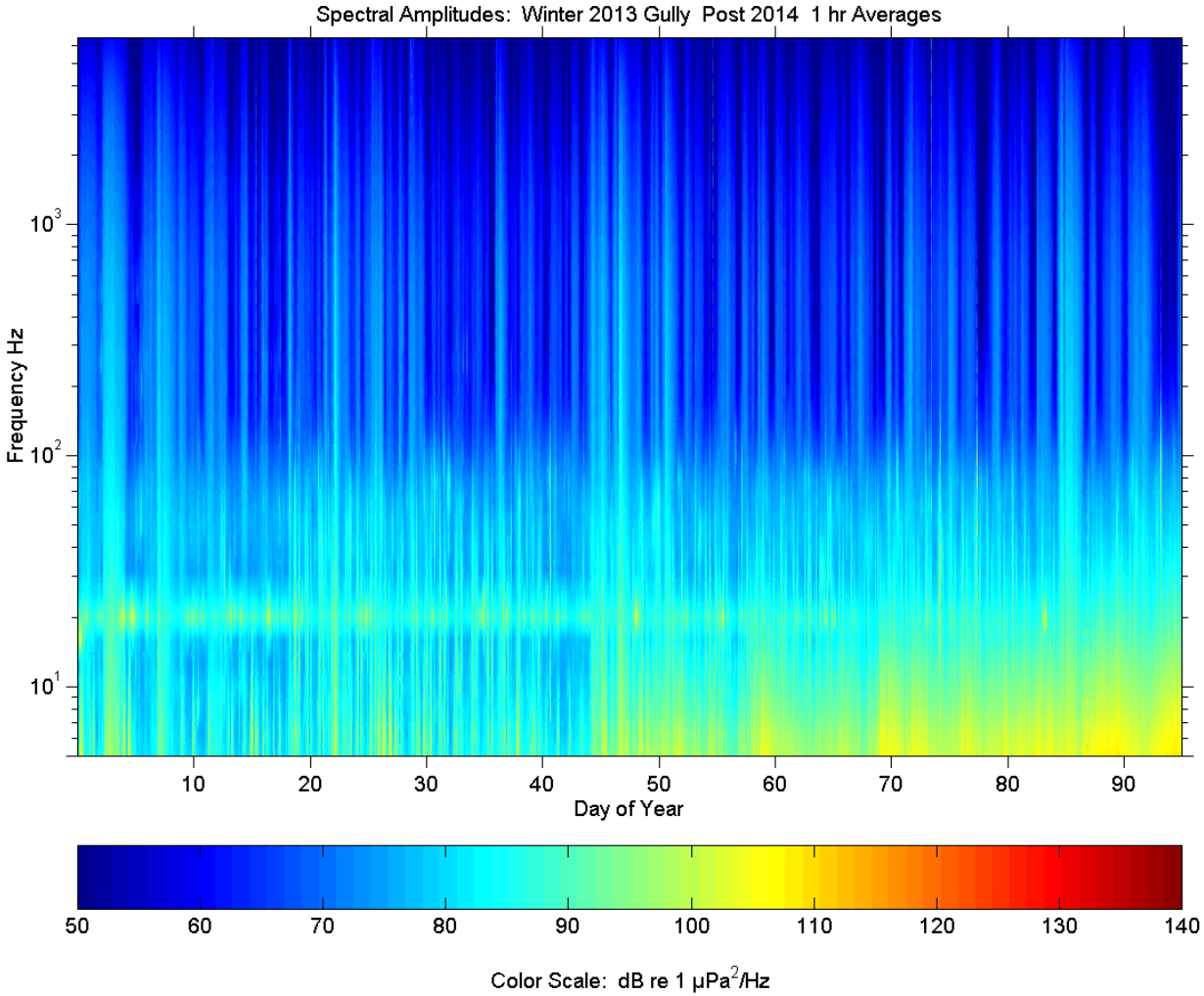


**Figure A4-3-MidGul-W2013-2.** Power spectral density sections in time x frequency space for **post** New Year deployment period. Power spectral amplitudes averaged over 1/3 octave in frequency and 1 hour in time and plotted in colour-encoded format in accordance with the displayed scale.

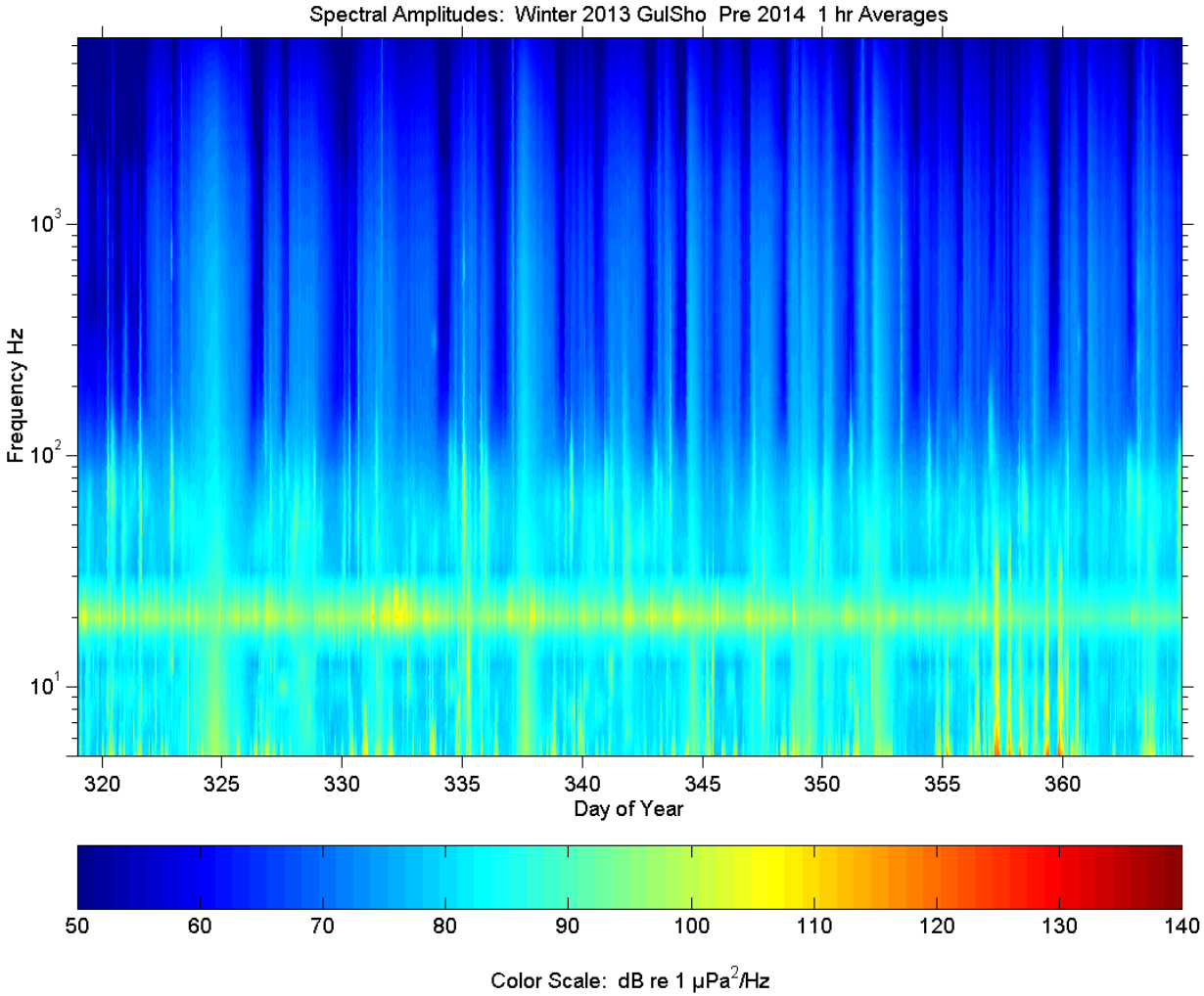


**Figure A4-3-GulSho-W2013-1.** Power spectral density sections in time x frequency space for **pre** New Year deployment period. Power spectral amplitudes averaged over 1/3 octave in frequency and 1 hour in time and plotted in colour-encoded format in accordance with the displayed scale.

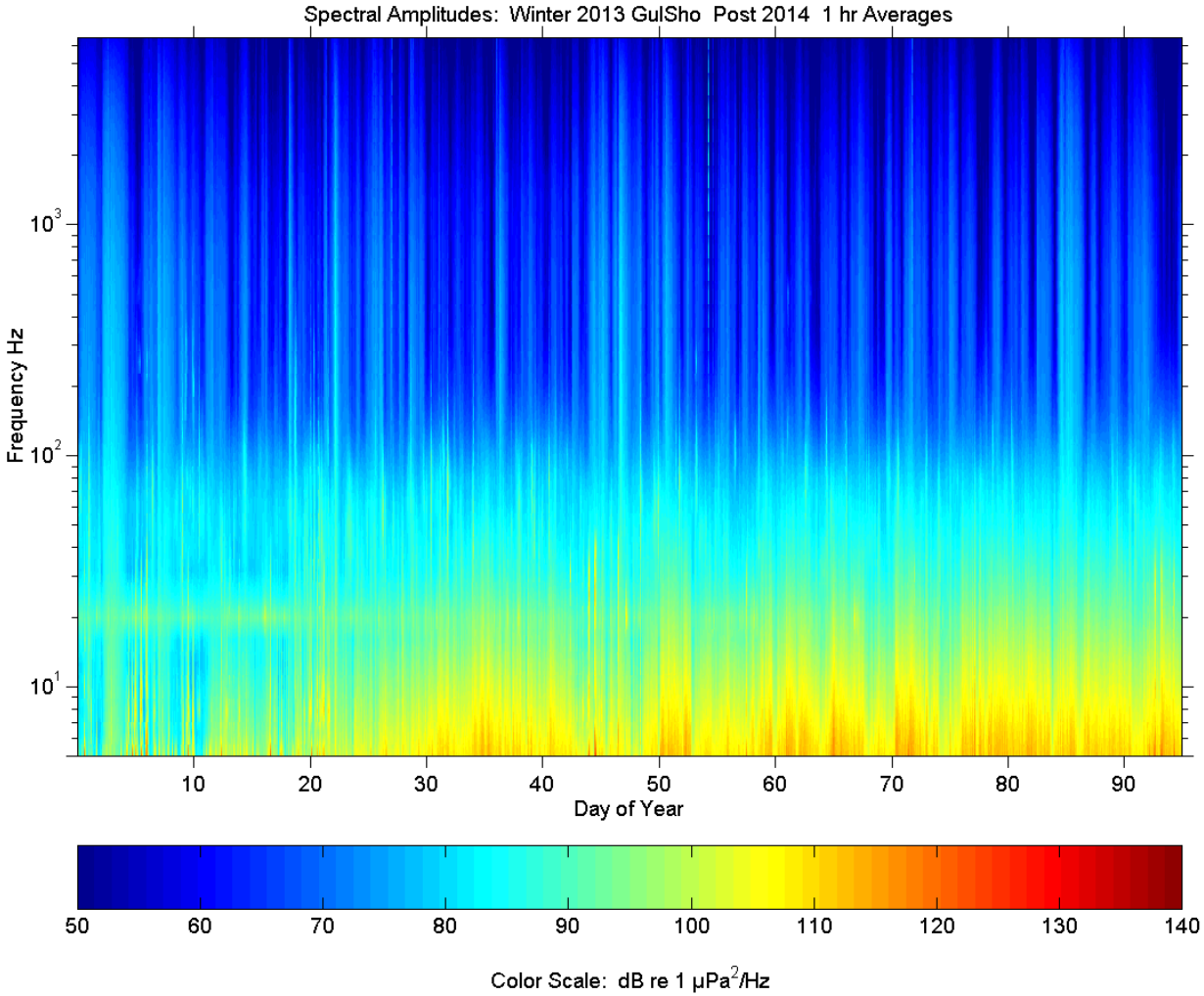


**Figure A4-3-GulSho-W2013-2.** Power spectral density sections in time x frequency space for **post** New Year deployment period. Power spectral amplitudes averaged over 1/3 octave in frequency and 1 hour in time and plotted in colour-encoded format in accordance with the displayed scale.

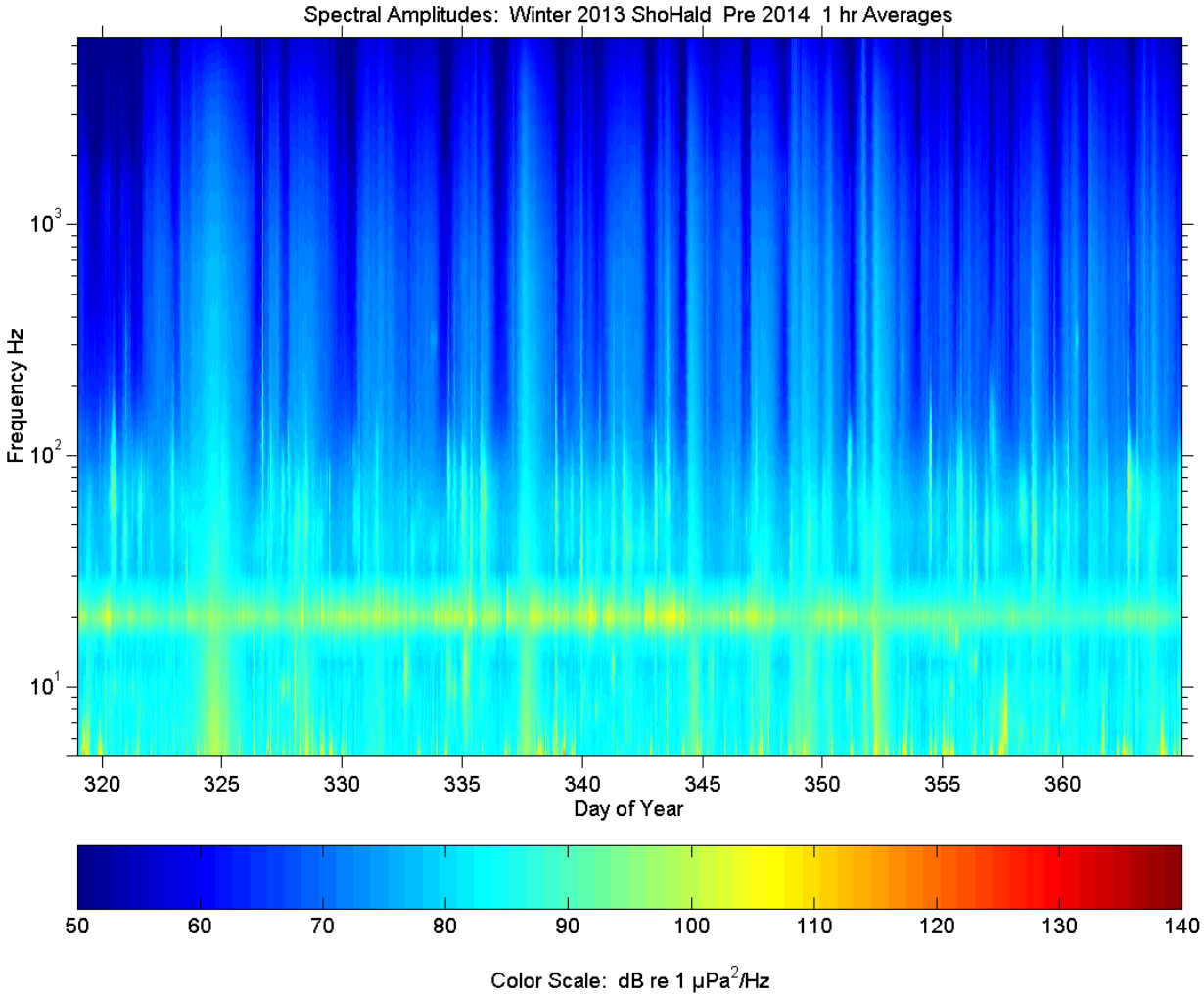


**Figure A4-3-ShoHald-W2013-1.** Power spectral density sections in time x frequency space for **pre** New Year deployment period. Power spectral amplitudes averaged over 1/3 octave in frequency and 1 hour in time and plotted in colour-encoded format in accordance with the displayed scale.

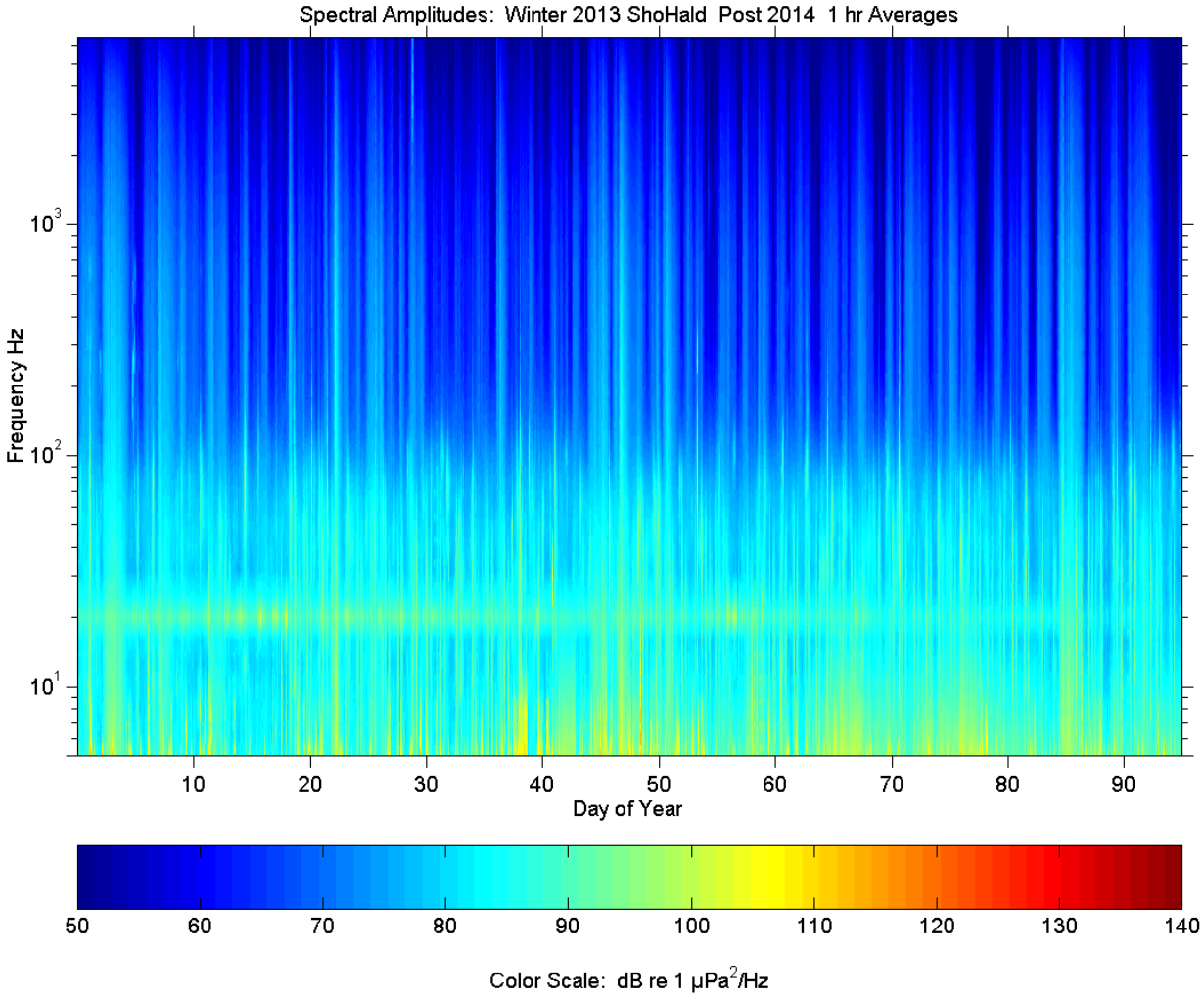


**Figure A4-3-ShoHald-W2013-2.** Power spectral density sections in time x frequency space for **post** New Year deployment period. Power spectral amplitudes averaged over 1/3 octave in frequency and 1 hour in time and plotted in colour-encoded format in accordance with the displayed scale.

### *A4.3.4. Summer 2014 Deployments*

**Figure (series) A4-3-Summer 2014 Deployments** - Power spectral density sections in time x frequency space.

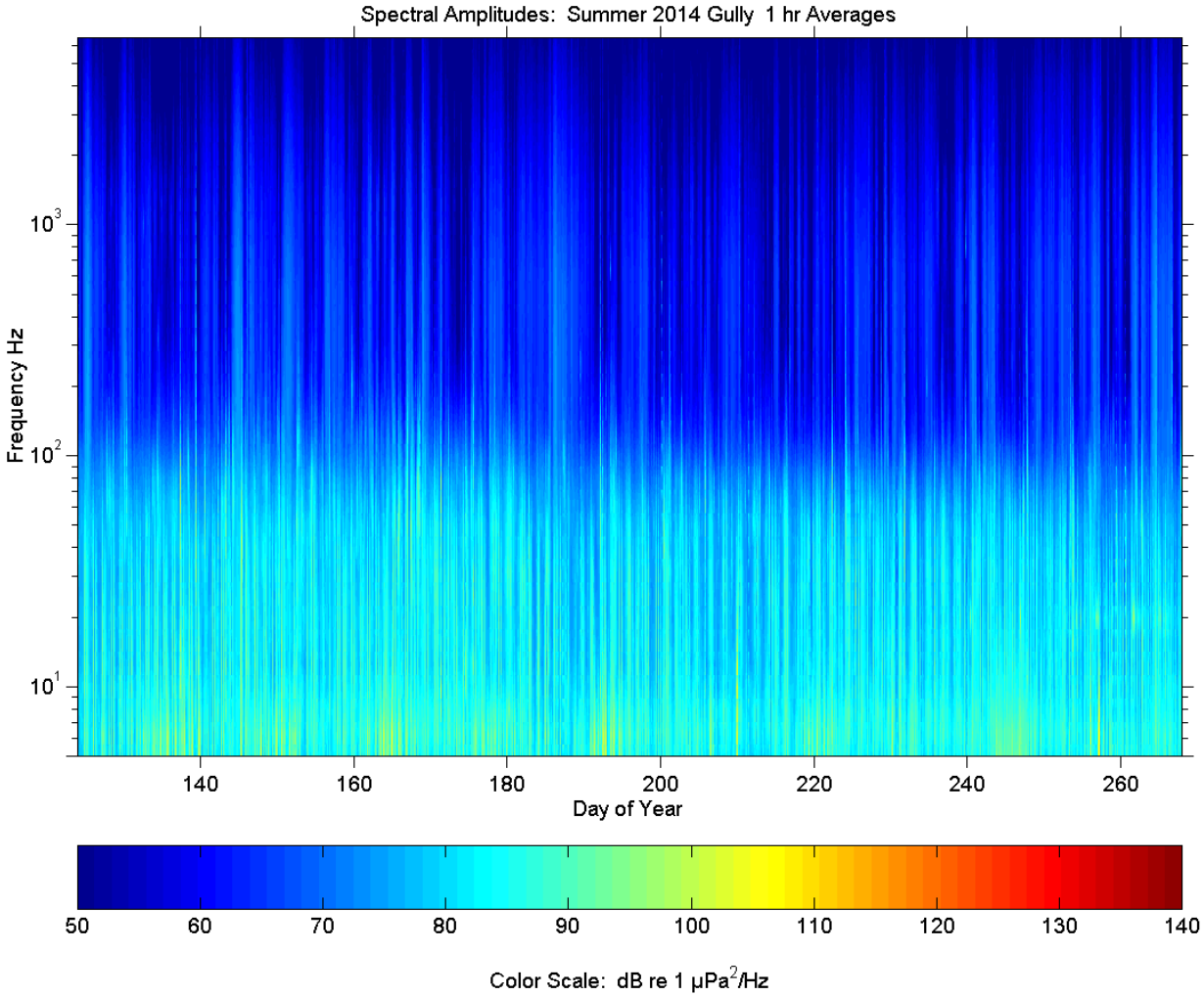


**Figure A4-3-MidGul-S2014.** Power spectral density section in time x frequency space. Power spectral amplitudes averaged over 1/3 octave in frequency and 1 hour in time and plotted in colour-encoded format in accordance with the displayed scale.

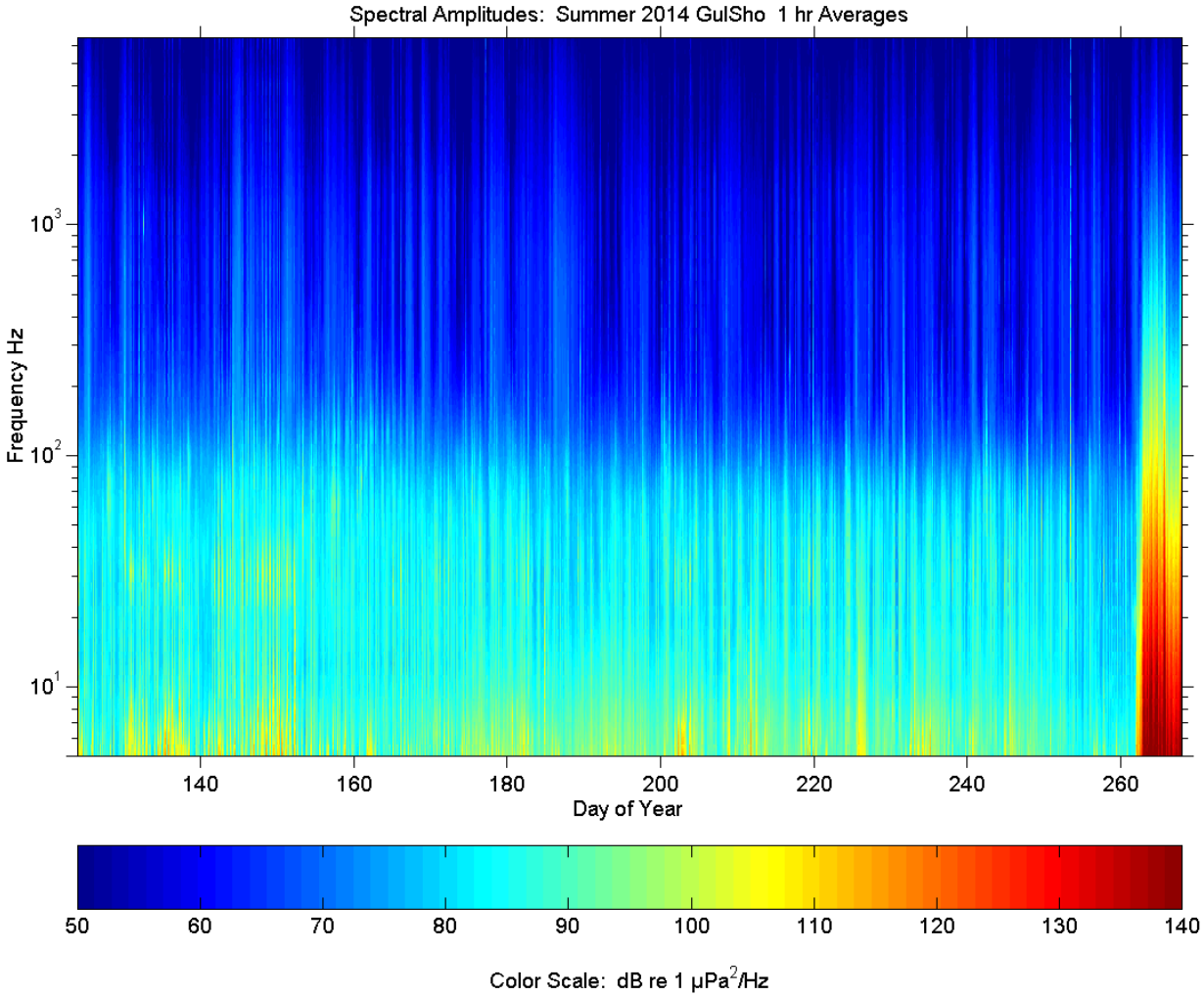


**Figure A4-3-GulSho-S2014.** Power spectral density section in time x frequency space. Power spectral amplitudes averaged over 1/3 octave in frequency and 1 hour in time and plotted in colour-encoded format in accordance with the displayed scale.

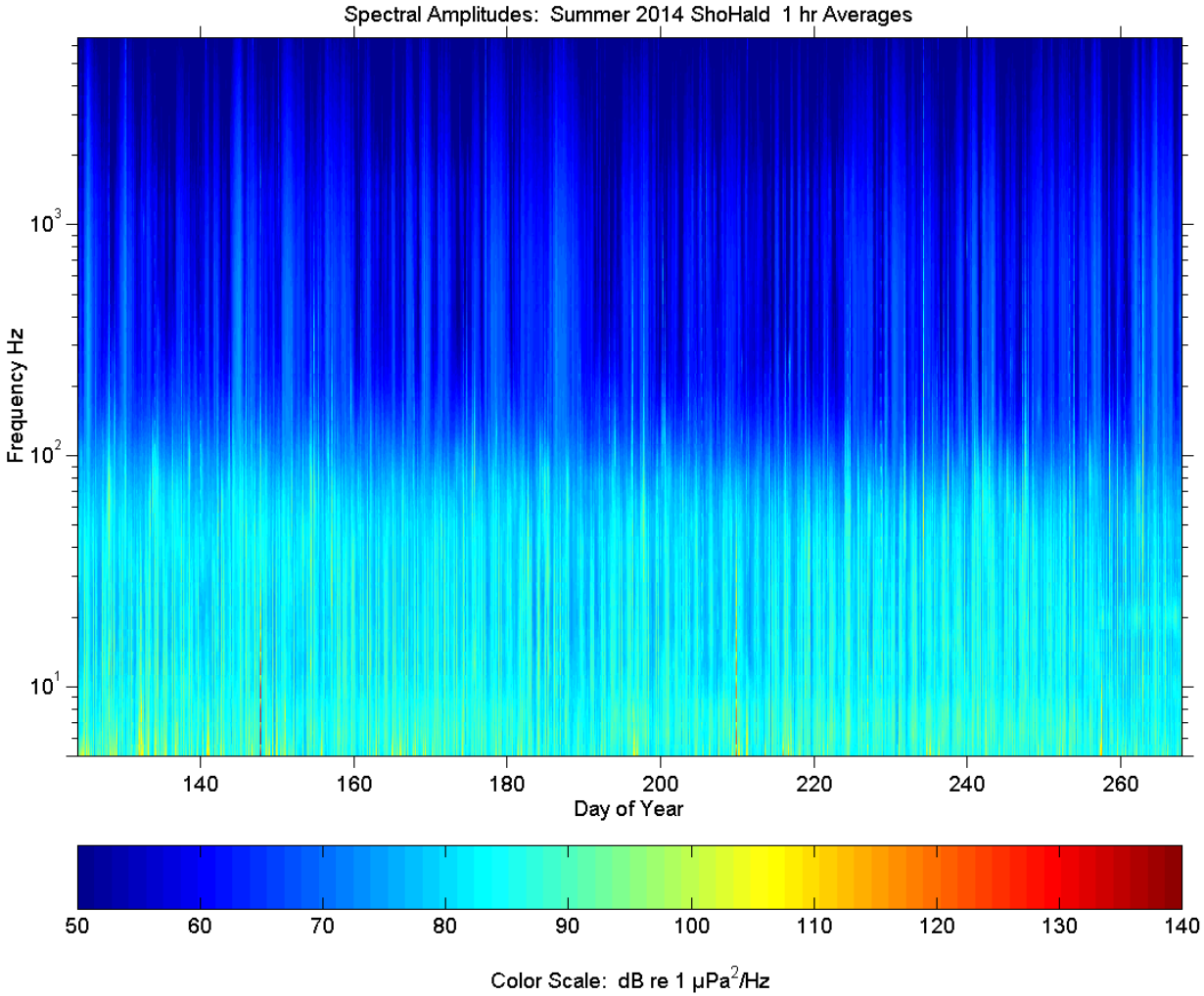


**Figure A4-3-ShoHald-S2014.** Power spectral density section in time x frequency space. Power spectral amplitudes averaged over 1/3 octave in frequency and 1 hour in time and plotted in colour-encoded format in accordance with the displayed scale.